



HAL
open science

Reduced-order models for blood flow in networks of large arteries

Arthur Ghigo

► **To cite this version:**

Arthur Ghigo. Reduced-order models for blood flow in networks of large arteries. Fluid mechanics [physics.class-ph]. Université Pierre et Marie Curie - Paris VI, 2017. English. NNT : 2017PA066422 . tel-01666313v2

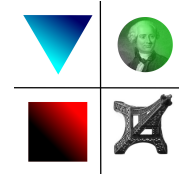
HAL Id: tel-01666313

<https://theses.hal.science/tel-01666313v2>

Submitted on 23 Apr 2018

HAL is a multi-disciplinary open access archive for the deposit and dissemination of scientific research documents, whether they are published or not. The documents may come from teaching and research institutions in France or abroad, or from public or private research centers.

L'archive ouverte pluridisciplinaire **HAL**, est destinée au dépôt et à la diffusion de documents scientifiques de niveau recherche, publiés ou non, émanant des établissements d'enseignement et de recherche français ou étrangers, des laboratoires publics ou privés.



THÈSE DE DOCTORAT

UNIVERSITÉ PIERRE ET MARIE CURIE

Spécialité : Mécanique des Fluides

École Doctorale de Sciences Mécaniques, Acoustique, Electronique et Robotique de Paris (ED 391)

Présentée par :

Arthur Ghigo

Pour obtenir le grade de

DOCTEUR DE L'UNIVERSITÉ PIERRE ET MARIE CURIE

**Modèles simplifiés d'écoulements sanguins
appliqués à des réseaux de grandes artères**

**Reduced-order models for blood flow
in networks of large arteries**

Dirigée par

D.R. CNRS Pierre-Yves Lagrée et Pr. UPMC Jose-Maria Fullana

à l'Institut Jean le Rond d'Alembert

Soutenue a l'UPMC le 29 Septembre 2017 devant le jury composé de

Jordi Alastruey	Examineur
Valérie Deplano	Examineur
Jose-Maria Fullana	Directeur de thèse
Pierre-Yves Lagrée	Directeur de thèse
Sylvie Lorthois	Rapporteur
Franck Nicoud	Rapporteur
Eleuterio Toro	Examineur
Irène Vignon-Clémentel	Examineur

Abstract

Every cardiac cycle, the heart contracts and ejects blood into the vascular network. This periodic inflow translates into the propagation of a pulse wave, which, through interactions with the elastic arterial wall, the blood and the complex arterial network, shapes itself into the pulsatile signal clinicians observe on a daily basis. Understanding these complex wave propagation dynamics is of great clinical relevance as large arteries are a breeding ground for many common cardiovascular pathologies which are often triggered by hemodynamical factors.

Unfortunately, hemodynamics in large arteries are too complex to be apprehended using only non-invasive measurements and medical imaging techniques. Patient-specific numerical simulations of blood flow have therefore been developed to provide clinicians with valuable insights on pathogenesis and the outcome of surgeries. As three-dimensional models are usually used only in small portions of the cardiovascular system due to their high modeling and computational costs, we have used reduced-order models to reproduce complex wave propagation behaviors in large networks of arteries.

We have first focused on one-dimensional models for blood flow and developed novel approaches that take into account the non-Newtonian behavior of blood and the viscoelastic response of the arterial wall. Next, we have proposed a fluid-structure interaction two-dimensional blood flow model to capture the complex flow patterns in stenoses and aneurysms unavailable to classical one-dimensional models. Finally, we have applied these models to compute the flow in large arterial networks and to predict the outcome of bypass surgeries.

Keywords: Blood flow – Network – 1D model – 2D model – Non-Newtonian – Viscoelasticity.

Résumé

La contraction périodique du cœur est à l'origine de l'onde de pouls qui, de part son interaction avec les artères élastiques, le sang et le réseau artériel lui-même, devient le signal observé quotidiennement par les médecins. Cette dynamique ondulatoire est d'une importance primordiale dans la compréhension de la genèse de nombreuses maladies cardiovasculaires. En effet, ce sont souvent des facteurs hémodynamiques qui sont à l'origine de la croissance de ces pathologies.

Malheureusement, les mesures non-invasives et l'imagerie médicale sont souvent insuffisantes pour appréhender la complexité des écoulements sanguins. La simulation numérique est donc en plein essor car celle-ci permet d'obtenir des données précises dans des régions vasculaires difficiles d'accès. Bien que les modèles sanguins tridimensionnels soient très précis et permettent de reproduire fidèlement la géométrie vasculaire, leur coût, à la fois numérique et paramétrique, est trop important pour que ceux-ci soient utilisés dans de grands réseaux vasculaires. Nous avons donc choisi d'utiliser des modèles simplifiés qui permettent d'accéder à cette dynamique de réseau si importante.

Premièrement, nous nous sommes intéressés aux modèles unidimensionnels et nous avons développé de nouvelles approches permettant de prendre en compte l'aspect non-Newtonien du sang et la viscoélasticité des parois artérielles. Secondement, nous avons proposé un modèle bidimensionnel, que nous avons utilisé pour simuler l'écoulement dans des sténoses et anévrismes. Finalement, nous avons utilisé ces modèles pour décrire l'écoulement du sang dans de grands réseaux artériels et pour optimiser un pontage extracorporel.

Mots Clés: Ecoulement sanguin – Réseau – Modèle 1D – Modèle 2D – Non-Newtonien – Viscoélasticité.

Acknowledgments-Remerciements

J'aimerais tout d'abord, et surtout, remercier très sincèrement mes deux directeurs de thèse, Pierre-Yves Lagrée et Jose-Maria Fullana. Durant ces trois années, j'ai eu le plaisir et le privilège de côtoyer ces deux scientifiques exceptionnels, qui m'ont transmis leur passion pour la recherche et dont l'amitié et le soutien m'ont été essentiels, tant sur le plan scientifique que moral. Toujours à l'écoute, toujours disponibles, toujours d'excellents conseils, ils ont su me guider à la perfection tout en me laissant jouir d'une liberté de recherche précieuse et formatrice. Ils ont également su me pardonner mes nombreux séjours au ski, ce dont je leur serai éternellement reconnaissant. Je n'aurais pu rêver meilleurs encadrants, et sans eux ce manuscrit n'aurait pu exister. Merci encore, Pierre-Yves et Jose-Maria, pour tout ce que vous avez fait. J'espère sincèrement que notre amitié perdurera bien au-delà de ces trois années de thèse.

Je remercie également Sylvie Lorthois et Franck Nicoud pour avoir accepté la charge de rapporteur pour cette thèse, ainsi que les autres membres du jury, Jordi Alastruey, Valérie Deplano, Euleuterio Toro et Irène Vignon-Clémentel. Leurs remarques et questions ont grandement amélioré la qualité de ce manuscrit et m'ont donné des pistes de réflexions très intéressantes. Je tiens tout particulièrement à témoigner ma reconnaissance à Irène Vignon-Clémentel pour son implication dans cette thèse dès la seconde année et pour son aide dans mes recherches de financements postdoctoraux. J'adresse de la même manière un grand merci à Jordi Alastruey pour nos nombreuses discussions via Skype et la confiance qu'il m'a accordée dans l'élaboration d'un sujet postdoctoral. Je souhaite également exprimer ma très grande gratitude envers Sylvie Lorthois, qui m'a accepté au sein de son équipe en tant que postdoctorant pour les deux prochaines années.

J'ai également une pensée toute particulière pour tous les professeurs que j'ai eu la chance d'avoir en cours à l'UPMC durant mes années de licence et de master. Parmi eux, je tiens surtout à remercier Hélène Dumontet, qui m'a accueilli à l'UPMC à bras ouverts et sans qui je ne serais pas là aujourd'hui.

Un thèse n'étant pas un travail individuel mais le fruit de nombreuses collaborations avec des scientifiques de divers horizons, je tiens à remercier chaleureusement tous ceux qui, de près ou de loin, ont contribué aux travaux réalisés pendant cette thèse. Merci à Olivier Delestre et Minh Le, qui m'ont fait découvrir l'univers passionnant des méthodes numériques et qui sont maintenant de véritables amis. C'est avec grand plaisir que j'envisage nos futures collaborations. Merci à Teresa Politi, pour son amitié, son énergie, son enthousiasme et sa bienveillance. Je n'aurais pu rêver meilleure collaboratrice de recherche. Merci pour tout. Merci également à Juan Fernández et Sandy Wray pour leur amitié, leur gentillesse et bien évidemment l'asado dominical. Merci à Julien Gaudric et Salam Abou Taam, sans qui les aspects cliniques de cette thèse n'auraient pu exister. Je ne peux que regretter de ne pas avoir plus interagi avec vous. Merci à Mami Matsukawa et Shimpei Ono, qui m'ont accueilli au Japon et qui m'ont permis d'utiliser leurs données expérimentales indispensables à la validation de nos résultats numériques. Merci à Ricardo Armentano et Manuel Alfonso pour nos nombreux échanges scientifiques et leur accueil en Argentine.

Je tiens à remercier toute l'équipe administrative de l'Institut ∂ Alembert pour avoir facilité toutes mes démarches au cours de cette thèse. Je pense notamment à Olivier Labbey, qui a été d'une aide précieuse.

Je remercie l'ensemble des doctorants et postdoctorants de l'Institut ∂ Alembert qui m'ont accompagné au cours de ces trois années. Je pense particulièrement à Antoine, Paul, Bruno, Jan, Raph, Vincent, Alessio ainsi que tous mes co-bureaux. Je remercie également les permanents du labo, Pierre-Yves et Jose-Maria évidemment, mais aussi Sophie, Thomas,

Stéphane, Jean-Camille et Arnaud, dont la gentillesse à éclairé ces trois années.

Je tiens à remercier l'ensemble de mes amis pour m'avoir soutenu tout au long de cette thèse. Merci à Bertrand, Joseph, Vincent, Serena, Arthur, Charles et tous mes autres amis de Ginette. Merci à Dahmun pour les séances de squash hebdomadaire et nos discussions passionnantes sur le fonctionnement du cœur. Merci à mes amis du volley, Lucas, Théo, Blog, Charline, Raph, Thomas, Romane, Manu, Steph, Mathilde et tous les autres pour avoir égayé mes soirées volleybalistiquement, coinchement et de bien d'autres manières, me permettant de me ressourcer.

En dernier lieu, je suis extrêmement reconnaissant envers mes parents, qui m'ont toujours soutenu, accompagné et encouragé pendant ces trois années et sans qui je ne serais jamais arrivé jusqu'ici. Merci également à ma sœur Zoé pour sa bonne humeur, ses encouragements et sa complicité, sans qui la vie serait bien triste et vide. Merci infiniment à tous les trois, du fond du cœur. Enfin, merci à Bérengère pour sa patience, sa compréhension et ses encouragements qui m'ont été indispensables au cours de ces trois années.

Merci à tous!

Contents

<i>Abstract</i>	i
<i>Résumé</i>	i
<i>Acknowledgments-Remerciements</i>	ii
Chapter 1 Introduction	1
1.1 Motivation	1
1.2 The cardiovascular system and wave dynamics	2
1.2.1 Cardiovascular physiology	2
1.2.2 Wave dynamics in a network of arteries	3
1.3 Existing blood flow models	4
1.3.1 In vitro models	5
1.3.2 Three-dimensional models	6
1.3.3 Zero-dimensional models	6
1.3.4 One-dimensional models	8
1.4 Specific aims and outline of the thesis	8
Chapter 2 One-dimensional equations for blood flow in an elastic artery	11
2.1 Introduction	11
2.2 Simplified solid equations	12
2.2.1 Simplifying hypotheses	12
2.2.2 Thin cylinder wall law	13
2.3 Simplified fluid equations	16
2.3.1 Simplifying hypotheses	16
2.3.2 The reduced Navier-Stokes-Prandtl equations	17
2.4 Validity of the combined fluid and solid models	19
2.4.1 The steady linear elastic Poiseuille solution	19
2.4.2 The Womersley solution	20
2.5 One-dimensional equations	21
2.5.1 One-dimensional fluid and solid equations	21
2.5.2 Velocity profile approximations	24
2.6 Dimensional and mathematical analysis	26
2.6.1 Dimensional analysis	26
2.6.2 Mathematical analysis	28
2.7 Conclusion	30
Chapter 3 One-dimensional equations for blood flow in a viscoelastic artery	31
3.1 Introduction	31
3.2 Material and methods	33

3.2.1	Data acquisition	33
3.2.2	Nonlinear wall model	34
3.2.3	Parameter estimation	34
3.3	Results and discussion	36
3.3.1	Comparison of the linear and nonlinear Kelvin-Voigt models	36
3.3.2	Validation of the parameter estimation strategy	36
3.3.3	Analysis of the nonlinear Kelvin-Voigt model	37
3.4	One-dimensional viscoelastic blood flow equations	40
3.5	Conclusion	42
Chapter 4 Numerical methods		43
4.1	Problem splitting	43
4.2	Hyperbolic subproblem	45
4.2.1	Kinetic numerical flux	46
4.2.2	Second-order extensions	47
4.2.3	Subcritical boundary condition	48
4.3	Parabolic and reaction subproblems	50
4.3.1	Parabolic subproblem	50
4.3.2	Reaction subproblem	51
4.3.3	Initial condition	51
4.4	Validation examples in one artery	51
4.4.1	Inviscid tourniquet	51
4.4.2	Inviscid wave propagation	52
4.4.3	Inviscid particular solution	54
4.4.4	Viscous and viscoelastic wave propagation	56
4.4.5	Asymptotic front propagation	58
4.5	Conclusion	62
Chapter 5 Hydrostatic reconstruction		63
5.1	Introduction	63
5.2	Mathematical model	65
5.2.1	One-dimensional equations with varying geometrical and mechanical properties	65
5.2.2	Additional mathematical properties	66
5.3	Hydrostatic reconstruction	67
5.3.1	The hydrostatic reconstruction: HR	67
5.3.2	The low-Shapiro hydrostatic reconstruction: HR-LS	68
5.3.3	The subsonic hydrostatic reconstruction: HR-S	71
5.4	First-order validation examples in one artery	74
5.4.1	Inviscid steady solutions	76
5.4.2	Inviscid wave propagation	79
5.5	Second-order extension	86
5.6	Second-order validation examples in one artery	87
5.6.1	Inviscid steady solutions	87
5.6.2	Wave propagation in a tapered tube	88
5.6.3	Inviscid Thacker solution	91
5.7	Conclusion	94
Chapter 6 Networks and boundary conditions		97
6.1	Introduction	97
6.2	Bifurcation boundary conditions	98
6.2.1	Point bifurcation model	98

6.2.2	Control-volume bifurcation model	99
6.2.3	Validation and comparison	102
6.3	Outflow boundary conditions	107
6.3.1	Zero-dimensional blood flow equations	109
6.3.2	Resistance outflow model	110
6.3.3	Windkessel outflow model	111
6.3.4	Numerical method	112
6.3.5	Validation and comparison	112
6.4	Structured-tree outflow boundary condition	114
6.4.1	Construction of a structured-tree	116
6.4.2	Terminal vessel impedance	116
6.4.3	Equivalent Windkessel outflow model	117
6.5	Conclusion	124
Chapter 7 Biomedical applications		127
7.1	The dicrotic notch analyzed by a one-dimensional numerical model	128
7.1.1	Introduction	128
7.1.2	Methods	129
7.1.3	Results	131
7.1.4	Discussion	142
7.2	A one-dimensional arterial network model for bypass graft assessment	144
7.2.1	Introduction	144
7.2.2	Numerical model	145
7.2.3	Numerical methods and results	145
7.2.4	Conclusion	155
7.3	Impact of arterial cross-clamping during vascular surgery on arterial stiffness measured by the augmentation index and fractal dimension of arterial pressure	156
7.3.1	Introduction	156
7.3.2	Methods	158
7.3.3	Results	160
7.3.4	Discussion	162
7.4	Conclusion	165
Chapter 8 Two-dimensional multiring model for blood flow		166
8.1	Introduction	167
8.2	A multiring discretization of the RNSP equations	169
8.2.1	Radial decomposition of the fluid domain	169
8.2.2	System of equations for one layer	170
8.2.3	System of equations for the artery	171
8.2.4	Radial boundary conditions	172
8.2.5	Multiring system of equations	172
8.2.6	Radial velocity	173
8.2.7	Link to the one-dimensional blood flow equations	173
8.3	Mathematical properties	174
8.3.1	Single layer system of equations	174
8.3.2	Two layers system of equations	175
8.3.3	Multiring system of equations	176
8.4	Numerical methods	176
8.4.1	Problem splitting	176
8.4.2	Explicit convective numerical scheme	177
8.4.3	Implicit viscous numerical scheme	180

8.5	Boundary conditions	182
8.5.1	Imposed flow rate	182
8.5.2	Imposed cross-sectional area	183
8.5.3	Imposed reflection coefficient	183
8.6	Linear examples in an elastic artery	183
8.6.1	The Womersley solution	183
8.6.2	The steady linear elastic Poiseuille solution	185
8.7	Nonlinear examples in a rigid artery	189
8.7.1	Nonlinear transition from a flat to a Poiseuille velocity profile	189
8.7.2	Rigid wall stenosis and aneurysm	191
8.8	Unsteady flow in an elastic stenosis	195
8.9	Conclusion	196
Chapter 9 One-dimensional non-Newtonian blood flow equations		200
9.1	Introduction	201
9.2	1D time-dependent non-Newtonian blood flow model	202
9.2.1	The 1D blood flow model	202
9.2.2	Stress model: Newtonian	203
9.2.3	Stress model: non-Newtonian	204
9.2.4	Time-dependent 1D non-Newtonian blood flow model	205
9.2.5	Numerical scheme	205
9.3	Analysis of the non-Newtonian stress model	206
9.3.1	Steady flow: Analogy with the simplified Cross model	206
9.3.2	Constant shear rate	207
9.3.3	Zero shear rate	208
9.4	Comparison with experimental data	208
9.4.1	Single shear-step	209
9.4.2	Multiple shear-steps	210
9.4.3	Triangle shear solicitation	211
9.5	Elementary bifurcation	211
9.6	Idealized asymmetric network	213
9.6.1	Healthy network	214
9.6.2	Pathological network	215
9.7	Conclusion	215
Chapter 10 Conclusion and perspectives		219
10.1	Conclusion	220
10.2	Perspectives	220
10.2.1	Short term perspectives	221
10.2.2	Long term perspectives	221

Introduction

Contents

1.1	Motivation	1
1.2	The cardiovascular system and wave dynamics	2
	1.2.1 Cardiovascular physiology	2
	1.2.2 Wave dynamics in a network of arteries	3
1.3	Existing blood flow models	4
	1.3.1 In vitro models	5
	1.3.2 Three-dimensional models	6
	1.3.3 Zero-dimensional models	6
	1.3.4 One-dimensional models	8
1.4	Specific aims and outline of the thesis	8

1.1 Motivation

Since the early work of Harvey in 1628 [Harvey 1957], clinicians have made tremendous steps forward in understanding the cardiovascular system. They are now able to propose efficient treatment strategies at low negative outcome. Yet cardiovascular pathologies remain the leading cause of death in developed countries, with rising risk factors such as high blood pressure, cholesterol, overweight, tobacco and alcohol consumption, lack of physical activity. In France, they represent more than 150.000 deaths every year and are the principal cause of death for women and people over 65 years old.

These cardiovascular pathologies include, among others, heart failure, atherosclerosis which leads to stenoses and embolisms, and aneurysms. They are usually slowly progressing diseases which remain asymptomatic until their very late stages, when the patient is already in a critical health condition. Clinicians have therefore developed a wide variety of treatment strategies to prevent their progression. However, despite progress in the comprehension of the cardiovascular system and advances made in medical imaging, their early and accurate diagnosis has been and still is a pressing issue of cardiovascular medicine, a fact that is elegantly summarized by Sir Thomas Lewis (1933): "*The very essence of cardiovascular practice is the early detection of heart failure*". Indeed, the development of cardiovascular pathologies is a complex multiscale process involving a combination of geometrical, mechanical, hemodynamical and biological factors which can not be apprehended using non-invasive pressure measurements and geometrical considerations alone.

Fortunately, there is now a widespread recognition that mathematical models and numerical simulations can help to better understand physiological and pathological processes

[Formaggia et al. 2010; Ambrosi et al. 2012]. More than complementing data obtained by noninvasive measurements and medical imaging, they provide means to analyze and predict the hemodynamics at a wide variety of vascular scales. They are now being progressively integrated into modern cardiovascular medicine to help clinicians perform early diagnosis and patient-specific surgical planning and companies such as *Heart flow* [Chinnaiyan et al. 2017] are now developing help-to-decision tools using these mathematical models.

However, the relevancy and accuracy of the numerical predictions of a mathematical blood flow model are inherently conditioned by its modeling limits. And unfortunately all cardiovascular blood flow models have their limits. The overall goal of this thesis is therefore to revisit classical reduced-order mathematical models for blood flow and try to improve their modeling capabilities. The emphasis is set on developing complementary models, appropriate numerical methods and realistic boundary conditions to solve hemodynamics in networks of large arteries. In the following, we briefly describe the cardiovascular system along with a short literature and historical review on blood flow models, before presenting the specific aims and the outline of the thesis.

1.2 The cardiovascular system and wave dynamics

We present here the physiology of the cardiovascular system and more specifically the wave dynamics in the arterial systemic circulation. The content of this section can be found in most textbooks on the cardiovascular system and we have made extensive use of the following references [Caro et al. 1974; Thiriet 2007; Formaggia et al. 2010; Nichols et al. 2011].

1.2.1 Cardiovascular physiology

The cardiovascular system is a closed-loop circuit composed of three principal blocks (see Figure 1.1): the heart, the pulmonary circulation and the systemic circulation.

The heart is a muscular organ made of two synchronized pumps working in parallel, each composed of two cavities. The right pump collects deoxygenated blood from the systemic veins in the right atrium and ejects blood into the pulmonary circulation from the right ventricle. The left pump collects oxygenated blood from the pulmonary veins in the left atrium and ejects blood into the systemic circulation from the left ventricle. The heart itself is perfused by the right and left coronary arteries, originating from two of the three sinuses of Valsalva just above the aortic valve (orifice of the left ventricle).

The pulmonary circulation is responsible for reoxygenating the blood leaving the right ventricle and returning oxygenated blood in the left atrium. On the contrary, the systemic circulation provides oxygenated blood from the left ventricle to the rest of the body and returns deoxygenated blood to the right atrium.

In both the pulmonary and the systemic circulations, a network of vessels is responsible for the transport of blood from the large vessels to the small capillaries and back. Indeed, the large arteries connected to the ventricles progressively branch out into smaller arteries and arterioles, who themselves divide into millions of smaller capillaries which constitute the capillary bed present in all organs, muscles and tissues and where exchanges of oxygen and nutrients occur. The smallest capillaries then connect to venules who progressively merge into veins until only the largest veins remain and deliver blood to the atria.

Despite their similar network topology, the pulmonary circulation differs from the systemic circulation. The most striking difference is that, contrary to the systemic circulation, the pulmonary circulation is a low pressure, low resistance system [Davidson and Fee 1990]. Even within the systemic circulation, strong differences exist between the arterial system

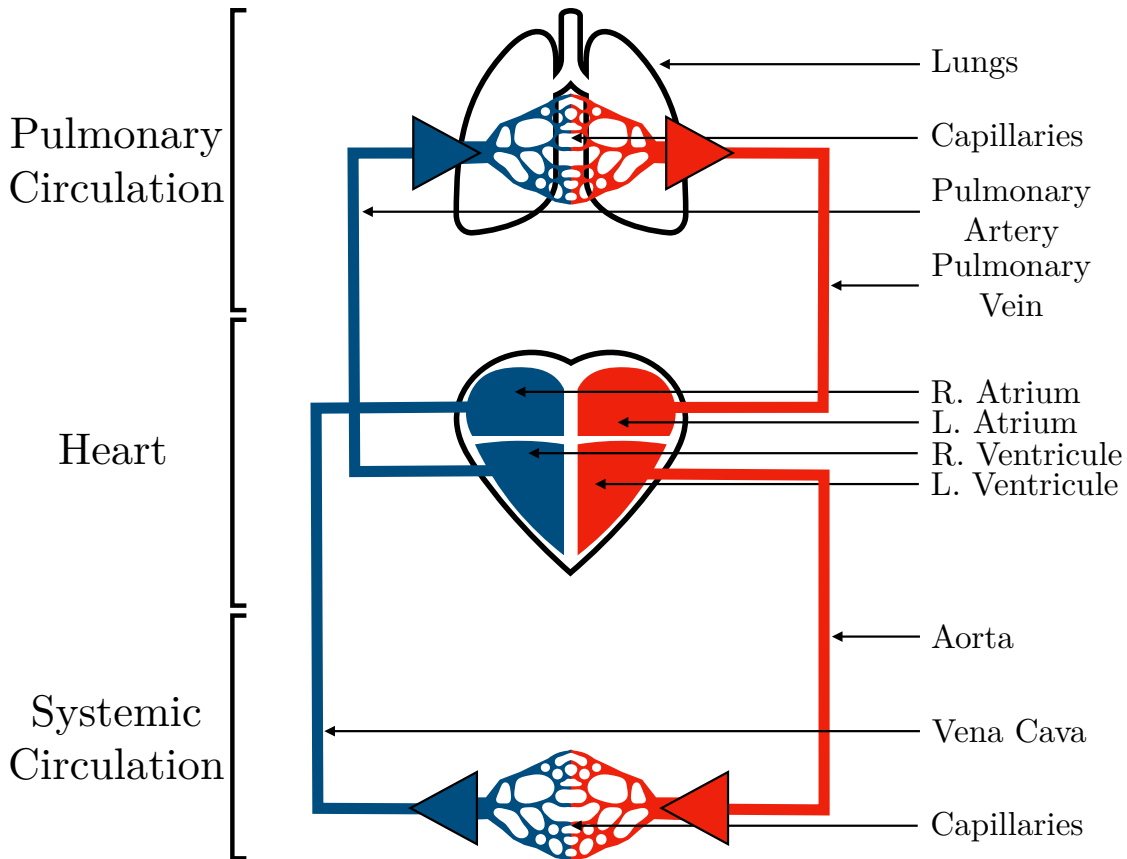


Figure 1.1 – Schematic of the cardiovascular system, including the heart, the pulmonary circulation and the systemic circulation.

and the venous system. Indeed, the venous pressure is much lower than the arterial pressure and the venous flow is essentially driven by arterio-venous pressure differences.

For these reasons, we intentionally restrict our analysis to the systemic circulation, and more particularly to the arterial systemic circulation. The arterial systemic circulation still represents a challenge from clinical, imaging and modeling standpoints as it involves multiple scales (large arteries to capillaries, one heart beat to years of vascular remodeling), multiple flow regimes (pulsatile near the heart, quasi-steady in the capillaries) and is a breeding ground for most cardiovascular pathologies. In the following, we detail the nature of blood flow in the arterial systemic circulation and the complex interactions between blood, the arterial wall and the arterial network.

1.2.2 Wave dynamics in a network of arteries

The flow in the arterial systemic circulation is driven by the heart. Every cardiac cycle is constituted of four successive stages: the inflow phase, the isovolumetric contraction, the outflow phase and the isovolumetric relaxation. The first and fourth stages constitute the diastole, or relaxation period, during which the ventricle fills up with blood coming from the atrium. The second and third stages correspond to the systole, or contraction period, during which blood exits the ventricle and enters the systemic circulation.

Blood first travels in the large and small arteries. These arteries are generally elastic as their walls are made of elastic tissue and smooth muscle cells. During systole, blood ejected from the left ventricle causes these arteries to elastically dilate. As the ventricular flow rate decreases during diastole, the vessel walls elastically relax towards their equilibrium state. This dilatation-relaxation process propagates at a finite speed along the arteries in the form

	Radius [cm]	Number of vessels
Large arteries	0.85 - 0.2	50
Small arteries	0.065 - 0.0075	10^5
Arterioles	0.0025	10^6
Capillaries	0.0004	10^9
Venules	0.005	10^7
Veins	0.014 - 0.7	10^5

Table 1.1 – Orders of magnitude of the systemic circulation, taken from Milnor 1989.

of a wave, which modifies blood pressure and flow rate and allows, in combination with fluid inertia, to maintain blood flow during diastole.

Following the waves, blood then reaches the arterioles, which are very small arteries lined with muscle cells. They are the primary site of both resistance and regulation of blood pressure, which they control by changing the contraction of their muscle fibers. As a consequence of high resistance, blood pressure drops sharply in the arterioles and blood pulsatility reduces to a minimum as most of the incoming pulse waves are reflected back into the large and small arteries. The passage of blood in the arterioles marks the final stage of the transformation of the very pulsatile flow generated by the left ventricle into the steady laminar flow suitable for the continuous exchange of oxygen and nutrients in the capillaries.

We further restrict our analysis to the study of the large and small arteries only, as the range of scales necessary to describe both the propagation of pulse waves in elastic arteries and the steady transfer of oxygen and nutrients through the capillary walls is too vast to be apprehended simultaneously (see Table 1.1). Removing the systemic microcirculation from the arterial systemic circulation, we are left with a network of large and small elastic arteries in which pulse waves propagate. These pulse waves are a combination of forward waves traveling from the heart and backward waves originating from the reflection of forward waves at arterial junctions and in the arterioles [Alastruey et al. 2012].

Understanding and predicting the wave dynamics in this network of elastic arteries using mathematical models is of great clinical relevance and is the main point of interest of this thesis. Next, we briefly review the different mathematical models that have been used up to now to describe blood flow in large arteries.

1.3 Existing blood flow models

Many clinicians have contributed to our understanding of the form and function of the cardiovascular system. However, faced with the complexity of the cardiovascular system, clinicians have progressively discarded modeling approaches to focus on *a posteriori* studies of large cohorts of patients to identify statistically meaningful trends concerning risk factors, treatments and surgical strategies. While these studies provide precious guidelines to clinicians, they usually lack a deep understanding of the geometrical, hemodynamical and biological factors influencing their results.

With the advent of medical imaging and computer sciences, clinicians are renewing with the idea of cardiovascular models to represent hemodynamics at different vascular scales. While mathematical blood flow models were initially developed to complement clinicians' understanding of the cardiovascular system, they have now outgrown this purpose and are being used as predictive tools for patient-specific clinical studies. In the following, we present a brief literature and historical review on the different blood flow models, inspired from the work presented in [Parker 2009].

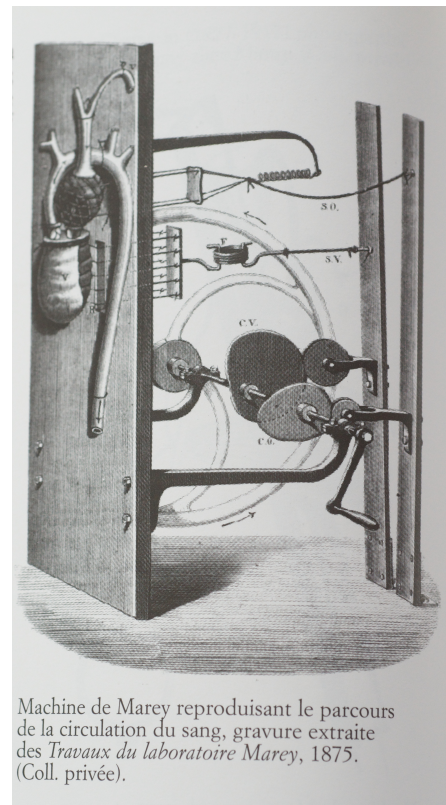
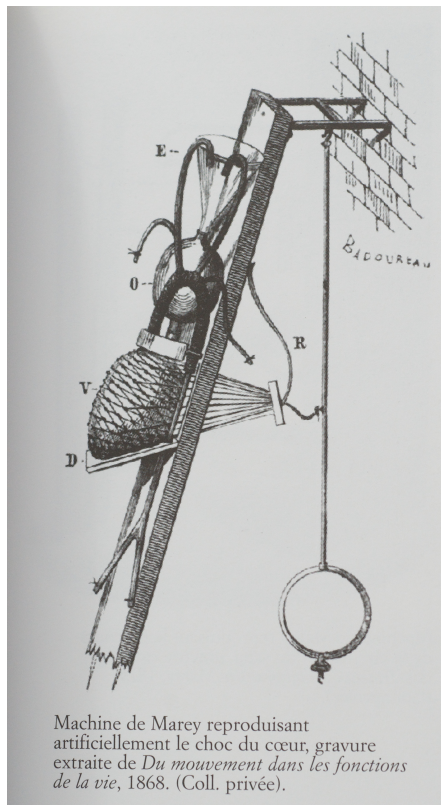


Figure 1.2 – Two examples a machines built by Marey, reproducing the contraction of the heart and the flow in the systemic circulation. The images are taken from [Mannoni and Marey 1999].

1.3.1 In vitro models

Étienne-Jules Marey, in collaboration with Jean-Baptiste Auguste Chauveau, are among the first to have developed *in vitro* models of the heart and the arterial circulation (see Figure 1.2) [Marey 1863]. Indeed, the initial work of Marey on the sphygmographe has allowed him to accurately measure and analyze the nature of pulse waves. However, he felt that the analysis of measured data is not sufficient to establish the reality of physiological mechanisms, and that a synthetic proof-of-concept was necessary to validate the results. These *in vitro* models gave him new insights on cardiovascular physiology and pathologies and laid the groundwork for modern blood flow models and numerical simulations. The essence of his approach is summarized by the following partial citation taken from p. 26-27 of [Marey 1863]:

... la plupart des phénomènes liés au mouvement du sang pouvaient être reproduits artificiellement dans une sorte de contre-épreuve synthétique. ... Chaque fois que nous avons supposé qu'une forme du pouls tenait à certaines conditions, nous avons essayé de la reproduire artificiellement en simulant, à l'aide de certains appareils, les conditions auxquelles nous l'avions attribuée. ... Nous espérons ainsi avoir suivi la voie la plus sûre dans ces études, s'il est vrai, comme on s'accorde à le dire, que le plus haut degré de certitude auquel on puisse arriver dans toute science, c'est de déduire de l'observation des faits une théorie que l'expérience sanctionne.

Since then, such *in vitro* circulation models have been used to replicated *in vivo* conditions in a controlled environment. In [Segers et al. 1998], the authors construct a 28-artery network and find striking correspondence between *in vivo* and *in vitro* results. In [Saito et al. 2011], an arterial bifurcation and a 9-artery network model are used to study the propagation and reflection of pulse waves and the effects of blood viscosity and wall viscoelasticity. In

[Matthys et al. 2007; Alastruey et al. 2011] a similar approach is considered but in a 37-artery network, and the *in vitro* results are used as validation for *in silico* blood flow models.

Much can still be learned from *in vitro* models and they remain an active field of research. Indeed, they accurately reproduce data unattainable in *in vivo* conditions, useful in particular to validate *in silico* blood flow models which are the subject of the following subsections.

1.3.2 Three-dimensional models

Blood flow in the large arteries is three-dimensional (3D), pulsatile and a transition to turbulence occurs in healthy conditions in the heart, at the root of the aorta and may occur in pathological vessels [Nerem et al. 1972; Chnafa et al. 2014]. It is therefore natural to describe the flow of blood using the incompressible Navier-Stokes equations. Additionally, the behavior of the arterial wall is assumed to obey an elastic law relating stress to strain in the arterial tissue, even though the behavior of the arterial wall is far more complex [Holzapfel et al. 2000; Holzapfel and Ogden 2010].

These 3D blood flow models are the numerical counterpart to the *in vitro* models presented above, in the sense that they enable a complete description of all relevant scales. As such, they have been solved using a variety of fluid structure interaction (FSI) numerical methods coupling the motion of blood and the deformation of the arterial wall [Hughes et al. 1981; Farhat et al. 2001; Tezduyar 2003; Figueroa et al. 2006; Tezduyar et al. 2007; Mayr et al. 2015].

They are usually used to compute blood flow in small regions of interest such as arterial bifurcations [Taylor et al. 1998], aneurysms [Cebal et al. 2005] and in small portions of the systemic network [Vignon-Clementel et al. 2010; Sankaran et al. 2012], even though 3D FSI blood flow simulations in large arterial network simulations are possible [Xiao et al. 2013]. In each of these applications, these 3D blood flow models provide relevant information on the flow patterns in patient-specific geometries [Steinman et al. 2002; Cebal et al. 2005].

Despite the work proposed in [Xiao et al. 2013], 3D blood flow models are difficult to apply to extended arterial networks due to their high computational and modeling costs. Multiscale approaches have therefore been developed, where 3D blood flow models are coupled to simpler reduced-order models that describe the global behavior of large portions of the vascular tree. Such zero-dimensional (0D) and one-dimensional (1D) blood flow models are presented in the following subsections.

1.3.3 Zero-dimensional models

Zero-dimensional (0D) blood flow models can be obtained by integrating the 3D equations governing blood flow over the cross-sectional area and the length of an artery, assuming that the characteristic axial lengthscale is much longer than the radial one and that the flow is axisymmetric. In this integration process, the axial and radial dependencies are lost. Hence 0D models only describe the relations linking the inlet and outlet variables of an artery, which provide valuable information on flow and pressure at low computational and modeling costs.

The first 0D blood flow model is the Windkessel and was proposed by Otto Frank in [Frank 1899] to describe the systemic circulation. In this work, Frank considered the systemic circulation as a single compliant compartment and used the conservation of mass to analyze changes of volume during diastole and systole. While the Windkessel theory is successful in describing pressure variations during diastole, it fails to capture the behavior of pressure during systole and was progressively abandoned by clinicians, as is summarized by William Milnor in [Milnor 1989]:

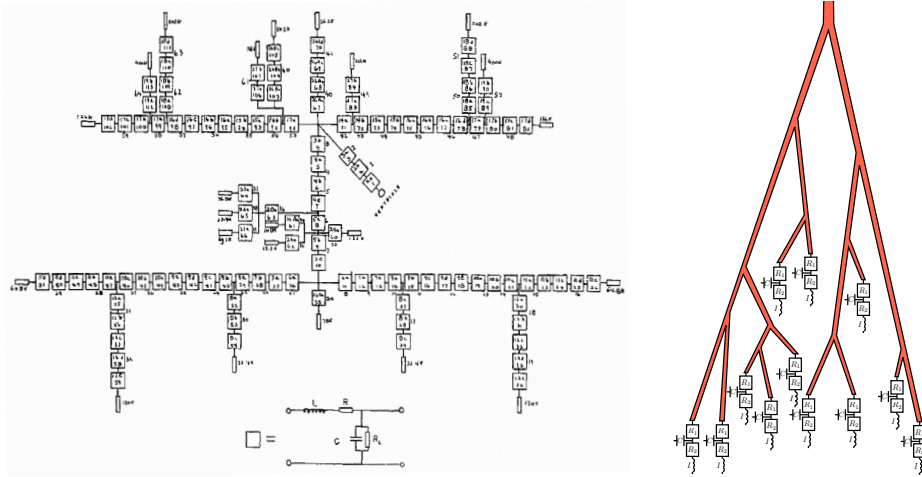


Figure 1.3 – Two representations of the systemic network:

Left: Representation of an electrical circuit analogue to the systemic arterial tree taken from [Noordergraaf et al. 1963]. Blood flow in each segment is described by the electrical equivalent of a 0D Windkessel model.

Right: Representation of a systemic arterial tree where the flow in each segment is described by a complex blood flow model (1D, 2D, 3D) and where 0D Windkessel models are used as physiological terminal boundary conditions.

The great virtue of the initial Windkessel model was its simplicity, and it still has an explanatory value as a rough approximation that is readily grasped. For almost all research purposes, however, a more detailed and realistic model that conforms to the distribution of properties in the vascular tree is to be preferred.

Indeed, to derive the Windkessel model, Frank assumed that pressure is uniform in all the systemic circulation and discarded wave propagation and reflection, which play an important role during systole. To overcome these limitations, 0D blood flow models similar to the Windkessel were introduced to describe the flow in a single artery. Using an analogy with the telegraph equations representing the transmission of an electrical pulse through a uniform cable [Noordergraaf et al. 1963], these 0D blood flow models were represented using electrical components (resistance, inductance, capacity) and connected together to form an electrical circuit representing the systemic arterial tree with distributed properties [Noordergraaf et al. 1963; Westerhof et al. 1969]. Such an analog systemic arterial tree is illustrated in Figure 1.3 Left, taken from [Noordergraaf et al. 1963]. By actually constructing these analog systemic arterial trees, the authors were able to reproduce electrical behaviors similar to those of an *in vivo* system.

These 0D circulation models were progressively replaced by more complex blood flow models that are now solved numerically. However, 0D models still play an important role in cardiovascular simulations as they are now used as physiological boundary conditions for more complex cardiovascular models (see Figure 1.3 Right) [Vignon and Taylor 2004; Vignon-Clementel et al. 2006; Alastruey et al. 2008, 2011; Cousins and Gremaud 2012; Xiao et al. 2013; Perdikaris and Karniadakis 2014; Guan et al. 2016] and to represent at a low computational cost large portions of the systemic circulation [Liang et al. 2009; Sankaran et al. 2012; Müller and Toro 2014; Audebert et al. 2017a].

Finally, the Windkessel model was recently revisited in [Tyberg et al. 2009; Westerhof and Westerhof 2017; Parker 2017] in the reservoir-wave approach, where the pressure waveform is no longer decomposed as a forward and backward component [Westerhof et al. 1972] but as a reservoir pressure (the Windkessel pressure, uniform in the system) and an excess pressure, containing the forward and backward waves.

1.3.4 One-dimensional models

In the same spirit as 0D models, one-dimensional (1D) blood flow models can be obtained by integrating the 3D equations governing blood flow over the cross-sectional area of an artery, assuming that the characteristic axial lengthscale is much longer than the radial one and that the flow is axisymmetric. In this integration process, only the radial dependency is lost, and 1D blood flow models still retain the ability to propagate elastic waves. Indeed, their hyperbolic nature is well adapted to reproduce the wave propagation phenomena in the systemic arterial tree. These 1D models give accurate predictions of pressure and flow waveforms in all the main arteries at a low computational cost, which offers a distinct advantage for clinical applications using patient-specific data.

In fact, Leonhard Euler was the first to write the 1D equations for the conservation of mass and the continuity of momentum describing blood flow [Euler 1844]. Unfortunately, he was unable to properly solve them. Since then, the progress of mathematics (solution of hyperbolic systems) and of computer sciences has enabled to solve the 1D equations for blood in single arteries as well as in large networks [Sherwin et al. 2003a,b; Formaggia et al. 2003] using a wide variety of numerical methods [Delestre and Lagrée 2013; Boileau et al. 2015; Wang et al. 2015; Puelz et al. 2017].

To obtain physiological waveforms in 1D systemic network models, much effort was put into obtaining realistic boundary conditions accurately modeling the behavior of the heart [Mynard and Nithiarasu 2008], the flow in junctions [Fullana and Zaleski 2009; Mynard and Valen-Sendstad 2015; Contarino et al. 2016; Müller et al. 2016b; Chnafa et al. 2017] and the vascular network distal to the terminal vessels [Olufsen et al. 2000; Alastruey et al. 2008; Cousins and Gremaud 2012; Perdikaris et al. 2015; Guan et al. 2016]. These 1D models have then been extensively used to study the flow in the main systemic arteries, from the ascending aorta to the upper and lower limbs [Matthys et al. 2007; Müller and Blanco 2015; Müller et al. 2016a]. Other studies have considered the cerebral circulation in detail [Zagzoule and Marc-Vergnes 1986; Alastruey et al. 2007]. More recently, simulation of the complete systemic circulation [Reymond et al. 2009; Liang et al. 2011; Reymond et al. 2011; Watanabe et al. 2013; Blanco et al. 2014, 2015] and the complete cardiovascular system [Müller and Toro 2014] have been performed.

Some studies have gone beyond reproducing healthy networks and have considered pathological networks with stenoses and aneurysms [Müller et al. 2013; Delestre and Lagrée 2013; Murillo and García-Navarro 2015; Ghigo et al. 2017b; Sazonov et al. 2017] and have modeled their treatment using endovascular or extracorporeal surgeries [Willemet et al. 2013; Drzisga et al. 2016; Ghigo et al. 2017a; Strocchi et al. 2017]. In time, these 1D models will be integrated in daily clinical practice to provide clinicians with rapid information on hemodynamics in patient-specific networks and on the possible outcome of surgical treatments.

1.4 Specific aims and outline of the thesis

Despite their obvious success, 1D blood flow models have several limitations. Interestingly, the limitations are not inherent to the long wave approximation which is valid in physiological conditions, but rather to the different closure hypotheses used to solve the 1D blood flow equations.

The first closure hypothesis concerns the Newtonian aspect of blood. Indeed, in almost all 1D simulations, blood is assumed to be Newtonian. However, in many regions of the systemic network, low shear regimes are reached as a consequence of the pulsatility of blood flow, of recirculation areas created by stenoses, aneurysms and bifurcations and of the decrease in shear with vessel ramification. In such low shear regions, blood behaves as a non-Newtonian

fluid and exhibits shear-thinning, viscoelastic and thixotropic behaviors. At low shear rates, molecular mechanisms trigger the aggregation of red blood cells (RBCs) into long column-like structures called "rouleaux", whereas at higher shear rates, these structures are deformed, disaggregated and the RBCs re-align in the direction of the flow. This reversible aggregation-disaggregation process is responsible for the shear-thinning behavior of blood. The different timescales of the aggregation and disaggregation processes are at the origin of the thixotropic response of blood. Finally, viscoelasticity stems from the elasticity of RBCs and the change of dissipation mechanisms at low and high shear rates [Cross 1965; Thurston 1972, 1975; Bureau et al. 1980; Quemada and Droz 1982]. As there exists strong evidence that this non-Newtonian behavior of blood influences the progression of many cardiovascular pathologies, such as atherosclerosis, through local modifications of the hemodynamics [Verdier 2003], it is crucial to take into account these non-Newtonian behaviors in 1D blood flow simulations.

The second closure hypothesis concerns the constitutive law used to describe the behavior of the arterial wall. Many 1D simulations assume that the arterial wall is a purely elastic material. However, the arterial wall displays both elastic and viscous behaviors [Taylor 1959; Westerhof and Noordergraaf 1970; Valdez-Jasso et al. 2009] and wall viscosity is a key element of the mechanical response of the arterial wall. Indeed, it acts as a protection mechanism by dissipating energy and filtering high-frequency components of the pressure signal, preventing structural injuries of the arterial wall [Armentano et al. 2007]. Different viscoelastic constitutive equations have been used in combination with 1D blood flow models [Alastruey et al. 2011; Reymond et al. 2009; Raghu et al. 2011; Reymond et al. 2011; Perdikaris and Karniadakis 2014; Montecinos et al. 2014; Müller et al. 2016b; Ghigo et al. 2017a], yet none of these have considered the nonlinear response of the arterial wall.

The third and most important closure hypothesis concerns the shape of the velocity profile, which is lost in the averaging process used to derive 1D blood flow equations. A carefully chosen *a priori* velocity profile is then selected [Ikenaga et al. 2013; Wang et al. 2016b; Puelz et al. 2017], thereby preventing any time or spatial variations of the velocity profile. Alternative dynamical approaches have been proposed based on the Womersley theory [Lagrée 2000; Reymond et al. 2009]. However, a more general approach is necessary for which no additional hypothesis is required, especially to compute the flow in pathological segments [Lagrée and Lorthois 2005].

The bulk of this thesis is designed to provide new insights on the three issues raised above. Each new model developed is extensively validated using analytic, linear and asymptotic solutions and then tested in large network simulations when possible. Other problematics are also addressed such as the treatment of boundary conditions, numerical methods to deal with arteries with varying geometrical and mechanical properties and possible applications of 1D blood flow models in large networks of arteries. That being said, this thesis is organized as follows:

Chapter 2 Chapter 2 deals with the derivation of the 1D blood flow equations, and we carefully explicit and justify the different hypotheses made.

Chapter 3 In Chapter 3, we present a nonlinear viscoelastic constitutive law designed to fit experimental pressure-radius hysteresis loops obtained in sheep. The experimental data were graciously provided by Pr. Armentano and his team in Favaloro University, Argentina. We then incorporate the viscoelastic wall model into the 1D system of equations derived in Chapter 2.

Chapter 4 In Chapter 4, we propose *finite volume* and *finite difference* methods to solve in one artery the 1D viscoelastic blood flow system presented in Chapter 2 and Chapter 3. We validate our numerical methods using exact and asymptotic solutions.

Chapter 5 In Chapter 5, we expose a numerical strategy called the hydrostatic reconstruction designed to deal with arteries that present variations of their geometrical and mechanical properties. This method allows to accurately preserve steady states and to capture wave reflections and transmissions. As in Chapter 4, we validate our numerical methods using exact and asymptotic solutions.

Chapter 6 In Chapter 6, we discuss the very important issue of junction and outflow boundary conditions used in large network simulations. Junction boundary conditions link one parent artery with two daughter arteries, while outflow boundary conditions represent the response of the vascular bed at the end of each terminal vessel of the network.

Chapter 7 In Chapter 7, we present three biomedical applications where we use the 1D blood flow equations to provide insights on medical issues. We first propose a didactic investigation of the origin of the aortic notch. We then study different extracorporeal bypass graft treatments of a severe stenosis of the right Iliac artery (in the leg). Finally, we analyze experimental data on aortic and iliac clamping.

Chapter 8 In Chapter 8, we derive what we refer to as the multiring blood flow model. It is a two-dimensional model designed to dynamically compute the velocity profile in elastic arteries without resorting to mesh adaptation strategies. We show that the multiring model can compute classical blood flow solutions such as the Poiseuille and Womersley solutions as well as recirculation areas in stenosed vessels.

Chapter 9 In Chapter 9, we propose a non-Newtonian extension of the 1D blood flow equations, taking into account time-dependent non-Newtonian behaviors using a structure function that describes the state of aggregation of red blood cells. We validate our model using experimental data and analytic solutions and then study its effects in structured arterial trees.

Chapter 10 In Chapter 10, we summarize the thesis, discuss the results and present some perspectives.

One-dimensional equations for blood flow in an elastic artery

We present here the derivation of the one-dimensional blood flow equations. Purposefully, the presentation is synthetic to clearly highlight the successive simplification steps.

Contents

2.1	Introduction	11
2.2	Simplified solid equations	12
2.2.1	Simplifying hypotheses	12
2.2.2	Thin cylinder wall law	13
2.3	Simplified fluid equations	16
2.3.1	Simplifying hypotheses	16
2.3.2	The reduced Navier-Stokes-Prandtl equations	17
2.4	Validity of the combined fluid and solid models	19
2.4.1	The steady linear elastic Poiseuille solution	19
2.4.2	The Womersley solution	20
2.5	One-dimensional equations	21
2.5.1	One-dimensional fluid and solid equations	21
2.5.2	Velocity profile approximations	24
2.6	Dimensional and mathematical analysis	26
2.6.1	Dimensional analysis	26
2.6.2	Mathematical analysis	28
2.7	Conclusion	30

2.1 Introduction

In Chapter 1, we have introduced the context of this study and the motivations for considering a simplified fluid structure interaction model of blood flow in large arteries. We now describe the hypotheses and the derivation of both solid and fluid reduced-order models that we then combine to obtain a monolithic one-dimensional blood flow model. Further details on the hypotheses and the derivation steps are found in [Fung 2013; van de Vosse and van Dongen 1998].

Coming from a fluid mechanics background, we use dimensional analysis to simplify the fluid and solid equations by keeping only the terms of highest orders of magnitude. We use the *centimeter-gram-second* or *cgs* unit system to express the value of all dimensional

variables. Indeed, the *cgs* unit system is the natural unit system for blood flow as the radius of a large artery is 1 cm, blood density is $1 \text{ g} \cdot \text{cm}^{-3}$ and a heart beat lasts 1 s. It is worth pointing out that the value of the fluid pressure is high in the *cgs* unit system (of the order of $10^5 \text{ dyn} \cdot \text{cm}^{-2}$). Yet this poses no problem as only the pressure gradient plays a role in blood flow dynamics.

In most of the work presented in this thesis, the equations are written in dimensional form, contrary to the fluid mechanics common practice to write all equations in non-dimensional form. However, as we use the *cgs* unit system, most quantities are equal to 1.

In Section 2.2 we present successive simplifications of the mechanical behavior of the arterial wall leading to the description of the arterial wall as an elastic spring (loi des chaudroniers). In Section 2.3 we use a similar approach to derive, starting from the Navier-Stokes equations governing the motion of blood, a simplified system of equations that we refer to as the reduced Navier-Stokes-Prandtl equations (RNSP). Finally, in Section 2.4 and Section 2.6 we test the validity of these hypotheses and derive the one-dimensional equations describing blood flow in an elastic artery.

2.2 Simplified solid equations

Following ideas exposed in [Jager 1965; Westerhof 1968], we derive a simplified model of the mechanical response of the arterial wall. We detail the hypotheses in Subsection 2.2.1 and the derivation in Subsection 2.2.2. We recall that all dimensional quantities are expressed in the *cgs* unit system.

2.2.1 Simplifying hypotheses

Axisymmetric thin cylinder

We represent the artery in its simplest form as a thin, long and straight axisymmetric cylinder of length L , width h , neutral radius R_0 and instantaneous radius R (see Figure 2.1).

Small perturbation assumption

In physiological conditions the wall displacement is small. We therefore assume that the small perturbation assumption is valid (small displacement \mathbf{u} and strain $\boldsymbol{\epsilon}$). The strain tensor $\boldsymbol{\epsilon}$ then writes:

$$\boldsymbol{\epsilon} = \frac{1}{2} [\nabla \mathbf{u} + \nabla \mathbf{u}^T]. \quad (2.1)$$

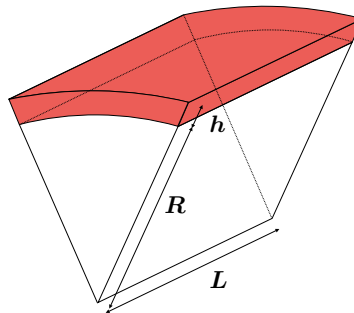


Figure 2.1 – Schematics of a portion of a thin straight axisymmetric cylinder of length L , width h and radius R .

Linear elasticity

We describe the arterial wall in the simplest possible way as an homogeneous, isotropic, isothermal, linear elastic material. Consequently, the relationship between the Cauchy stress tensor $\boldsymbol{\sigma}$ and the strain tensor $\boldsymbol{\epsilon}$ is given by Hooke's law:

$$\boldsymbol{\sigma} = \lambda_w \text{tr}(\boldsymbol{\epsilon}) \mathbb{I} + 2\mu_w \boldsymbol{\epsilon} \quad \text{or} \quad \boldsymbol{\epsilon} = -\frac{\nu_w}{E} \text{tr}(\boldsymbol{\sigma}) \mathbb{I} + \frac{1 + \nu_w}{E} \boldsymbol{\sigma}. \quad (2.2)$$

The tensor \mathbb{I} is the identity matrix, the coefficients λ_w and μ_w are the first and second Lamé parameters and E and ν_w are respectively the Young's modulus and the Poisson coefficient.

We do not assume that the material is incompressible. The justification for this assumption is provided in the following.

Quasi-static equilibrium

The general momentum balance equation for an incompressible material writes:

$$\rho_w \frac{D\mathbf{v}}{Dt} = \rho_w \mathbf{f}_v + \text{div}(\boldsymbol{\sigma}), \quad (2.3)$$

where ρ_w is the density of the material, \mathbf{v} the velocity vector and \mathbf{f}_v the vector of volume forces. To assess the importance of each term in Equation (2.3), we introduce in Table 2.1 non-dimensional variables and their respective orders of magnitude.

$t = T\bar{t}$	$\mathbf{x} = R_0\bar{\mathbf{x}}$	$\mathbf{v} = \frac{R_0}{T}\bar{\mathbf{v}}$	$\boldsymbol{\sigma} = \mu_w\bar{\boldsymbol{\sigma}}$	$\mathbf{f}_v = g\bar{\mathbf{f}}_v$
$\rho_w = 1$	$T = 1$	$R_0 = 1$	$\frac{R_0}{T} = 1$	$\mu_w = 10^5 \quad g = 10^3$

Table 2.1 – Non-dimensional solid variables and their orders of magnitude.

Injecting these non-dimensional variables into Equation (2.3), we obtain:

$$\frac{D\bar{\mathbf{v}}}{D\bar{t}} = \left[\frac{gT^2}{R_0} \right] \bar{\mathbf{f}}_v + \left[\frac{\mu_w}{\rho_w \frac{R_0^2}{T^2}} \right] \bar{\text{div}}(\bar{\boldsymbol{\sigma}}), \quad (2.4)$$

where the values of the non-dimensional numbers are:

$$\frac{gT^2}{R_0} = 10^3, \quad \frac{\mu_w}{\rho_w \frac{R_0^2}{T^2}} = 10^5. \quad (2.5)$$

These values indicate that the acceleration and volume forces are negligible compared to the surface forces. Equation (2.3) then simplifies to the quasi-static equilibrium equation:

$$\text{div}(\boldsymbol{\sigma}) = 0. \quad (2.6)$$

2.2.2 Thin cylinder wall law

Combining these hypotheses, we obtain simplified equations for the displacement of the arterial wall, usually referred to as the Navier-Lamé equations:

$$[\lambda_w + 2\mu_w] \nabla(\text{div}(\mathbf{u})) - \mu_w \text{rot}(\text{rot}(\mathbf{u})) = 0. \quad (2.7)$$

The final and very important step is to provide boundary conditions for Equation (2.7). We assume that the idealized artery does not deform in the axial direction, or more accurately that the axial displacement is small compared to the length of the artery ($u_x \ll L$), and that pressure is the only significant stress applied on the internal and external sides of the artery:

$$\begin{cases} \epsilon_{xx} = 0 & (2.8a) \\ \boldsymbol{\sigma} \cdot \mathbf{n} = -p\mathbf{n} & \text{in } r = R & (2.8b) \\ \boldsymbol{\sigma} \cdot \mathbf{n} = -p_{ext}\mathbf{n} & \text{in } r = R + h, & (2.8c) \end{cases}$$

where p and p_{ext} are respectively the internal and external fluid pressures. In the following, we assume that p_{ext} is constant.

Thick wall

We solve System (2.7) by choosing a kinetically admissible form for the displacement \mathbf{u} :

$$\mathbf{u} = rf(r) \mathbf{e}_r + g(x) \mathbf{e}_x. \quad (2.9)$$

Injecting this expression in System (2.7) and using the boundary condition (2.8a) we obtain the expressions for f and g :

$$\begin{cases} f(r) = a + \frac{b}{r^2} \\ g(x) = c, \end{cases} \quad (2.10a)$$

and for the strain tensor ϵ :

$$\epsilon = \begin{bmatrix} a - \frac{b}{r^2} & 0 & 0 \\ 0 & a + \frac{b}{r^2} & 0 \\ 0 & 0 & c \end{bmatrix}. \quad (2.11)$$

We then find the expression for the Cauchy stress tensor σ using Equation (2.2) and the boundary conditions (2.8b) and (2.8c):

$$\sigma = \begin{bmatrix} \sigma_{rr} & 0 & 0 \\ 0 & \sigma_{\theta\theta} & 0 \\ 0 & 0 & \sigma_{xx} \end{bmatrix}, \quad (2.12)$$

with:

$$\begin{cases} \sigma_{rr} = A - \frac{B}{r^2} \\ \sigma_{\theta\theta} = A + \frac{B}{r^2} \\ \sigma_{xx} = C, \end{cases} \quad (2.13a)$$

$$\sigma_{\theta\theta} = A + \frac{B}{r^2} \quad (2.13b)$$

$$\sigma_{xx} = C, \quad (2.13c)$$

and

$$\begin{cases} A = p \left[\frac{1}{\left[1 + \frac{h}{R}\right]^2} - \frac{p_{ext}}{p} \right] \frac{\left[1 + \frac{h}{R}\right]^2}{\left[1 + \frac{h}{R}\right]^2 - 1} \\ B = p \left[1 - \frac{p_{ext}}{p} \right] R^2 \frac{\left[1 + \frac{h}{R}\right]^2}{\left[1 + \frac{h}{R}\right]^2 - 1} \\ C = 2\lambda_w a. \end{cases} \quad (2.14a)$$

$$B = p \left[1 - \frac{p_{ext}}{p} \right] R^2 \frac{\left[1 + \frac{h}{R}\right]^2}{\left[1 + \frac{h}{R}\right]^2 - 1} \quad (2.14b)$$

$$C = 2\lambda_w a. \quad (2.14c)$$

Under the assumption that the displacement is given by Equation (2.9), the boundary conditions (2.8) are sufficient to completely solve System (2.7). If we additionally assume that the material is incompressible, the system becomes hyperstatic. Indeed, we have in this case $\text{tr}(\epsilon) = 0$ and therefore $2a - c = 0$. The boundary condition (2.8a) gives $c = 0$ and therefore $a = 0$. The Cauchy stress writes as $\sigma = 2\mu_w \epsilon$ and the boundary conditions (2.8b) and (2.8c) are no longer verified simultaneously.

Thin wall

In the previous paragraph, we have considered an arbitrary width of the arterial wall. In reality, the width of the arterial wall is small compared to the radius of the artery. We therefore introduce the small parameter ϵ_w :

$$\epsilon_w = \frac{h}{R_0}, \quad (2.15)$$

and write r and R as:

$$\begin{cases} r = R_0 [1 + \epsilon_w \bar{r}] & \text{with } \bar{r} = O(1) \\ R = R_0 [1 + \epsilon_w \bar{R}] & \text{with } \bar{R} = O(1). \end{cases} \quad (2.16a)$$

We then have:

$$\begin{cases} \sigma_{rr} = p \left[\frac{1}{[1 + \epsilon_w]^2} - \frac{[1 + \epsilon_w \bar{R}]^2}{[1 + \epsilon_w \bar{r}]^2} - \frac{p_{ext}}{p} \left[1 - \frac{[1 + \epsilon_w \bar{R}]^2}{[1 + \epsilon_w \bar{r}]^2} \right] \right] \frac{[1 + \epsilon_w]^2}{[1 + \epsilon_w]^2 - 1} \\ \sigma_{\theta\theta} = p \left[\frac{1}{[1 + \epsilon_w]^2} + \frac{[1 + \epsilon_w \bar{R}]^2}{[1 + \epsilon_w \bar{r}]^2} - \frac{p_{ext}}{p} \left[1 + \frac{[1 + \epsilon_w \bar{R}]^2}{[1 + \epsilon_w \bar{r}]^2} \right] \right] \frac{[1 + \epsilon_w]^2}{[1 + \epsilon_w]^2 - 1}. \end{cases} \quad (2.17a)$$

$$\begin{cases} \sigma_{\theta\theta} = p \left[\frac{1}{[1 + \epsilon_w]^2} + \frac{[1 + \epsilon_w \bar{R}]^2}{[1 + \epsilon_w \bar{r}]^2} - \frac{p_{ext}}{p} \left[1 + \frac{[1 + \epsilon_w \bar{R}]^2}{[1 + \epsilon_w \bar{r}]^2} \right] \right] \frac{[1 + \epsilon_w]^2}{[1 + \epsilon_w]^2 - 1}. \end{cases} \quad (2.17b)$$

Keeping only terms up to order $O(\epsilon_w)$ we obtain:

$$\begin{cases} \sigma_{rr} \approx p \left[[\bar{r} - \bar{R} - 1] - \frac{p_{ext}}{p} [\bar{r} - \bar{R}] \right] \\ \sigma_{\theta\theta} \approx \frac{p}{\epsilon_w} \left[1 - \frac{p_{ext}}{p} \right]. \end{cases} \quad (2.18a)$$

$$\begin{cases} \sigma_{\theta\theta} \approx \frac{p}{\epsilon_w} \left[1 - \frac{p_{ext}}{p} \right]. \end{cases} \quad (2.18b)$$

Equation (2.18a) and Equation (2.18b) indicate that $\sigma_{rr} \ll \sigma_{\theta\theta}$ and that the transmural pressure applied on the arterial wall is balanced only by the tangential stress $\sigma_{\theta\theta}$.

To link $\sigma_{\theta\theta}$ to $\epsilon_{\theta\theta}$, we use the constitutive Equation (2.2), System (2.18) and the boundary condition (2.8a):

$$\begin{cases} \epsilon_{\theta\theta} = \frac{1}{E} [\sigma_{\theta\theta} - \nu_w \sigma_{xx}] \\ \epsilon_{xx} = 0 = \frac{1}{E} [\sigma_{xx} - \nu_w \sigma_{\theta\theta}]. \end{cases} \quad (2.19a)$$

$$\begin{cases} \epsilon_{xx} = 0 = \frac{1}{E} [\sigma_{xx} - \nu_w \sigma_{\theta\theta}]. \end{cases} \quad (2.19b)$$

We then obtain:

$$\sigma_{\theta\theta} = \frac{E}{1 - \nu_w^2} \epsilon_{\theta\theta}. \quad (2.20)$$

Noticing that $\epsilon_{\theta\theta} = \frac{u_r}{r}$, this relation writes in $r = R$:

$$\sigma_{\theta\theta} = \frac{E}{1 - \nu_w^2} \frac{R - R_0}{R}. \quad (2.21)$$

Combining Equation (2.18b) and Equation (2.21), we finally obtain the linearized thin cylinder wall law, or Hoop law (loi des chaudronniers), relating variations of the transmural pressure with the deformation of the arterial wall:

$$p - p_{ext} = \frac{E}{1 - \nu_w^2} \frac{h}{R_0^2} [R - R_0]. \quad (2.22)$$

Equation (2.22) is usually written under the more general form:

$$p - p_{ext} = K \left[\sqrt{A} - \sqrt{A_0} \right], \quad (2.23)$$

where K is the rigidity of the arterial wall:

$$K = \frac{E}{1 - \nu_w^2} \frac{\sqrt{\pi} h}{A_0}. \quad (2.24)$$

Equation (2.23) describes the arterial wall as a spring of rigidity K .

We have derived a very simple relation able to describe the elastic deformation of the arterial with variations of the transmural pressure. A more realistic arterial wall model is presented in Chapter 3, where viscoelastic effects are taken into account.

2.3 Simplified fluid equations

Following [Prandtl 1928], we derive simplified equations for blood flow in large arteries. We detail the hypotheses in Subsection 2.3.1 and the derivation in Subsection 2.3.2. We recall that all dimensional quantities are expressed in the *cgs* unit system.

2.3.1 Simplifying hypotheses

Homogeneous Newtonian fluid

In large arteries, the average size of red blood cells (RBCs) (6×10^{-4} in diameter) is four orders of magnitude smaller than the average vessel size (1 in diameter). Moreover, the average shear rate is high ($\dot{\gamma} \geq 100$), preventing the aggregation of RBCs. As a first approximation, we consider that blood is a homogeneous Newtonian fluid. The validity of this hypothesis is discussed in Chapter 9.

Incompressible flow

The compressibility of the flow can play an important role in the propagation of waves in elastic cylinders. Indeed, in pipe flows, which are the industrial analogue of arterial flows, the water hammer phenomenon has been studied for many years. A water hammer describes the wave generated when a fluid in motion is forced to stop and change direction, which commonly occurs when a valve closes. According to water hammer theory [Allievi 1913; Ghidaoui et al. 2005], both the compressibility of the flow and the elasticity of the arterial wall are responsible for the propagation of the water hammer wave, even though the Mach number $M_a \ll 1$. Indeed, the conservation of mass on a control-volume of compressible fluid in an elastic pipe writes:

$$\frac{\partial}{\partial t} [\rho A] + \frac{\partial}{\partial x} [\rho A U_x] = 0, \quad (2.25)$$

which can be rewritten as:

$$\frac{1}{\rho} \frac{D\rho}{Dt} + \frac{1}{A} \frac{DA}{Dt} + \frac{\partial U_x}{\partial x} = 0. \quad (2.26)$$

A rigorous derivation of Equation (2.25) for an incompressible flow is presented in Subsection 2.5.1.

As the fluid is compressible and the wall elastic, both the fluid density ρ and the cross-sectional area A of the tube vary with the fluid pressure p ($\rho(p)$ and $A(p)$). This pressure dependence allows us to write the mass conservation equation as:

$$\frac{1}{\rho c_{wh}^2} \frac{Dp}{Dt} + \frac{\partial U_x}{\partial x} = 0, \quad (2.27)$$

where c_{wh} is the water hammer wave speed:

$$\frac{1}{c_{wh}^2} = \frac{1}{\frac{dp}{d\rho}} + \frac{1}{\frac{A}{\rho} \frac{dA}{dA}}. \quad (2.28)$$

This formula is also obtained in [Korteweg 1878]. As the flow is slightly compressible ($dp/d\rho \gg 1$) and the pipe wall very rigid ($A/\rho (dA/dA) \gg 1$), both terms in Equation (2.28) have the same order of magnitude.

By analogy, we assume that the pulse wave speed in an artery is given by Equation (2.28). We therefore introduce the acoustic wave speed of blood [Szabo 2004]:

$$c_\rho = \sqrt{\frac{dp}{d\rho}} = 1.584 \times 10^5, \quad (2.29)$$

and the elastic wave speed in the large arteries [Moens 1878; Korteweg 1878]:

$$c = \frac{A}{\rho} \frac{dp}{dA} \approx 1 \times 10^2. \quad (2.30)$$

Applying Equation (2.28), we conclude that the acoustic wave speed c_p can be neglected with respect to the elastic wave speed c and that blood flow is incompressible in the large arteries.

Axisymmetric flow

In accordance with the geometrical assumptions made in Section 2.2, we assume that blood flow is axisymmetric ($\partial_\theta = 0$) and that:

$$\left\{ \begin{array}{l} \frac{\partial u_x}{\partial r} \Big|_{r=0} = 0 \end{array} \right. \quad (2.31a)$$

$$\left\{ \begin{array}{l} u_r|_{r=0} = 0 \end{array} \right. \quad (2.31b)$$

$$\left\{ \begin{array}{l} u_\theta = 0. \end{array} \right. \quad (2.31c)$$

Long wavelength

The average radius in large arteries is $R_0 \approx 1$, the pulse wave speed $c \approx 10^2$ and the heart ejection period $T \approx 1$. The wavelength of the pulse wave is then $\lambda = cT \approx 10^2$. We can therefore introduce a small parameter ϵ_λ , called the long wave parameter:

$$\epsilon_\lambda = \frac{R_0}{\lambda} \ll 1. \quad (2.32)$$

This small parameter is used in Subsection 2.3.2 to simplify the governing equations for the motion of blood.

2.3.2 The reduced Navier-Stokes-Prandtl equations

These hypotheses, that we have briefly discussed, lead us to describe blood flow in the idealized artery presented in Section 2.2 with the incompressible axisymmetric Navier-Stokes equations for a homogeneous Newtonian fluid:

$$\left\{ \begin{array}{l} \frac{1}{r} \frac{\partial}{\partial r} [r u_r] + \frac{\partial u_x}{\partial x} = 0 \end{array} \right. \quad (2.33a)$$

$$\left\{ \begin{array}{l} \frac{\partial u_r}{\partial t} + u_r \frac{\partial u_r}{\partial r} + u_x \frac{\partial u_r}{\partial x} = -\frac{1}{\rho} \frac{\partial p}{\partial r} + \nu \left[\frac{1}{r} \frac{\partial}{\partial r} \left[r \frac{\partial u_r}{\partial r} \right] - \frac{u_r}{r^2} + \frac{\partial^2 u_r}{\partial x^2} \right] \end{array} \right. \quad (2.33b)$$

$$\left\{ \begin{array}{l} \frac{\partial u_x}{\partial t} + u_r \frac{\partial u_x}{\partial r} + u_x \frac{\partial u_x}{\partial x} = -\frac{1}{\rho} \frac{\partial p}{\partial x} + \nu \left[\frac{1}{r} \frac{\partial}{\partial r} \left[r \frac{\partial u_x}{\partial r} \right] + \frac{\partial^2 u_x}{\partial x^2} \right], \end{array} \right. \quad (2.33c)$$

where ρ is the density of blood, ν the kinematic viscosity of blood, p the fluid pressure and $\mathbf{u} = [u_r, u_\theta, u_x]^{-1}$ the fluid velocity vector. Equation (2.33) is completed by the following material interface and axisymmetric conditions for a viscous fluid:

$$\left\{ \begin{array}{l} u_r = \frac{\partial R}{\partial t} + u_x \frac{\partial R}{\partial x} \end{array} \right. \quad \text{in } r = R \quad (2.34a)$$

$$\left\{ \begin{array}{l} u_x = 0 \end{array} \right. \quad \text{in } r = R \quad (2.34b)$$

$$\left\{ \begin{array}{l} \frac{\partial u_x}{\partial r} \Big|_{r=0} = 0 \end{array} \right. \quad (2.34c)$$

$$\left\{ \begin{array}{l} u_r|_{r=0} = 0 \end{array} \right. \quad (2.34d)$$

$$\left\{ \begin{array}{l} u_\theta = 0. \end{array} \right. \quad (2.34e)$$

Indeed, the equation for the interface between the fluid and the arterial wall can be written as $F = r - R(x, t) = 0$. As $F = 0$ on the interface at all times, the derivative with respect

effects:

$$\alpha = R_0 \sqrt{\frac{\omega}{\nu}}, \quad (2.41)$$

with $\omega = 2\pi/T$. The physiological orders of magnitude presented in Table 2.2 give us:

$$0 \leq S_h \leq 1 \quad (2.42a)$$

$$0 \leq \alpha \leq 25, \quad (2.42b)$$

which confirms the fact that the viscous and nonlinear effects are small compared to the pressure gradient and the unsteady inertial term. Using the long wave hypothesis (2.32) and keeping only terms of order $O(1)$, System (2.39) simplifies to what we refer to as the reduced Navier-Stokes-Prandtl equations (RNSP) [Lagrée and Lorthois 2005]:

$$\begin{cases} \frac{1}{\bar{r}} \frac{\partial}{\partial \bar{r}} [\bar{r} \bar{u}_r] + \frac{\partial \bar{u}_x}{\partial \bar{x}} = 0 & (2.43a) \\ \frac{\partial \bar{u}_x}{\partial \bar{t}} + S_h \left[\bar{u}_r \frac{\partial \bar{u}_x}{\partial \bar{r}} + \bar{u}_x \frac{\partial \bar{u}_x}{\partial \bar{x}} \right] = -\frac{\partial \tilde{p}}{\partial \bar{x}} + \frac{1}{\alpha^2} \left[\frac{1}{\bar{r}} \frac{\partial}{\partial \bar{r}} \left[\bar{r} \frac{\partial \bar{u}_x}{\partial \bar{r}} \right] \right] & (2.43b) \\ \tilde{p}(\bar{x}, \bar{r}, \bar{t}) = \tilde{p}(\bar{x}, \bar{t}). & (2.43c) \end{cases}$$

System (2.43) was originally derived by Prandtl in [Prandtl 1928], hence the name reduced Navier-Stokes-Prandtl equations.

Starting from the incompressible Navier-Stokes equations, we have derived a simplified system of equations for blood flow. The RNSP equations (2.43) are a rich dynamical system [Womersley 1955; Smith 1976; Lagrée and Lorthois 2005] and we show in the Section 2.4 that they contain all necessary physical ingredients to describe blood flow in large arteries.

2.4 Validity of the combined fluid and solid models

Before going any further, we assess the validity of the hypotheses made in Section 2.2 and Section 2.3 and the ability of the combined fluid and solid models to reproduce classical blood flow solutions. Apart from numerical solutions, there are, to our knowledge, two analytic solutions of the Navier-Stokes equations in straight elastic tubes:

- the steady, linear and elastic Poiseuille solution, proposed in [Fung 2013] as the analogue of the Hagen-Poiseuille solution in a rigid tube [Sutera and Skalak 1993];
- the linear and harmonic Womersley solution, proposed in [Womersley 1955] as a solution of the linearized Navier-Stokes equations both in rigid and elastic axisymmetric tubes.

In Subsection 2.4.1 and Subsection 2.4.2, we derive both solutions from the RNSP equations (2.43) coupled to the wall law (2.23) and thereby validate the reduced-order fluid and solid models.

2.4.1 The steady linear elastic Poiseuille solution

Starting from the RNSP equations (2.43), we use the long wave hypothesis (2.32) and consider a steady linear flow ($\partial_t \cdot = 0$ and $S_h \ll 1$). We obtain using Equation (2.43b), written here in dimensional form, the classical Poiseuille governing equation (valid both in elastic and rigid tubes):

$$0 = -\frac{1}{\rho} \frac{dp}{dx} + \frac{\nu}{r} \frac{\partial}{\partial r} \left[r \frac{\partial u_x}{\partial r} \right]. \quad (2.44)$$

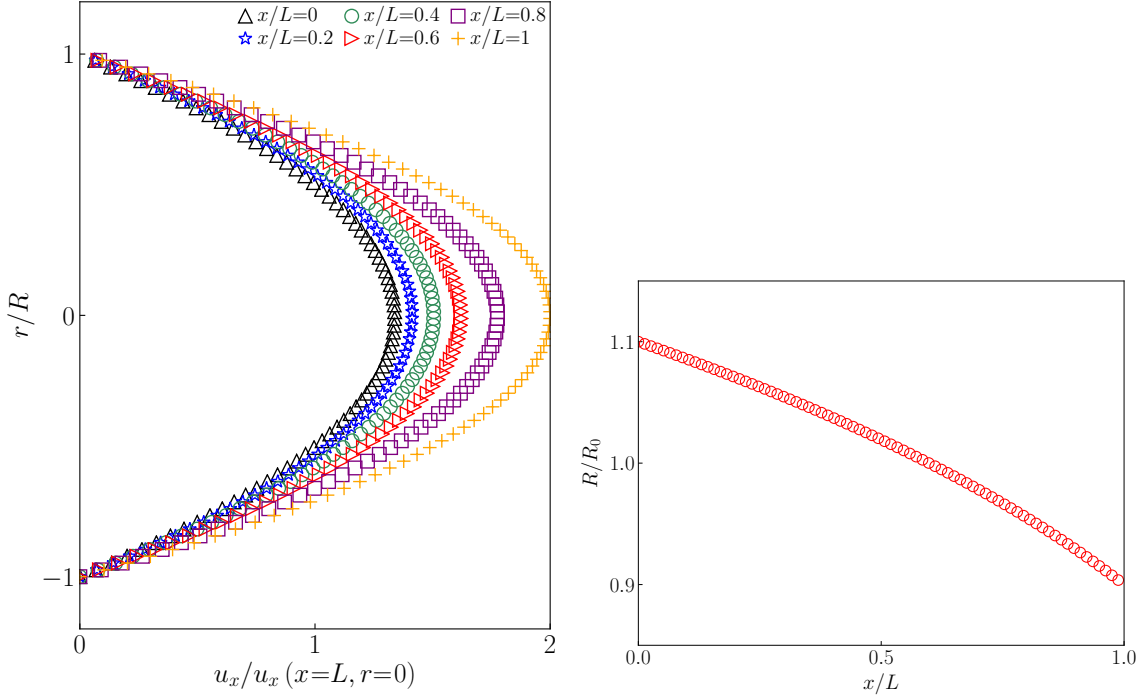


Figure 2.2 – Axial evolution of the Poiseuille velocity profile and radius solutions: **Left:** Velocity profile u_x at $x/L \in \{0 (\Delta), 0.2 (\star), 0.4 (\bigcirc), 0.6 (\triangleright), 0.8 (\square), 1 (+)\}$. **Right:** Radius R (\bigcirc).

Integrating twice Equation (2.44) and using the no-slip boundary condition (2.34b), we recover the classical Poiseuille solution (valid both in elastic and rigid tubes):

$$u_x = -\frac{R^2}{4\mu} \frac{dp}{dx} \left[1 - \frac{r^2}{R^2} \right] = 2 \frac{Q}{\pi R^2} \left[1 - \frac{r^2}{R^2} \right], \quad (2.45)$$

where Q is the steady flow rate. Finally, injecting the solution (2.45) into Equation (2.44) and using the elastic wall law (2.23), we find the expression for the elastic variation of the radius:

$$R^5 - R^5(x=0) = -\frac{40\nu}{\pi^{\frac{3}{2}} K} Qx, \quad (2.46)$$

which allows us to deduce an expression for the flow rate Q :

$$Q = \frac{\pi^{\frac{3}{2}} K}{40\nu L} [R^5(x=0) - R^5(x=L)]. \quad (2.47)$$

If $K \rightarrow \infty$, than from Equation (2.46) we see that $R = R(x=0)$ and we recover the classical Poiseuille solution in a rigid tube.

We plot in Figure 2.2 analytic Poiseuille velocity profiles at positions $x/L \in \{0, 0.2, 0.4, 0.6, 0.8, 1\}$ and the axial variations of the radius R . We observe that the maximum velocity increases with x to compensate the elastic decrease in radius and maintain a constant flow rate (mass conservation).

2.4.2 The Womersley solution

Starting from the RNSP equations (2.43), we assume that the flow is linear ($S_h \ll 1$) and periodic and search for a harmonic solution of the axial velocity u_x and the pressure p :

$$\begin{cases} u_x = \hat{u}_x(r) e^{i[\omega t - kx]} \\ p = p_0 + \hat{p} e^{i[\omega t - kx]}, \end{cases} \quad (2.48)$$

where $p_0 = 0$ for simplicity. Injecting these expressions into Equation (2.43b) we recover the classical Womersley equation:

$$\frac{\partial^2 \hat{u}_x}{\partial r^2} + \frac{1}{r} \frac{\partial \hat{u}_x}{\partial r} - i \frac{\alpha^2}{R^2} \hat{u}_x = -\frac{i\omega}{\mu c} \hat{p}, \quad (2.49)$$

where α is the Womersley number (2.41) and $c = \omega/k$ is the wave celerity. The solution of Equation (2.49) is obtained using the Bessel function J_0 and the no-slip boundary condition (2.34b), and writes:

$$\hat{u}_x = \frac{\hat{p}}{\rho c} \left[1 - \frac{J_0\left(i^{\frac{3}{2}} \alpha \frac{r}{R}\right)}{J_0\left(i^{\frac{3}{2}} \alpha\right)} \right]. \quad (2.50)$$

Using Equation (2.50), we compute the flow rate Q and the wall shear stress (WSS) τ_w :

$$\begin{cases} Q = \hat{Q} e^{i[\omega t - kx]} & \text{with} & \hat{Q} = \pi R^2 \frac{\hat{p}}{\rho c} [1 - F_{10}(\alpha)] \\ \tau_w = \hat{\tau}_w e^{i[\omega t - kx]} & \text{with} & \hat{\tau}_w = i \frac{\nu \alpha^2}{2R} \frac{\hat{p}}{\rho c} F_{10}(\alpha), \end{cases} \quad (2.51a)$$

where F_{10} is defined as:

$$F_{10}(\alpha) = \frac{2}{i^{\frac{3}{2}} \alpha} \frac{J_1(i^{\frac{3}{2}} \alpha)}{J_0(i^{\frac{3}{2}} \alpha)}. \quad (2.52)$$

Finally, Equation (2.43a) integrated over the cross-sectional area of the artery combined with Equation (2.23) allows us to obtain a linearized expression for the wave celerity c :

$$c^2 = \frac{K \sqrt{\pi} R_0}{2\rho} [1 - F_{10}(\alpha)] \quad \text{with} \quad \hat{p} = \sqrt{\pi} K \hat{R}. \quad (2.53)$$

The inlet boundary condition imposes the value of either \hat{p} or \hat{R} , which closes the problem.

The Womersley solution is obtained in the frequency domain. It can therefore be used as a validation case for blood oscillating at a single frequency. To use this solution to describe more realistic multi-frequencies flows, knowledge of the local flow waveform is required.

We plot in Figure 2.3 the real part of the analytic Womersley velocity profiles obtained for $T = 1$ at a fixed position $x/L = 0.5$ at times $t/T \in \{0, 0.1, 0.2, 0.3, 0.4, 0.5\}$ for different Womersley numbers $\alpha \in \{1, 10, 20, 30\}$. We observe that for small Womersley numbers, at which viscous effects dominate, the velocity profiles are parabolic and similar to those presented in Figure 2.2. On the contrary, for high Womersley numbers, at which inertial effects dominate, the velocity profiles flatten in the center of the tube and a boundary layer develops near the wall to match the no-slip boundary condition (2.34b).

2.5 One-dimensional equations

In Section 2.2 and Section 2.3, we have derived simplified equations governing the deformation of the arterial wall and the flow of blood in the large arteries. These equations are summarized in Table 2.3. The main difficulty now lies in proposing an efficient coupling of the fluid and solid problems. To that effect, we derive in Subsection 2.5.1 the one-dimensional (1D) monolithic fluid-structure interaction (FSI) system of equations and discuss in Subsection 2.5.2 the approximations made on the shape of the axial velocity profile.

2.5.1 One-dimensional fluid and solid equations

The elastic wall law (2.23) depends on two dynamic variables: the internal fluid pressure p and the instantaneous radius of the artery R . Only the fluid pressure p is an explicit

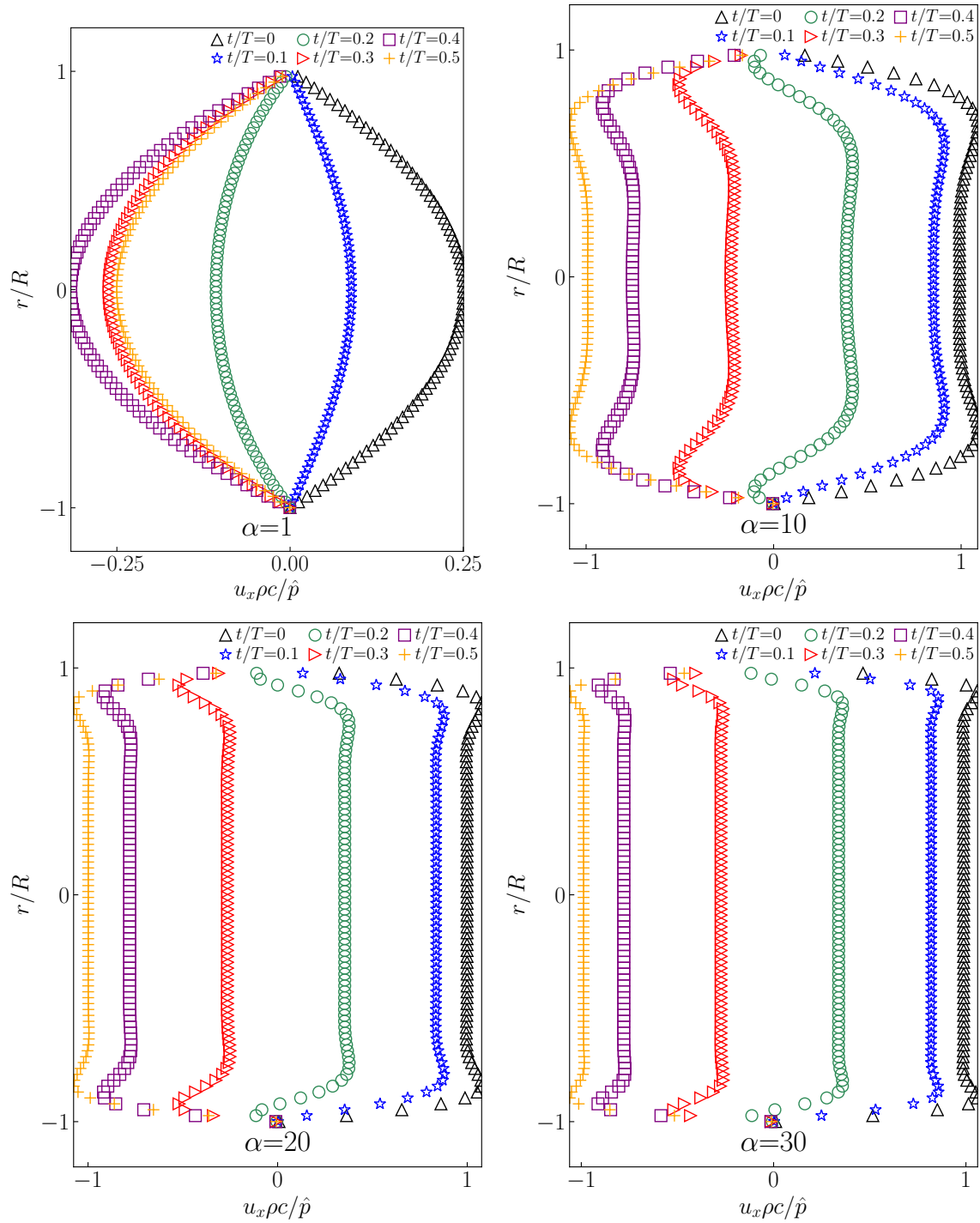


Figure 2.3 – Temporal evolution of analytic Womersley velocity profiles obtained for $T = 1$ at a fixed position $x/L = 0.5$ at times $t/T \in \{0 (\Delta), 0.1 (\star), 0.2 (\bigcirc), 0.3 (\triangleright), 0.4 (\square), 0.5 (+)\}$ for different Womersley numbers:

Top left: $\alpha = 1$.

Top right: $\alpha = 10$.

Bottom left: $\alpha = 20$.

Bottom right: $\alpha = 30$.

	Hypotheses	Non-dimensional numbers	Equations
Solid	$\boldsymbol{\sigma} = \lambda_w \text{tr}(\boldsymbol{\epsilon}) \mathbb{I} + 2\mu_w \boldsymbol{\epsilon}$	$gT^2/R_0 = 10^3$	$\Delta p = K \left[\sqrt{A} - \sqrt{A_0} \right]$
	$\text{div}(\boldsymbol{\sigma}) = 0$	$\mu_w T^2 / (\rho_w R_0^2) = 10^5$	
	$\partial_\theta = 0$		$K = \frac{E}{1 - \nu_w^2} \frac{\sqrt{\pi} h}{A_0}$
	$\epsilon_{xx} = 0$ $\epsilon_w = h/R_0 \ll 1$		
Fluid	$\rho = \text{cst}$	$0 \leq S_h = U_x/c \leq 1$	$\begin{aligned} \frac{1}{r} \frac{\partial}{\partial r} [ru_r] + \frac{\partial u_x}{\partial x} &= 0 \\ \frac{\partial u_x}{\partial t} + u_r \frac{\partial u_x}{\partial r} + u_x \frac{\partial u_x}{\partial x} &= -\frac{1}{\rho} \frac{\partial p}{\partial x} \\ &+ \frac{\nu}{r} \frac{\partial}{\partial r} \left[r \frac{\partial u_x}{\partial r} \right] \\ p(x, r, t) &= p(x, t) \end{aligned}$
	$\mu = \text{cst}$	$0 \leq \alpha = R_0 \sqrt{\omega/\nu} \leq 25$	
	$\partial_\theta = 0$ and $u_\theta = 0$		
	$u_r = \partial_t R$ in $r = R$ $\epsilon_\lambda = R_0/\lambda \ll 1$		

Table 2.3 – Summary of the hypotheses and equations for blood flow in large elastic arteries.

variable of the RNSP equations (2.43). To introduce the variable R into the fluid equations and simplify the coupling of the fluid and solid models, we integrate the RNSP equations (2.43) over the cross-sectional area A of the artery:

$$\int_0^{2\pi} \int_0^R \left\{ \begin{array}{l} \frac{1}{r} \frac{\partial}{\partial r} [ru_r] + \frac{\partial u_x}{\partial x} = 0 \\ \frac{\partial u_x}{\partial t} + u_r \frac{\partial u_x}{\partial r} + u_x \frac{\partial u_x}{\partial x} = -\frac{1}{\rho} \frac{\partial p}{\partial x} + \frac{\nu}{r} \frac{\partial}{\partial r} \left[r \frac{\partial u_x}{\partial r} \right] \\ p(x, r, t) = p(x, t) \end{array} \right\} r \, dr \, d\theta. \quad (2.54)$$

Through this exact integration or averaging process, we obtain the 1D mass and momentum equations expressed at time t in the axial position x (see [Wang et al. 2015] for details):

$$\left\{ \begin{array}{l} \frac{\partial A}{\partial t} + \frac{\partial Q}{\partial x} = 0 \end{array} \right. \quad (2.55a)$$

$$\left\{ \begin{array}{l} \frac{\partial Q}{\partial t} + \frac{\partial}{\partial x} \left[\psi \frac{Q^2}{A} \right] + \frac{A}{\rho} \frac{\partial p}{\partial x} = \frac{2\pi R}{\rho} \tau_{rx}, \end{array} \right. \quad (2.55b)$$

where A and Q are respectively the cross-sectional area and the axial flow rate:

$$A = 2\pi \int_{r=0}^R r \, dr, \quad Q = 2\pi \int_{r=0}^R u_x r \, dr. \quad (2.56)$$

The coefficient ψ is the nonlinear shape factor:

$$\psi = 2\pi \frac{A}{Q^2} \int_{r=0}^R r u_x^2 \, dr, \quad (2.57)$$

and τ_{rx} is the WSS:

$$\tau_{rx} = \mu \left. \frac{\partial u_x}{\partial r} \right|_{r=R}. \quad (2.58)$$

We can now use the elastic wall law (2.23) to couple the fluid and solid problems. Injecting Equation (2.23) into System (2.55), we obtain:

$$\left\{ \begin{array}{l} \frac{\partial A}{\partial t} + \frac{\partial Q}{\partial x} = 0 \end{array} \right. \quad (2.59a)$$

$$\left\{ \begin{array}{l} \frac{\partial Q}{\partial t} + \frac{\partial}{\partial x} \left[\psi \frac{Q^2}{A} + \frac{K}{3\rho} A^{\frac{3}{2}} \right] = \frac{2\pi R}{\rho} \tau_{rx}. \end{array} \right. \quad (2.59b)$$

We assume here that A_0 and K are constants. However, in pathological situations such as in stenoses and aneurysms, these quantities can vary with space and time (growth and remodeling). The mathematical and numerical implications of these behaviors are discussed in Chapter 5.

2.5.2 Velocity profile approximations

To close System (2.59), we need to express the nonlinear shape factor ψ and the WSS τ_{rx} in terms of the flow rate Q and the cross-sectional area A . One-dimensional closure hypotheses [Hughes and Lubliner 1973; Formaggia et al. 2003] suggest that we may write the axial velocity u_x as:

$$u_x = \phi \left(\frac{r}{R} \right) U, \quad (2.60)$$

where $U = Q/A$ is the averaged velocity and ϕ is the dimensionless shape of the velocity profile. Using this expression, we can rewrite ψ and τ_{rx} as:

$$\left\{ \begin{array}{l} \psi = 2 \int_0^1 \bar{r} \phi^2 d\bar{r} \\ \tau_{rx} = \mu \frac{U}{R} \frac{d\phi}{d\bar{r}} \Big|_{\bar{r}=1}, \end{array} \right. \quad (2.61a)$$

$$\left. \right\} \quad (2.61b)$$

where $\bar{r} = r/R$. Unfortunately, the shape of the axial velocity profile is lost in the averaging process and remains an unknown of the problem. An *a priori* shape must therefore be carefully chosen. Indeed, in [Ikenaga et al. 2013; Wang et al. 2016b; Puelz et al. 2017] the authors show that the choices for ψ and $d_{\bar{r}}\phi|_{\bar{r}=1}$ significantly affect the computed numerical results.

For blood flow in a straight artery, we can reasonably assume that the velocity profile is given by the Womersley solution (2.50), presented in Subsection 2.4.2 and valid only for linear harmonic flow, for which we have:

$$\phi = \Re \left(\frac{u_x}{U} \right) = \Re \left(\frac{1 - \frac{J_0(i^{\frac{3}{2}}\alpha\bar{r})}{J_0(i^{\frac{3}{2}}\alpha)}}{1 - F_{10}(\alpha)} \right). \quad (2.62)$$

From Equation (2.62) we obtain the expressions for ψ and $d_{\bar{r}}\phi|_{\bar{r}=1}$ using the software *Mathematica*:

$$\left\{ \begin{array}{l} \psi = \Re \left(\frac{J_1(i^{\frac{3}{2}}\alpha)^2 + 2J_0(i^{\frac{3}{2}}\alpha) \left[J_0(i^{\frac{3}{2}}\alpha) - \frac{{}_0F_1(2, \frac{i\alpha^2}{4})}{\Gamma(2)} \right]}{I_2(i^{\frac{1}{2}}\alpha)} \right) \\ \frac{d\phi}{d\bar{r}} \Big|_{\bar{r}=1} = \Re \left(-2 \frac{\Gamma(3) {}_0F_1(2, \frac{i\alpha^2}{4})}{\Gamma(2) {}_0F_1(3, \frac{i\alpha^2}{4})} \right), \end{array} \right. \quad (2.63a)$$

$$\left. \right\} \quad (2.63b)$$

where ${}_0F_1(a, z)$ is the confluent hypergeometric function, $\Gamma(x)$ the Gamma function and $I_n(z)$ the modified Bessel function of the first kind. These expressions are parametrized by the value of the Womersley number α (2.41) which can be estimated in experiments and numerical simulations.

A more classical approach consists in using the power-law velocity profile introduced in

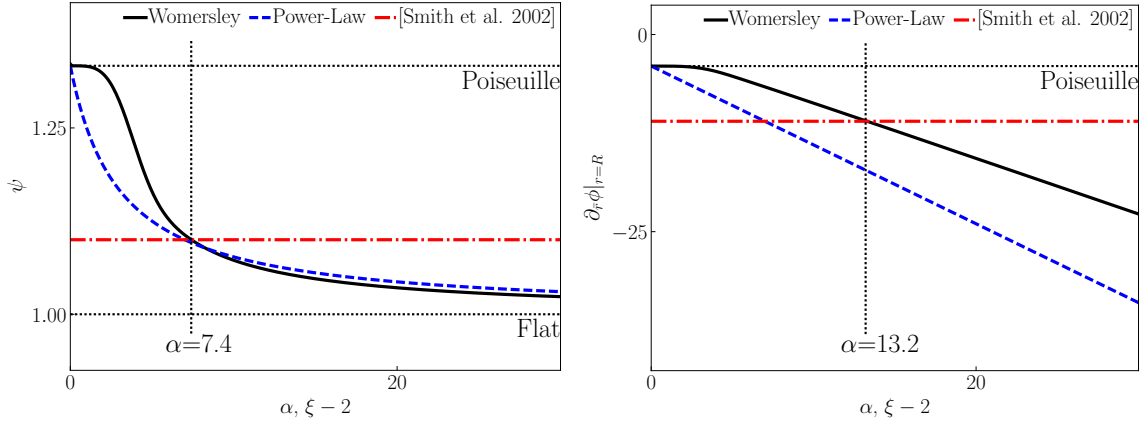


Figure 2.4 – Evolution of the advection coefficient ψ (left) and wall friction $\partial_{\bar{r}}\phi|_{r=R}$ (right) computed with the Womersley closure (2.63) (—) and the power-law closure relations (2.65) (---). The straight lines correspond to the coefficients obtained in [Smith et al. 2002] (—, $\psi = 1.1$, $d_{\bar{r}}\phi = -11$), with a Poiseuille profile (---, $\psi = 4/3$, $d_{\bar{r}}\phi = -4$) and with a flat profile (---, $\psi = 1$, $d_{\bar{r}}\phi = -\infty$). Note that the advection and wall friction coefficients obtained in [Smith et al. 2002] correspond respectively to Womersley coefficients obtained for $\alpha = 7.4$ and $\alpha = 13.2$.

[Hughes and Lubliner 1973]:

$$\phi = \frac{\xi + 2}{\xi} \left[1 - \bar{r}^\xi \right], \quad (2.64)$$

for which we have:

$$\begin{cases} \psi = 1 + \frac{1}{1 + \xi} & (2.65a) \\ \left. \frac{d\phi}{d\bar{r}} \right|_{\bar{r}=1} = -[2 + \xi]. & (2.65b) \end{cases}$$

These expressions are parametrized by the user-defined value of ξ .

To compare both the Womersley and power-law closure relations, we plot in Figure 2.4 the variations of the coefficients ψ and $d_{\bar{r}}\phi|_{\bar{r}=1}$ given by System (2.63) and System (2.65). We notice that both the Womersley and power-law closure relations recover the classical bounds for ψ and $d_{\bar{r}}\phi|_{\bar{r}=1}$:

$$\begin{cases} 1 \leq \psi \leq 4/3 & (2.66a) \\ d_{\bar{r}}\phi|_{\bar{r}=1} \leq -4. & (2.66b) \end{cases}$$

However, we observe that their respective variations with α and ξ differ, whether for ψ or $d_{\bar{r}}\phi|_{\bar{r}=1}$. Indeed, the Womersley closure relations (2.63) are based on a physical analysis of blood flow equations and are able to capture the complex behavior of the flow near the arterial wall. Furthermore, they are parametrized by the Womersley number α , which is the natural blood flow non-dimensional parameter and can be estimated in experiments and numerical simulations. On the contrary, the power-law closure relations (2.65) stem from an *ad hoc* expression for the shape of the velocity profile designed to match the no-slip condition (2.34b), the axisymmetric condition $d_{\bar{r}}\phi|_{\bar{r}=0} = 0$, the Poiseuille velocity profile for $\xi = 2$ ($\alpha = 0$) and a flat velocity profile (plug flow) for $\xi \gg 1$ ($\alpha \gg 1$). They are parametrized by the variable ξ , which has no physical meaning and can not be measured experimentally or numerically. The Womersley closure relations (2.63) are therefore the better choice.

Despite this analysis, we conform to the literature on 1D blood flow and set $\psi = 1$ and use the power-law closure relations (2.65) in the following to compute $d_{\bar{r}}\phi|_{\bar{r}=1}$. These hypotheses allow us to write the final closed form of System (2.59):

$$\begin{cases} \frac{\partial A}{\partial t} + \frac{\partial Q}{\partial x} = 0 & (2.67a) \\ \frac{\partial Q}{\partial t} + \frac{\partial}{\partial x} \left[\frac{Q^2}{A} + \frac{K}{3\rho} A^{\frac{3}{2}} \right] = -C_f \frac{Q}{A}, & (2.67b) \end{cases}$$

where C_f is the friction coefficient, defined as:

$$C_f = 2\pi\nu [2 + \xi]. \quad (2.68)$$

The value $\xi = 9$, proposed in [Smith et al. 2002], is commonly used in the literature on 1D blood flow [Alastruey et al. 2011; Montecinos et al. 2014; Wang et al. 2016c; Ghigo et al. 2017a]. We observe in Figure 2.4 that the advection and wall friction coefficients computed with this value correspond to Womersley coefficients obtained for a Womersley number $7 \leq \alpha \leq 13$, which is a physiological Womersley number range.

However, as blood flow is a strongly multiscale problem, a realistic model can not assume that ψ and $d_{\bar{r}}\phi|_{\bar{r}=1}$ are fixed in space and time and must allow for their dynamic evolution. The Womersley closure relations (2.65) could be used to dynamically update ψ and $d_{\bar{r}}\phi|_{\bar{r}=1}$ using the Womersley number computed in all positions for all times. Other dynamical approach also based on the Womersley theory are proposed in [Lagrée 2000; Reymond et al. 2009]. However, a more general approach is necessary for which no additional hypothesis is required. In Chapter 8, we propose such an approach where we dynamically compute the velocity profile and therefore completely eliminate the need for a velocity profile closure.

2.6 Dimensional and mathematical analysis

To better understand the behaviors of System (2.67), we propose its dimensional analysis in Subsection 2.6.1 and its mathematical analysis in Subsection 2.6.2.

2.6.1 Dimensional analysis

We perform here a dimensional analysis of System (2.67), similar to the analysis performed in Subsection 2.3.2. To assess the importance of each term in System (2.67), we introduce in Table 2.4 non-dimensional variables.

$$\rho = 1 \quad C_f = C_f \quad t = T\bar{t} \quad x = X\bar{x} \quad R = R_0 [1 + \Delta_R \bar{R}] \quad Q = Q\bar{Q} \quad p = p_{ext} + \Pi\bar{p}$$

Table 2.4 – Non-dimensional 1D variables. The parameter Δ_R represents the deformation amplitude of the radius of the artery and the parameter Π characterizes the fluid pressure variations.

Using these non-dimensional variables, the wall law (2.23) rewrites:

$$\Pi\bar{p} = \sqrt{\pi} K R_0 \Delta_R \bar{R}, \quad (2.69)$$

which gives:

$$\Pi = 2\rho c^2 \Delta_R. \quad (2.70)$$

The variable c is the Moens-Korteweg wave speed [Moens 1878; Korteweg 1878], introduced in Equation (2.30) in Subsection 2.3.1:

$$c = \sqrt{\frac{K}{2\rho}} \sqrt{A}. \quad (2.71)$$

Then, injecting these non-dimensional variables into System (2.67), we obtain the 1D blood

flow equations written in non-dimensional form (see [Saito et al. 2011] for details):

$$\left\{ \begin{array}{l} \left[2\Delta_R \frac{X}{UT} \right] [1 + \Delta_R \bar{R}] \frac{\partial \bar{R}}{\partial \bar{t}} + \frac{\partial \bar{Q}}{\partial \bar{x}} = 0 \end{array} \right. \quad (2.72a)$$

$$\left\{ \begin{array}{l} \frac{\partial \bar{Q}}{\partial \bar{t}} + \left[\frac{UT}{X} \right] \frac{\partial}{\partial \bar{x}} \left[\frac{\bar{Q}^2}{[1 + \Delta_R \bar{R}]^2} \right] \\ + \left[2\Delta_R \frac{c^2 T}{UX} \right] [1 + \Delta_R \bar{R}]^2 \frac{\partial \bar{p}}{\partial \bar{x}} = - \left[\frac{1}{\alpha^2} \right] \frac{\bar{Q}}{[1 + \Delta_R \bar{R}]^2}, \end{array} \right. \quad (2.72b)$$

where $U = Q/[\pi R_0^2]$ is the average flow velocity and $\alpha^2 = \pi R_0^2/[C_f T]$ is the 1D analogue of the Womersley number (2.41). The least degeneracy principle applied to Equation (2.72a) gives:

$$2\Delta_R \frac{X}{UT} = 1, \quad (2.73)$$

which allows us to rewrite System (2.72) as:

$$\left\{ \begin{array}{l} [1 + \Delta_R \bar{R}] \frac{\partial \bar{R}}{\partial \bar{t}} + \frac{\partial \bar{Q}}{\partial \bar{x}} = 0 \end{array} \right. \quad (2.74a)$$

$$\left\{ \begin{array}{l} \frac{\partial \bar{Q}}{\partial \bar{t}} + [2\Delta_R] \frac{\partial}{\partial \bar{x}} \left[\frac{\bar{Q}^2}{[1 + \Delta_R \bar{R}]^2} \right] \\ + \left[2\frac{\Delta_R}{S_h} \right]^2 [1 + \Delta_R \bar{R}]^2 \frac{\partial \bar{p}}{\partial \bar{x}} = - \left[\frac{1}{\alpha^2} \right] \frac{\bar{Q}}{[1 + \Delta_R \bar{R}]^2}, \end{array} \right. \quad (2.74b)$$

where $S_h = |U/c|$ is the Shapiro number (2.40).

Linear wave propagation regime

We consider a linear pulsatile flow regime. The least degeneracy principle applied to Equation (2.74b) states that in the linear wave propagation regime the pressure gradient must balance the unsteady inertial term, which gives:

$$\left\{ \begin{array}{l} \Delta_R \ll 1 \end{array} \right. \quad (2.75a)$$

$$\left\{ \begin{array}{l} S_h = 2\Delta_R. \end{array} \right. \quad (2.75b)$$

Nonlinear Wave propagation regime

We now consider a nonlinear pulsatile flow regime. The least degeneracy principle applied to Equation (2.74b) states that in the nonlinear wave propagation regime the pressure gradient must balance the inertial terms, which gives:

$$\left\{ \begin{array}{l} \Delta_R = 1 \end{array} \right. \quad (2.76a)$$

$$\left\{ \begin{array}{l} S_h = 2\Delta_R. \end{array} \right. \quad (2.76b)$$

For both linear and nonlinear flow regimes, we show using Equation (2.73) and Equation (2.75b) (or Equation (2.76b)) that the characteristic length scale is the wavelength of the pulse wave:

$$X = cT. \quad (2.77)$$

This analysis is an *a posteriori* confirmation that the 1D equations (2.67) are valid in the long wave approximation framework used to derive the RNSP equations (2.43) and that in this framework blood flow dynamics are indeed governed by a balance between the inertial and pressure forces. The dimensional analysis also shows that viscous effects are of secondary importance as long as the Womersley number $\alpha \geq 1$, which highlights the importance of

choosing correct velocity profile closure relations as they directly influence the value of C_f and therefore the importance of viscous effects.

Equation (2.75a) and Equation (2.76a) show that the nonlinearity of blood flow, characterized by the Shapiro number S_h (2.40), is also represented by the deformation amplitude of the wall Δ_R , which is easily measurable in *in vitro* and *in vivo* experiments.

2.6.2 Mathematical analysis

In the continuity of the dimensional analysis performed in Subsection 2.6.1, we analyze here the mathematical properties of System (2.67). Indeed, the mathematical structure of System (2.67) provides valuable information on the nature of the flow it describes and aids in the choice of its numerical treatment. As viscous effects are second-order behaviors (see Subsection 2.6.1), we simplify the analysis and consider the inviscid form of System (2.67), rewritten as a system of conservation laws:

$$\frac{\partial \mathbf{U}}{\partial t} + \frac{\partial \mathbf{F}}{\partial x} = 0. \quad (2.78)$$

The vectors \mathbf{U} and \mathbf{F} are respectively the vector of conservative variables and the vector of mass and momentum fluxes:

$$\mathbf{U} = \begin{bmatrix} A \\ Q \end{bmatrix}, \quad (2.79)$$

and:

$$\mathbf{F} = \begin{bmatrix} F_A \\ F_Q \end{bmatrix}, \quad (2.80)$$

where F_A is the mass flux and F_Q the momentum flux:

$$\begin{cases} F_A = Q \\ F_Q = \frac{Q^2}{A} + \frac{K}{3\rho} A^{\frac{3}{2}}. \end{cases} \quad (2.81a)$$

$$\quad (2.81b)$$

The conservative System (2.78) has been thoroughly studied by many authors and we only briefly recall its properties. Additional details can be found in [Formaggia et al. 2003; Sherwin et al. 2003a; Alastruey et al. 2012; Müller et al. 2013].

The Jacobian matrix of the flux vector \mathbf{F} (2.81) is:

$$\mathbf{J} = \frac{\partial \mathbf{F}}{\partial \mathbf{U}} = \begin{bmatrix} 0 & 1 \\ c^2 - \frac{Q^2}{A^2} & 2\frac{Q}{A} \end{bmatrix}, \quad (2.82)$$

and has two real eigenvalues λ_1 and λ_2 :

$$\begin{cases} \lambda_1 = \frac{Q}{A} - c \\ \lambda_2 = \frac{Q}{A} + c, \end{cases} \quad (2.83a)$$

$$\quad (2.83b)$$

respectively associated to two right eigenvectors \mathbf{R}_1 and \mathbf{R}_2 :

$$\begin{cases} \mathbf{R}_1 = \begin{bmatrix} 1 \\ \lambda_1 \end{bmatrix} \\ \mathbf{R}_2 = \begin{bmatrix} 1 \\ \lambda_2 \end{bmatrix}. \end{cases} \quad (2.84a)$$

$$\quad (2.84b)$$

where c is the Moens-Korteweg wave speed (2.71).

The hyperbolicity of System (2.78) is characterized by the Shapiro number S_h , defined in

[Shapiro 1977] and introduced in Subsection 2.3.2:

$$S_h = \left| \frac{U}{c} \right| = \left| \frac{1}{c} \frac{Q}{A} \right|. \quad (2.85)$$

The Shapiro number S_h is the analogue of the Froude number F_r for the shallow-water equations or of the Mach number M_a for compressible flows. Depending on the value of S_h , we distinguish two flow regimes, represented respectively by the subcritical velocity domain \mathbb{U}_{sub} and the supercritical velocity domain \mathbb{U}_{sup} :

$$\begin{cases} \mathbb{U}_{sub} = \left\{ \frac{Q}{A} \in \mathbb{R} \mid A > 0, K > 0, S_h < 1 \right\} \\ \mathbb{U}_{sup} = \left\{ \frac{Q}{A} \in \mathbb{R} \mid A > 0, K > 0, S_h > 1 \right\}. \end{cases} \quad (2.86)$$

In both regions \mathbb{U}_{sub} and \mathbb{U}_{sup} , system (2.78) is strictly hyperbolic as $\lambda_1 \neq \lambda_2$ and the right eigenvectors \mathbf{R}_1 and \mathbf{R}_2 are linearly independent. When $S_h = 1$, the flow is critical and the system loses its strict hyperbolicity. In this case resonance phenomena can occur, leading to a possible loss of uniqueness of the solution [Liu 1987; Isaacson and Temple 1992; LeVeque 2002; Han et al. 2012]. However, in physiological conditions blood flow is always subcritical, except maybe in very specific pathologies. Hence only subcritical solutions of system (2.78) are considered here.

For solutions of system (2.78) in \mathbb{U}_{sub} , linear algebra shows that the Jacobian matrix \mathbf{J} (2.82) is diagonalizable in the form $\mathbf{J} = \mathbf{R}\mathbf{\Delta}\mathbf{R}^{-1}$, where $\mathbf{R} = [\mathbf{R}_1, \mathbf{R}_2]$ and $\mathbf{\Delta}$ is a diagonal matrix containing the eigenvalues of \mathbf{J} . Introducing a new vector $\mathbf{W} = [W_1, W_2]^T$ such that $\partial_U \mathbf{W} = \mathbf{R}^{-1}$, system (2.78) can be written as:

$$\frac{\partial \mathbf{W}}{\partial t} + \mathbf{\Delta} \frac{\partial \mathbf{W}}{\partial x} = 0. \quad (2.87)$$

Finally, by integrating the equation $\partial_U \mathbf{W} = \mathbf{R}^{-1}$, an expression for \mathbf{W} is obtained:

$$\mathbf{W} = \begin{bmatrix} W_1 \\ W_2 \end{bmatrix} = \begin{bmatrix} \frac{Q}{A} - 4c \\ \frac{Q}{A} + 4c \end{bmatrix}. \quad (2.88)$$

The vector \mathbf{W} is often referred to as the Riemann invariant vector and is linked to the conservative variables through the relations:

$$\begin{cases} A = \left(\frac{2\rho}{K} \right)^2 \left(\frac{W_2 - W_1}{8} \right)^4 \\ Q = A \frac{W_1 + W_2}{2}. \end{cases} \quad (2.89)$$

In Chapter 6, the relations (2.89) are useful to define the boundary conditions at the inlet and outlet of the computational domain.

If $\psi \neq 1$:

$$\lambda_1 = \psi \frac{Q}{A} - \sqrt{[\psi^2 - \psi] \frac{Q^2}{A^2} + c^2}, \quad \lambda_2 = \psi \frac{Q}{A} + \sqrt{[\psi^2 - \psi] \frac{Q^2}{A^2} + c^2}. \quad (2.90)$$

Then, since $0 \leq \psi^2 - \psi \leq 4/9$ as $1 < \psi \leq 4/3$ and $Q^2/A^2 \ll c^2$ as $S_h \ll 1$, we write:

$$\sqrt{[\psi^2 - \psi] \frac{Q^2}{A^2} + c^2} \approx c. \quad (2.91)$$

This simplification allow us to solve solve $\partial_{\mathbf{U}}\mathbf{W} = \mathbf{R}^{-1}$ and obtain:

$$\mathbf{W} = \begin{bmatrix} W_1 \\ W_2 \end{bmatrix} = \begin{bmatrix} \frac{Q}{A^\psi} - \frac{4}{[5-4\psi]A^{\psi-1}}c \\ \frac{Q}{A^\psi} + \frac{4}{[5-4\psi]A^{\psi-1}}c \end{bmatrix}. \quad (2.92)$$

However, in this case, System (2.67) does not verify a Galilean invariance.

The vector \mathbf{U} also satisfies an entropy inequality linked to the entropy pair (η, G) :

$$\frac{\partial \eta}{\partial t} + \frac{\partial G}{\partial x} \leq 0, \quad (2.93)$$

where η is the entropy and G is the entropy flux:

$$\begin{cases} \eta = \frac{Q^2}{2A} + \frac{2K}{3\rho}A^{\frac{3}{2}} \\ G = \left[\frac{Q^2}{2A} + \frac{K}{\rho}A^{\frac{3}{2}} \right] \frac{Q}{A}. \end{cases} \quad (2.94)$$

This entropy inequality is closely linked to the variation of the physical energy of the system. The existence of such an inequality is essential in order to select the correct physical solution across discontinuities [Gosse 2013].

2.7 Conclusion

In Chapter 2, we have carefully presented the hypotheses for the solid and fluid problems that have allowed us to derive simplified equations for the mechanical response of the arterial wall (spring law, Equation (2.23)) and for the flow of blood in an axisymmetric artery (RNSP equations, System (2.43)). We have shown that both Equation (2.23) and System (2.43) form the minimal system of equations necessary to accurately describe blood flow in large elastic arteries (they reproduce the Poiseuille and Womersley solutions). Then, we have coupled both fluid and solid simplified equations and obtained the 1D system of equations (2.67) describing simultaneously the flow of blood in an axisymmetric artery and the elastic deformation of the arterial wall. Finally, we have shown through a dimensional and mathematical analysis that System (2.67) is able to describe wave propagation in an elastic artery (hyperbolic system). System (2.67) is the origin from which all work presented in this thesis departs from, with the objective of improving its ability to describe the flow of blood in large elastic arteries.

One-dimensional equations for blood flow in a viscoelastic artery

We present here an extension of the one-dimensional model presented in Chapter 1, where we include viscoelastic effects. First we propose a nonlinear viscoelastic wall model designed to fit experimental pressure-radius hysteresis loops obtained in sheep. The experimental data were graciously provided by Pr. Armentano and his team in Favaloro University, Argentina. We then incorporate this viscoelastic wall model into the 1D system of equations. The text in this chapter is greatly inspired from the following *published* article:

- A.R. Ghigo, X.-F. Wang, R. Armentano, J.-M. Fullana, and P.-Y. Lagrée. Linear and nonlinear viscoelastic arterial wall models: application on animals. *Journal of Biomechanical Engineering*, 139(1):011003, 2017e.

Contents

3.1	Introduction	31
3.2	Material and methods	33
	3.2.1 Data acquisition	33
	3.2.2 Nonlinear wall model	34
	3.2.3 Parameter estimation	34
3.3	Results and discussion	36
	3.3.1 Comparison of the linear and nonlinear Kelvin-Voigt models	36
	3.3.2 Validation of the parameter estimation strategy	36
	3.3.3 Analysis of the nonlinear Kelvin-Voigt model	37
3.4	One-dimensional viscoelastic blood flow equations	40
3.5	Conclusion	42

3.1 Introduction

In Chapter 2, we have proposed a model (Equation (2.23)) describing the elastic deformation of the arterial wall through variations of the transmural pressure. We have shown that this model is suitable for the propagation of pulse wave in an artery. However, the arterial wall displays both elastic and viscous behaviors [Taylor 1959; Westerhof and Noordergraaf 1970; Valdez-Jasso et al. 2009]. Indeed, wall viscosity is a key element of the mechanical response of the arterial wall and acts as a protection mechanism by dissipating energy and

filtering high-frequency components of the pressure signal, preventing structural injuries of the arterial wall [Armentano et al. 2007].

Considerable efforts have been made to accurately model the three characteristic viscoelastic properties of the arterial wall: stress relaxation, creep and hysteresis. The proposed viscoelastic models fall roughly into three categories:

Integer-order model They describe the arterial viscoelastic strain-stress relation using an arrangement of spring (purely elastic response) and dashpots (purely viscous response) [Armentano et al. 1995]. Integer-order models include the Maxwell, Voigt, Kelvin-Voigt and Standard Linear Solid (SLS) viscoelastic models.

Quasi-linear model They relate the strain and stress in the arterial wall through a convolution between a normalized relaxation (or creep) function and a nonlinear elastic function [Holenstein et al. 1980; Fung 1993].

Fractional-order model They describe the viscoelastic properties of the arterial wall using fractional-order differential equations [Craiem and Armentano 2007; Craiem et al. 2008] and are in fact a subcategory of quasi-linear models. Using the fractional order $0 \leq \alpha_f \leq 1$, a new flexible element is created, called the spring-pot, which can be viewed of as a large set of weighted integer-order spring (zero order element) and dashpot (first order element) pairs arranged in parallel.

Each of these models depends on a set a parameters that must be estimated in order to correctly describe the viscoelastic properties of the arterial wall. Therefore difficulties arise when performing patient-specific simulations as the number of model parameters increases with the number of simulated arterial segments. This is especially true for quasi-linear models, as their parameters can exhibit dynamic variations during a cardiac cycle. Additionally, the parameters describing the viscoelasticity of the arterial wall are difficult to measure and are often hard to distinguish from those characterizing the viscoelastic properties of blood. For the reasons, most existing 1D blood flow simulations adopt an elastic wall model such as Equation (2.23).

Nonetheless, quasi-linear models have been successfully used in combination with a 1D blood flow model. In [Reymond et al. 2009, 2011], comparison between numerical results and *in vivo* measurements reveal a considerable impact of the viscoelasticity on the pulse waves. Similar results are obtained in [Raghu et al. 2011]. In [Perdikaris and Karniadakis 2014] a fractional-order model is used to compute blood flow in a patient-specific cranial network and the sensitivity of the model to the fractional order is quantified.

Simpler integer-order model have also been used in 1D blood flow simulations. In [Alastruey et al. 2011; Montecinos et al. 2014; Müller et al. 2016b; Ghigo et al. 2017a], a Kelvin-Voigt model is adopted and used to simulate the pulsatile flow in an *in vitro* experimental setup. The success of the Kelvin-Voigt viscoelastic model is greatly due to its mathematical and modeling simplicity (it has only two parameters). Unfortunately, when confronted with experimental data, the Kelvin-Voigt model fails to capture the nonlinearities in the response of the arterial wall (see Figure 3.2). We therefore propose in this chapter a modified Kelvin-Voigt model in which a nonlinear viscoelastic component is added. A similar nonlinear viscoelastic term is used in [Erbay et al. 1992] to study wave propagation in nonlinear viscoelastic tubes, and the theoretical basis of the approach is described in [Bird et al. 1977]. We use experimental pressure-radius hysteresis loops acquired in a group of sheep at different arterial sites (experimental data from [Valdez-Jasso et al. 2009] provided by Pr. Armentano and his team for Favaloro University, Argentina) to estimate the parameters of the model and to assess the quality of the numerical results.

In Section 3.2, we present the experimental protocol for data acquisition, the proposed

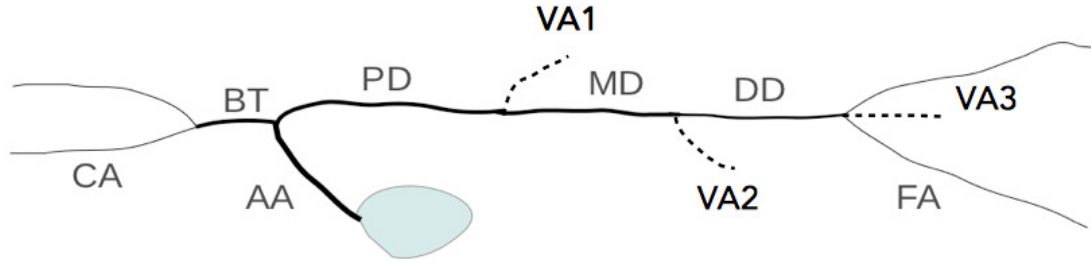


Figure 3.1 – Arterial tree of a sheep. Experimental data are collected from eleven sheep at the following seven locations: Ascending Aorta (AA), Proximal Descending aorta (PD), Medial Descending aorta (MD), Distal Descending aorta (DD), Brachiocephalic Trunk (BT), Carotid Artery (CA) and Femoral Artery (FA). There are three virtual arteries (VA), which are indicated by dashed lines, to model the side branches when pulse waves are simulated. Parameters for all the arteries are shown in Table 3.3.

nonlinear Kelvin-Voigt model and the optimization approach to estimate the model parameters. In Section 3.3, we discuss the optimization results and numerical findings. Finally, in Section 3.4, we integrate the Kelvin-Voigt model into the 1D blood flow equations (2.67).

3.2 Material and methods

3.2.1 Data acquisition

The experimental data were provided by Pr. Armentano and his team in Favaloro University, Argentina. We describe in this subsection the protocol they used to acquire the data.

The experimental data were obtained from a group of eleven sheep (male Merino, between 25 and 35 kg). Before each surgery, the animals were anesthetized with sodium pentobarbital (35 mg/kg). The arterial segments of interest (6 cm long) were separated from the surrounding tissues. To measure the diameter, two miniature piezoelectric crystal transducers (5 MHz, 2 mm in diameter) were sutured on opposite sides into the arterial adventitia. The animals were then sacrificed and the arterial segments of interest were excised for *ex vivo* tests.

The arterial segments were mounted on a test bench where a periodical flow was generated by an artificial heart (Jarvik Model 5, Kolff Medical Inc., Salt Lake City, USA). The input signal was as close as possible to a physiological waveform. We obtained the desired pressure waveforms by simple adjustments of tuning resistances and Windkessel chambers.

The circulating liquid was an aqueous solution of Tyrode. In each arterial segment the internal pressure was measured using a solid-state pressure micro-transducer (Model P2.5, Konigsberg Instruments, Inc., Pasadena, USA), previously calibrated using a mercury manometer at 37°C. The arterial diameter signal was calibrated in millimeters using the 1 mm step calibration option of the sono-micrometer (Model 120, Triton Technology, San Diego, USA). The transit time of the ultrasonic signal with a velocity of $1580 \text{ m} \cdot \text{s}^{-1}$ was converted to the vessel diameter. The experimental protocol was in agreement with the *European Convention for the Protection of Vertebrate Animals used for Experimental and Other Scientific Purposes*. For more details on the animal experiments, please refer to [Valdez-Jasso et al. 2009].

Simultaneous synchronized measurements of transmural pressure and diameter were performed on the following seven anatomical locations as shown in Figure 3.1: Ascending Aorta (AA), Proximal Descending Aorta (PD), Medial Descending Aorta (MD), Distal Descending Aorta (DD), Brachiocephalic Trunk (BT), Carotid Artery (CA) and Femoral Artery (FA).

That experimental data were acquired from blood vessels that were extracted from their surrounding tissue, which affects the experimental pressure-radius hysteresis loops. Other modifying factors are listed in [Cabrera Fischer et al. 2006] where it is shown that the viscosity and elasticity of the arterial wall are influenced by adventitia removal in *in vivo* studies, possibly due to a smooth muscle mechanism.

3.2.2 Nonlinear wall model

In Section 2.2, we have described the arterial wall as an homogeneous, isotropic, isothermal, linear elastic material and we have carefully derived the hoop law relating variations of the transmural pressure with the elastic deformation of the arterial wall, written here in its general form:

$$[1 - \nu_w^2] \frac{R}{h} [p - p_{ext}] = E\epsilon_{\theta\theta}. \quad (3.1)$$

Conforming to the experimental setup, we set $p_{ext} = 0$ and write the strain $\epsilon_{\theta\theta} = \epsilon$ for simplicity.

We now include viscoelastic behaviors using a linear Kelvin-Voigt model and add the viscoelastic term $\phi\dot{\epsilon}$ to the right hand side of Equation (3.1):

$$[1 - \nu_w^2] \frac{R}{h} p = E\epsilon + \phi\dot{\epsilon}, \quad (3.2)$$

where ϕ is the wall viscosity coefficient and $\dot{\epsilon} = \partial_t \epsilon$. We then construct a more general nonlinear Kelvin-Voigt model by performing a second-order expansion of Equation (3.2) in both ϵ and $\dot{\epsilon}$, which writes:

$$[1 - \nu_w^2] \frac{R}{h} p = E\epsilon + E_{nl}\epsilon^2 + \phi\dot{\epsilon} + \phi_{nl}\dot{\epsilon}^2. \quad (3.3)$$

We show in Section 3.3 that the strain ϵ measured in the experimental data is small, confirming the hypothesis of small perturbation made in Section 2.2. We therefore assume that the nonlinear term in ϵ^2 does not play an important role in the pressure dynamics and set $E_{nl} = 0$. A similar assumption is made in [Segers et al. 1997].

In order to use the measured pressure and radius experimental data, we rewrite Equation (3.3), recalling that:

$$\epsilon = \frac{R - R_0}{R_0}, \quad (3.4)$$

and obtain the following relationship connecting the pressure p and the radius R :

$$p = \frac{Eh}{[1 - \nu_w]^2} \frac{1}{R_0} - \frac{Eh}{[1 - \nu_w]^2} \frac{1}{R} + \frac{\phi h}{[1 - \nu_w]^2} \frac{\dot{R}}{R_0} + \frac{\phi_{nl} h}{[1 - \nu_w]^2} \frac{\dot{R}^2}{R_0^2}. \quad (3.5)$$

3.2.3 Parameter estimation

Equation (3.5) shows that the pressure p is a linear combination of the quantities 1 , $1/R$, \dot{R}/R and \dot{R}^2/R . We therefore estimate the coefficients of Equation (3.5) using a linear regression method. As the thickness h and the neutral radius R_0 are measured experimentally, the optimization process provides the values of the Young's modulus E and the viscosity coefficients ϕ and ϕ_{nl} . However, we assume that the value of R_0 is also unknown and we show that the measured and optimized values for R_0 are equivalent, which validates our method. Written in matrix form, the problem is:

$$\mathbf{p} = \mathbf{MC}, \quad (3.6)$$

where \mathbf{M} is a $N \times 4$ matrix:

$$\mathbf{M} = \begin{bmatrix} 1 & \frac{1}{R} & \frac{\dot{R}}{R} & \frac{\dot{R}^2}{R} \\ \vdots & \vdots & \vdots & \vdots \\ 1 & \frac{1}{R} & \frac{\dot{R}}{R} & \frac{\dot{R}^2}{R} \end{bmatrix}_N, \quad (3.7)$$

with N the number of experimental data points, \mathbf{C} the unknown coefficient vector:

$$\mathbf{C} = \begin{bmatrix} \frac{Eh}{[1-\nu_w]^2} \frac{1}{R_0} \\ -\frac{Eh}{[1-\nu_w]} \\ \frac{\phi h}{[1-\nu_w]R_0} \\ \frac{\phi_n h}{[1-\nu_w]R_0^2} \end{bmatrix}, \quad (3.8)$$

and \mathbf{p} the vector of experimental pressure values. We assume that the columns of \mathbf{M} are independent in the linear space and that the measurement errors are independent and identically distributed. Then, according to the theory of the least square method the optimal value of \mathbf{C} is:

$$\mathbf{C}_{opt} = [\mathbf{M}^T \mathbf{M}]^{-1} \mathbf{M}^T \mathbf{p}. \quad (3.9)$$

Unfortunately, the experimental data contains high-frequency noise that prevents us from accurately computing the time derivative of R in the temporal domain, which is required to compute the matrix \mathbf{M} (3.7). We therefore evaluate the time derivative of R using a spectral numerical method. Given a time series $R(t)$ with a period T , we can expand it in Fourier series:

$$R = \sum_{k=-\infty}^{\infty} \hat{R}_k e^{i2\pi k \frac{t}{T}}, \quad (3.10)$$

where \hat{R}_k is the k^{th} Fourier coefficient, defined as:

$$\hat{R}_k = \frac{1}{T} \int_0^T R(t) e^{-i2\pi k \frac{t}{T}} dt. \quad (3.11)$$

The time derivative of R can then be computed as:

$$\dot{R} = \sum_{k=-\infty}^{\infty} \frac{i2\pi k}{T} \hat{R}_k e^{i2\pi k \frac{t}{T}}. \quad (3.12)$$

In the computation, we take advantage of the Discrete Fourier Transform (DFT). We also filter out the experimental noise using an optimization approach based on a criterion γ , selected to minimize the following cost function:

$$J(\mathbf{C}) = \frac{1}{N} \sqrt{\sum_i^N [p_{m,i} - p_i]^2}, \quad (3.13)$$

with \mathbf{p}_m the pressure vector predicted by Equation (3.5).

The pseudo-code for the parameter estimation procedure is:

- **Step 1:** Evaluate the DFT of R (assume N as an even number without loss of generality)

:

$$\hat{R}_k = \frac{1}{N} \sum_{n=-\frac{N}{2}+1}^{\frac{N}{2}} R_n e^{-\frac{2\pi i}{N} nk} \quad \text{with } k \in \left\{ \frac{N}{2} + 1, \dots, \frac{N}{2} \right\}. \quad (3.14)$$

- **Step 2:** $|\hat{R}_k|$ represents the amplitude of the k^{th} wave. To filter out the high frequency experimental noise, we impose a criterion γ such that if $|\hat{R}_k| < \gamma$, \hat{R}_k is set to 0. The

value of γ is optimized by minimizing the cost function $J(\mathbf{C})$ (3.13).

- **Step 3:** Multiply \hat{R}_k by $\frac{i2\pi k}{T}$ to obtain \widehat{DR}_k .
- **Step 4:** Evaluate the inverse DFT of \widehat{DR} :

$$\dot{R}_k = \sum_{k=-\frac{N}{2}+1}^{\frac{N}{2}} \widehat{DR} e^{i2\pi k \frac{n}{N}}. \quad (3.15)$$

- **Step 5:** Solve the least square problem and evaluate the objective function $J(\mathbf{C})$ (3.13).
- **Step 6:** Change γ and return back to Step 2 until the value of the objective function $J(\mathbf{C})$ (3.13) stops decreasing.

We have performed the optimization process using the frequency imposed by the Jarvik device. However, we know that the model parameters are frequency-dependent. Therefore, we assume here that the models (both linear or nonlinear) are valid for all frequencies. This is a strong hypothesis as we use only one frequency to obtain the experimental data. To confirm this hypothesis, we should design an optimization process for large band frequencies and show that the optimal parameters are independent of the input frequency.

3.3 Results and discussion

3.3.1 Comparison of the linear and nonlinear Kelvin-Voigt models

We discuss here the differences in the numerical results obtained with the linear and nonlinear Kelvin-Voigt models (Equation (3.2) and Equation (3.3)) and assess the relative importance of the elastic nonlinear term $E_{nl}\epsilon^2$.

In Figure 3.2, we represent experimental pressure-radius hysteresis loops obtained in the Ascending Aorta (AA) and compare them to the predictions of the linear and nonlinear Kelvin-Voigt models (Equation (3.2) and Equation (3.3)). The estimated viscoelastic parameters of the linear and nonlinear models are presented in Table 3.1. We observe that the linear model fits poorly the curvature observed in the experimental data (Figure 3.2 Left) whereas the nonlinear model accurately predicts the experimental pressure-radius loops (Figure 3.2 Right). A similar observation is made in [Valdez-Jasso et al. 2009], where a stress relaxation constant is integrated into a linear Kelvin-Voigt model.

	$E \times 10^7$	$\phi \times 10^4$
Linear (3.2)	1.475	26.156
Nonlinear (3.3)	1.539	25.451

Table 3.1 – Viscoelastic parameters of the linear and nonlinear Kelvin-Voigt models in the Ascending Aorta.

Furthermore, from the experimental data presented Figure 3.2, we evaluate the order of magnitude of ϵ and find that $\epsilon \approx 10^{-1}$, confirming the observation made in [Segers et al. 1997] that the nonlinear elastic term $E_{nl}\epsilon^2$ is small and therefore can be neglected.

This preliminary analysis shows the necessity of using a nonlinear Kelvin-Voigt model (Equation (3.3)) to describe the viscoelastic properties of the arterial wall.

3.3.2 Validation of the parameter estimation strategy

In Figure 3.3 we present the estimated values of the neutral radius R_0 with error bars. These values compare extremely well the experimentally measured neutral radius represented by

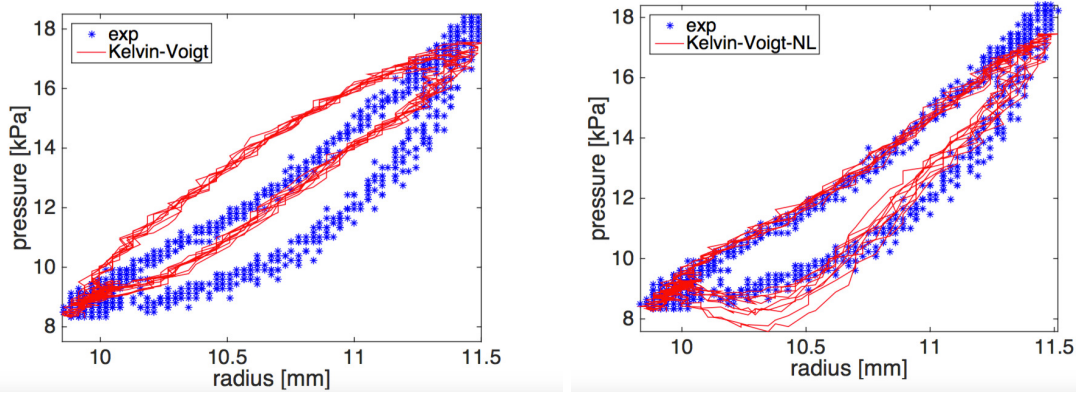


Figure 3.2 – Pressure-radius loop in the Ascending Aorta.

Left: Experimental data (\star) and prediction of the linear Kelvin-Voigt model ($-$).

Right: Experimental data (\star) and prediction of the nonlinear Kelvin-Voigt model ($-$).

Only the nonlinear Kelvin-Voigt model is able to reproduce the curvature of the experimental data.

crosses (\times) in Figure 3.3 and detailed in Table 3.2. In combination with the data presented in Subsection 3.3.1, these results validate the linear regression strategy used to estimate the model parameters.

	AA	PD	MD	DD	BT	CA	FA
Experimental R_0	0.9360	0.8600	0.8500	0.8250	0.8900	0.4060	0.2810
Estimated R_0	0.9489	0.8809	0.8554	0.8286	0.9002	0.4069	0.2826

Table 3.2 – Measured and estimated neutral radius R_0 in the seven arterial sites.

As experimental measurements of neutral vessel radii are only possible in *in vitro* experiments (impossible *in vivo*), this approach could be used in an *in vivo* study to accurately estimate the neutral radius R_0 .

3.3.3 Analysis of the nonlinear Kelvin-Voigt model

In Figure 3.2 and Figure 3.4, we present experimental pressure-radius hysteresis loops obtained in 7 different arterial sites of sheep: the Proximal Descending Aorta, the Medial Descending Aorta, the Distal Descending Aorta, the Brachiocephalic Trunk, the Carotid

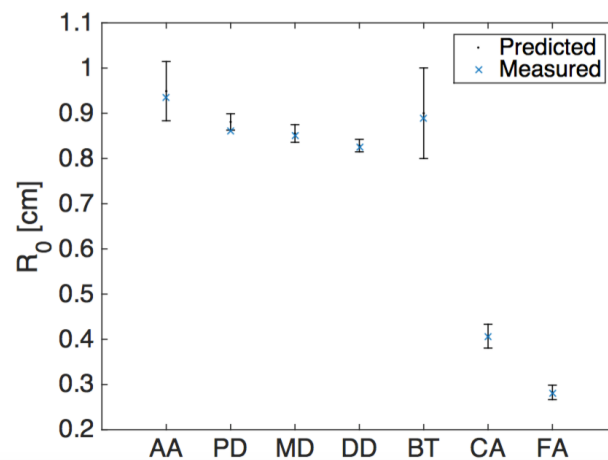


Figure 3.3 – Estimated and measured neutral radius R_0 in the seven arterial sites (Ascending Aorta, Proximal Descending Aorta, Medial Descending Aorta, Distal Descending Aorta, Brachiocephalic Trunk, Carotid Artery, Femoral Artery).

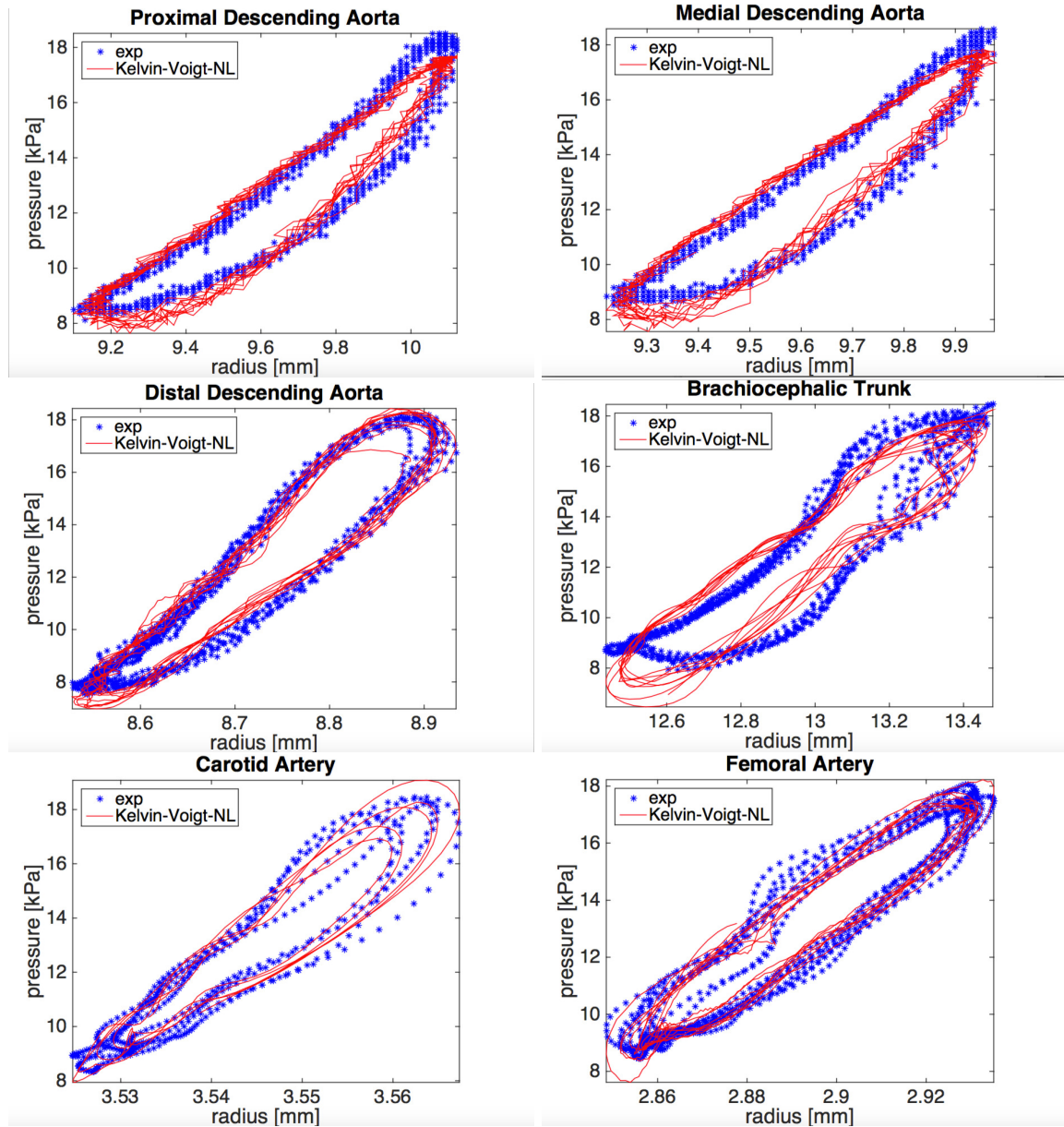


Figure 3.4 – Experimental data (\star) and the fitted nonlinear Kelvin-Voigt model ($-$). Parameter values are found in Table 3.3.

Artery, and the Femoral Artery. For each arterial site, we compare the experimental results to those obtained with the nonlinear Kelvin-Voigt model (3.3). The geometrical and mechanical parameters describing the arterial wall in each arterial site are presented in Table 3.3. We find good agreement everywhere which validates the ability of the nonlinear Kelvin-Voigt model to describe the viscoelastic properties of the arterial wall in large arteries and confirms the validity of the linear regression method used to estimate the model parameters. Finally, we observe that the nonlinearity decreases from the proximal to the distal end of the Aorta and that in the peripheral arteries, represented here by the Carotid and Femoral Arteries, the nonlinearity is negligible.

Next, we perform a detailed analysis of the parameters estimated using the linear regression method and presented in Table 3.3. In Figure 3.5, we plot the estimated values of the Young's modulus E and the viscous coefficient ϕ in the seven selected arterial sites. We observe that the smaller arteries tend to be stiffer, as pointed out by previous studies [Valdez-Jasso et al. 2009, 2011], and that the variations of E and ϕ are similar.

	L	R_0	$h \times 10^{-1}$	$E \times 10^7$	$\phi \times 10^4$
AA	4	0.948	0.38	1.539	25.451
PD	10	0.880	0.91	0.842	12.746
MD	10	0.855	1.26	0.617	11.651
DD	15	0.828	1.10	1.427	24.514
BT	4	0.900	1.06	0.683	12.048
CA	15	0.406	0.78	4.142	77.082
FA	10	0.282	0.31	2.260	43.426

Table 3.3 – Geometrical and mechanical parameters of the simulated arterial tree. The length L is from literature and the thickness h is directly measured. From the optimization process we computed the Young’s modulus E and the viscosity coefficients ϕ and the neutral radius R_0 .

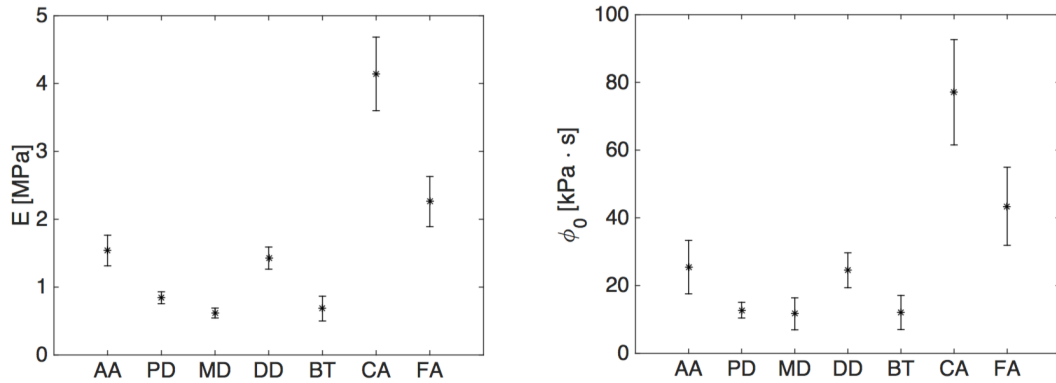


Figure 3.5 – Mean values of the reference Young’s modulus E (Left), and viscosity coefficient ϕ (Right) with standard deviations among the group of sheep at the seven arterial sites.

We therefore represent in Figure 3.6 the ratio ϕ/E and observe that this quantity is indeed constant. This ratio is in fact the relaxation time $t_r = \phi/E$ of the linear Kelvin-Voigt, characterizing the viscous time delay in the response of the arterial wall to external forcing. Assuming that the wall is submitted to a pressure perturbation oscillating at a frequency ω , two mechanical response are expected:

- if $\omega t_r \gg 1$, then the perturbation frequency is too high and the arterial wall filters out these high frequency oscillations;
- if $\omega t_r \ll 1$, the opposite occurs and the wall deforms at the frequency ω , with a phase shift $\delta = \arctan(\omega t_r)$ introduced by viscous wall effects.

Therefore, should the coefficient ϕ remain unchanged, the arteries would be submitted to higher frequency deformations as the Young’s modulus increases when moving distally in the network. The fact that the relaxation time t_r remains constant indicates that the arteries increase their viscous dissipation to compensate the increase in Young’s modulus and maintain the same high-frequency damping behavior. This damping effect may be a protective mechanisms to eliminate high-frequencies before reaching the microcirculation.

	AA	PD	MD	DD	BT	CA	FA
$\frac{\phi_{nl}}{\phi}$	-0.915	-0.999	-0.888	-0.975	-1.380	0.524	-0.395

Table 3.4 – Estimated ratio ϕ_{nl}/ϕ in the seven arterial sites.

Finally the mean values of the ratio ϕ_{nl}/ϕ are presented in Table 3.4 and we observe that:

$$\frac{\phi_{nl}}{\phi} \approx -1. \quad (3.16)$$

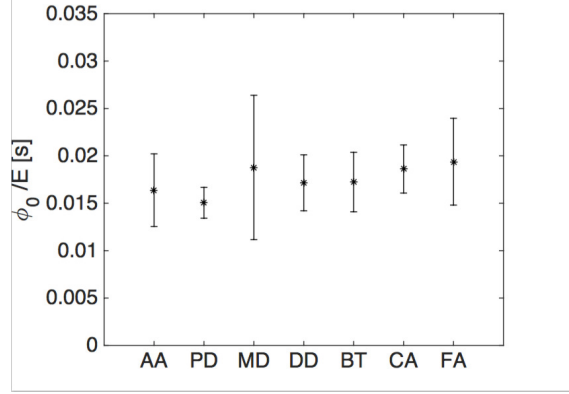


Figure 3.6 – Relaxation time ϕ/E with standard deviations in the seven arterial sites.

This result allows us to estimate the order of magnitude of the viscoelastic linear and nonlinear terms. Writing $\phi\dot{\epsilon} + \phi_{nl}\dot{\epsilon}^2$ as:

$$\phi\dot{\epsilon} \left[1 + \frac{\phi_{nl}}{\phi}\dot{\epsilon} \right], \quad (3.17)$$

and $\dot{\epsilon} = i\omega\epsilon \approx i\omega/10$, we conclude that linear and nonlinear effects are comparable as long as $\omega/10 \sim 1$.

3.4 One-dimensional viscoelastic blood flow equations

In Section 3.2, we have showed the importance of linear and nonlinear viscoelastic effects to accurately capture the deformation of the arterial wall. We must therefore include these effects in the 1D blood flow equations (2.67). We therefore rewrite Equation (3.5) as:

$$p - p_{ext} = K \left[\sqrt{A} - \sqrt{A_0} \right] + K_\nu \frac{\partial A}{\partial t} + K_{\nu, nl} \left[\frac{\partial A}{\partial t} \right]^2, \quad (3.18)$$

where K is given by Equation (2.24) and K_ν and $K_{\nu, nl}$ are defined as:

$$\left\{ \begin{array}{l} K_\nu = \frac{\phi}{1 - \nu_w^2} \frac{\sqrt{\pi}h}{2\sqrt{A_0}} \frac{1}{A} \\ K_{\nu, nl} = \frac{\phi_{nl}}{1 - \nu_w^2} \frac{\sqrt{\pi}h}{4A_0} \frac{1}{A^{\frac{3}{2}}}. \end{array} \right. \quad (3.19a)$$

$$\left\{ \begin{array}{l} K_\nu = \frac{\phi}{1 - \nu_w^2} \frac{\sqrt{\pi}h}{2\sqrt{A_0}} \frac{1}{A} \\ K_{\nu, nl} = \frac{\phi_{nl}}{1 - \nu_w^2} \frac{\sqrt{\pi}h}{4A_0} \frac{1}{A^{\frac{3}{2}}}. \end{array} \right. \quad (3.19b)$$

As in Subsection 2.5.1, we couple the fluid and solid problems by injecting Equation (3.18) into System (2.55):

$$\left\{ \begin{array}{l} \frac{\partial A}{\partial t} + \frac{\partial Q}{\partial x} = 0 \end{array} \right. \quad (3.20a)$$

$$\left\{ \begin{array}{l} \frac{\partial Q}{\partial t} + \frac{\partial}{\partial x} \left[\psi \frac{Q^2}{A} + \frac{K}{3\rho} A^{\frac{3}{2}} \right] = \frac{2\pi R}{\rho} \tau_{rx} + \frac{A}{\rho} \frac{\partial}{\partial x} \left[K_\nu \frac{\partial Q}{\partial x} - K_{\nu, nl} \left[\frac{\partial Q}{\partial x} \right]^2 \right]. \end{array} \right. \quad (3.20b)$$

Unfortunately, contrary to the linear elastic coefficient K , both K_ν and $K_{\nu, nl}$ depend on the variable A which prevents us from writing System (3.20) in a conservative form.

However, we have shown in Subsection 2.6.1 that the deformation of the arterial $\Delta R = 2S_h$ (2.75b), where S_h is the Shapiro number (2.85). In physiological conditions, the flow is subcritical (or quasi-linear) and therefore $S_h \ll 1$. Consequently, we linearize the viscoelastic coefficients K_ν and $K_{\nu, nl}$ around the neutral cross-sectional area A_0 and obtain:

$$\left\{ \begin{array}{l} \frac{\partial A}{\partial t} + \frac{\partial Q}{\partial x} = 0 \end{array} \right. \quad (3.21a)$$

$$\left\{ \begin{array}{l} \frac{\partial Q}{\partial t} + \frac{\partial}{\partial x} \left[\psi \frac{Q^2}{A} + \frac{K}{3\rho} A^{\frac{3}{2}} \right] = \frac{2\pi R}{\rho} \tau_{rx} + C_\nu \frac{\partial^2 Q}{\partial x^2} - C_{\nu, nl} \frac{\partial}{\partial x} \left[\frac{\partial Q}{\partial x} \right]^2, \end{array} \right. \quad (3.21b)$$

where:

$$\left\{ \begin{array}{l} C_\nu = \frac{\phi}{\rho [1 - \nu_w]^2} \frac{\sqrt{\pi} h}{2\sqrt{A_0}} \end{array} \right. \quad (3.22a)$$

$$\left\{ \begin{array}{l} C_{\nu, nl} = \frac{\phi_{nl}}{\rho [1 - \nu_w]^2} \frac{\sqrt{\pi} h}{4A_0^{\frac{3}{2}}}. \end{array} \right. \quad (3.22b)$$

Typically $C_\nu \approx 10^4$ and $C_{\nu, nl} \approx 10^4$. Note here that $C_{\nu, nl}$ is a non-dimensional number.

Finally, using the same velocity profile closure assumptions as in Subsection 2.5.2, we obtain the closed form of the 1D viscoelastic blood flow equations (3.21):

$$\left\{ \begin{array}{l} \frac{\partial A}{\partial t} + \frac{\partial Q}{\partial x} = 0 \end{array} \right. \quad (3.23a)$$

$$\left\{ \begin{array}{l} \frac{\partial Q}{\partial t} + \frac{\partial}{\partial x} \left[\frac{Q^2}{A} + \frac{K}{3\rho} A^{\frac{3}{2}} \right] = -C_f \frac{Q}{A} + C_\nu \frac{\partial^2 Q}{\partial x^2} - C_{\nu, nl} \frac{\partial}{\partial x} \left[\frac{\partial Q}{\partial x} \right]^2. \end{array} \right. \quad (3.23b)$$

An alternative to this linearized approach is proposed in [Montecinos et al. 2014]. The idea is to use a relaxation approach and rewrite System (3.23) in a quasi-linear form using the variables $\Psi = \partial_x Q$ and $\Psi_{nl} = [\partial_x Q]^2$ governed by the following equations:

$$\left\{ \begin{array}{l} \frac{\partial \Psi}{\partial t} = \frac{1}{\epsilon} \left[\frac{\partial Q}{\partial x} - \Psi \right] \end{array} \right. \quad (3.24a)$$

$$\left\{ \begin{array}{l} \frac{\partial \Psi_{nl}}{\partial t} = \frac{1}{\epsilon_{nl}} \left[\left[\frac{\partial Q}{\partial x} \right]^2 - \Psi_{nl} \right]. \end{array} \right. \quad (3.24b)$$

A similar dimensional analysis than the one performed in Subsection 2.6.1 allows us to write System (3.23) in the following non-dimensional form:

$$\left\{ \begin{array}{l} [1 + \Delta_R \bar{R}] \frac{\partial \bar{R}}{\partial \bar{t}} + \frac{\partial \bar{Q}}{\partial \bar{x}} = 0 \end{array} \right. \quad (3.25a)$$

$$\left\{ \begin{array}{l} \frac{\partial \bar{Q}}{\partial \bar{t}} + [2\Delta_R] \frac{\partial}{\partial \bar{x}} \left[\frac{\bar{Q}^2}{[1 + \Delta_R \bar{R}]^2} \right] \\ \quad + \left[2 \frac{\Delta_R}{S_h} \right]^2 [1 + \Delta_R \bar{R}]^2 \frac{\partial \bar{p}}{\partial \bar{x}} = - \left[\frac{1}{\alpha^2} \right] \frac{\bar{Q}}{[1 + \Delta_R \bar{R}]^2} \\ \quad + \left[\frac{1}{\alpha_\nu^2} \right] \frac{\partial^2 \bar{Q}}{\partial \bar{x}^2} - [\epsilon \lambda^2 C_{\nu, nl} S_h] \frac{\partial}{\partial \bar{x}} \left[\frac{\partial \bar{Q}}{\partial \bar{x}} \right]^2, \end{array} \right. \quad (3.25b)$$

where α_ν is the non-dimensional number characterizing the linear viscoelastic effects:

$$\alpha_\nu = c \sqrt{\frac{T}{C_\nu}}. \quad (3.26)$$

The orders of magnitude previously defined enable us to show that $\alpha_\nu \approx 1$, which confirms the importance of viscoelastic effects in large arteries. Concerning the nonlinear viscoelastic effects, a similar analysis shows that $\epsilon \lambda^2 C_{\nu, nl} S_h \approx S_h$. This proves that the nonlinear viscoelastic effects must be accounted for when the flow is critical or supercritical (nonlinear) and $S_h \geq 1$. However, as stated in Subsection 2.6.2, in physiological conditions blood flow is almost always subcritical. We therefore neglect nonlinear viscoelastic effects in the following and set $C_{\nu, nl} = 0$.

Neglecting the nonlinear viscoelastic effects is not in complete contradiction with the results presentend in Section 3.3. Indeed, these results where acquired *ex vivo* in flow conditions more nonlinear than physiological flow conditions.

3.5 Conclusion

In Chapter 3, we have estimated the viscoelasticity of the arterial network of a sheep by examining pressure-radius hysteresis loops. We have found good agreement between the experimental measurements and the proposed nonlinear Kelvin-Voigt model, where the parameters were estimated using a linear regression method. We have shown the damping effect of the wall viscosity on the high frequency waves, especially in the peripheral arteries, and explained this behavior as a defense mechanisms against the rigidification of the peripheral arteries. Finally, we have integrated linear viscoelastic effects into the 1D equations (2.67) governing blood flow in large arteries. Overall, we have shown the importance of viscoelastic effects.

Numerical methods

We present here the *finite volume* and *finite difference* methods we use in practice to solve the 1D viscoelastic blood flow system presented in Chapter 2 and Chapter 3. The text in this chapter deals therefore almost exclusively with numerical methods, and is partly inspired from the following *published* articles:

- O. Delestre, A.R. Ghigo, J.-M. Fullana, and P.-Y. Lagrée. A shallow water with variable pressure model for blood flow simulation. *Networks and Heterogeneous Media*, 11(1):69–87, 2016;
- A.R. Ghigo, O. Delestre, J.-M. Fullana, and P.-Y. Lagrée. Low-Shapiro hydrostatic reconstruction technique for blood flow simulation in large arteries with varying geometrical and mechanical properties. *Journal of Computational Physics*, 331: 108–136, 2017b.

Contents

4.1	Problem splitting	43
4.2	Hyperbolic subproblem	45
4.2.1	Kinetic numerical flux	46
4.2.2	Second-order extensions	47
4.2.3	Subcritical boundary condition	48
4.3	Parabolic and reaction subproblems	50
4.3.1	Parabolic subproblem	50
4.3.2	Reaction subproblem	51
4.3.3	Initial condition	51
4.4	Validation examples in one artery	51
4.4.1	Inviscid tourniquet	51
4.4.2	Inviscid wave propagation	52
4.4.3	Inviscid particular solution	54
4.4.4	Viscous and viscoelastic wave propagation	56
4.4.5	Asymptotic front propagation	58
4.5	Conclusion	62

4.1 Problem splitting

In Chapter 2 and Chapter 3, we have derived the 1D viscoelastic equations (3.23) governing blood flow in large arteries. Unfortunately, System (3.23) is nonlinear and can not be solved analytically. We therefore propose numerical methods to obtain a numerical approximation of the solution of System (3.23) in an artery. To simplify the notations, we write System (3.23)

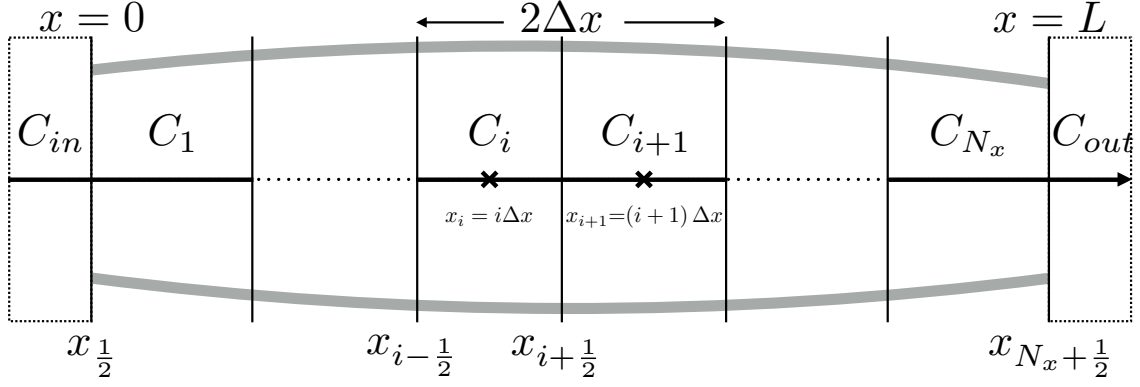


Figure 4.1 – Representation of the spatial mesh with the inlet and outlet ghost cells C_{in} and C_{out} .

in vectorial form:

$$\frac{\partial \mathbf{U}}{\partial t} + \frac{\partial \mathbf{F}}{\partial x} = \mathbf{S}_f + \mathbf{S}_\nu. \quad (4.1)$$

Vectors $\mathbf{U} = [A, Q]^\top$ and $\mathbf{F} = [F_A, F_Q]^\top$ are respectively defined by Equation (2.79) and Equation (2.80). The vectors \mathbf{S}_f and \mathbf{S}_ν represent the viscous and viscoelastic source terms and write:

$$\mathbf{S}_f = \begin{bmatrix} 0 \\ -C_f \frac{Q}{A} \end{bmatrix}, \quad (4.2)$$

and

$$\mathbf{S}_\nu = \begin{bmatrix} 0 \\ C_\nu \frac{\partial^2 Q}{\partial x^2} \end{bmatrix}. \quad (4.3)$$

The first step towards obtaining a numerical approximation of the solution of System (4.1) is to discretize both time and space. We first divide the time domain using a constant time step Δt and the discrete times are defined as:

$$t^n = n\Delta t, \quad n \in \{0, \dots, N_t\}, \quad (4.4)$$

and the final time $t_f = N_t\Delta t$. We note $\mathbf{U}^n = \mathbf{U}(t^n)$. We then introduce a mesh in the axial direction and divide the length L of the artery in a series of cells C_i defined as:

$$C_i = \left[x_{i-1/2}, x_{i+1/2} \right] = [(i-1)\Delta x, i\Delta x] \quad \text{for } i \in \{1, \dots, N_x\}, \quad (4.5)$$

where Δx is the cell size, supposed constant for simplicity, and $L = N_x\Delta x$. This spatial mesh is represented in Figure 4.1.

In Subsection 2.6.2, we have shown that System (4.1), in the absence of friction and viscoelastic source terms, is hyperbolic. On the contrary, the viscoelastic source term \mathbf{S}_ν has a parabolic mathematical structure. We therefore decompose System (4.1) into three subproblems:

Hyperbolic subproblem

$$\frac{\partial \mathbf{U}}{\partial t} + \frac{\partial \mathbf{F}}{\partial x} = 0. \quad (4.6)$$

Parabolic subproblem

$$\frac{\partial \mathbf{U}}{\partial t} = \mathbf{S}_\nu. \quad (4.7)$$

Reaction subproblem

$$\frac{\partial \mathbf{U}}{\partial t} = \mathbf{S}_f. \quad (4.8)$$

Following [Wang et al. 2015], we use a first-order Godunov operator splitting technique

[LeVeque 2002] to combine the solution of each subproblem and update the numerical solution from time t^n to time t^{n+1} in each cell C_i :

$$\begin{cases} A_i^n \xrightarrow{\text{Sys. (4.6)}} A_i^{n+1} \\ Q_i^n \xrightarrow{\text{Sys. (4.6)}} Q_i^* \xrightarrow{\text{Sys. (4.7)}} Q_i^{**} \xrightarrow{\text{Sys. (4.8)}} Q_i^{n+1}. \end{cases} \quad (4.9)$$

4.2 Hyperbolic subproblem

We first solve the hyperbolic System (4.6) describing pulse wave propagation. Multiple approaches have been used and include essentially finite element methods such as Galerkin [Sherwin et al. 2003a; Mynard and Nithiarasu 2008] and Taylor-Galerkin [Martin et al. 2005; Formaggia et al. 2006; Melicher and Gajdošík 2008] methods, discontinuous Galerkin methods [Xiu and Sherwin 2007; Willemet et al. 2011; Alastruey et al. 2011; Puelz et al. 2017], finite difference methods [Saito et al. 2011; Fullana and Zaleski 2009; Wang et al. 2015] and finite volume methods [Cavallini et al. 2008; Cavallini and Coscia 2010; Delestre and Lagrée 2013; Müller and Toro 2014; Montecinos et al. 2014; Murillo and García-Navarro 2015; Audebert et al. 2017b]. These methods are compared in [Wang et al. 2015; Boileau et al. 2015] in a series of test cases and give similar results. The choice of the numerical method used to solve System (4.6) is therefore left to the user's preference. Coming from a fluid mechanics background, we select a *finite volume* approach allowing us to derive a robust, conservative and shock-capturing numerical scheme preserving the positivity of the numerical solution if the chosen numerical flux is positive [Bouchut 2004].

To obtain a *finite volume* numerical scheme, we first derive the integral form of the conservative System (4.6) by integrating it with respect to t and x over $]t^n, t^*[\times C_i$:

$$\int_{C_i} [\mathbf{U}^* - \mathbf{U}^n] dx + \int_{t^n}^{t^*} [\mathbf{F}|_{x_{i+\frac{1}{2}}} - \mathbf{F}|_{x_{i-\frac{1}{2}}}] dt = 0. \quad (4.10)$$

We then approximate the integrals in System (4.10) using the discrete vector of conservative variables \mathbf{U}_i^n and the numerical flux vector $\mathbf{F}_{i+\frac{1}{2}}^n$, corresponding respectively to an approximation of the space average of the exact solution vector \mathbf{U} over the cell C_i at time t^n :

$$\mathbf{U}_i^n \approx \frac{1}{\Delta x} \int_{C_i} \mathbf{U}^n dx, \quad (4.11)$$

and to an approximation of the time average of the flux vector \mathbf{F} at the cell interface $x_{i+\frac{1}{2}}$:

$$\mathbf{F}_{i+\frac{1}{2}}^n \approx \frac{1}{\Delta t} \int_{t^n}^{t^*} \mathbf{F}|_{x_{i+\frac{1}{2}}} dt. \quad (4.12)$$

Using these definitions, we obtain the explicit *finite volume* numerical scheme:

$$\mathbf{U}_i^* = \mathbf{U}_i^n - \frac{\Delta t}{\Delta x} [\mathbf{F}_{i+\frac{1}{2}}^n - \mathbf{F}_{i-\frac{1}{2}}^n]. \quad (4.13)$$

We define $\mathbf{F}_{i+\frac{1}{2}}^n$ as a two-points numerical flux vector, namely:

$$\mathbf{F}_{i+\frac{1}{2}}^n = \mathcal{F}(\mathbf{U}_L, \mathbf{U}_R) = \begin{bmatrix} \mathcal{F}_A(\mathbf{U}_L, \mathbf{U}_R) \\ \mathcal{F}_Q(\mathbf{U}_L, \mathbf{U}_R) \end{bmatrix}. \quad (4.14)$$

The vectors \mathbf{U}_L and \mathbf{U}_R correspond respectively to numerical approximations of the vector \mathbf{U}^n at the left and right of the cell interface $x_{i+\frac{1}{2}}$ and are defined in Subsection 4.2.2. The vector function \mathcal{F} is the numerical flux and is defined in Subsection 4.2.1.

4.2.1 Kinetic numerical flux

We choose to compute the vector function \mathcal{F} using a kinetic approach, and a review of this method applied to different systems of equations can be found in [Bouchut 1999]. The kinetic method was first introduced for shallow water equations in [Perthame and Simeoni 2001] and adapted to the blood flow in [Delestre and Lagrée 2013; Audebert et al. 2017b; Ghigo et al. 2017b]. Our principal motivation for choosing a kinetic numerical flux is that it does not require information on the characteristic structure of the jacobian matrix \mathbf{J} (2.82), which proves useful in Chapter 8 to solve the multiring system of equations (8.21). Additionally, the kinetic flux is suitable for the computation of venous blood flow [Audebert et al. 2017b]. Other possible numerical fluxes are presented in [Delestre and Lagrée 2013; Müller et al. 2013; Wang et al. 2015; Murillo and García-Navarro 2015; Müller et al. 2016a; Audebert et al. 2017b].

Following [Perthame and Simeoni 2001; Audusse and Bristeau 2005], we introduce the real, positive, even and compactly supported function χ , verifying the properties:

$$\chi(-w) = \chi(w) \quad \text{and} \quad \int_{\mathbb{R}} \chi(w) dw = \int_{\mathbb{R}} w^2 \chi(w) dw = 1. \quad (4.15)$$

We choose the function χ as:

$$\chi(w) = \begin{cases} \frac{1}{2\sqrt{3}} & \text{if } |w| \leq \sqrt{3} \\ 0 & \text{else.} \end{cases} \quad (4.16)$$

We then define the kinetic Maxwellian, or so-called *Gibbs equilibrium*, which represents the density of microscopic particles moving at the velocity $\xi \in \mathbb{R}$:

$$M(x, t, \xi) = M(A, \xi - u) = \frac{A(x, t)}{\tilde{c}} \chi\left(\frac{\xi - u}{\tilde{c}}\right), \quad (4.17)$$

where:

$$\tilde{c} = \sqrt{\frac{K}{3\rho}} \sqrt{A}. \quad (4.18)$$

Noticing that the integral and the first and second moments on \mathbb{R} of M respectively allow to recover A , Q and F , it can be proved [Perthame and Simeoni 2001] that \mathbf{U} is solution of System (4.6) if and only if M satisfies the following linear kinetic equation:

$$\frac{\partial M}{\partial t} + \xi \frac{\partial M}{\partial x} = \mathcal{Q}(x, t, \xi), \quad (4.19)$$

where \mathcal{Q} is a collision term that satisfies:

$$\int_{\mathbb{R}} \mathcal{Q} d\xi = \int_{\mathbb{R}} \xi \mathcal{Q} d\xi = 0. \quad (4.20)$$

As Equation (4.19) is linear, it can be approximated by a simple upwind scheme. The flux function \mathcal{F} is then obtained using the integral and the first moment of the upwind numerical flux used to solve the linear kinetic equation (4.19), and writes:

$$\mathcal{F}(\mathbf{U}_L, \mathbf{U}_R) = \mathcal{F}^+(\mathbf{U}_L) + \mathcal{F}^-(\mathbf{U}_R), \quad (4.21)$$

where fluxes \mathcal{F}^+ and \mathcal{F}^- are defined as:

$$\mathcal{F}^+ = \int_{\xi \geq 0} \xi \begin{bmatrix} 1 \\ \xi \end{bmatrix} M(A, \xi - u) d\xi \quad \text{and} \quad \mathcal{F}^- = \int_{\xi \leq 0} \xi \begin{bmatrix} 1 \\ \xi \end{bmatrix} M(A, \xi - u) d\xi. \quad (4.22)$$

Using Equation (4.17), we find that:

$$\mathcal{F}^+ = \frac{A}{2\sqrt{3}\tilde{c}} \begin{bmatrix} \frac{1}{2} \left((\xi_p^+)^2 - (\xi_m^+)^2 \right) \\ \frac{1}{3} \left((\xi_p^+)^3 - (\xi_m^+)^3 \right) \end{bmatrix} \quad \text{and} \quad \mathcal{F}^- = \frac{A}{2\sqrt{3}\tilde{c}} \begin{bmatrix} \frac{1}{2} \left((\xi_p^-)^2 - (\xi_m^-)^2 \right) \\ \frac{1}{3} \left((\xi_p^-)^3 - (\xi_m^-)^3 \right) \end{bmatrix}, \quad (4.23)$$

and the function minmod is a slope limiter defined as:

$$\text{minmod}(x, y) = \begin{cases} \min(x, y) & \text{if } x, y \geq 0 \\ \max(x, y) & \text{if } x, y \leq 0 \\ 0 & \text{else} \end{cases} \quad (4.30)$$

and designed to prevent non-physical oscillations of the numerical solution. We finally obtain a second-order scheme by choosing at each cell interface $x_{i+\frac{1}{2}}$:

$$\begin{cases} U_L = U_{i+\frac{1}{2}}^{+,n} \\ U_R = U_{i+\frac{1}{2}}^{-,n} \end{cases} \quad (4.31a)$$

$$\begin{cases} U_L = U_{i+\frac{1}{2}}^{+,n} \\ U_R = U_{i+\frac{1}{2}}^{-,n} \end{cases} \quad (4.31b)$$

where $U_{i+\frac{1}{2}}^{+,n}$ and $U_{i+\frac{1}{2}}^{-,n}$ are obtained using the MUSCL reconstruction previously defined. As a reminder, vector \mathbf{U} contains the conservative variables A and Q , which are therefore the variables we reconstruct here. We also reconstruct the arterial wall rigidity K as it plays a role in the computation of the numerical flux (4.14).

Second-order time integration

To increase the temporal order of accuracy of the numerical scheme, we use a second-order Adam-Bashforth (AB2) integration scheme initialized by a Strong Stability Preserving second-order Runge-Kutta (SSPRK2 or Heun) integration scheme [Gottlieb 2005]:

SSPRK2

$$\begin{cases} U_i^{*,1} = U_i^n + \Delta t \mathbf{RHS}_{Sys.(4.6)}(U_i^n) \\ U_i^{*,2} = U_i^{*,1} + \Delta t \mathbf{RHS}_{Sys.(4.6)}(U_i^{*,1}) \\ U_i^* = U_i^n + \frac{\Delta t}{2} \left[\mathbf{RHS}_{Sys.(4.6)}(U_i^n) + \mathbf{RHS}_{Sys.(4.6)}(U_i^{*,1}) \right] \end{cases} \quad (4.32)$$

AB2

$$U_i^* = U_i^n + \Delta t \left[\frac{3}{2} \mathbf{RHS}_{Sys.(4.6)}(U_i^n) - \frac{1}{2} \mathbf{RHS}_{Sys.(4.6)}(U_i^{n-1}) \right] \quad (4.33)$$

We choose the AB2 integration scheme (4.33) to facilitate the use of time-dependent boundary conditions. Indeed, it does not require any intermediate boundary condition, contrary to the SSPRK2 integration scheme (4.32). Moreover, AB2 requires one less time integration step than SSPRK2.

Once U_i^* is computed, we use the discrete parabolic and reaction schemes, described in Subsection 4.3.1 and Subsection 4.3.2, to compute U_i^{**} and then U_i^{n+1} .

4.2.3 Subcritical boundary condition

The hyperbolic System (4.6) describes the leading-order wave propagation behavior of blood flow. Boundary conditions must therefore be imposed in the hyperbolic framework of System (4.6). In each artery at time t^n , we impose these hyperbolic boundary conditions in inlet and outlet ghost cells, respectively noted C_{in} and C_{out} , by setting the value of their associated vector of conservative variable $U_{in}^n = [A_{in}^n, Q_{in}^n]^T$ and $U_{out}^n = [A_{out}^n, Q_{out}^n]^T$. As we compute subcritical solutions of system (4.6) in \mathbb{U}_{sub} , one boundary condition is imposed in the inlet ghost cell C_{in} and one boundary condition is imposed in the outlet ghost cell C_{out} , respectively allowing to determine one component of U_{in}^n and one component of U_{out}^n . To compute the remaining unknown components of U_{in}^n and U_{out}^n , we follow methodologies proposed in [Bristeau and Coussin 2001; Alastruey et al. 2008], assuming that in each cell C_i at time t^n , the discrete vector of conservative variables U_i^n is known. As the implementation

of inlet and outlet boundary conditions is very similar, we describe only the derivation of the inlet boundary conditions.

Imposed flow rate Q_{in}

We describe here a methodology to impose the flow rate $Q_{in}(t^n) = Q_{in}^n$ at the interface between the first cell of the computational domain C_1 and the inlet ghost cell C_{in} , namely:

$$\mathcal{F}_A(\mathbf{U}_{in}^n, \mathbf{U}_1^n) = Q_{in}^n. \quad (4.34)$$

Taking advantage of the fact that the kinetic flux function \mathcal{F}_A can be split in two parts, Equation (4.34) rewrites:

$$\mathcal{F}_A^+(\mathbf{U}_{in}^n) + \mathcal{F}_A^-(\mathbf{U}_1^n) = Q_{in}^n. \quad (4.35)$$

To ensure the stability of the scheme, this condition is imposed in an upwind manner. Following [Bristeau and Coussin 2001], we define the quantity:

$$a_1 = Q_{in}^n - \mathcal{F}_A^-(\mathbf{U}_1^n), \quad (4.36)$$

and distinguish two cases:

- If $a_1 \leq 0$, the dominant part of the information is coming from inside the computational domain. As we are performing an upwind evaluation of the inlet boundary condition, we impose:

$$\begin{cases} \mathcal{F}_A^+(\mathbf{U}_{in}^n) = 0 & (4.37a) \\ \mathcal{F}_Q^+(\mathbf{U}_{in}^n) = 0. & (4.37b) \end{cases}$$

- If $a_1 > 0$, the dominant part of the information is coming from outside the computational domain. In this case, we impose:

$$\begin{cases} \mathcal{F}_A^+(\mathbf{U}_{in}^n) = a_1 & (4.38a) \\ W_1(\mathbf{U}_{in}^n) = W_1(\mathbf{U}_1^n). & (4.38b) \end{cases}$$

Equation (4.38b) translates the fact that the Riemann invariant $W_1(\mathbf{U}_{in}^n)$ (2.88) is constant along the outgoing characteristic and that it can be correctly estimated by $W_1(\mathbf{U}_1^n)$.

The vector \mathbf{U}_{in}^n is obtained by solving either System (4.37) or System (4.38) using a Newton's method in a limited number of iterations (~ 5).

Imposed cross-sectional area A_{in} .

We describe here a methodology to impose the cross-sectional area $A_{in}(t^n) = A_{in}^n$ at the inlet of the computational domain. We first set this value in the inlet ghost cell C_{in} . We then compute Q_{in}^n to completely determine the inlet vector of conservative variables \mathbf{U}_{in}^n . To do so, we use Equation (4.38b) and solve the following system:

$$\begin{cases} W_1(\mathbf{U}_{in}^n) = W_1(\mathbf{U}_1^n) & (4.39a) \\ W_2(\mathbf{U}_{in}^n) = W_1(\mathbf{U}_{in}^n) + 8c_{in}^n. & (4.39b) \end{cases}$$

We then compute \mathbf{U}_{in}^n using the relations (2.89).

Imposed characteristic reflection $R_{t,in}$

We propose here a methodology to reflect part of the outgoing information at the inlet of the computational domain. In practice, we estimate the incoming Riemann invariant $W_2(\mathbf{U}_{in}^n)$ as a fraction R_t of the outgoing Riemann invariant $W_1(\mathbf{U}_{in}^n)$ [Wang et al. 2015; Alastruey et al. 2008, 2009; Murillo and García-Navarro 2015]. To do so, we use Equation (4.38b) and

solve the following system:

$$\begin{cases} W_1(\mathbf{U}_{in}^n) = W_1(\mathbf{U}_1^n) & (4.40a) \\ W_2(\mathbf{U}_{in}^n) - W_2(\mathbf{U}_{in}^0) = -R_t [W_1(\mathbf{U}_{in}^n) - W_1(\mathbf{U}_{in}^0)] & (4.40b) \end{cases}$$

where $W_1(\mathbf{U}_{in}^0)$ and $W_2(\mathbf{U}_{in}^0)$ are the initial Riemann invariants of the ghost cell C_{in} . We then compute \mathbf{U}_{in}^n using the relations (2.89).

The methodologies described here are only first-order accurate, preventing ever reaching second-order accuracy in boundary-dominated problems.

4.3 Parabolic and reaction subproblems

4.3.1 Parabolic subproblem

We now solve the parabolic System (4.7) describing viscoelastic effects. Following [Wang et al. 2015], we choose a semi-implicit unconditionally stable second-order Crank-Nicolson *finite difference* scheme, which writes in the cell C_i as:

$$-\alpha_{cn}Q_{i-1}^{**} + [1 + 2\alpha_{cn}]Q_i^{**} - \alpha_{cn}Q_{i+1}^{**} = \alpha_{cn}Q_{i-1}^* + [1 - 2\alpha_{cn}]Q_i^* + \alpha_{cn}Q_{i+1}^*, \quad (4.41)$$

where:

$$\alpha_{cn} = C_\nu \frac{\Delta t}{2\Delta x^2}. \quad (4.42)$$

We then provide homogeneous Neumann boundary conditions in the cells C_1 and C_{N_x} , written here in discrete form:

$$\begin{cases} Q_{in}^{*,**} = Q_1^{*,**} & (4.43a) \\ Q_{out}^{*,**} = Q_{N_x}^{*,**} & (4.43b) \end{cases}$$

Combining Equation (4.41) and the boundary conditions 4.43, we write the Crank-Nicolson *finite difference* scheme in matrix form:

$$\mathbf{A}\mathbf{Q}^{**} = \mathbf{B}\mathbf{Q}^*, \quad (4.44)$$

where:

$$\mathbf{A} = \begin{bmatrix} 1 + 2\alpha_{cn} & -2\alpha_{cn} & & & & \\ -\alpha_{cn} & 1 + 2\alpha_{cn} & -\alpha_{cn} & & & \\ & \ddots & \ddots & \ddots & & \\ & & -\alpha_{cn} & 1 + 2\alpha_{cn} & -\alpha_{cn} & \\ & & & -2\alpha_{cn} & 1 + 2\alpha_{cn} & \end{bmatrix}, \quad (4.45)$$

and:

$$\mathbf{B} = \begin{bmatrix} 1 - 2\alpha_{cn} & 2\alpha_{cn} & & & & \\ \alpha_{cn} & 1 - 2\alpha_{cn} & \alpha_{cn} & & & \\ & \ddots & \ddots & \ddots & & \\ & & \alpha_{cn} & 1 - 2\alpha_{cn} & \alpha_{cn} & \\ & & & 2\alpha_{cn} & 1 - 2\alpha_{cn} & \end{bmatrix}. \quad (4.46)$$

We solve System (4.44) using the Thomas algorithm [Thomas 1949], well-suited for solving tridiagonal matrix systems.

The boundary conditions (4.43) are more or less equivalent to neglecting viscoelastic effects in the boundary cells. In [Müller et al. 2016b], this approximation is shown to give small inconsistencies of the physical solutions at the inlet and outlet of the artery.

4.3.2 Reaction subproblem

We finally solve the reaction System (4.8) describing viscous effects. As the source term \mathbf{S}_f (4.2) does not involve any spatial gradients, we simply solve System (4.8) using the explicit time integration scheme presented in Subsection 4.2.2. Such an approach is possible as the viscous effects are always dissipative (opposite to the flow direction), the arteries do not collapse and the cross-sectional area A never goes to zero. For shallow-water equations, such an explicit numerical treatment is not possible as transitions between wet and dry states occur. Overall, our main motivation to use this approach is consistency with the treatment of the time-dependent non-Newtonian viscous model presented in Chapter 9.

Other approaches are possible, such as the semi-implicit formulation:

$$Q_i^{n+1} = \frac{Q_i^{**}}{1 + \frac{C_f \Delta t}{A_i^{n+1}}}. \quad (4.47)$$

4.3.3 Initial condition

Most numerical simulations presented in this study are initialized by the following solution of System (4.1):

$$Q = 0 \quad \text{and} \quad A = A_0, \quad (4.48)$$

and the initial vector of conservative variable in the cell C_i is then:

$$\mathbf{U}_i^0 = \begin{bmatrix} A_{0,i} \\ 0 \end{bmatrix}. \quad (4.49)$$

4.4 Validation examples in one artery

We present a series of test cases in a single uniform artery, designed to assess the implementation of the different numerical schemes and their respective boundary conditions. In each test case, we systematically compare the results obtained with the first-order and MUSCL variable reconstructions and assess the accuracy of both methods using the following L_1 , L_2 and L_∞ errors:

$$\left\{ \begin{array}{l} L_1 [s] = \frac{1}{L} \int_{x=0}^L |s - s_{ref}| dx \end{array} \right. \quad (4.50a)$$

$$\left\{ \begin{array}{l} L_2 [s] = \sqrt{\frac{1}{L} \int_{x=0}^L |s - s_{ref}|^2 dx} \end{array} \right. \quad (4.50b)$$

$$\left\{ \begin{array}{l} L_\infty [s] = \max_{x \in L} (|s - s_{ref}|). \end{array} \right. \quad (4.50c)$$

which represent the differences between a reference solution and the corresponding numerical solution. More particularly, we plot the evolution of these errors with the number cells N_x to assess the convergence and accuracy of the numerical schemes. The convergence error of a first-order numerical solution is expected to decrease at the rate 10^{-N_x} , whereas the convergence error of a second-order numerical scheme is expected to decrease at the rate 10^{-2N_x} .

4.4.1 Inviscid tourniquet

A tourniquet (garrot in french) is a compressing device used to temporarily occlude arteries and veins. We describe here the inviscid elastic relaxation of an artery initially occluded by

a tourniquet:

$$\begin{cases} A(x, t = 0) = \begin{cases} A_L = A_0 [1 + S_h]^2 & \text{if } x \in \left[-\frac{L}{2}, 0\right] \\ A_R = A_0 & \text{if } x \in \left]0, \frac{L}{2}\right] \end{cases} \\ Q(x, t = 0) = 0. \end{cases} \quad (4.51a)$$

We recall that the Shapiro number $S_h = 2\Delta R$ (2.76b), which explains the parametrization of Equation (4.51). This test case is in fact a Riemann problem, first introduced in compressible gas dynamics with the Sod tube (see [Lighthill 1978; LeVeque 1992]) and extended to blood flow in [Delestre and Lagrée 2013]. The inviscid nonlinear solution of this Riemann problem is obtained using the method of characteristics and we refer the reader to [Delestre and Lagrée 2013; Delestre et al. 2016] for further details.

In addition to the initial condition (4.51), we impose non-reflecting boundary conditions at each end of the artery to remove any backward traveling wave and suppress the effect of boundary conditions. The parameters used in this test case are described in Table 4.1.

ρ	L	R_0	K	C_f	C_ν	S_h	R_t	Δt	t	order
1	10	1	10^4	0	0	10^{-1}	0	10^{-5}	2	

Table 4.1 – Geometrical, mechanical, numerical and boundary parameters used in the inviscid tourniquet test case.

In Figure 4.2 Left, we compare at times $t \in \{0, 0.001, 0.002, 0.003, 0.004\}$ the spatial evolution of the analytic solutions for the cross-sectional area A , the flow rate Q and the average velocity U with the spatial evolution of the first-order and MUSCL numerical solutions obtained with $N_x = 100$. We observe that for each variable, the analytic solution is correctly described and the MUSCL solution is more accurate than the first-order solution.

For larger values of N_x such as $N_x = 3200$, the analytic and numerical solutions are almost indiscernible.

In Figure 4.2 Right, we plot at time $t = 0.002$ the evolution with the number of cells N_x of the first-order and MUSCL L_1 , L_2 and L_∞ errors for the cross-sectional area A , the flow rate Q and the average velocity U . We observe that for each variable, the L_1 and L_2 errors decrease with an increasing number of cells N_x , indicating that the first-order and MUSCL numerical solutions converge towards the analytic solution. However, only first-order accuracy is achieved as the analytic solutions are discontinuous. This is highlighted in particular by the L_∞ error that does not decrease when the number of cells N_x is increased as the error at the discontinuities remains constant.

4.4.2 Inviscid wave propagation

We reproduce a test case presented in [Delestre and Lagrée 2013; Delestre et al. 2016] describing the linear inviscid propagation of a pulse wave starting from an initial perturbation of the cross-sectional area A of the artery:

$$\begin{cases} A(x, t = 0) = \begin{cases} A_0 \left[1 + S_h \cos \left(\pi + 2\pi \frac{x - x_s}{x_e - x_s} \right) \right] & \text{if } x_s \leq x \leq x_e \\ A_0 & \text{else} \end{cases} \\ Q(x, t = 0) = 0, \end{cases} \quad (4.52a)$$

$$(4.52b)$$

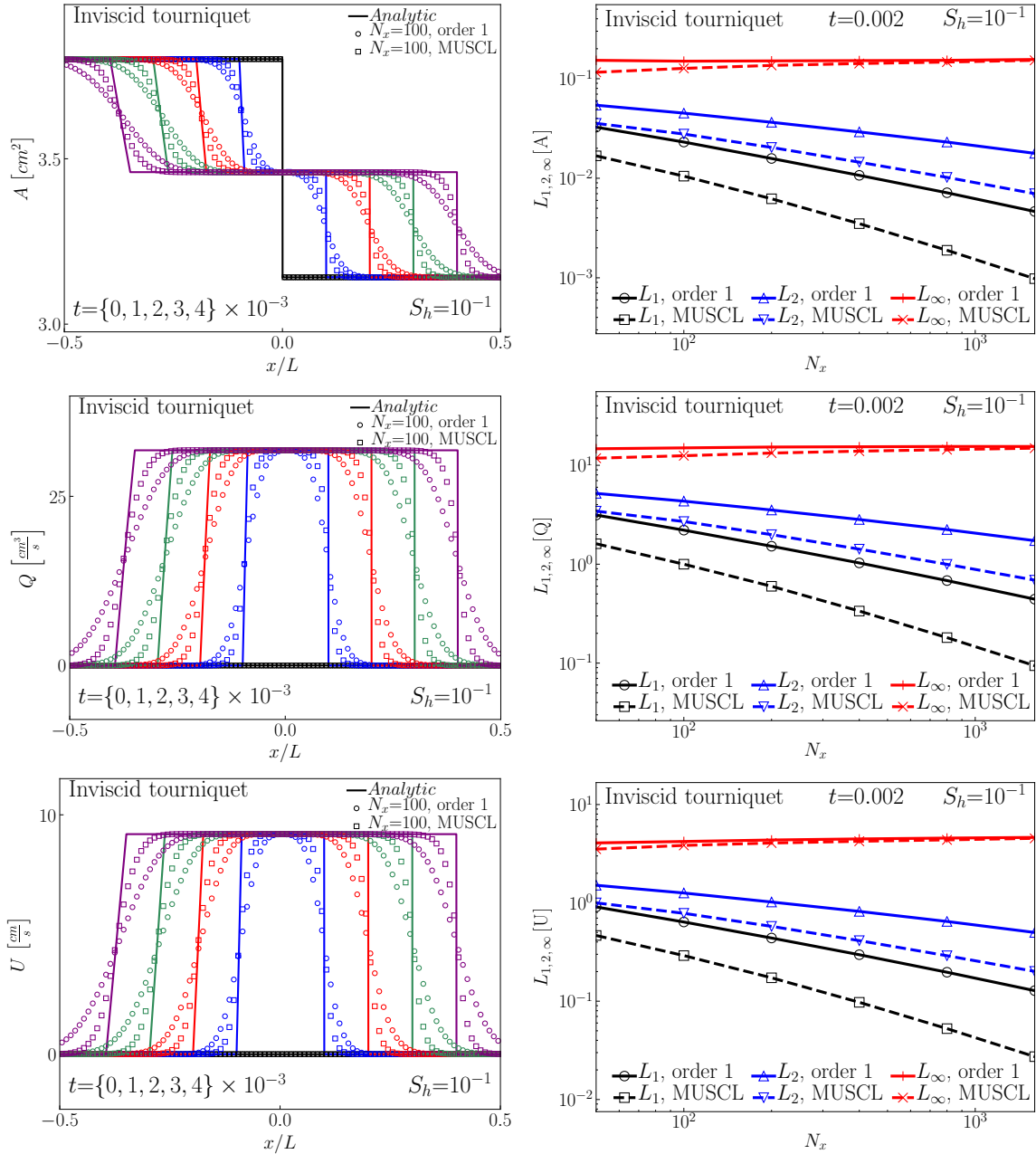


Figure 4.2 – The inviscid tourniquet test case:

Left: Comparison between the analytic solution (—) and the first-order (○) and MUSCL (□) numerical solutions obtained with $N_x = 100$ at times $t \in \{0, 0.001, 0.002, 0.003, 0.004\}$.

Right: Spatial convergence of the first-order (○, △, +) and MUSCL (□, ▽, ×) L_1 , L_2 and L_∞ errors obtained at time $t = 0.002$ with $N_x \in \{50, 100, 200, 400, 800, 1600\}$.

The first-order and MUSCL solutions converge towards the analytic solution. However, only first-order accuracy is achieved as the analytic solution is discontinuous.

where $x_s = \frac{2}{5L}$ and $x_e = \frac{3}{5L}$. Once again, we use the Shapiro number S_h (2.85) to parametrize the perturbation of the cross-sectional area A , chosen small to remain in the linear regime. The solution described here is a linear inviscid solution of System (3.23), which reduces in this case to the well-known d'Alembert equation.

In addition to the initial condition (4.52), we impose non-reflecting boundary conditions at each end of the artery to remove any backward traveling wave and suppress the effect of boundary conditions. The parameters used in this test case are described in Table 4.2.

ρ	L	R_0	K	C_f	C_ν	S_h	R_t	Δt	t	order
1	10	1	10^4	0	0	$\{10^{-3}, 10^{-4}, 10^{-5}\}$	0	10^{-5}		2

Table 4.2 – Geometrical, mechanical, numerical and boundary parameters used in the inviscid wave propagation test case.

In Figure 4.3 Left, we compare at times $t \in \{0, 0.001, 0.002, 0.003, 0.004\}$ the spatial evolution of the linear wave solution for the cross-sectional area A , the flow rate Q and the average velocity U with the spatial evolution of the first-order and MUSCL numerical solutions obtained with $N_x = 100$ for $S_h = 10^{-3}$. We observe that for each variable, the linear wave solution is correctly described and the MUSCL solution is more accurate than the first-order solution.

In Figure 4.3 Right, we plot at time $t = 0.002$ the evolution with the number of cells N_x of the first-order and MUSCL L_1 errors for the cross-sectional area A , the flow rate Q and the average velocity U obtained for $S_h \in \{10^{-3}, 10^{-4}, 10^{-5}\}$. We observe that for each variable and each value of S_h , the L_1 errors decrease with an increasing number of cells N_x , indicating that the first-order and MUSCL numerical solutions converge towards the analytic solution. However, only first-order accuracy is achieved. Indeed, for large values of N_x , the MUSCL L_1 error saturates and remains constant as the error reaches the amplitude of the nonlinearity of the numerical solution, proportional to S_h . Indeed, the analytic wave propagation solutions described here are linear whereas the numerical solutions are intrinsically nonlinear.

4.4.3 Inviscid particular solution

We derive an inviscid particular solution of System (3.23) driven mainly by the inlet and outlet boundary conditions. We search for a solution of the form:

$$\begin{cases} A = a(t)x + b(t) & (4.53a) \\ U = c(t)x + d(t), & (4.53b) \end{cases}$$

describing the elastic relaxation of an artery towards its equilibrium state. Injecting the expressions (4.53a) and (4.53b) in the inviscid System (3.23), rewritten in nonconservative form, we obtain the following ordinary differential equations for the quantities a , b , c and d :

$$\begin{cases} a = 0 \\ b' + bc = 0 \\ c' + c^2 = 0 \\ d' + dc = 0. \end{cases} \quad (4.54)$$

Finally, we obtain the expressions for the cross-sectional area A and the average velocity U :

$$A = \frac{C_2}{C_1 + t} \quad (4.55a)$$

$$U = \frac{C_3 + x}{C_1 + t} \quad (4.55b)$$

$$Q = AU, \quad (4.55c)$$

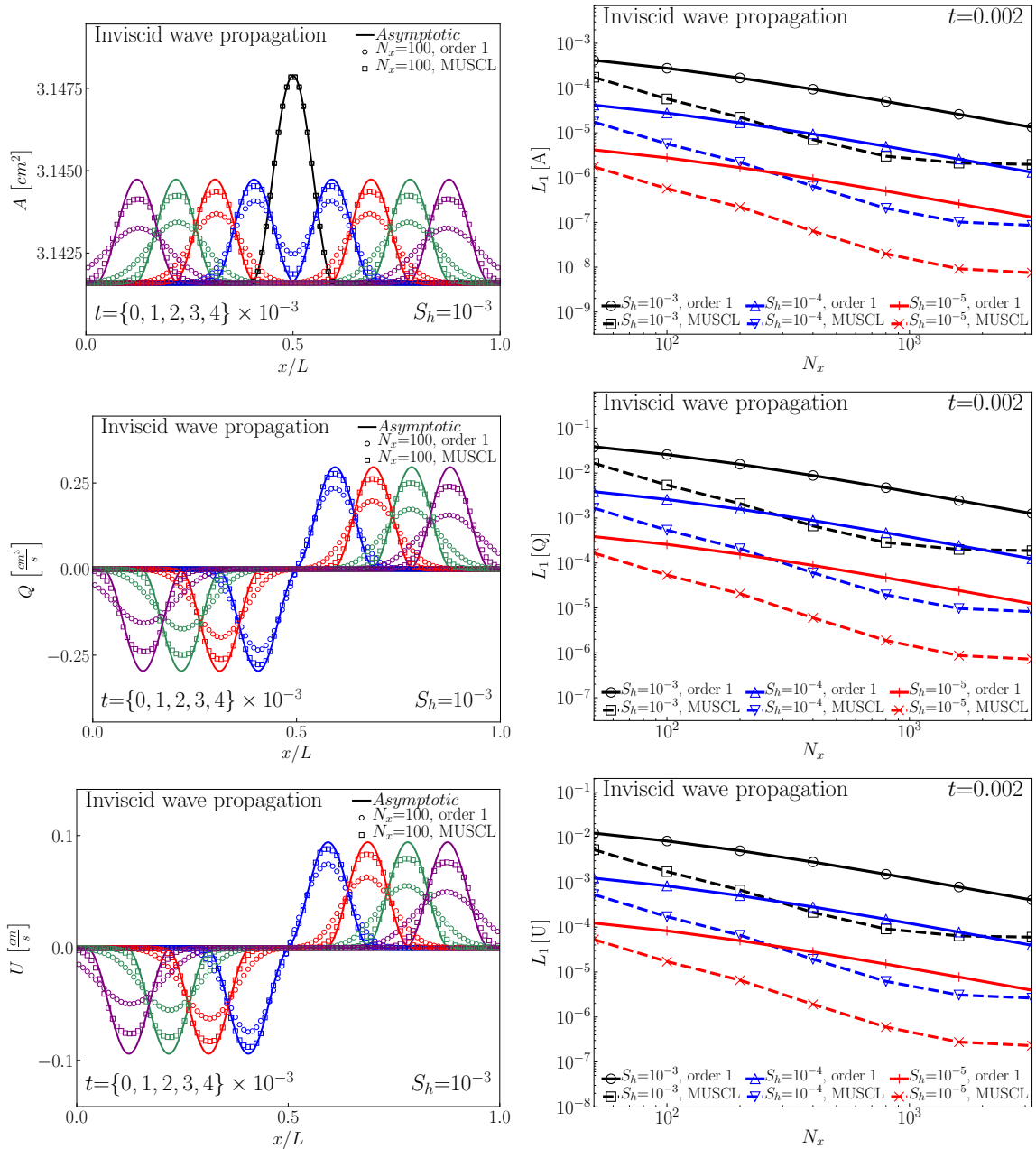


Figure 4.3 – The inviscid wave propagation test case:

Left: Comparison between the linear wave solution (—) and the first-order (○) and MUSCL (□) numerical solutions obtained with $N_x = 100$ at times $t \in \{0, 0.001, 0.002, 0.003, 0.004\}$ for $S_h = 10^{-3}$.

Right: Spatial convergence of the first-order (○, △, +) and MUSCL (□, ▽, ×) L_1 errors obtained at time $t = 0.002$ with $N_x \in \{50, 100, 200, 400, 800, 1600, 3200\}$ for $S_h \in \{10^{-3}, 10^{-4}, 10^{-5}\}$.

The first-order and MUSCL solutions converge towards the linear wave solution and first-order accuracy is achieved. For large values of N_x , the L_1 errors saturate as the analytic wave propagation solutions described here are linear whereas the numerical solutions are intrinsically nonlinear.

where C_1 , C_2 and C_3 are chosen constants, imposed through the inlet and outlet boundary conditions.

We start from the initial condition $\mathbf{U}^0 = [A(t=0), Q(x, t=0)]^\top$ and impose the flow rate $Q(x=0, t)$ (4.55c) at the inlet of the artery and the cross-sectional area $A(t)$ (4.55a) at the outlet. The parameters used in this test case are described in Table 4.3. With this choice of parameters, System (4.55) indeed describes the elastic relaxation of an artery towards its equilibrium state.

ρ	L	R_0	K	C_f	C_ν	C_1	C_2	C_3	Δt	t order
1	10	1	10^4	0	0	-1	$-\pi$	$\frac{L}{2}$	10^{-5}	2

Table 4.3 – Geometrical, mechanical, numerical and boundary parameters used in the inviscid particular solution test case.

In Figure 4.4 Left, we compare at times $t \in \{0, 0.1, 0.2, 0.3, 0.4\}$ the spatial evolution of the inviscid particular solutions (4.55) for the cross-sectional area A , the flow rate Q and the average velocity U with the spatial evolution of the first-order and MUSCL numerical solutions obtained with $N_x = 50$. We observe that for each variable, the inviscid particular solution is correctly described and the MUSCL solution is more accurate than the first-order solution.

In Figure 4.4 Right, we plot at time $t = 0.3$ the evolution with the number of cells N_x of the first-order and MUSCL L_1 , L_2 and L_∞ errors for the cross-sectional area A , the flow rate Q and the average velocity U . We observe that for each variable, the L_1 , L_2 and L_∞ errors decrease with an increasing number of cells N_x , indicating that the first-order and MUSCL numerical solutions converge towards the analytic solution. Only first-order accuracy is achieved as this particular solution is driven by the boundary conditions and boundary conditions are only implemented at first-order (see Subsection 4.2.3).

4.4.4 Viscous and viscoelastic wave propagation

We reproduce two linear asymptotic solutions of system (3.23) presented in [Wang et al. 2015] and describing the propagation of a pulse wave perturbed by viscous and viscoelastic effects. These solutions are obtained by considering small perturbations of System (3.23) linearized around the equilibrium state $\mathbf{U}^0 = [0, A_0]^\top$ and are summarized in Table 4.4.

Viscous wave propagation	Viscoelastic wave propagation
$\begin{cases} p = p_{in}(\xi) \exp\left(-\frac{\tau}{2}\right) \\ \epsilon = \frac{1}{\alpha^2}. \end{cases}$	$\begin{cases} p = \int_{-\infty}^{\infty} p_{in}(\eta) G(\tau, \xi - \eta) d\eta \\ G = \frac{1}{\sqrt{2\pi\tau}} \exp\left(-\frac{\xi^2}{2\tau}\right) \\ \epsilon = \frac{\sqrt{\pi}}{\alpha_\nu^2}. \end{cases}$

Table 4.4 – Summary of the viscous and viscoelastic asymptotic wave propagation solutions presented in [Wang et al. 2015], where $\xi = \frac{1}{T} \left[t - \frac{x}{c_0} \right]$ and $\tau = \epsilon \frac{t}{T}$.

Before proceeding to the presentation of the numerical results, we briefly recall the strategy to derive asymptotic solutions. Given a small parameter, here referred to as ϵ , the idea is to search for solutions using an asymptotic expansion of the variables (here A and Q) in

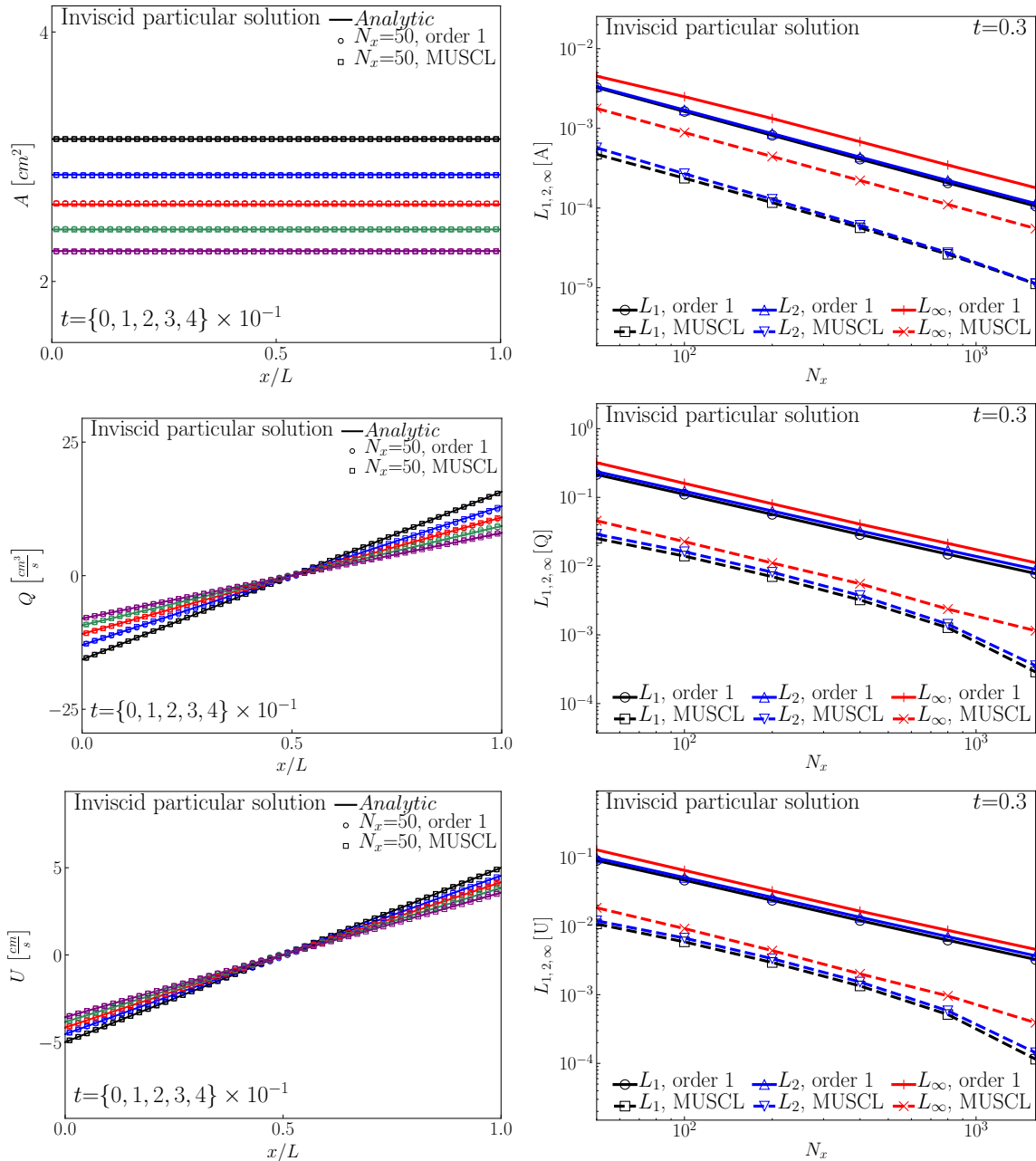


Figure 4.4 – The inviscid particular solution test case:

Left: Comparison between the inviscid particular solution (—) and the first-order (\circ) and MUSCL (\square) numerical solutions obtained with $N_x = 50$ at times $t \in \{0, 0.1, 0.2, 0.3, 0.4\}$.

Right: Spatial convergence of the first-order (\circ , Δ , $+$) and MUSCL (\square , ∇ , \times) L_1 , L_2 and L_∞ errors obtained at time $t = 0.3$ with $N_x \in \{50, 100, 200, 400, 800, 1600\}$.

The first-order and MUSCL solutions converge towards the analytic solutions. Only first-order accuracy is achieved as boundary conditions are only implemented at first-order.

powers of ϵ :

$$\begin{cases} A = A_0 + \epsilon A_1 + \epsilon^2 A_2 + \dots & (4.56a) \\ Q = Q_0 + \epsilon Q_1 + \epsilon^2 Q_2 + \dots, & (4.56b) \end{cases}$$

where $A_i|_{i=0}^\infty = O(1)$ and $Q_i|_{i=0}^\infty = O(1)$. These expressions are then injected into the governing equations, here System (3.23), and the terms of similar order in ϵ are collected, starting from the terms $O(1)$ and so on. As the governing equations usually are nonlinear and explicitly depend on the small parameter ϵ , non-trivial combinations of the functions $A_i|_{i=0}^\infty = O(1)$ and $Q_i|_{i=0}^\infty = O(1)$ are obtained and lead to the derivation of an asymptotic solution.

To compute the numerical solutions, we impose at the inlet of the artery the pressure wave p_{in} :

$$p_{in}(t) = \begin{cases} \frac{\hat{p}}{2} \left[1 + \cos \left(\pi + 2\pi \frac{t}{T} \right) \right] & \text{if } 0 \leq \frac{t}{T} \leq 1 \\ 0 & \text{else} \end{cases} \quad (4.57)$$

where $\hat{p} = \sqrt{A_0 K S_h}$ (see Equation (2.53)). The Shapiro number S_h (2.85) is chosen small to remain in the linear regime. At the outlet of the artery, we impose a non-reflecting boundary condition to remove any backward traveling wave. The parameters used in these two test cases are described in Table 4.5.

ρ	L	R_0	K	α	α_ν	S_h	T	R_t	Δt	t order
1	200	1	10^4	5	5.6	$\{10^{-3}, 10^{-4}, 10^{-5}\}$	1	0	10^{-4}	2

Table 4.5 – Geometrical, mechanical, numerical and boundary parameters used in the asymptotic wave propagation test cases.

In Figure 4.5 Left, we compare at times $t \in \{0.5, 1, 1.5, 2, 2.5\}T$ the spatial evolution of the viscous and viscoelastic asymptotic solutions for the pressure p with the spatial evolution of the first-order and MUSCL numerical solutions obtained with $N_x = 100$ for $S_h = 10^{-3}$. We observe that the viscous and viscoelastic asymptotic solutions are correctly described and that the MUSCL solutions are more accurate than the first-order solutions.

In Figure 4.5 Right, we plot at time $t = 1.5T$ the evolution with the number of cells N_x of the first-order and MUSCL L_1 errors for the pressure p obtained for $S_h \in \{10^{-3}, 10^{-4}, 10^{-5}\}$. We observe that for each value of S_h , the L_1 errors initially decrease with an increasing number of cells N_x , indicating that the first-order and MUSCL numerical solutions converge towards the analytic solution. However, the L_1 errors then saturate as the viscous and viscoelastic solutions presented here are linear asymptotic solutions and therefore not exact solutions of System (3.23). The values at which the L_1 errors saturate are proportional to the Shapiro number of S_h and to the value of the small parameter ϵ used to derive the asymptotic solutions.

4.4.5 Asymptotic front propagation

This test case describes the propagation of a wave front created when filling an elastic tube. This phenomenon is studied in [Kamm and Shapiro 1979; Fullana et al. 2003; Flaud et al. 2012]. We present here an asymptotic solution of System (3.23) describing the moving front of a wave propagating in an infinitely long artery initially rest.

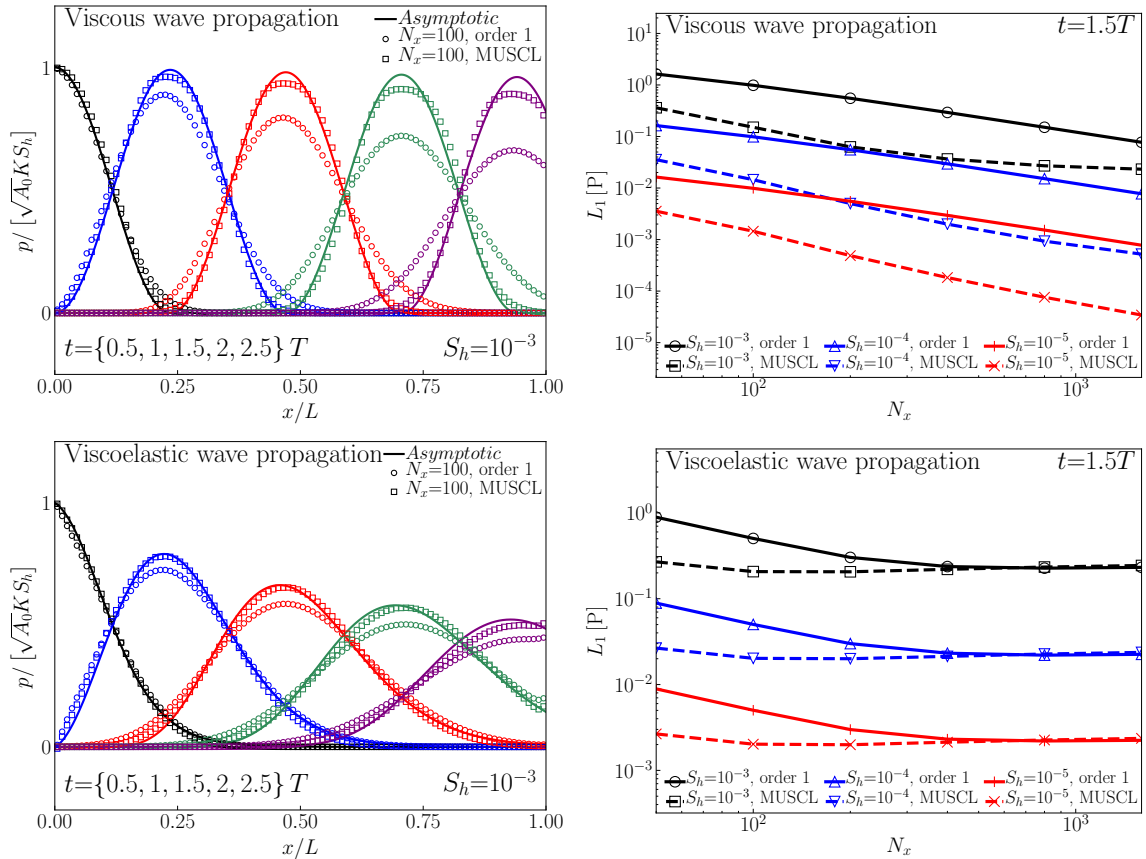


Figure 4.5 – The viscous and viscoelastic asymptotic wave propagation test cases:

Left: Comparison between the asymptotic (—), first-order (\circ) and MUSCL (\square) waveforms obtained with $N_x = 100$ at times $t \in \{0.5, 1, 1.5, 2, 2.5\}T$ for $S_h = 10^{-3}$.

Right: Spatial convergence of the first-order (\circ , \triangle , $+$) and MUSCL (\square , ∇ , \times) L_1 errors obtained at time $t = 1.5T$ with $N_x \in \{50, 100, 200, 400, 800, 1600\}$ for $S_h \in \{10^{-3}, 10^{-4}, 10^{-5}\}$.

The first-order and MUSCL solutions initially converge towards the asymptotic solutions and then saturate. Indeed, the viscous and viscoelastic solutions presented here are linear asymptotic solutions and therefore not exact solutions of System (3.23).

Asymptotic solution

Near the front of the wave, the inertial effects are negligible and System (3.23) simplifies to:

$$\left\{ \begin{array}{l} \frac{\partial A}{\partial t} + \frac{\partial Q}{\partial x} = 0 \\ \frac{\partial}{\partial x} \left[\frac{K}{3\rho} A^{\frac{3}{2}} \right] = -C_f \frac{Q}{A}, \end{array} \right. \quad (4.58a)$$

$$\left\{ \begin{array}{l} \frac{\partial A}{\partial t} + \frac{\partial Q}{\partial x} = 0 \\ \frac{\partial}{\partial x} \left[\frac{K}{3\rho} A^{\frac{3}{2}} \right] = -C_f \frac{Q}{A}, \end{array} \right. \quad (4.58b)$$

Combining Equation (4.58a) and Equation (4.58b), we obtain:

$$\frac{\partial A}{\partial t} = C_{wf} \frac{\partial}{\partial x} \left[A^{\frac{3}{2}} \frac{\partial A}{\partial x} \right], \quad (4.59)$$

where:

$$C_{wf} = \frac{K}{2\rho C_f}. \quad (4.60)$$

We complete Equation (4.59) with the following inlet and outlet boundary conditions:

$$\left\{ \begin{array}{l} A(x=0, t) = A|_{x=0} = \text{cst} \\ \lim_{x \rightarrow \infty} A(x, t) = A_0. \end{array} \right. \quad (4.61a)$$

$$\left\{ \begin{array}{l} A(x=0, t) = A|_{x=0} = \text{cst} \\ \lim_{x \rightarrow \infty} A(x, t) = A_0. \end{array} \right. \quad (4.61b)$$

We then introduce in Table 4.6 non-dimensional variables.

$$\overline{t = \tau \bar{t} \quad x = X \bar{x} \quad A = A|_{x=0} \bar{A}}$$

Table 4.6 – Wave front propagation non-dimensional variables.

Injecting these non-dimensional variables into Equation (4.59) and Equation (4.61), we obtain:

$$\left\{ \begin{array}{l} \frac{\partial \bar{A}}{\partial \bar{t}} = \left[C_{wf} A^{\frac{3}{2}}|_{x=0} \frac{\tau}{X^2} \right] \frac{\partial}{\partial \bar{x}} \left[\bar{A}^{\frac{3}{2}} \frac{\partial \bar{A}}{\partial \bar{x}} \right] \\ \bar{A}(\bar{x}=0, \bar{t}) = 1 \\ \lim_{\bar{x} \rightarrow \infty} \bar{A}(\bar{x}, \bar{t}) = \Psi, \end{array} \right. \quad (4.62a)$$

$$\left\{ \begin{array}{l} \bar{A}(\bar{x}=0, \bar{t}) = 1 \\ \lim_{\bar{x} \rightarrow \infty} \bar{A}(\bar{x}, \bar{t}) = \Psi, \end{array} \right. \quad (4.62b)$$

$$\left\{ \begin{array}{l} \bar{A}(\bar{x}=0, \bar{t}) = 1 \\ \lim_{\bar{x} \rightarrow \infty} \bar{A}(\bar{x}, \bar{t}) = \Psi, \end{array} \right. \quad (4.62c)$$

where $\Psi = A_0/A|_{x=0}$. The least degeneracy principle applied to Equation (4.62a) states that:

$$\frac{X}{\sqrt{\tau}} = \sqrt{C_{wf} A^{\frac{3}{2}}|_{x=0}}. \quad (4.63)$$

We now search for a self-similar solution of System (4.62). A classical analysis (not detailed here) shows that the variable of similitude is:

$$\eta = \frac{\bar{x}}{\sqrt{\bar{t}}}, \quad (4.64)$$

and that System (4.62) rewrites as:

$$\left\{ \begin{array}{l} -\frac{1}{2} \eta \frac{\partial \bar{A}}{\partial \eta} = \frac{\partial}{\partial \eta} \left[\bar{A}^{\frac{3}{2}} \frac{\partial \bar{A}}{\partial \eta} \right] \\ \bar{A}(\eta=0) = 1 \\ \lim_{\eta \rightarrow \infty} \bar{A}(\eta) = \Psi. \end{array} \right. \quad (4.65a)$$

$$\left\{ \begin{array}{l} \bar{A}(\eta=0) = 1 \\ \lim_{\eta \rightarrow \infty} \bar{A}(\eta) = \Psi. \end{array} \right. \quad (4.65b)$$

$$\left\{ \begin{array}{l} \bar{A}(\eta=0) = 1 \\ \lim_{\eta \rightarrow \infty} \bar{A}(\eta) = \Psi. \end{array} \right. \quad (4.65c)$$

To solve System (4.65), we assume that $\psi \approx 1$, which allows us to linearize System (4.65) around the neutral cross-sectional area ψ :

$$\left\{ \begin{array}{l} -\frac{1}{2} \eta \frac{\partial \bar{A}}{\partial \eta} = \Psi^{\frac{3}{2}} \frac{\partial^2 \bar{A}}{\partial \eta^2} \\ \bar{A}(\eta=0) = 1 \\ \lim_{\eta \rightarrow \infty} \bar{A}(\eta) = \Psi. \end{array} \right. \quad (4.66a)$$

$$\left\{ \begin{array}{l} \bar{A}(\eta=0) = 1 \\ \lim_{\eta \rightarrow \infty} \bar{A}(\eta) = \Psi. \end{array} \right. \quad (4.66b)$$

$$\left\{ \begin{array}{l} \bar{A}(\eta=0) = 1 \\ \lim_{\eta \rightarrow \infty} \bar{A}(\eta) = \Psi. \end{array} \right. \quad (4.66c)$$

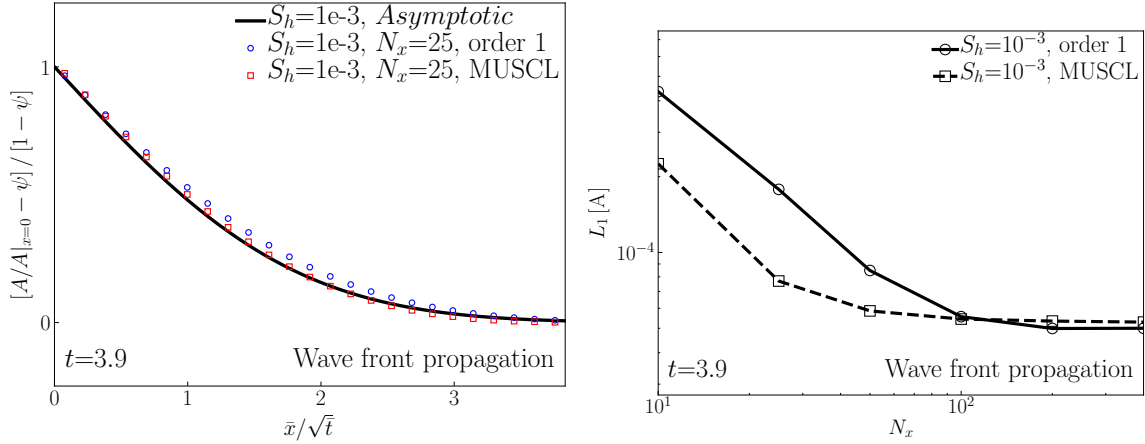


Figure 4.6 – The wave front propagation test case:

Left: Comparison between the linear (—), first-order (○) and MUSCL (□) waveforms obtained with $N_x = 25$ at time $t = 3.9$ for $S_h = 10^{-3}$.

Right: Spatial convergence of the first-order (○) and the MUSCL (□) L_1 errors obtained at time $t = 3.9$ with $N_x \in \{10, 25, 50, 100, 200, 400\}$ for $S_h = 10^{-3}$.

The first-order and MUSCL solutions converge towards the linear wave front solution. The L_1 errors decrease with an increasing number of cells N_x and then saturate as the wave front propagation solution is only a linear solution of System (3.23).

Finally, the solution of System (4.66) is:

$$\bar{A} = 1 - [1 - \Psi] \operatorname{erf} \left(\frac{\eta}{2\Psi^{\frac{3}{4}}} \right), \quad (4.67)$$

where the function erf is the classical error function.

Numerical simulations

We impose at the inlet of the artery a constant cross-section area $A|_{x=0}$, defined as:

$$A|_{x=0} = A_0 [1 + S_h]^2. \quad (4.68)$$

The Shapiro number S_h (2.85) is chosen small to remain in the linear regime. At the outlet, we impose a non-reflecting boundary condition to mimic an infinitely long elastic tube. The parameters used in this test case are described in Table 4.7.

ρ	L	R_0	K	C_f	C_ν	S_h	R_t	Δt	t	order
1	400	1	10^4	10	0	10^{-3}	0	10^{-4}	2	

Table 4.7 – Geometrical, mechanical, numerical and boundary parameters used in the wave front propagation test case.

In Figure 4.6 Left, we compare at time $t = 3.9$ the linear wave front solution for the cross-sectional area A with first-order and MUSCL numerical solutions obtained with $N_x = 25$ for $S_h = 10^{-3}$. We observe that the linear solution is correctly described and that the MUSCL solution is more accurate than the first-order solution.

In Figure 4.6 Right, we plot at time $t = 3.9$ the evolution with the number of cells N_x of the first-order and MUSCL L_1 errors for the cross-sectional area A obtained for $S_h = 10^{-3}$. We observe that the L_1 errors decrease with an increasing number of cells N_x and then saturate as the wave front propagation solution is only a linear solution of System (3.23).

In Section 4.4, we have presented a series of test cases in a single uniform artery that have enabled us to validate the hyperbolic, parabolic and reaction numerical schemes as well

as the implementation of the different boundary conditions and assess the accuracy of the MUSCL reconstruction strategy.

4.5 Conclusion

In Chapter 4, we have presented and validated numerical methods to solve the 1D viscoelastic blood flow system of equations (3.23) in one artery using an operator splitting technique. We have used a *finite volume* kinetic numerical scheme to solve the hyperbolic System (4.6) describing the propagation of elastic waves. Then, we have described the Crank-Nicolson *finite difference* scheme we use to solve the parabolic System (4.7) describing viscoelastic diffusion. Finally, we have briefly commented on the temporal scheme we use to solve the reaction System (4.8) describing viscous dissipation. To limit numerical dissipation of propagating pulse waves, we have also described a MUSCL reconstruction strategy to achieve second-order accuracy for smooth solutions. We have implemented each of these numerical methods in our in-house code and then tested their accuracy in different test cases. The results show that our implementation is second-order accurate except when:

- the analytic solution is driven by boundary conditions;
- the analytic solution is discontinuous;
- the numerical solution is compared to a linear or asymptotic solution, which is therefore not an exact solution of System (3.23).

Overall, MUSCL solutions have proven to be always more accurate and less dissipative than first-order solutions.

We are now working towards numerical reconstruction techniques better suited to capture discontinuities using the boundary-value diminishing (BVD) reconstruction framework proposed in [Sun et al. 2016]. This is particularly important when considering bolus injections of passive tracers in an artery, since sharp interfaces naturally exist at each end of the bolus. We are also studying numerical strategies to increase the order of accuracy of our boundary conditions implementation strategies.

Hydrostatic reconstruction

We present here a numerical strategy called the hydrostatic reconstruction designed to deal with arteries that present variations of their geometrical and mechanical properties (typically A_0 and K). As in Chapter 4, this chapter deals exclusively with numerical methods and is greatly inspired from the following *published* articles:

- O. Delestre, A.R. Ghigo, J.-M. Fullana, and P.-Y. Lagrée. A shallow water with variable pressure model for blood flow simulation. *Networks and Heterogeneous Media*, 11(1):69–87, 2016;
- A.R. Ghigo, O. Delestre, J.-M. Fullana, and P.-Y. Lagrée. Low-Shapiro hydrostatic reconstruction technique for blood flow simulation in large arteries with varying geometrical and mechanical properties. *Journal of Computational Physics*, 331: 108–136, 2017b.

Contents

5.1	Introduction	63
5.2	Mathematical model	65
5.2.1	One-dimensional equations with varying geometrical and mechanical properties	65
5.2.2	Additional mathematical properties	66
5.3	Hydrostatic reconstruction	67
5.3.1	The hydrostatic reconstruction: HR	67
5.3.2	The low-Shapiro hydrostatic reconstruction: HR-LS	68
5.3.3	The subsonic hydrostatic reconstruction: HR-S	71
5.4	First-order validation examples in one artery	74
5.4.1	Inviscid steady solutions	76
5.4.2	Inviscid wave propagation	79
5.5	Second-order extension	86
5.6	Second-order validation examples in one artery	87
5.6.1	Inviscid steady solutions	87
5.6.2	Wave propagation in a tapered tube	88
5.6.3	Inviscid Thacker solution	91
5.7	Conclusion	94

5.1 Introduction

Up to now, we have only considered uniform arteries, in which the geometrical and mechanical properties of the arterial wall are constant. However, in physiological situations, these prop-

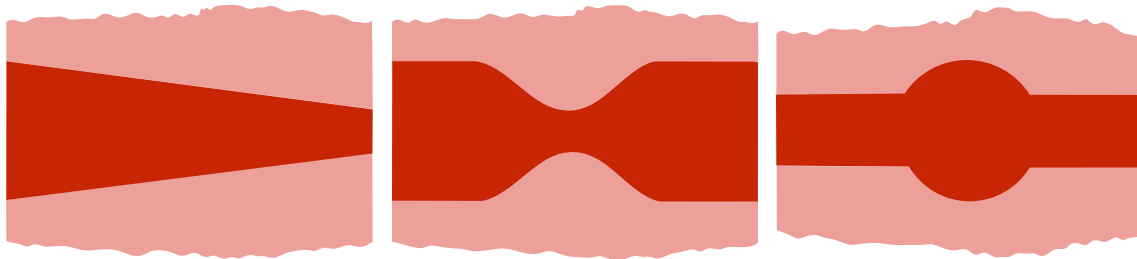


Figure 5.1 – Schematic representations of possible arterial geometrical configurations. *Left: Taper; Center: Stenosis; Right: Aneurysm.*

erties vary locally. The variations are caused by tapering (Figure 5.1 left), pathologies such as stenoses (Figure 5.1 center) or aneurysms (Figure 5.1 right) and endovascular prosthesis (stent). Mathematically, they result in a source term in the momentum conservation equation that prevents from writing the system in a conservation-law form. A naive discretization of this nonconservative source term can lead to spurious oscillations of the numerical solution and the failure of the numerical method, especially close to steady states [Delestre and Lagrée 2013]. This problem was originally pointed out by Roe [Roe 1987] for the scalar equation with source terms and reflects a truncation error between the discretization of the conservative flux gradient and the nonconservative source term that does not vanish close to steady states. Since the works of Bermúdez and Vázquez [Bermúdez and Vázquez 1994] and LeRoux [Gosse and LeRoux 1996; Greenberg and LeRoux 1996] in the context of shallow-water equations, numerical schemes that preserve some steady states at a discrete level are called well-balanced.

The aim of this chapter is to propose a simple, robust and efficient well-balanced numerical method for blood flow in an artery with variations of its mechanical and geometrical properties. As blood flow equations are mathematically similar to shallow water equations, several well-balanced numerical schemes have been derived for 1D blood flow equations with varying geometrical and mechanical properties. A popular approach consists in expressing the system in terms of primitive variables, namely the cross-sectional area (A) and the flow velocity U . The resulting system can be written in a conservation-law form, even in the presence of varying geometrical and mechanical properties. However, it has been proved for shallow water equations that this formulation is not mass-conservative and can lead to erroneous estimations of the wave celerity [Toro 2001]. This analysis is also valid for blood flow equations and the numerical solutions obtained with a nonconservative system will be incorrect in the presence of elastic jumps. Indeed, the Rankine-Hugoniot jump relation of the nonconservative form is different from the one of the conservative form. Čanić [Čanić 2002] and Sherwin [Sherwin et al. 2003a] were among the first to address the issue of the nonconservative source term for blood flow simulation. Čanić proposed to treat the nonconservative product in this source term through jump conditions, while Sherwin used a two-rarefaction Riemann solver when the material properties vary abruptly. More recently, Toro and Siviglia [Toro and Siviglia 2013] reformulated the 1D conservative system with varying geometrical and mechanical properties as a homogeneous quasi-linear system and solved the associated Riemann problem. To do so, they introduced an auxiliary steady variable containing the geometrical and mechanical properties of the artery, and also included variations of the external pressure. In the framework of path-conservative methods [Parés 2006], Müller and Toro [Müller et al. 2013] used this augmented quasi-linear system to propose an exactly well-balanced numerical scheme for all steady states (subcritical, transcritical and supercritical). Murillo and García-Navarro [Murillo and García-Navarro 2015] derived an energy balanced numerical scheme in the framework of augmented solvers for arteries with varying mechanical and geometrical properties, and also variations of the

external pressure. In [Delestre and Lagrée 2013], Delestre and Lagrée successfully applied the hydrostatic reconstruction (HR), proposed in [Audusse et al. 2004] for shallow water equations, to compute blood flow in arteries with varying cross-sectional area. In more recent work [Delestre et al. 2016], Delestre extended the hydrostatic reconstruction (HR) to arteries with varying cross-sectional area and arterial wall rigidity.

The hydrostatic reconstruction (HR) meets the simplicity and efficiency requirements for 1D blood flow simulation and is the reference well-balanced method used in this study. HR can be used with any *finite volume* numerical flux for a conservative problem and guarantees the following natural properties of shallow water flows:

- well-balanced for the steady states at rest, or hydrostatic equilibria;
- the conservation of mass;
- the non-negativity of the water-height h ;
- the ability to compute dry states and transcritical flows;
- a discrete or semi-discrete entropy inequality, which enables to compute the entropic solution in the presence of a discontinuity.

Unfortunately, the steady states at rest preserved by HR are not relevant for blood flow as they only occur in "dead men" [Delestre and Lagrée 2013]. We therefore propose two extensions of the hydrostatic reconstruction adapted to blood flow simulation in large arteries.

By relaxing some of the properties of HR such as the ability to compute dry states, we derive an extension of the hydrostatic reconstruction, that we refer to as the "low-Shapiro" hydrostatic reconstruction (HR-LS). HR-LS accurately preserves low-Shapiro number steady states that may occur in large network simulations. We also adapt the subsonic hydrostatic reconstruction (HR-S), proposed by Bouchut [Bouchut and Morales De Luna 2010], to blood flow equations with variable geometrical and mechanical properties. HR-S exactly preserves all subcritical steady states, including low-Shapiro number steady states. By construction, both HR-LS and HR-S are able to accurately compute wave reflections and transmissions. The different numerical methods are then tested and compared in a series of steady and unsteady physiological flow configurations, where both the geometrical and mechanical wall properties vary.

5.2 Mathematical model

5.2.1 One-dimensional equations with varying geometrical and mechanical properties

In Subsection 2.2.2, we have derived the thin cylinder wall law (2.23) valid for a uniform elastic artery. If we now consider that the neutral cross-sectional area A_0 and the arterial rigidity K vary in the x -direction, Equation (2.23) simply rewrites:

$$p - p_{ext} = K(x) \left[\sqrt{A} - \sqrt{A_0(x)} \right]. \quad (5.1)$$

The variations of the geometry of the arterial wall should remain small to stay in the long wavelength asymptotic limit.

Following the derivation presented in Section 2.5, we obtain the 1D system of equations describing blood flow in an artery with varying geometrical and mechanical properties:

$$\left\{ \begin{array}{l} \frac{\partial A}{\partial t} + \frac{\partial Q}{\partial x} = 0 \end{array} \right. \quad (5.2a)$$

$$\left\{ \begin{array}{l} \frac{\partial Q}{\partial t} + \frac{\partial}{\partial x} \left[\frac{Q^2}{A} + \frac{K}{3\rho} A^{\frac{3}{2}} \right] = S_T, \end{array} \right. \quad (5.2b)$$

where S_T is a source term taking into account the possible variations of the geometrical and mechanical properties of the arterial wall:

$$S_T = \frac{A}{\rho} \left[\frac{\partial}{\partial x} \left[K \sqrt{A_0} \right] - \frac{2}{3} \sqrt{A} \frac{\partial K}{\partial x} \right]. \quad (5.3)$$

Notice that System (5.2) does not include viscous or viscoelastic terms that we neglect in this chapter.

5.2.2 Additional mathematical properties

To simplify the analysis, we write System (5.2) as a system of balance laws:

$$\frac{\partial \mathbf{U}}{\partial t} + \frac{\partial \mathbf{F}}{\partial x} = \mathbf{S} \frac{\partial \boldsymbol{\sigma}}{\partial x}. \quad (5.4)$$

The vectors $\mathbf{U} = [A, Q]^\top$ and $\mathbf{F} = [F_A, F_Q]^\top$ are respectively defined by Equation (2.79) and Equation (2.80). The vector $\boldsymbol{\sigma}$ and the matrix \mathbf{S} are defined as:

$$\boldsymbol{\sigma} = \begin{bmatrix} K \\ Z \end{bmatrix} = \begin{bmatrix} K \\ K \sqrt{A_0} \end{bmatrix}, \quad (5.5)$$

and:

$$\mathbf{S} = \begin{bmatrix} 0 & 0 \\ -\frac{2}{3} \frac{A^{\frac{3}{2}}}{\rho} & \frac{A}{\rho} \end{bmatrix}. \quad (5.6)$$

The main difficulty with System (5.4) lies in the presence of the nonconservative source term $\mathbf{S} \partial_x \boldsymbol{\sigma}$. This nonconservative term vanishes when the neutral cross-sectional area A_0 and the arterial wall rigidity K are constant, and System (5.4) reduces to System (2.78). The mathematical properties of System (2.78) have been presented in Subsection 2.6.2. We therefore only recall the modifications introduced by the presence of the nonconservative source term $\mathbf{S} \partial_x \boldsymbol{\sigma}$.

The entropy inequality (2.93) is extended to solutions of System (5.4) through a new entropy pair $(\tilde{\eta}, \tilde{G})$ taking into account the vector $\boldsymbol{\sigma}$:

$$\begin{cases} \tilde{\eta} = \eta - \frac{Z}{\rho} A \\ \tilde{G} = G - \frac{Z}{\rho} Q, \end{cases} \quad (5.7)$$

that verify the following entropy inequality:

$$\frac{\partial \tilde{\eta}}{\partial t} + \frac{\partial \tilde{G}}{\partial x} \leq 0. \quad (5.8)$$

Most importantly, System (5.4) now admits non-trivial steady solutions, verifying the following steady state system of equations:

$$\begin{cases} Q = C_1 & (5.9a) \\ E = \frac{1}{2} \frac{Q^2}{A^2} + \frac{1}{\rho} [K \sqrt{A} - Z] = C_2, & (5.9b) \end{cases}$$

where C_1 and C_2 are two constants and E is the energy discharge. A particular family of steady states are the steady states at rest, or "man at eternal rest" equilibria, defined by:

$$\begin{cases} Q = 0 & (5.10a) \\ p = K \sqrt{A} - Z = C_2. & (5.10b) \end{cases}$$

For shallow water flows, steady states mainly occur in "lakes at rest", which are the analogue of the "man at eternal rest" equilibria (5.10). In arteries, steady or quasi-steady flow regimes are observed in small segments when the frequency of the pulse wave is greatly reduced due to a high resistance of the flow, for example after severe stenoses or in smaller arteries. In these cases, the relevant equilibria are no longer the steady states at rest but the non-zero flow steady states described by System (5.9).

5.3 Hydrostatic reconstruction

To prevent spurious oscillations of the numerical solution of system (5.4) close to steady states, a well-balanced numerical scheme is required to properly balance the source term $\mathcal{S}\partial_x\sigma$ and the flux gradient $\partial_x\mathbf{F}$. To make an explicit analogy with the well-balanced methods derived for shallow water equations, we introduce the following notations:

$$\begin{cases} \mathcal{P} = \frac{K}{3\rho}A^{\frac{3}{2}} \\ \mathcal{E} = \frac{2K}{3\rho}\sqrt{A} \\ H = K\sqrt{A}. \end{cases} \quad (5.11)$$

With these notations, the flux vector \mathbf{F} (2.80) is expressed as:

$$\mathbf{F} = \begin{bmatrix} Q \\ \frac{Q^2}{A} + \mathcal{P} \end{bmatrix}, \quad (5.12)$$

and the steady state System (5.9) and System (5.10) respectively write:

$$\begin{cases} Q = C_1 & (5.13a) \\ \frac{1}{2}\frac{Q^2}{A^2} + \mathcal{E} + \frac{\mathcal{P}}{A} - \frac{Z}{\rho} = C_2, & (5.13b) \end{cases}$$

and:

$$\begin{cases} Q = 0 & (5.14a) \\ H - Z = C_2. & (5.14b) \end{cases}$$

In the context of shallow water equations, Equation (5.13b) is a generalized Bernoulli equation and Equation (5.14b) describes the hydrostatic equilibria.

5.3.1 The hydrostatic reconstruction: HR

The hydrostatic reconstruction (HR) was introduced by Audusse [Audusse et al. 2004] for shallow water equations and applied to blood flow equations by Delestre [Delestre and Lagr ee 2013; Delestre et al. 2016]. Through a reconstruction of the conservative variables, HR allows to obtain a simple and efficient well-balanced numerical scheme given any *finite volume* numerical flux for the conservative System (2.78). It is simple to implement and can easily be adapted to different pressure laws with multiple varying parameters, which is useful when considering veins, collapsible tubes and external pressure variations [Pedley et al. 1996; Cavallini and Coscia 2010; M uller and Toro 2014]. This technique allows to preserve at a discrete level the steady states at rest (5.14) and guarantees that the scheme verifies some natural properties of the shallow water equations (listed as bullets in the introduction), such as the positivity of the water height (equivalent of the cross-sectional area A), the ability to compute dry states and transcritical flows and a discrete entropy inequality with an error term that tends to zero when the mesh size decreases [Audusse et al. 2016]. This last property is necessary to select the admissible entropy solution across a discontinuity, as explained in [Gosse 2013].

On both sides of each cell interface $x_{i+\frac{1}{2}}$, reconstructed conservative variables are defined to preserve the following system of equations, which coincides with the steady states at rest (5.14) when the flow rate Q or the velocity U are zero:

$$\begin{cases} U = \frac{Q}{A} = C_1 & (5.15a) \\ H - Z = C_2. & (5.15b) \end{cases}$$

Details on the derivation of HR for blood flow in an artery with variable neutral cross-sectional area A_0 and variable arterial wall rigidity K are found in [Delestre et al. 2016].

In large arteries, the steady states at rest preserved by HR only occur for "dead men" or distal to an obliterated segment and are of little interest when simulating blood flow in the systemic network. However, in regions of large flow resistance such as small arteries, arterioles or arteries severely constricted by a stenosis, the flow loses its pulsatility and reaches steady or near-steady states with a non-zero flow rate. These quasi-steady flow configurations can occur in large network simulations when the level of arterial precision extends to small arteries and arterioles or in the presence of a very severe stenosis. They are described by the steady state System (5.13). Therefore, a modification of HR is necessary to capture these relevant steady states for blood flow in large arteries.

5.3.2 The low-Shapiro hydrostatic reconstruction: HR-LS

System (5.13) is nonlinear and difficult to solve in practice. However, in physiological conditions, blood flow is subcritical with a Shapiro number of the order of $S_h \approx 10^{-2}$ (2.85). Therefore, the nonlinear advection term $U^2 = Q^2/(2A^2)$ in System (5.13) can be neglected at first-order with respect to the term $\mathcal{E} + \mathcal{P}/A - Z/\rho$ that scales as c^2 , where c is the Moens-Korteweg celerity (2.71). Doing so, we obtain the following simplified low-Shapiro number steady state system of equations:

$$\begin{cases} Q = C_1 & (5.16a) \\ H - Z = C_2. & (5.16b) \end{cases}$$

System (5.16) coincides with the steady state at rest (5.14) when Q or U are zero and is an asymptotically correct approximation of the steady state system (5.13) in low-Shapiro number flow regimes. It also contains the correct conservation properties to obtain low-Shapiro number wave reflections if a change of impedance occurs at the interface between two cells of the computational domain. Indeed, the conservation properties of System (5.16) are identical to those of System (6.1), which prove to be adequate to compute wave reflections and transmissions at junction points [Alastruey et al. 2009; Wang et al. 2015] (see Subsection 6.2.1 for more details). System (5.16) is the basis for the derivation of the modification of HR we propose in this study, referred to as the low-Shapiro hydrostatic reconstruction (HR-LS) and better suited to compute blood flow in physiological conditions.

HR-LS aims at preserving low-Shapiro number steady states (5.16) in an artery with a varying neutral cross-sectional area A_0 and arterial wall rigidity K . Similarly to HR, the well-balanced property is enforced by defining reconstructed variables on both sides of the interface $x_{i+\frac{1}{2}}$ according to the reconstruction procedure (5.16). In the following, variables noted with "*" will refer to the reconstructed variables. Given the vectors of conservative variables \mathbf{U}_L and \mathbf{U}_R and the vectors $\boldsymbol{\sigma}_L$ and $\boldsymbol{\sigma}_R$ on the left and right of the interface $x_{i+\frac{1}{2}}$

between cells C_i and C_{i+1} , the discrete analogue of System (5.16) writes:

$$\begin{cases} Q_L^* = Q_L \\ H_L^* - Z^* = H_L - Z_L \\ Q_R^* = Q_R \\ H_R^* - Z^* = H_R - Z_R. \end{cases} \quad (5.17)$$

By solving System (5.17) and preserving the positivity of H , we obtain the following reconstructed variables:

$$\begin{cases} H_L^* = \max(0, Z^* + H_L - Z_L) \\ Q_L^* = Q_L \\ H_R^* = \max(0, Z^* + H_R - Z_R) \\ Q_R^* = Q_R. \end{cases} \quad (5.18)$$

The reconstructed variable Z^* is chosen considering nonlinear stability arguments that require that:

$$\begin{cases} 0 \leq H_L^* \leq H_L \\ 0 \leq H_R^* \leq H_R, \end{cases}$$

to preserve the positivity of H . A simple choice is the downwind value:

$$Z^* = \min(Z_L, Z_R). \quad (5.19)$$

In order to obtain the reconstructed values A_L^* and A_R^* , we select a reconstruction for K^* . Following [Bouchut 2004; Delestre et al. 2016] we choose:

$$K^* = \max(K_L, K_R). \quad (5.20)$$

Therefore, we directly have:

$$\begin{cases} A_L^* = \left(\frac{H_L^*}{K^*}\right)^2 \\ A_R^* = \left(\frac{H_R^*}{K^*}\right)^2. \end{cases} \quad (5.21)$$

Finally, we obtain the reconstructed conservative vectors:

$$\begin{cases} \mathbf{U}_L^* = \begin{bmatrix} A_L^* \\ Q_L^* \end{bmatrix} \\ \mathbf{U}_R^* = \begin{bmatrix} A_R^* \\ Q_R^* \end{bmatrix}, \end{cases} \quad (5.22)$$

that are used to compute the numerical flux $\mathcal{F}(\mathbf{U}_L^*, \mathbf{U}_R^*)$ (4.14). This reconstruction process is represented in Figure 5.2.

A *finite volume* formulation for the source term S_T (5.3) is obtained by integrating over the cell C_i the steady flux gradient in which the nonlinear advection term is neglected. This approximation is valid in low-Shapiro number flow regimes, and therefore particularly appropriate for blood flow in large arteries. The following *finite volume* expression for S_T is obtained, expressed in terms of the reconstructed conservative vector \mathbf{U}^* :

$$S_{T,i} = \frac{1}{\Delta x} \int_{C_i} S_T dx = \mathcal{P}\left(A_{L,i+\frac{1}{2}}^*, K_{i+\frac{1}{2}}^*\right) - \mathcal{P}\left(A_{R,i-\frac{1}{2}}^*, K_{i-\frac{1}{2}}^*\right), \quad (5.23)$$

where $\left[A_{L,i+\frac{1}{2}}^*, A_{R,i-\frac{1}{2}}^*\right]$ are the reconstructed cross-sectional areas on the left of the cell interface $x_{i+\frac{1}{2}}$ and on the right of the cell interface $x_{i-\frac{1}{2}}$ respectively and $\left[K_{i+\frac{1}{2}}^*, K_{i-\frac{1}{2}}^*\right]$ are the reconstructed arterial wall rigidities on the cell interfaces $x_{i+\frac{1}{2}}$ and $x_{i-\frac{1}{2}}$ respectively.

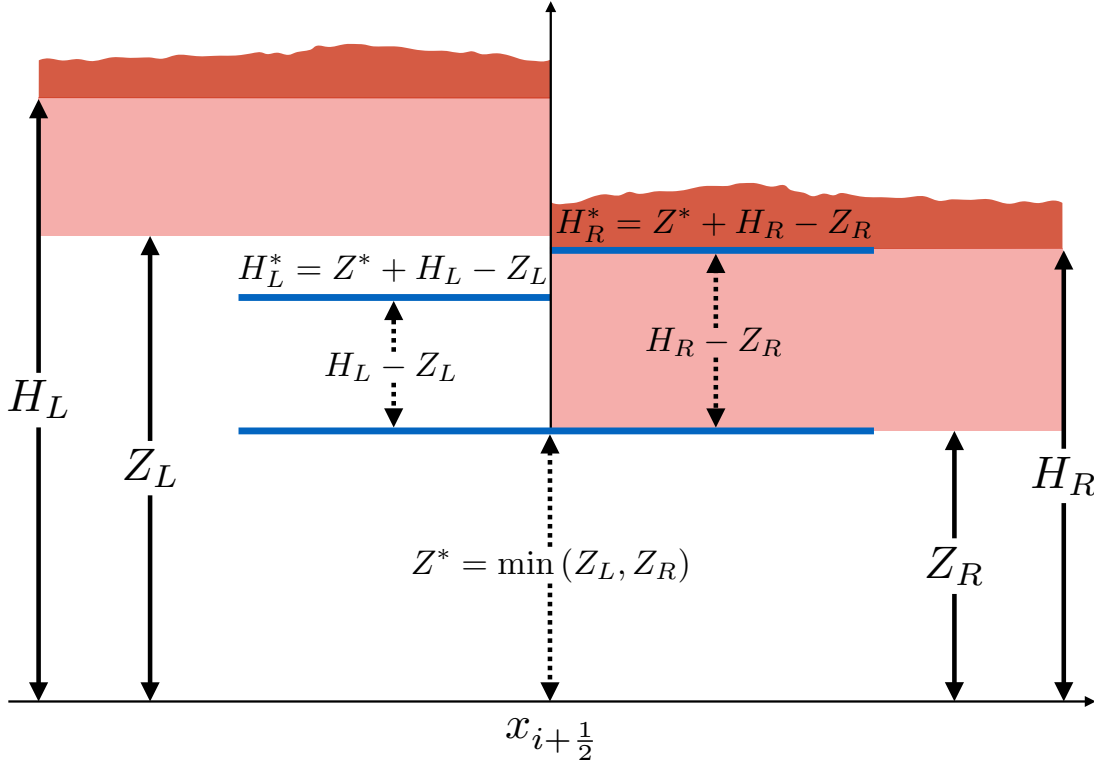


Figure 5.2 – Schematics of the HR-LS reconstruction. Given the vectors of conservative variables \mathbf{U}_L and \mathbf{U}_R and the vectors $\boldsymbol{\sigma}_L$ and $\boldsymbol{\sigma}_R$ on the left and right of the interface $x_{i+\frac{1}{2}}$, we reconstruct the variables H_L^* and H_R^* using Equation (5.18).

For consistency reasons, we modify the previous expression and write:

$$S_{T,i} = \mathcal{P} \left(A_{L,i+\frac{1}{2}}, A_{L,i+\frac{1}{2}}^*, K_{L,i+\frac{1}{2}}, K_{i+\frac{1}{2}}^* \right) - \mathcal{P} \left(A_{R,i-\frac{1}{2}}, A_{R,i-\frac{1}{2}}^*, K_{R,i-\frac{1}{2}}, K_{R,i-\frac{1}{2}}^* \right), \quad (5.24)$$

with the notation:

$$\mathcal{P}(A, A^*, K, K^*) = \mathcal{P}(A^*, K^*) - \mathcal{P}(A, K). \quad (5.25)$$

With these notations, the first-order well-balanced *finite volume* scheme (4.13) proposed in Section 4.2 and applied to System (5.4) is simply:

$$\mathbf{U}_i^{n+1} = \mathbf{U}_i^n - \frac{\Delta t}{\Delta x} \left[\mathbf{F}_{i+\frac{1}{2}}^{n*} - \mathbf{F}_{i-\frac{1}{2}}^{n*} \right], \quad (5.26)$$

with:

$$\left\{ \begin{array}{l} \mathbf{F}_{i+\frac{1}{2}}^{n*} = \mathcal{F} \left(\mathbf{U}_{L,i+\frac{1}{2}}^*, \mathbf{U}_{R,i+\frac{1}{2}}^*, K_{i+\frac{1}{2}}^* \right) + \left[\begin{array}{c} 0 \\ \mathcal{P} \left(A_{L,i+\frac{1}{2}}, A_{L,i+\frac{1}{2}}^*, K_{L,i+\frac{1}{2}}, K_{i+\frac{1}{2}}^* \right) \end{array} \right] \end{array} \right. \quad (5.27a)$$

$$\left\{ \begin{array}{l} \mathbf{F}_{i-\frac{1}{2}}^{n*} = \mathcal{F} \left(\mathbf{U}_{L,i-\frac{1}{2}}^*, \mathbf{U}_{R,i-\frac{1}{2}}^*, K_{i-\frac{1}{2}}^* \right) + \left[\begin{array}{c} 0 \\ \mathcal{P} \left(A_{R,i-\frac{1}{2}}, A_{R,i-\frac{1}{2}}^*, K_{R,i-\frac{1}{2}}, K_{i-\frac{1}{2}}^* \right) \end{array} \right]. \end{array} \right. \quad (5.27b)$$

It is straightforward to see that HR-LS is well-balanced for the steady states at rest (5.14) and provides a good approximation of the steady states (5.13) in low-Shapiro number flow regimes. It also guarantees the following natural properties of blood flow equations:

- the conservation of mass;
- the non-negativity of the cross-sectional area A ;
- correct reflection and transmission conditions when variations of vessel impedance occur.

In physiological conditions, the arteries never completely collapse, therefore the numerical scheme no longer needs to be able to compute dry states. Furthermore, as the flow is subcritical and the heart input signal is not discontinuous, transcritical or supercritical regimes and discontinuities of the conservative variables do not occur. Hence the discrete entropy inequality as well as the ability to compute transcritical flows are no longer crucial requirements of the numerical scheme. Finally, the viscosity of the blood and of the arterial wall, that are not taken into account here, are of great importance in arteries and have diffusive and dissipative effects that remove high frequency components and therefore any discontinuity in the conservative variables.

5.3.3 The subsonic hydrostatic reconstruction: HR-S

In [Bouchut and Morales De Luna 2010], an extension of HR was proposed, referred to as the subsonic hydrostatic reconstruction (HR-S), ideal for blood flow simulations in large arteries. HR-S is well-balanced for all subcritical steady states (5.13) and also preserves the good properties of HR (listed as bullets in the introduction), that is the positivity of the water height (equivalent of the cross-sectional area A), the ability to compute dry states and transcritical flows and a semi-discrete entropy inequality. HR-S is also able to correctly capture wave reflections and transmissions in regions where the impedance of the arterial wall changes. Indeed, the subcritical steady states (5.13) coincide with the junction conservation properties (6.1). However, HR-S requires the resolution of the nonlinear System (5.13) at each time step at every cell interface presenting a gradient of the artery's geometrical or mechanical properties. This increases the computational cost compared to HR and HR-LS, especially if the region requiring a well-balanced treatment is not limited to a few mesh cells.

In this section, we present the derivation of HR-S adapted to blood flow in an artery where both variations of cross-sectional area at rest A_0 and variations of the arterial wall rigidity K are taken into account. HR-S serves as the reference exactly well-balanced method to be compared to HR and HR-LS. In particular, HR-S allows us to assess if relaxing the dry-state property and the semi-discrete entropy inequality in HR-LS impacts solutions of blood flow in physiological conditions. With the notations (5.11), we are in the framework introduced in [Bouchut and Morales De Luna 2010] and therefore we only briefly recall the main steps of the derivation of HR-S. Additional details can be found in the cited publication.

Well-balanced subsonic positivity-preserving reconstruction procedure for the cross-sectional area A .

Similarly to HR and HR-LS, the well-balanced property is enforced by defining reconstructed variables on both sides of each cell interface $x_{i+\frac{1}{2}}$ according to the reconstruction procedure (5.13). Variables noted with "*" will refer to the reconstructed variables. Following [Bouchut and Morales De Luna 2010], we introduce the function f :

$$\begin{aligned} f : \mathbb{R} \times (\mathbb{R}^{++})^2 &\longrightarrow \mathbb{R} \\ (Q, A, K) &\longrightarrow \frac{1}{2} \frac{Q^2}{A^2} + \mathcal{E}(A, K) + \frac{\mathcal{P}(A, K)}{A}, \end{aligned} \tag{5.28}$$

and given the vectors of conservative variables \mathbf{U}_L and \mathbf{U}_R and the vectors $\boldsymbol{\sigma}_L$ and $\boldsymbol{\sigma}_R$ at the left and right of the interface $x_{i+\frac{1}{2}}$, the discrete analogue of system (5.13) writes:

$$\begin{cases} Q_L^* = Q_L \\ f(Q_L^*, A_L^*, K^*) = f(Q_L, A_L, K_L) + \delta_L \\ Q_R^* = Q_R \\ f(Q_R^*, A_R^*, K^*) = f(Q_R, A_R, K_R) + \delta_R, \end{cases} \tag{5.29}$$

with:

$$\begin{cases} \delta_L = \frac{1}{\rho} (Z^* - Z_L) \\ \delta_R = \frac{1}{\rho} (Z^* - Z_R). \end{cases} \quad (5.30)$$

Similarly to HR-LS, the reconstruction of the flow rate Q^* is straightforward. However, contrary to HR and HR-LS, System (5.29) is nonlinear in A^* and is difficult to solve analytically. To help with the resolution of System (5.29), we recall the following properties (see [Bouchut and Morales De Luna 2010] for details).

For fixed values of Q and K , the function f admits a minimum in $A_s(Q, K)$ and $m_s(Q, K)$ is the minimum value of f :

$$\begin{cases} A_s(Q, K) = \left[\frac{2\rho}{K} Q^2 \right]^{\frac{2}{5}} \\ m_s(Q, K) = \frac{5}{4} \frac{K}{\rho} \left[\frac{2\rho}{K} Q^2 \right]^{\frac{1}{5}}. \end{cases} \quad (5.31)$$

For fixed values of Q and K and since the function f is convex, System (5.29) admits a subcritical and a supercritical solution for the cross-sectional area A if $f(Q, A, K) > m_s(Q, K)$. Furthermore, if $A > A_s(Q, K)$ the flow is subcritical with $\mathbf{U} \in \mathbb{U}_{sub}$ and inversely if $A < A_s(Q, K)$ the flow is supercritical with $\mathbf{U} \in \mathbb{U}_{sup}$ (see Figure 5.3).

Using these properties, a reconstruction procedure for the cross-sectional area is proposed in [Bouchut and Morales De Luna 2010]. The first step is to select reconstructions of the variables Z^* and K^* that preserve the positivity of A and select the subcritical solution of System (5.29). These conditions are met if the following inequalities are verified:

$$\begin{cases} A_L^* \leq A_L \\ A_R^* \leq A_R, \end{cases} \quad (5.32)$$

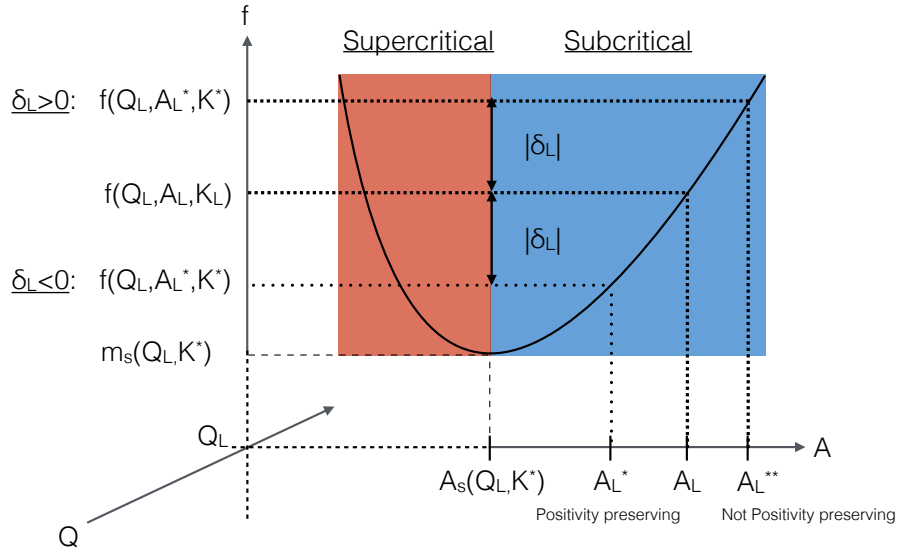


Figure 5.3 – Representation of the function $f(Q_L, \cdot, \cdot)$. The abscissa of the intersections between function f and the straight lines representing the different values of $f(Q_L, A_L^*, K^*)$ give the possible values of A_L^* . A graphical analysis shows that conditions (5.32) and (5.33) are met only for $\delta_L < 0$.

and:

$$\begin{cases} A_s \leq A_L^* \\ A_s \leq A_R^*. \end{cases} \quad (5.33)$$

The inequalities (5.33) are naturally verified as we consider only subcritical flow configurations. On the contrary, the inequalities (5.32) are verified if inequalities (5.33) are true and if Z^* and K^* are chosen such that $\delta_{L,R} \leq 0$. A simple choice for Z^* and K^* is:

$$\begin{cases} Z^* = \min(Z_L, Z_R) \\ K^* = \max(K_L, K_R). \end{cases} \quad (5.34)$$

Given the expressions (5.34) for Z^* and K^* , we adapt the reconstruction procedure for the cross-sectional area A^* proposed by Bouchut [Bouchut and Morales De Luna 2010] to blood flow in arteries with variable neutral cross-sectional area A_0 and variable arterial wall rigidity K . The procedure is summarized in Figure 5.3 and is presented in the Algorithm (5.1). The Algorithm (5.1) describes the steps that need to be followed to obtain the reconstructed cross-sectional area A_L^* , solution of system (5.29). The same algorithm can be applied to reconstruct A_R^* .

Algorithm 5.1 Algorithm to compute the reconstructed cross-sectional area A_L^* to enforce the well-balanced property by interface for the steady states (5.13).

```

if  $\delta_L = 0$  then
     $A_L^* \leftarrow A_L$ 
else
    if  $u_L \geq c_L$  then
         $A_L^* \leftarrow A_L$ 
    else
        if  $f(Q_L, A_L, K_L) + \delta_L > m_s(Q_L, K^*)$  then
             $\begin{cases} Q_L^* = Q_L \\ f(Q_L^*, A_L^*, K^*) = f(Q_L, A_L, K_L) + \delta_L \end{cases}$ 
            The solution of the system can be obtained numerically using a recursive procedure.
        else
             $A_L^* \leftarrow A_s(Q_L, K^*)$ 
    
```

Well-balanced subsonic first-order numerical scheme.

Similarly to HR and HR-LS, a *finite volume* formulation for the source term S_T is obtained by integrating over the cell C_i the steady flux gradient. However, the nonlinear advection term is no longer neglected and an additional flux term $\mathcal{T}_{L,R}$ is introduced to take it into account:

$$\begin{aligned} S_{T,i} = & \mathcal{P} \left(A_{L,i+\frac{1}{2}}, A_{L,i+\frac{1}{2}}^*, K_{L,i+\frac{1}{2}}, K_{i+\frac{1}{2}}^* \right) + \mathcal{T}_L \left(U_{L,i+\frac{1}{2}}, U_{L,i+\frac{1}{2}}^*, U_{R,i+\frac{1}{2}}, K_{i+\frac{1}{2}}^* \right) - \\ & \mathcal{P} \left(A_{R,i-\frac{1}{2}}, A_{R,i-\frac{1}{2}}^*, K_{R,i-\frac{1}{2}}, K_{i-\frac{1}{2}}^* \right) - \mathcal{T}_R \left(U_{R,i-\frac{1}{2}}, U_{L,i-\frac{1}{2}}^*, U_{R,i-\frac{1}{2}}, K_{i-\frac{1}{2}}^* \right), \end{aligned} \quad (5.35)$$

where $\left[A_{L,i+\frac{1}{2}}^*, A_{R,i-\frac{1}{2}}^* \right]$ are the reconstructed cross-sectional areas on the of left the cell interface $x_{i+\frac{1}{2}}$ and on the right of the cell interface $x_{i-\frac{1}{2}}$ respectively and $\left[K_{i+\frac{1}{2}}^*, K_{i-\frac{1}{2}}^* \right]$ are the reconstructed arterial wall rigidities at the cell interfaces $x_{i+\frac{1}{2}}$ and $x_{i-\frac{1}{2}}$ respectively. The additional fluxes \mathcal{T}_L and \mathcal{T}_R are chosen such that the numerical scheme satisfies an entropy inequality by interface (see [Bouchut and Morales De Luna 2010] for details). The computation of \mathcal{T}_L and \mathcal{T}_R is presented in the Algorithm (5.2). Only the steps that need to be followed to obtain \mathcal{T}_L are detailed in Algorithm (5.2) but similar results are obtained for \mathcal{T}_R .

With these notations, the first-order well-balanced *finite volume* scheme (4.13) proposed in

Algorithm 5.2 Algorithm to compute the flux \mathcal{T}_L used in HR-S to balance the nonlinear advection term Q^2/A and the source term S_T .

To simplify the expression of \mathcal{T}_L we use the following notations:

$$\begin{cases} \mathcal{F}_A = \mathcal{F}_A(\mathbf{U}_L^*, \mathbf{U}_R^*, K^*), & \mathcal{F}_Q = \mathcal{F}_Q(\mathbf{U}_L^*, \mathbf{U}_R^*, K^*) \\ \mathcal{P} = \mathcal{P}(A_L, A_L^*, K_L, K^*), & \Delta f = f(Q_L^*, A_L^*, K^*) - f(Q_L, A_L, K_L) - \delta_L. \end{cases}$$

if $\delta_L = 0$ then

$$\mathcal{T}_L \leftarrow 0$$

else

if $u_L \geq c_L$ then

$$\mathcal{T}_L \leftarrow -\frac{A_L}{Q_L} \mathcal{F}_A \delta_L$$

else

if $f(Q_L, A_L, K_L) + \delta_L > m_s(Q_L, K^*)$ then

$$\mathcal{T}_L \leftarrow \frac{A_L - A_L^*}{A_L^*} \left[\mathcal{F}_Q - \mathcal{P} - \frac{Q_L^*}{A_L^*} \mathcal{F}_A \right] - \mathcal{F}_A \left[\frac{Q_L^*}{A_L^*} - \frac{Q_L}{A_L} \right]$$

else

$$\mathcal{T}_L \leftarrow \frac{A_L - A_L^*}{A_L^*} \left[\mathcal{F}_Q - \mathcal{P} - \frac{Q_L^*}{A_L^*} \mathcal{F}_A \right] - \mathcal{F}_A \left[\frac{Q_L^*}{A_L^*} - \frac{Q_L}{A_L} \right] + \frac{A_L}{Q_L} \mathcal{F}_A \Delta f$$

Section 4.2 and applied to System (5.4) is:

$$\mathbf{U}_i^{n+1} = \mathbf{U}_i^n - \frac{\Delta t}{\Delta x} \left[\mathbf{F}_{i+\frac{1}{2}}^{n*} - \mathbf{F}_{i-\frac{1}{2}}^{n*} \right], \quad (5.36)$$

with:

$$\begin{cases} \mathbf{F}_{i+\frac{1}{2}}^{n*} = \mathcal{F} \left(\mathbf{U}_{L,i+\frac{1}{2}}^*, \mathbf{U}_{R,i+\frac{1}{2}}^*, K_{i+\frac{1}{2}}^* \right) + \\ \left[\begin{array}{c} 0 \\ \mathcal{P} \left(A_{L,i+\frac{1}{2}}, A_{L,i+\frac{1}{2}}^*, K_{L,i+\frac{1}{2}}, K_{i+\frac{1}{2}}^* \right) + \mathcal{T}_L \left(\mathbf{U}_{L,i+\frac{1}{2}}, \mathbf{U}_{L,i+\frac{1}{2}}^*, \mathbf{U}_{R,i+\frac{1}{2}}^*, K_{i+\frac{1}{2}}^* \right) \end{array} \right] \end{cases} \quad (5.37a)$$

$$\begin{cases} \mathbf{F}_{i-\frac{1}{2}}^{n*} = \mathcal{F} \left(\mathbf{U}_{L,i-\frac{1}{2}}^*, \mathbf{U}_{R,i-\frac{1}{2}}^*, K_{i-\frac{1}{2}}^* \right) + \\ \left[\begin{array}{c} 0 \\ \mathcal{P} \left(A_{R,i-\frac{1}{2}}, A_{R,i-\frac{1}{2}}^*, K_{R,i-\frac{1}{2}}, K_{i-\frac{1}{2}}^* \right) + \mathcal{T}_R \left(\mathbf{U}_{R,i-\frac{1}{2}}, \mathbf{U}_{L,i-\frac{1}{2}}^*, \mathbf{U}_{R,i-\frac{1}{2}}^*, K_{i-\frac{1}{2}}^* \right) \end{array} \right]. \end{cases} \quad (5.37b)$$

In the following section, we present a series of numerical test-cases where we systematically compare the first-order results obtained with HR, HR-LS and HR-S.

5.4 First-order validation examples in one artery

In this section we present a series of numerical computations designed to evaluate the performances in physiological conditions of the low-Shapiro hydrostatic reconstruction (HR-LS) in comparison with the hydrostatic reconstruction (HR) and the subsonic hydrostatic reconstruction (HR-S).

The following numerical simulations are performed in a single artery representative of a large artery such as the aorta. Table 5.1 summarizes the values of the characteristic properties of blood and of the artery, namely the blood density ρ , the length L of the artery and the inlet neutral radius and arterial wall rigidity R_{in} and K_{in} .

ρ	L	R_{in}	K_{in}
1	10	0.5	10^5

Table 5.1 – Parameters describing the artery used in the different test-cases: the density ρ , the length L , the inlet radius R_{in} and the inlet rigidity K_{in} .

We study two geometrical configurations in which both the neutral cross-sectional area A_0 and the arterial wall rigidity K vary. Both are idealized representations of variations of arteries' geometrical and mechanical properties encountered in arterial networks. The

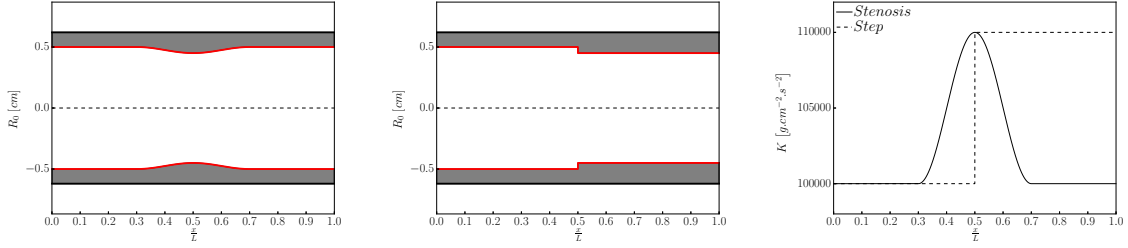


Figure 5.4 – Representation of the neutral radius R_0 and the arterial wall rigidity K for the smooth stenosis (5.38) and the decreasing step (5.39) configurations obtained for $\Delta\mathcal{G} = 10\%$:
Left: R_0 for the stenosis.
Center: R_0 for the step.
Right: K for the stenosis (—) and the step (--).

first configuration is a smooth stenosis and corresponds to a local reduction of the neutral cross-sectional area A_0 . It is a classical arterial pathology caused by the formation of plaque that deposits on the arterial wall and slowly obliterates the vessel. The stenosis is represented in Figure 5.4 and is defined by the following neutral radius R_0 and arterial wall rigidity K :

$$\begin{cases} R_0 = \begin{cases} R_{in} & \text{if } x < x_s \text{ or } x > x_e \\ R_{in} \left(1 - \frac{\Delta\mathcal{G}}{2} \left[1 + \cos \left(\pi + 2\pi \frac{x - x_s}{x_e - x_s} \right) \right] \right) & \text{if } x_s \leq x \leq x_e \end{cases} \\ K = \begin{cases} K_{in} & \text{if } x < x_s \text{ or } x > x_e \\ K_{in} \left(1 + \frac{\Delta\mathcal{G}}{2} \left[1 + \cos \left(\pi + 2\pi \frac{x - x_s}{x_e - x_s} \right) \right] \right) & \text{if } x_s \leq x \leq x_e. \end{cases} \end{cases} \quad (5.38)$$

We choose $x_s = \frac{3L}{10}$ and $x_e = \frac{7L}{10}$. The second configuration we investigate is a decreasing step, or decreasing discontinuity. It is an idealized representation of a pointwise transition between a parent artery and a smaller daughter artery and is useful to evaluate the wave reflection behavior of a numerical method. A similar configuration is studied in Subsection 6.2.3. The decreasing step is represented in Figure 5.4 and is defined by the following neutral radius R_0 and arterial wall rigidity K :

$$\begin{cases} R_0 = \begin{cases} R_{in} & \text{if } x < x_m \\ R_{in} (1 - \Delta\mathcal{G}) & \text{if } x \geq x_m \end{cases} \\ K = \begin{cases} K_{in} & \text{if } x < x_m \\ K_{in} (1 + \Delta\mathcal{G}) & \text{if } x \geq x_m. \end{cases} \end{cases} \quad (5.39)$$

We choose $x_m = \frac{L}{2}$. In both configurations, the amplitude of the geometrical and mechanical variations depends on the wall deformation parameter $\Delta\mathcal{G}$. The values of $\Delta\mathcal{G}$ used in the following simulations are taken from Table 5.2 and are chosen to test the limits of the well-balanced methods while staying in the subcritical flow regime. From a well-balanced point of view, each of these two configurations has a different behavior with respect to the cell size Δx . Indeed, the step configuration is a discontinuity of the neutral cross-sectional area A_0 and of the arterial wall rigidity K , and therefore the amplitude of the variations of the geometrical and mechanical properties of the artery, proportional to $\Delta\mathcal{G}$, is independent of Δx . On the contrary, the stenosis configuration describes smooth variations of A_0 and K , and therefore the local variations of the artery's geometrical and mechanical properties at each cell interface decrease with a decreasing cell size Δx .

We now provide the values of the conservative variables at the inlet and outlet of the computational domain. We impose the flow rate Q_{in} at the inlet, in $x = 0$. To control the flow regime, we parametrize the inlet flow rate Q_{in} using the inlet Shapiro number $S_{h,in}$

(2.85):

$$Q_{in} = S_{h,in} A_{in} c_{in}. \quad (5.40)$$

where A_{in} and c_{in} are respectively the inlet cross-sectional area and Moens-Korteweg wave speed (2.71) and are unknown. However, the dimensional analysis of System (2.67) performed in Subsection 2.6.1 shows that the inlet Shapiro number $S_{h,in} = 2\Delta R$ (2.76b). With this scaling law, we estimate a value of the inlet cross-sectional area A_{in} consistent with the inlet Shapiro number $S_{h,in}$:

$$A_{in} = A_0|_{x=0} [1 + S_{h,in}]^2. \quad (5.41)$$

At the outlet of the computational domain, in $x = L$, we either impose the reflection coefficient $R_t = 0$ or the cross-sectional area A_{out} , depending on the test case. Similarly to the inlet cross-sectional area A_{in} , we compute the outlet cross-sectional area as a function of $S_{h,in}$:

$$A_{out} = A_0|_{x=L} [1 + S_{h,in}]^2. \quad (5.42)$$

The values of the inlet Shapiro number $S_{h,in}$ and the wall deformation parameter $\Delta\mathcal{G}$ used in the following simulations are presented in Table 5.2. They cover a wide range of physiological configurations, allowing us to assess the behavior of the three hydrostatic reconstruction techniques in the limit of the low-Shapiro number flow regime. We recall that in arteries the average Shapiro number is $S_h \approx 10^{-2}$.

$S_{h,in}$	0	10^{-3}	10^{-2}	10^{-1}
$\Delta\mathcal{G}$	1%	10%	30%	

Table 5.2 – Values of the inlet Shapiro number $S_{h,in}$ and the wall deformation parameter $\Delta\mathcal{G}$ used in the single artery test-cases. These values are chosen to test the well-balanced methods in the limits of the low-Shapiro number flow regime.

5.4.1 Inviscid steady solutions

We evaluate the well-balanced properties of HR, HR-LS and HR-S by computing steady solutions of System (5.2) in the smooth stenosis (5.38) and the decreasing step (5.39). Steady flow configurations in arterial geometries similar to the stenosis (5.38) are studied by Müller [Müller et al. 2013], where only variations of the wall rigidity K are taken into account. In [Murillo and García-Navarro 2015], the authors compute steady solutions in tapered tubes. In the context of the shallow water equations, steady flow solutions over a bump (analogue of the stenosis) or a step are studied by many authors [Castro et al. 2007; Noelle et al. 2007; Castro Díaz et al. 2013; Delestre et al. 2013].

The steady numerical solutions are obtained for $t = 200$. The time step Δt is constant and chosen such that the CFL condition (4.25) is always satisfied. We impose the flow rate Q_{in} (5.40) at the inlet and the cross-sectional area A_{out} (5.42) at the outlet. We therefore select a specific steady state characterized by its associated flow rate Q_{st} and energy discharge E_{st} . These values can be computed analytically and provide exact solutions to compare with our numerical results:

$$\begin{cases} Q_{st} = Q_{in} \\ E_{st} = \frac{1}{2} \frac{Q_{st}^2}{A_{out}^2} + \frac{K|_{x=L}}{\rho} \left[\sqrt{A_{out}} - \sqrt{A_0|_{x=L}} \right]. \end{cases} \quad (5.43)$$

In both configurations (5.38) and (5.39), we perform a series of 12 numerical computations for all combinations of the inlet Shapiro number $S_{h,in}$ and the wall deformation parameter $\Delta\mathcal{G}$ taken from Table 5.2. Table 5.3 shows L^1 relative errors between the analytic solutions and the results obtained with HR, HR-LS and HR-S for a fixed number of cells $N_x = 50$.

$\Delta\mathcal{G}$		Stenosis			Step		
		1%	10%	30%	1%	10%	30%
$S_{h,in} = 0$							
$L^1[Q]$	HR	0	0	0	0	0	0
	HR-LS	0	0	0	0	0	0
	HR-S	0	0	0	0	0	0
$L^1[E]$	HR	0	0	0	0	0	0
	HR-LS	0	0	0	0	0	0
	HR-S	0	0	0	0	0	0
$S_{h,in} = 1 \times 10^{-3}$							
$L^1[Q]$	HR	4.0×10^{-4}	4.2×10^{-3}	1.4×10^{-2}	2.2×10^{-4}	2.3×10^{-3}	7.4×10^{-3}
	HR-LS	3.6×10^{-7}	4.1×10^{-6}	1.9×10^{-5}	1.8×10^{-7}	2.1×10^{-6}	9.4×10^{-6}
	HR-S	5.4×10^{-13}	5.3×10^{-13}	4.2×10^{-14}	2.9×10^{-13}	3.1×10^{-13}	5.8×10^{-13}
$L^1[E]$	HR	3.0×10^{-4}	5.1×10^{-3}	4.2×10^{-2}	2.1×10^{-4}	9.4×10^{-3}	1.3×10^{-1}
	HR-LS	2.1×10^{-7}	2.6×10^{-6}	1.5×10^{-5}	1.1×10^{-7}	1.4×10^{-6}	1.0×10^{-5}
	HR-S	4.6×10^{-13}	4.9×10^{-13}	6.1×10^{-13}	6.7×10^{-13}	6.5×10^{-13}	1.4×10^{-12}
$S_{h,in} = 1 \times 10^{-2}$							
$L^1[Q]$	HR	4.0×10^{-4}	4.2×10^{-3}	1.4×10^{-2}	2.3×10^{-4}	2.3×10^{-3}	7.4×10^{-3}
	HR-LS	3.6×10^{-6}	4.1×10^{-5}	1.9×10^{-4}	1.8×10^{-6}	2.1×10^{-5}	9.4×10^{-5}
	HR-S	2.6×10^{-13}	2.7×10^{-13}	9.6×10^{-14}	2.4×10^{-13}	9.5×10^{-14}	1.8×10^{-13}
$L^1[E]$	HR	3.0×10^{-4}	5.1×10^{-3}	4.2×10^{-2}	2.1×10^{-4}	9.4×10^{-3}	1.2×10^{-1}
	HR-LS	2.1×10^{-6}	2.6×10^{-5}	1.5×10^{-4}	1.1×10^{-6}	1.4×10^{-5}	8.1×10^{-5}
	HR-S	2.7×10^{-13}	2.7×10^{-13}	3.3×10^{-13}	2.7×10^{-13}	3.4×10^{-13}	5.9×10^{-13}
$S_{h,in} = 1 \times 10^{-1}$							
$L^1[Q]$	HR	4.0×10^{-4}	4.2×10^{-3}	1.4×10^{-2}	2.3×10^{-4}	2.3×10^{-3}	7.5×10^{-3}
	HR-LS	3.6×10^{-5}	4.1×10^{-4}	1.8×10^{-3}	1.8×10^{-5}	2.1×10^{-4}	9.0×10^{-4}
	HR-S	2.6×10^{-13}	3.4×10^{-13}	2.0×10^{-13}	2.8×10^{-13}	2.4×10^{-13}	1.4×10^{-13}
$L^1[E]$	HR	3.2×10^{-4}	5.4×10^{-3}	4.4×10^{-2}	2.2×10^{-4}	9.9×10^{-3}	1.2×10^{-1}
	HR-LS	2.2×10^{-5}	2.8×10^{-4}	1.8×10^{-3}	1.2×10^{-5}	2.0×10^{-4}	2.2×10^{-3}
	HR-S	2.3×10^{-13}	2.4×10^{-13}	2.9×10^{-13}	2.3×10^{-13}	2.9×10^{-13}	3.4×10^{-13}

Table 5.3 – Relative errors $L^1[Q]$ and $L^1[E]$ for the steady case computed in the stenosis (5.38) and the step (5.39) configurations for $N_x = 50$ cells for all combinations of values of the inlet Shapiro number $S_{h,in}$ and the wall deformation parameter $\Delta\mathcal{G}$ taken for Table 5.2. Only HR-S is exactly well-balanced, but HR-LS is more accurate than HR.

N_x	Stenosis				Step			
	$L^1 [Q]$	Order	$L^1 [E]$	Order	$L^1 [Q]$	Order	$L^1 [E]$	Order
HR								
50	4.22×10^{-3}		5.09×10^{-3}		2.34×10^{-3}		9.41×10^{-3}	
100	2.11×10^{-3}	-1.01	2.56×10^{-3}	-1.01	1.17×10^{-3}	-1.01	8.64×10^{-3}	-0.12
200	1.05×10^{-3}	-1.01	1.28×10^{-3}	-1.01	5.86×10^{-4}	-1.01	8.26×10^{-3}	-0.07
400	5.26×10^{-4}	-1.00	6.38×10^{-4}	-1.00	2.93×10^{-4}	-1.00	8.07×10^{-3}	-0.03
HR-LS								
50	4.14×10^{-5}		2.61×10^{-5}		2.08×10^{-5}		1.39×10^{-5}	
100	2.07×10^{-5}	-1.01	1.31×10^{-5}	-1.01	1.04×10^{-5}	-1.01	7.24×10^{-6}	-0.96
200	1.04×10^{-5}	-1.01	6.58×10^{-6}	-1.00	5.19×10^{-6}	-1.01	3.91×10^{-6}	-0.90
400	5.19×10^{-6}	-1.00	3.30×10^{-6}	-1.00	2.59×10^{-6}	-1.00	2.24×10^{-6}	-0.80
HR-S								
50	2.68×10^{-13}		2.73×10^{-13}		9.53×10^{-14}		3.43×10^{-13}	
100	1.40×10^{-15}		3.39×10^{-13}		9.20×10^{-14}		3.97×10^{-13}	
200	1.94×10^{-12}		7.30×10^{-13}		2.26×10^{-12}		8.44×10^{-13}	
400	8.83×10^{-12}		1.45×10^{-12}		1.01×10^{-11}		1.63×10^{-12}	

Table 5.4 – Relative convergence errors $L^1 [Q]$ and $L^1 [E]$ for the steady case computed in the stenosis (5.38) and the step (5.39) for $S_{h,in} = 10^{-2}$ and $\Delta\mathcal{G} = 10\%$ obtained for $N_x \in \{50, 100, 200, 400\}$. HR and HR-LS converge with order 1 whereas HR-S is exactly well-balanced up to machine precision.

In both the stenosis (5.38) and the step (5.39) configurations, the results are similar and indicate that, as expected, each numerical method is exactly well-balanced for the steady states at rest ($S_{h,in} = 0$). Only HR-S is exactly well-balanced for all considered subcritical steady states. For the low-Shapiro number steady states ($S_{h,in} \in \{10^{-3}, 10^{-2}, 10^{-1}\}$), HR-LS is more accurate than HR. However, the accuracy of HR-LS diminishes when the values of $S_{h,in}$ and $\Delta\mathcal{G}$ increase, and for $S_{h,in} = 10^{-1}$ and $\Delta\mathcal{G} = 30\%$, in the limit of the low-Shapiro number flow regime, HR-LS is only one order of magnitude more accurate than HR. Interestingly, the errors obtained with HR are independent of the inlet Shapiro number $S_{h,in}$, but increase significantly with the wall deformation parameter $\Delta\mathcal{G}$.

To test the consistency and the accuracy of the different methods, we perform a convergence study for the average low-Shapiro steady configuration $S_{h,in} = 10^{-2}$ and $\Delta\mathcal{G} = 10\%$ in both the stenosis and the step configurations. L^1 relative errors with analytic solutions are presented in Table 5.4 for the following number of cells $N_x \in \{50, 100, 200, 400\}$.

In the stenosis configuration (5.38), both HR and HR-LS converge with order 1, whereas in the step configuration (5.39), they do not achieve order 1 convergence. Indeed, in the stenosis configuration, the variations of the artery's geometrical and mechanical properties at each cell interface decrease when the number of cells N_x increases, enabling the convergence of both methods. On the contrary, the geometrical and mechanical variations remain unchanged in the step configuration when the number of cells N_x increases. These observations are illustrated by Figure 5.5 and Figure 5.6, where we respectively plot the spatial evolution of the flow rate Q and the energy discharge E obtained with increasing values of the number of cells N_x in the stenosis and step configurations.

In both configurations, the values of the errors obtained in Table 5.4 with HR-S are of the order of machine precision, indicating that HR-S is exactly well-balanced for the considered low-Shapiro steady state. However, the errors increase slightly with the number of cells. Similar behaviors are observed in convergence studies presented in [Castro Díaz et al. 2013] for an exactly well-balanced method. In our case, this phenomenon is due to a small error between the computed boundary conditions and those required to obtain the desired steady state, and is not caused by HR-S.

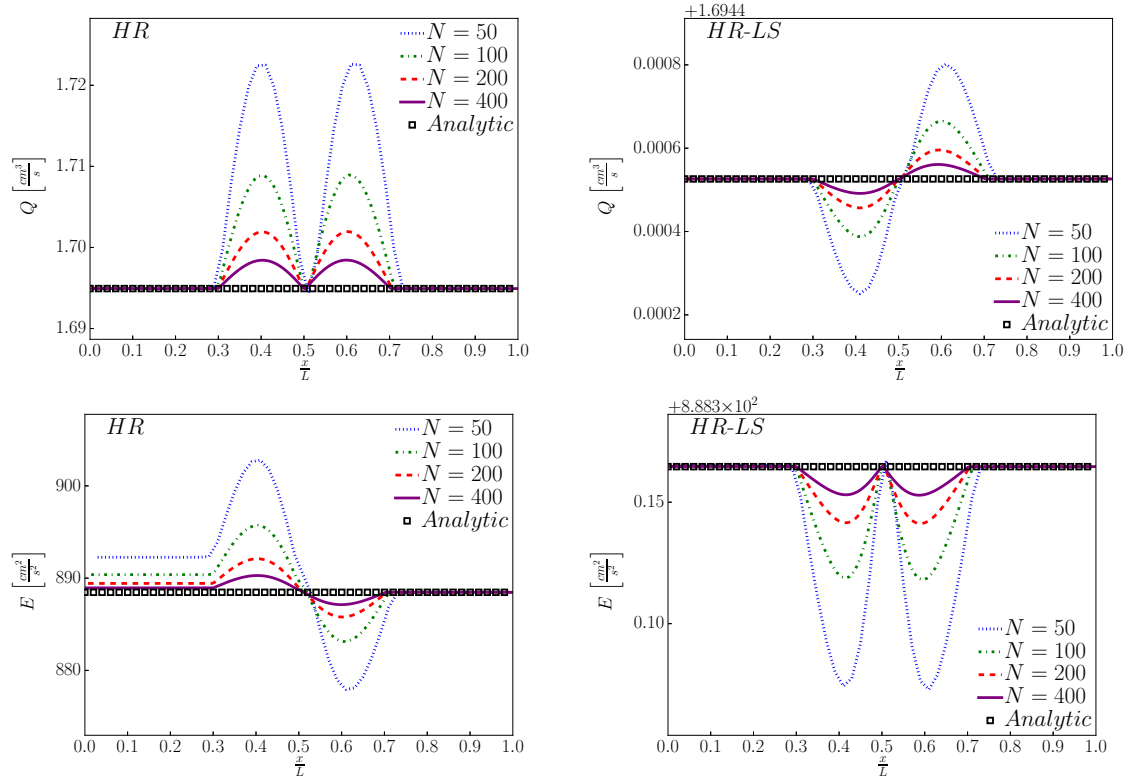


Figure 5.5 – Spatial evolution of the flow rate Q (top) and the energy discharge E (bottom) for the steady case in the stenosis configuration (5.38), at $t = 200$ for $S_{h,in} = 10^{-2}$ and $\Delta\mathcal{G} = 10\%$ obtained with different numbers of cells $N_x = \{50, 100, 200, 400\}$ and compared to the analytic solution (5.43) (\square):

Left: HR.

Right: HR-LS.

We observe that for both HR and HR-LS, the errors with the analytic solution decrease when the number of cells N_x increases, indicating the convergence of the method.

The results indicate that among the three well-balanced methods considered, HR is the least accurate when computing low-Shapiro number steady solutions in an artery presenting smooth and discontinuous variations of its neutral cross-sectional area A_0 and of its arterial wall rigidity K . On the contrary, HR-S is the only exactly well-balanced method for the considered low-Shapiro number steady states. Finally, even though HR-LS is not exactly well-balanced for the considered low-Shapiro number steady states, it allows to compute with satisfying accuracy steady solutions for smooth and discontinuous variations of the artery's geometrical and mechanical properties. These results show that System (5.16) is a better approximation than System (5.15) of the steady state system (5.13) in low-Shapiro flow configurations.

5.4.2 Inviscid wave propagation

The wave-capturing properties of HR, HR-LS and HR-S are now evaluated. We simulate the propagation of a single wave in the smooth stenosis (5.38) and decreasing step (5.39) configurations. The step configuration is studied in [Delestre and Lagr e 2013; Delestre et al. 2016; Wang et al. 2016c] for an artery with only variations of its neutral cross-sectional area A_0 .

The results are obtained for $t = 0.045$. The time step Δt is constant and chosen such that the CFL condition (4.25) is always satisfied. We impose a single pulse of flow at the inlet of

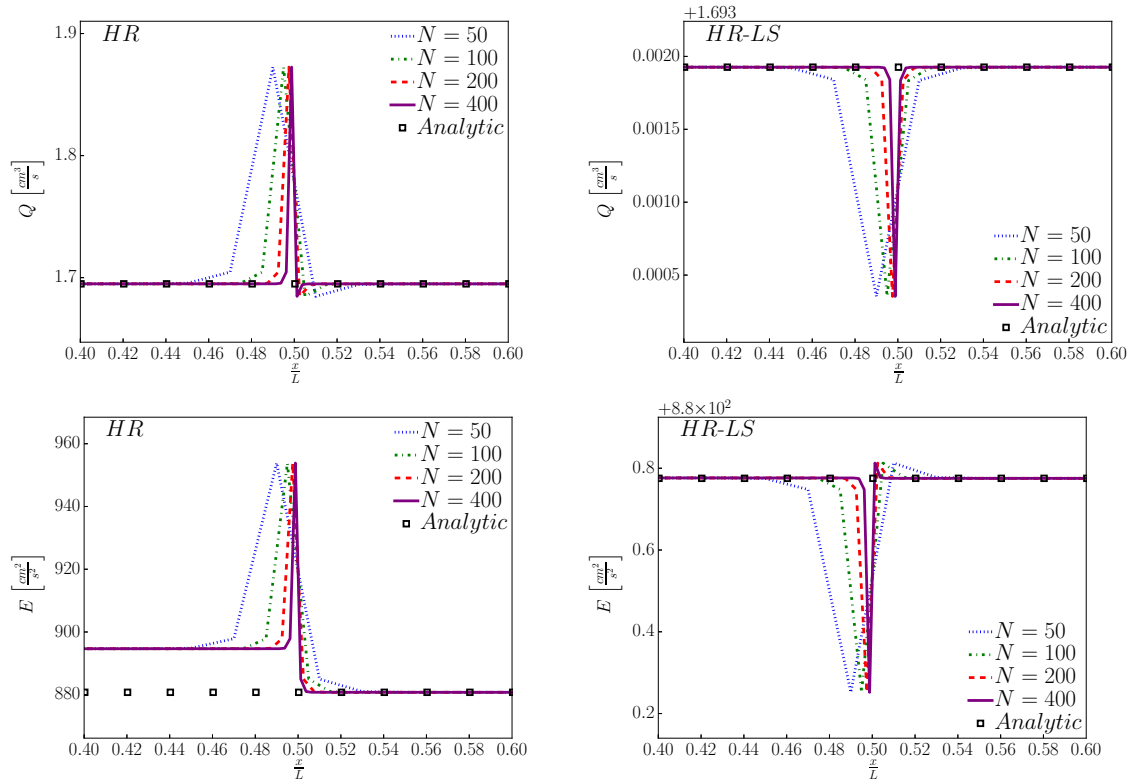


Figure 5.6 – Spatial evolution (zoom for $0.4 \leq \frac{z}{L} \leq 0.6$) of the flow rate Q (top) and the energy discharge E (bottom) for the steady case in the step configuration (5.39), at $t = 200$ for $S_{h,in} = 10^{-2}$ and $\Delta\mathcal{G} = 10\%$ obtained with different numbers of cells $N_x = \{50, 100, 200, 400\}$ and compared to the analytic solution (5.43) (\square):

Left: HR.

Right: HR-LS.

We observe that for both HR and HR-LS, the maximal amplitude of the errors with the analytic solution remains unchanged when the number of cells N_x increases. However, the region of error is more localized when the number of cells increases, explaining why the error decreases.

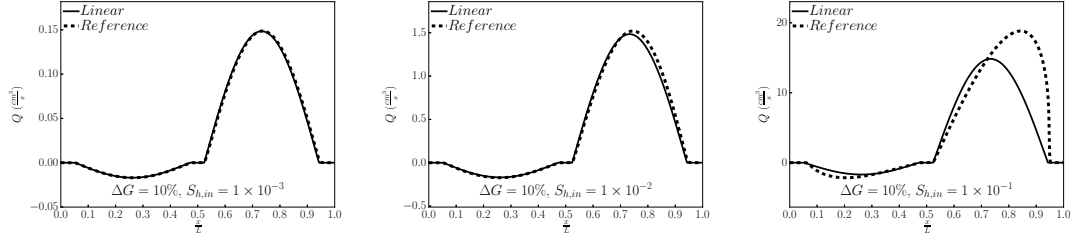


Figure 5.7 – Comparison between the linear solution (—) and the reference solution (--) in the wave propagation case for the step configuration (5.39), obtained using HR-S for $N_x = 25600$, for the flow rate Q at $t = 0.045$ for $\Delta\mathcal{G} = 10\%$.

Left: $S_h = 10^{-3}$.

Center: $S_h = 10^{-2}$.

Right: $S_h = 10^{-1}$.

the computational domain and the unsteady inlet flow rate $Q_{in}(t)$ is defined as:

$$Q_{in}(t) = \begin{cases} Q_{pulse} \sin\left(2\pi \frac{t}{T_{pulse}}\right) & \text{if } t \leq \frac{T_{pulse}}{2} \\ 0 & \text{else} \end{cases} \quad (5.44)$$

We choose $T_{pulse} = 0.04$ to artificially reduce the wave length of the pulse for visualization purposes and the value of Q_{pulse} is a function of the inlet Shapiro number $S_{h,in}$ and is defined by Equation (5.40). At the outlet of the computational domain, we set the reflection coefficient $R_t = 0$ to remove any terminal reflection.

The step configuration

We focus on the decreasing step configuration (5.39). Given the inlet condition (5.44), the pulse wave propagates in the artery starting from the left-hand side of the domain until it reaches the step. The change of impedance of the vessel creates reflected and transmitted waves that need to be captured by the numerical scheme. A linear analytic solution was proposed in [Raines et al. 1974] and validated in [Delestre and Lagrée 2013; Delestre et al. 2016; Wang et al. 2015], and gives the expression of the reflection coefficient R_t and the transmission coefficient T_t , based on the point junction conservation properties (6.1) presented in Subsection 6.2.1:

$$\begin{cases} R_t = \frac{Y_L - Y_R}{Y_L + Y_R} \\ T_t = 1 + R_t, \end{cases} \quad (5.45)$$

where $Y = A/[\rho c]$ is the vessel admittance. Subscripts L and R respectively refer to the values at the left and right of the step. As the coefficients R_t and T_t do not depend on the frequency of the incoming wave, we can analytically predict the position, shape and amplitude of the linear reflected and transmitted waves. However, as the inlet Shapiro number $S_{h,in}$ is non-zero, the flow is nonlinear and the linear analytic solution (5.45) is only valid in the linear limit $S_{h,in} \rightarrow 0$. To evaluate the quality of the results obtained with HR, HR-LS and HR-S, we compute reference solutions, obtained with HR-S for $N_x = 25600$ and values of $S_{h,in}$ and $\Delta\mathcal{G}$ taken from Table 5.2. To assess the validity of these reference solutions, we compare them to the linear analytic solutions (5.45) in Figure 5.7. We observe that for low values of the inlet Shapiro number $S_{h,in}$ (Figure 5.7 Left), for which the linear approximation is valid, the analytic and reference solutions match. As expected, for higher values of $S_{h,in}$, the flow is no longer linear and the propagation speed as well as the amplitude of the reflected and transmitted waves change (Figure 5.7 Center and Right).

We present results only for the flow rate Q to reduce the number of variables and simplify the analysis of the results. Similar conclusions to those presented hereafter would have been

drawn if we had considered the pressure p or the wall perturbation $R - R_0$.

We perform a series of 9 numerical computations with different combinations of the non-zero inlet Shapiro number $S_{h,in}$ and the wall deformation parameter $\Delta\mathcal{G}$ taken from Table 5.2. Table 5.5 shows $L^1[Q]$ relative errors between the reference solutions and the results obtained with HR, HR-LS and HR-S for a fixed number of cells $N_x = 1600$. We choose a high value of N_x to reduce the numerical dissipation and highlight the effects of the well-balanced methods.

$\Delta\mathcal{G}$		1%	10%	30%
$S_{h,in} = 1 \times 10^{-3}$				
$L^1[Q]$	HR	2.3×10^{-2}	5.5×10^{-2}	5.5×10^{-1}
	HR-LS	2.3×10^{-2}	2.8×10^{-2}	6.6×10^{-2}
	HR-S	2.3×10^{-2}	2.8×10^{-2}	6.6×10^{-2}
$S_{h,in} = 1 \times 10^{-2}$				
$L^1[Q]$	HR	2.3×10^{-2}	5.5×10^{-2}	5.5×10^{-1}
	HR-LS	2.3×10^{-2}	2.8×10^{-2}	6.6×10^{-2}
	HR-S	2.3×10^{-2}	2.8×10^{-2}	6.6×10^{-2}
$S_{h,in} = 1 \times 10^{-1}$				
$L^1[Q]$	HR	2.9×10^{-2}	6.1×10^{-2}	5.1×10^{-1}
	HR-LS	2.9×10^{-2}	3.5×10^{-2}	7.6×10^{-2}
	HR-S	2.9×10^{-2}	3.5×10^{-2}	7.5×10^{-2}

Table 5.5 – Relative error $L^1[Q]$ for the wave propagation case computed in the step (5.39) for values of $S_{h,in}$ and $\Delta\mathcal{G}$ taken from Table 5.2 obtained for $N_x = 1600$. HR, HR-LS and HR-S present similar results except for $\Delta\mathcal{G} = 30\%$.

The results obtained with HR, HR-LS and HR-S are almost identical and indicate that each method is able to correctly compute the expected reflected and transmitted waves. For each method, the error $L^1[Q]$ is independent of the inlet Shapiro number $S_{h,in}$ but increases with the wall deformation parameter $\Delta\mathcal{G}$. However, the error obtained with HR increases faster with $\Delta\mathcal{G}$ than with the other methods. In particular, for $\Delta\mathcal{G} = 30\%$, the value of $L^1[Q]$ obtained with HR is one order of magnitude higher than the one obtained with HR-LS or HR-S.

This last point is corroborated by Figure 5.8, Figure 5.9 and Figure 5.10, where we represent the spatial evolution of the flow rate Q at $t = 0.045$, obtained using $N_x = 100$ (Left) and $N_x = 1600$ (Right) for $S_{h,in} = 10^{-2}$ and $\Delta\mathcal{G} \in \{10\%, 30\%, 60\%\}$. In each figure, we compare the results obtained using HR, HR-LS and HR-S to the corresponding reference solution and observe if increasing the number of cells allows the numerical solution to converge towards the reference solution. In Figure 5.8, the results obtained for $\Delta\mathcal{G} = 10\%$ with HR, HR-LS and HR-S are similar and indicate that each numerical solution converges towards the reference solution. On the contrary, in Figure 5.9 for $\Delta\mathcal{G} = 30\%$ and in Figure 5.10 for $\Delta\mathcal{G} = 60\%$, only the solutions obtained with HR-LS and HR-S converge towards the reference solution. HR is unable to compute the expected amplitude of the reflected and transmitted waves and overestimates the amplitude of the reflected wave and underestimates the amplitude of the transmitted wave.

The results indicate that HR-LS and HR-S are able to compute wave reflections and transmissions in an artery presenting arbitrary large discontinuous variations of its cross-sectional area at rest A_0 and arterial wall rigidity K . On the contrary, HR is unable to compute the correct amplitude of the reflected and transmitted waves when the discontinuous variations of the artery's geometrical and mechanical properties are too large, independently of the number of cells N_x . Moreover, these results show that System (5.16) has the appropriate conservation properties to compute wave reflections for arbitrary large discontinuous geometrical and mechanical variations in low-Shapiro number flow regimes. On the contrary, HR, using

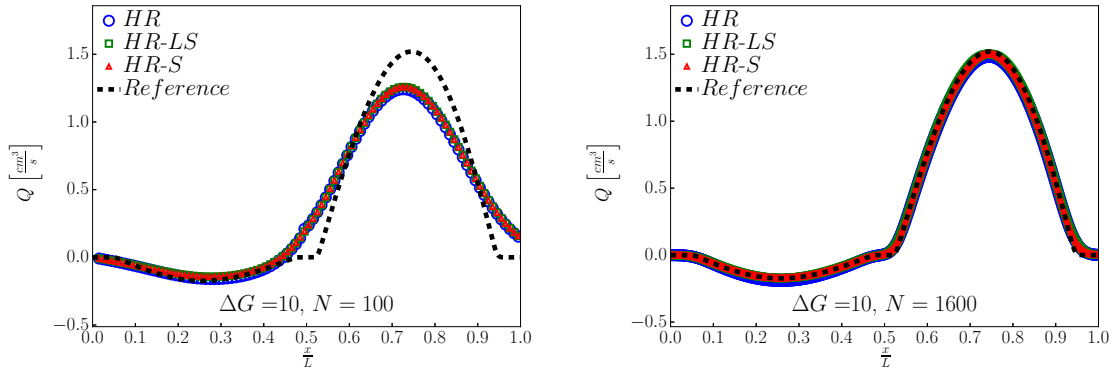


Figure 5.8 – Flow rate Q for the wave propagation case in the step configuration (5.39) at $t = 0.045$ for the reference solution (---), HR (○), HR-LS (□) and HR-S (△) for $S_h = 10^{-2}$ and $\Delta\mathcal{G} = 10\%$:

Left: $N_x = 100$.

Right: $N_x = 1600$.

For $N_x = 100$ and $N_x = 1600$, all solutions are comparable, and for $N_x = 1600$, HR, HR-LS and HR-S converge towards the reference solution.

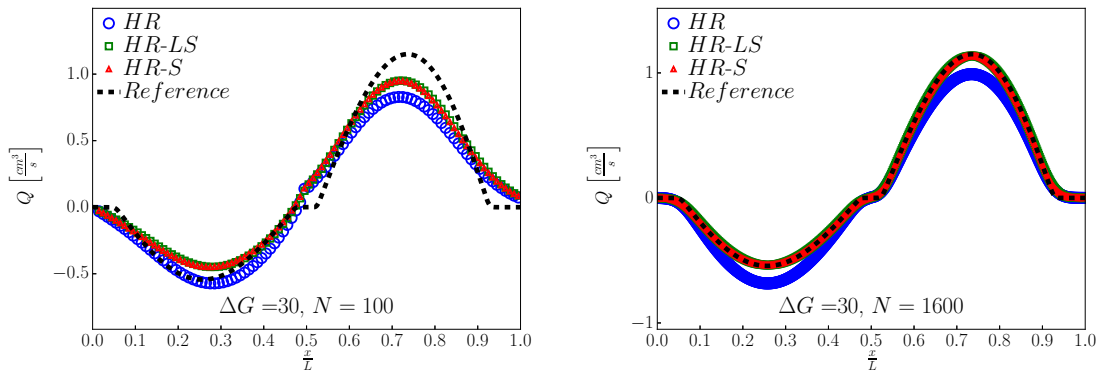


Figure 5.9 – Flow rate Q for the wave propagation case in the step configuration (5.39) at $t = 0.045$ for the reference solution (---), HR (○), HR-LS (□) and HR-S (△) for $S_h = 10^{-2}$ and $\Delta\mathcal{G} = 30\%$:

Left: $N_x = 100$.

Right: $N_x = 1600$.

HR-LS and HR-S converge towards the reference solution while HR does not.

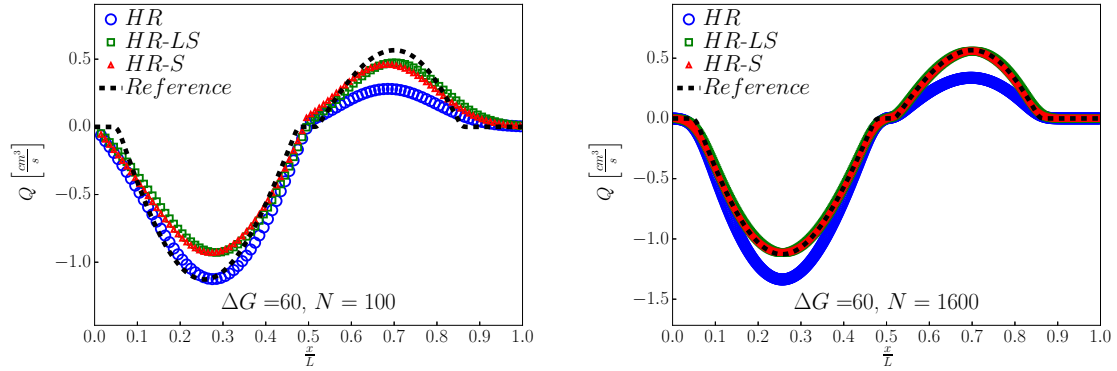


Figure 5.10 – Flow rate Q for the wave propagation case in the step configuration (5.39) at $t = 0.045$ for the reference solution (–), HR (\circ), HR-LS (\square) and HR-S (\triangle) for $S_h = 10^{-2}$ and $\Delta\mathcal{G} = 60\%$:

Left: $N_x = 100$.

Right: $N_x = 1600$.

HR-LS and HR-S converge towards the reference solution while HR does not.

System (5.15), is only able to compute wave reflections for small discontinuous variations of the artery's properties ($\Delta\mathcal{G} = 10\%$, see Figure 5.8). This last point can be problematic as large variations of the artery's geometrical and mechanical properties can be encountered when modeling arterial pathologies such as stenoses.

The stenosis configuration

In this subsection we focus on the stenosis configuration (5.38). To evaluate the quality of the results obtained with HR, HR-LS and HR-S, we compute reference solutions, obtained with HR-S for $N_x = 25600$ and values of $S_{h,in}$ and $\Delta\mathcal{G}$ taken from Table 5.2. As the variation of geometrical and mechanical properties of the artery is smooth, the observed flow rate is constituted of a continuum of reflected and transmitted waves that are created at each cell interface, where the artery's geometrical and mechanical properties are discontinuous.

Similar results to those of the previous paragraph are obtained, and therefore we do not completely repeat the previous analysis. In Figure 5.11, Figure 5.12 and Figure 5.13, we present the spatial evolution of the flow rate Q at $t = 0.045$, obtained using $N_x = 100$ (Left) and $N_x = 1600$ (Right) for $S_{h,in} = 10^{-2}$ and $\Delta\mathcal{G} = \{10\%, 30\%, 60\%\}$ respectively. In each figure, we compare the results obtained using HR, HR-LS and HR-S to the corresponding reference solution and observe if increasing the number of cells allows the numerical solution to converge towards the reference solution. Contrary to the step configuration studied in Subsection 5.4.2, the results obtained with HR, HR-LS and HR-S are similar and indicate that each numerical solution converges towards the reference solution. However, for $\Delta\mathcal{G} = \{30\%, 60\%\}$ and $N_x = 100$, HR is less accurate than HR-LS and HR-S.

These results are coherent with those of the previous paragraph. Indeed, when studying the step configuration, we showed that contrary to HR-LS and HR-S, HR overestimates the amplitude of the reflected wave and underestimates the amplitude of the transmitted wave when a large discontinuous variation of the artery's geometrical and mechanical properties is considered ($\Delta\mathcal{G} = \{30\%, 60\%\}$). As the stenosis is a smooth variation of the neutral cross-sectional area A_0 and of the arterial wall rigidity K , discontinuous variations of the arterial wall's geometrical and mechanical properties occur at each cell interface and the amplitude of these variations decreases with the number of cells N_x . Hence, for $\Delta\mathcal{G} = \{30\%, 60\%\}$ and $N_x = 100$, the local discontinuous variations of the artery's properties are large enough for HR to be inaccurate. On the contrary, for $N_x = 1600$, the local discontinuous

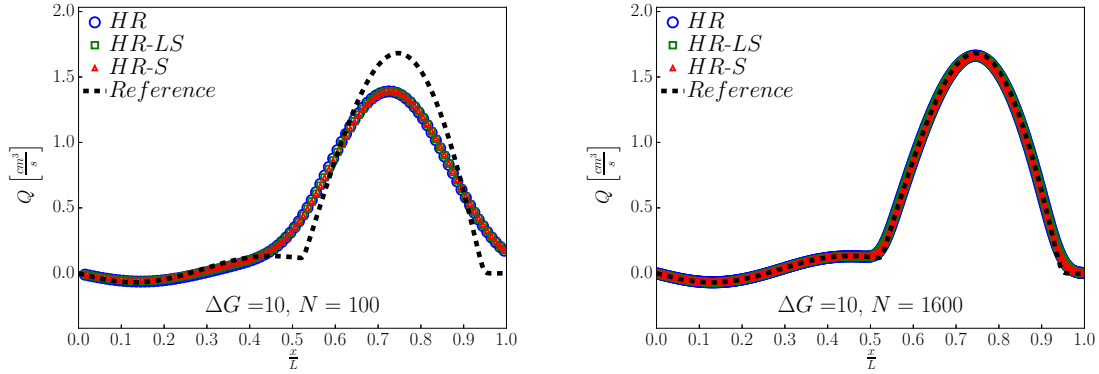


Figure 5.11 – Flow rate Q for the wave propagation case in the stenosis configuration (5.38) at $t = 0.045$ for the reference solution (---), HR (\circ), HR-LS (\square) and HR-S (\triangle) for $S_h = 10^{-2}$ and $\Delta\mathcal{G} = 10\%$:

Left: $N_x = 100$.

Right: $N_x = 1600$.

For $N_x = 100$ and $N_x = 1600$, all solutions are comparable, and for $N_x = 1600$, HR, HR-LS and HR-S converge towards the reference solution.

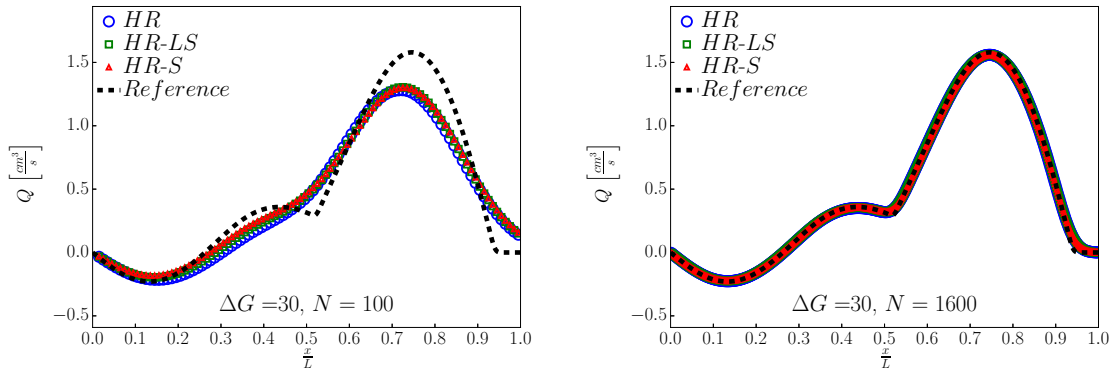


Figure 5.12 – Flow rate Q for the wave propagation case in the stenosis configuration (5.38) at $t = 0.045$ for the reference solution (---), HR (\circ), HR-LS (\square) and HR-S (\triangle) for $S_h = 10^{-2}$ and $\Delta\mathcal{G} = 30\%$:

Left: $N_x = 100$.

Right: $N_x = 1600$.

For $N_x = 100$ and $N_x = 1600$, all solutions are comparable, and for $N_x = 1600$, HR, HR-LS and HR-S converge towards the reference solution.

variation of the artery's geometrical and mechanical properties are sufficiently small for HR to be as accurate as HR-LS and HR-S.

We have studied the wave capturing behavior of HR, HR-LS and HR-S. We showed that for arbitrary large smooth or discontinuous variations of the artery's neutral cross-sectional area A_0 and arterial wall rigidity K , both HR-LS and HR-S are able to compute the expected reflected and transmitted waves. On the contrary, HR is unable to correctly compute reflected and transmitted waves when large discontinuous variations of the artery's properties are considered. In particular, HR overestimates the reflected wave and underestimates the transmitted wave. Therefore, HR-LS and HR-S are good choices to compute wave reflections and transmissions in low-Shapiro flow regimes.

The analysis conducted in this section allows us to conclude that both HR-LS and HR-S are adequate well-balanced methods to compute blood flow in large arteries with varying cross-sectional area at rest and arterial wall rigidity. However, in large networks where many

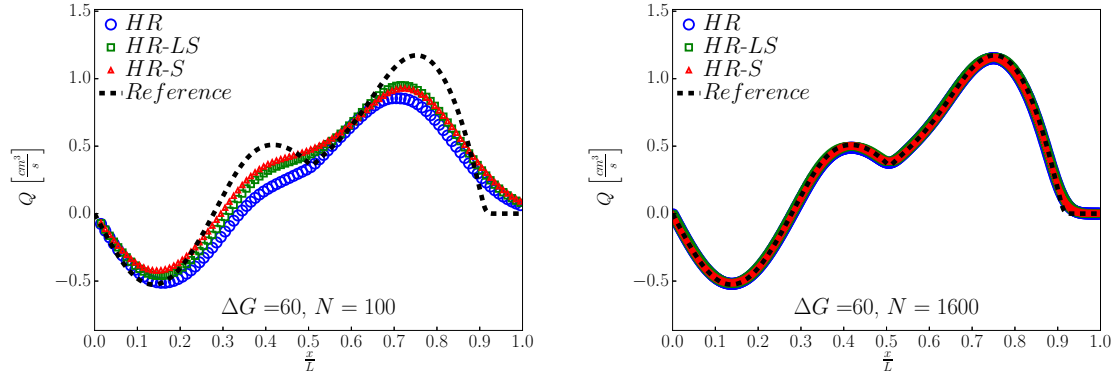


Figure 5.13 – Flow rate Q for the wave propagation case in the stenosis configuration (5.38) at $t = 0.045$ for the reference solution (---), HR (○), HR-LS (□) and HR-S (△) for $S_h = 10^{-2}$ and $\Delta G = 60\%$:

Left: $N_x = 100$.

Right: $N_x = 1600$.

For $N_x = 100$, HR is less accurate than HR-LS and HR-S, and for $N_x = 1600$, HR, HR-LS and HR-S converge towards the reference solution.

arteries present variations of their geometrical and mechanical properties, the additional iterations required by HR-S increase the computational cost compared to HR-LS. We therefore recommended using HR-LS in this case, as it is a good compromise between simplicity, numerical accuracy and efficiency. In the following section, we present the extension of HR-LS to second-order, using the methodology presented in Subsection 4.2.2.

5.5 Second-order extension

We describe here the numerical strategy we use to increase the spatial accuracy of the HR-LS well-balanced numerical scheme (5.26). As in Subsection 4.2.2, we use the monotonic upwind scheme for conservation law (MUSCL) linear variable reconstruction strategy. At each cell interface $x_{i+\frac{1}{2}}$, we define the vectors \mathbf{U}_L and \mathbf{U}_R at time t^n based on the MUSCL reconstruction (4.28):

$$\begin{cases} \mathbf{U}_L = \mathbf{U}_{i+\frac{1}{2}}^{+,n} \\ \mathbf{U}_R = \mathbf{U}_{i+\frac{1}{2}}^{-,n}. \end{cases} \quad (5.46a)$$

$$\quad (5.46b)$$

However, the neutral cross-sectional area A_0 and the arterial wall rigidity K also vary with the axial position. They must therefore be reconstructed as they play a role in the HR-LS numerical flux (5.27) and their reconstruction should account for the low-Shapiro steady states (5.16). Following [Bouchut 2004], we reconstruct the variables A , Q , A_0 and K at the cell interface $x_{i+\frac{1}{2}}$ using the procedure described below:

Step 1: We reconstruct the variables Q and K using the MUSCL reconstruction (4.28) and their respective MUSCL reconstructions at the left and right of the cell interface $x_{i+\frac{1}{2}}$ are:

$$\begin{cases} Q_L = Q_{i+\frac{1}{2}}^{+,n}, & Q_R = Q_{i+\frac{1}{2}}^{-,n} \\ K_L = K_{i+\frac{1}{2}}^{+,n}, & K_R = K_{i+\frac{1}{2}}^{-,n}. \end{cases} \quad (5.47)$$

Step 2: We reconstruct the following intermediate variables that preserve the low-Shapiro steady states (5.16):

$$\begin{cases} H = K\sqrt{A} \end{cases} \quad (5.48a)$$

$$\begin{cases} [H - Z] = H - Z, \end{cases} \quad (5.48b)$$

and their respective MUSCL reconstructions at the left and right of the cell interface $x_{i+\frac{1}{2}}$ are:

$$\begin{cases} H_L = H_{i+\frac{1}{2}}^{+,n}, & H_R = H_{i+\frac{1}{2}}^{-,n} \\ [H - Z]_L = [H - Z]_{i+\frac{1}{2}}^{+,n}, & [H - Z]_R = [H - Z]_{i+\frac{1}{2}}^{-,n}. \end{cases} \quad (5.49)$$

Step 3: We finally reconstruct the variables A_0 and A as:

$$\begin{cases} A_{0,L} = \left[\frac{[H - Z]_{i+\frac{1}{2}}^{+,n} - H_{i+\frac{1}{2}}^{+,n}}{K_{i+\frac{1}{2}}^{+,n}} \right]^2, & A_{0,R} = \left[\frac{[H - Z]_{i+\frac{1}{2}}^{-,n} - H_{i+\frac{1}{2}}^{-,n}}{K_{i+\frac{1}{2}}^{-,n}} \right]^2 \\ A_L = \left[\frac{H_{i+\frac{1}{2}}^{+,n}}{K_{i+\frac{1}{2}}^{+,n}} \right]^2, & A_R = \left[\frac{H_{i+\frac{1}{2}}^{-,n}}{K_{i+\frac{1}{2}}^{-,n}} \right]^2. \end{cases} \quad (5.50)$$

If used, the variable U is reconstructed using a variant of the MUSCL procedure (4.28) to conserve mass [Bouchut 2004]:

$$U_{i-\frac{1}{2}}^- = U_i - \frac{\Delta x}{2} \mathcal{D}(U_i) \frac{A_{i-\frac{1}{2}}^-}{A_i}, \quad U_{i+\frac{1}{2}}^+ = U_i + \frac{\Delta x}{2} \mathcal{D}(U_i) \frac{A_{i+\frac{1}{2}}^+}{A_i}. \quad (5.51)$$

We finally obtain a second-order well-balanced scheme by applying the HR-LS reconstruction presented in Subsection 5.3.2 to the MUSCL reconstructed variables (5.46) and then using the following modified well-balanced *finite volume* scheme:

$$\mathbf{U}_i^{n+1} = \mathbf{U}_i^n - \frac{\Delta t}{\Delta x} \left[\mathbf{F}_{i+\frac{1}{2}}^{n*} - \mathbf{F}_{i-\frac{1}{2}}^{n*} + \begin{bmatrix} 0 \\ F_{c,i} \end{bmatrix} \right], \quad (5.52)$$

where the momentum centered flux F_c is added for consistency reasons and is defined in the cell C_i as:

$$F_{c,i} = \mathcal{P} \left(A_{L,i+\frac{1}{2}}, A_{c,L,i+\frac{1}{2}}, K_{L,i+\frac{1}{2}}, K_{c,i} \right) - \mathcal{P} \left(A_{R,i-\frac{1}{2}}, A_{c,R,i-\frac{1}{2}}, K_{R,i-\frac{1}{2}}, K_{c,i} \right). \quad (5.53)$$

The centered variables K_c and Z_c are defined in the cell C_i as:

$$\begin{cases} K_{c,i} = \sqrt{K_{L,i+\frac{1}{2}} K_{R,i-\frac{1}{2}}} \\ Z_{c,i} = \frac{1}{2} \left[Z_{L,i+\frac{1}{2}} + Z_{R,i-\frac{1}{2}} \right] \\ A_{c,L,i+\frac{1}{2}} = \left[\frac{Z_{c,i} + [H - Z]_{L,i+\frac{1}{2}}}{K_{c,i}} \right]^2 \\ A_{c,R,i-\frac{1}{2}} = \left[\frac{Z_{c,i} + [H - Z]_{R,i-\frac{1}{2}}}{K_{c,i}} \right]^2. \end{cases} \quad (5.54)$$

5.6 Second-order validation examples in one artery

We present a series of test cases in an artery with varying geometrical and mechanical properties. These test cases are designed to assess the accuracy of the MUSCL reconstruction procedure presented in Section 5.5 for HR-LS. In each test case, we systematically compare the results obtained with the first-order and MUSCL variable reconstructions used in combination with HR-LS and evaluate the accuracy of both methods using the errors (4.50).

5.6.1 Inviscid steady solutions

This steady test case is identical to the one presented in Subsection 5.4.1. We use the same parameters, presented in Table 5.1, and the same inlet (5.40) and outlet (5.41) boundary

conditions, computed for $\Delta\mathcal{G} = 10^{-1}$ and $S_h \in \{10^{-3}, 10^{-2}, 0\}$. However, contrary to the steady test case presented in Subsection 5.4.1, we use the inviscid steady solution (5.43) as an initial condition to accelerate the convergence towards the steady state.

In Figure 5.14 Left, we compare at time $t = 2.49$ the spatial evolution of the steady solutions (5.43) for the energy discharge E , the pressure p and the flow rate Q with the spatial evolution of the first-order and MUSCL numerical solutions obtained with $N_x = 100$ for $\Delta\mathcal{G} = 10^{-1}$ and $S_h = 10^{-3}$. We observe that for each variable, the steady solution is correctly described and the MUSCL solution is more accurate than the first-order solution.

In Figure 5.14 Right, we plot at time $t = 2.49$ the evolution with the number of cells N_x of the first-order and MUSCL L_1 errors for the energy discharge E , the pressure p and the flow rate Q obtained for $\Delta\mathcal{G} = 10^{-1}$ and $S_h \in \{10^{-3}, 10^{-2}, 0\}$. We observe that for each variable, the L_1 errors decrease with an increasing number of cells N_x , indicating that the first-order and MUSCL numerical solutions converge towards the steady solution. Moreover, first-order and second-order accuracy is achieved. Note that for $S_h = 0$, the errors reach machine precision as HR-LS is exactly well-balanced for the steady state at rest (5.14).

5.6.2 Wave propagation in a tapered tube

This test case describes the propagation of a pulse wave in a slightly tapered artery, where the neutral cross-sectional area A_0 and the arterial wall rigidity K vary slowly in the x -direction. We derive an asymptotic solution following the work presented in [Bois 2000], where similar solutions are obtained for acoustic or river waves. This solution is relevant as a validation test case but is not physiologically significant as takes place at large x , far from the inlet of the artery. Such a long unperturbed propagation length is never encountered in physiological conditions.

Asymptotic solution

To capture the perturbations induced by vessel tapering, we introduce in Table 5.6 non-dimensional variables.

$$\underline{t = T\bar{t} \quad x = X\bar{x} \quad R_0 = R_0\bar{f} \quad R = R_0 [\bar{f} + \Delta_R\bar{R}] \quad K = K_0\bar{g} \quad Q = Q\bar{Q} \quad p = p_0 + \Pi\bar{p}}$$

Table 5.6 – *Tapering non-dimensional variables.*

The geometrical and mechanical functions f and g characterize the slow tapering of the artery and therefore vary slowly in the x -direction. A dimensional analysis similar to the one performed in Subsection 2.6.1 allows us to write System (5.2) as:

$$\left\{ \begin{array}{l} [\bar{f} + \Delta_R\bar{R}] \frac{\partial\bar{R}}{\partial\bar{t}} + \frac{\partial\bar{Q}}{\partial\bar{x}} = 0 \end{array} \right. \quad (5.55a)$$

$$\left\{ \begin{array}{l} \frac{\partial\bar{Q}}{\partial\bar{t}} + [2\Delta_R] \frac{\partial}{\partial\bar{x}} \left[\frac{\bar{Q}^2}{[\bar{f} + \Delta_R\bar{R}]^2} \right] + \left[2\frac{\Delta_R}{S_h} \right]^2 [\bar{f} + \Delta_R\bar{R}]^2 \frac{\partial}{\partial\bar{x}} [\bar{g}\bar{R}] = 0. \end{array} \right. \quad (5.55b)$$

We then consider a linear pulsatile regime, and using the relations (2.75) derived in Subsection 2.6.1, we linearize System (5.55) and obtain:

$$\left\{ \begin{array}{l} \bar{f} \frac{\partial\bar{R}}{\partial\bar{t}} + \frac{\partial\bar{Q}}{\partial\bar{x}} = 0 \end{array} \right. \quad (5.56a)$$

$$\left\{ \begin{array}{l} \frac{\partial\bar{Q}}{\partial\bar{t}} = -\bar{f}^2 \frac{\partial}{\partial\bar{x}} [\bar{g}\bar{R}]. \end{array} \right. \quad (5.56b)$$

We finally rewrite System (5.56) as a single equation by combining Equation (5.56a) and

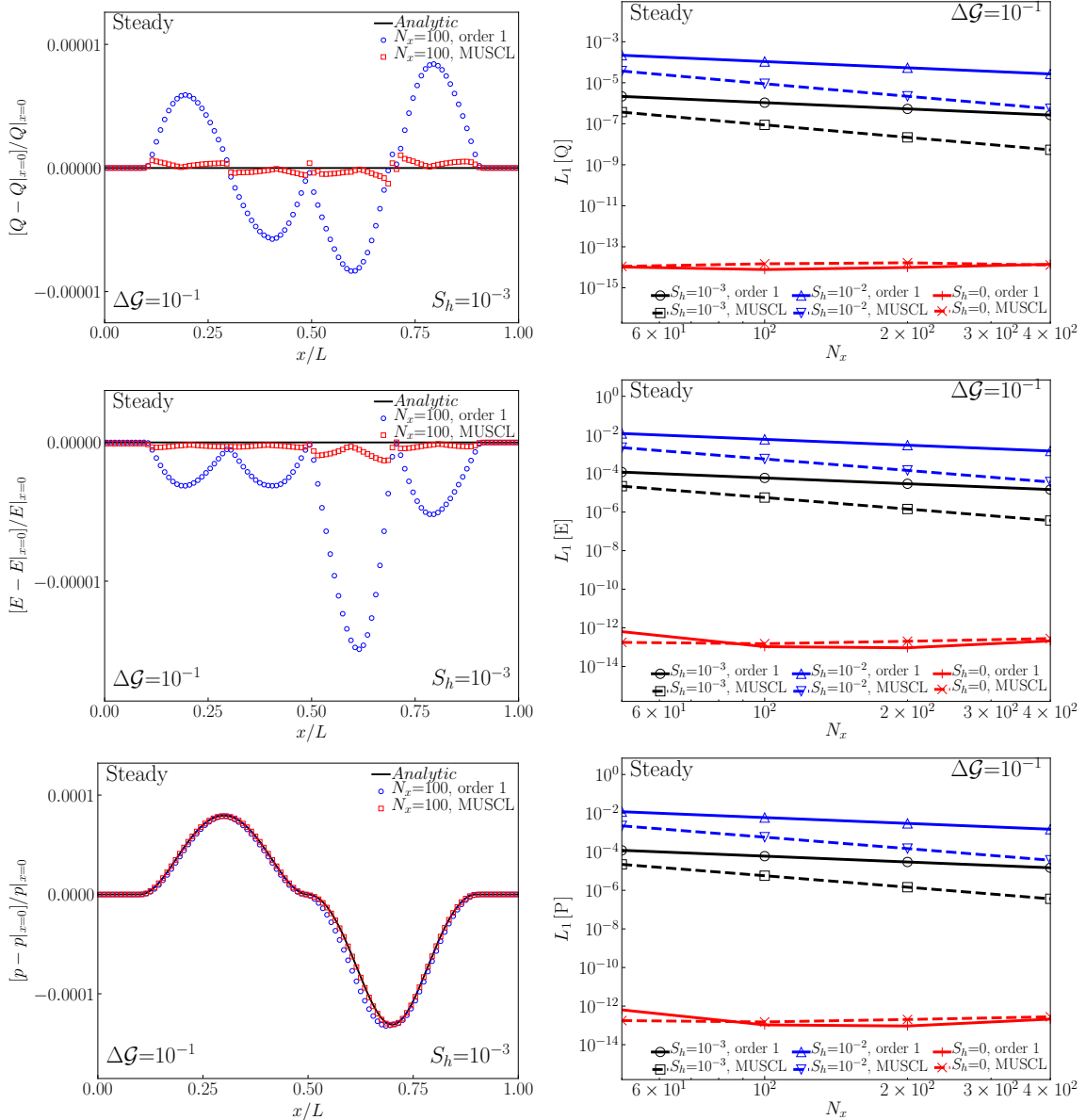


Figure 5.14 – The inviscid steady test case:

Left: Comparison between the steady solution (—) and the first-order (○) and MUSCL (□) numerical solutions obtained with $N_x = 100$ at time $t = 2.49$ for $\Delta\mathcal{G} = 10^{-1}$ and $S_h = 10^{-3}$.

Right: Spatial convergence of the first-order (○, △, +) and MUSCL (□, ▽, ×) L_1 errors obtained at time $t = 2.49$ for $\Delta\mathcal{G} = 10^{-1}$ and $S_h \in \{10^{-3}, 10^{-2}, 0\}$ with $N_x \in \{50, 100, 200, 400\}$.

The first-order and MUSCL solutions converge towards the steady solution and first-order and second-order accuracy is achieved.

Equation (5.56b):

$$\frac{1}{\bar{f}\bar{g}} \frac{\partial^2 \bar{Q}}{\partial \bar{t}^2} - \frac{\partial^2 \bar{Q}}{\partial \bar{x}^2} = \left[\frac{1}{\bar{g}} \frac{\partial \bar{g}}{\partial \bar{x}} - \frac{1}{\bar{f}} \frac{\partial \bar{f}}{\partial \bar{x}} \right] \frac{\partial \bar{Q}}{\partial \bar{x}}. \quad (5.57)$$

Introducing the dimensionless wave speed:

$$\bar{c} = \sqrt{\bar{f}\bar{g}}, \quad (5.58)$$

Equation (5.57) rewrites:

$$\frac{1}{\bar{c}^2} \frac{\partial^2 \bar{Q}}{\partial \bar{t}^2} - \frac{\partial^2 \bar{Q}}{\partial \bar{x}^2} = \left[\frac{1}{\bar{g}} \frac{\partial \bar{g}}{\partial \bar{x}} - \frac{1}{\bar{f}} \frac{\partial \bar{f}}{\partial \bar{x}} \right] \frac{\partial \bar{Q}}{\partial \bar{x}}. \quad (5.59)$$

As Equation (5.59) is linear in t , we search for a wave solution of the form:

$$\bar{Q} = \tilde{Q}(\bar{x}) \exp(i\omega \bar{t}), \quad \omega \in \mathbb{R}. \quad (5.60)$$

Injecting the expression (5.60) into Equation (5.59), we obtain:

$$\frac{d^2 \tilde{Q}}{d\bar{x}^2} + \frac{\omega^2}{\bar{c}^2} \tilde{Q} = - \left[\frac{1}{\bar{g}} \frac{d\bar{g}}{d\bar{x}} - \frac{1}{\bar{f}} \frac{d\bar{f}}{d\bar{x}} \right] \frac{d\tilde{Q}}{d\bar{x}}. \quad (5.61)$$

To keep track of the slowly varying neutral radius R_0 and arterial wall rigidity K , we use the following change of variables, to place ourselves at long x while keeping track of local variations of the wave speed:

$$\frac{d\xi}{d\bar{x}} = \Phi'(X), \quad X = \epsilon \bar{x}, \quad (5.62)$$

where ϵ is the small parameter characterizing the slow variations of the neutral radius R_0 and the arterial wall rigidity K . The function Φ' represents the wave distortion. Using this change of variables, we have:

$$\begin{cases} \frac{\partial}{\partial \bar{x}} = \frac{\partial \xi}{\partial \bar{x}} \frac{\partial}{\partial \xi} + \frac{\partial X}{\partial \bar{x}} \frac{\partial}{\partial X} = \Phi' \frac{\partial}{\partial \xi} + \epsilon \frac{\partial}{\partial X} \\ \frac{\partial^2}{\partial \bar{x}^2} = \Phi'^2 \frac{\partial^2}{\partial \xi^2} + 2\epsilon \Phi' \frac{\partial^2}{\partial X \partial \xi} + \epsilon \Phi'' \frac{\partial}{\partial \xi} + O(\epsilon^2), \end{cases} \quad (5.63)$$

and Equation (5.61) rewrites:

$$\Phi'^2 \frac{\partial^2 \tilde{Q}}{\partial \xi^2} + \frac{\omega^2}{\bar{c}^2} \tilde{Q} = -\epsilon \left[2\Phi' \frac{\partial^2 \tilde{Q}}{\partial X \partial \xi} + \Phi'' \frac{\partial \tilde{Q}}{\partial \xi} + \Phi' \left[\frac{\bar{g}'}{\bar{g}} - \frac{\bar{f}'}{\bar{f}} \right] \frac{\partial \tilde{Q}}{\partial \xi} \right] + O(\epsilon^2). \quad (5.64)$$

We now use an asymptotic expansion of \tilde{Q} in ϵ :

$$\tilde{Q} = \tilde{Q}_0 + \epsilon \tilde{Q}_1 + \epsilon^2 \tilde{Q}_2 + \dots \quad (5.65)$$

Injecting expression (5.65) into Equation (5.64) and regrouping the terms of order $O(1)$, we obtain:

$$\Phi'^2 \frac{\partial^2 \tilde{Q}_0}{\partial \xi^2} + \frac{\omega^2}{\bar{c}^2} \tilde{Q}_0 = 0. \quad (5.66)$$

The solution of Equation (5.66) writes:

$$\tilde{Q}_0 = A(X) e^{i\Omega \xi} + C.C., \quad (5.67)$$

where $C.C.$ refers to the complex conjugate and:

$$\Omega = \frac{\omega}{\bar{c}\Phi'}. \quad (5.68)$$

Without loss of generality, we set $\Omega = 1$ (if this is not the case, we use the change of variables $\eta = \Omega \xi$). Using expression (5.67) and regrouping the terms of order $O(\epsilon)$ we obtain:

$$\Phi'^2 \frac{\partial^2 \tilde{Q}_1}{\partial \xi^2} + \frac{\omega^2}{\bar{c}^2} \tilde{Q}_1 = -i \left[2\Phi' A' + \Phi'' A + \Phi' A \left[\frac{\bar{g}'}{\bar{g}} - \frac{\bar{f}'}{\bar{f}} \right] \right] e^{i\xi} + C.C. \quad (5.69)$$

Since $e^{i\Omega \xi}$ (here $\Omega = 1$) is solution of Equation (5.66), the right hand side of Equation (5.69)

is a secular term that we set to zero to keep the solution bounded. Therefore we have:

$$2\Phi'A' + \Phi''A + \Phi'A \left[\frac{\bar{g}'}{\bar{g}} - \frac{\bar{f}'}{\bar{f}} \right] = 0, \quad (5.70)$$

and the solution to Equation (5.70) writes:

$$A = B \sqrt{\frac{\bar{f}}{\bar{g}\Phi'}} = \frac{B}{\sqrt{\omega}} \frac{\bar{f}^{\frac{3}{4}}}{\bar{g}^{\frac{1}{4}}}, \quad B = cst. \quad (5.71)$$

Finally, the first-order solution \bar{Q}_0 writes:

$$\bar{Q}_0 = \frac{B}{\sqrt{\omega}} \frac{\bar{f}^{\frac{3}{4}}}{\bar{g}^{\frac{1}{4}}} \exp \left(i\omega \left[\bar{t} - \frac{1}{\epsilon} \int_0^X \frac{1}{c} dX \right] \right) + C.C. \quad (5.72)$$

Numerical solution

We consider a tapered artery for which:

$$\begin{cases} \bar{f} = 1 + \epsilon_R \bar{x} \\ \bar{g} = 1 + \epsilon_K \bar{x}. \end{cases} \quad (5.73a)$$

We impose at the inlet the flow wave Q_{in} :

$$Q_{in}(t) = \begin{cases} \frac{\hat{Q}}{2} \left[1 + \cos \left(\pi + 2\pi \frac{t}{T} \right) \right] & \text{if } 0 \leq \frac{t}{T} \leq 1 \\ 0 & \text{else.} \end{cases} \quad (5.74)$$

At the outlet, we impose a non-reflecting boundary condition to remove any backward traveling wave. The parameters used in this test case are described in Table 5.7.

ρ	L	R_0	K	ϵ_R	ϵ_K	\hat{Q}	T	R_t	Δt	t order
1	200	1	10^4	-0.1	0.1	1	1	0	10^{-4}	2

Table 5.7 – Geometrical, mechanical, numerical and boundary parameters used in the taper test case.

In Figure 5.15 Left, we compare at times $t \in \{0.5, 1, 1.5, 2, 2.5\}T$ the spatial variations of the inviscid asymptotic taper solution for the flow rate Q with the spatial variations of the first-order and MUSCL numerical solutions obtained with $N_x = 100$ for $[\epsilon_R = -0.1, \epsilon_K = 0]$ and $[\epsilon_R = 0, \epsilon_K = 0.1]$. In both cases, we observe that the inviscid asymptotic solutions are correctly described and that the MUSCL solutions are more accurate than the first-order solutions.

In Figure 5.15 Right, we plot at time $t = 1.5T$ the evolution with the number of cells N_x of the first-order and MUSCL L_1 , L_2 and L_∞ errors for the flow rate Q obtained for $[\epsilon_R = -0.1, \epsilon_K = 0]$ and $[\epsilon_R = 0, \epsilon_K = 0.1]$. In both cases, the L_1 , L_2 and L_∞ errors decrease with an increasing number of cells N_x , indicating that the first-order and MUSCL numerical solutions converge towards the analytic solution. For $50 \leq N_x \leq 400$, first-order accuracy is achieved. However, for larger values of N_x , the MUSCL L_1 , L_2 and L_∞ errors saturate as the taper solution is a linear asymptotic solution of System (5.2).

5.6.3 Inviscid Thacker solution

This test case describes inviscid pressure oscillations in a parabolic aneurysm and is greatly inspired from the solutions of Thacker [Thacker 1981] and Sampson [Sampson et al. 2006], well-known in the shallow water community.

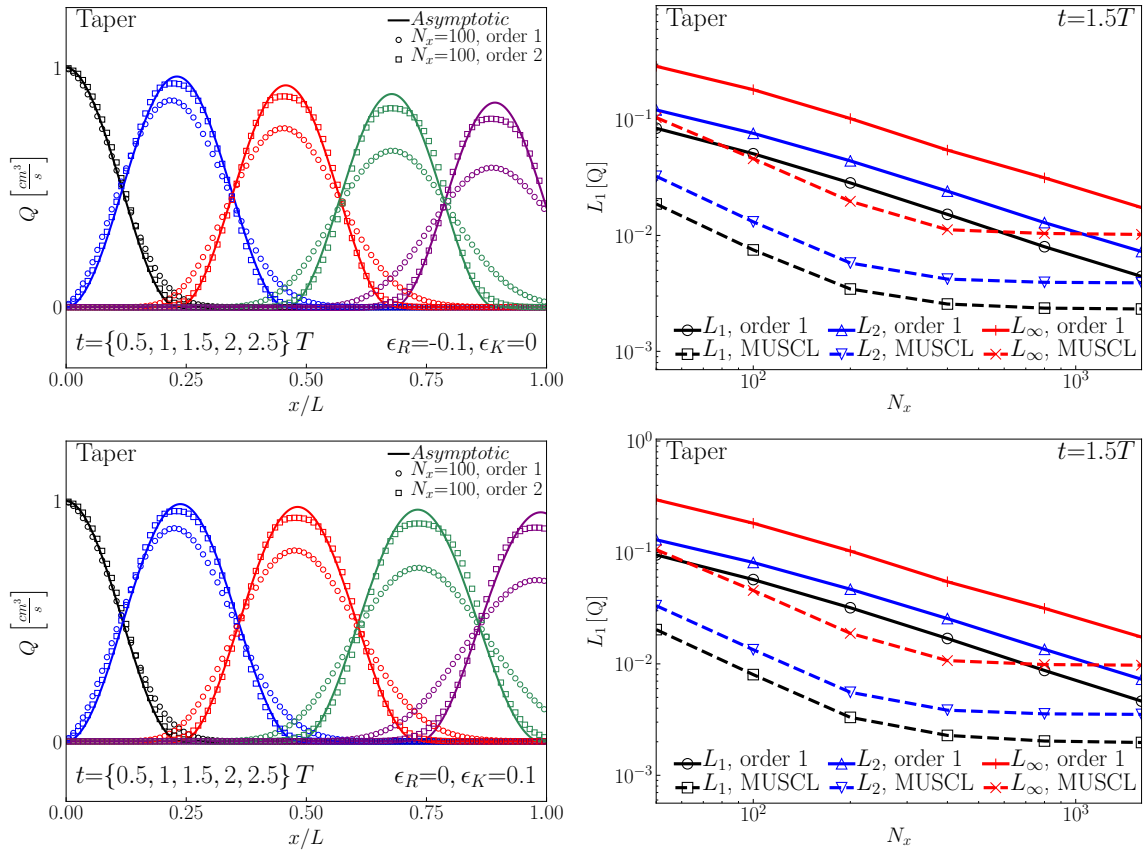


Figure 5.15 – *The inviscid taper test cases:*

Left: Comparison between the asymptotic (—), first-order (\circ) and MUSCL (\square) waveforms obtained with $N_x = 100$ at times $t \in \{0.5, 1, 1.5, 2, 2.5\}T$ for $[\epsilon_R = -0.1, \epsilon_K = 0]$ (top) and $[\epsilon_R = 0, \epsilon_K = 0.1]$ (bottom).

Right: Spatial convergence of the first-order ($\circ, \Delta, +$) and MUSCL (\square, ∇, \times) L_1 , L_2 and L_∞ errors obtained at time $t = 1.5T$ with $N_x \in \{50, 100, 200, 400, 800, 1600\}$ for $[\epsilon_R = -0.1, \epsilon_K = 0]$ (top) and $[\epsilon_R = 0, \epsilon_K = 0.1]$ (bottom).

The first-order and MUSCL solutions converge towards the asymptotic solutions. Only first-order accuracy is achieved and the MUSCL L_1 , L_2 and L_∞ errors saturate as the taper solution is a linear asymptotic solution of System (5.2).

Analytic solution

We look for a regular solution of System (5.2) rewritten in its nonconservative form:

$$\left\{ \begin{array}{l} \frac{\partial}{\partial t} [\pi R^2] + \frac{\partial}{\partial x} [\pi R^2 U] = 0 \end{array} \right. \quad (5.75a)$$

$$\left\{ \begin{array}{l} \frac{\partial U}{\partial t} + U \frac{\partial U}{\partial x} + \frac{1}{\rho} \frac{\partial p}{\partial x} = 0. \end{array} \right. \quad (5.75b)$$

We first assume that:

$$U(x, t) = U_0(t). \quad (5.76)$$

This strong assumption enables us to rewrite Equation (5.75b) as:

$$p = F_0(t) - \rho x \frac{dU_0}{dt}, \quad (5.77)$$

where $F_0(t) \in \mathbb{R}$. We then obtain from Equation (5.75a) and Equation (5.77) combined with the thin wall law (5.1) the following simplified governing equation:

$$\frac{dF_0}{dt} - \frac{d}{dt} \left[\frac{\rho U_0^2}{2} \right] - \rho x \frac{d^2 U_0}{dt^2} + K' U_0 \frac{dR_0}{dx} - U_0 \frac{p}{K'} \frac{dK'}{dx} = 0, \quad (5.78)$$

where $K' = \sqrt{\pi} K$. To describe aneurysms (expansions) as well as stenoses (constrictions), we choose the following spatial variations of the neutral cross-sectional area A_0 and the arterial wall rigidity K' in the domain $x \in [-a, a]$:

$$\left\{ \begin{array}{l} R_0 = \bar{R}_0 \left[1 + \Delta \mathcal{G} \left[1 - \frac{x^2}{a^2} \right] \right] \\ K' = \text{cst} \end{array} \right. \quad \begin{array}{l} \text{with } \bar{R}_0 > 0, a > 0, \Delta \mathcal{G} > -1 \\ \text{with } K' > 0. \end{array} \quad (5.79a)$$

Injecting the expressions (5.79a) and (5.79b) into Equation (5.78) and identifying the powers of x , we obtain for $(x, t) \in [-a, a] \times [0, +\infty]$:

$$\left\{ \begin{array}{l} \frac{d^2 U_0}{dt^2} + \Delta \mathcal{G} \omega^2 U_0 = 0 \\ \frac{dF_0}{dt} - \frac{d}{dt} \left[\frac{\rho U_0^2}{2} \right] = 0. \end{array} \right. \quad (5.80a)$$

$$\left\{ \begin{array}{l} \frac{d^2 U_0}{dt^2} + \Delta \mathcal{G} \omega^2 U_0 = 0 \\ \frac{dF_0}{dt} - \frac{d}{dt} \left[\frac{\rho U_0^2}{2} \right] = 0. \end{array} \right. \quad (5.80b)$$

The parameter $\omega = 2c/a$ is the characteristic pulsation and $c = \sqrt{\frac{K'}{2\rho} \bar{R}_0}$ is the Moens-Korteweg celerity (2.71). We complete System (5.80) with the initial condition:

$$U_0(t=0) = 0. \quad (5.81)$$

To describe aneurysms, we choose $\Delta \mathcal{G} > 0$ and simple analysis allows us to obtain the solution of System (5.80):

$$\left\{ \begin{array}{l} U_0 = U \sin \left(\frac{t}{\tau} \right) \\ p = -\frac{1}{4} \rho U^2 \cos \left(2 \frac{t}{\tau} \right) - \rho \frac{x}{\tau} U \cos \left(\frac{t}{\tau} \right), \end{array} \right. \quad \text{with } U = \text{cst} \quad (5.82a)$$

$$\left\{ \begin{array}{l} U_0 = U \sin \left(\frac{t}{\tau} \right) \\ p = -\frac{1}{4} \rho U^2 \cos \left(2 \frac{t}{\tau} \right) - \rho \frac{x}{\tau} U \cos \left(\frac{t}{\tau} \right), \end{array} \right. \quad (5.82b)$$

where:

$$\tau = |\Delta \mathcal{G} \omega^2|^{-\frac{1}{2}}. \quad (5.83)$$

Finally, we choose U with respect to the following nonlinear stability arguments, namely that the radius R remains positive:

$$R(x, t) > 0, \quad \forall (x, t) \in [-a, a] \times [0, +\infty], \quad (5.84)$$

and that the flow remains subcritical:

$$S_h^2(x, t) < 1, \quad \forall (x, t) \in [-a, a] \times [0, +\infty]. \quad (5.85)$$

Numerical solution

We use the inviscid Thacker solution (5.82) as an initial condition for the numerical simulations and to impose the flow rate at the inlet and the cross-sectional area at the outlet. The parameters used in this test case are described in Table 5.8.

ρ	a	R_0	$\Delta\mathcal{G}$	K	U	$T = 2\pi\omega$	Δt	t	order
1	4	1	10^{-1}	10^4	10	0.42	10^{-5}	2	

Table 5.8 – Geometrical, mechanical, numerical and boundary parameters used in the inviscid Thacker test case.

In Figure 5.16 Left, we compare at times $t \in \{0, 0.1, 0.3, 0.6, 0.8\}T$ the spatial evolution of the inviscid Thacker solutions (5.82) for the pressure p , the average speed U and the flow rate Q with the spatial evolution of the first-order and MUSCL numerical solutions obtained with $N_x = 100$. We observe that for each variable, the inviscid Thacker solution is correctly described.

In Figure 5.16 Right, we plot at time $t = 0.8T$ the evolution with the number of cells N_x of the first-order and MUSCL L_1 , L_2 and L_∞ errors for the pressure p , the average speed U and the flow rate Q . We observe that for the average speed U and the flow rate Q , the L_1 , L_2 and L_∞ errors decrease with an increasing number of cells N_x , indicating that the first-order and MUSCL numerical solutions converge towards the steady solution. However, only first-order accuracy is achieved as boundary conditions are implemented at first-order and the Riemann invariants (2.88) do not account for geometrical and mechanical variations of the properties of the arterial wall.

The Thacker solution is an excellent test case as it is very sensitive to errors in the implementation of the numerical scheme and the boundary conditions. Therefore, even though we do not recover the expected order of accuracy and the errors for the pressure p behave poorly, the fact that visually the numerical results match the analytic solutions is satisfactory.

A viscous Thacker solution can be derived by modifying the friction term such that $C_f Q/A = \bar{C}_f Q$. This solution writes:

$$\begin{cases} U_0 = U \sin\left(\frac{t}{\tau}\right) e^{-\frac{\bar{C}_f}{2}t}, & U = \text{cst} \end{cases} \quad (5.86a)$$

$$\begin{cases} p = -\frac{1}{2}\rho\frac{U^2}{\delta\omega^2\tau^2}H(\bar{C}_f, \tau, t)^2 - \rho x\frac{U}{\tau}H(\bar{C}_f, \tau, t), \end{cases} \quad (5.86b)$$

with:

$$\tau = \frac{2}{\sqrt{|\bar{C}_f^2 - 4\delta\omega^2|}}, \quad (5.87)$$

and:

$$H = \left[\cos\left(\frac{t}{\tau}\right) + \frac{\bar{C}_f\tau}{2} \sin\left(\frac{t}{\tau}\right) \right] e^{-\frac{\bar{C}_f}{2}t}. \quad (5.88)$$

5.7 Conclusion

In Chapter 5, we have introduced three well-balanced hydrostatic reconstruction techniques for blood flow in large arteries with varying geometrical and mechanical properties, designed to treat the nonconservative source term introduced in the 1D blood flow momentum equation due to these variations. The first is the classical hydrostatic reconstruction (HR) originally proposed for shallow water equations to preserve steady states at rest. The second is the

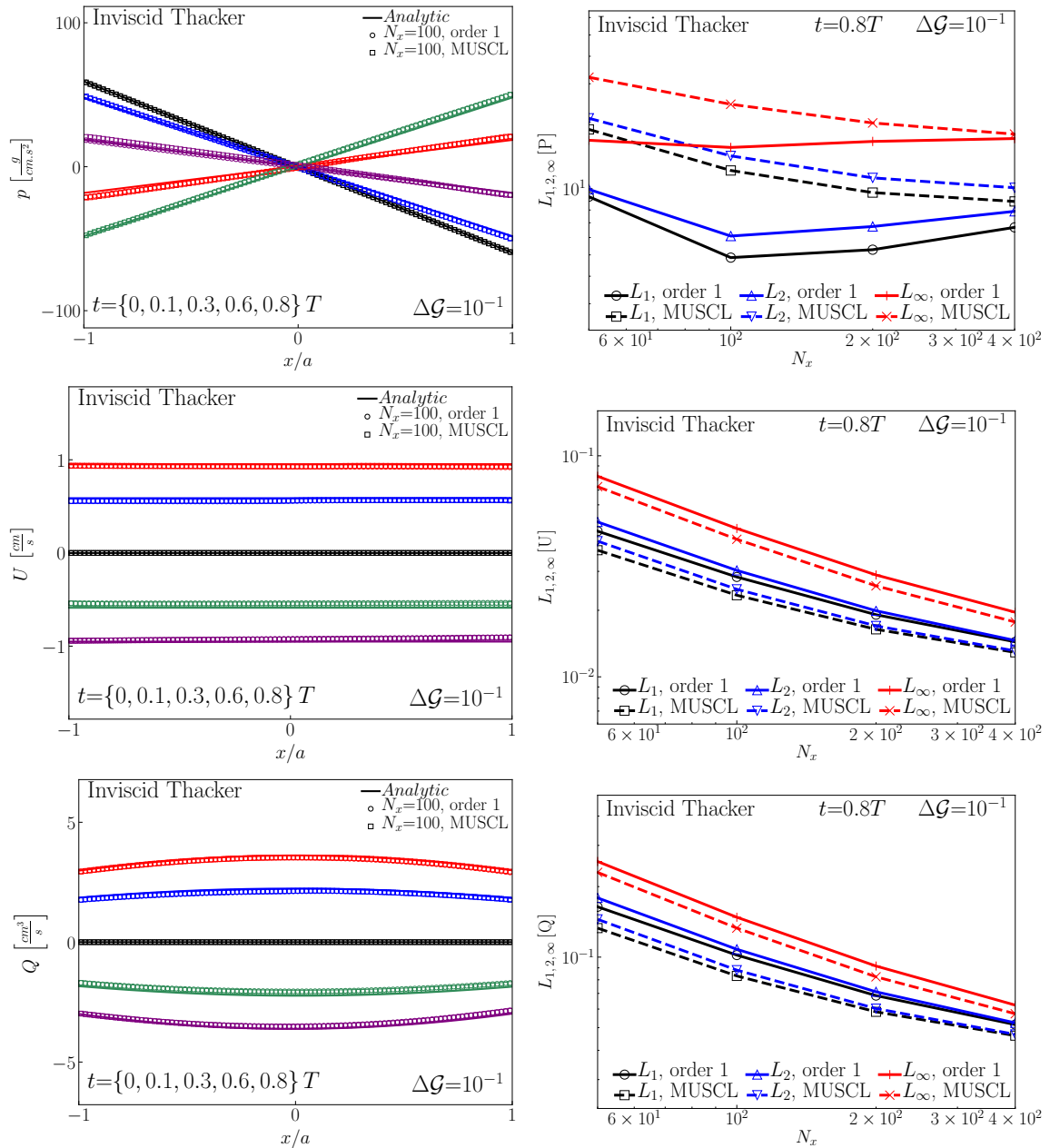


Figure 5.16 – The inviscid Thacker test case:

Left: Comparison between the inviscid Thacker solution (—) and the first-order (○) and MUSCL (□) numerical solutions obtained with $N_x = 100$ at times $t \in \{0, 0.1, 0.3, 0.6, 0.8\}T$.

Right: Spatial convergence of the first-order (○, △, +) and MUSCL (□, ▽, ×) L_1 , L_2 and L_∞ errors obtained at time $t = 0.8T$ with $N_x \in \{50, 100, 200, 400\}$.

The first-order and MUSCL solutions converge towards the steady solution and first-order accuracy is achieved.

low-Shapiro hydrostatic reconstruction (HR-LS), which is a simple and efficient variation of HR, designed to accurately preserve low-Shapiro number steady states. These steady states may occur in large network simulations and also characterize the wave reflections and transmissions occurring at discontinuities of the geometrical and mechanical properties of the artery. The third is the subsonic hydrostatic reconstruction (HR-S), introduced in [Bouchut and Morales De Luna 2010] and adapted here to blood flow. HR-S exactly preserves all subcritical steady states. We have performed a series of numerical computations to compare the properties of HR, HR-LS and HR-S. In all numerical computations, HR was the least accurate method and was unable to correctly compute wave reflection and transmission when large variations of the artery's geometrical and mechanical properties were considered. HR-S proved to be exactly well-balanced for all low-Shapiro number steady states and the most accurate reconstruction technique. We showed that HR-LS is well-balanced only for steady states at rest, but provides satisfactory approximations of low-Shapiro steady states. HR-LS is also able to capture wave reflections and transmissions for arbitrary large variations of the artery's geometrical and mechanical properties, which is an essential property to compute realistic flow and pressure waveforms. We therefore concluded that both HR-LS and HR-S are adequate well-balanced methods to compute blood flow in large arteries with varying cross-sectional area at rest and arterial wall rigidity. However, in large networks where many arteries present variations of their geometrical and mechanical properties, the extra iterations required by HR-S increase the computational cost compared to HR-LS. We have therefore recommended using HR-LS in this case, as it is a good compromise between simplicity, numerical accuracy and efficiency. We have then proposed a second-order extension of HR-LS using the MUSCL variable reconstruction strategy proposed in Subsection 4.2.2. Using a series of test cases for blood flow in one artery, we have validated the second-order extension in arteries presenting both variations of the neutral cross-sectional area A_0 and the arterial wall rigidity K .

We are now working towards a simpler well-balanced strategy that does not required the introduction of reconstructed variable. This well-balanced strategy uses the HLL numerical flux and a linearization of the equilibrium states (5.13) and is well suited for arteries presenting geometrical and mechanical property variations.

Networks and boundary conditions

We present here what we refer to as network boundary conditions, which allow us to construct an arterial network as an ensemble of single arteries connected together. The first boundary conditions we study are bifurcation boundary conditions, that typically link one parent artery with two daughter arteries. The second boundary conditions we consider are zero-dimensional outflow models (resistance, Windkessel), representing the response of the vascular bed at the end of each terminal vessel of the network. Once again, our approach is rather numerical but we also focus on the physical and mechanical aspects of these network boundary conditions.

Contents

6.1	Introduction	97
6.2	Bifurcation boundary conditions	98
6.2.1	Point bifurcation model	98
6.2.2	Control-volume bifurcation model	99
6.2.3	Validation and comparison	102
6.3	Outflow boundary conditions	107
6.3.1	Zero-dimensional blood flow equations	109
6.3.2	Resistance outflow model	110
6.3.3	Windkessel outflow model	111
6.3.4	Numerical method	112
6.3.5	Validation and comparison	112
6.4	Structured-tree outflow boundary condition	114
6.4.1	Construction of a structured-tree	116
6.4.2	Terminal vessel impedance	116
6.4.3	Equivalent Windkessel outflow model	117
6.5	Conclusion	124

6.1 Introduction

In Chapter 4 and Chapter 5, we have presented numerical methods and validation test cases for the 1D blood flow system of equations (3.23) in a single artery. However, waveforms observed *in vivo* can not be reproduced by considering only one artery. Indeed, these waveforms are greatly influenced by the topology of the arterial network [Westerhof et al. 1972], as reflections occur at each arterial bifurcation and in the arterioles (see Chapter 1).

To reproduce physiological waveforms, we therefore construct large networks by connecting different arteries together using two types boundary conditions:

- bifurcations boundary conditions, which link parent arteries with their daughter arteries;
- terminal boundary conditions, which essentially represent the resistive response of the distal vascular bed not taken into account in the model network.

Indeed, the computational and modeling costs are too high to consider all vessels of systemic circulation. Moreover, the assumptions used to derive the 1D blood flow equations become less valid as the radius of the vessels decreases. Consequently, any 1D network model must be truncated after a few generation of vessels and the response of the truncated vascular bed must be taken into account through terminal boundary conditions. The behavior of these vessels beyond the modeled arteries is usually simulated using lumped parameter or zero-dimensional (0-D) models [Alastruey et al. 2008]. Alternatively, structured-tree models can also be used [Olufsen 1999; Olufsen et al. 2000; Cousins and Gremaud 2012; Perdikaris and Karniadakis 2014].

Bifurcation and terminal boundary conditions are responsible for the reflection of pulse waves generated by the heart [Alastruey et al. 2009, 2011; Politi et al. 2016a]. The terminal boundary conditions are particularly important as they represent the principal sites of reflection and govern the pressure levels in the arterial network. Moreover, as the wave length of the pulse wave is at least one order of magnitude larger than the average length of an artery (see Chapter 1), these boundary conditions essentially drive large network numerical simulations.

In this context, we present in Section 6.2 classical and novel bifurcation models and in Section 6.4 a comparison between 0D and structured-tree outflow boundary conditions.

6.2 Bifurcation boundary conditions

A bifurcation is a characteristic network structure where parent arteries (proximal or closest to the heart) connect to their daughter arteries (distal or furthest from the heart). A typical bifurcation connects one parent artery to two daughter arteries. The flow in a bifurcation is complex and intrinsically 3D. Nevertheless, it can still be represented by means of a 1D blood flow model if one is not interested in the flow details in the bifurcation. We present two methods to impose bifurcation boundary conditions compatible with the 1D framework we have described in the previous chapters. We refer to these two methods as the point bifurcation model and the control-volume bifurcation model.

6.2.1 Point bifurcation model

Bifurcation modelization

The most commonly used bifurcation boundary condition in the 1D blood flow literature assumes that a bifurcation is a single point where the general conservation principles of fluid mechanics still apply. These conservation principles are the conservation of mass and the continuity of the energy discharge E , defined in Subsection 5.2.2. They are used to link the flow in each $p \in [1, N_p]$ parent and $d \in [1, N_d]$ daughter arteries connecting at a bifurcation J and are written in this case as:

$$\left\{ \begin{array}{l} \sum_{p=1}^{N_p} Q_p - \sum_{d=1}^{N_d} Q_d = 0 \\ E_p = E_d + \Delta p_{loss} \quad \forall [p, d] \in [1, N_p] \times [1, N_d]. \end{array} \right. \quad (6.1a)$$

$$\left. \right\} \quad (6.1b)$$

The variable Δp_{loss} represents the pressure losses in the bifurcation and is thoroughly studied in [Mynard and Valen-Sendstad 2015]. However, we set $\Delta p_{loss} = 0$ as in practice, these losses have only secondary effects on the pulse waves [Alastruey et al. 2011]. System (6.1) is

successfully used in [Segers et al. 1997; Formaggia et al. 2003; Sherwin et al. 2003a; Matthys et al. 2007; Liang et al. 2009; Müller and Toro 2014; Müller and Blanco 2015; Mynard and Valen-Sendstad 2015; Quarteroni et al. 2016; Ghigo et al. 2017a]. As the Shapiro number S_h (2.85) is small in physiological conditions, System (6.1) can be linearized and reduces to:

$$\begin{cases} \sum_{p=1}^{N_p} Q_p - \sum_{d=1}^{N_d} Q_d = 0 & (6.2a) \\ p_p = p_d + \Delta p_{loss} \quad \forall [p, d] \in [1, N_p] \times [1, N_d], & (6.2b) \end{cases}$$

where Equation (6.2b) represents the continuity of pressure. System (6.2) is used in [Alastruey et al. 2009; Wang et al. 2015] and gives satisfying results. It is also a generalization of the low-Shapiro steady states (5.16) preserved by HR-LS.

System (6.1) (and System (6.2)) allows to accurately compute wave reflections and transmissions if a change of impedance occurs between the parent and the daughter arteries, which is crucial to obtain physiological wave forms in large network simulations [Sherwin et al. 2003a; Alastruey et al. 2012]. Indeed, it is identical to the steady state system of equations (5.9).

In the following, we propose a classical numerical strategy to implement the point bifurcation model.

Numerical method

We consider a point bifurcation where N_p parent arteries $[p]_{p=1}^{N_p}$ connect to N_d daughter arteries $[d]_{d=1}^{N_d}$. As in Subsection 4.2.3, we impose the bifurcation boundary conditions by setting the value of the vectors of conservative variables $\mathbf{U}_{out}^n|_{p=1}^{N_p}$ and of $\mathbf{U}_{in}^n|_{d=1}^{N_d}$ in the ghost cells $C_{out}|_{p=1}^{N_p}$ and $C_{in}|_{d=1}^{N_d}$. In total, $2[N_p + N_d]$ unknown variables must be determined.

$N_p + N_d$ equations are obtained by estimating the outgoing Riemann invariants of the parent and daughter arteries using Equation (4.38b):

$$\begin{cases} W_2(\mathbf{U}_{out}^n)|_p = W_2(\mathbf{U}_{N_x}^n)|_p, & \text{for } p \in [1, N_p] & (6.3a) \\ W_1(\mathbf{U}_{in}^n)|_d = W_1(\mathbf{U}_1^n)|_d, & \text{for } d \in [1, N_d]. & (6.3b) \end{cases}$$

The $N_p + N_d$ missing equations are provided by System (6.1). The global system is solved using a Newton's method in a limited number of iterations (~ 5) in every bifurcation at every time step.

Other implementation strategies are proposed in [Contarino et al. 2016], based on a generalized Riemann problem, which has no accuracy limit, both in space and time. Here, the implementation is only first-order accurate.

Despite its success, the point bifurcation model lacks any compliant behavior and requires a time-consuming resolution of System (6.1) to update the boundary properties of each artery connecting at the bifurcation. Moreover, its lack of volume poses difficulties when considering the transfer of passive scalars through the bifurcation. We therefore propose an alternative approach based on a time-dependent control-volume bifurcation model inspired from the bifurcation model for veins proposed in [Fullana and Zaleski 2009].

6.2.2 Control-volume bifurcation model

Bifurcation geometrical and mechanical properties

Following [Fullana and Zaleski 2009], we consider a bifurcation J connecting N_p parent $[p]_{p=1}^{N_p}$ arteries and N_d daughter arteries $[d]_{d=1}^{N_d}$. We define bifurcation J as an elastic volume

of undefined shape characterized by a length L_J , a neutral cross-sectional area $A_{0,J}$ and a arterial wall rigidity K_J . See Figure 6.1 for a schematic of the control-volume bifurcation model.

We define $A_{0,J}$ as:

$$A_{0,J} = \begin{cases} \max_{d \in [1, N_d]} A_{0,d} & \text{if } \max_{d \in [1, N_d]} A_{0,d} \leq \min_{p \in [1, N_p]} A_{0,p} \\ \frac{1}{2} \left[\frac{1}{N_p} \sum_{p=1}^{N_p} A_{0,p} + \frac{1}{N_d} \sum_{d=1}^{N_d} A_{0,d} \right] & \text{else ,} \end{cases} \quad (6.4)$$

where $A_{0,p}$ (*resp.* $A_{0,d}$) is the neutral cross-sectional area of the parent artery p (*resp.* daughter artery d). This choice provides a smooth transition at the bifurcation between the larger parent arteries and the smaller daughter arteries. We then define the length L_J and the arterial wall rigidity K_J as:

$$\left\{ L_J = C_L \left[\sum_{p=1}^{N_p} \Delta x_p + \sum_{d=1}^{N_d} \Delta x_d \right] \right. \quad (6.5a)$$

$$\left. \left\{ K_J = \frac{1}{2} \left[\frac{1}{N_p} \sum_{p=1}^{N_p} K_p + \frac{1}{N_d} \sum_{d=1}^{N_d} K_d \right] \right. \right. \quad (6.5b)$$

where Δx_p and K_p (*resp.* Δx_d and K_d) are the mesh size and arterial wall rigidity of parent artery p (*resp.* daughter artery d). The parameter C_L allows us to control the length and volume of bifurcation J . Finally, the neutral volume $V_{0,J}$ of bifurcation J is:

$$V_{0,J} = L_J A_{0,J}. \quad (6.6)$$

With these definitions, bifurcation J provides a smooth geometrical and mechanical transition between the parent and daughter arteries connecting at bifurcation J . Bifurcation J is parametrized only by the length scaling factor C_L , and its influence on numerical solutions is studied in Subsection 6.2.3.

Bifurcation governing equations

During a cardiac cycle, multiple reflected and transmitted pulse waves pass through bifurcation J and modify its volume and flow patterns. To account for these time-dependent behaviors, we introduce the time-dependent cross-sectional area A_J , volume V_J and flow rate Q_J of bifurcation J . As for the point bifurcation model, the time evolution of the quantities A_J , V_J and Q_J should respect the general conservation principles of fluid mechanics.

To that effect, we first derive the governing equation for V_J based on the 1D mass conservation equation (2.67a). Using a control-volume approach, we integrate Equation (2.67a) over the characteristic length L_J of bifurcation J and obtain the integral mass conservation equation for bifurcation J :

$$\frac{dV_J}{dt} + \sum_{p=1}^{N_p} F_{A,p} - \sum_{d=1}^{N_d} F_{A,d} = 0. \quad (6.7)$$

where $F_A = Q$ is the mass flux (2.81a). Equation (6.7) enables us to dynamically update the volume V_J depending on the incoming and outgoing mass fluxes. For parent artery p , the mass flux is counted positively ($F_{A,p} > 0$) coming into bifurcation J , whereas for daughter artery d , the mass flux are counted negatively ($F_{A,d} < 0$) coming into bifurcation J . From the volume V_J we obtain the cross-sectional A_J using the following relation:

$$A_J = \frac{V_J}{L_J}. \quad (6.8)$$

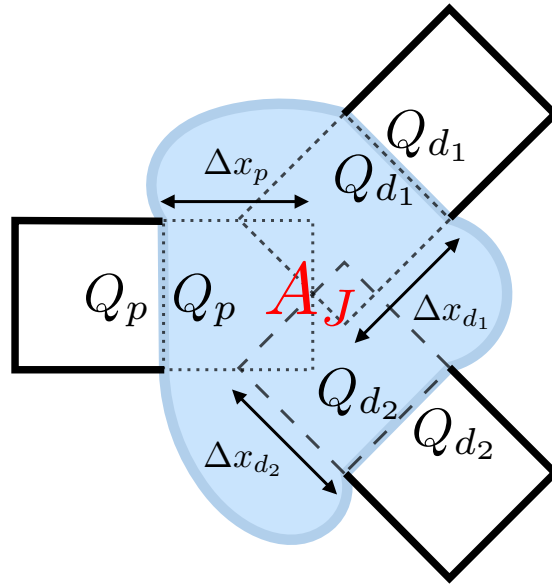


Figure 6.1 – Representation of the control-volume bifurcation model, connecting the parent artery p to the daughter arteries d_1 and d_2 . The blue surface represents the bifurcation J containing the ghost cells of the parent and daughter arteries. The cross-sectional area A_J of the bifurcation is updated using the mass conservation equation (6.7) and homogeneous Neumann boundary conditions are used to update the flow rate.

Whereas the volume V_J is a scalar quantity, the flow rate Q_J is a vector (or directional) quantity. It is therefore difficult to derive a control-volume equation for Q_J from the 1D momentum continuity equation (2.67b) or the 1D entropy equation (2.93) without precise knowledge on the bifurcation's geometry and flow patterns. We therefore choose to discard the variable Q_J and prescribe boundary conditions for the flow rate at each of bifurcation's inlets and outlets. We use the long wave framework described in Subsection 2.3.1 and assume that local spatial variations of the flow rate are small at the inlets and outlets of bifurcation J . This assumption leads us to impose homogeneous Neumann boundary conditions for the flow rate at each of bifurcation J 's inlets and outlets:

$$\begin{cases} \frac{\partial Q_p}{\partial x} = 0, & \forall p \in [1, N_p] \\ \frac{\partial Q_d}{\partial x} = 0, & \forall d \in [1, N_d]. \end{cases} \quad (6.9)$$

The boundary conditions (6.9) are valid only in a subcritical flow regime. Indeed, in the presence of shocks the solution becomes discontinuous. Fortunately, in physiological conditions blood flow is always subcritical.

In the following, we present a numerical strategy to implement the control-volume bifurcation model.

Numerical method

We consider a control-volume bifurcation J where N_p parent arteries $[p]_{p=1}^{N_p}$ connect to N_d daughter arteries $[d]_{d=1}^{N_d}$. As in Subsection 6.2.1, we impose the bifurcation boundary conditions by setting the value of the vectors conservative variables $\mathbf{U}_{out}^n|_{p=1}^{N_p}$ and of $\mathbf{U}_{in}^n|_{d=1}^{N_d}$ in the ghost cells $C_{out}|_{p=1}^{N_p}$ and $C_{in}|_{d=1}^{N_d}$.

We first define the geometrical and mechanical properties of bifurcation J using Equation (6.4) and System (6.5). We then replace the values of A_0 and K in the ghost cells $C_{out}|_{p=1}^{N_p}$ and $C_{in}|_{d=1}^{N_d}$ by the computed bifurcation values $A_{0,J}$ and K_J . Doing so, the bifurcation's geometrical and mechanical properties are now uniformly distributed in the ghost cells $C_{out}|_{p=1}^{N_p}$ and $C_{in}|_{d=1}^{N_d}$ and the bifurcation's volume is preserved.

We then update the bifurcation volume V_J by discretizing Equation (6.7) with an explicit Euler integration scheme:

$$V_J^{n+1} = V_J^n - \Delta t \left[- \sum_{p=1}^{N_p} \mathcal{F}_{\mathcal{A}}^n|_p + \sum_{d=1}^{N_d} \mathcal{F}_{\mathcal{A}}^n|_d \right], \quad (6.10)$$

where Δt is the time step presented in Section 4.1 and $\mathcal{F}_{\mathcal{A}}^n|_p$ (*resp.* $\mathcal{F}_{\mathcal{A}}^n|_d$) is the mass numerical flux (4.14) defined at the interface between the last cell of artery p (*resp.* the first cell of artery d) and ghost cell $C_{out}|_p$ (*resp.* $C_{in}|_d$). We then compute A_J^{n+1} using Equation (6.8) and impose this value in the ghost cells $C_{out}|_{p=1}^{N_p}$ and $C_{in}|_{d=1}^{N_d}$.

Finally, we use the boundary conditions (6.9) to impose the flow rate in the ghost cells $C_{out}|_{p=1}^{N_p}$ and $C_{in}|_{d=1}^{N_d}$:

$$\begin{cases} Q_{out}^{n+1}|_p = \mathcal{F}_{\mathcal{Q}}^n|_{N_x+\frac{1}{2},p} & \text{for } p \in [1, N_p] \\ Q_{in}^{n+1}|_d = \mathcal{F}_{\mathcal{Q}}^n|_{\frac{1}{2},d} & \text{for } d \in [1, N_d], \end{cases} \quad (6.11)$$

where $\mathcal{F}_{\mathcal{Q}}^n|_{N_x+\frac{1}{2},p}$ (*resp.* $\mathcal{F}_{\mathcal{Q}}^n|_{\frac{1}{2},d}$) is the momentum numerical flux (4.14) defined at the interface between the last cell of artery p (*resp.* the first cell of artery d) and ghost cell $C_{out}|_p$ (*resp.* $C_{in}|_d$). The use of $\mathcal{F}_{\mathcal{Q}}^n|_{p,d}$ guarantees a well-balanced treatment of the flux at the bifurcation's inlets and outlets.

Viscous effects are easily included in the control-volume bifurcation model following the methodology presented in Subsection 4.3.2.

6.2.3 Validation and comparison

To validate both bifurcation models and their implementation, we propose a series of test cases where we study the propagation of pressure pulse waves in simplified arterial networks and systematically compare the results obtained with the point and control-volume bifurcation models.

Two arteries

We consider a single artery of length $2L$ described by the following neutral radius R_0 and arterial wall rigidity K :

$$\begin{cases} R_0(x) = \begin{cases} R_0 & \text{if } x < x_m \\ R_0(1 - \Delta_R) & \text{if } x \geq x_m \end{cases} \\ K(x) = \begin{cases} K & \text{if } x < x_m \\ K(1 + \Delta_K) & \text{if } x \geq x_m. \end{cases} \end{cases} \quad (6.12)$$

where $x_m = L$. This artery is identical to the step configuration presented in Section 5.4. We divide this artery in two at $x = x_m$ and connect the resulting two arteries with the point bifurcation and control-volume bifurcation models and compare the computed results with those obtained with the low-Shapiro hydrostatic reconstruction technique (HR-LS, see Subsection 5.3.2) in the single artery of length $2L$. In all configurations, we impose a

pressure wave p_{in} at the inlet:

$$p_{in}(t) = \begin{cases} \frac{\hat{p}}{2} \left[1 + \cos \left(\pi + 2\pi \frac{t}{T} \right) \right] & \text{if } 0 \leq \frac{t}{T} \leq 1 \\ 0 & \text{else ,} \end{cases} \quad (6.13)$$

where $\hat{p} = \sqrt{A_0} K S_h$ (see Equation (2.53)), and a non-reflecting boundary condition at the outlet. To assess the long wave and wave propagation properties of both bifurcation models, we choose $T \in \{0.1, 1\}$, $\Delta_R \in \{0, 0.5\}$ and $\Delta_K \in \{0, 2\}$. The other parameters used in this test case are described in Table 6.1.

ρ	L	R_0	K	C_f	C_ν	S_h	T	R_t	N_x	x order	Δt	t order
1	10	1	10^4	0	0	$\{10^{-3}, 10^{-1}\}$	$\{0.1, 1\}$	0	50	2	10^{-4}	2

Table 6.1 – Geometrical, mechanical, numerical and boundary parameters used in the inviscid two arteries bifurcation comparison test cases.

In Figure 6.2, we consider a straight artery for which $\Delta_R = \Delta_K = 0$ and we compare at times $t \in \{0.06, 0.12, 0.19, 0.25\}$ for $T = 0.1$ (Left) and times $t \in \{0.25, 0.5, 0.75, 1\}$ for $T = 1$ (Right) the spatial evolution of the pressure p and flow rate Q solutions obtained for $S_h \in \{10^{-3}, 10^{-1}\}$ with the single artery configuration, the point bifurcation configuration and the control-volume bifurcation configuration with $C_L = 0.1$. We observe that for each variable, both values of T and both Shapiro numbers S_h , the single artery solutions match the point and control-volume bifurcations solutions. These results indicate that both bifurcation models do not create spurious reflections at a bifurcation connecting two identical arteries and that the homogeneous Neumann conditions (6.9) used in the control-volume bifurcation model are valid outside of the long wave framework, when $T = 0.1$.

We now assess the influence of the length scaling factor C_L . In geometrical and flow conditions identical to those of Figure 6.2, we compare in Figure 6.3 the spatial evolution of the pressure p and flow rate Q solutions obtained with the single artery configuration and the control-volume bifurcation configuration, where we choose $C_L \in \{1, 0.1, 0.01\}$. We observe that for each variable, both Shapiro numbers S_h and $T = 1$, the single artery solutions match the control-volume bifurcation solutions for all values of C_L . However, for $T = 0.1$, the single artery solutions match the control-volume bifurcation solutions only for $C_L \in \{0.1, 0.01\}$. Indeed, for $C_L = 1$, the control-volume bifurcation model generates a flow aspiration that propagates towards the inlet of the artery. This aspiration behavior is probably due to the pulse wave that takes too long to go through the length of the bifurcation. Based on these results, we choose $C_L = 0.1$ in the following test-cases.

Finally, in Figure 6.4, we consider a step ($\Delta_R = 0.5$, $\Delta_K = 2$) and we compare at times $t \in \{0.06, 0.12, 0.19, 0.25\}$ for $T = 0.1$ (Left) and times $t \in \{0.25, 0.5, 0.75, 1\}$ for $T = 1$ (Right) the spatial evolution of the pressure p and flow rate Q solutions obtained for $S_h \in \{10^{-3}, 10^{-1}\}$ with the single artery configuration, the point bifurcation configuration and the control-volume bifurcation configuration with $C_L = 0.1$. We observe that for each variable, both values of T and $S_h = 10^{-3}$, all solutions match and the wave reflections and transmissions are correctly computed (represented by the dashed lines in Figure 6.4). For $S_h = 10^{-1}$, the single artery and the point bifurcation solutions are similar as they preserve similar conservation properties at the bifurcation, described by System (6.1). On the contrary, the control-volume bifurcation solutions differ due to the compliance of the bifurcation and additional reflections introduced by the chosen definition of K_J (6.5).

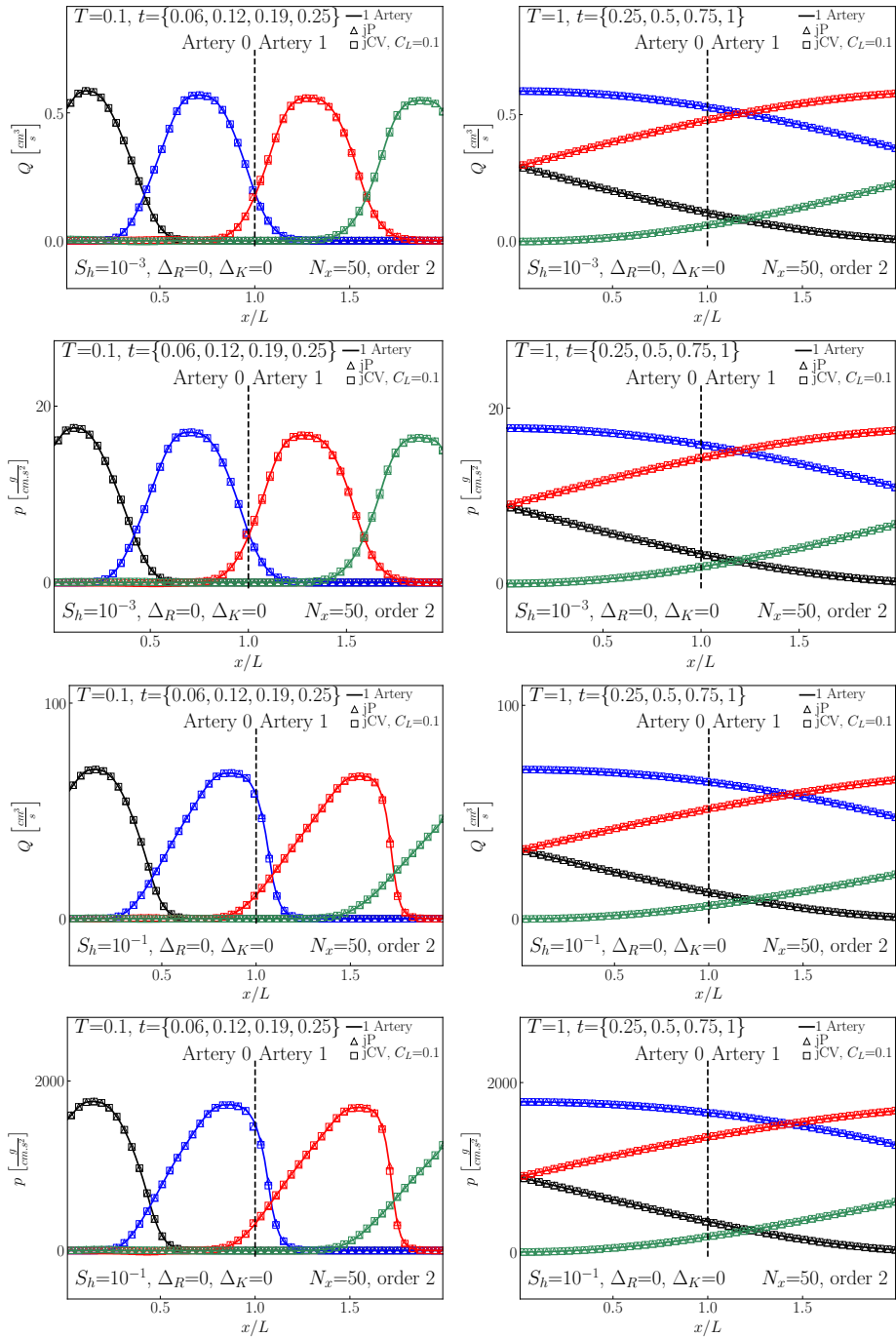


Figure 6.2 – The straight two arteries test case. Comparison between the single artery solutions (—), the point bifurcation solutions (Δ) and the control-volume bifurcation solutions (\square) with $C_L = 0.1$ for the pressure p and the flow rate Q obtained in a straight artery ($\Delta_R = \Delta_K = 0$):

Left: $T = 0.1$ at times $t \in \{0.06, 0.12, 0.19, 0.25\}$.

Right: $T = 1$ at times $t \in \{0.25, 0.5, 0.75, 1\}$.

Top: $S_h = 10^{-3}$.

Bottom: $S_h = 10^{-1}$.

The single artery solutions match the point and control-volume bifurcation solutions.

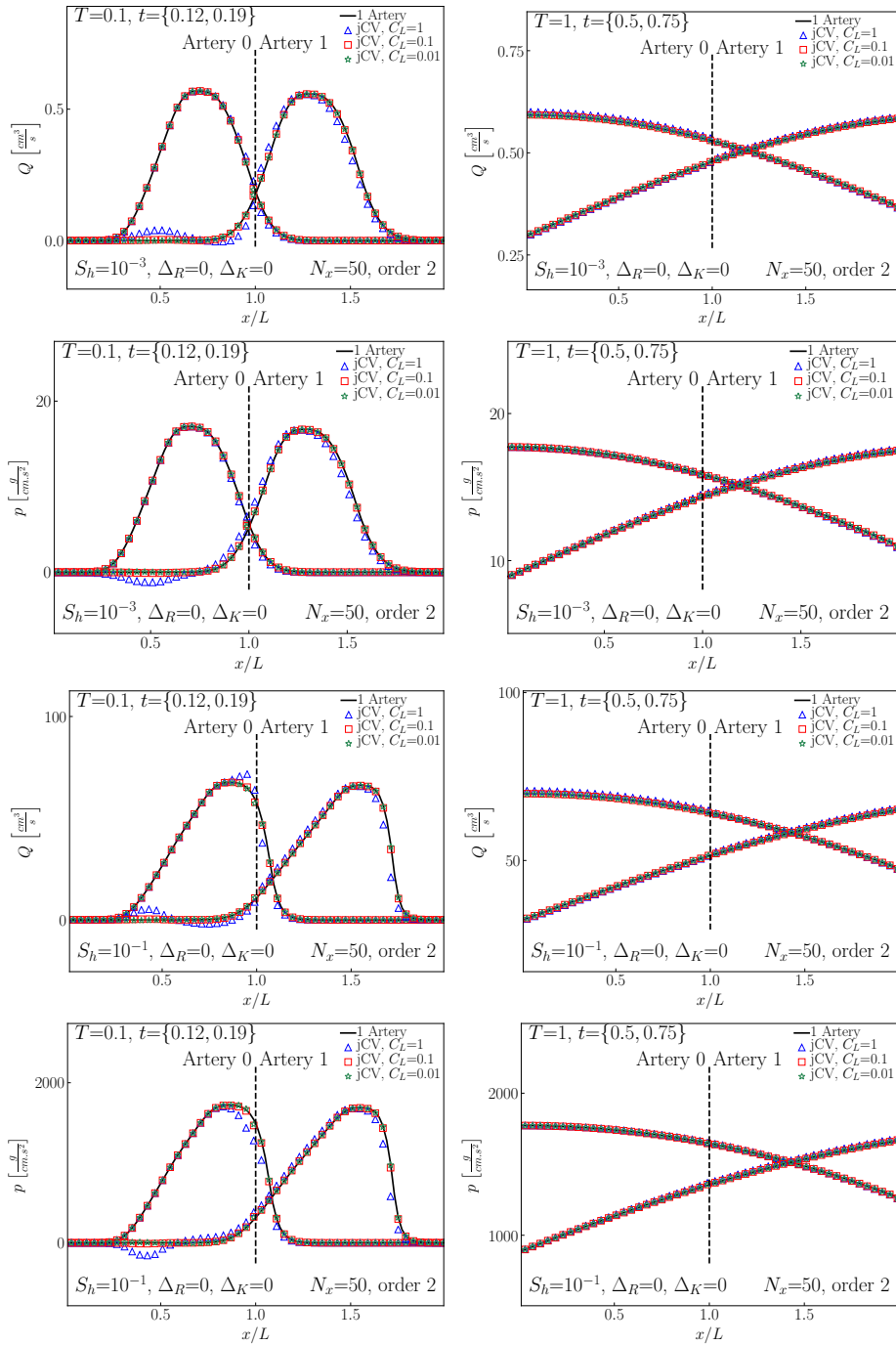


Figure 6.3 – Effect of the length scaling factor C_L in the two arteries test case. Comparison between the single artery solutions (—) and the control-volume bifurcation solutions with $C_L \in \{1 (\Delta), 0.1 (\square), 0.01 (\star)\}$ for the pressure p and the flow rate Q in a straight artery ($\Delta_R = \Delta_K = 0$):

Left: $T = 0.1$ at times $t \in \{0.12, 0.19\}$.

Right: $T = 1$ at times $t \in \{0.5, 0.75\}$.

Top: $S_h = 10^{-3}$.

Bottom: $S_h = 10^{-1}$.

The single artery solutions match the control-volume bifurcation solutions for $C_L \in \{0.1, 0.01\}$. For $C_L = 1$, the control-volume bifurcation model generates a flow aspiration due to its larger control-volume.

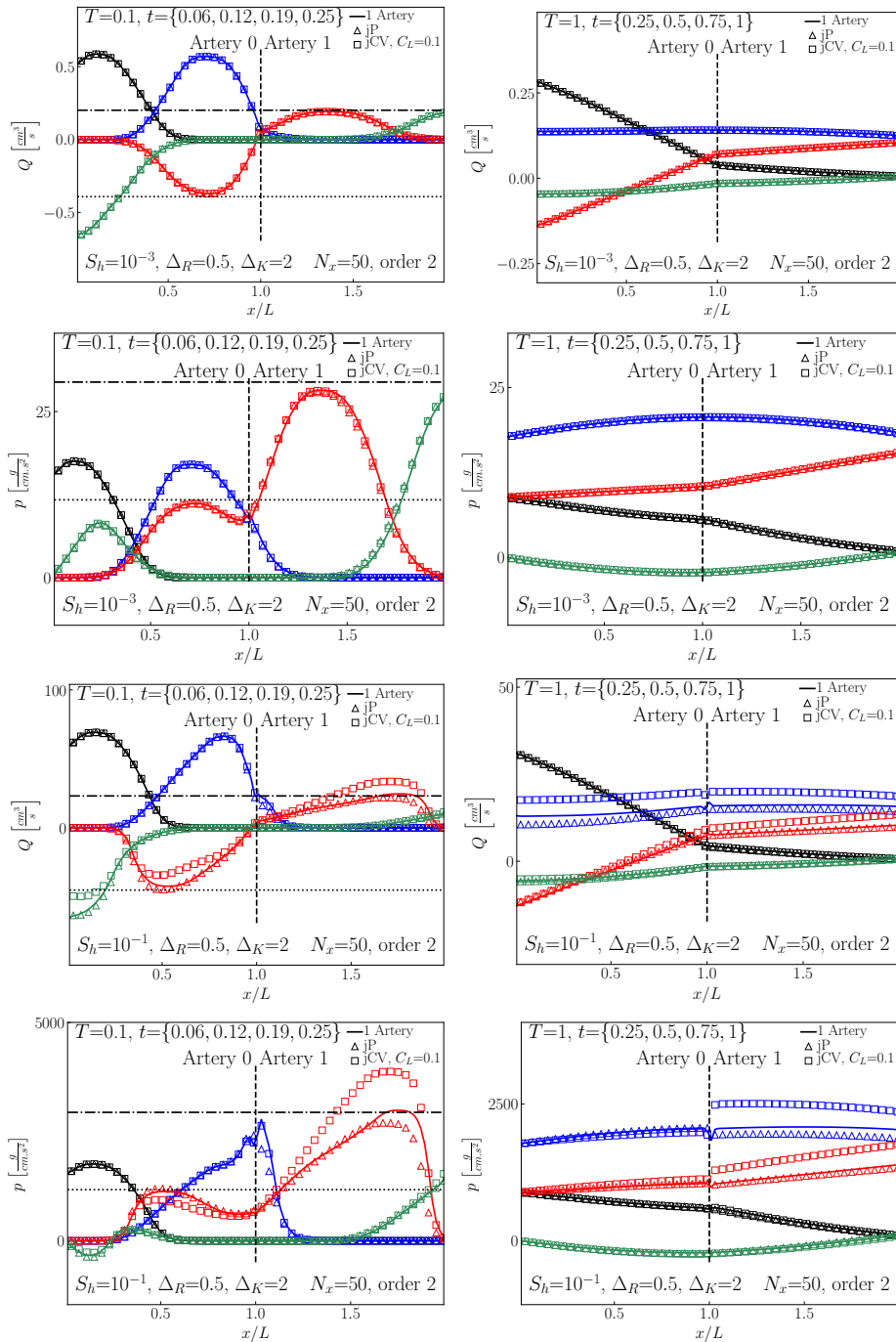


Figure 6.4 – The step two arteries test case. Comparison between the single artery solutions (—), the point bifurcation solutions (Δ) and the control-volume bifurcation solutions (\square) with $C_L = 0.1$ for the pressure p and the flow rate Q obtained in a step ($\Delta_R = 0.5$, $\Delta_K = 2$):

Left: $T = 0.1$ at times $t \in \{0.06, 0.12, 0.19, 0.25\}$. The point line (---) represents the expected amplitude of the reflected wave and the point-dashed line (-·-) the expected amplitude of the transmitted wave.

Right: $T = 1$ at times $t \in \{0.25, 0.5, 0.75, 1\}$.

Top: $S_h = 10^{-3}$.

Bottom: $S_h = 10^{-1}$.

For $S_h = 10^{-3}$, all solutions match and the reflections are correctly computed. For $S_h = 10^{-1}$, only the single artery and the point bifurcation solutions are similar.

Three arteries

We consider an elementary arterial bifurcation where one parent artery p connects to two daughter arteries d_1 and d_2 . We impose the pressure pulse wave p_{in} (6.13) at the inlet of the parent artery and non-reflecting boundary conditions at the outlet of the two daughter arteries. As in the two arteries test case, we choose $T \in \{0.1, 1\}$. The other parameters used in this test case are described in Table 6.2 (geometrical and mechanical properties) and Table 6.1 (boundary and numerical parameters).

	ρ	L	R_0	K	C_f	C_ν
Artery p	1	10	1	1×10^4	0	0
Artery d_1	1	10	0.5	3×10^4	0	0
Artery d_2	1	10	0.5	3×10^4	0	0

Table 6.2 – Geometrical and mechanical parameters used in the inviscid three arteries bifurcation comparison test case.

In Figure 6.5, we compare at times $t \in \{0.06, 0.12, 0.19, 0.25\}$ for $T = 0.1$ (Left) and times $t \in \{0.25, 0.5, 0.75, 1\}$ for $T = 1$ (Right) the spatial evolution of the pressure p and flow rate Q solutions obtained in the parent artery p and the daughter artery d_1 for $S_h \in \{10^{-3}, 10^{-1}\}$ with the point bifurcation configuration and the control-volume bifurcation configuration with $C_L = 0.1$. We observe that for each variable, both values of T and $S_h = 10^{-3}$, both bifurcation models give similar results and the wave reflections and transmissions are correctly computed (represented by the dashed lines in Figure 6.5). As in the two arteries test case, the point bifurcation solutions and the control-volume bifurcation solutions slightly differ for $S_h = 10^{-1}$.

These test cases show that both the point bifurcation model and the control-volume bifurcation model are able to accurately compute long and short wave reflections and transmissions in linear flow regimes. As expected, their solutions differ in nonlinear flow regimes due to the control-volume and compliant aspects of the control-volume bifurcation model. The control-volume bifurcation model therefore provides an interesting alternative to the classical point bifurcation model and is particularly well suited for the transport of passive scalars. Further comparison against experimental and 3D numerical results is necessary to determine which bifurcation model is best suited to describe blood flow in large arteries.

6.3 Outflow boundary conditions

The systemic network is constituted of millions of arteries that can be categorized as large arteries, arterioles and capillaries. For obvious computational and modeling reasons, blood flow in the entire systemic network can not be numerically computed. Network numerical simulations are usually restricted to large arteries and eventually arterioles [Watanabe et al. 2013; Blanco et al. 2014; Perdikaris et al. 2015] and the terminal arteries in these numerical networks do not represent the actual end of the systemic network but are rather arbitrarily chosen end points. The boundary conditions at the outlet of these terminal vessels must then model the response of the vascular bed distal to these terminal segments. These boundary conditions usually take the form of zero-dimensional (0D) models, which can be interpreted as electrical circuits formed of resistances, capacities and inductances. In the following sections, we first derive from the 1D blood flow equations (2.67) a 0D artery model to better understand the different constituents of classical outflow models. We then present and compare different outflow models for arterial networks. In Figure 6.6, we represent the three outflow models we consider here: the resistance, the Windkessel and the structured-tree.

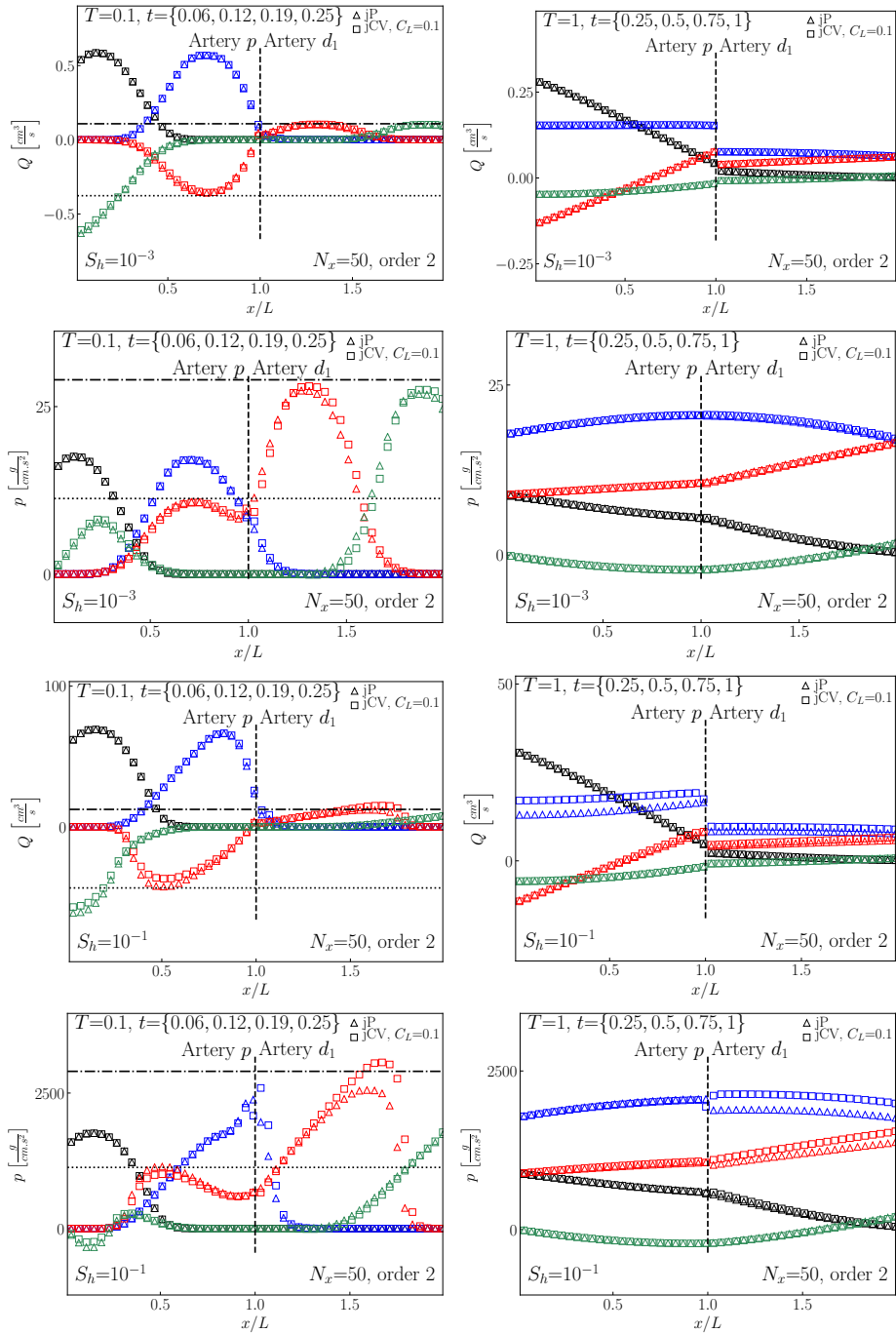


Figure 6.5 – The three arteries test case. Comparison between the point bifurcation solutions (Δ) and the control-volume bifurcation solutions (\square) with $C_L = 0.1$ for the pressure p and the flow rate Q obtained in parent artery p and daughter artery d_1 :

Left: $T = 0.1$ at times $t \in \{0.06, 0.12, 0.19, 0.25\}$. The point line (---) represents the expected amplitude of the reflected wave and the point-dashed line (—) the expected amplitude of the transmitted wave.

Right: $T = 1$ at times $t \in \{0.25, 0.5, 0.75, 1\}$.

Top: $S_h = 10^{-3}$.

Bottom: $S_h = 10^{-1}$.

For $S_h = 10^{-3}$, all solutions match and the reflections are correctly computed. For $S_h = 10^{-1}$, the two bifurcation models give different results.

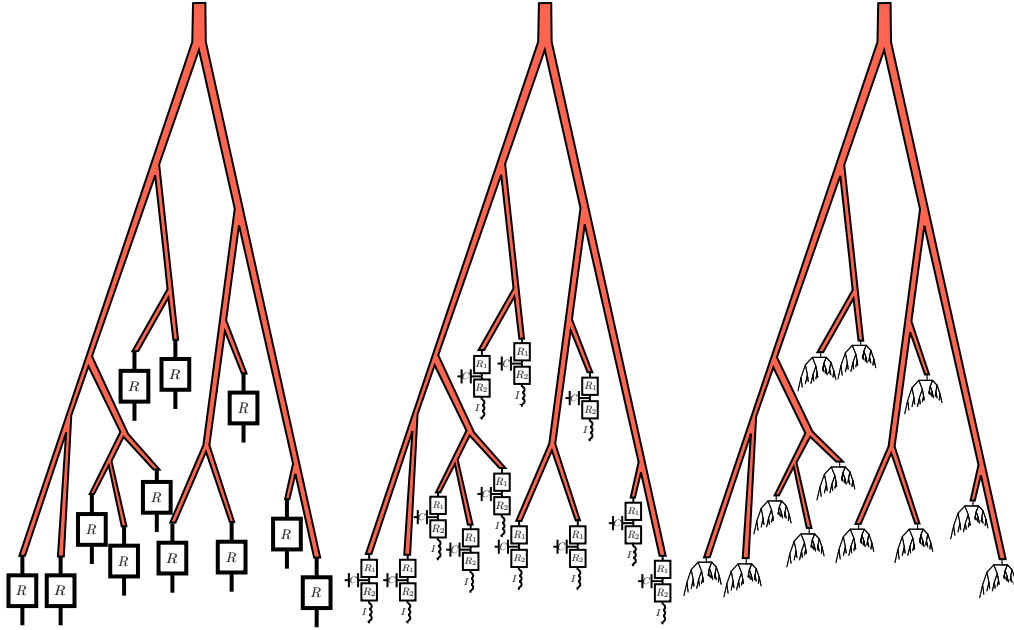


Figure 6.6 – Representation of the three principal outflow models applied to a model network:
Left: Resistance (see Figure 6.8).
Middle: Windkessel (see Figure 6.9).
Left: Structured-tree (see Figure 6.12).

6.3.1 Zero-dimensional blood flow equations

We derive here 0D blood flow equations to better understand the different building blocks of the classical 0D outflow models. We first linearize System (2.67) around the reference state $\mathbf{U} = [A = A_0, Q]^\top$ and obtain:

$$\begin{cases} C \frac{\partial p}{\partial t} + \frac{\partial Q}{\partial x} = 0 \end{cases} \quad (6.14a)$$

$$\begin{cases} I \frac{\partial Q}{\partial t} + \frac{\partial p}{\partial x} = -R_f Q, \end{cases} \quad (6.14b)$$

where R_f is the viscous resistance, C the vessel compliance and I the flow inertia which are defined as:

$$\begin{cases} R_f = \frac{\rho C_f}{A_0^2} \end{cases} \quad (6.15a)$$

$$\begin{cases} C = 2 \frac{\sqrt{A_0}}{K} = \frac{A_0}{\rho c_0^2} \end{cases} \quad (6.15b)$$

$$\begin{cases} I = \frac{\rho}{A_0}. \end{cases} \quad (6.15c)$$

To simplify the problem even further, we integrate System (6.14) over the length L of the artery and obtain 0D blood flow equations linking the inlet ($x = 0$) and outlet ($x = L$) of the artery:

$$\begin{cases} C \frac{d\hat{p}}{dt} + Q|_{x=L} - Q|_{x=0} = 0 \end{cases} \quad (6.16a)$$

$$\begin{cases} I \frac{d\hat{Q}}{dt} + p|_{x=L} - p|_{x=0} = -R_f \hat{Q}, \end{cases} \quad (6.16b)$$

where:

$$\hat{p} = \frac{1}{L} \int_{x=0}^L p dx \quad \text{and} \quad \hat{Q} = \frac{1}{L} \int_{x=0}^L Q dx. \quad (6.17)$$

To close System (6.16), we follow [Alastruey et al. 2012] and assume that:

$$\begin{cases} \hat{p} = p|_{x=0} \\ \hat{Q} = Q|_{x=L}. \end{cases} \quad (6.18)$$

This allows us to rewrite System (6.16) as a single equation that depends only on $p|_{x=0}$, $p|_{x=L}$ and $Q|_{x=0}$:

$$\left(1 + R_f C \frac{d \cdot}{dt} + C I \frac{d^2 \cdot}{dt^2}\right) p|_{x=0} - p|_{x=L} = \left(R_f + I \frac{d \cdot}{dt}\right) Q|_{x=0}. \quad (6.19)$$

Equation (6.19) connects the inlet flow rate and pressure with the outlet pressure of the artery and shows that a resistance, a capacity and an inductance are sufficient to describe blood flow in an artery. In Figure 6.7, we represent the electrical circuit equivalent to the 0D blood flow equation (6.19).

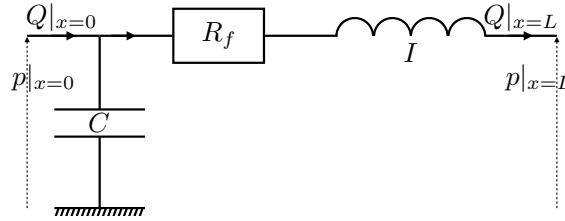


Figure 6.7 – Electrical representation of the 0D blood flow equation (6.19).

Due to the integration of System (2.67) over the length L of the artery, the viscoelastic effects that involve a spatial gradient can not be represented by the 0D Equation (6.19). We reach here the limitations of such a simplified approach.

These three electrical elements are therefore the building blocks of any relevant outflow model. Next, we follow the literature and construct two classical outflow models as combinations of resistances, capacities and inductances. We refer to these models as the resistance and the Windkessel outflow models.

6.3.2 Resistance outflow model

The resistance outflow model is obtained by considering that the response of the distal vascular bed is purely resistive. This is equivalent to assuming that each artery in this distal network is rigid and that blood flow behaves as a Poiseuille flow, therefore neglecting any compliant or inertial effect. The governing equation for the resistance outflow model writes:

$$p|_{x=0} - p|_{x=L} = R_f Q|_{x=0}. \quad (6.20)$$

In Figure 6.8, we represent the electrical circuit equivalent to this resistance model.

A characteristic analysis of System (6.14), presented in detail in [Vignon and Taylor 2004; Alastruey et al. 2012], enables to link the resistance R_f and the

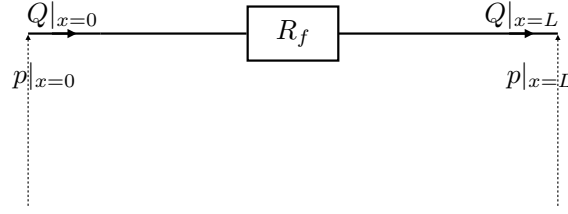


Figure 6.8 – Electrical representation of the resistance 0D outflow model (6.22).

reflection coefficient R_t :

$$R_t = \frac{R_f - Z_0}{R_f + Z_0}, \quad (6.21)$$

where Z_0 is the impedance of the terminal vessel.

The resistance outflow model is the equivalent of the reflection boundary condition presented in Subsection 4.2.3 and is responsible for the reflection of incoming waves, which is one of the most important feature of any network outflow boundary condition. The value of the resistance also governs the mean pressure levels for a given mean flow rate.

6.3.3 Windkessel outflow model

The Windkessel outflow model is a modified version of the 0D blood flow equation (6.19), where an additional resistance is added at the inlet, before the capacity, to model the resistive behavior of the terminal vessel itself. It is the most common 0D outflow model used in the literature on 1D blood flow.

The governing equation of the Windkessel outflow model linking the inlet flow rate and pressure with the outlet pressure writes:

$$\left(1 + R_2 C \frac{d \cdot}{dt} + I C \frac{d^2 \cdot}{dt^2}\right) p|_{x=0} - p|_{x=L} = \left([R_1 + R_2] + R_1 \left[R_2 C \frac{d \cdot}{dt} + I C \frac{d^2 \cdot}{dt^2}\right] + I \frac{d \cdot}{dt}\right) Q|_{x=0}. \quad (6.22)$$

Equation (6.22) contains the resistance model (6.20) if $C = I = 0$, in which case $R_f = R_1 + R_2$. In Figure 6.9, we represent the electrical circuit equivalent to this Windkessel outflow model.

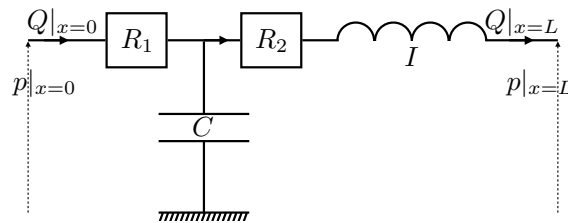


Figure 6.9 – Electrical representation of the Windkessel 0D outflow model (6.22).

To better understand the behavior of the Windkessel model (6.22), we compute its response to a constant flow input which is essentially a crude approximation of the flow in a terminal vessel. Considering a constant inlet flow rate $Q|_{x=0}$ and a zero outlet pressure $p|_{x=L} = 0$, Equation (6.22) writes:

$$\left(1 + R_2 C \frac{d \cdot}{dt} + I C \frac{d^2 \cdot}{dt^2}\right) p|_{x=0} = [R_1 + R_2] Q|_{x=0}. \quad (6.23)$$

The solution of Equation (6.23) is:

$$\begin{aligned}
 p|_{x=0} = [R_1 + R_2] Q|_{x=0} &+ A \exp\left(-t \frac{\tau_C}{2\tau_I^2} \left[1 + \sqrt{1 - 4 \frac{\tau_I^2}{\tau_C^2}}\right]\right) \\
 &+ B \exp\left(-t \frac{\tau_C}{2\tau_I^2} \left[1 - \sqrt{1 - 4 \frac{\tau_I^2}{\tau_C^2}}\right]\right),
 \end{aligned} \tag{6.24}$$

where $\tau_C = R_2 C$ and $\tau_I = \sqrt{CI}$. In physiological conditions, we have $\tau_I/\tau_C < 0.5$ and therefore:

$$\lim_{t \rightarrow +\infty} p|_{x=0} = [R_1 + R_2] Q_{in} \tag{6.25}$$

This analysis shows that the Windkessel outflow model is essentially a resistance model where inertia and compliance introduce delays in the resistive response, characterized by τ_C and τ_I .

In the following, we propose a numerical strategy to implement the Windkessel outflow model (6.22).

6.3.4 Numerical method

We propose here a numerical method to implement the Windkessel outflow model (6.22). As in Subsection 6.2.1, we impose the Windkessel outflow boundary condition by setting the value of the vector conservative variables \mathbf{U}_{out}^n in the ghost cell C_{out} placed at the outlet of the considered terminal vessel. We consider here that $I = 0$ for simplicity, which is a common assumption used in the literature on 1D blood flow equations.

The first equation is obtained by estimating the outgoing Riemann invariant using Equation (4.38b):

$$W_2\left(\mathbf{U}_{out}^{n+1}\right) = W_2\left(\mathbf{U}_{N_x}^{n+1}\right). \tag{6.26}$$

The second equation is derived by discretizing Equation (6.22) with an implicit Euler integration scheme:

$$p_{out}^{n+1} + R_2 C \frac{p_{out}^{n+1} - p_{out}^n}{\Delta t} - p|_{x=L} = [R_1 + R_2] Q_{out}^{n+1} + R_1 R_2 C \frac{Q_{out}^{n+1} - Q_{out}^n}{\Delta t}, \tag{6.27}$$

where Δt is the time step presented in Section 4.1 and $p|_{x=L}$ is the constant pressure at the distal end of the terminal vascular bed. Usually, we assume that $p|_{x=L} = 0$. The global system is solved using a Newton's method in a limited number of iterations (~ 5) in every terminal artery at every time step.

6.3.5 Validation and comparison

We use two network test cases presented in [Boileau et al. 2015] to validate the resistance and Windkessel outflow models and continue the comparison between the point and control-volume bifurcation models.

Aortic bifurcation

We consider the arterial bifurcation test case presented in [Boileau et al. 2015] and describing blood flow in an aortic bifurcation between the thoracic aorta and the two iliac arteries. Following [Boileau et al. 2015], we impose the flow rate at the inlet and Windkessel outflow conditions at the outlet of both iliac arteries. The geometrical, mechanical and boundary parameters are found in [Boileau et al. 2015] and the numerical parameters are described in Table 6.3.

N_x	x order	Δt	t order
50	2	10^{-5}	2

Table 6.3 – Numerical parameters used in the aortic bifurcation test case presented in [Boileau et al. 2015].

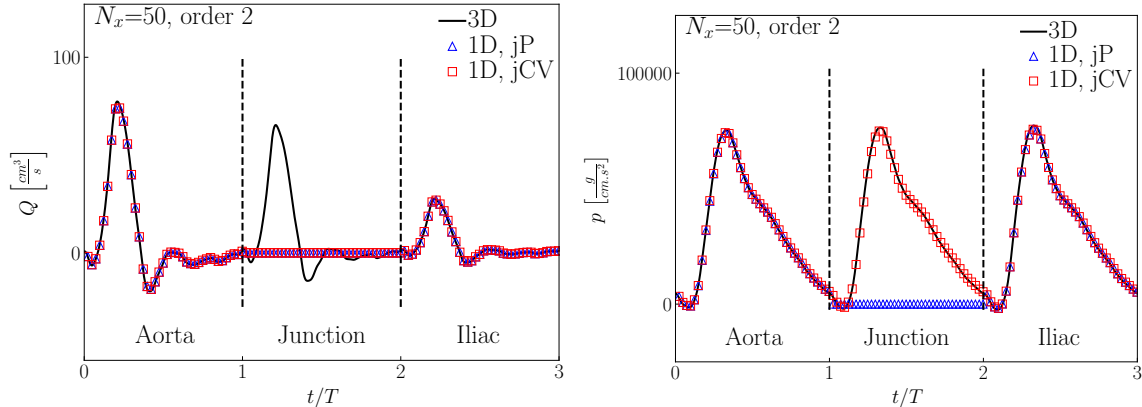


Figure 6.10 – Aortic bifurcation test case. Comparison between 3D solutions (—), the 1D point bifurcation solutions (Δ) and the 1D control-volume bifurcation solutions (\square) with $C_L = 0.1$ for the time evolution of the pressure p (Left) and the flow rate Q (Right) obtained in the aorta, the bifurcation and one iliac artery. Both 1D solutions perfectly match the 3D solutions, but only the control-volume bifurcation model can describe the variation of pressure inside the bifurcation.

In Figure 6.10, we compare the time evolution of the pressure p and flow rate Q solutions obtained in the aorta, the bifurcation and the iliac artery with a 3D model to results computed with the 1D point bifurcation model and the 1D control-volume bifurcation model with $C_L = 0.1$. We observe that for each variable, both 1D bifurcation models (point and control-volume) give results identical to those obtained with the 3D model. The pressure in the bifurcation is correctly captured by the control-volume bifurcation model, whereas the point bifurcation model by definition does not have a bifurcation pressure.

In this test case, the length of each artery is small compared to the wavelength of the pulse wave. The flow is therefore mainly driven by the Windkessel outflow boundary conditions, which explains the perfect match between the 3D and 1D solutions. This somewhat reduces the pertinence of this test case as we are essentially testing the implementation of the inlet and outlet boundary conditions more than the blood flow and bifurcation models.

37-artery network

We now consider a 37-artery *in vitro* network presented in [Matthys et al. 2007; Alastruey et al. 2011] and benchmarked in [Boileau et al. 2015]. Following [Boileau et al. 2015], we impose the flow rate at the inlet and use both resistance and Windkessel outflow conditions at the outlet of each terminal segment. The geometrical, mechanical and boundary parameters are found in [Boileau et al. 2015] and the numerical parameters are described in Table 6.4. The capacity of the Windkessel outflow model is set to 10^{-5} in all terminal segments.

In Figure 6.11, we plot the time evolution of the pressure p and flow rate Q solutions obtained in different arteries (Aortic Arch 2, Left Subclavian 1, Right Anterior Tibial) with the 1D point bifurcation model and the 1D control-volume bifurcation model with $C_L = 0.1$

N_x	x order	Δt	t order
3	2	10^{-5}	2

Table 6.4 – Numerical parameters used in the 37-artery *in vitro* test case used in [Boileau et al. 2015] and presented in [Matthys et al. 2007; Alastruey et al. 2011].

where we apply both resistance and Windkessel boundary conditions. These results are compared to the experimental data measured in the *in vitro* network and to numerical solutions computed with a 1D *finite volume* model presented in [Boileau et al. 2015] coupled to resistance outflow conditions. We observe that for each variable computed with resistance outflow conditions, both 1D bifurcation models give the same results as the 1D *finite volume* model. However only the experimental pressure p is well-matched by the numerical solutions. Finally, the effects of the Windkessel outflow conditions are noticeable in the flow rate signal. In addition to the expected smoothing effect, the Windkessel outflow condition increases flow rate during systole and consequently decreases flow rate during diastole in the arteries close to the terminal segments (Left Subclavian 1, Right Anterior Tibial). However, the solutions obtained with the Windkessel outflow conditions do not provide a better estimation of the experimental flow rate signal.

These results validate the implementation of the resistance and Windkessel outflow conditions and again show the potential of the control-volume bifurcation boundary condition.

6.4 Structured-tree outflow boundary condition

In physiological conditions the wavelength of the pulse wave is large, therefore outflow boundary conditions greatly influence the shape and amplitude of the numerical pulse wave. Fortunately, the 0D outflow models presented in Section 6.3 give satisfactory results in large network simulations. However, they depend on parameters that are difficult to estimate in the absence of local measurements and the numerical results are highly sensitive to the value of these parameters. Data assimilation and parameter estimation strategies are being developed to numerically determine the value of these outflow parameters for specific patients and show very promising results [Alastruey et al. 2008; Pant et al. 2014; Lal et al. 2016].

Other approaches are also considered that focus on finding alternative outflow models that do not depend on a large number of unknown parameters. To that effect, the structured-tree outflow model was originally proposed in [Olufsen 1999; Olufsen et al. 2000] and then applied in [Vignon and Taylor 2004; Olufsen et al. 2012; Cousins and Gremaud 2012; Perdikaris et al. 2015; Qureshi et al. 2014; Guan et al. 2016]. The idea is to replace at the outlet of each terminal vessel the classical resistance and Windkessel outflow flow models by a user-defined structured network representing the vascular bed distal to each terminal segment (see Figure 6.7 Right and Figure 6.12). In practice, the flow is not computed in these very large structured-trees. Rather, their frequency response is evaluated and represented through their root impedance Z_{ST} , representing the impedance response at the outlet of their corresponding terminal vessel, which also their first (or root) artery. The root impedance then links the outlet pressure and flow rate p_{out} and Q_{out} in the ghost cell C_{out} , similarly to the resistance outflow condition (6.20).

In the following, we detail the construction of a structured tree and the methodology to compute the root impedance Z_{ST} of a terminal vessel. As the structured-tree outflow model is computationally more expensive than the Windkessel outflow model, we investigate if the frequency response of the structured-tree can be accurately represented by a Windkessel model.

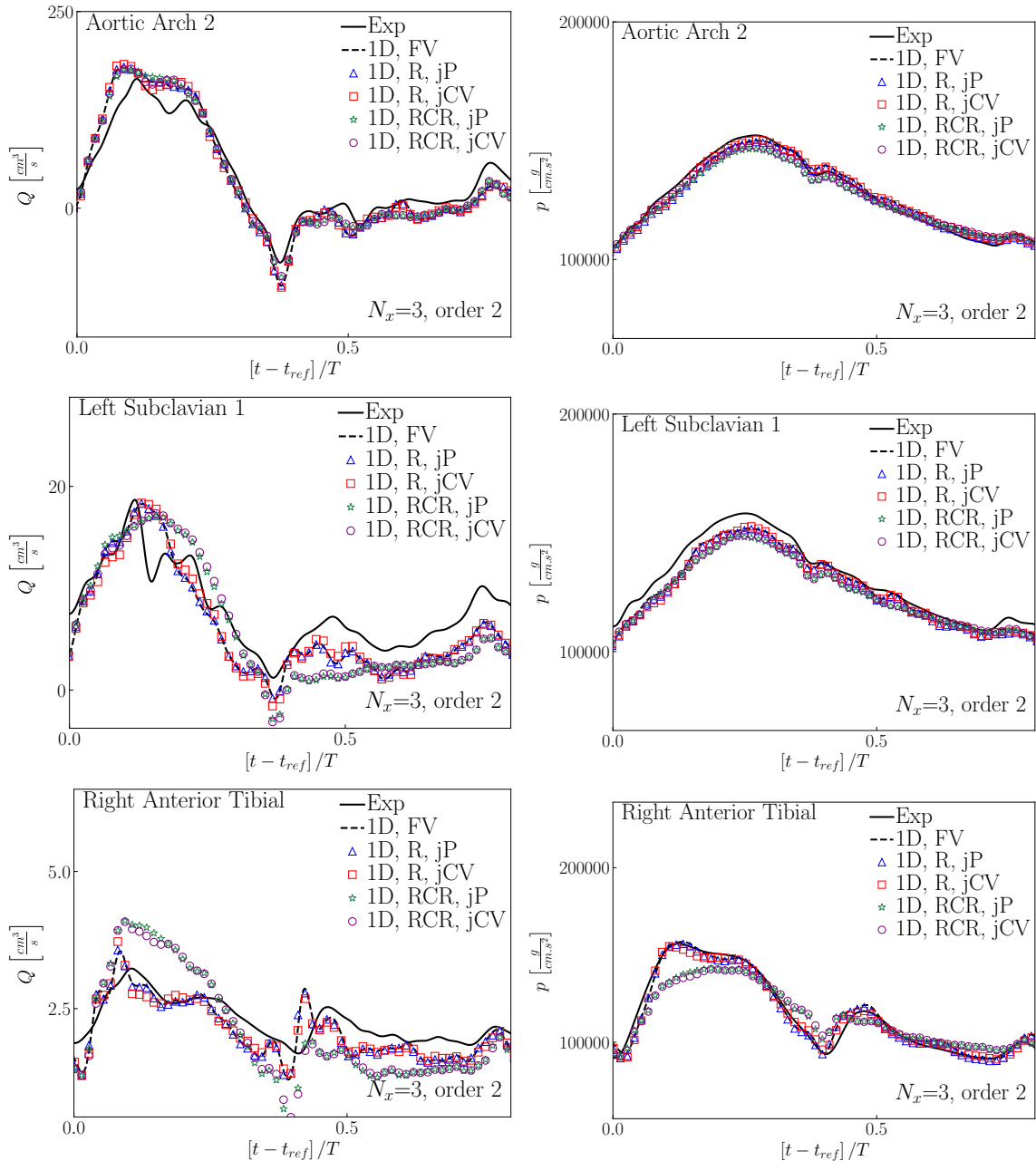


Figure 6.11 – 37-artery in vitro network test case. Comparison between experimental measurements (—), a 1D finite volume solution (resistance --), the 1D point bifurcation solutions (resistance \triangle , Windkessel \star) and the 1D control-volume bifurcation solutions (resistance \square , Windkessel \circ) with $C_L = 0.1$ for the time evolution of the pressure p and the flow rate Q .

Top: Aortic Arch 2.

Middle: Left Subclavian 1.

Bottom: Right Anterior Tibial.

The 1D solutions coupled to resistance outflow conditions perfectly match the 1D finite volume solutions and are a good approximation the experimental pressure solutions.

6.4.1 Construction of a structured-tree

A structured tree is constructed based on the simple rule stating that each vessel in the structured tree divides into two daughter arteries until a minimum radius R_{min} is reached. The properties of the daughter arteries are computed using the following relationships, fitted from data presented in [Avolio 1980]:

- the structured-tree bifurcates up to a minimal radius R_{min} , usually chosen as:

$$10 \mu\text{m} \leq R_{min} \leq 100 \mu\text{m}. \quad (6.28)$$

- the radii of the two daughter arteries are proportional to the radius of the parent artery:

$$R_\alpha = \alpha_{ST} R_p \quad ; \quad R_\beta = \beta_{ST} R_p, \quad (6.29)$$

and usually $\alpha_{ST} = 0.9$ and $\beta_{ST} = 0.6$.

- the radius-length ratio is constant, but varies from one vascular region to the other [Zamir 1999]:

$$\lambda_{ST} = \frac{L}{R} = \text{cst}, \quad (6.30)$$

and usually $\lambda_{ST} = 50$.

- the rigidity increases towards the more distal arteries according to the expression:

$$K = \frac{4}{3} \frac{1}{\sqrt{\pi} R} \left[k_1 e^{k_2 R} + k_3 \right], \quad (6.31)$$

where $k_1 = 2 \times 10^7$, $k_2 = -22.53$ and $k_3 = 8.65 \times 10^5$. In [Perdikaris et al. 2015], the authors point-out that Equation (6.31) should be truncated when $R < 500 \mu\text{m}$ to prevent abnormally high rigidity values.

Assuming that the properties propagation laws described above are valid, the structured-tree model depends on four parameters: R_{min} , α_{ST} , β_{ST} , λ_{ST} . This may seem as more unknown parameters than the 0D outflow models described in Section 6.3, but these parameters, once chosen, can be used to describe terminal vessels in large regions of the network. The entire outflow boundary conditions are then parametrized by only a few parameters.

6.4.2 Terminal vessel impedance

We follow the methodology proposed in [Cousins and Gremaud 2012] to compute the root impedance Z_{ST} of the terminal segment at the root of the structured tree. The impedance Z_{ST} represents the response of the structured-tree distal to the considered terminal vessel. Rather than computing Z_{ST} in the time domain, we use the natural periodicity of blood pressure and flow rate to write the equations in the frequency domain and compute the Fourier coefficients $Z_{ST,\omega}$ of Z_{ST} .

Starting from the linear System (6.14), we assume that the pressure and flow signals are periodic, which allows us to rewrite System (6.14) in the frequency domain as:

$$\begin{cases} j\omega C \hat{p}_\omega + \frac{\partial \hat{Q}_\omega}{\partial x} = 0 \end{cases} \quad (6.32a)$$

$$\begin{cases} j\omega I \hat{Q}_\omega + \frac{\partial \hat{p}_\omega}{\partial x} = -R_f \hat{Q}_\omega, \end{cases} \quad (6.32b)$$

where \hat{p}_ω and \hat{Q}_ω are the Fourier coefficients of the pressure p and the flow rate Q associated to the characteristic frequency ω and $j = \sqrt{-1}$. Following [Cousins and Gremaud 2012], we

solve System (6.32) for $x \in [0, L]$ and find:

$$\begin{cases} \hat{p}_\omega = \hat{p}_\omega(L) \cos\left([L-x] \sqrt{\omega C [\omega I - jR_f]}\right) \\ \quad + \hat{Q}_\omega(L) j \sqrt{\frac{\omega I - jR_f}{\omega C}} \sin\left([L-x] \sqrt{\omega C [\omega I - jR_f]}\right) \end{cases} \quad (6.33a)$$

$$\begin{cases} \hat{Q}_\omega = \hat{Q}_\omega(L) \cos\left([L-x] \sqrt{\omega C [\omega I - jR_f]}\right) \\ \quad + \hat{p}_\omega(L) j \sqrt{\frac{\omega C}{\omega I - jR_f}} \sin\left([L-x] \sqrt{\omega C [\omega I - jR_f]}\right). \end{cases} \quad (6.33b)$$

We then obtain an expression derived in [Cousins and Gremaud 2012] linking the inlet and outlet impedances of the artery:

$$Z_{ST,\omega}(0) = \frac{Z_{ST,\omega}(L) \cos(L \sqrt{\omega C [\omega I - jR_f]}) + j \sqrt{\frac{\omega I - jR_f}{\omega C}} \sin(L \sqrt{\omega C [\omega I - jR_f]})}{\cos(L \sqrt{\omega C [\omega I - jR_f]}) + Z_{ST,\omega}(L) j \sqrt{\frac{\omega C}{\omega I - jR_f}} \sin(L \sqrt{\omega C [\omega I - jR_f]})}, \quad (6.34)$$

where $Z_{ST,\omega}$ is the Fourier coefficient of Z_{ST} associated to the frequency ω . In particular, we have for $\omega = 0$:

$$Z_{ST,0}(0) = Z_{ST,0}(L) + LR_f. \quad (6.35)$$

which gives the link between the impedance Z_{ST} and the viscous resistance R_f . Finally, we connect at each bifurcation of the structured-tree the parent and daughter arteries together by imposing as in Subsection 6.2.1 the conservation of mass and the continuity of pressure at the bifurcation, which translates as:

$$Z_{ST,\omega,p}(L) = \frac{Z_{ST,\omega,\alpha}(0) Z_{ST,\omega,\beta}(0)}{Z_{ST,\omega,\alpha}(0) + Z_{ST,\omega,\beta}(0)}. \quad (6.36)$$

Methodologies are then proposed in [Olufsen et al. 2000; Cousins and Gremaud 2012] to update the pressure and flow rate at each time step in the ghost cell C_{out} of the terminal vessel. Essentially, these methods use the Fourier coefficients of the root impedance Z_{ST} to compute in a discrete manner the pressure p_{out} in the ghost cell C_{out} as a function of the flow rate Q_{out} :

$$p_{out} = \sum_{k=-\infty}^{\infty} \hat{p}_{out,\omega_k} e^{i\omega_k t} = \sum_{k=-\infty}^{\infty} Z_{ST,\omega_k} \hat{Q}_{out,\omega_k} e^{i\omega_k t} \quad (6.37)$$

Note that in [Perdikaris et al. 2015], this frequency approach is not used and the 1D nonlinear blood flow equations (2.67) are solved in each terminal structured-trees using a highly parallelized numerical code.

6.4.3 Equivalent Windkessel outflow model

Using the structured-tree outflow model following the methodologies proposed in [Olufsen et al. 2000; Cousins and Gremaud 2012] has a higher computational cost than using classical 0D outflow models. Alternatively, directly solving the 1D equations in each structured-tree is computationally expensive and requires very large computational resources and well parallelized code [Perdikaris et al. 2015]. The structured-tree outflow model comes therefore at a higher computational cost than the other classical 0D outflow models. Moreover, its complex structure does not permit the simple understanding of the parameter effects we are able to achieve with the resistance or Windkessel outflow models (see Subsection 6.3.2 and Subsection 6.3.3). This renders the interpretation of the results difficult.

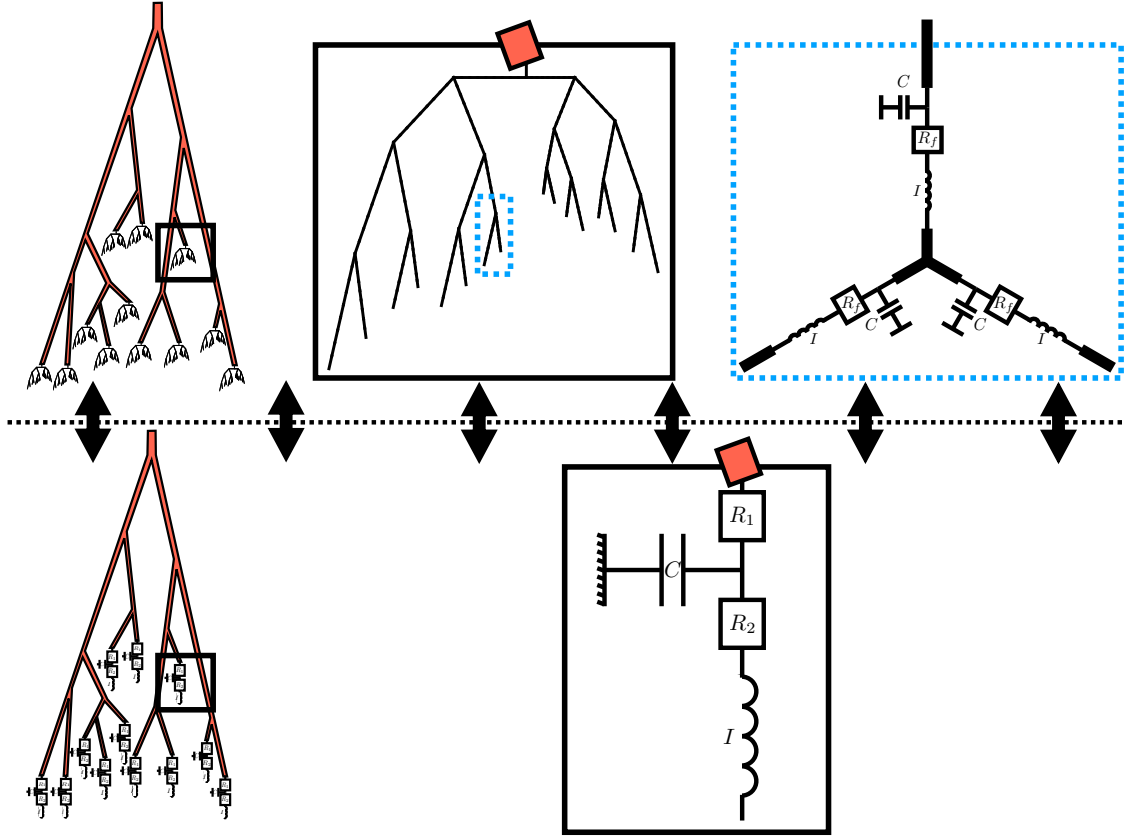


Figure 6.12 – Schematic of the equivalent Windkessel approach.

Top: Model arterial network using structured-tree outflow conditions. Each structured-tree is an assemblage of 0D arteries governed by the 0D blood flow equation (6.19).

Bottom: Same model arterial network using equivalent Windkessel outflow conditions designed to match the behavior of their corresponding target structured-tree.

However, recent studies [Cousins and Gremaud 2012; Guan et al. 2016] that compare the results obtained using a structured-tree outflow model and an equivalent Windkessel model find a very good match between the results computed with both models. We seek to confirm these results and propose a methodology to estimate the parameters of the Windkessel outflow model (6.22) to match the response of a target structured-tree. We then evaluate the sensitivity of the resistances R_1 and R_2 , the compliance C and inductance I of the equivalent Windkessel model to variations of the parameters of the target structured-tree outflow model, namely R_{root} and R_{min} . A schematic of our approach is presented in Figure 6.12.

Terminal Windkessel impedance

We derive from Equation (6.22) the root impedance Z_{WK} of the Windkessel outflow model and express here its Fourier coefficient associated to the frequency ω :

$$Z_{WK,\omega} = R_1 + \frac{R_2 + j\omega I}{1 - \omega^2 IC + j\omega R_2 C} \quad (6.38)$$

The modulus of $Z_{WK,\omega}$ writes:

$$|Z_{WK,\omega}|^2 = R_1^2 \frac{I^2 \omega^2 + 2R_1 R_2 + R_2^2}{1 + C\omega^2 [CR_2^2 + I[CI\omega^2 - 2]]} \quad (6.39)$$

and its asymptotic behaviors are:

$$\begin{cases} \lim_{\omega \rightarrow 0} |Z_{WK,\omega}| = R_1 + R_2 & (6.40a) \\ \lim_{\omega \rightarrow +\infty} |Z_{WK,\omega}| = R_1 & (6.40b) \end{cases}$$

We recover here the limit behavior (6.25). This analysis confirms that the resistances R_1 and R_2 govern the asymptotic response of the Windkessel, whereas the compliance C and the inductance I characterize the transition between the two asymptotic regimes.

Parameter estimation algorithm

Based on the analysis performed in the previous subsections, we propose an algorithm to estimate the parameters R_1 , R_2 , C and I of the Windkessel model (6.22) such that the Fourier coefficients $Z_{WK,\omega}$ (6.38) of the Windkessel impedance Z_{WK} match the Fourier coefficients $Z_{ST,\omega}$ (6.34) of the root impedance of the structured-tree Z_{ST} for a large band of frequencies ω . We proceed as follows:

1. We compute the Fourier coefficients Z_{ST,ω_k} for different frequencies $\omega_k = \frac{2k\pi}{T}$, assuming that the impedance Z_{leaf} of the vessels at the distal end of the structured-tree is 0. This process can be time-consuming when the difference between R_{root} and R_{min} is great.
2. We compute the resistances R_1 and R_2 using a *bounded limited-memory Broyden-Fletcher-Goldfarb-Shanno* (L-BFGS-B) minimization algorithm [Byrd et al. 1995], taken from the *Python2.7 scipy* library, which minimizes the cost-function:

$$\mathcal{F} = \frac{1}{N} \sqrt{\sum_{k=0}^{N-1} \Re [Z_{ST,\omega_k} - Z_{WK,\omega_k}]^2 + \Im [Z_{ST,\omega_k} - Z_{WK,\omega_k}]^2}, \quad (6.41)$$

within the bounds:

$$1 \leq R_1 \leq \infty \quad 1 \leq R_2 \leq \infty. \quad (6.42)$$

3. We compute the compliance C and inductance I using a *bounded Brent* minimization algorithm [Brent 2013], taken from the *Python2.7 scipy* library, which minimizes the cost-function:

$$\mathcal{F} = \frac{1}{N} \frac{\sqrt{\sum_{k=0}^{N-1} [\Re [Z_{ST,\omega_k} - Z_{WK,\omega_k}]^2 + \Im [Z_{ST,\omega_k} - Z_{WK,\omega_k}]^2]}}{\max_{k \in [1, N]} \sqrt{[\Re [Z_{ST,\omega_k} - Z_{WK,\omega_k}]^2 + \Im [Z_{ST,\omega_k} - Z_{WK,\omega_k}]^2]}} \quad (6.43)$$

within the bounds:

$$0 \leq C \leq 10^{-3} \quad 0 \leq I \leq \frac{R_2 C}{4}. \quad (6.44)$$

Both C and I are computed in separate minimization procedures as their values are of different magnitude rendering a common minimization procedure difficult (different step size in the phase space or line search).

From experience, $k \in [0, 50]$ is sufficient to capture the asymptotic behaviors of the impedance of the structured tree.

Validation

As a precaution, we first assess the performances of the parameter estimation algorithm and compute an equivalent Windkessel model for a given target structured-tree outflow model. We set $\alpha_{ST} = 0.9$, $\beta_{ST} = 0.6$ and $\lambda_{ST} = 50$ and vary the value of R_{min} and R_{root} , defined as the radius of the terminal vessel, which corresponds to the root (or first vessel) of the structured tree. We choose $R_{root} \in \{0.05, 0.15, 0.25, 0.35\}$ and $R_{min} \in \{30, 50, 70, 90\} \times 10^{-4}$.

In Figure 6.13, we compare the frequency response of the modulus $|Z|$ of both the structured-tree impedance Z_{ST} and the Windkessel impedance Z_{WK} . We observe a good match between $|Z_{ST}|$ and $|Z_{WK}|$ and recover similar results to those presented in [Cousins and Gremaud 2012; Guan et al. 2016]. We note that the quality of the Windkessel approximation essentially depends on the value of R_{root} . Indeed, as R_{root} increases (from left to right in Figure 6.13),

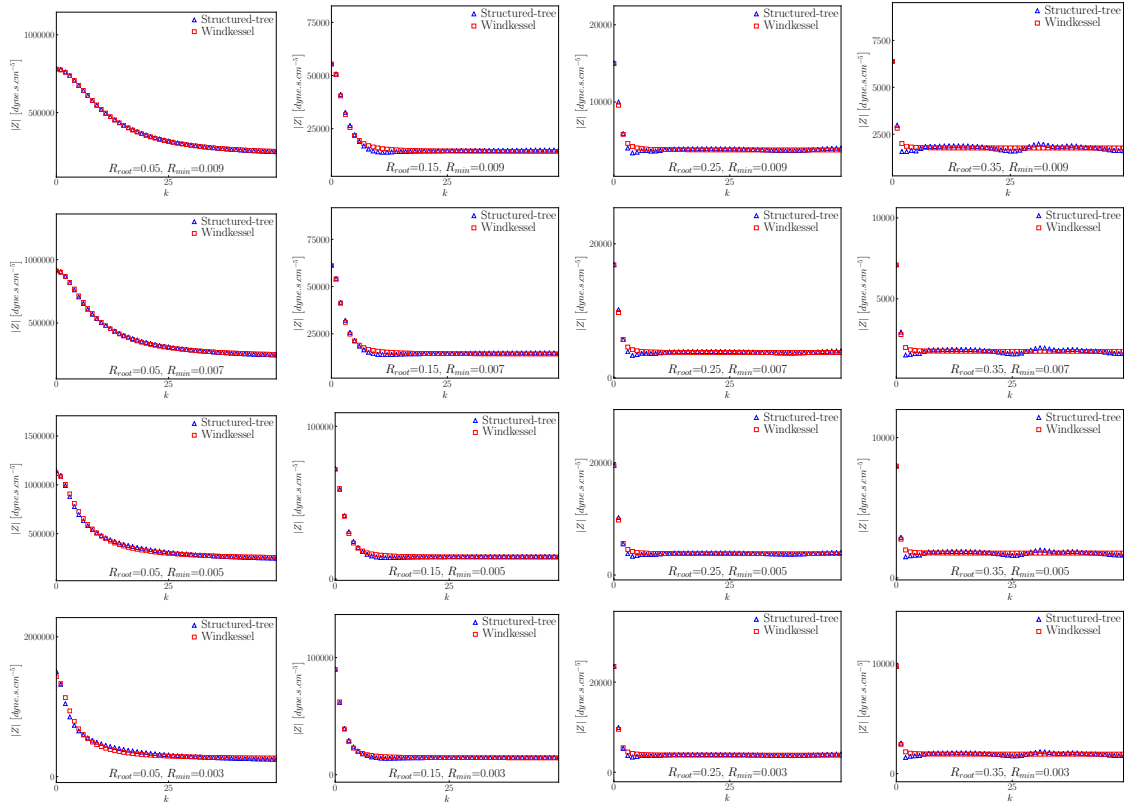


Figure 6.13 – Comparison between the frequency response of the modulus of the structured-tree impedance $|Z_{ST}|$ (Δ) and the modulus of the Windkessel impedance $|Z_{WK}|$ (\square) obtained with $\alpha_{ST} = 0.9$, $\beta_{ST} = 0.6$ and $\lambda_{ST} = 50$ for $R_{root} \in \{0.05, 0.15, 0.25, 0.35\}$.

Top: $R_{min} = 0.009$.

Middle top: $R_{min} = 0.007$.

Middle bottom: $R_{min} = 0.005$.

Bottom: $R_{min} = 0.003$.

The Windkessel and structured-tree impedance moduli are well-matched and the quality of the Windkessel approximation essentially depends on the value of R_{root} .

a local minimum of $|Z_{ST}|$ appears for $k \approx 5$ and oscillations occur for $k \geq 20$, which are frequency-dependent behaviors that the Windkessel model is unable to reproduce.

These results are confirmed in Figure 6.14 where we plot the final value of the cost-function \mathcal{F} (6.43) as a function of R_{root} and R_{min} . Indeed, a global minimum is reached for $\{R_{root} \approx 0.05, R_{min} \approx 0.008\}$ and the error increases with R_{root} , all the while remaining acceptably low. The values of R_{root} and R_{min} used in Figure 6.14 are presented in Table 6.5.

Overall, the results presented in Figure 6.13 and Figure 6.14 establish the validity of the parameter estimation algorithm and confirm the results presented in [Spilker et al. 2007; Cousins and Gremaud 2012; Guan et al. 2016] indicating that an equivalent Windkessel model can accurately describe the frequency response of a structured-tree.

Parameter sensitivity

All studies on structured-tree outflow conditions show that among the parameters α_{ST} , β_{ST} , λ_{ST} and R_{min} , the cutoff radius R_{min} is the most important parameter [Cousins and Gremaud 2012; Perdikaris et al. 2015]. We therefore perform a detailed analysis of the sensitivity of the estimated Windkessel parameters to variations of R_{min} and of the root radius R_{root} . The values of the structured-tree parameters we use are presented in Table 6.5.

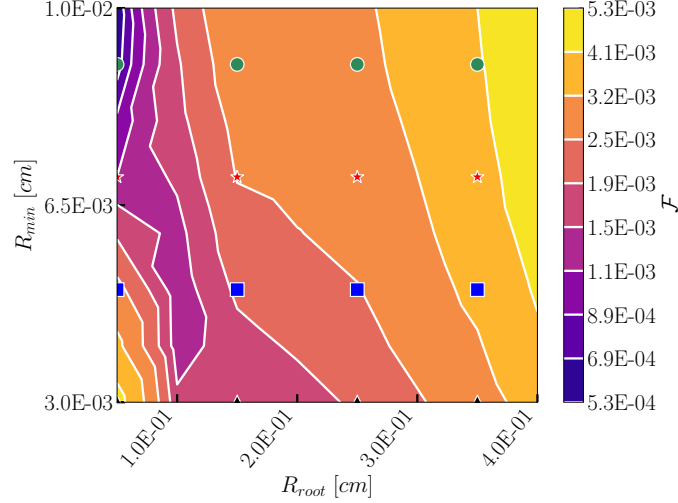


Figure 6.14 – Phase diagram representing the final value of the cost-function \mathcal{F} (6.43) as a function of R_{root} and R_{min} . The marks (Δ , \square , \star , \circ) represent the data points used in Figure 6.13. The final value of \mathcal{F} increases with R_{root} and a global minimum is reached for $\{R_{root} \approx 0.05, R_{min} \approx 0.008\}$

α_{ST}	β_{ST}	λ_{ST}	$R_{root} \times 10^{-2}$	$R_{min} \times 10^{-4}$
0.9	0.6	50	5	30
			\vdots	\vdots
			40	100

Table 6.5 – Values of the structured-tree parameters.

Figure 6.15 describes how variations of R_{root} and R_{min} affect the values of the Windkessel's resistances R_1 and R_2 . We observe that the value of R_1 decreases only when R_{root} increases, whereas R_2 decreases as R_{root} and R_{min} increase. Indeed, the variations of R_1 are accurately fitted by the functions:

$$\begin{cases} f_{R_{min}} = a_1 \exp(-b_1 R_{root}) + c_1 & \text{for } R_{min} = \text{cst and } a_1, b_1, c_1 > 0 \\ f_{R_{root}} = a_2 x^2 + b_2 x + c_2 & \text{for } R_{root} = \text{cst and } a_2, b_2, c_2 > 0, \end{cases} \quad (6.45)$$

and the variations of R_2 by the functions:

$$\begin{cases} f_{R_{min}} = a_3 \exp(-b_3 R_{root}) + c_3 & \text{for } R_{min} = \text{cst and } a_3, b_3, c_3 > 0 \\ f_{R_{root}} = a_4 \exp(-b_4 R_{min}) + c_4 & \text{for } R_{root} = \text{cst and } a_4, b_4, c_4 > 0. \end{cases} \quad (6.46)$$

These results are coherent with the fact that smaller vessels have a larger impedance and that the impedance matching conditions (6.36) favor vessels of small impedance (if $Z_\alpha \gg Z_\beta$ then $Z_p \approx Z_\beta$), i.e. of large radius. We note, both from the orientation of the isolines and the slopes of the fitted curves, that the influence of R_{root} is stronger than the influence of R_{min} . These results confirm the observation made in [Alastruey et al. 2008] concerning the Windkessel outflow model, stating that the resistance R_1 essentially represents the impedance of the terminal vessel whereas the resistance R_2 characterizes the impedance of the distal vascular bed.

Figure 6.16 describes how variations of R_{root} and R_{min} affect the values of the Windkessel's compliance C and inductance I . We observe that the compliance C increases only when R_{root} increases and remains constant when R_{min} changes. Indeed, the variations of C are accurately fitted using the functions:

$$\begin{cases} f_{R_{min}} = a_5 \exp(-b_5 R_{root}) + c_5 & \text{for } R_{min} = \text{cst and } a_5, c_5 < 0, b_5 > 0 \\ f_{R_{root}} = a_6 R_{min}^2 + b_6 R_{min} + c_6 & \text{for } R_{root} = \text{cst and } a_6, c_6, b_6 > 0. \end{cases} \quad (6.47)$$

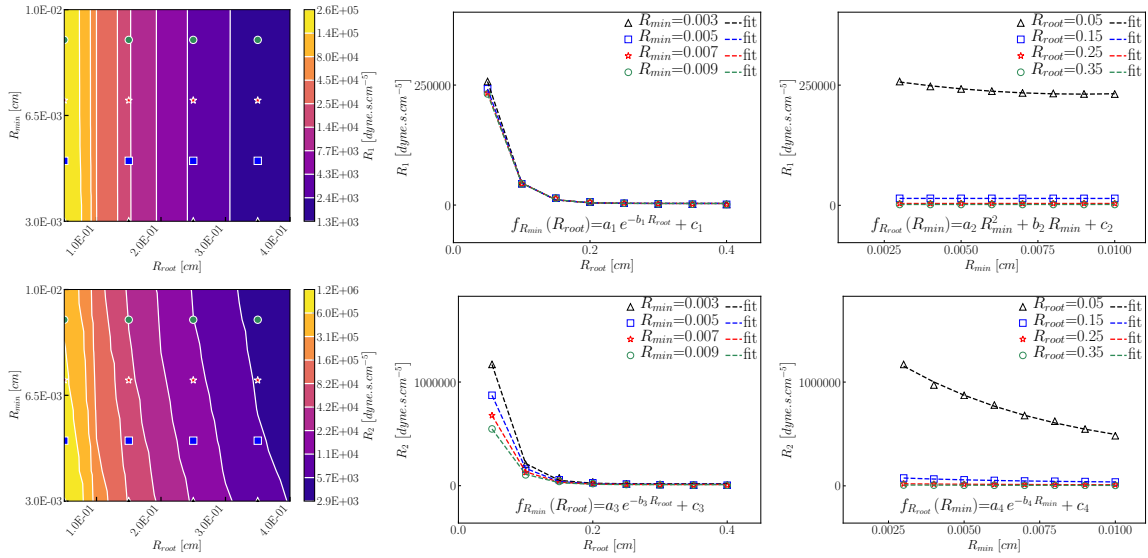


Figure 6.15 – Evolution of the Windkessel’s resistances R_1 (top) and R_2 (bottom) depending on the values of R_{root} and R_{min} .

Left: Phase diagram where the marks (Δ , \square , \star , \circ) represent the data points used in Figure 6.13.

Middle: Evolution of the Windkessels’ resistances with R_{root} for fixed values of $R_{min} \in \{30 \Delta, 50 \square, 70 \star, 90 \circ\} \times 10^{-4}$. The dotted lines (---) represented the fitted curves for each value of R_{min} using System (6.45) and System (6.46).

Right: Evolution of the Windkessels’ resistances with R_{min} for fixed values of $R_{root} \in \{5 \Delta, 15 \square, 25 \star, 35 \circ\} \times 10^{-2}$. The dotted lines (---) represented the fitted curves for each value of R_{root} using System (6.45) and System (6.46).

The resistance R_1 decreases only when R_{root} increases whereas the resistance R_2 decreases as R_{root} and R_{min} increase.

On the contrary, the inductance I exhibits a maximum for intermediate values of R_{root} and R_{min} and its variations are accurately fitted using the functions:

$$\begin{cases} f_{R_{min}} = a_7 R_{root}^2 + b_7 R_{root} + c_7 & \text{for } R_{min} = \text{cst and } a_7, c_7 < 0, b_7 > 0 \\ f_{R_{root}} = a_8 R_{min}^2 + b_8 R_{min} + c_8 & \text{for } R_{root} = \text{cst and } a_8, c_8 > 0, b_8 < 0. \end{cases} \quad (6.48)$$

Indeed, from System (6.15) we have $C \propto \frac{\sqrt{A_0}}{K}$ and $I \propto \frac{1}{A_0}$, which explains the previous results.

Finally, we plot in Figure 6.17 the variations of the characteristic time of the Windkessel model τ_I^2/τ_C (see Equation (6.24)) with R_{root} and R_{min} . We observe that τ_I^2/τ_C increases with R_{root} but remains smaller than the pulse period $T = 1$. This indicates that the Windkessel and structured-tree models essentially behave as pure resistances, which is expected as resistance is the essential behavior of any outflow model. This also means that in the parameter range considered here, using a pure resistance outflow condition rather than a Windkessel outflow condition generates a 10% error at the most (see Figure 6.11). We note that for large radius values with $R_{root} \approx 1$, $\tau_I^2/\tau_C \rightarrow T$ and the compliant and inertial effects become significant.

The analysis conducted here allows us to conclude that the root radius R_{root} is the most influential parameter, as it dictates the values of R_1 , R_2 and C . Fortunately, the radius R_{root} is not a parameter of the structured-tree outflow model but rather a geometrical parameter of the numerical network considered. These results therefore indicate that the value of R_{root} must be correctly estimated from medical imaging data to prevent non-physiological behaviors of the structured-tree outflow model. Variations of R_{min} are also important as

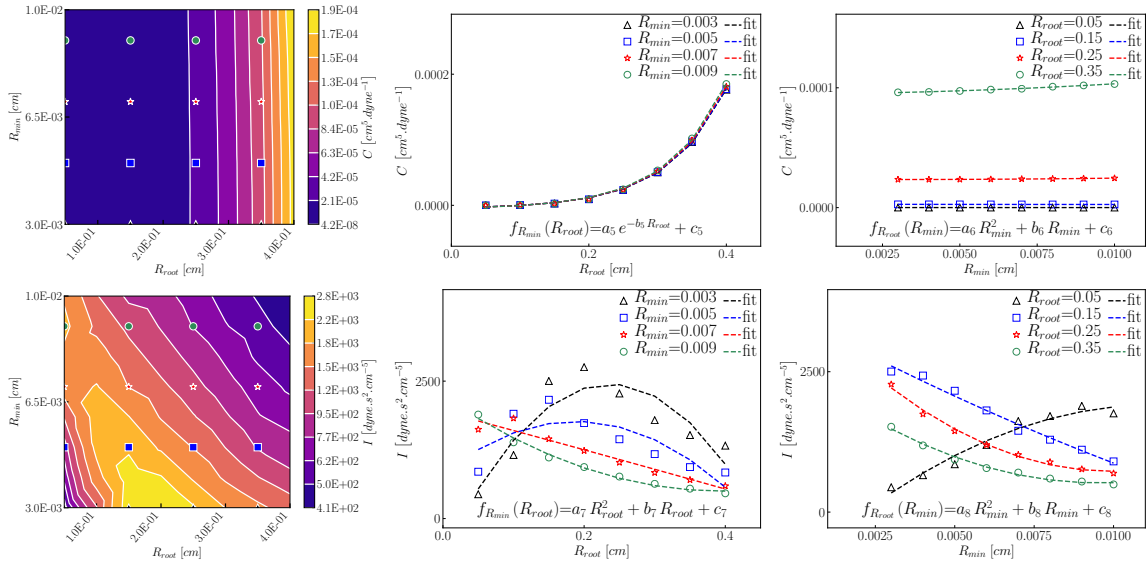


Figure 6.16 – Evolution of the Windkessel’s compliance C (top) and inductance I (bottom) depending on the values of R_{root} and R_{min} .

Left: Phase diagram where the marks (Δ , \square , \star , \circ) represent the data points used in Figure 6.13

Middle: Evolution of the Windkessel’s compliance and inductance with R_{root} for fixed values of $R_{min} \in \{30 \Delta, 50 \square, 70 \star, 90 \circ\} \times 10^{-4}$. The dotted lines (---) represented the fitted curves for each value of R_{min} using System (6.47) and System (6.48).

Right: Evolution of the Windkessel’s compliance and inductance with R_{min} for fixed values of $R_{root} \in \{5 \Delta, 15 \square, 25 \star, 35 \circ\} \times 10^{-2}$. The dotted lines (---) represented the fitted curves for each value of R_{root} using System (6.47) and System (6.48).

The compliance C increases only when R_{root} increases and the inductance I exhibits a maximum for intermediate values of R_{root} and R_{min} .

they lead to small but significant variations of the resistance R_2 , which lead to small but significant changes in the total resistance $R_1 + R_2$ and therefore in the value of pressure. Indeed, a change by a factor of 2 in the pressure amplitude is significant when trying to match experimental measurements.

77-artery network

To conclude the analysis on the structured-tree outflow model, we consider the 77-artery network used in [Boileau et al. 2015] and originally presented in [Blanco et al. 2014, 2015], representing the 55 principal arteries of the systemic circulation.

We do not use the 37-artery network presented in Subsection 6.3.5 as it is an *in vitro* network. Therefore, its boundary conditions can not be represented by structured-tree outflow conditions using the propagation law presented in Subsection 6.4.1, as they are fitted to *in vivo* data.

As before, we impose the flow rate at the inlet and Windkessel outflow conditions at the outlet of each terminal segment. However, the Windkessel parameters are now computed to match an equivalent structured-tree outflow model using the algorithm described previously. The geometrical and mechanical properties are found in [Boileau et al. 2015] and the boundary and numerical parameters are described in Table 6.6, where we vary the cutoff radius R_{min} to assess its influence on the numerical results.

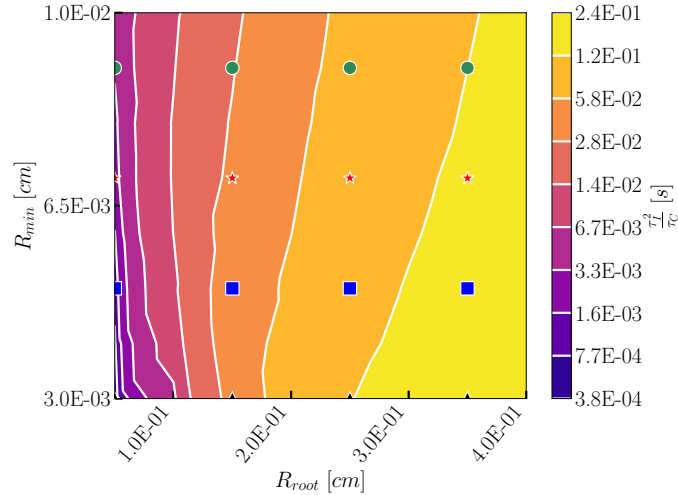


Figure 6.17 – Phase diagram representing the value of the Windkessel’s characteristic time τ_I^2/τ_C depending on the values of R_{root} and R_{min} . The marks (Δ , \square , \star , \circ) represent the data points used in Figure 6.13. The characteristic time τ_I^2/τ_C is much smaller than the pulse period $T = 1$, which indicates that the Windkessel and structured-tree models essentially behave as pure resistances.

α_{ST}	β_{ST}	λ_{ST}	$R_{min} \times 10^{-4}$	N_x	x order	Δt	t order
0.9	0.6	50	{100, 75, 50}	3	2	10^{-5}	2

Table 6.6 – Numerical parameters used in the 77-artery network test case used in [Boileau et al. 2015] and presented in [Blanco et al. 2014, 2015].

In Figure 6.18, we plot the time evolution of the pressure p and flow rate Q solutions obtained in different arteries (Aortic Arch 1, Right Posterior Interosseus, Right Internal Iliac) with the 1D point bifurcation model coupled to structured-tree Windkessel boundary conditions computed with $R_{min} \in \{100, 75, 50\} \times 10^{-4}$. These results are compared to numerical solutions computed with a 1D *finite volume* model coupled to Windkessel boundary conditions and presented in [Boileau et al. 2015]. We observe that in each artery, the pressure p levels predicted by the structured-tree Windkessel outflow model are higher than those obtained in [Boileau et al. 2015] with a Windkessel model, and, as expected, they increase when R_{min} decreases. On the contrary, the flow rate Q is correctly matched in both the Aortic Arch 1 and the Right Internal Iliac arteries, and the value of R_{min} has very little influence on the computed flow rates. An exception must be made for the flow rate computed in the Right Posterior Interosseus, which is much lower than the one computed in [Boileau et al. 2015] with Windkessel boundary conditions. In conclusion, the structured-tree Windkessel outflow conditions generate different but overall similar results to those obtained the Windkessel outflow condition.

The increased pressure levels obtained with the structured-tree Windkessel outflow model can also originate from a high value of the input stroke volume.

6.5 Conclusion

In Chapter 6, we have studied what we refer to as network boundary conditions, that is bifurcation and terminal boundary conditions. We have first proposed a control-volume bifurcation model that we have compared to the classical point bifurcation model. We have shown that in linear flow regimes, both model give identical results. In nonlinear flow regimes, their behaviors differ due to the compliant and control-volume aspects of the control-volume

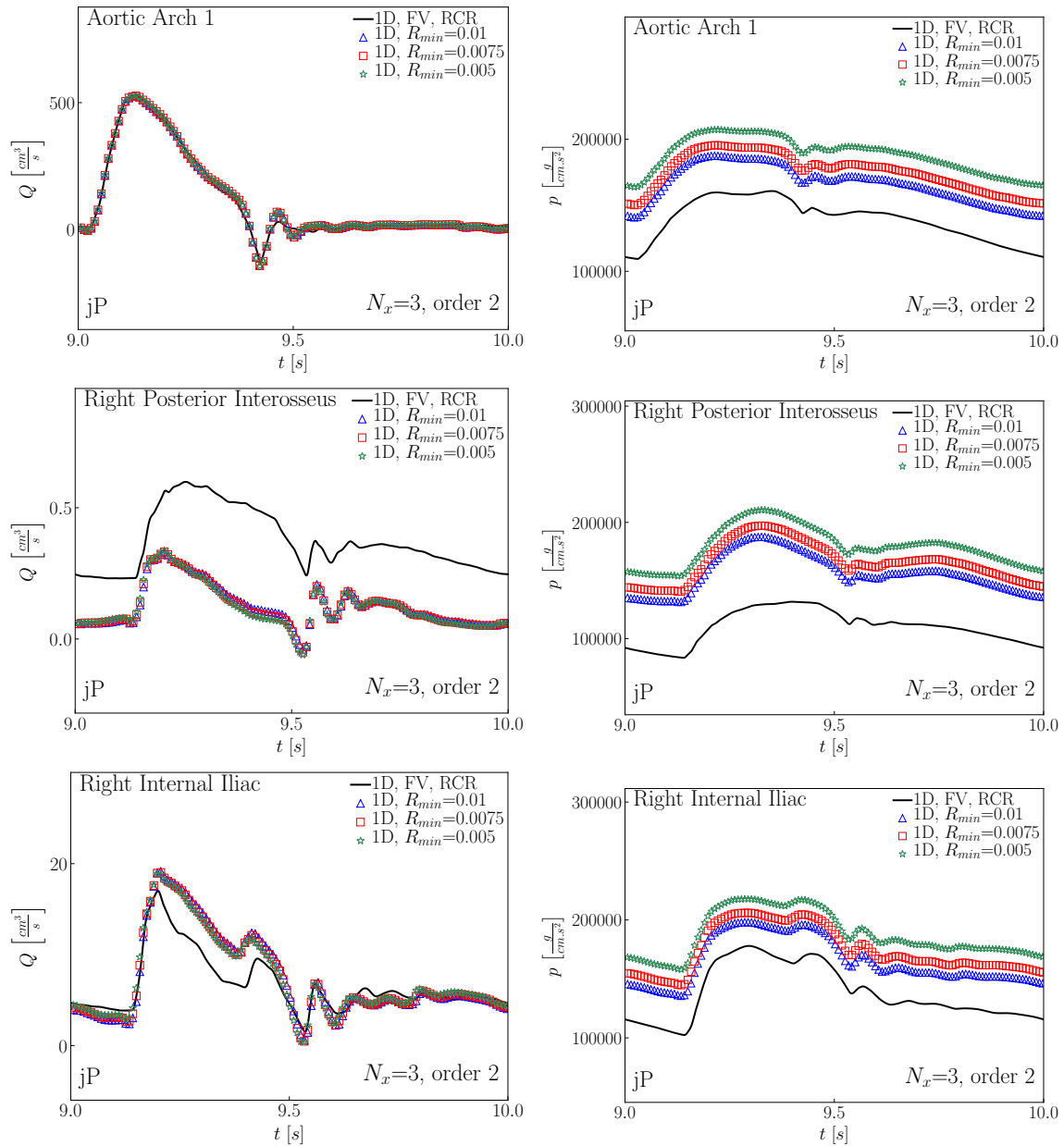


Figure 6.18 – 77-artery network test case with structured-tree equivalent Windkessel boundary conditions. Comparison between a 1D finite volume solution (—) presented in [Boileau et al. 2015] obtained with Windkessel boundary conditions and 1D point bifurcation solutions obtained with structured-tree equivalent Windkessel boundary conditions using $R_{min} \in \{100 \Delta, 75 \square, 50 \star\} \times 10^{-4}$ for the time evolution of the pressure p and the flow rate Q .

Top: Aortic Arch 1.

Middle: Right Posterior Interosseus.

Bottom: Right Internal Iliac.

bifurcation model. We have then studied different 0D outflow models, namely the resistance and the Windkessel, designed to represent the behavior of the vascular bed distal to a terminal segment. In particular, we have shown that Windkessel model with well-chosen parameters can accurately represent the frequency response of the structured-tree outflow model.

We are now implementing the structured-tree outflow condition and trying to add a non-Newtonian blood model to reduce the pressure in the structured-tree due to the Fahreus and Fahreus-Lindquist effects [[Pries et al. 1992](#)].

Biomedical applications

We present here three biomedical applications where we use the one-dimensional blood flow equations to provide insights on different medical problematic. We first propose a didactic investigation of the origin of the dicrotic notch. We then study different extracorporeal bypass graft treatments of a severe stenosis of the right Iliac artery (in the leg). Finally, we analyze experimental data on aortic and iliac clamping. The text in this chapter is greatly inspired from the following *published* articles:

- M.T. Politi, A.R. Ghigo, J.M. Fernández, I. Khelifa, J. Gaudric, J.-M. Fullana, and P.-Y. Lagrée. The dicrotic notch analyzed by a numerical model. *Computers in Biology and Medicine*, 72:54–64, 2016a;
- A.R. Ghigo, S. Abou Taam, X. Wang, P.-Y. Lagrée, and J.-M. Fullana. A one-dimensional arterial network model for bypass graft assessment. *Medical Engineering & Physics*, 2017a;
- M.T. Politi, S.A. Wray, J.M. Fernández, J. Gaudric, A.R. Ghigo, P.-Y. Lagrée, C. Capurro, J.-M. Fullana, and R. Armentano. Impact of arterial cross-clamping during vascular surgery on arterial stiffness measured by the augmentation index and fractal dimension of arterial pressure. *Health and Technology*, 6(3):229–237, 2016b.

Contents

7.1	The dicrotic notch analyzed by a one-dimensional numerical model . . .	128
	7.1.1 Introduction	128
	7.1.2 Methods	129
	7.1.3 Results	131
	7.1.4 Discussion	142
7.2	A one-dimensional arterial network model for bypass graft assessment . .	144
	7.2.1 Introduction	144
	7.2.2 Numerical model	145
	7.2.3 Numerical methods and results	145
	7.2.4 Conclusion	155
7.3	Impact of arterial cross-clamping during vascular surgery on arterial stiffness measured by the augmentation index and fractal dimension of arterial pressure	156
	7.3.1 Introduction	156
	7.3.2 Methods	158
	7.3.3 Results	160
	7.3.4 Discussion	162

7.1 The dicrotic notch analyzed by a one-dimensional numerical model

7.1.1 Introduction

The dicrotic notch is a small and brief increase in arterial blood pressure that appears when the aortic valve closes. This landmark has been widely referred to in the descriptive analysis of the arterial waveform (especially of aortic and radial arteries) and is commonly used as an equivalent of end-systolic left ventricular pressure [Dahlgren et al. 1991; Hébert et al. 1995].

Most medical textbooks explain the origin of the dicrotic notch as caused by the aortic valve closure itself [Boulpaep et al. 2009; Guyton and Hall 2006; Mann et al. 2014; Pinsky et al. 2006; Zundel et al. 2015]. These authors claim that towards the end of the ejection phase, blood flow across the aortic valve falls to very low values, until it actually reverses, producing a backflow that closes the aortic valve. As both flow and pressure are strongly coupled, this momentary backflow would produce a small positive shift in the aortic pressure trace. The dicrotic notch would therefore be the result of a short period of backward flow of blood immediately before the aortic valve closes. Many studies support this theory and have stressed that both events occur simultaneously [Higashidate et al. 1995; Hirschfeld et al. 1977].

On the other hand, there are clinical data that emphasize that the morphology of the dicrotic notch is related to the value of mean arterial pressure and, therefore, to peripheral vascular resistance [Chemla et al. 1996; Hébert et al. 1995]. Peripheral vascular resistance is mainly influenced by the vascular tone of small distal arteries (diameter smaller than 500 μm), called arterioles [Levy et al. 2005]. Pressure waves created by the heart travel through the arteries and reflect back towards the heart at places with high-vascular tone (such as the arterioles) and also at every vascular bifurcation [Marino 2013]. Hence, blood pressure waveforms can be viewed as a large addition of the forward pressure waves generated by the heart and the backward components due to multiple reflections, in particular, from the sites of distal resistance [Latham et al. 1985; O'Rourke and Avolio 1980; Westerhof et al. 2006]. This backward component would modify the mean arterial pressure and also change the morphology of the forward pressure wave, resulting in the creation of the dicrotic notch. The speed of these reflected waves depends on the mechanical and geometrical characteristics of the vessels [O'Rourke et al. 2002] but their amplitude depends directly on the value of peripheral resistance, that is, on the degree of vasoconstriction or vasodilation of the arterioles [Van den Bos et al. 1982; Westerhof et al. 1972]. In the following, the influence of the peripheral resistance will be quantified by a reflection coefficient ($R_t = R_a/I_a$), which is the ratio of the reflected amplitude (R_a) to the incident amplitude (I_a). Some authors state that a high vascular tone also increases the speed of the reflected waves [Zundel et al. 2015]. We consider that this would only change the amplitude of the reflected waves, not the speed, and will be addressing this matter in our experiments.

Based on this hypothesis, the presence of the dicrotic notch, created by the reflected waves, would induce a secondary pressure peak in the aorta, interrupting the aortic pressure downslope during end-systole. The increased pressure gradient between the aorta and the left ventricle would be sufficient to create a momentary backflow and close the aortic valve at higher diastolic levels, explaining why both the dicrotic notch and the aortic valve closure occur at the same time. We have arguments to put forward that this second approach responds to a better understanding of how the cardiovascular system actually works.

Understanding the dicrotic notch as a result of reflected pressure waves suggests that this landmark contains valuable information on the peripheral vascular network. We believe that this is an important concept to underline in cardiovascular physiology courses; therefore we present a teaching example that combines theoretical reasoning, numerical modeling and human experimental data. We propose a 1D model to study the role of reflected waves in the origin of the dicrotic notch, and compare the results from numerical simulations to experimental data from adult patients.

7.1.2 Methods

Invasive arterial pressure measurements in representative patients

Experimental data were obtained from continuous invasive arterial pressure measurements with a fluid-filled catheter from the right radial artery of adult patients undergoing peripheral vascular surgery at the *Hôpital Universitaire Pitié-Salpêtrière* in Paris, France. The study was approved by the IRB of the *Hôpitaux Universitaires La Pitié-Salpêtrière*, adheres to the requirements of the U.S. Federal Policy for the Protection of Human Subjects (45 CFR, Part 46), and is in accordance with the ethical principles of the Declaration of Helsinki. We used a disposable pressure transducer (TruWave, Edwards Lifesciences®) with a natural frequency of 40 Hz for a standard kit, which has shown to be appropriate for measuring blood pressure [Falsetti et al. 1974; Shinozaki et al. 1980]. Data were registered using an analog-digital converter (MP150, BIOPAC Systems Inc.) and the AcqKnowledge software. Data acquisition rate was 100 Hz.

Quantitative waveform analysis was done by measuring the time between the minimum value of the original radial pressure wave and the peak value of the reflection wave. Additionally, the relative time-position of the reflected wave within the pressure cycle (i.e., time between the minimum value of the original pressure wave and the peak value of the reflection wave divided by the overall cycle length) was studied to test the hypothesis of the reflection wave traveling faster as a result of the increased vascular tone. Systolic and diastolic arterial pressure values were computed from the maximum and minimum values of the original radial pressure wave. The amplitude of the dicrotic notch was computed from the peak value of the reflection wave. After defining a time window for each of these points by visual assessment, exact locations were identified using the first time-derivative of the pressure signal (dp/dt). Values were averaged over a 10 second interval. We compared data from before and after an intravenous bolus of phenylephrine (50 – 100 μg), which is a selective alpha 1-receptor agonist and thus a potent vasoconstrictor without any direct effect on heart rate and contractility. A brief transitional period was allowed between one state and the other. To better compare the dicrotic notch before and after the phenylephrine IV bolus, time was normalized to the duration of one cycle and pressure was normalized to the nearest inflexion point before the dicrotic notch (identified as the local minimum of the first time-derivative). Statistical analysis involved paired-Student's t-test (two-tailed) for before-after testing and independent Student's t-test (two-tailed) for comparisons among groups ($\alpha = 0.05$) using R studio free statistical software. Data are presented as mean \pm standard deviation.

Theoretical reasoning and numerical model

The aim of the numerical model is to accurately describe the flow of blood in the systemic network. In the previous chapters, we have shown that despite its simplification, the 1D viscoelastic system of equations (3.23) contains all the necessary physical behaviors to accurately describe blood flow in a network. The most important feature is its ability to capture the propagation of waves along the arteries, as a result of the elastic properties (or compliance) of the arterial wall, represented by the coefficient K in Equation (3.23b). As

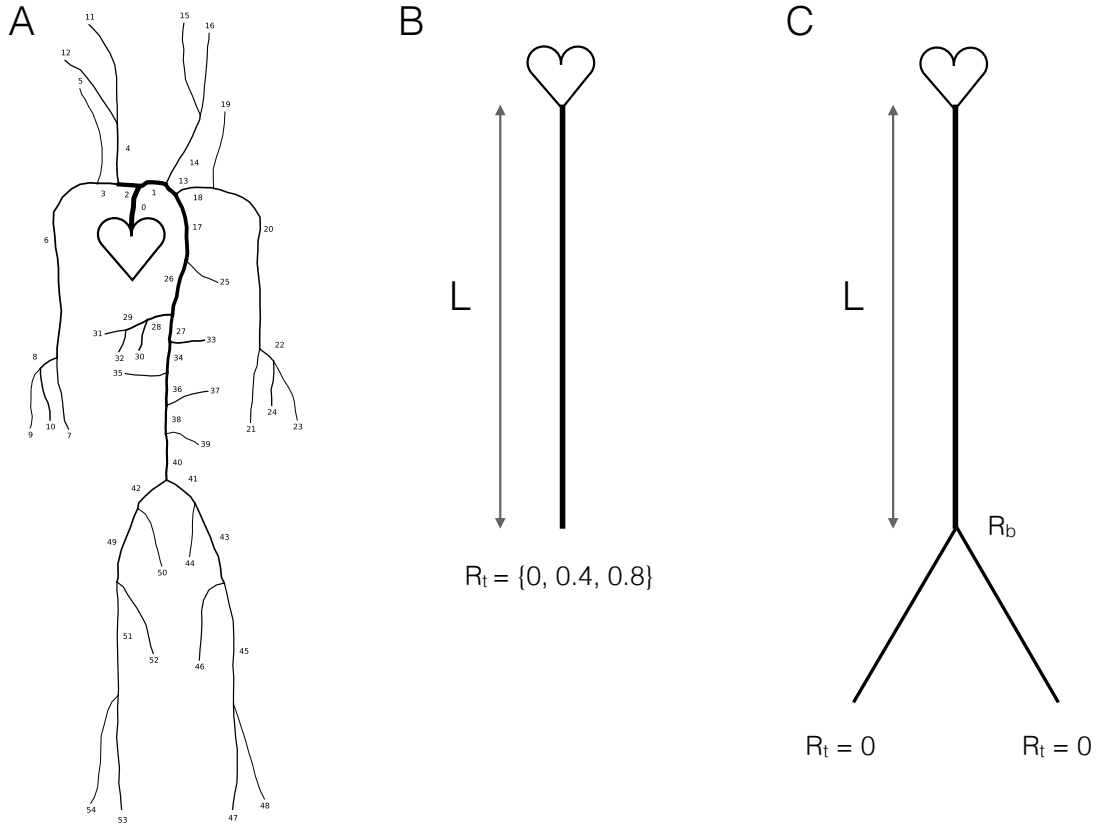


Figure 7.1 – Three different artery models used in our simulations.

- A* A human arterial network of 55 segments based on vascular nuclear magnetic resonance images. The influence of the peripheral vascular bed was taken into account through terminal reflection coefficients (R_t), which could be modified and, for the sake of simplicity, had the same value for all terminal segments.
- B* A single segment model considering one straight artery without bifurcations, where the terminal coefficient (R_t) could be modified. The mechanical and geometrical parameters of this single segment were identical to those of the aorta of the 55 arteries model and can be found in Table 7.1.
- C* A single bifurcation model formed of one parent artery that divides into two identical daughter arteries. The geometrical and mechanical parameters of the parent artery were the same as the single artery model. The two daughter arteries were identical and their parameters are presented in Table 7.2. The terminal coefficient (R_t) of the daughter arteries were set to 0 in order to study the value of the reflection coefficient (R_b) at the bifurcation, which could be modified.

these waves propagate in the network, the viscosity of the wall (described by the coefficient C_v in Equation (3.23b)) and the viscosity of the fluid (described by the coefficient C_f in Equation (3.23b)) are responsible respectively for the diffusion of the signal in the axial direction and its attenuation. The model also describes the reflection of the waves at each junction and terminal segment. The reflections occurring at junctions are characterized by the coefficient R_b which depends on the geometrical and mechanical properties of the parent and daughter arteries of the bifurcation. On the contrary, terminal reflection coefficients (R_t) are imposed numerically. These terminal reflection coefficients are set to model the reflective (or resistive) behavior of the peripheral vascular network. It is important to note that both internal and terminal reflections play an important role in modifying the waveforms as they propagate in the network.

In the following numerical computations, we used three different simplified models of the systemic network (Figure 7.1). The first was taken from the literature and represents the 55 principal segments of the human arterial network, which is a simplified construction based on vascular nuclear magnetic resonance images. The geometrical and mechanical parameters for each of the 55 segments were taken from the literature [Wang et al. 2015]. For the sake of

simplicity, the reflection coefficients for all terminal segments had the same value, R_t . The second model describes a single artery. The mechanical and geometrical parameters of this single segment are identical to those of the aorta of the 55 arteries model and can be found in Table 7.1. The third model is a single bifurcation formed of one parent artery and two daughter arteries. The geometrical and mechanical parameters of the parent artery are those of the single artery model. The two daughter arteries are identical and their parameters are presented in Table 7.2.

L	R	h	E
20-100	1.47	0.163	4×10^6

Table 7.1 – Geometrical and mechanical parameters describing the single artery network model and the parent artery of the bifurcation network model.

The governing equations are solved using the *finite volume* method presented and validated in Chapter 4.

L	R	h	E
10	0.5	0.1	4×10^6

Table 7.2 – Geometrical and mechanical parameters describing the daughter arteries of the bifurcation network model.

7.1.3 Results

Experimental data

In order to test the hypothesis that the presence of the dicrotic notch is related to the degree of peripheral vasoconstriction, we recorded the arterial pressure waveform registered continuously from the arterial line of patients undergoing peripheral vascular surgery. Data were taken from short, stable periods during the surgery, in which the only modification introduced was the injection of an intravenous bolus of phenylephrine. No vascular clamping or additional drug modifications were taking place at the time. Periodic oscillations in pressure waves were due to respiratory variations, which may be emphasized in patients under mechanical ventilation.

Figure 7.2 A shows data from Patient 1, an 81 year-old female smoker with arterial hypertension undergoing abdominal aorta prosthetic replacement after the diagnosis of an infrarenal abdominal aortic aneurysm. After an IV bolus of 100 μg of phenylephrine, not only did the systolic arterial pressure increase significantly from 94.1/52.3 to 109.5/56.1 mmHg ($p < 0.01$), but also the peak value of the dicrotic notch became higher (56.2 ± 2.9 vs. 60.2 ± 2.8 mmHg; $p < 0.01$) (Figure 7.2 A; left and middle panels). To additionally compare the dicrotic notch before and after the phenylephrine IV bolus, time was normalized to the duration of one cycle and pressure was normalized to the nearest inflexion point before the dicrotic notch. There was a statistically significant increase in the normalized peak value of the main wave (1.28 ± 0.04 vs. 1.31 ± 0.03 ; $p < 0.03$) and in the normalized peak value of the dicrotic notch (0.71 ± 0.01 vs. 0.76 ± 0.02 ; $p < 0.01$) after the IV bolus of phenylephrine. The proportional increase in the normalized peak value of the main wave (2%) was significantly smaller than the proportional increase in the normalized peak value of the dicrotic notch (6%) ($p < 0.01$) (Figure 7.2 A; right panel). The time between the minimum value of the original pressure wave and the peak value of the dicrotic notch did not change after phenylephrine injection (0.40 ± 0.02 vs. 0.41 ± 0.03 s; $p < 0.35$) nor did the relative time-position of the dicrotic notch within the pressure cycle (0.69 ± 0.03 vs.

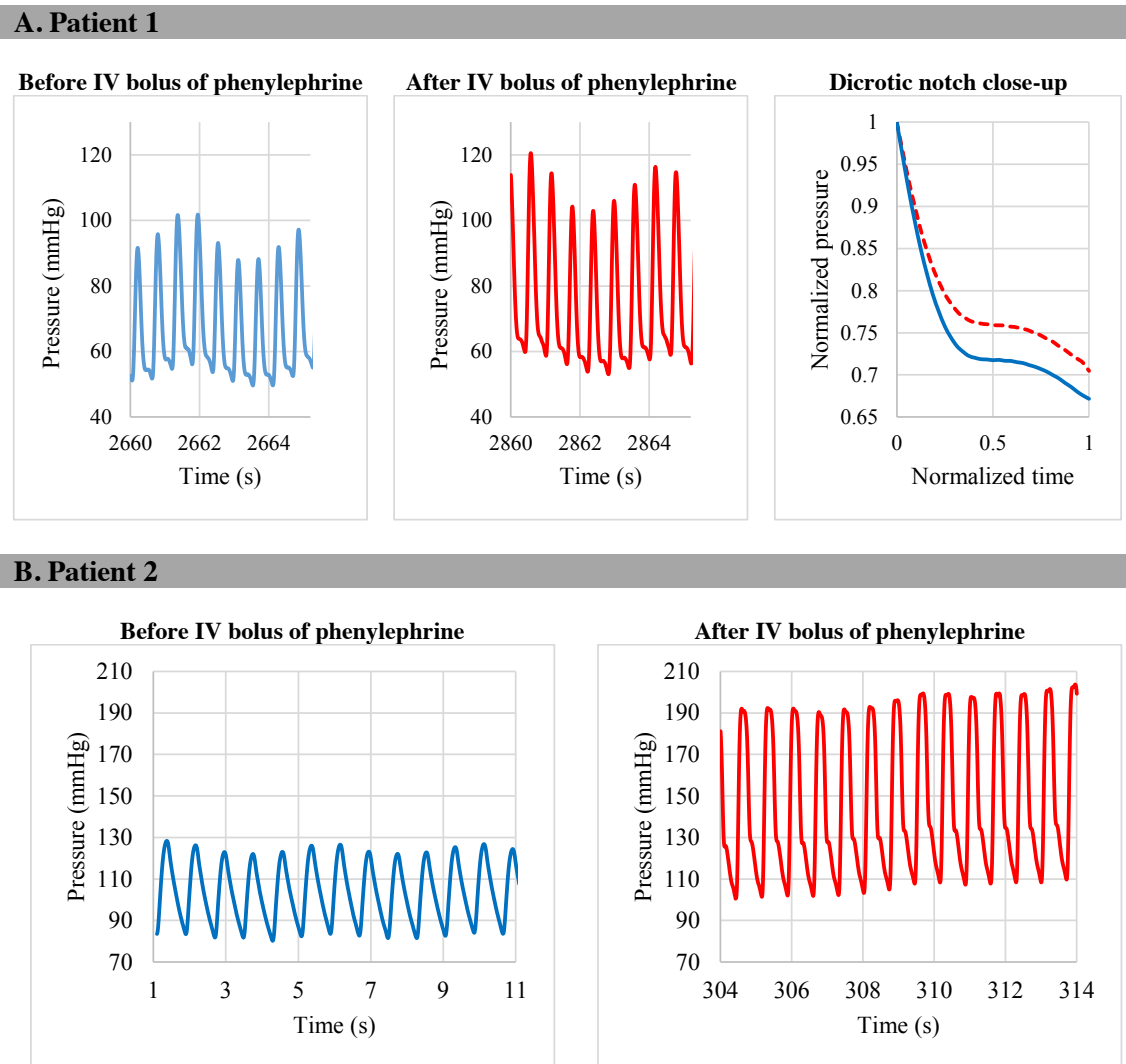


Figure 7.2 –

- A Left and middle panel: Invasive arterial pressure-time waves for Patient 1 undergoing abdominal aorta prosthetic replacement. Periodic oscillations in pressure waves were due to respiratory variations, which were enhanced due to mechanical ventilation settings. Initially the patient had a small dicrotic notch. Notice that, after an IV bolus of phenylephrine, the dicrotic notch increased its peak amplitude without changing its relative time-position within the pressure cycle. This could indicate that vasoconstriction induced by phenylephrine increases the amplitude of the dicrotic notch without modifying pressure wave travel time. Right panel: Comparison of mean pressure tracings over a 10-second interval before (continuous line) and after (dotted line) an IV bolus of phenylephrine with time normalized to the duration of one cycle and pressure normalized to the nearest inflexion point before the dicrotic notch. The proportional increase in the normalized peak value of the main wave (2%) was smaller than the proportional increase in the normalized peak value of the dicrotic notch (6%).*
- B Invasive arterial pressure-time waves for Patient 2 undergoing a right femoral-popliteal bypass. Initially the patient had a monophasic waveform that lacked any noticeable dicrotic notch. After an IV bolus of phenylephrine, blood pressure increased significantly and waveform morphology changed, with the dicrotic notch interrupting the end of the diastolic slope.*

0.69 ± 0.04 ; $p < 0.88$). These results indicate that, after vasoconstriction, the dicrotic notch only increases its amplitude; it does not appear earlier in the cycle.

Figure 7.2 B shows the arterial pressure waveform of Patient 2, a 56 year-old obese female without any known history of heart disease, undergoing a right femoral-popliteal bypass. Continuous invasive pressure measurements show that with an initial blood pressure of 124.5/82.4 mmHg the patient had a monophasic waveform that lacked any noticeable dicrotic notch. After an IV bolus of 50 μ g of phenylephrine, blood pressure increased significantly up to 195.6/105.2 mmHg ($p < 0.01$) and waveform morphology changed showing a clear dicrotic wave interrupting the end of the diastolic slope.

Since in both cases the only modification introduced between the two states was the addition of a powerful and selective vasoconstrictor, phenylephrine, the presence (or the increased amplitude) of the dicrotic notch could be attributed to an increase in the peripheral vascular tone. These experimental results suggest that the presence and the amplitude of the dicrotic notch are correlated with the value of peripheral resistance. Nevertheless, since we did not measure cardiac output or pulse wave velocity, we cannot assure there is a causal relationship between the two, based on our experimental data. Given the complexity of a human experimental model, a theoretical model of the human vascular network is required to explore the relationship between the amplitude of the dicrotic wave and the value of peripheral resistance.

Numerical simulations

In order to explore the hidden mechanisms behind the relationship between the amplitude of the dicrotic notch and vascular tone, while overcoming the difficulties of obtaining invasive data from humans under different conditions, we propose a numerical model of the human systemic arterial tree.

We first present the results obtained using the arterial network of 55 segments, then with the single segment model considering one straight artery without bifurcations, and finally with a single segment model with a bifurcation (one parent artery that divides into two daughter arteries).

55-artery model Numerical simulations compute the flow rate (Q) and the pressure (P) at every chosen record point of the 55-artery vascular network. The time evolution of these variables was studied in the proximal aorta, as to correlate with experimental data from other studies. To study the influence of the shape of the signal as well as backflow, three different inlet flow rate signals were considered in order: a parabolic signal without backflow (normal), a parabolic signal with backflow (backflow), and a triangular signal without backflow (triangular) (Figure 7.3). The amplitude of the different signals was set so that the total volume of blood ejected during each cycle is identical for each input signal considered. Backflow was simulated considering a maximum amplitude that is one fifth of overall aortic flow ($Q_{max}/5$) and a period that is one sixth of overall aortic flow period ($T_c/6$), which probably overestimates real values. Results show that for each inlet signal considered, a terminal coefficient of $R_t = 0$ yields a monophasic pressure-time curve that perfectly mirrors flow-time curves and lacks a dicrotic notch. On the other hand, a terminal coefficient of $R_t = 0.4$ results in a clear dicrotic notch which interrupts the downward pressure slope. An even higher terminal coefficient of $R_t = 0.8$ produces a higher dicrotic notch that is overlaid on the first pressure wave.

These numerical results from entire network simulations suggest that

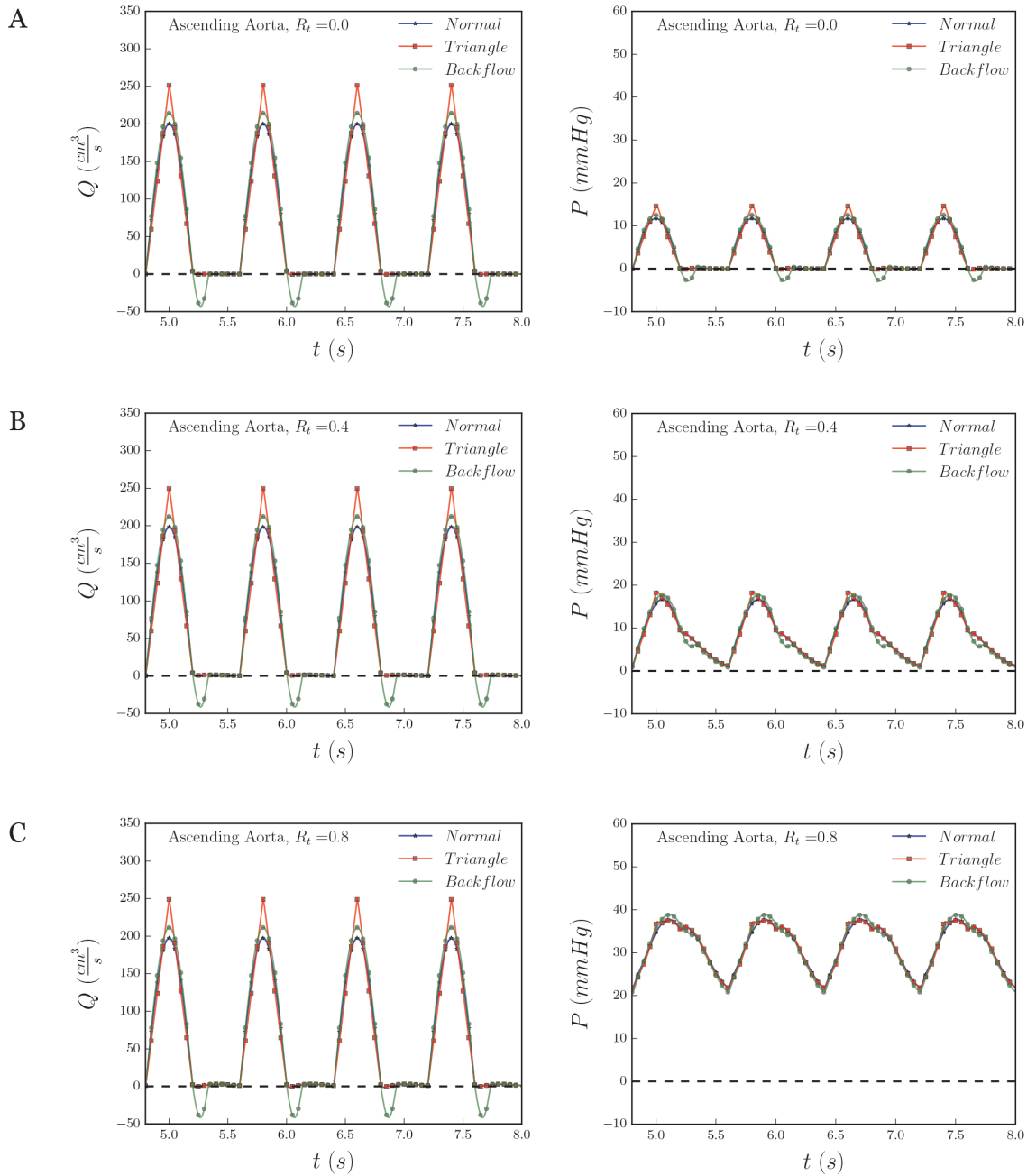


Figure 7.3 – Numerical simulation of flow rate (Q) and pressure (P) time curves in the proximal aorta of the 55-artery vascular network, using different terminal reflection coefficients (R_t).

A A terminal coefficient of $R_t = 0$ yields a monophasic pressure-time curve that practically mirrors flow-time curves. Note that the dicrotic notch is undetectable.

B A terminal coefficient of $R_t = 0.4$ results in a clear dicrotic notch which interrupts the downward pressure slope of the original pressure wave.

C A high terminal reflection coefficient of $R_t = 0.8$ produces a higher dicrotic notch that is superimposed on the original pressure wave nearly at its peak.

Three different inlet flow rate signals are illustrated: a parabolic signal without backflow (normal), a parabolic signal with backflow (backflow), and a triangular signal without backflow (triangular). The presence of backflow, as well as the shape of the inlet signal, modifies the shape but not the time-position of the dicrotic notch.

1. the presence and the amplitude of the dicrotic notch can be modified by simply changing the terminal reflection coefficient
2. the presence of the dicrotic notch does not depend on the shape of the inlet flow signal.

Backflow in the aorta is not required to create a dicrotic notch. However, using different inlet signals will modify the shape of the dicrotic notch, since the reflected waves will not be the same.

These results are in good accordance with our hypothesis that inlet backflow does not create the dicrotic notch by itself. In the following simulations, we will therefore consider only parabolic inlet signals without backflow.

Single segment model without bifurcations In real experiments as well as in numerical simulations using the 55-artery model, it is difficult to understand the underlying mechanism responsible for the creation of the dicrotic notch, since so many effects come into play. To simplify the problem, we used a very reduced model of the 55-artery network, considering only one artery without bifurcations. In this situation, the variables of interest that influence wave morphology (such as terminal reflection (R_t) coupled with classical compliant (K), viscous (C_f) and viscoelastic (C_ν) effects) can be easily modified, identified and therefore studied. We sought to evaluate the influence of each of these variables on the dicrotic notch through numerical simulation.

We computed the pressure-time curve of a single-beat impulse in arteries of different lengths ($L = 100$ cm, 60 cm, 40 cm, 20 cm) and plotted these curves in the same figure. We chose this strategy because the reflection waves resulting from the original pressure wave can be clearly identified in single-beat simulations. Likewise, individual reflection waves can be easily pointed out in longer vessels, since the increased vessel length prolongs the traveling time between the original pressure wave and the reflection point, separating the waves apart. Regardless of the overall length of the artery, the signal was always measured in the same location (i.e., at 15 cm from the beginning of the artery). Since the heart signal is periodic and has two phases (systole and diastole) and ejection occurs only during systole, we considered that ejection time was half the pulse period by supposing that each phase occupies half of the entire pulse period and that the systolic phase is mainly occupied by the ejection period (which is only slightly different from physiologic findings).

Pure wave propagation

We considered first a pure wave propagation, suppressing all source of attenuation and diffusion (meaning that no viscous or viscoelastic effects were taken into account, that is, both coefficients C_f and $C_\nu = 0$), with a pulse period of 0.1 s (i.e., ejection time = 0.05 s). We initially considered a reflection coefficient (R_t) of 0. As expected, our simulation showed a single original pressure wave, that was identical regardless of the vessel length, and no reflected waves (Figure 7.4 A). When we increased the reflection coefficient up to $R_t = 0.4$ (Figure 7.4 B), two additional reflected pressure waves appeared, which had identical amplitudes but were recorded at different times for each vessel length. These two waves are the result of the reflection of the original pressure wave at the end of the artery and the reflection of the first reflected wave at the beginning of the artery. In shorter vessels the two reflection waves are much closer to the original pressure wave than in longer vessels (e.g., compare the reflection waves from the 60 cm vessel and the 100 cm vessel). As the length of the artery decreases, the two reflection waves move closer and closer to the original pressure wave, since the first reflection wave is traveling a smaller distance at the same speed. Eventually, at very short vessel lengths, the two reflection waves merge together with the original wave by forming a notch (i.e., the 20 cm vessel). This clearly shows how the final morphology of the

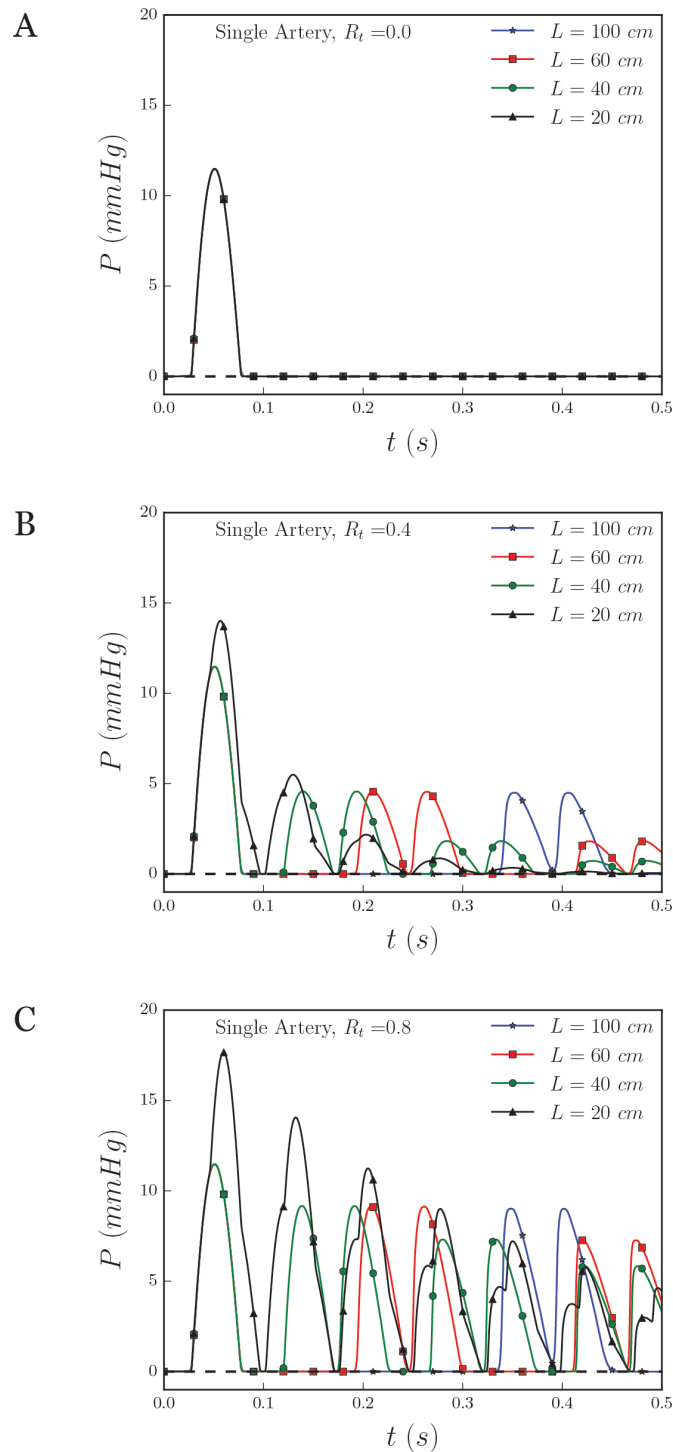


Figure 7.4 – Pressure-time curve of a single beat impulse in a one-artery model without bifurcations, measured at 150 mm from the beginning of the artery, in arteries of different lengths. These simulations considered a pulse period of 0.1 s and only pure wave propagation.

- A Considering a reflection coefficient of $R_t = 0$, our simulation shows a single original pressure wave that is similar regardless of the vessel length, and no reflected waves at all.
- B At an $R_t = 0.4$, our simulation shows two reflected waves that are much closer to the original pressure wave in shorter vessels than in longer vessels (e.g., compare the reflected waves from the 60 cm vessel and the 100 cm vessel). Eventually, at very short vessel lengths, the two reflection waves merge together with the original wave by forming a notch (i.e., the 20 cm vessel).
- C At an $R_t = 0.8$ our simulation shows that by increasing the reflection coefficient, only the amplitudes of the waves change. The reflected waves do not get closer to one another or to the original pressure wave, indicating that they do not change their propagation velocity.

pressure-time waveform is the addition of the original pressure wave and several reflection waves. When we increased again the reflection coefficient up to $R_t = 0.8$ (Figure 7.4 C), the pressure-time waveform was similar to Figure 7.4 B but had a higher amplitude. It is important to note that by increasing the reflection coefficient, only the amplitudes of the waves change. The reflected waves do not get closer to one another nor to the original pressure wave, that is, they do not increase their propagation velocity: the waves arrive at 15 cm at the same time, regardless of the reflection coefficient.

These numerical simulations show that the reflection waves originated at the terminal reflection site can create a notch on the original pressure and that the amplitude of these waves depends on the value of the terminal coefficient (R_t).

Up to this point, we have considered a pulse period of 0.1 s, since this allows us to identify individual waves more easily. Nevertheless, this would imply a heart rate of 600 beats per minute. A pulse period of 0.8 s would be a more realistic approach, yielding a heart rate of 75 beats per minute. Pressure-time curve simulations considering a pulse period of 0.8 s (i.e., ejection time = 0.4 s) show that, once again, reflected waves disappear when the terminal reflection is zero (Figure 7.5 A) and increase in amplitude as the terminal reflection does (Figure 7.5 B and C). With a longer pulse period, the reflected waves merge with the original pressure wave even in vessels with long lengths (e.g., in the 60 cm vessel they are almost completely merged together) (Figure 7.5 B) and the individual elements of these pressure waves are harder to point out.

Considering only the propagation of a wave without viscous attenuation or viscoelastic diffusion, we were able to show that in the scope of our experiments, it was possible to form a dicrotic notch through positive interactions between reflected waves originated at the terminal reflection site and the original pressure wave. Furthermore, we showed that when considering a realistic pulse period of 0.8 s, the interactions between the forward and backward traveling wave were strengthened.

Viscous and viscoelastic effects

The influence of viscous and viscoelastic effects (respectively governed by the coefficients C_f and C_ν) was added in the following series of simulations. Once again, we considered a pulse period of 0.1 s in order to compare with pure wave propagation curves. Figure 7.6 A shows that with a reflection coefficient (R_t) of 0 there is a single original pressure wave and no reflected waves. Figure 7.6 B and C represent numerical solutions for reflection coefficients (R_t) of 0.4 and 0.8, respectively, and we observe reflected waves that have higher amplitude for higher reflection coefficient. In comparison to pure wave propagation, the reflected waves merge with the original pressure wave at longer lengths (e.g., in the 40 cm vessel) when influenced by viscous and viscoelastic effects.

These simulations show that the presence of viscosity and viscoelasticity “smoothens the curves out”, resulting in the overlap of waves that previously were identified as individual elements when considering only pure wave propagation. These results show that, when considering viscous and viscoelastic effects, the overlap between waves is greater but still dependent on the reflection terminal coefficient.

Changes in elasticity

The effects of changing the vessel elasticity (E) were studied using the same single artery model as before, this time with a length of 60 cm. Figure 7.7 A indicates how, as the elasticity increases, the incoming pressure wave appears earlier (since the propagation speed is increased) and reaches higher values; however since the reflection coefficient (R_t) is 0, the

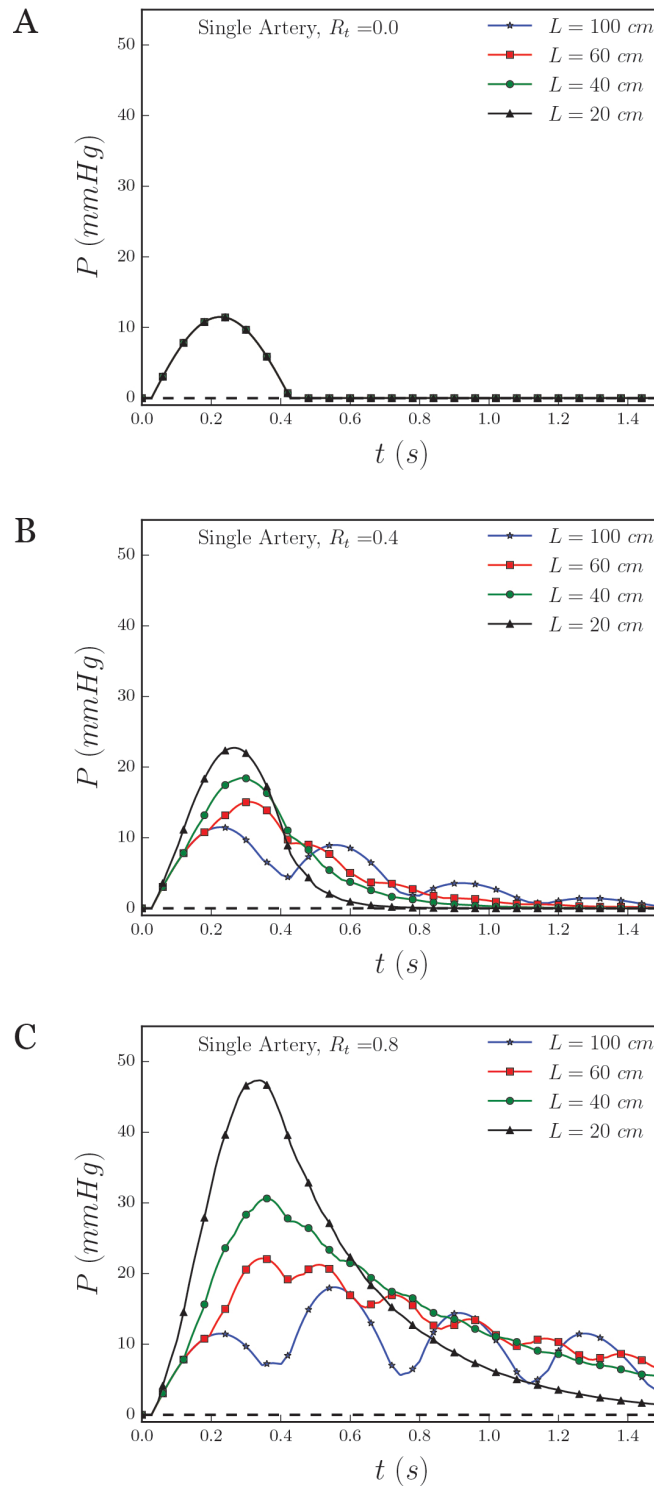


Figure 7.5 – Pressure–time curve of a single beat impulse in a one-artery model without bifurcations measured at 15 cm from the beginning of the artery, in arteries of different lengths. These simulations considered a pulse period of 0.8 s and only pure wave propagation.

- A At an $R_t = 0$, once again our simulation shows a single original pressure wave that is similar regardless of the vessel length, and no reflected waves at all.
- B At an $R_t = 0.4$ and a longer pulse period than in Figure 7.4, our simulation shows two reflected waves that merge with the original pressure wave even in vessels with long lengths (e.g., in the 60 cm vessel they are almost completely merged together).
- C At an $R_t = 0.8$, by increasing the reflection coefficient, the amplitudes of the waves change. With a longer pulse period, the individual elements of these pressure waves are harder to point out.

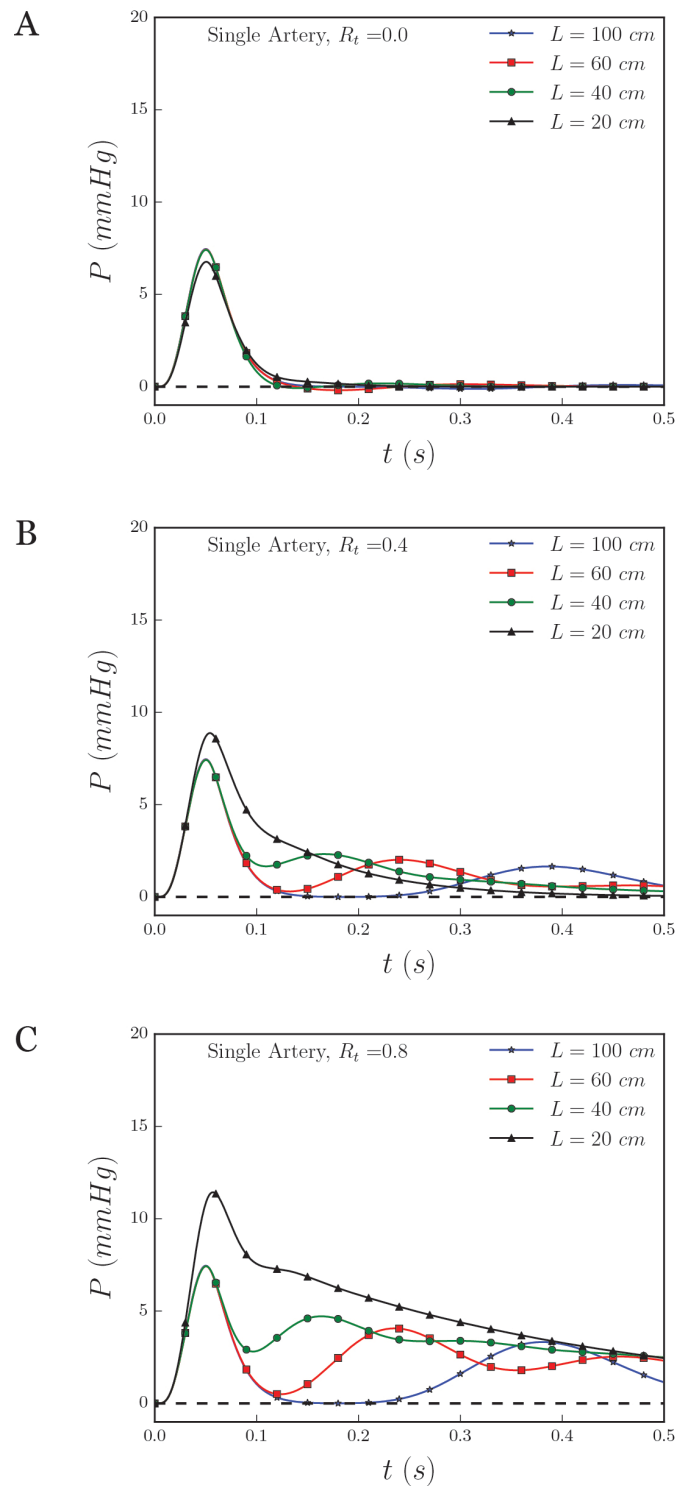


Figure 7.6 – Pressure–time curve of a single beat impulse in a one-artery model without bifurcations measured at 15 cm from the beginning of the artery, in arteries of different lengths. These simulations considered a pulse period of 0.1 s and the influence of viscous and viscoelastic effects on wave propagation.

A At an $R_t = 0$ our simulation shows a single original pressure wave that is similar regardless of the vessel length, and no reflected waves.

B At an $R_t = 0.4$, in comparison to pure wave propagation, reflected waves merge with the original pressure wave at longer lengths (e.g., in the 40 cm vessel).

C . At an $R_t = 0.8$ the compliant effect of viscoelasticity “smoothens the curves out”, resulting in the overlap of waves that previously were identified as individual elements when considering only pure wave propagation.

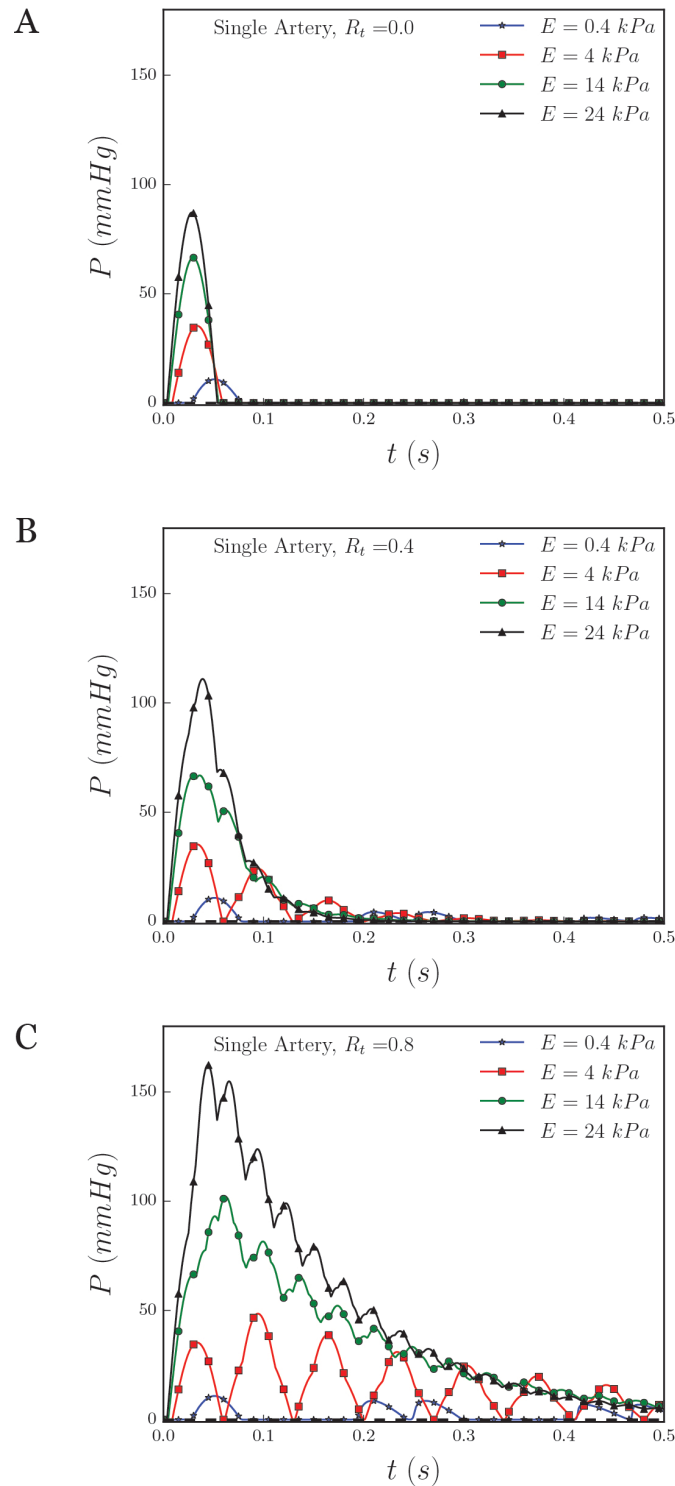


Figure 7.7 – Pressure (p) time curves of a single beat impulse in a one-artery model without bifurcations measured at 15 cm from the beginning of an artery with a length of 60 cm. These simulations considered a pulse period of 0.1 s and only pure wave propagation.

- A Considering a reflection coefficient (R_t) of 0 – therefore, in the absence of reflection waves – increases in vessel elasticity (E) raised the propagation speed but did not create a dicrotic notch.
- B Considering a reflection coefficient (R_t) of 0.4, reflection waves appear. An increase in the vessel's elasticity (E) increased the amplitude and the propagation speed of both the original pressure wave and the reflected wave, which therefore appear earlier.
- C Considering a reflection coefficient (R_t) of 0.8, reflection waves increased their amplitude and reduced their timing.

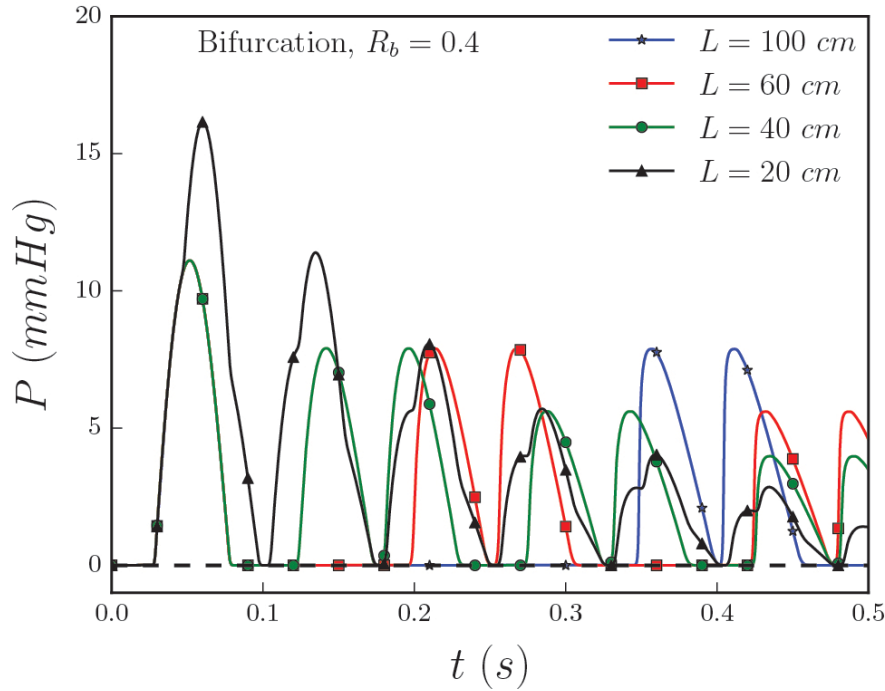


Figure 7.8 – Pressure–time curve of a single beat impulse in an artery model with bifurcations, measured at 15 cm from the beginning of the parent artery, in arteries of different lengths. These simulations considered a pulse period of 0.1 s, a bifurcation reflection coefficient (R_b) of 0.4 and only pure wave propagation. Our simulation is identical to that obtained for the single-artery model without bifurcations (Figure 7.4 B) and demonstrates that internal reflection can also play an important role and influence the shape of the dirotic notch.

shape of the signal remains the same and does not form a dirotic notch. Figure 7.7 B and C consider a reflection coefficient (R_t) of 0.4 and 0.8, respectively; thus reflected waves now appear and modify the shape of the signal, creating a dirotic notch. In both these figures, vessels with a higher elasticity have higher and earlier reflected waves.

These results suggest that an increase in the vessel elasticity could change the overall morphology of the wave by increasing the propagation speed and therefore changing the timing of interaction between the incoming and the reflected waves. However, this depends on the creation of reflected waves, which are caused by terminal reflections – and not changes in elasticity.

Single segment model with a bifurcation

As we mentioned previously, reflection can also occur at vessel bifurcations. We considered only one parent artery that divides into two daughter arteries. We studied the pressure–time curve of a single-beat impulse in parent arteries of different lengths (100 cm, 60 cm, 40 cm and 20 cm), keeping the geometrical and mechanical properties of the two daughter arteries constant. Furthermore, we set the reflection coefficients at the end of the daughter arteries to zero ($R_t = 0$), ensuring that if a reflection occurred, it could only come from the bifurcation. The value of the reflection coefficient produced by the bifurcation depends on the geometrical and mechanical properties of the parent and the two daughter arteries, and in the configuration we consider its value is $R_b = 0.4$. Regardless of the overall length of the artery, the signal was always measured in the same location (i.e., at 15 cm from the beginning of the parent artery) and a pulse period of 0.1 s (i.e., ejection time = 0.05 s) was used. As for the single-artery model without bifurcations, we considered only pure wave propagation (Figure 7.8). The results presented in Figure 7.8 are identical to those obtained for the single-artery model without bifurcations with a non-zero reflection coefficient (Figure 7.4

B). Hence we demonstrated that internal reflection could also play an important role in the reflective behavior of the network and influence the shape of the dicrotic notch.

7.1.4 Discussion

Although the dicrotic notch withholds valuable information on cardiovascular hemodynamics, medical textbooks and literature explain its origin in very different ways, often leading to divergent interpretations among medical professionals.

We have shown through both numerical simulations and experimental data from adult patients that reflected waves may have a role in the origin of the dicrotic notch. Our results also suggest that increases in peripheral resistance increase the amplitude but not the propagation speed. A commonly considered etiology of the dicrotic notch is that it is a manifestation of aortic valve closure [Boulpaep et al. 2009; Guyton and Hall 2006; Mann et al. 2014; Pinsky et al. 2006]. However, this explanation could be incomplete. While the closure of the aortic valve generates a transient reversal of blood flow in the aorta which can contribute slightly to the shape of the notch (Figure 7.3), the only reasonable explanation for the aortic valve to close at all is the presence of a pressure gradient in that direction. This pressure gradient may be caused by the declining ventricular pressure during diastole and by the transient increase in aortic pressure caused by reflection waves, commonly referred to as the dicrotic notch. We therefore believe that even though the appearance of the dicrotic notch is simultaneous to the aortic valve closure, this explanation on its own may not be enough, and could be a lost chance for reinforcing important hemodynamic concepts.

Other authors do recognize the role of reflected waves in the origin of the dicrotic notch, but consider that a rise in the value of the reflection coefficient increases not only the amplitude of the reflection waves but also the speed at which they travel Zundel et al. [2015]. Our experiments in patients undergoing vascular surgery show that after an IV bolus of phenylephrine the dicrotic notch either appeared if it was previously absent or it increased its amplitude if it was previously present (Figure 7.2). Nevertheless, in our experiments the relative time-position of the reflection wave in the overall pressure wave cycle remained unchanged. Although our experimental data have some limitations, since continuous pressure was not recorded using a high-fidelity transducer (only a fluid-filled system) and did not assess other variables in the cardiovascular system (such as cardiac output, pulse wave velocity or vasoactive responses), these findings are in accordance with our numerical simulations and with the concept that the speed at which pressure waves travel in a vascular network depends only on the structural characteristics of the network. For example, in elderly patients with vascular stiffening, reflected waves may move faster and reach the original arterial pressure waveform before it has time to decrease, which causes an amplification of the systolic pressure and, as a consequence, isolated systolic hypertension. This clinical condition illustrates clearly how changes in vascular elasticity can have an influence on the time-position and the amplitude of the dicrotic notch. Indeed, several studies have used the dicrotic notch as a time-reference point to measure pulse wave velocity and as an indicator of arterial stiffness [Hermeling et al. 2009, 2010]. However, our results suggest that this effect would be greatly influenced by modifications in reflected waves, as shown in Figure 7.7, where, in the absence of reflected waves, changes in elasticity do not generate a dicrotic notch.

This problem was approached using a 1D model, which has been previously used to study the effects of reflected waves on vascular networks both numerically [Alastruey et al. 2009; Segers et al. 1997] and experimentally [Khir and Parker 2002; Borlotti et al. 2014; Matthys et al. 2007; Murgo et al. 1980]. Alastruey et al. used this method to conclude that the dicrotic notch is a combination of several mechanisms –mainly left ventricle outflow, arterial junction reflections and aortic valve closure. However these results were obtained through a

linear model that did not include viscoelasticity, complementary experimental data, or a systematical study of the dicrotic notch [Alastruey et al. 2009]. Mynard et al. also studied arterial wave reflections using a 1D model, this time introducing a heart model [Mynard and Nithiarasu 2008]. However these authors did not systematically study the dicrotic notch either. These previous studies support the accuracy of this modeling approach for wave reflection analysis. The main contribution of our research is the systematical study of the role of reflected waves in the origin of the dicrotic notch, starting from experimental data from adult patients, and then complementing our analysis with data from a 1D numerical model – first with a 55 artery model and then with a single artery, progressively making the system simpler.

There are some limitations in the 1D numerical model. First, it does not include a heart model, so it does not take into account any feedback between the heart and the vascular network. A possible solution for this problem could be the heart model proposed by Mynard et al. [Mynard and Nithiarasu 2008]. Second, the arterioles, capillaries and veins are all simulated by the terminal reflection coefficient (R_t). A more accurate alternative would be to use a Windkessel model to estimate systemic resistance and characteristic impedance, with the additional costs in complexity.

Both our experimental and numerical data show that increased vasoconstriction is related to a higher dicrotic notch. This study is proof of concept that the dicrotic notch is mainly determined by the reflection waves and their characteristics.

We propose these experimental and numerical examples as a conceptual and educational tool to illustrate how changes in reflection waves can produce modifications in the morphology of the dicrotic notch.

7.2 A one-dimensional arterial network model for bypass graft assessment

7.2.1 Introduction

Arterial diseases such as stenoses are frequent clinical pathologies, and their prevalence is evaluated from 3% to 10% in the global population with a significant growth from 15% to 20% in persons over 70 years old [Norgren et al. 2007]. Stenoses correspond to the partial or total obstruction of an artery and can cause symptoms going from intermittent claudication to severe ischemia. These symptoms result from a decrease in blood supply as the diseased vessel providing vascularization is narrowed or occluded. When untreated, stenoses can have severe consequences and can lead to the amputation of the stenosed member, especially when they occur in the arteries of the lower members, such as in the Iliac arteries.

When the symptoms are too severe or when medical treatment fails, surgery is necessary to restore blood flow downstream of the stenosed member. This can be done by angioplasty stenting, where the obstructed segment is replaced by a prosthesis (stent) during an endovascular substitution surgery. An alternative solution consists in inserting a bypass graft to redirect the flow of blood from a healthy artery to bypass the obstructed vessel and restore blood flow downstream of the stenosis. In both cases, the mechanical role of these grafts or conduits is to replace or bypass vessels that have become occluded or severely obstructed by a disease process [Abbott et al. 1993].

Numerical studies of local endovascular graft replacements have been reported previously (e.g., [Marchandise et al. 2009; Willemet et al. 2013]). We propose to study instead extracorporeal bypass graft procedures. To do so, we consider a detailed model of the systemic network which presents a stenosis of the Right Iliac artery. In this pathological case, the most common bypass graft configurations are: Aorto-Femoral, Axillo-Femoral and cross-over Femoral, defined by the combination of the name of the healthy or donor artery (Aorto for Aorta, Axillo for Axillary and cross-over for the opposite artery, the Left Femoral Artery) and the name of the receptor artery, in our case the Right Femoral artery which follows distally the narrowed site.

The aim of this section is to use the 1D model (3.23) to compute blood flow in each segment of the considered model network before and after extracorporeal bypass graft surgery. To help clinicians optimize surgical repair, we evaluate the viability of each bypass graft by computing the flow rate and pressure downstream of the stenosed member, which is an a posteriori evaluation of the quality of the surgery. Clinicians often prefer the Aorto-Femoral bypass graft. However, for weak patients who can not tolerate the aortic clamping required to insert the Aorto-Femoral bypass graft, the preferred solution is an extra-anatomic Axillo-Femoral bypass graft [Appleton et al. 2010]. Furthermore, it has the shortest graft survival time among the three previously named bypass grafts ([Greenwald and Berry 2000; Musicant et al. 2003]). We therefore study in detail the optimization of the geometrical and mechanical characteristics of the Axillo-Femoral bypass graft. We hope that this numerical approach will be used in the future to define the optimal parameters of new prosthesis and help clinicians plan surgeries.

In the following, we present the numerical model and the model arterial network, as applied to the study of flow through three different arterial bypass graft configurations, along with the results of a parametric study of the Axillo-Femoral bypass graft. We propose only hemodynamic predictions based on fluid mechanics equations, regardless of biological phenomena and their consequences. Nevertheless, we are aware that short term graft failures can be caused by infections or hemorrhages, while long-term failures are the result of intimal

hyperplasia of the graft site, with a proliferation and a migration of vascular smooth muscle cells near the arterial wall [Greenwald and Berry 2000].

7.2.2 Numerical model

To compute the hemodynamics in an artery, we use the one-dimensional (1D) viscoelastic blood flow equations (3.23). The network used in the numerical simulations is constructed by connecting different arterial segments together using the point junction model described in Subsection 6.2.1. To drive the flow through the network, we prescribe inlet and outlet boundary conditions. These boundary conditions are:

1. an imposed physiological flow rate at the inlet of the ascending aorta;
2. reflection coefficients imposed at the outlet of each terminal segment and characterizing the resistance of the vascular bed that is not taken into account in our model. These values are given in the last column of the table presented in [Ghigo et al. 2017a].

The input flow rate signal we use in the numerical simulations is:

$$Q = \begin{cases} Q_{max} \sin\left(\frac{2\pi}{T}t\right) & \text{if } t \leq \frac{T}{2} \\ 0 & \text{else,} \end{cases} \quad (7.1)$$

where T is the period of the heart cycle. To define the maximum flow rate Q_{max} , we introduce the ejection fraction EF , defined as:

$$EF = \frac{EDV - ESV}{EDV} \times 100, \quad (7.2)$$

where EDV is the End Diastolic Volume and ESV is the End Systolic Volume. Healthy patients typically have an EF between 50% and 65%. On the contrary, people with heart muscles damages (principally on the myocardium) have a low EF . The ejected volume $V_e = EDV - ESV$ during one period is computed by integrating $Q(t)$ over one period, which gives here:

$$V_e = Q_{max} \frac{T}{\pi}. \quad (7.3)$$

Finally we have:

$$Q_{max} = EF \pi \frac{EDV}{T}, \quad (7.4)$$

and we can now define Q_{max} , for a given period T and a given EDV as a function of EF . With this approach we propose a simple heart model that allows us to define a pathological heart by reducing EF . This behavior is physiologically meaningful if in the case of a pathological heart, the system reacts by either increasing EDV by expanding the muscle fibers or by reducing the period T by increasing the cardiac rhythm.

7.2.3 Numerical methods and results

In this section we present the numerical protocol and detail the numerical results obtained with the healthy network, the pathological network presenting an obstruction of the Right Iliac artery and the pathological network treated with three different bypass grafts (Axillo-Femoral, Femoral-Femoral and cross-over Femoral bypass grafts). The numerical protocol is the following:

1. we first simulate blood flow in a healthy network (Figure 7.9 (a)). We use the computed numerical data as the target blood flow we compare the other numerical results to;
2. we then build the pathological network by narrowing the cross-sectional area of the Right Iliac artery (Figure 7.9 (b)). As we record all hemodynamic variables everywhere in the

network for different degrees of obstruction of the stenosis, we are able to observe the global changes depending on the degree of obstruction;

3. we finally build three repaired networks by introducing in the pathological network the Axillo-Femoral, Femoral-Femoral and cross-over Femoral bypass grafts using elastic tubes inserted between the donor and the receptor arteries of each bypass graft (Figure 7.9 (c) for the Axillo-Femoral, the other two are presented in Figure 7.11). We then compare the numerical results obtained with the three repaired networks to those obtained with pathological and healthy networks.

The key points of clinical repair are:

1. first the ability of the bypass graft to restore blood flow in the previously non-perfused region (here the network downstream of Right Femoral artery, number 52 in Figure 7.9);
2. second, ensuring that the repair does not ill-balance the rest of the hemodynamic circulation.

In the following, both key points are systematically tested for each repaired network.

Healthy case

The healthy network we consider represents the principal arteries of the great circulation (55 segments). It is used in the literature as the basic model of the systemic network. Its topology is presented in Figure 7.9 (a), where every artery is given a number (ID) useful to understand the numerical results. Each artery of the healthy network is described by geometrical and mechanical parameters adapted from [Sherwin et al. 2003a] and presented in the table in [Ghigo et al. 2017a]. Compared to [Sherwin et al. 2003a], we have added a viscoelastic term to the wall model. This viscoelastic term exists in physiological conditions and is very important from the hemodynamic point of view [Alastruey et al. 2011; Wang et al. 2016b]. Without it, high frequency components would be present in the pulse wave signal [Wang et al. 2016b]. In the literature on 1D network models, this viscoelastic term is usually not included as its coefficients are hard to evaluate experimentally. Here, we use the work of [Armentano et al. 1995], where the viscosity of the aortic walls of dogs was modeled by a Kelvin-Voigt model and where the values of ϕ range between $3.8 \pm 1.3 \times 10^3 \text{ Pa} \cdot \text{s}$ and $7.8 \pm 1.1 \times 10^3 \text{ Pa} \cdot \text{s}$. Hence, in all numerical simulations we assume $\phi = 5 \times 10^3 \text{ Pa} \cdot \text{s}$ to calculate the coefficient C_v .

The flow in each arterial segment is computed using the 1D numerical model presented in Chapter 4. The simulations are performed over 10 heart periods T . Any data we present is taken from the final period to ensure that a permanent state is reached, where each heart period is identical to the next. The recorded data for the healthy network contains the values of the blood flow rate $Q_{healthy}$, the cross-sectional area $A_{healthy}$ and the blood pressure $P_{healthy}$ in every artery and at every recorded time of the final period. These numerical results are the target values we use from now on to evaluate the severity of the pathological situation with respect to the healthy reference case and to assess the curative properties of each bypass graft.

Pathological case

Numerical protocol We model the stenosis by narrowing the cross-sectional area of a portion of the Right Iliac artery (number 50 in Figure 7.9 (b)). The length of the occlusion is 5 cm and the degree of obstruction is directly related to the ratio of the cross-sectional area of the stenosed artery $A_{\%}$ over the cross-sectional area of the healthy artery $A_{healthy}$. We define this ratio as:

$$I_s = \frac{A_{healthy} - A_{\%}}{A_{healthy}} \times 100. \quad (7.5)$$

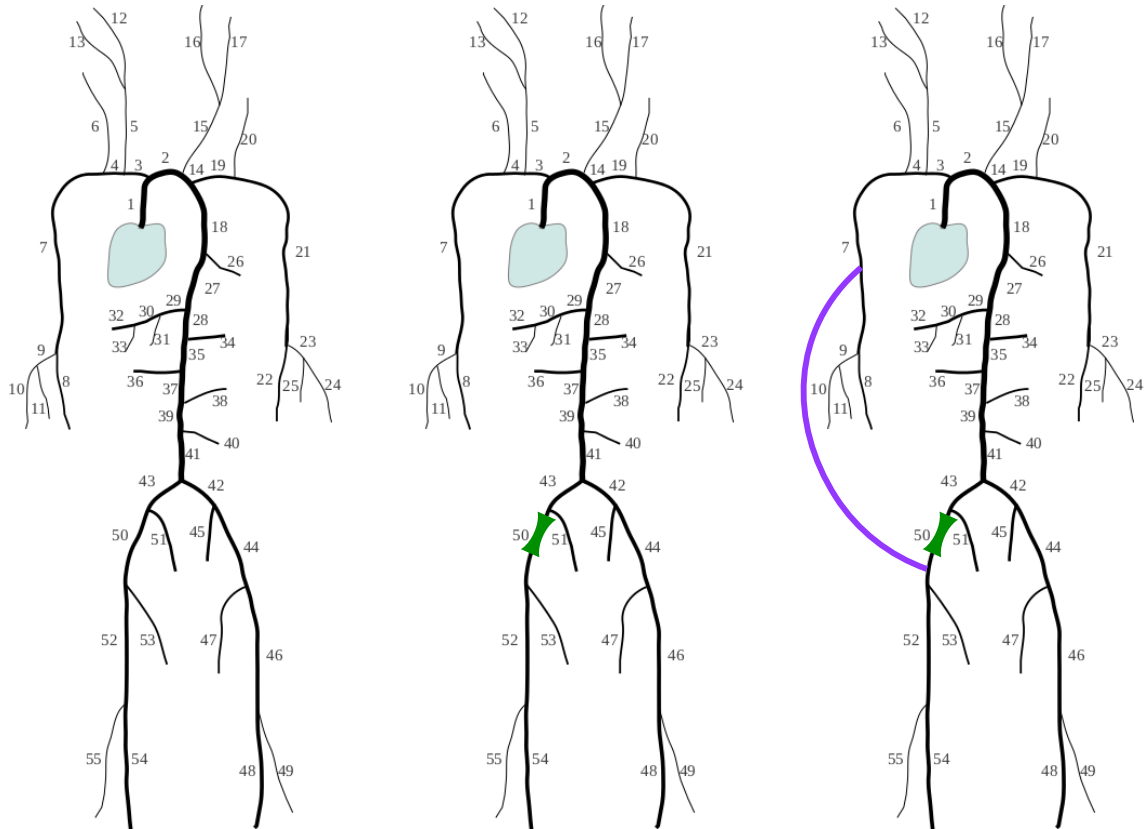


Figure 7.9 – Arterial tree. (a) "Healthy" network. (b) Pathological network. (c) "Repaired" network. The pathological network (b) is modeled by narrowing the cross-sectional area of the Right Iliac artery (number 50, green) and the extracorporeal bypass graft by an elastic tube (purple). In each segment, a 1D model of fluid flow with viscoelastic wall is solved numerically. The flow is imposed by given heart pulses, with a realistic reflection coefficient at the end of each terminal arteries. The geometrical and mechanical data used in numerical computations are presented in the table in [Ghigo et al. 2017a].

The data presented here were obtained before the development of the well-balanced methods presented in Chapter 5. The stenosis is therefore not treated with a well-balanced method. It is created by dividing the artery into three parts (2 healthy, 1 stenosis) connected with the point junction model.

Four control sites are chosen to evaluate the hemodynamical influence of the stenosis on the flow rate and pressure waveforms. Two are located in the lower legs, in the Right Femoral artery (number 52) and in Left Femoral artery (number 46). The other two are located in the arms, in the Right Subclavian artery (number 7) and in the Left Subclavian artery (number 21). The Right Femoral artery (number 52) is the principal assessment point of our numerical study as the flow rate passing through it characterizes the leg's perfusion and therefore the degree of ischemia. The other control sites (Left Femoral, Left and Right Subclavian) are used in clinical routines to evaluate if a bypass graft surgery is successful.

Results Figure 7.10 (a) shows the variation with the degree of obstruction I_s of the blood flow rate Q averaged over the final period at the four previously defined control sites. The first observation is that under 60% to 70% of obstruction there is no significant variation of flow rate with respect to the healthy state ($I_s = 0\%$). This behavior is well known in the medical community (i.e. renal arteries in pigs and human carotid arteries [Lanzino et al.

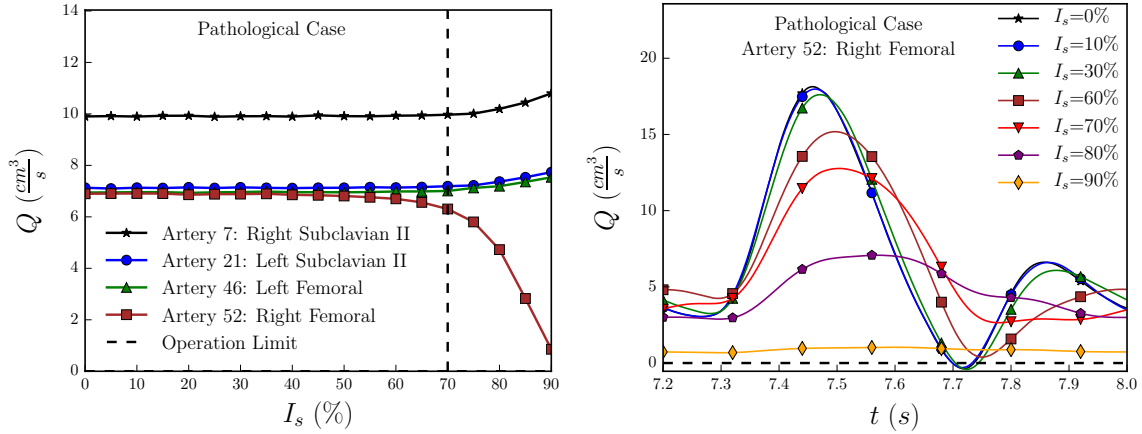


Figure 7.10 – (a) Flow rate averaged over a cycle as function of the obstruction degree I_s for the following arteries: Right Femoral, (number 52), Left Femoral, (number 46), Right Subclavian (number 7) and Left Subclavian, (number 21). As the ratio I_s increases, the flow rate drops in the Right Femoral artery, distal to the stenosis, whereas the flow rate increases in all other segments to compensate this drop. (b) Instantaneous flow rate as function of time over a cycle in the Right Femoral artery (number 52) for different degree of obstruction. As the ratio I_s increases, the waveform loses its pulsatility and flattens and the average flow rate drops.

2009; Rognant et al. 2010]). Above 70% of obstruction, the flow rate drastically decreases in the Right Femoral artery (number 52) due to the obstruction of its proximal artery, the Right Iliac artery (number 50). We note that for an occlusion of 90% there is almost no blood flow in the Right Femoral artery (number 52). Conversely, the flow rate moderately increases in the other control sites to compensate for the reduction of flow rate in the network distal to the stenosis. This as a clear example of how we can monitor global variations in the network caused by a local perturbation.

Figure 7.10 (b) presents the time evolution of the blood flow rate Q over the final period in the Right Femoral artery (artery 52). These results are correlated to those of Figure 7.10 (a) but provide additional information: first, as expected, the flow rate decreases in average as the ratio I_s increases; second the positions of the maximum and minimum peaks are shifted, due to a time shift in the traveling waves; third the maximum amplitude decreases significantly as the ration I_s increases and we observe that for $I_s = 70\%$ the amplitude drops by 30% and for $I_s = 80\%$ it drops by 60%. For $I_s = 90\%$, the amount of blood perfusion in the leg is minimal and the waveform is a flat line. This last point indicates that as the degree of obstruction I_s increases, the signal loses its pulsatility and flattens.

Bypass grafts

Numerical protocol We study here the three most commonly used bypass grafts to treat a stenosis of the Right Iliac arteries: the Axilo-Femoral (AxF) where the donor artery is the Axillary artery (artery 7), the cross-over Femoral (FF) where the donor artery is the opposite Common Femoral artery (artery 44) and the Aorto-Femoral (ArF) where the donor artery is the Abdominal Aorta (artery 39). Each bypass graft is connected to the pathological network using two connection points: the proximal anastomosis, connecting the bypass graft to the donor artery, and the distal anastomosis, linking the bypass graft to the receptor artery. For each of these three bypass grafts, the distal anastomosis is located downstream of the stenosis, in the distal part of the Right Iliac artery (artery 50). In Figure 7.11 we represent the topology of the three different pathological network treated with a bypass graft.

Each bypass graft we study is made of the same composite material which is constituted

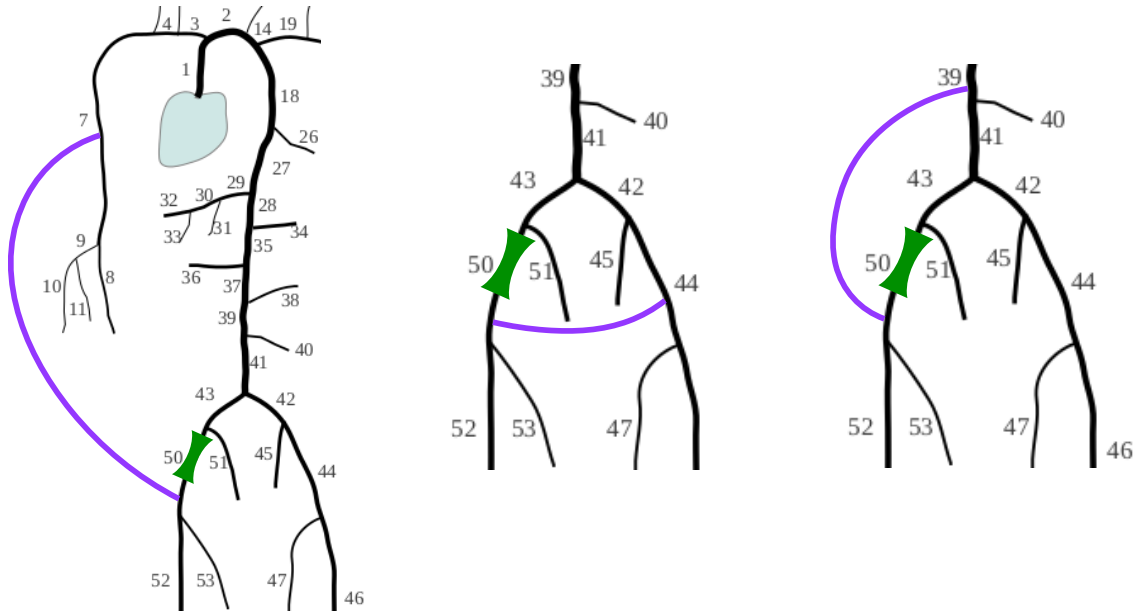


Figure 7.11 – Sketch of three bypasses with the donor artery : (left) Axillo-Femoral (AxF) and donor artery, Right Axillary artery (number 7), (center) cross-over-Femoral (FF) and donor artery, Left Femoral artery (number 44) and (right) Aorto-Femoral (ArF) and donor artery, Abdominal Aorta (number 39).

principally of polyethylene terephthalate (Dacron). From the literature [Sarkar et al. 2006], we obtain their mechanical and geometrical characteristics, that is a Young's modulus equal to $9 \times 10^6 Pa$, an internal diameter of $0.8 cm$ and a thickness of $0.05 cm$. The length L of each bypass graft depends on the geometric distance between the proximal and distal anastomoses: Axillo-Femoral, $40 cm$, cross-over-Femoral, $20 cm$ and Aorto-Femoral, $20 cm$.

To assess the performances of each bypass graft, we define three control sites where we compare the healthy, pathological and repaired data. The first is located in the Right Femoral artery (number 52), downstream of the stenosis and the distal anastomosis, and is identical to the control site used previously to analyze the pathological network. The second and third control sites are respectively situated in the upstream and downstream segments of the proximal anastomosis.

Results For each bypass graft we first study the predicted perfusion hemodynamics in the first control site located downstream of the stenosis, in the Right Femoral artery (number 52). Figure 7.12 (a) presents the evolution with the degree of obstruction I_s of the time-averaged blood flow rate in the pathological network (same as Figure 7.10 (a) for the artery 52) and in the three repaired networks obtained using the AxF, ArF and FF bypass grafts. Figure 7.12 (b) shows the temporal evolution of the blood flow rate over the final heart cycle for $I_s = 90 \%$. These figures should be compared to Figure 7.10 (a) and Figure 7.10 (b). We observe in Figure 7.12 (a) that for all three bypass grafts configurations, we retrieve in average the blood flow rate of the healthy case for every value of I_s considered. Figure 7.12 (b) indicates that the repaired waveforms are similar to the target healthy ones, although the amplitudes of the peaks are slightly underestimated. The delay in the position of the maximum and minimum flow rate peaks is caused by a change in the length of vessel traveled by the wave starting from the heart. Overall we retrieve for all three bypass graft configurations the target average blood flow rate as well as the approximate shape of the waveform. From the analysis of Figure 7.12 we conclude that all three bypass graft are successful in retrieving the healthy flow rate in the first control site distal to the obstructed segment (Right Femoral

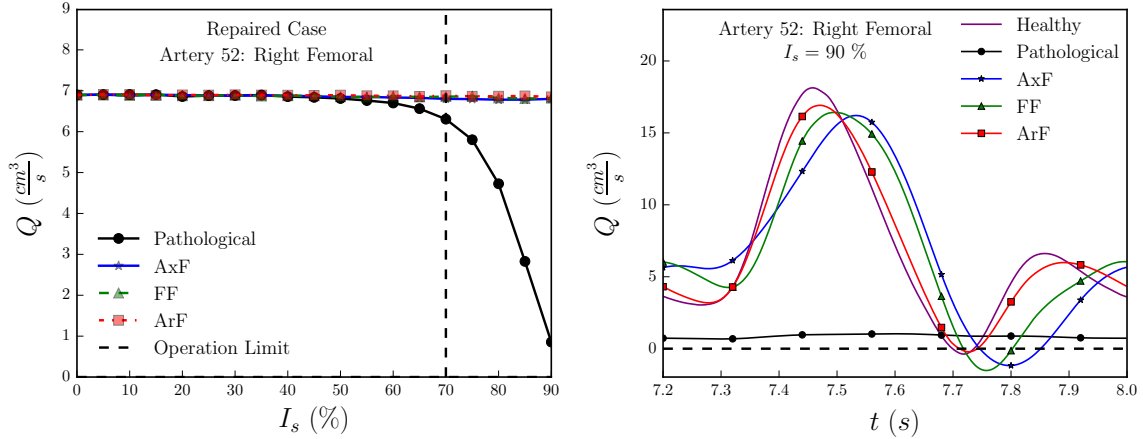


Figure 7.12 – (a) Averaged flow rate over a cycle as function of the degree of obstruction I_s (Artery 52 : Right Femoral) (b) Instantaneous flow rate as function of time over a cycle (Artery 52 : Right Femoral) for healthy, pathological with $I_s = 90\%$ and for the three bypasses. We observe that for all three bypass graft configurations, we are able to recover the target healthy flow rate (average values and waveform) distal to the stenosis.

artery 52).

We complete our study by analyzing the time-averaged blood flow rate in each donor artery. In the subsequent numerical results we focus on the remaining two control sites: the upstream and downstream segments of the proximal anastomosis, which differ from one bypass graft configuration to the next. We expect that each bypass graft will supply the missing blood flow rate to the diseased lower leg (Right Femoral artery 52) whilst maintaining a healthy perfusion in the donor site (downstream segments of the proximal anastomosis).

For the FF bypass graft the donor artery is the opposite Femoral artery (Left Femoral artery, number 44 in Figure 7.9). Figure 7.13 presents the evolution of the time-averaged blood flow rate with the degree of obstruction I_s in the two control sites, upstream and downstream of the proximal anastomosis. We observe that upstream of the donor site the flow rate increases proportionally to the degree of obstruction. Indeed the donor artery must now supply blood to both its downstream segment and the stenosed member and therefore increases its flow rate, in comparison with the healthy case ($I_s = 0\%$). The downstream blood flow rate does not change compared to the healthy case ($I_s = 0\%$) indicating that the opposite lower leg, downstream of the proximal anastomosis, is correctly supplied. We note that for a severe stenosis (obstruction of 90 %) the upstream blood flow rate is twice the basal one.

For the ArF bypass graft the donor artery is the Abdominal Aorta (artery 39), the principal path carrying blood to both lower legs. Figure 7.14 presents the evolution of the time-averaged blood flow rate with the degree of obstruction I_s in the two control sites, upstream and downstream of the proximal anastomosis. We observe that upstream of the proximal anastomosis, the blood flow rate does not change with the degree of obstruction I_s , contrary to the FF bypass graft configuration. Indeed, in the healthy configuration the Abdominal Aorta already carries blood to the Right Femoral artery, therefore no compensation mechanism is required upstream of the donor site. Conversely we observe that the downstream of the proximal anastomosis, the blood flow rate decreases as the degree of obstruction increases, in comparison to the healthy configuration ($I_s = 0\%$). Indeed, since the blood that supplies the stenosed member (Right Femoral artery 52) now flows through the bypass graft, only the blood supply for the left leg remains downstream of the donor site. This behavior shows that the bypass graft is indeed carrying blood to the stenosed member. Finally, we note that in absence of stenosis ($I_s = 0\%$) the downstream blood flow is symmetrically shared between

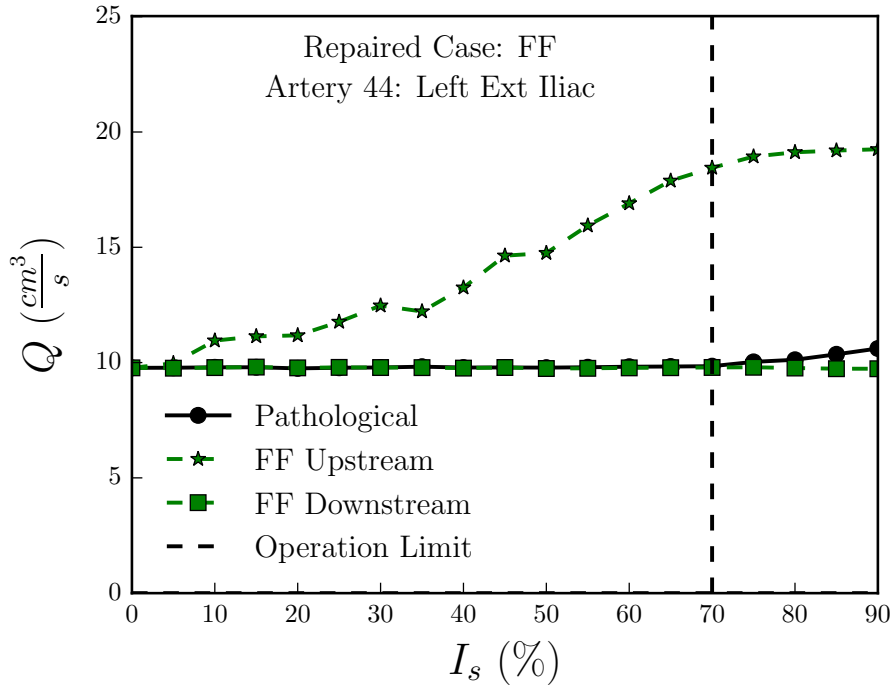


Figure 7.13 – *Cross-over Femoral bypass graft: average flow rate over a cycle in the opposite Femoral artery (Artery 44). Upstream of the proximal anastomosis, the flow rate increases to properly vascularize the bypass graft, depending on the degree of obstruction I_s . Downstream of the proximal anastomosis, we recover the healthy ($I_s = 0\%$) flow rate.*

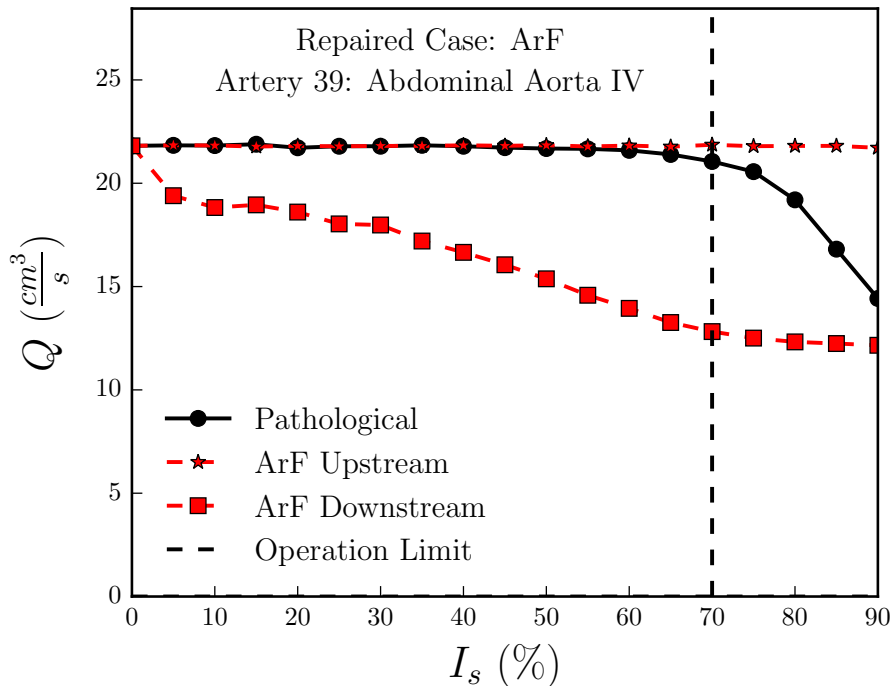


Figure 7.14 – *Aorto-Femoral bypass graft: average flow rate over a cycle at the donor artery (Artery 39). Upstream of the proximal anastomosis, the flow rate remains unchanged since blood flow passing through the bypass graft to vascularize the right leg was already supplied by the Aorta in the healthy case. Downstream of the proximal anastomosis, the flow rate decreases with the degree of obstruction I_s since now only the blood supplying the left leg is passing downstream of the proximal anastomosis.*

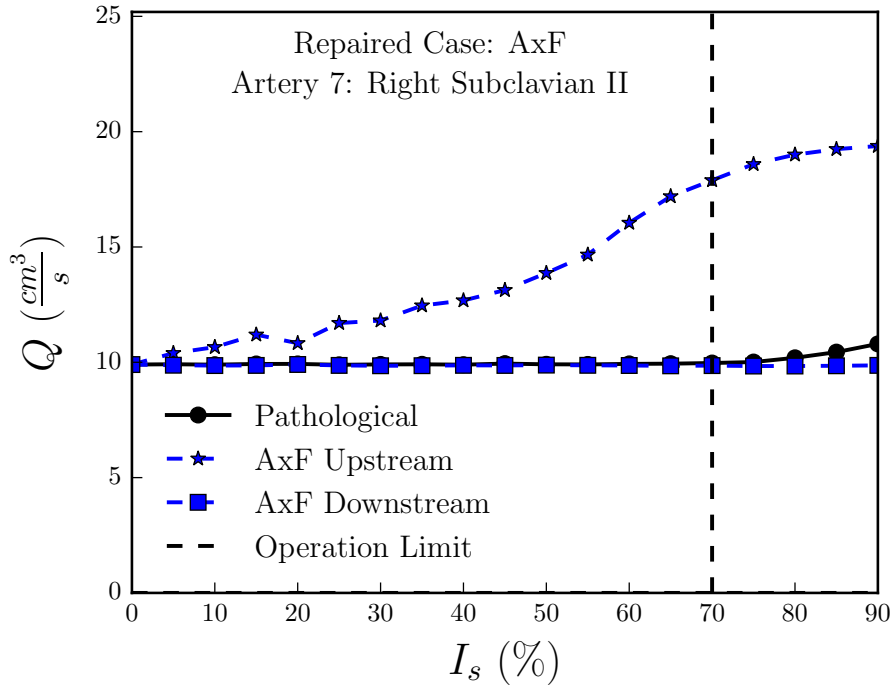


Figure 7.15 – Axillo-Femoral bypass graft: averaged flow rate over a cycle at the donor artery (number 7). Upstream of the proximal anastomosis, the flow rate increases to properly vascularize the bypass graft, depending on the degree of obstruction I_s . Downstream of the proximal anastomosis, we recover the healthy ($I_s = 0\%$) flow rate.

the two legs and that for a severe stenosis ($I_s = 90\%$) the downstream blood flow rate is half the basal one.

Figure 7.15 presents the evolution for the AxF bypass graft of the time-averaged blood flow rate with the degree of obstruction I_s in the two control sites, upstream and downstream of the proximal anastomosis. The results are identical to those obtained with the FF bypass graft (Figure 7.13). The same analysis can be performed and we conclude that this bypass graft configuration correctly supplies the stenosed member while maintaining the healthy flow rate downstream of the donor site. We also note that for an obstruction of 90% the upstream blood flow rate is twice the basal one.

These results show that for all three bypass graft configurations, the target behaviors are obtained and the bypass graft surgery is successful.

Optimization

Of the three bypass grafts considered here, the AxF has the highest chance of graft failure. Indeed, the AxF is the longest bypass graft. Moreover, the AxF bypass graft surgery is performed on patients who are not healthy enough to survive the more invasive surgical procedures required to implement the FF or ArF bypass grafts.

For these reasons we choose to perform a detailed analysis to determine the optimal mechanical (the Young modulus E) and geometrical (the radius R) parameters of the AxF bypass graft. In order to give arguments for discussion we perform hundreds of simulations where we vary the values of the Young modulus [0.1 – 50 MPa] and radius R [0.01 – 5 cm] of the AxF bypass graft. As before, we use as a target the healthy data in the Right Femoral artery (number 52 in Figure 7.9).

Figure 7.16 presents a log-log scale contour plot of the normalized flow rate $Q/Q_{healthy}$ in

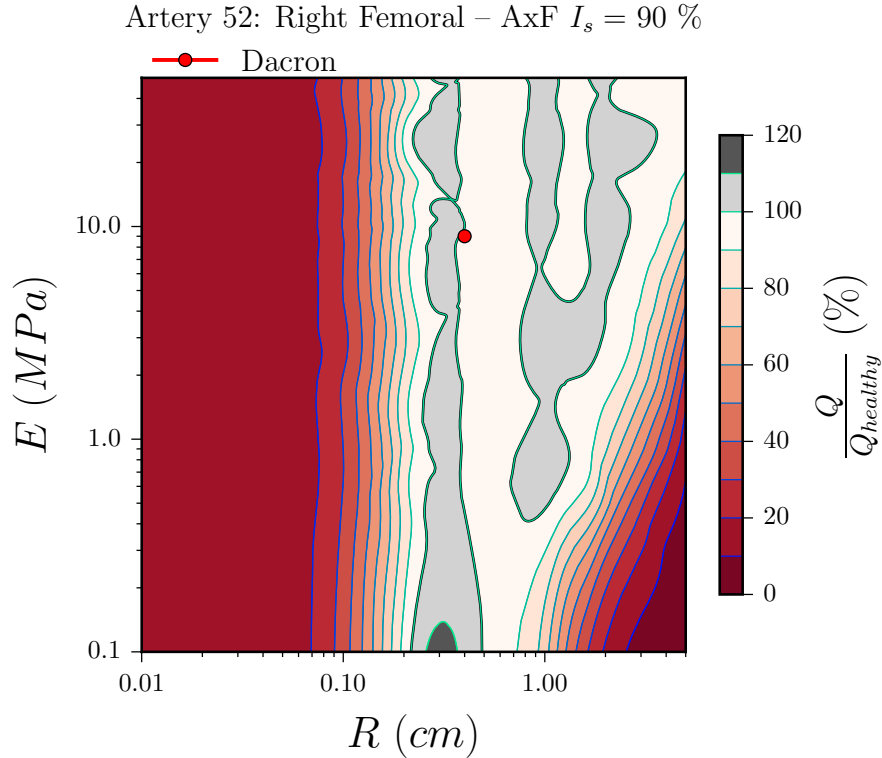


Figure 7.16 – Contour plot for the normalized time-averaged flow rate $Q/Q_{healthy}$ as a function of the Young modulus E and the radius R for a stenosis of $I_s = 90\%$. The red circle corresponds to the actual values of the Young modulus E and the radius R used in numerical simulations, which are situated in an optimal zone (100%). When the radius decreases, the resistance of the tube increases and therefore less flow is bypassing through the bypass graft. When the Young's modulus decreases, the tube becomes more compliant and stores more flow. Both behaviors reduce the quality of the bypass graft.

the AxF bypass graft obtained for different values of the Young modulus E and the radius R in a pathological network with $I_s = 90\%$. The red circle in the middle of the Figure 7.16 indicates the actual values of the bypass graft's Young's modulus E and radius R . For these values the normalized flow rate $Q/Q_{healthy} \approx 100\%$ indicating that the healthy flow rate is restored in average downstream of the stenosis. Starting from this point we analyze the results by moving along the horizontal and vertical directions, that is for E constant and varying R (horizontal) and for R constant and varying E (vertical).

For a constant Young's modulus E , we analyze the effect of changing the radius R of the bypass graft. Moving along the horizontal direction towards the left starting from the red circle, the radius R decreases. Consequently the hydraulic resistance of the bypass graft increases leading to a decrease of the the normalized flow rate $Q/Q_{healthy}$. Moving now towards the right, the radius R increases. Even though for a large range of values of the Young's modulus E the value of $Q/Q_{healthy}$ is close to 100%, it is clear that as the radius increase the blood volume inside of the bypass also increases. This results in a decrease of the flow rate distal to the proximal anastomosis and could lead to the ischemia of the right hand. Increasing the radius R also implies decreasing blood flow velocity in the bypass graft which results in a smaller shear rate along the bypass. This increases aggregation and coagulation processes which are key factors in the onset of graft failure. From a physiological and mechanical point of view for a given value of the Young's modulus E , the optimal radius R should be taken from a $Q/Q_{healthy} \approx 100\%$ region and be as small as possible to ensure an optimal distal and proximal blood perfusion.

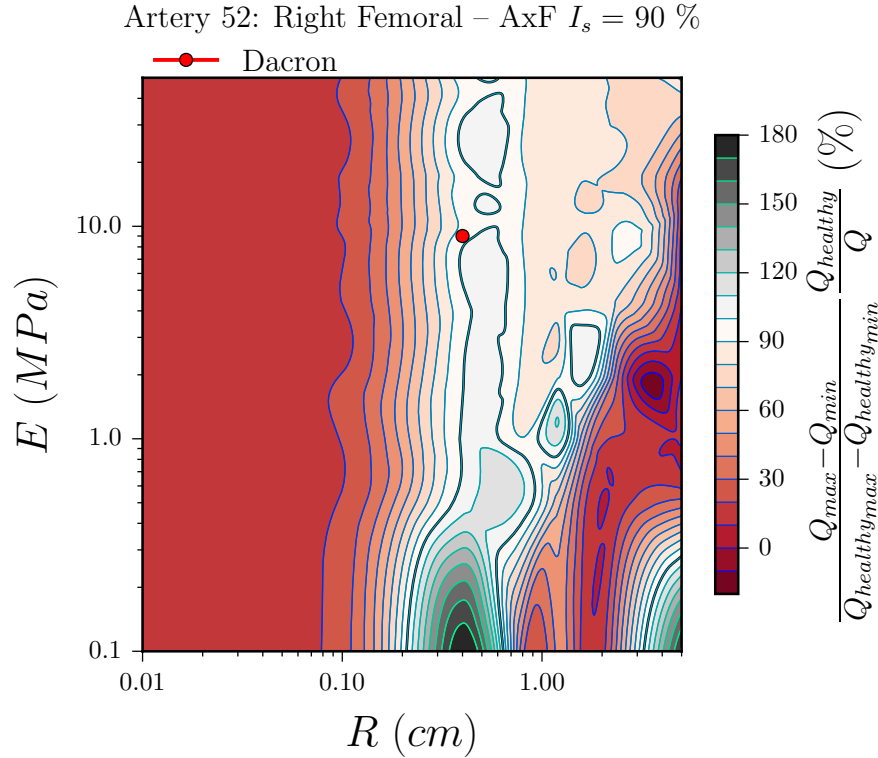


Figure 7.17 – Contour plot for the normalized peak to peak flow rate $\frac{Q_{max}-Q_{min}}{Q_{max}-Q_{min}^{healthy}} \frac{Q_{healthy}}{Q}$ as function of the Young modulus E and the radius R for a stenosis of 90 %. The red circle corresponds to the actual values of the Young modulus E and the radius R used in numerical simulations.

For a constant radius R , we analyze the effect of changing the Young's modulus E of the bypass graft. Moving along the vertical direction towards the top or the bottom starting from the red circle, $Q/Q_{healthy} \approx 100\%$ for every value of the Young's modulus E . However, the bypass graft's Young's modulus E should be taken as close as possible to the arteries' Young's modulus since elasticity jumps lead to impedance discontinuities and therefore higher reflected pressure waves. Moreover, if the bypass graft's elasticity is too small, the bypass graft will become more compliant and inflate, increasing the blood volume inside the bypass graft. Conversely, if the bypass graft's elasticity is too large, high pressure peaks will be generated due to increased wave reflections.

Figure 7.17 presents a log-log scale contour plot of the normalized peak to peak flow rate $\frac{Q_{max}-Q_{min}}{Q_{max}-Q_{min}^{healthy}} \frac{Q_{healthy}}{Q}$ in the AxF bypass graft obtained for different values of the Young modulus E and the radius R in a pathological network with an obstruction degree of 90 %. This quantity measures the pulsatility of the flow rate signal (and consequently the pressure signal). We observe that both Figure 7.16 and Figure 7.17 are similar, and the previous analysis of Figure 7.16 can be applied. Nevertheless, Figure 7.17 provides additional information especially in the region of large radii. For a fixed Young's modulus E , increasing the radius significantly decreases the value of $\frac{Q_{max}-Q_{min}}{Q_{max}-Q_{min}^{healthy}} \frac{Q_{healthy}}{Q}$. We previously described this situation as a correlation between an increase of radius and an increase of the blood volume inside the bypass graft. We prove here that this increase in blood volume in the bypass graft reduces its quality as the signal loses its pulsatility.

7.2.4 Conclusion

We have presented a model network comprising 55 viscoelastic arteries in which we modeled blood flow using a 1D fluid-structure system of equations. We performed simulations of this complex nonlinear dissipative system in a healthy and a pathological network presenting a stenosis of the Right Iliac artery. We then computed blood flow in a repaired network where we considered the three classical bypass grafts used to treat a stenosis of the Iliac artery. Our numerical results showed that all three bypass grafts are able to retrieve the healthy hemodynamics downstream of the stenosed member whilst maintaining a global healthy circulation.

However, little is known about the evolution of the hemodynamics in a bypass graft when its geometrical and mechanical characteristics are changed. We therefore studied the optimization of the geometrical and mechanical characteristics of the Axillo-Femoral bypass. Indeed, this bypass graft is used on unhealthy weak patients who can not sustain other types of bypass graft surgeries and because it has the smallest graft survival time of the three studied bypass grafts. The optimization results (Figure 7.16 and Figure 7.17) indicated that the mechanical characteristic of the bypass grafts used by clinicians are optimal and allow to retrieve the healthy circulation in the pathological network. Moreover, the numerical findings showed that choosing another set of parameters would lead to diminished performances of the bypass graft.

Besides the numerical approach, our numerical findings over an "averaged patient" proved that numerical hemodynamic predictions could be used to optimize or plan surgeries for specific patients, under the conditions that the pathologies were well defined and the physiological parameters known. Indeed, the numerical tool is very fast in terms of computing time, and therefore is suited for computational intensive simulations such as parametric analyses and error propagation tasks, and for the evaluation of new bypass procedures.

7.3 Impact of arterial cross-clamping during vascular surgery on arterial stiffness measured by the augmentation index and fractal dimension of arterial pressure

7.3.1 Introduction

Arterial cross-clamping is a necessary strategy for vascular surgery procedures, such as aortic aneurysm repair or peripheral vascular bypass [Dalman 2015]. Within the human vascular network, the aorta is the most thoroughly studied vessel during cross-clamping procedures [Gelman 1995]. Both arterial clamping and unclamping can produce several clinical disturbances, such as myocardial infarction, heart failure, acute lung injury, coagulopathies, visceral ischemia, acute kidney failure, and eventually, postoperative multiorgan failure and death [Katseni et al. 2015; Lim et al. 2016; Wartman et al. 2014; Wynn et al. 2015; Kotake et al. 2012]. In clinical studies, the clamping time of aortic cross-clamping has shown to be an independent predictor of overall surgical outcomes [Svensson et al. 1993]. Some of the proposed pathophysiological mechanisms behind these clinical outcomes are ischemia and reperfusion injury, oxidative stress damage, systemic inflammatory response, and microcirculatory dysfunction [Erkut and Onk 2015; Charles et al. 2011; Pottecher et al. 2013; Guillot et al. 2014; Kalder et al. 2012]. However, the impact of arterial cross-clamping on the viscoelastic properties of the arterial system and its underlying mechanisms remain unclear. Furthermore, the comparative effects of clamping and unclamping in common vascular surgery sites (such as the aorta and the iliofemoral artery) on the biomechanical characteristics of the vascular system have not been systematically studied.

We hypothesized that arterial clamping and unclamping would produce significant changes in the viscoelastic properties of the vascular system, mainly affecting arterial stiffness. A practical approach towards studying arterial stiffness is to analyze the morphology of the arterial pressure wave under different hemodynamic states. The Augmentation Index (AIx) and the Fractal Dimension (FD) of arterial pressure are indexes that are commonly used as indirect measures of wave reflections and arterial stiffness [Armentano et al. 2013]. One of the main advantages of these vascular indexes is that they can be assessed with pressure wave morphology only [Swillens and Segers 2008].

The augmentation index (AIx) is a ratio calculated from the analysis of blood pressure waveform morphology. It is defined as the augmentation pressure (i.e., the difference between the late systolic pressure shoulder and the early systolic pressure shoulder) divided by the pulse pressure (i.e., the difference between the maximum systolic pressure and the end diastolic pressure), and is usually expressed as a percentage (Figure 7.18) [Fantin et al. 2007]. The AIx is a measure of the relative contribution of wave reflection to the systolic arterial pressure [Liao and Farmer 2014]. Under normal conditions, the arterial pressure waveform is determined by the sum of a forward traveling wave coming from the heart, and backward reflected waves coming from the periphery vessels. The amplitude and propagation speed of the reflected waves depend on the peripheral resistance and on the functional and structural characteristics of the arterial network [O'Rourke et al. 2002; Westerhof et al. 1972, 2006]. For example, arterial stiffening increases the speed of propagation of both forward and backward waves, resulting in an earlier return of reflected waves, a higher degree of overlap among forward and backward waves, and a change in the morphology and amplitude of the waveform [Politi et al. 2016a; Borlotti et al. 2014; Khir and Parker 2002]. Therefore, both the magnitude and the sign of the AIx provide information on arterial pressure wave morphology and, indirectly, on arterial stiffness and the influence of wave reflections [Beckmann et al. 2015].

Arterial pressure waves can be classified into three different wave types according to wave

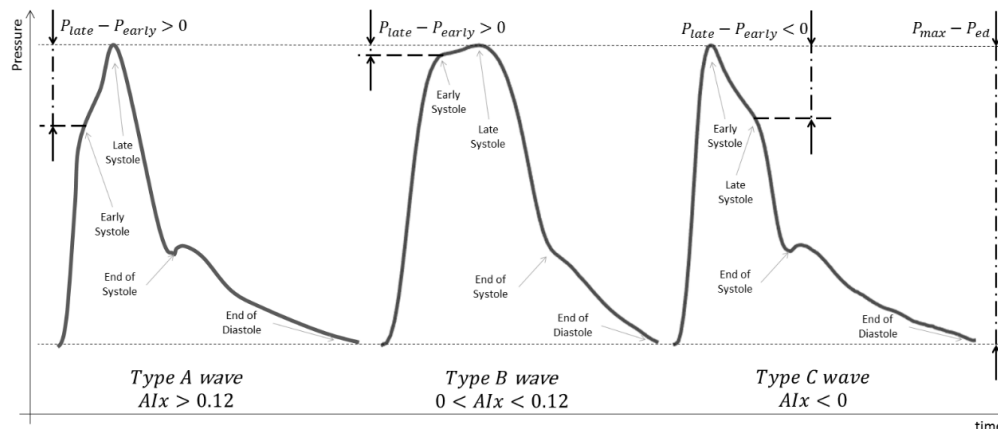


Figure 7.18 – Classification of arterial pressure waves according to wave morphology. In type A waves the early systolic pressure shoulder is lower than the late systolic pressure shoulder and the Augmentation Index (AIx) has a positive value, which is above 0.12. Type B waves are similar to type A waves except for the fact that the AIx has a positive value below 0.12. In type C waves the early systolic pressure shoulder is higher than the late systolic pressure shoulder and the AIx has a negative value.

morphology, which can be quantified through their AIx value (Figure 7.18) [Murgo et al. 1975]. A study of the aortic input impedance (i.e., a measure of effective hemodynamic resistance) in human subjects undergoing catheterism, proposed that the variations in pressure waveforms are due to differences in wave reflections in the arterial tree. Type A waves suggest considerable reflection in the arterial system, while type C waves imply smaller or more diffuse reflections. Type B waves would be an intermediate pattern between the two [Murgo et al. 1980].

The Fractal Dimension (FD) of arterial pressure is another indirect index for arterial stiffness. A fractal is a set of data that shows self-similarity throughout a certain dimension (e.g. time or space), which means it has a repeating pattern at every scale. The vascular system may have a fractal architecture related to its open tree structure, which is based on repeated bifurcations [Mandelbrot 1977]. The fractal character of the vascular system is produced by a) the fact that the same general rule or pattern of dichotomous divisions is applied in the growth of each portion of the tree from the previous portion, and b) a self-similarity shown at many different levels; for example, in the fact that any portion of the tree, taken as a whole, has the same branching structure as the overall tree [Zamir 2001]. Similarly, flow distributions in the systemic circulation may also follow a fractal pattern since its arrangement is heterogeneous, although not random. A fractal characterization of blood flow may arise from the logarithmic relation between flow dispersion and element size, showing an increase in the degree of heterogeneity as the size of the elements decrease. The fractality of blood flow could be related to the fact that flow is delivered through a branching vascular tree, which appears to have a fractal structure itself [Bassingthwaight 1992]. Arterial blood pressure may also have an underlying fractal structure that could describe the multiple changes in the waveform complexity of arterial pressure time series [Cymberknop et al. 2015, 2012].

Daily physiological variations and adjustments of the cardiovascular system have a complex behavior that is related to the inherent complexity of its own structure [Sharma 2009]. A straightforward way of measuring this complex behavior is by determining the FD of a given time-based parameter of the cardiovascular system. Conceptually, the FD is a way of quantifying the self-similarity of a parameter (e.g. blood pressure) throughout a dimension (e.g. time), that is, a measure of resemblance at different observation scales [Cymberknop

et al. 2011]. Fractal physiological signals –such as blood pressure– may lose their fractal nature (i.e., decrease their FD) in pathological states, thus making FD an indicator of cardiovascular health. Previous in-vitro studies show that the loss of fractal complexity of blood pressure is related to an increase in arterial stiffness. [Cymberknop et al. 2012] Clinical studies have also suggested that FD may have diagnostic and prognostic value in patients with heart failure and could be a predictor of mortality [Sharma 2009].

The aim of this study is to evaluate the impact of arterial cross-clamping on the biomechanical properties of the vascular system by using data from continuous radial arterial pressure tracings during vascular surgery. We chose AIx and FD as indirect indicators of the arterial stiffness of the vascular network for several hemodynamic states. We proposed that the clamping and unclamping events during vascular surgery would have a significant impact on these indicators. We additionally sought to explore the relationship between these two indicators throughout the vascular surgery.

7.3.2 Methods

Study design

A cross-section, observational, analytical, before-after study was designed. We evaluated the effect of arterial clamping and unclamping during vascular surgery at two different locations in the vascular network: iliofemoral and infrarenal abdominal aorta. The effect of these interventions on arterial stiffness was estimated indirectly by the Augmentation Index normalized to 75 beats-per-minute (AIx@75) and the Fractal Dimension (FD) of invasive radial arterial pressure tracings during each clamping condition.

Patient enrollment

The study enrolled adult patients undergoing peripheral vascular surgery at the *Hôpital Universitaire Pitié-Salpêtrière* in Paris, France. Exclusion criteria were having:

- a) an irregular heart rhythm;
- b) an undetectable pressure notch.

The study protocol was approved by the IRB of the *Hôpital Universitaire Pitié-Salpêtrière*. The study is in accordance with the ethical principles of the Declaration of Helsinki [34].

Invasive radial arterial pressure measurements

Experimental data were obtained from continuous invasive arterial pressure measurements using a fluid-filled catheter from the radial artery of adult patients undergoing peripheral vascular surgery. We used a disposable pressure transducer (TruWave, Edwards Lifesciences®) with a natural frequency of 40 Hz for a standard kit for measuring blood pressure. Data were registered using an analogue-digital converter with internal hardware filters ((low pass frequency set at 20 kHz, high pass frequency set at 0.05 Hz, MP150, BIOPAC Systems Inc.) and the AcqKnowledge software. Data acquisition rate was 100 Hz.

Waveform analysis

A stable set of beats from radial arterial pressure tracings were chosen manually throughout a 20-s interval immediately before and after each clamp and unclamp event. A brief transitional period was allowed after each event. The time values for end diastolic, end systolic, early systolic shoulder, late systolic shoulder and maximum pressure were computed for each beat with a custom software developed in Matlab (R2014b, The MathWorks, Inc., Natick,

Massachusetts). The median heart rate (HR) was calculated using the foot-to-foot time differences of the radial arterial pressure.

In order to identify the early and late systolic pressure shoulders, a two-term Gaussian model was used to separate the first and second components of the systolic portion of each beat, where the modeled systolic pressure ($PS(t)$) for each beat was expressed as [Liu et al. 2013]:

$$P_S(t) = a_1 e^{-\left(\frac{t-b_1}{c_1}\right)^2} + a_2 e^{-\left(\frac{t-b_2}{c_2}\right)^2}. \quad (7.6)$$

This method has shown to yield good results when modeling peripheral pressure waveforms [Liu et al. 2013, 2014]. In our data, we estimated for each beat the coefficient of determination (R^2) between the model and the data. The minimum value for all beats from all patients in all states was $R^2 = 0.987$.

The time centroids b_1 and b_2 were recorded and their difference was established as the time-distance between the early and late systolic pressure shoulders. The maximum pressure was assigned to one of the shoulders, depending on the wave morphology (i.e., type A, type B or type C) (Figure 7.18) [Murgo et al. 1980]. The other shoulder was located by using the time difference between centroids (e.g., in a type C beat, the maximum pressure matches the early shoulder, while the late shoulder is found $|b_2 - b_1|$ seconds later). This technique produced successful results that were visually validated, and double-checked using the method described by Takazawa et al. [Armentano et al. 2013; Takazawa et al. 1995].

The Augmentation Index (AIx) was calculated as following:

$$AIx = \frac{P_{late} - P_{early}}{P_{max} - P_{ed}} \times 100. \quad (7.7)$$

where P_{late} , P_{early} , P_{max} and P_{ed} are late systolic pressure, early systolic pressure, maximum systolic pressure, and end diastolic pressure, respectively. All AIx values were normalized to a heart rate of 75 beats-per-minute (AIx@75), using the well-known conversion formula [Gallagher et al. 2004]:

$$AIx@75 = AIx - 0.39(75 - HR). \quad (7.8)$$

The Fractal Dimension (FD) was calculated for each set of data using a custom software developed in Matlab following the Higuchi method [Higuchi 1988]. The software was validated using several fractal signals with a known FD, yielding acceptable mean and SD values (test signal: FD = 1.2; calculated FD = 1.231 ± 0.069 ; test signal: FD = 1.5; calculated FD = 1.514 ± 0.134).

The Higuchi method uses different scales to measure the length of the curve of a given parameter [Higuchi 1988]. The log-log relationship between the resulting lengths and their corresponding scales is given by:

$$L(k) \propto k^{-FD}. \quad (7.9)$$

where $L(k)$ is the measured length with the scale k .

As in most natural phenomena, FD may not be constant over all time scales. Instead, there are two ranges in which the property of self-similarity holds, which are separated by a critical breaking point [Higuchi 1988]. FD was calculated for all scales, and the critical point where

lower and higher ranges break was detected by optimizing the linear adjustments of the length $L(k)$. The reported FD value is the median FD for the lower range scales.

Statistical analysis

Since FD and AIx@75 distributions deviate from normal when tested formally (AIX@75 has a skewed distribution and FD has a logarithmic distribution), data are presented as median and interquartile range (IQR) and non-parametric tests were chosen. The statistical analysis involved Wilcoxon matched-pairs signed-ranks test for before-after testing and Spearman's rank-order correlation using R studio free statistical software. All statistical tests were two-tailed. Statistical significance was considered at 5 % ($\alpha = 0.05$).

7.3.3 Results

Patient clinical data

The radial arterial pressure tracings of 9 patients undergoing vascular surgery were evaluated in this study; one patient was excluded for having an irregular heart rhythm. The arterial pressure tracings from a total final of 8 patients were analyzed. The surgeries involved were 4 infrarenal abdominal aorta prosthesis placements and 4 iliofemoral bypass surgeries. Some surgeries required more than one arterial intervention; overall, there were 4 aortic and 11 iliofemoral interventions. Mean age was 69 years. Most patients were non-diabetic males with hypertension who were current or former smokers. All patients had a baseline type C waveform. Of the 60 hemodynamic states analyzed, 58 hemodynamic states had type C waveforms; only one patient switched to a type A waveform during two hemodynamic states. Table 7.3 displays main patient clinical characteristics. Figure 7.19 illustrates the results of one representative patient.

	($n = 8$)
Age -years	68.9 \pm 14.5
Males - no (%)	5 (62.5)
Hypertension	6 (75.0)
Hypercholesterolemia	7 (87.5)
Diabetes	0 (0.0)
Smokers	5 (62.5)
Pack-year among smokers	46.3 \pm 24.3
BMI – kg · m ² -1	23.8 \pm 3.3
Baseline type C waveform – no (%)	8 (100.0)

Table 7.3 – Patient clinical characteristics. Data are presented as mean \pm SD. BMI =body mass index

Augmentation index normalized to 75 beats-per-minute (AIx@75)

Experimental data included continuous invasive radial arterial pressure tracings from 4 infrarenal abdominal aorta clamps and unclamps, and from 11 iliofemoral artery clamps and unclamps.

Table 7.4 presents the overall results for the median AIx@75 over a 20-s interval before and after aortic clamping and unclamping for all aortic interventions. After infrarenal abdominal aorta clamping, the median AIx@75 increased significantly (-14.8 to -14.2; $\Delta AIx@75 + 4.1$ %; $p < 0.01$), while after unclamping, it decreased significantly (-0.142 to -0.177; $\Delta AIx@75 -24.6$ %; $p < 0.001$). Notice that the sign of the median AIx@75 remained unchanged after

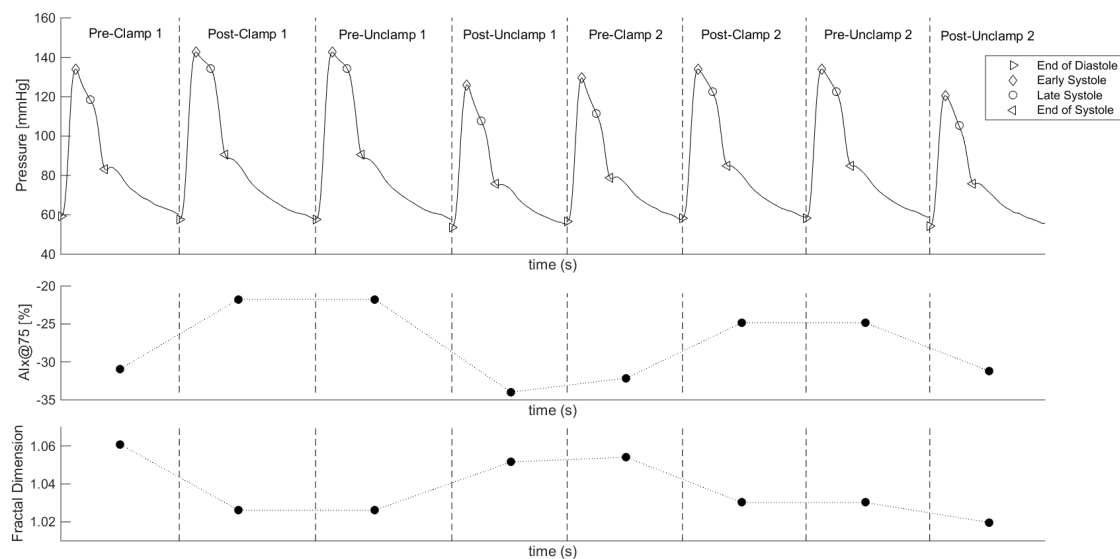


Figure 7.19 – Average arterial radial pressure tracings over 20-s intervals before and after each event (clamping/unclamping) for one representative patient undergoing vascular surgery. The end of diastole, end of systole, early systole and late systole pressures were detected on arterial pressure tracings. The Augmentation Index normalized to 75 beats-per-minute ($AIx@75$) and the Fractal Dimension (FD) were calculated for each state.

	Pre-clamp	Post-clamp	Pre-unclamp	Post-unclamp
Median	-14.8	-14.2	-14.2	-17.7
IQR	-20.7 to -2.9	-20.6 to -10.6	-20.9 to 10.0	-34.1 to -7.4
$\Delta AIx@75$ (%)		+4.1		-24.6
p		< 0.01		< 0.001

Table 7.4 – Changes in Augmentation Index normalized to 75 beats-per-minute ($AIx@75$) following aortic clamp and unclamp. IQR interquartile range. $\Delta AIx@75$ (%): relative percentage change in AIx .

both clamping and unclamping events.

	Pre-clamp	Post-clamp	Pre-unclamp	Post-unclamp
Median	-15.9	-13.9	-15.3	-15.7
IQR	-19.8 to -11.0	-17.3 to -5.5	-17.5 to -8.8	-19.0 to -10.8
$\Delta AIx@75$ (%)		+12.6		-2.6
p		< 0.001		< 0.001

Table 7.5 – Changes in Augmentation Index normalized to 75 beats-per-minute ($AIx@75$) following iliofemoral clamp and unclamp. IQR interquartile range. $\Delta AIx@75$ (%): relative percentage change in AIx .

Table 7.5 presents the overall results for the median $AIx@75$ over a 20-s interval before and after iliofemoral artery clamping and unclamping for all iliofemoral interventions. After iliofemoral artery clamping, the median $AIx@75$ increased significantly (-15.9 to -13.9; $\Delta AIx@75$ + 12.6 %; $p < 0.001$), while after unclamping, it decreased significantly (-15.3 to -15.7; $\Delta AIx@75$ -2.6 %; $p < 0.001$). Once again, the sign of the median $AIx@75$ remained unchanged after both clamping and unclamping events.

Fractal dimension (FD)

Table 7.6 shows data for the median FD over a 20-s interval before and after aortic clamping and unclamping for all aortic interventions. After infrarenal abdominal aorta clamping, the median FD was reduced significantly (1.039 to 1.027; ΔFD -1.2 %; $p < 0.01$), while after unclamping, it increased significantly (1.031 to 1.040; ΔFD + 0.9 %; $p < 0.001$).

	Pre-clamp	Post-clamp	Pre-unclamp	Post-unclamp
Median	1.039	1.027	1.031	1.040
<i>IQR</i>	1.006 to 1.154	1.004 to 1.135	1.004 to 1.138	1.007 to 1.178
ΔFD (%)		-1.2		+0.9
<i>p</i>		< 0.01		< 0.001

Table 7.6 – Changes in Fractal Dimension (FD) following aortic clamp and unclamp. *IQR* interquartile range. ΔFD (%): relative percentage change in FD.

Table 7.7 shows data for the median FD over a 20-s interval before and after iliofemoral artery clamping and unclamping for all iliofemoral interventions. After iliofemoral artery clamping, the median FD was reduced significantly (1.032 to 1.029; ΔFD -0.3 %; $p < 0.01$), while after unclamping, it increased significantly (1.029 to 1.033; ΔFD + 0.4 %; $p < 0.001$).

	Pre-clamp	Post-clamp	Pre-unclamp	Post-unclamp
Median	1.032	1.029	1.029	1.033
<i>IQR</i>	1.005 to 1.154	1.003 to 1.138	1.004 to 1.143	1.005 to 1.151
ΔFD (%)		-0.3		+0.4
<i>p</i>		< 0.01		< 0.001

Table 7.7 – Changes in Fractal Dimension (FD) following iliofemoral clamp and unclamp. ΔFD (%): relative percentage change in FD.

Correlation between augmentation index normalized to 75 beats-per-minute (AIx@75) and fractal dimension (FD)

In the light of these results, we decided to explore the relationship between the two indicators, median AIx@75 and FD, during different hemodynamic states through Spearman’s rank-order correlation. The relation between these variables was monotonic, though non-linear, as assessed by visual inspection of a scatterplot. A strong significant negative correlation between median AIx@75 and FD for each hemodynamic state was found for aortic interventions ($rs = -0.95$; $p < 0.05$), though not for iliofemoral interventions nor overall data. These results are illustrated in Figure 7.20

7.3.4 Discussion

The results show that arterial clamping and unclamping during vascular surgery have a significant impact on the biomechanical properties of the vascular system, as assessed by the Augmentation Index normalized to 75 beats-per-minute (AIx@75) and the Fractal Dimension (FD), calculated from radial arterial pressure tracings. After arterial clamping, median AIx@75 rises and median FD drops; the opposite occurs after arterial unclamping. This effect was observed in both aortic and iliofemoral interventions.

The increase in the median values of AIx@75 during arterial clamping may indicate a higher arterial stiffness during this hemodynamic state [Armentano et al. 2013; Laurent et al. 2006]. However, the magnitude of this effect on median AIx@75 was relatively small (4.1 % in aortic interventions and 12.6 % in iliofemoral interventions). Additionally, the sign of the median

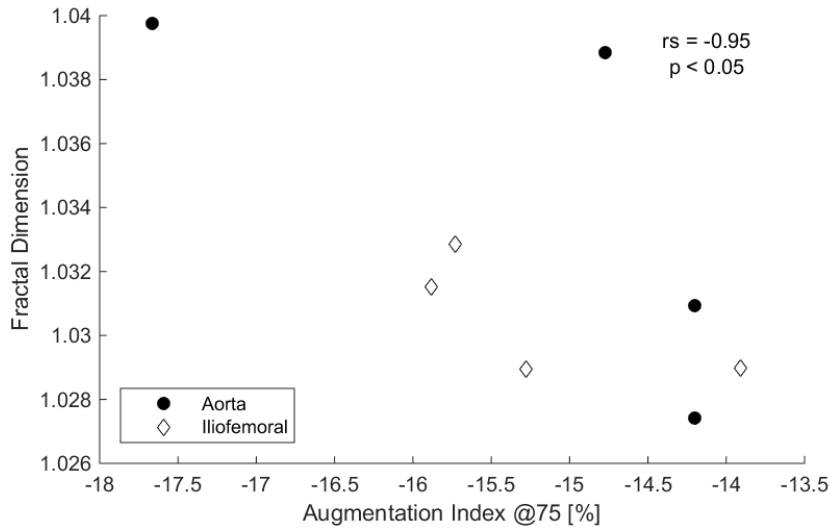


Figure 7.20 – Spearman’s rank-order correlation between the Augmentation Index normalized to 75 beats-per-minute ($AIx@75$) and the Fractal Dimension (FD). A strong significant correlation between median $AIx@75$ and FD for each hemodynamic state was found for aortic interventions ($r_s = -0.95$; $p < 0.05$), though not for iliofemoral interventions nor overall data.

$AIx@75$ did not change, which possibly indicates that the increase in arterial stiffness was not large enough to change the wave morphology into a type A or B wave. The decrease in median FD during arterial clamping also suggests a higher arterial stiffness [Cymberknop et al. 2012, 2011]. Once again, the magnitude of this effect on median FD was small (1.2 % in aortic interventions and 0.3 % in iliofemoral interventions). Despite the small effect size, our results are consistent at many levels:

- a) opposite events (i.e., clamping and unclamping) produce changes in different directions;
- b) two different indicators (i.e., $AIx@75$ and FD) suggest the same underlying phenomenon;
- c) similar results are observed at different vascular locations (i.e., aortic and iliofemoral).

Overall, our data consistently suggests an increase in arterial stiffness during clamping and a reduction in arterial stiffness during unclamping.

Similar results were published by Armentano et al. by measuring the simultaneous aortic pressure and diameter in 14 conscious dogs before and after occluding the distal descending aorta with a pneumatic cuff [Armentano et al. 2013]. These authors observed that, during aortic occlusion, the aortic pressure FD decreased and the pressure-strain elastic modulus (E) of the aortic wall increased (i.e., the aorta became stiffer). The magnitude of the FD drop reported by these authors was -4.7 %, which is only slightly higher than our own findings, -1.2 % (1.039 to 1.027; $p < 0.01$), especially when taking into account that:

- a) our protocol involved a more distal occlusion site (infrarenal aorta instead of descending aorta);
- b) our protocol involved a larger distance between the pressure measurement site (i.e., radial artery) and the occlusion site (i.e., infrarenal aorta or iliofemoral artery) whereas Armentano et al. measured the aortic pressure just proximal to the occlusion site.

Therefore, these results would be in accordance with our own findings.

Given this apparent association between changes in arterial stiffness and changes in $AIx@75$ and FD , what remains to be addressed are the possible underlying mechanisms involved. Armentano et al. suggest that reflected waves may participate in changes in FD during

arterial occlusion. Through wave separation analysis, these authors studied the forward and backward traveling components of the aortic pressure wave before and after the occlusion of the descending aorta in dogs. The authors analyzed only the first two heartbeats after aortic occlusion, as to avoid the participation of regulation mechanisms (which take place around the fifth heartbeat after occlusion) in the resulting waveform. They proposed that, during total occlusion of the descending aorta, aortic incident waves reflect almost completely and immediately at the descending aorta occlusion site, thus overlapping the incident wave with the reflected wave and increasing overall aortic pressure and modifying waveform morphology. Since multiple branching reflection sites are avoided during aortic occlusion, the fractal complexity of the aortic pressure wave is reduced (i.e., aortic FD decreases). The authors conclude that arterial pressure fractality depends highly on the wave reflection [Armentano et al. 2013]. In the light of these conclusions, in our results, the decrease in median FD during clamping could be associated to loss in the complexity of the pressure waveform due to reduced reflection sites during clamping. Additionally -and since in our own protocol both AIx@75 and FD were calculated from 20-s intervals before and after each event- reflex regulation mechanisms (i.e., reduced heart rate and increased contractile force) probably pay a contribution to the waveform structure in our analysis, as in actual real-life patients.

Murgo et al. also studied the aortic pressure waveform after arterial occlusion [Murgo et al. 1980]. These authors invasively measured pressure in the ascending aorta of 4 patients undergoing coronary catheterism after the external occlusion of the iliac artery. These authors describe significant changes in the aortic waveform related to an increase in the late systolic pressure shoulder, without observing changes in the end-diastolic pressure. Just as in our protocol, the authors measure the arterial pressure at a distant site from the vascular occlusion; however, it is still a central arterial pressure measurement. Therefore, the effect of reflection waves may be larger than on peripheral arterial pressure measurements [Nichols and Edwards 2001]. Through the study of the impedance spectral patterns, these authors suggest that type A waveforms are associated to a stiffer vascular profile, with considerable wave reflections returning from the periphery; whereas type C waves imply smaller or more diffuse reflections [Murgo et al. 1980]. Our results are in accordance with these reports, since clamping increased the magnitude of AIx@75, although the waveform type did not change.

Cyberknop et al. studied the variation of the complexity of the arterial pressure waveform in relation to its anatomical location. The authors compared the continuous arterial pressure waveforms of the carotid and femoral arteries through non-invasive applanation tonometry in human subjects. They found that the arterial pressure FD of the carotid artery was higher than the arterial pressure FD of the femoral artery ($+56.51 \pm 13.62\%$). Though the authors did not evaluate clamping or unclamping interventions, these findings could possibly indicate that the higher pressure FD reported in the carotid artery is related to a higher waveform complexity, due to a higher exposure to multiple wave reflection at central vascular sites. The lower pressure FD reported in the femoral artery could be related to the loss of complexity at vascular sites distant from the heart pump, a process often described as an "unwrinkling" phenomenon [Cyberknop et al. 2015]. This "unwrinkling" phenomenon or loss of complexity could also possibly occur during arterial clamping, and would explain the decrease in pressure FD during clamping and its increase during unclamping.

Finally, although wave reflections occur at multiple locations in the arterial system, in human subjects the "effective" reflection site is the region of the terminal abdominal aorta and the bifurcation of the iliac and femoral arteries [Murgo et al. 1980; Mills et al. 1970; Latham et al. 1985]. These vessels would produce reflections that dominate over those arising from other locations. The fact that the surgical interventions of our study are located at the dominant reflection sites suggests that reflection waves could participate in the observed changes in AIx@75 and FD.

As opposed to others, our results have demonstrated changes in arterial pressure $AIx@75$ and FD during clamping with an effect size smaller than previously reported [Armentano et al. 2013; Murgo et al. 1980]. However, these studies involved intraortic measurements in invasive animal experiments or in human subjects undergoing coronary catheterization. Our study analyzed the arterial pressure $AIx@75$ and FD through a radial artery catheter, which is a minimally-invasive monitoring instrument that is widely used in surgical settings. Despite the large distance from the event taking place at the aortic or iliofemoral intervention sites, radial artery pressure monitoring was still able to detect consistently these vascular events.

The question on the role of FD in hemodynamic monitoring and in the study of the viscoelastic properties of the vascular network is yet to be answered. Due to the influence of peripheral reflected waves on this index, the FD may be able to address issues related to peripheral microcirculation, such as the skin or retinal vessels [Crystal et al. 2016; Gryglewska et al. 2011; Takahashi 2014]. As a measure of complexity, it may also have a higher capacity than the AIx to discriminate the incident wave and the reflected wave in the overall waveform.

In summary, in both the aorta and the iliofemoral artery, arterial clamping and unclamping significantly modify the Augmentation Index normalized to 75 beats-per-minute ($AIx@75$) and the Fractal Dimension (FD) measured by invasive radial arterial pressure monitoring, suggesting changes in arterial stiffness. After arterial clamping, median $AIx@75$ rises and median FD drops; the opposite occurs after arterial unclamping. A strong significant negative correlation between median $AIx@75$ and FD for each hemodynamic state was found for aortic interventions ($rs = 0.95$; $p < 0.05$), though not for iliofemoral interventions nor overall data. Overall, our data consistently suggests an increase in arterial stiffness during clamping and a reduction during unclamping.

7.4 Conclusion

In Chapter 7, we have studied three biomedical situations. We have first investigated the origin of the dicrotic notch, which is a small and brief increase in arterial blood pressure occurring at the end of systole, creating a notch in the pressure signal. In a didactic approach, we have used the 1D blood flow equations (3.23) to show that the dicrotic notch could be explained by the overlap of the incoming pressure wave generated by the heart and the reflected waves originating from the distal vasculature. We then have presented a numerical study of the consequences of a stenosis of the Iliac artery on global network hemodynamics and showed that the 1D blood flow equations (3.23) are able to provide information on the design of extracorporeal bypass grafts used to treat such a pathology. Finally, we have analyzed experimental data on aortic clamping and showed that clamping affects both the augmentation index and the fractal dimension. The first two applications are proof that the 1D blood flow equations (3.23) can and are necessary to capture wave propagation and reflection dynamics at the scale of the systemic network. Moreover, the second applications shows that even a local perturbation such as a stenosis of the Iliac artery generates perturbation in the whole network, and that therefore any relevant blood flow application should consider a large network to capture these effects.

We are now performing the numerical equivalent of the experiments analyzed in the third application, in the hope of recovering similar results for the augmentation index.

Two-dimensional multiring model for blood flow

We present here a two-dimensional multiring blood flow model designed to solve the RNSP equations (8.1) in an elastic axisymmetric artery. The text in this chapter deals with the derivation and numerical resolution of the multiring model and is greatly inspired from the following published article:

- A.R. Ghigo, J.-M. Fullana, and P.-Y. Lagrée. A 2D nonlinear multiring model for blood flow in large elastic arteries. *Journal of Computational Physics*, 350:136–165, 2017c.

Contents

8.1	Introduction	167
8.2	A multiring discretization of the RNSP equations	169
8.2.1	Radial decomposition of the fluid domain	169
8.2.2	System of equations for one layer	170
8.2.3	System of equations for the artery	171
8.2.4	Radial boundary conditions	172
8.2.5	Multiring system of equations	172
8.2.6	Radial velocity	173
8.2.7	Link to the one-dimensional blood flow equations	173
8.3	Mathematical properties	174
8.3.1	Single layer system of equations	174
8.3.2	Two layers system of equations	175
8.3.3	Multiring system of equations	176
8.4	Numerical methods	176
8.4.1	Problem splitting	176
8.4.2	Explicit convective numerical scheme	177
8.4.3	Implicit viscous numerical scheme	180
8.5	Boundary conditions	182
8.5.1	Imposed flow rate	182
8.5.2	Imposed cross-sectional area	183
8.5.3	Imposed reflection coefficient	183
8.6	Linear examples in an elastic artery	183
8.6.1	The Womersley solution	183
8.6.2	The steady linear elastic Poiseuille solution	185
8.7	Nonlinear examples in a rigid artery	189
8.7.1	Nonlinear transition from a flat to a Poiseuille velocity profile	189

	8.7.2 Rigid wall stenosis and aneurysm	191
8.8	Unsteady flow in an elastic stenosis	195
8.9	Conclusion	196

8.1 Introduction

The numerical simulation of blood flow in large elastic arteries requires the resolution of a complex fluid-structure interaction (FSI) problem (see Chapter 2). Indeed, the motion of blood is governed by the three-dimensional (3D) Navier-Stokes equations for an incompressible homogeneous Newtonian fluid [Quarteroni et al. 2016] and the deformation of the arterial wall is described by a nonlinear elastic constitutive law [Holzapfel et al. 2000]. Several numerical methods have been proposed to solve this nonlinear 3D FSI problem [Hughes et al. 1981; Farhat et al. 2001; Tezduyar 2003; Figueroa et al. 2006; Tezduyar et al. 2007; Mayr et al. 2015]. Due to their modelling complexity and high computational cost, they have only been used to accurately compute blood flow in small regions of interest such as in arterial pathologies or small portions of the systemic network [Taylor et al. 1998; Vignon-Clementel et al. 2010; Sankaran et al. 2012]. However, an accurate local analysis is not sufficient to obtain physiological results (see Chapter 6). Indeed, the observed waveforms in large arteries are the result of the reflection, damping and diffusion throughout the systemic network of the waves emanating from the heart [Alastruey et al. 2009; Poli et al. 2016a]. Realistic waveforms can only be computed by performing a global simulation taking into account a large portion of the arterial network. Unfortunately, such large network 3D FSI simulations are too computationally expensive. Reduced-order models have therefore been proposed to compute physiological waveforms at a lower modeling and computational cost [Kim et al. 2010; Müller and Toro 2014; Ramachandra et al. 2016; Arthurs et al. 2016; Audebert et al. 2017b]. The aim of this paper is to propose a novel two-dimensional (2D) reduced-order model that accurately computes linear and nonlinear blood flow features in rigid and axisymmetric elastic arteries at a reasonable computational cost with minimal modeling parameters and could prove to be an alternative to 3D FSI simulations in simple arterial configurations.

In [Xiao et al. 2013], a 3D FSI simulation in a large network is performed to prove that such simulations are possible. Nevertheless, the computational and modeling costs are high and these 3D FSI simulations are still inadapted to real-time medical applications.

Reduced-order models for blood flow rely on a simplified system of equations for the motion of blood and a single equation for the deformation of the arterial wall, both of which are thoroughly discussed in Chapter 2. As a reminder, the reduced Navier-Stokes-Prandtl equations (RNSP) (2.43) are derived from the Navier-Stokes equations assuming that the flow is axisymmetric and noticing that the characteristic length scale in the axial direction is much larger than the one in the radial direction. The RNSP equations describe the conservation of mass and the balance of axial momentum of blood flow in an axisymmetric artery in which the pressure is hydrostatic (a function of x at t only):

$$\begin{cases} \frac{1}{r} \frac{\partial}{\partial r} [ru_r] + \frac{\partial u_x}{\partial x} = 0 & (8.1a) \\ \frac{\partial u_x}{\partial t} + u_r \frac{\partial u_x}{\partial r} + u_x \frac{\partial u_x}{\partial x} = -\frac{1}{\rho} \frac{\partial p}{\partial x} + \frac{\nu}{r} \frac{\partial}{\partial r} \left[r \frac{\partial u_x}{\partial r} \right] & (8.1b) \\ p(x, r, t) = p(x, t). & (8.1c) \end{cases}$$

The axial and radial boundary conditions for System (8.1) are described in Chapter 2 (see System (2.34)) and are recalled in the next section. Similarly, using simplifying assumptions,

different hydrostatic pressure laws $p(x, t)$ can be found linking the motion of the fluid and the displacement of the wall. Depending on the problem addressed, they can describe for example the behavior of flexible viscoelastic rubber tubes in hydraulic systems, the propagation of a water hammer (Allevi's equations, see Subsection 2.3.1) or the deformation of an elastic artery. The later is used in this study and its exact form is given by Equation (5.1). See Section 2.2 for further details.

System (8.1) is a rich dynamical system able to describe many asymptotic flow regimes in rigid tubes [Womersley 1955; Smith 1976; Lagrée and Lorthois 2005] and is numerically solved in [Barrenechea and Chouly 2009; Chouly and Lagrée 2012] in a rigid axisymmetric tube using a variety of numerical methods. However, similar numerical difficulties to those encountered in 3D FSI problems arise when solving System (8.1) in a deformable elastic tube.

One-dimensional (1D) models were therefore introduced as simple and efficient methods to obtain averaged quantities in elastic arteries [Euler 1844; Lambert 1958; Formaggia et al. 2003; Müller et al. 2013; Wang et al. 2015]. They are obtained by averaging over the cross-sectional area of the artery the mass (8.1a) and momentum (8.1b) equations. A detailed derivation of the 1D blood flow equations (2.67) is performed in Section 2.5. Unfortunately, they depend on coefficients which themselves depend on the shape of the velocity profile, lost in the averaging process. These coefficients are therefore estimated *a priori*, which often results in unrealistic viscous dissipation and pressure losses. This issue is discussed in Subsection 2.5.2.

One-and-a-half-dimensional (3/2D) models were then proposed as intermediates between 1D models and the complete resolution of the RNSP equations (8.1). In [Čanić et al. 2005, 2006], the authors used an asymptotic analysis of the RNSP equations (8.1) and homogenization theory to propose a 3/2D model for blood flow in an elastic artery. This model allows to compute, without any *a priori* coefficient estimation, the zero-th and first order components of the wall displacement and the axial and radial velocities. In [Bessems et al. 2007], an approximate velocity profile function was obtained depending on the instantaneous pressure gradient and the thickness of the boundary layer. This function was then used in a 1D model to compute the velocity profile-dependent coefficients. In [Lagrée 2000], a Von Kármán-Pohlhausen integral method closed using the Womersley velocity profiles was studied. This integral method accurately computes linear solutions such as the Womersley solution [Womersley 1955] (see Subsection 2.4.2) but is limited by the chosen linear closure relation. More recently, in [Flores et al. 2016], the authors proposed an analytic model for blood flow in an elastic artery based on a generalized Darcy's model and the linear Womersley theory. Despite their added modeling precision, 3/2D models still only provide approximate solutions of the RNSP equations (8.1).

Several authors have therefore proposed numerical methods to directly solve the RNSP equations (8.1) in elastic arteries. A noteworthy attempt was presented in [Ling and Atabek 1972] but the problem was simplified by introducing an explicit dependence with experimental data. In [Lagrée 2000], the author derived a boundary layer method which gives good results in the linear regime but behaves poorly in the nonlinear regime. To our knowledge, the most advanced numerical method was proposed in [Casulli et al. 2012]. There, a semi-implicit efficient numerical method was introduced based on an Eulerian-Lagrangian method to treat the advection term and a nested Newton algorithm to iteratively compute the pressure matching the desired wall displacement. The main drawback of this approach is that it can not deal with arbitrary large wall deformation and requires that the flow stays mildly nonlinear.

In this work, we propose a novel 2D model to solve without any approximations the

RNSP equations (8.1) in elastic arteries for arbitrary large arterial wall deformations. By decomposing the fluid domain in concentric rings, we derive what we refer to as the "multiring model with mass exchange". This model is inspired from the multilayer model with mass exchange presented in [Audusse et al. 2011] in the context of shallow water equations. This multiring system of balance laws provides a unified framework in which both the motion of the fluid and the displacement of the wall are dealt with simultaneously. Its mathematical structure allows us to use a *finite volume* numerical method that guarantees the conservation of mass and the positivity of the numerical solution and can deal with nonlinear flows and large deformations of the arterial wall. We will show that the multiring model can compute all relevant flow features in elastic arteries.

In the first section, we present the derivation of the multiring model. Next, we discuss its mathematical properties and details of the numerical method. In the last sections, we propose a series of examples where we compare the solution of the multiring model to reference solutions in elastic and quasi-rigid arteries.

8.2 A multiring discretization of the RNSP equations

We describe a multiring model with mass exchange for blood flow based on the axisymmetric RNSP equations (8.1) coupled to the elastic wall model (5.1). As stated in the introduction, this multiring model is the analog of the multilayer model with mass exchange for shallow water flows [Audusse et al. 2011].

8.2.1 Radial decomposition of the fluid domain

In the framework of the axisymmetric RNSP equations (8.1), the arteries are modeled as axisymmetric cylinders of radius R , cross-sectional area $A = \pi R^2$ and length L . Therefore, we can divide the fluid region delimited by the arterial wall into N_r concentric axisymmetric rings of width h_α , with $\alpha = 1, \dots, N_r$. This decomposition of the fluid domain is illustrated in Figure 8.1.

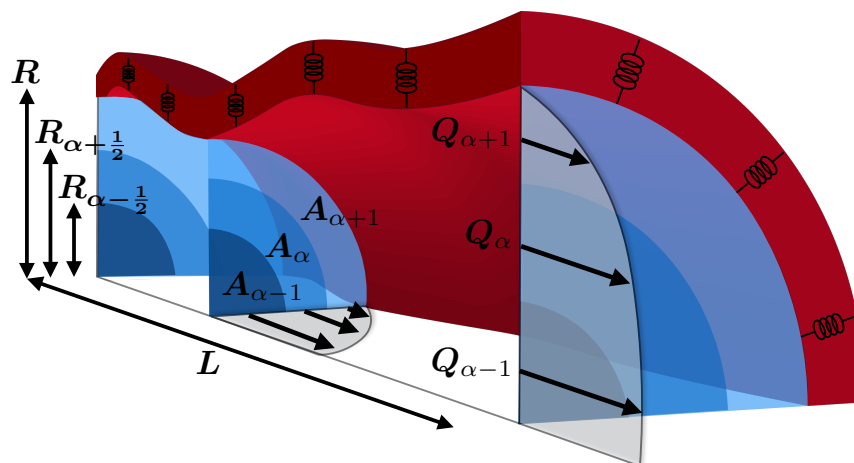


Figure 8.1 – Representation of the decomposition in several concentric rings of the fluid domain contained in an axisymmetric cylindrical artery. For clarity, only one-fourth of the artery of length L is represented. The springs in the arterial wall represent its elastic behavior. The variable Q_α is the flow rate in the ring α and A_α is the area delimited by the radii $R_{\alpha-\frac{1}{2}}$ and $R_{\alpha+\frac{1}{2}}$

To simplify the notations, we refer to the fluid ring of width h_α as the ring α . Each ring α is delimited by an upper and lower interface, respectively defined by the radii $R_{\alpha+\frac{1}{2}}$ and $R_{\alpha-\frac{1}{2}}$, with:

$$h_\alpha = R_{\alpha+\frac{1}{2}} - R_{\alpha-\frac{1}{2}}. \quad (8.2)$$

The interface position $R_{\alpha+\frac{1}{2}}$ and the radius of the artery R can now respectively be written as:

$$R_{\alpha+\frac{1}{2}} = \sum_{j=1}^{\alpha} h_j, \quad \text{and} \quad R = \sum_{j=1}^{N_r} h_j. \quad (8.3)$$

We also define the cross-sectional area of the ring α , noted A_α , the average flow rate in the ring α , noted Q_α , and the mean velocity in the ring α , noted u_α :

$$\left\{ \begin{array}{l} A_\alpha = \int_0^{2\pi} \int_{R_{\alpha-\frac{1}{2}}}^{R_{\alpha+\frac{1}{2}}} r dr d\theta \\ Q_\alpha = \int_0^{2\pi} \int_{R_{\alpha-\frac{1}{2}}}^{R_{\alpha+\frac{1}{2}}} u_x r dr d\theta \\ u_\alpha = \frac{Q_\alpha}{A_\alpha}. \end{array} \right. \quad (8.4a)$$

$$\left\{ \begin{array}{l} Q_\alpha = \int_0^{2\pi} \int_{R_{\alpha-\frac{1}{2}}}^{R_{\alpha+\frac{1}{2}}} u_x r dr d\theta \\ u_\alpha = \frac{Q_\alpha}{A_\alpha}. \end{array} \right. \quad (8.4b)$$

$$\left\{ \begin{array}{l} u_\alpha = \frac{Q_\alpha}{A_\alpha}. \end{array} \right. \quad (8.4c)$$

Finally, we note $l_{r,\alpha}$ the proportion of the total radius R occupied by the ring α :

$$h_\alpha = l_{r,\alpha} R, \quad \text{with} \quad \sum_{\alpha=1}^{N_r} l_{r,\alpha} = 1, \quad (8.5)$$

and l_α the proportion of the total cross-sectional area A occupied by the ring α :

$$A_\alpha = l_\alpha A, \quad \text{with} \quad l_\alpha = \left[\sum_{j=1}^{\alpha} l_{r,j} \right]^2 - \left[\sum_{j=1}^{\alpha-1} l_{r,j} \right]^2. \quad (8.6)$$

Without loss of generality, we prescribe the radial decomposition of the artery in concentric rings and set the proportion $l_{r,\alpha}$ in each ring α . This proportion is therefore a given constant number which can differ from one ring to another:

$$\forall t \geq 0, \forall x \in [0, L], \quad l_{r,\alpha} = \text{cst with } \alpha = 1, \dots, N_r. \quad (8.7)$$

As a consequence, we have:

$$\forall t \geq 0, \forall x \in [0, L], \quad l_\alpha = \text{cst with } \alpha = 1, \dots, N_r. \quad (8.8)$$

Assumption (8.7) indicates that the interfaces $R_{\alpha-\frac{1}{2}}$ and $R_{\alpha+\frac{1}{2}}$ of the ring α are not impermeable interfaces but rather interfaces of a radial mesh, and therefore mass exchanges exist between neighboring rings. This radial mesh automatically adapts itself to the movement of the arterial wall and can sustain arbitrary large wall deformation as long as $R > 0$.

In the following, we use this decomposition of the fluid domain in concentric rings to introduce a *finite volume* discretization of the axisymmetric RNSP equations (8.1) in the radial direction.

8.2.2 System of equations for one layer

Inspired by *finite volume* methods and the 1D approach presented in Subsection 2.5.1, we integrate the axisymmetric RNSP equations (8.1) over the cross-sectional area the ring α . Using the Leibniz integration rule, we obtain an integral form of the axisymmetric RNSP

mass (8.1a) and momentum (8.1b) equations in the ring α :

$$\left\{ \begin{array}{l} \frac{\partial A_\alpha}{\partial t} + \frac{\partial Q_\alpha}{\partial x} = G_{\alpha+\frac{1}{2}} - G_{\alpha-\frac{1}{2}} \end{array} \right. \quad (8.9a)$$

$$\left\{ \begin{array}{l} \frac{\partial Q_\alpha}{\partial t} + \frac{\partial}{\partial x} \left[\psi_\alpha \frac{Q_\alpha^2}{A_\alpha} \right] + \frac{A_\alpha}{\rho} \frac{\partial p}{\partial x} = S_{M,\alpha} + S_{\nu,\alpha}. \end{array} \right. \quad (8.9b)$$

The term $G_{\alpha+\frac{1}{2}}$ represents the radial mass exchanges at the interface $R_{\alpha+\frac{1}{2}}$ and is defined as:

$$G_{\alpha+\frac{1}{2}} = \frac{\partial}{\partial t} \left[\pi R_{\alpha+\frac{1}{2}}^2 \right] + u_{x,\alpha+\frac{1}{2}} \frac{\partial}{\partial x} \left[\pi R_{\alpha+\frac{1}{2}}^2 \right] - 2\pi R_{\alpha+\frac{1}{2}} u_{r,\alpha+\frac{1}{2}}. \quad (8.10)$$

The source term $S_{M,\alpha}$ characterizes the momentum associated to the radial mass exchanges in the ring α and writes:

$$S_{M,\alpha} = u_{x,\alpha+\frac{1}{2}} G_{\alpha+\frac{1}{2}} - u_{x,\alpha-\frac{1}{2}} G_{\alpha-\frac{1}{2}}, \quad (8.11)$$

where $u_{x,\alpha+\frac{1}{2}} = u_x(x, R_{\alpha+\frac{1}{2}}, t)$ is the axial velocity in $R_{\alpha+\frac{1}{2}}$. The source term $S_{\nu,\alpha}$ describes the viscous dissipation in the ring α and writes:

$$S_{\nu,\alpha} = 2\pi\nu \left[\left[r \frac{\partial u_x}{\partial r} \right]_{R_{\alpha+\frac{1}{2}}} - \left[r \frac{\partial u_x}{\partial r} \right]_{R_{\alpha-\frac{1}{2}}} \right]. \quad (8.12)$$

Finally, the nonlinear advection correction coefficient ψ_α writes:

$$\psi_\alpha = \frac{A_\alpha}{Q_\alpha^2} \int_{R_{\alpha-\frac{1}{2}}}^{R_{\alpha+\frac{1}{2}}} 2\pi r u_x^2 dr. \quad (8.13)$$

It is important to note that up to this point, the integration process is exact and no approximation has been made in this *finite volume* radial discretization of the axisymmetric RNSP equations (8.1). We now derive the system of equations governing the motion of blood in the entire artery.

8.2.3 System of equations for the artery

To obtain the system of equations governing blood flow in the entire artery, we must combine the N_r systems of equations (8.9) describing the conservation of mass and axial momentum in each ring α . The unknowns of the global system are therefore the cross-sectional area A_α and the flow rate Q_α of each ring α .

However, an important consequence of assumption (8.7) is that the local cross-sectional area A_α can be deduced from the cross-sectional area A using the prescribed proportion l_α . The unknowns of the system are then reduced to the cross-sectional area A and the flow rate Q_α of each ring α . Similarly, by adding the N_r mass conservation equations (8.9a), we obtain a single mass conservation equation depending on the cross-sectional area A and the flow rate Q_α of each ring α :

$$\frac{\partial A}{\partial t} + \frac{\partial}{\partial x} \left[\sum_{j=1}^{N_r} Q_j \right] = G_{N_r+\frac{1}{2}} - G_{\frac{1}{2}}. \quad (8.14)$$

Performing the same operation but adding only up to the ring α , we obtain the following expression for the mass exchange term $G_{\alpha+\frac{1}{2}}$:

$$G_{\alpha+\frac{1}{2}} - \left[G_{N_r+\frac{1}{2}} \sum_{j=1}^{\alpha} l_j + G_{\frac{1}{2}} \sum_{j=\alpha+1}^{N_r} l_j \right] = \sum_{j=1}^{\alpha} \left[\frac{\partial Q_j}{\partial x} - l_j \sum_{p=1}^{N_r} \left[\frac{\partial Q_p}{\partial x} \right] \right]. \quad (8.15)$$

Finally, by combining the previous remarks, we obtain a simplified global system of equations

describing the conservation of mass in the artery and the balance of axial momentum in each ring α . We refer to this system as the multiring system of equations, which depends on the variables $[A, Q_1, \dots, Q_\alpha, \dots, Q_{N_r}, p]$ and writes:

$$\left\{ \begin{array}{l} \frac{\partial A}{\partial t} + \frac{\partial}{\partial x} \left[\sum_{j=1}^{N_r} Q_j \right] = G_{N_r+\frac{1}{2}} - G_{\frac{1}{2}} \end{array} \right. \quad (8.16a)$$

$$\left\{ \begin{array}{l} \frac{\partial Q_\alpha}{\partial t} + \frac{\partial}{\partial x} \left(\psi_\alpha \frac{Q_\alpha^2}{l_\alpha A} \right) + l_\alpha \frac{A}{\rho} \frac{\partial p}{\partial x} = S_{M,\alpha} + S_{\nu,\alpha}, \quad \text{for } \alpha = 1, \dots, N_r. \end{array} \right. \quad (8.16b)$$

8.2.4 Radial boundary conditions

To complete the description of System (8.16), we provide boundary conditions at the center of the artery, in $r = R_{\frac{1}{2}} = 0$, and at the arterial wall, in $r = R_{N_r+\frac{1}{2}} = R$. These boundary conditions are identical those described in System (2.34).

In the center of the artery, in $r = R_{\frac{1}{2}}$, the velocity must verify the following axisymmetric boundary conditions:

$$\frac{\partial u_x}{\partial r} \Big|_{R_{\frac{1}{2}}} = 0 \quad \text{and} \quad u_r \Big|_{R_{\frac{1}{2}}} = 0. \quad (8.17)$$

At the arterial wall, in $r = R_{N_r+\frac{1}{2}}$, the following classical kinematic boundary condition is verified stating that the arterial wall is a material interface:

$$2\pi R_{N_r+\frac{1}{2}} u_{r,N_r+\frac{1}{2}} - \frac{\partial}{\partial t} \left[\pi R_{N_r+\frac{1}{2}}^2 \right] - u_{x,N_r+\frac{1}{2}} \frac{\partial}{\partial x} \left[\pi R_{N_r+\frac{1}{2}}^2 \right] = 0. \quad (8.18)$$

Finally, a no-slip boundary conditions is also verified at the arterial wall:

$$u_{x,N_r+\frac{1}{2}} = 0. \quad (8.19)$$

As a result, the expressions of the mass exchange terms $G_{\frac{1}{2}}$ and $G_{N_r+\frac{1}{2}}$ can be simplified using the boundary conditions (8.17) and (8.18):

$$G_{\frac{1}{2}} = 0, \quad G_{N_r+\frac{1}{2}} = 0. \quad (8.20)$$

Equation (8.20) indicates that there is no mass exchange at the arterial wall due to its impermeability and that there is no mass exchange in the center of the artery due to the axisymmetry of the flow.

8.2.5 Multiring system of equations

We use the thin wall pressure law (5.1) as a closure relation linking the pressure p with the cross-sectional area A . Injecting this pressure law and the boundary conditions (8.20) in the multiring system of equations (8.16), we obtain the final closed-form of the multiring system of equations describing the conservation of mass and the balance of axial momentum in an elastic impermeable axisymmetric artery:

$$\frac{\partial A}{\partial t} + \frac{\partial F_A}{\partial x} = 0 \quad (8.21a)$$

$$\frac{\partial Q_\alpha}{\partial t} + \frac{\partial F_{Q_\alpha}}{\partial x} = S_{M,\alpha} + S_{\nu,\alpha} + l_\alpha S_T, \quad \text{for } \alpha = 1, \dots, N_r, \quad (8.21b)$$

where:

$$\left\{ \begin{array}{l} F_A = \sum_{j=1}^{N_r} Q_j \end{array} \right. \quad (8.22a)$$

$$\left\{ \begin{array}{l} F_{Q_\alpha} = \psi_\alpha \frac{Q_\alpha^2}{l_\alpha A} + l_\alpha \frac{K}{3\rho} A^{\frac{3}{2}}, \end{array} \right. \quad (8.22b)$$

and:

$$S_T = \frac{A}{\rho} \left(\frac{\partial}{\partial x} \left(K \sqrt{A_0} \right) - \frac{2}{3} \sqrt{A} \frac{\partial K}{\partial x} \right). \quad (8.23)$$

The source term S_T is the geometrical and mechanical source term and is non-zero when the neutral cross-sectional area A_0 or the arterial wall rigidity K vary with the axial position x . The mass exchange source term $S_{M,\alpha}$ is defined by Equation (8.11) and the viscous source term $S_{\nu,\alpha}$ by Equation (8.12). The Equation (8.15) for the mass exchange term $G_{\alpha+\frac{1}{2}}$ in each ring α can be simplified using the boundary conditions (8.20):

$$G_{\alpha+\frac{1}{2}} = \sum_{j=1}^{\alpha} \left[\frac{\partial Q_j}{\partial x} - l_j \sum_{p=1}^{N_r} \left[\frac{\partial Q_p}{\partial x} \right] \right] \quad (8.24)$$

In the remainder of the study, we assume that the advection correction coefficient $\psi_\alpha = 1$ in each ring α . Doing so, we suppose that the velocity profile is a piece-wise constant function of the variable r . This classical *finite volume* hypothesis is the only one used in the derivation of the multiring system of equations and is reasonable if we use a sufficiently large number of rings N_r .

8.2.6 Radial velocity

We compute the radial velocity u_r using the incompressibility condition (8.1a). By integrating equation (8.1a) over the cross-sectional area of the ring α , we obtain:

$$[ru_r]_{R_{\alpha+\frac{1}{2}}} = [ru_r]_{R_{\alpha-\frac{1}{2}}} - \int_{R_{\alpha-\frac{1}{2}}}^{R_{\alpha+\frac{1}{2}}} r \frac{\partial u_x}{\partial x} dx. \quad (8.25)$$

The axisymmetric boundary condition (8.17) imposes that:

$$u_{r,\frac{1}{2}} = 0. \quad (8.26)$$

We then iteratively compute the radial velocity $u_{r,\alpha+\frac{1}{2}}$ in each ring α using equation (8.25), and then an approximation of $u_{r,\alpha}$ as:

$$u_{r,\alpha} = \frac{u_{r,\alpha-\frac{1}{2}} + u_{r,\alpha+\frac{1}{2}}}{2}. \quad (8.27)$$

8.2.7 Link to the one-dimensional blood flow equations

The multiring system of equations (8.21) is a generalization of the classical 1D system of equations for blood flow (2.67). Indeed, by adding the momentum balance equations (8.21b) of all the rings α , we obtain the following global momentum balance equation:

$$\frac{\partial Q}{\partial t} + \frac{\partial}{\partial x} \left[\sum_{\alpha=1}^{N_r} F_{Q_\alpha} \right] = \sum_{\alpha=1}^{N_r} [S_{M,\alpha} + S_{\nu,\alpha} + l_\alpha S_T], \quad (8.28)$$

where:

$$Q = \sum_{\alpha=1}^{N_r} Q_\alpha. \quad (8.29)$$

Using the boundary conditions (8.20), Equation (8.28) simplifies to:

$$\frac{\partial Q}{\partial t} + \frac{\partial}{\partial x} \left[\left[\sum_{\alpha=1}^{N_r} \frac{Q_\alpha^2}{l_\alpha A} \right] + \frac{K}{3\rho} A^{\frac{3}{2}} \right] = 2\pi\nu \left[r \frac{\partial u_x}{\partial r} \right]_{R_{N_r+\frac{1}{2}}} + S_T. \quad (8.30)$$

Combining the mass conservation equation (8.21a) with Equation (8.30), we obtain the following 1D system of equations for blood flow, describing the conservation of mass and

axial momentum in an elastic artery:

$$\begin{cases} \frac{\partial A}{\partial t} + \frac{\partial Q}{\partial x} = 0 \end{cases} \quad (8.31a)$$

$$\begin{cases} \frac{\partial Q}{\partial t} + \frac{\partial}{\partial x} \left[\left[\sum_{\alpha=1}^{N_r} \frac{Q_\alpha^2}{l_\alpha A} \right] + \frac{K}{3\rho} A^{\frac{3}{2}} \right] = 2\pi\nu \left[r \frac{\partial u_x}{\partial r} \right]_{R_{N_r+\frac{1}{2}}} + S_T. \end{cases} \quad (8.31b)$$

System (8.31) is a discrete analogue of System (5.2). The remaining unknowns are the nonlinear advection term $\sum_{\alpha=1}^{N_r} Q_\alpha^2 / [l_\alpha A]$ and the viscous term $2\pi\nu [r \partial_r u_x]_{R_{N_r+\frac{1}{2}}}$. They depend of the shape of the axial velocity profile u_x . As it can not be computed by 1D models, it is classical to close system (8.31) by prescribing an *a priori* shape of the velocity profile (see Subsection 2.5.2 for details). As an example, if we assume that the velocity profile is a Poiseuille profile, we have as in [Saito et al. 2011]:

$$\sum_{\alpha=1}^{N_r} \frac{Q_\alpha^2}{l_\alpha A} \approx \frac{4}{3} \frac{Q^2}{A} \quad \text{and} \quad 2\pi\nu \left[r \frac{\partial u_x}{\partial r} \right]_{R_{N_r+\frac{1}{2}}} = -8\pi\nu \frac{Q}{A}. \quad (8.32)$$

Unfortunately, in the vast majority of flow configurations, the shape of the velocity profile is an unknown function of time and position and a correct estimation of the coefficients $\sum_{\alpha=1}^{N_r} Q_\alpha^2 / [l_\alpha A]$ and $2\pi\nu [r \frac{\partial u_x}{\partial r}]_{R_{N_r+\frac{1}{2}}}$ is impossible. We propose the multiring model (8.21) to overcome those difficulties. Indeed, by integrating over concentric rings of fluid the axisymmetric RNSP equations (8.1) coupled to the elastic pressure law (5.1), we have derived a quasi-analytic radial discretization of the RNSP equations (8.1). The resulting multiring system of equations can compute the velocity profile and therefore does not depend on unknown coefficients like all 1D models. It is a system of balance laws, where the left hand side is written as a system of conservation laws and the right hand side contains the mass, viscous and geometrical and mechanical source terms. This mathematical structure guarantees the conservation of mass, the balance of axial momentum and is conducive to a *finite volume* axial discretization.

Next, we study the mathematical properties of this system of balance laws.

8.3 Mathematical properties

We study the mathematical properties of both the single layer system of equations (8.9) and the multiring system of equations (8.21).

8.3.1 Single layer system of equations

We consider here the homogeneous form of the single layer system of equations (8.9):

$$\begin{cases} \frac{\partial A_\alpha}{\partial t} + \frac{\partial Q_\alpha}{\partial x} = 0 \end{cases} \quad (8.33a)$$

$$\begin{cases} \frac{\partial Q_\alpha}{\partial t} + \frac{\partial F_{Q_\alpha}}{\partial x} = 0. \end{cases} \quad (8.33b)$$

This conservative system has been thoroughly studied by many authors and we only briefly recall its properties. Additional details can be found in [Formaggia et al. 2003; Wang et al. 2015; Ghigo et al. 2017b] and in Subsection 2.6.2.

The Jacobian matrix of System (8.33) has two real eigenvalues $\lambda_{1,\alpha}$ and $\lambda_{2,\alpha}$, respectively associated to two right eigenvectors $\mathbf{R}_{1,\alpha}$ and $\mathbf{R}_{2,\alpha}$:

$$\lambda_{1,\alpha} = \frac{Q_\alpha}{A_\alpha} - c, \quad \lambda_{2,\alpha} = \frac{Q_\alpha}{A_\alpha} + c, \quad \mathbf{R}_{1,\alpha} = \begin{bmatrix} 1 \\ \lambda_{1,\alpha} \end{bmatrix}, \quad \mathbf{R}_{2,\alpha} = \begin{bmatrix} 1 \\ \lambda_{2,\alpha} \end{bmatrix}, \quad (8.34)$$

where c (2.71) is the Moens-Korteweg celerity [Moens 1878; Korteweg 1878] and corresponds to the celerity of a pulse wave:

$$c = \sqrt{\frac{K}{2\rho}} \sqrt{A}. \quad (8.35)$$

The hyperbolicity of System (8.33) is characterized by the Shapiro number $S_{h,\alpha}$, introduced by Shapiro in [Shapiro 1977]:

$$S_{h,\alpha} = \frac{u_\alpha}{c}. \quad (8.36)$$

The Shapiro number $S_{h,\alpha}$ is the analog of the Froude number F_r for the shallow water equations or of the Mach number M_a for compressible flows. Depending on the value of $S_{h,\alpha}$, we distinguish two flow regimes in the ring α : if $S_{h,\alpha} < 1$, the flow is subcritical and if $S_{h,\alpha} > 1$ the flow is supercritical. In both cases, System (8.33) is strictly hyperbolic as $\lambda_{1,\alpha} \neq \lambda_{2,\alpha}$ and the right eigenvectors $\mathbf{R}_{1,\alpha}$ and $\mathbf{R}_{2,\alpha}$ are linearly independent. In physiological conditions, blood flow is almost always subcritical [Siviglia and Toffolon 2013], and therefore we only consider the case $S_{h,\alpha} < 1$. The Riemann invariant vector \mathbf{W}_α associated with System (8.33) is:

$$\mathbf{W}_\alpha = \begin{bmatrix} W_{1,\alpha} \\ W_{2,\alpha} \end{bmatrix} = \begin{bmatrix} \frac{Q_\alpha}{A_\alpha} - 4c \\ \frac{Q_\alpha}{A_\alpha} + 4c \end{bmatrix}. \quad (8.37)$$

The vector \mathbf{W}_α is linked to the conservative variables through the following relations:

$$\begin{cases} A_\alpha = \left(\frac{2\rho}{K}\right)^2 \left(\frac{W_{2,\alpha} - W_{1,\alpha}}{8}\right)^4 \\ Q_\alpha = A_\alpha \frac{W_{1,\alpha} + W_{2,\alpha}}{2}. \end{cases} \quad (8.38)$$

The relations (8.38) are useful when defining the boundary conditions at the inlet and outlet of the computational domain.

8.3.2 Two layers system of equations

We now focus on the more complicated inviscid two layers system of equations:

$$\begin{cases} \frac{\partial A}{\partial t} + \frac{\partial F_A}{\partial x} = 0 \end{cases} \quad (8.39a)$$

$$\begin{cases} \frac{\partial Q_1}{\partial t} + \frac{\partial F_{Q_1}}{\partial x} = S_{M,1} \end{cases} \quad (8.39b)$$

$$\begin{cases} \frac{\partial Q_2}{\partial t} + \frac{\partial F_{Q_2}}{\partial x} = S_{M,2}. \end{cases} \quad (8.39c)$$

To simplify the analysis, we suppose that the geometrical and mechanical properties of the artery do not vary ($S_T = 0$). System (8.39) can then be written in the following quasi-linear form:

$$\mathbf{M}(\mathbf{X}) \frac{\partial \mathbf{X}}{\partial t} + \mathbf{H}(\mathbf{X}) \frac{\partial \mathbf{X}}{\partial x} = 0. \quad (8.40)$$

The vector \mathbf{X} and the matrices \mathbf{M} and \mathbf{H} are respectively defined as:

$$\mathbf{X} = \begin{bmatrix} A \\ \bar{Q}_1 \\ \bar{Q}_2 \end{bmatrix}, \quad \mathbf{M}(\mathbf{X}) = \begin{bmatrix} 1 & 0 & 0 \\ -u & 1 & 0 \\ -u & 0 & 1 \end{bmatrix}, \quad \mathbf{H} = \begin{bmatrix} 0 & l & 1-l \\ c^2 - \frac{\bar{Q}_1^2}{A^2} & 2\frac{\bar{Q}_1}{A} - u & 0 \\ c^2 - \frac{\bar{Q}_2^2}{A^2} & 0 & 2\frac{\bar{Q}_2}{A} - u \end{bmatrix}, \quad (8.41)$$

where $l = l_{\frac{3}{2}}$, $u = u_{x,\frac{3}{2}}$, $Q_1 = l\bar{Q}_1$ and $Q_2 = (1-l)\bar{Q}_2$. System (8.40) is identical to the quasi-linear strictly hyperbolic system obtained in [Audusse et al. 2011] for the two layers shallow water model with mass exchange. Therefore, the two layers system (8.39) is also strictly hyperbolic.

8.3.3 Multiring system of equations

In [Audusse et al. 2011], the authors have studied the hyperbolicity of the multilayer shallow water system with mass exchange. They performed numerous numerical tests showing that for a given number of layers, the multilayer system is hyperbolic when small shear flows are considered. In regions of high shear, some eigenvalues can become complex and lead to the development of a Kelvin-Helmoltz-like instability [Audusse et al. 2014]. This behavior is expected as the RNSP equations (8.1) are not a system of conservation laws. By analogy, this analysis is valid for the multiring system of equations (8.21) and we assume that in physiological conditions the multiring system (8.21) is hyperbolic.

8.4 Numerical methods

For simplicity, we rewrite system (8.21) in the following vectorial form:

$$\frac{\partial \mathbf{U}}{\partial t} + \frac{\partial}{\partial x} [\mathbf{F}(\mathbf{U})] = \mathbf{S}_M(\mathbf{U}) + \mathbf{S}_\nu(\mathbf{U}) + \mathbf{S}_T(\mathbf{U}), \quad (8.42)$$

where:

$$\mathbf{U} = \begin{bmatrix} A \\ Q_1 \\ \vdots \\ Q_{N_r} \end{bmatrix}, \quad \mathbf{F} = \begin{bmatrix} F_A \\ F_{Q_1} \\ \vdots \\ F_{Q_{N_r}} \end{bmatrix}, \quad (8.43)$$

and:

$$\mathbf{S}_M = \begin{bmatrix} 0 \\ S_{M,1} \\ \vdots \\ S_{M,N_r} \end{bmatrix}, \quad \mathbf{S}_\nu = \begin{bmatrix} 0 \\ S_{\nu,1} \\ \vdots \\ S_{\nu,N_r} \end{bmatrix}, \quad \mathbf{S}_T = S_T \begin{bmatrix} 0 \\ l_1 \\ \vdots \\ l_{N_r} \end{bmatrix}. \quad (8.44)$$

The structure of the multiring system of equation (8.42) as a system of balance laws naturally leads us to propose a *finite volume* numerical scheme to obtain an approximate solution of System (8.42). Doing so, we ensure that the numerical scheme is robust, conservative and shock-capturing and that the numerical solution is positive if the chosen numerical flux preserves the positivity of the solution.

8.4.1 Problem splitting

The first step towards obtaining a numerical approximation of the solution of System (8.42) in the *finite volume* framework is to discretize both the temporal and spatial domains. We use the same discretization as in Section 4.1 and divide the time domain using a constant time step Δt and the discrete times are defined as:

$$t^n = n\Delta t, \quad n \in \mathbb{N}. \quad (8.45)$$

We note $\mathbf{U}^n = \mathbf{U}(t^n)$. We then introduce a mesh in the axial direction and divide the length L of the artery in a series of cells C_i defined as:

$$C_i = \left[x_{i-\frac{1}{2}}, x_{i+\frac{1}{2}} \right] = [[i-1]\Delta x, i\Delta x], \quad \text{for } i = 1, \dots, N_x, \quad (8.46)$$

where Δx is the cell size, supposed constant for simplicity, and $L = N_x \Delta x$.

Finally, we discretize the multiring system of equations (8.42) using a time splitting method, similar to the one introduced in Section 4.1:

Convective subproblem

$$\frac{\mathbf{U}^* - \mathbf{U}^n}{\Delta t} + \frac{\partial}{\partial x} [\mathbf{F}(\mathbf{U}^n)] = \mathbf{S}_M(\mathbf{U}^n) + \mathbf{S}_T(\mathbf{U}^n). \quad (8.47)$$

Viscous (or reaction) subproblem

$$\frac{\mathbf{U}^{n+1} - \mathbf{U}^*}{\Delta t} = \mathbf{S}_\nu (\mathbf{U}^{n+1}). \quad (8.48)$$

Both the convective and viscous subproblems (resp. eq. (8.47) and (8.48)) are solved numerically in the following subsections.

8.4.2 Explicit convective numerical scheme

We first solve the convective system of equations (8.47) using an explicit *finite volume* scheme, which includes the mass exchange source term \mathbf{S}_M and the geometrical and mechanical source term \mathbf{S}_T .

Integrating System (8.47) over the cell C_i , we obtain the explicit *finite volume* scheme:

$$\frac{\mathbf{U}_i^* - \mathbf{U}_i^n}{\Delta t} + \frac{1}{\Delta x} \left[\mathbf{F}_{i+\frac{1}{2}}^n - \mathbf{F}_{i-\frac{1}{2}}^n \right] = \mathbf{S}_{M,i}^n + \mathbf{S}_{T,i}^n, \quad (8.49)$$

where \mathbf{U}_i^n is the space-average approximation of the vector \mathbf{U} in the cell C_i at the time t^n :

$$\mathbf{U}_i^n \approx \frac{1}{\Delta x} \int_{C_i} \mathbf{U}(x, t^n) dx. \quad (8.50)$$

The vector $\mathbf{F}_{i+\frac{1}{2}}^n$ is the two-points numerical flux vector, and corresponds to the numerical approximation of the flux vector \mathbf{F} at interface $x_{i+\frac{1}{2}}$ of the cell C_i at time t^n :

$$\mathbf{F}_{i+\frac{1}{2}}^n = \mathcal{F} \left(\mathbf{U}_{i+\frac{1}{2},L}^n, \mathbf{U}_{i+\frac{1}{2},R}^n \right) = \begin{bmatrix} \mathcal{F}_A \left(\mathbf{U}_{i+\frac{1}{2},L}^n, \mathbf{U}_{i+\frac{1}{2},R}^n \right) \\ \mathcal{F}_{Q_1} \left(\mathbf{U}_{i+\frac{1}{2},L}^n, \mathbf{U}_{i+\frac{1}{2},R}^n \right) \\ \vdots \\ \mathcal{F}_{Q_{N_r}} \left(\mathbf{U}_{i+\frac{1}{2},L}^n, \mathbf{U}_{i+\frac{1}{2},R}^n \right) \end{bmatrix}. \quad (8.51)$$

The flux \mathcal{F}_A can also be written as the sum of the contribution of each ring α :

$$\mathcal{F}_A \left(\mathbf{U}_{i+\frac{1}{2},L}^n, \mathbf{U}_{i+\frac{1}{2},R}^n \right) = \sum_{j=1}^{N_r} \mathcal{F}_{A_j} \left(\mathbf{U}_{i+\frac{1}{2},L}^n, \mathbf{U}_{i+\frac{1}{2},R}^n \right) \quad (8.52)$$

The choice of the vector function \mathcal{F} defines the numerical flux and thus the *finite volume* scheme. As we use only a first-order *finite volume* numerical scheme, the vectors $\mathbf{U}_{i+\frac{1}{2},L}^n$ and $\mathbf{U}_{i+\frac{1}{2},R}^n$ at the left and right of the interface $x_{i+\frac{1}{2}}$ of the cell C_i at time t^n are defined as:

$$\begin{cases} \mathbf{U}_{i+\frac{1}{2},L}^n = \mathbf{U}_i^n \\ \mathbf{U}_{i+\frac{1}{2},R}^n = \mathbf{U}_{i+1}^n. \end{cases} \quad (8.53)$$

The vectors $\mathbf{S}_{M,i}^n$ and $\mathbf{S}_{T,i}^n$ correspond respectively to the discretization of the mass exchange source term $\mathbf{S}_M(\mathbf{U}_i^n)$ and of the geometrical and mechanical source term $\mathbf{S}_T(\mathbf{U}_i^n)$ and will be specified in the following subsections.

Kinetic flux

As shown previously, there is no analytic expression for the eigenvalues of System (8.42). We therefore choose to use a kinetic flux function, which does not require the computation of the eigenstructure of System (8.42). Other approaches are possible, see [Fernández-Nieto et al. 2013; Audusse et al. 2014]. A review of the kinetic method applied to different systems of equations can be found in [Bouchut 1999] and more particularly to the 1D blood flow system in [Audebert et al. 2017b; Ghigo et al. 2017b] and in Subsection 4.2.1 and to the multilayer shallow water system with mass exchange in [Audusse et al. 2011].

In the following, we briefly present the derivation of the expression of the kinetic vector function \mathcal{F} for the multiring system of equations (8.42). This derivation is very similar to the one presented in Subsection 4.2.1.

According to kinetic theory, the vector function \mathcal{F} is defined as:

$$\mathcal{F}(\mathbf{U}_L, \mathbf{U}_R) = \mathcal{F}^+(\mathbf{U}_L) + \mathcal{F}^-(\mathbf{U}_R), \quad (8.54)$$

where $\mathcal{F}^+(U)$ and $\mathcal{F}^-(U)$ are:

$$\mathcal{F}^+(U) = \begin{bmatrix} \sum_{j=1}^{N_r} \mathcal{F}_{A_j}^+(U) \\ \mathcal{F}_{Q_1}^+(U) \\ \vdots \\ \mathcal{F}_{Q_{N_r}}^+(U) \end{bmatrix} \quad (8.55)$$

$$\mathcal{F}^-(U) = \begin{bmatrix} \sum_{j=1}^{N_r} \mathcal{F}_{A_j}^-(U) \\ \mathcal{F}_{Q_1}^-(U) \\ \vdots \\ \mathcal{F}_{Q_{N_r}}^-(U) \end{bmatrix}.$$

The fluxes $\mathcal{F}_{A_\alpha}^\pm(U)$ and $\mathcal{F}_{Q_\alpha}^\pm(U)$ in each ring α are defined as:

$$\begin{bmatrix} \mathcal{F}_{A_\alpha}^+(U) \\ \mathcal{F}_{Q_\alpha}^+(U) \end{bmatrix} = \int_{\xi \geq 0} \xi \begin{bmatrix} 1 \\ \xi \end{bmatrix} M_\alpha(A, \xi - u_\alpha) d\xi \quad (8.56)$$

$$\begin{bmatrix} \mathcal{F}_{A_\alpha}^-(U) \\ \mathcal{F}_{Q_\alpha}^-(U) \end{bmatrix} = \int_{\xi \leq 0} \xi \begin{bmatrix} 1 \\ \xi \end{bmatrix} M_\alpha(A, \xi - u_\alpha) d\xi.$$

The function M_α is the kinetic Maxwellian, or so-called *Gibbs equilibrium*, and represents a distribution function of the microscopic particle velocity $\xi \in \mathbb{R}$ in the ring α :

$$M_\alpha(A, \xi - u_\alpha) = \frac{l_\alpha A}{\tilde{c}} \chi\left(\frac{\xi - u_\alpha}{\tilde{c}}\right), \quad (8.57)$$

where:

$$\tilde{c} = \sqrt{\frac{K}{3\rho}} \sqrt{A}. \quad (8.58)$$

We choose the function χ as:

$$\chi(w) = \begin{cases} \frac{1}{2\sqrt{3}} & \text{if } |w| \leq \sqrt{3} \\ 0 & \text{else.} \end{cases} \quad (8.59)$$

Injecting the expressions of the functions χ and M_α in the definition of the fluxes (8.56), we obtain after some computation the expressions for the fluxes $\mathcal{F}_{A_\alpha}^\pm(U)$ and $\mathcal{F}_{Q_\alpha}^\pm(U)$ in each ring α :

$$\begin{bmatrix} \mathcal{F}_{A_\alpha}^+(U) \\ \mathcal{F}_{Q_\alpha}^+(U) \end{bmatrix} = \frac{l_\alpha A}{2\sqrt{3}\tilde{c}} \begin{bmatrix} \frac{1}{2} \left((\xi_{p,\alpha}^+)^2 - (\xi_{m,\alpha}^+)^2 \right) \\ \frac{1}{3} \left((\xi_{p,\alpha}^+)^3 - (\xi_{m,\alpha}^+)^3 \right) \end{bmatrix} \quad (8.60)$$

$$\begin{bmatrix} \mathcal{F}_{A_\alpha}^-(U) \\ \mathcal{F}_{Q_\alpha}^-(U) \end{bmatrix} = \frac{l_\alpha A}{2\sqrt{3}\tilde{c}} \begin{bmatrix} \frac{1}{2} \left((\xi_{p,\alpha}^-)^2 - (\xi_{m,\alpha}^-)^2 \right) \\ \frac{1}{3} \left((\xi_{p,\alpha}^-)^3 - (\xi_{m,\alpha}^-)^3 \right) \end{bmatrix},$$

with:

$$\begin{cases} \xi_{p,\alpha}^+ = \max(0, u_\alpha + \sqrt{3}\tilde{c}), & \xi_{m,\alpha}^+ = \max(0, u_\alpha - \sqrt{3}\tilde{c}) \\ \xi_{p,\alpha}^- = \min(0, u_\alpha + \sqrt{3}\tilde{c}), & \xi_{m,\alpha}^- = \min(0, u_\alpha - \sqrt{3}\tilde{c}). \end{cases} \quad (8.61)$$

Mass exchange source term

We define the discrete mass exchange source term $\mathbf{S}_{M,i}^n$ as:

$$\mathbf{S}_{M,i}^n = \begin{bmatrix} 0 \\ u_{\frac{3}{2},i}^n G_{\frac{3}{2},i}^n \\ \vdots \\ u_{\alpha+\frac{1}{2},i}^n G_{\alpha+\frac{1}{2},i}^n - u_{\alpha-\frac{1}{2},i}^n G_{\alpha-\frac{1}{2},i}^n \\ \vdots \\ -u_{N_r-\frac{1}{2},i}^n G_{N_r-\frac{1}{2},i}^n \end{bmatrix}. \quad (8.62)$$

Following [Audusse et al. 2011] and by analogy with expression (8.24), we compute $G_{\alpha+\frac{1}{2},i}^n$ in each ring α as:

$$G_{\alpha+\frac{1}{2},i}^n = \frac{1}{\Delta x} \sum_{j=1}^{\alpha} \left\{ \left[\mathcal{F}_{A_j} \left(\mathbf{U}_{i+\frac{1}{2},L}^n, \mathbf{U}_{i+\frac{1}{2},R}^n \right) - \mathcal{F}_{A_j} \left(\mathbf{U}_{i-\frac{1}{2},L}^n, \mathbf{U}_{i-\frac{1}{2},R}^n \right) \right] - l_j \left[\mathcal{F}_A \left(\mathbf{U}_{i+\frac{1}{2},L}^n, \mathbf{U}_{i+\frac{1}{2},R}^n \right) - \mathcal{F}_A \left(\mathbf{U}_{i-\frac{1}{2},L}^n, \mathbf{U}_{i-\frac{1}{2},R}^n \right) \right] \right\}. \quad (8.63)$$

We define $u_{\alpha+\frac{1}{2},i}^n$ in an upwind manner:

$$u_{\alpha+\frac{1}{2},i}^n = \begin{cases} u_{\alpha,i}^n & \text{if } G_{\alpha+\frac{1}{2},i}^n \leq 0 \\ u_{\alpha+1,i}^n & \text{if } G_{\alpha+\frac{1}{2},i}^n > 0. \end{cases} \quad (8.64)$$

This choice is motivated by the analysis of expression (8.10) for the mass exchange term $G_{\alpha+\frac{1}{2}}$. Indeed, $G_{\alpha+\frac{1}{2}} > 0$ if the cross-sectional area $\pi R_{\alpha+\frac{1}{2}}^2$ increases with time or if the interface velocity $u_{r,\alpha+\frac{1}{2}} < 0$. In both cases, from the perspective of the interface $R_{\alpha+\frac{1}{2}}$, the flow is coming from the upper ring $\alpha + 1$ and the upwind velocity is therefore $u_{\alpha+1}$.

Hydrostatic reconstruction of the source term \mathbf{S}_T

The considered kinetic flux function does not take into account the geometrical and mechanical source term \mathbf{S}_T , which results from axial variations of the neutral cross-sectional area A_0 or the arterial rigidity K . This source term must be treated using a well-balanced method to prevent spurious oscillations of the numerical solution close to steady states [Roe 1987; Bermúdez and Vázquez 1994; Gosse and LeRoux 1996; Greenberg and LeRoux 1996].

To that effect, we use the well-balanced hydrostatic reconstruction technique (HR) introduced in [Audusse and Bristeau 2005] for shallow water equations and discussed in Chapter 5. This technique was then applied to blood flow equations in [Delestre and Lagrée 2013; Delestre et al. 2016] and to the multilayer shallow water system with mass exchange in [Audusse et al. 2011]. Through a reconstruction of the conservative variables, HR allows to obtain a simple and efficient well-balanced numerical scheme given any *finite volume* numerical flux. We briefly recall the derivation of HR applied to the multiring system of equations (8.42).

We define the discrete geometrical and mechanical source term $\mathbf{S}_{T,i}^n$ as:

$$\mathbf{S}_{T,i}^n = S_{T,i}^n [0, l_1, \dots, l_{N_r}]^\top, \quad (8.65)$$

where $S_{T,i}^n$ is:

$$S_{T,i}^n = \frac{1}{3\rho\Delta x} \left[K_{i+\frac{1}{2}}^* \left[A_{i+\frac{1}{2},L}^{*n} \right]^{\frac{3}{2}} - K_{i+\frac{1}{2},L} \left[A_{i+\frac{1}{2},L}^n \right]^{\frac{3}{2}} - K_{i-\frac{1}{2}}^* \left[A_{i-\frac{1}{2},R}^{*n} \right]^{\frac{3}{2}} + K_{i-\frac{1}{2},R} \left[A_{i-\frac{1}{2},R}^n \right]^{\frac{3}{2}} \right]. \quad (8.66)$$

The reconstructed variables $A_{i+\frac{1}{2},L}^{*n}$, $A_{i+\frac{1}{2},R}^{*n}$ and $K_{i+\frac{1}{2}}^*$ are defined such that the steady states at rest are preserved as well as the positivity of the cross-sectional area A :

$$\begin{cases} A_{i+\frac{1}{2},L}^{*n} = \left(\frac{H_{i+\frac{1}{2},L}^{*n}}{K_{i+\frac{1}{2}}^*} \right)^2 \\ A_{i+\frac{1}{2},R}^{*n} = \left(\frac{H_{i+\frac{1}{2},R}^{*n}}{K_{i+\frac{1}{2}}^*} \right)^2 \\ K_{i+\frac{1}{2}}^* = \max \left(K_{i+\frac{1}{2},L}, K_{i+\frac{1}{2},R} \right), \end{cases} \quad (8.67)$$

with:

$$\begin{cases} H_{i+\frac{1}{2},L}^{*n} = \max \left(0, Z_{i+\frac{1}{2}}^* + \left[K\sqrt{A} \right]_{i+\frac{1}{2},L} - \left[K\sqrt{A_0} \right]_{i+\frac{1}{2},L} \right) \\ H_{i+\frac{1}{2},R}^{*n} = \max \left(0, Z_{i+\frac{1}{2}}^* + \left[K\sqrt{A} \right]_{i+\frac{1}{2},R} - \left[K\sqrt{A_0} \right]_{i+\frac{1}{2},R} \right) \\ Z_{i+\frac{1}{2}}^* = \min \left(\left[K\sqrt{A_0} \right]_{i+\frac{1}{2},L}, \left[K\sqrt{A_0} \right]_{i+\frac{1}{2},R} \right). \end{cases} \quad (8.68)$$

Finally, we obtain a well-balanced numerical scheme by replacing each occurrence of the conservative vectors $\mathbf{U}_{i+\frac{1}{2},L}^n$ and $\mathbf{U}_{i+\frac{1}{2},R}^n$ in the vector function \mathcal{F} by the reconstructed conservative vectors $\mathbf{U}_{i+\frac{1}{2},L}^{*n}$ and $\mathbf{U}_{i+\frac{1}{2},R}^{*n}$, defined as:

$$\mathbf{U}_{i+\frac{1}{2},L}^{*n} = \begin{bmatrix} A_{i+\frac{1}{2},L}^{*n} \\ Q_{1,i+\frac{1}{2},L}^n \\ \vdots \\ Q_{N_r,i+\frac{1}{2},L}^n \end{bmatrix}, \quad \mathbf{U}_{i+\frac{1}{2},R}^{*n} = \begin{bmatrix} A_{i+\frac{1}{2},R}^{*n} \\ Q_{1,i+\frac{1}{2},R}^n \\ \vdots \\ Q_{N_r,i+\frac{1}{2},R}^n \end{bmatrix}. \quad (8.69)$$

CFL condition

The stability of the convective numerical scheme is ensured if at each time t_n , the time step Δt verifies the following CFL (Courant, Friedrichs and Lewy) [Courant et al. 1967] condition:

$$\Delta t \leq \min_{i=1}^{N_x} \min_{j=1}^{N_r} \frac{l_j A_i^n \Delta x}{l_j A_i^n \left(|u_{j,i}^n| + \tilde{c}_i^n \right) + \Delta x \left(G_{j+\frac{1}{2},i}^n - G_{j-\frac{1}{2},i}^n \right)}. \quad (8.70)$$

This CFL condition ensures that the kinetic scheme preserves the positivity of the cross-sectional area A (for a detailed proof see [Audusse et al. 2011]). Note that it is more restrictive than the classical CFL condition used in 1D models as the flow can now exit the ring through both its axial and radial interfaces.

8.4.3 Implicit viscous numerical scheme

We now solve the viscous system of equations (8.48) using an implicit numerical scheme. The implicit form of the scheme is chosen for stability reasons.

Integrating System (8.48) over the cell C_i , we obtain the following implicit viscous numerical scheme:

$$\frac{\mathbf{U}_i^{n+1} - \mathbf{U}_i^*}{\Delta t} = \mathbf{S}_{\nu,i}^{n+1}, \quad (8.71)$$

where \mathbf{U}_i^* is the solution of the system of equations (8.49) and $\mathbf{S}_{\nu,i}^{n+1}$ is the discretization of

the viscous source term $\mathbf{S}_\nu(\mathbf{U}_i^{n+1})$ and writes:

$$\mathbf{S}_{\nu,i}^{n+1} = \begin{bmatrix} 0 \\ S_{\nu,1,i}^{n+1} \\ \vdots \\ S_{\nu,N_r,i}^{n+1} \end{bmatrix}. \quad (8.72)$$

In each ring α of the cell C_i at time t^{n+1} , we define $S_{\nu,\alpha,i}^{n+1}$ as the discrete analog of $S_{\nu,\alpha}$ (8.12). To compute $S_{\nu,\alpha,i}^{n+1}$, we use a centered *finite difference* discretization of the term $\left[r \frac{\partial u_x}{\partial r}\right]_{R_{\alpha+\frac{1}{2}}}$:

$$\left[r \frac{\partial u_x}{\partial r}\right]_{R_{\alpha+\frac{1}{2}}} = J_{r,\alpha} \left[u_{\alpha+1,i}^{n+1} - u_{\alpha,i}^{n+1} \right] \quad \text{for } \alpha = 1, \dots, N_r - 1, \quad (8.73)$$

where:

$$J_{r,\alpha} = 2 \frac{\sum_{j=1}^{\alpha} l_{r,j}}{l_{r,\alpha} + l_{r,\alpha+1}}. \quad (8.74)$$

At the interfaces $R_{\frac{1}{2}}$ and $R_{N_r+\frac{1}{2}}$, the previous discretization (8.73) of $r \partial_r u_x$ is not possible and the boundary conditions (8.17) and (8.19) must be taken into account. At the ring interface $r_{\frac{1}{2}}$, the axisymmetric boundary condition (8.17) imposes that:

$$\left[r \frac{\partial u_x}{\partial r}\right]_{R_{\frac{1}{2}}} = 0. \quad (8.75)$$

To express $[r \partial_r u_x]_{R_{N_r+\frac{1}{2}}}$ using only the conservative vector \mathbf{U} , we first perform the following asymptotic expansion of u_x in the ring N_r :

$$u_x(x, r, t) = u_x\left(x, R_{N_r+\frac{1}{2}}, t\right) + \left[r - R_{N_r+\frac{1}{2}}\right] \frac{\partial u_x}{\partial r} \Big|_{R_{N_r+\frac{1}{2}}} + O\left(\left[R_{N_r+\frac{1}{2}} - r\right]^2\right). \quad (8.76)$$

Neglecting the higher-order terms and using the no-slip boundary condition (8.19), we obtain the following expression:

$$u_x(x, r, t) \approx \left[r - R_{N_r+\frac{1}{2}}\right] \frac{\partial u_x}{\partial r} \Big|_{R_{N_r+\frac{1}{2}}}. \quad (8.77)$$

We then integrate the previous expression over the cross-sectional area of the ring N_r and we obtain:

$$\left[r \frac{\partial u_x}{\partial r}\right]_{R_{N_r+\frac{1}{2}}} = J_{r,\nu} \frac{Q_{N_r,i}^{n+1}}{A_i^{n+1}}, \quad (8.78)$$

with:

$$J_{r,\nu} = \frac{1}{-\frac{1}{3} + [1 - l_{r,N_r}]^2 - \frac{2}{3} [1 - l_{r,N_r}]^3}. \quad (8.79)$$

It is important to note that the discretization (8.78) of $\left[r \frac{\partial u_x}{\partial r}\right]_{R_{N_r+\frac{1}{2}}}$ imposes the no-slip boundary condition (8.19) at the wall, which is the natural boundary condition for viscous flows.

Finally, noticing that the first component of the source term \mathbf{S}_ν is zero, we obtain the following trivial solution of the system of equations (8.48) for the first component of \mathbf{U}_i^{n+1} :

$$A_i^{n+1} = A_i^*, \quad \text{for } i = 1, \dots, N_x. \quad (8.80)$$

We can therefore rewrite the implicit viscous scheme (8.71) in the following matrix form:

$$[\mathbf{I} + \Delta t \mathbf{M}_{\nu,i}^*] \cdot [Q_{1,i}^{n+1}, \dots, Q_{\alpha,i}^{n+1}, \dots, Q_{N_r,i}^{n+1}]^\top = [Q_{1,i}^*, \dots, Q_{\alpha,i}^*, \dots, Q_{N_r,i}^*]^\top, \quad (8.81)$$

where \mathbf{I} is the identity matrix and $\mathbf{M}_{\nu,i}^*$ is the following tridiagonal matrix:

$$\mathbf{M}_{\nu,i}^* = \frac{2\pi\nu}{A_i^*} \begin{bmatrix} \frac{J_{r,1}}{l_1} & -\frac{J_{r,1}}{l_2} & 0 & \cdots & 0 \\ \ddots & \ddots & \ddots & \ddots & \vdots \\ 0 & -\frac{J_{r,\alpha-1}}{l_{\alpha-1}} & \frac{J_{r,\alpha-1}+J_{r,\alpha}}{l_\alpha} & -\frac{J_{r,\alpha}}{l_{\alpha+1}} & 0 \\ \vdots & \ddots & \ddots & \ddots & \ddots \\ 0 & \cdots & 0 & -\frac{J_{r,N_r-1}}{l_{N_r-1}} & \frac{J_{r,N_r-1}}{l_{N_r}} - J_{r,\nu} \end{bmatrix}. \quad (8.82)$$

We then invert the System (8.81) using the Thomas algorithm [Thomas 1949], well-suited for solving tridiagonal matrix systems.

Next, we provide algorithms to impose classical inlet and outlet boundary conditions for blood flow.

8.5 Boundary conditions

As we compute subcritical solutions of System (8.21), boundary conditions are required at both ends of the computational domain, in the inlet and outlet ghost cells of the artery, respectively noted C_{in} and C_{out} . In both cells C_{in} and C_{out} , the corresponding conservative vectors \mathbf{U}_{in}^n and \mathbf{U}_{out}^n must be prescribed in order to update the numerical solution from time t^n to time t^{n+1} in each cell C_i of the computational domain. We propose here algorithms to impose boundary conditions in the inlet and outlet ghost cells of the artery. As the implementation of inlet and outlet boundary conditions is very similar, we describe only the derivation of the inlet boundary conditions.

8.5.1 Imposed flow rate

We wish to impose the flow rate $Q_{e,\alpha}^n$ at the interface between the first cell C_1 and the inlet ghost cell C_{in} of each ring α , namely:

$$\mathcal{F}_{A_\alpha}(\mathbf{U}_{in}^n, \mathbf{U}_1^n) = Q_{e,\alpha}^n \quad \text{for } \alpha = 1, \dots, N_r. \quad (8.83)$$

Following the methodology proposed in [Bristeau and Coussin 2001] and taking advantage of the fact that the kinetic flux function \mathcal{F}_{A_α} can be split in two, Equation (8.83) can be expressed as:

$$\mathcal{F}_{A_\alpha}^+(\mathbf{U}_{in}^n) + \mathcal{F}_{A_\alpha}^-(\mathbf{U}_1^n) = Q_{e,\alpha}^n \quad \text{for } \alpha = 1, \dots, N_r. \quad (8.84)$$

To ensure the stability of the scheme, the condition (8.84) in each ring α is imposed in an upwind manner. Consequently, we define the quantity:

$$a = \sum_{\alpha=1}^{N_r} Q_{e,\alpha}^n - \mathcal{F}_{A_\alpha}^-(\mathbf{U}_1^n), \quad (8.85)$$

and distinguish two cases:

- If $a \leq 0$, the dominant part of the information is coming from inside the computational domain. As we are performing an upwind evaluation of the inlet boundary condition, we impose:

$$\begin{aligned} \mathcal{F}_A^+(\mathbf{U}_{in}^n) &= 0 \\ \mathcal{F}_{Q_\alpha}^+(\mathbf{U}_{in}^n) &= 0 \quad \text{for } \alpha = 1, \dots, N_r. \end{aligned} \quad (8.86)$$

- If $a > 0$, the dominant part of the information is coming from outside the computational domain. In this case, we impose:

$$\begin{aligned} \mathcal{F}_{A_\alpha}^+(\mathbf{U}_{in}^n) &= Q_{e,\alpha}^n - \mathcal{F}_{A_\alpha}^-(\mathbf{U}_1^n) \quad \text{for } \alpha = 1, \dots, N_r \\ W_1(\mathbf{U}_{in}^n) &= W_1(\mathbf{U}_1^n). \end{aligned} \quad (8.87)$$

$W_1(\mathbf{U})$ is the 1D analog of the Riemann invariant $W_{1,\alpha}(\mathbf{U})$ in the ring α and characterizes the global outgoing characteristic. It writes:

$$W_1 = \frac{\sum_{\alpha=1}^{N_r} Q_\alpha}{A} - c. \quad (8.88)$$

Similarly, we write $W_2(\mathbf{U})$ as:

$$W_2 = \frac{\sum_{\alpha=1}^{N_r} Q_\alpha}{A} + c. \quad (8.89)$$

\mathbf{U}_{in}^n is obtained by solving either System (8.86) or System (8.87). This can be done using a classic Newton's method in a limited number of iterations.

8.5.2 Imposed cross-sectional area

We wish to impose the cross-sectional area A_e^n in the inlet ghost cell C_{in} . Therefore, we set:

$$A_{in}^n = A_e^n. \quad (8.90)$$

To completely determine the inlet vector of conservative variables \mathbf{U}_{in}^n , we estimate the outgoing Riemann invariant $W_{1,\alpha}(\mathbf{U}_{in}^n)$ in the ring α as:

$$W_{1,\alpha}(\mathbf{U}_{in}^n) = W_{1,\alpha}(\mathbf{U}_1^n) \quad \text{for } \alpha = 1, \dots, N_r, \quad (8.91)$$

and using Equation (8.37) and Equation (8.38), we compute $W_{2,\alpha}(\mathbf{U}_{in}^n)$ and then $Q_{in,\alpha}^n$ in each ring α :

$$\begin{cases} W_{2,\alpha}(\mathbf{U}_{in}^n) = W_{1,\alpha}(\mathbf{U}_{in}^n) + 8c_{in}^n \\ Q_{in,\alpha}^n = l_\alpha A_{in}^n \frac{W_{1,\alpha}(\mathbf{U}_{in}^n) + W_{2,\alpha}(\mathbf{U}_{in}^n)}{2}. \end{cases} \quad (8.92)$$

8.5.3 Imposed reflection coefficient

We wish to impose the reflection coefficient R_t in the inlet ghost cell C_{in} . The inlet reflection coefficient R_t is defined as:

$$W_2(\mathbf{U}_{in}^n) - W_2(\mathbf{U}_{in}^0) = -R_t [W_1(\mathbf{U}_{in}^n) - W_1(\mathbf{U}_{in}^0)], \quad (8.93)$$

and characterizes the proportion of the outgoing information reflected back into the computational domain. When we wish to remove any reflection of the outgoing information, we set $R_t = 0$. We first estimate the outgoing Riemann invariant $W_1(\mathbf{U}_{in}^n)$ as:

$$W_1(\mathbf{U}_{in}^n) = W_1(\mathbf{U}_1^n), \quad (8.94)$$

and using Equation (8.93), we compute $W_2(\mathbf{U}_{in}^n)$ and then A_{in}^n :

$$A_{in}^n = \left(\frac{2\rho}{K_{in}} \right)^2 \left(\frac{W_2(\mathbf{U}_{in}^n) - W_1(\mathbf{U}_{in}^n)}{8} \right)^4. \quad (8.95)$$

Finally, we use the algorithm presented in the previous subsection to completely determine the inlet vector of conservative variables \mathbf{U}_{in}^n .

In the following sections, we perform a series of numerical tests to validate the multiring model (8.21), the numerical scheme and the boundary conditions previously described.

8.6 Linear examples in an elastic artery

8.6.1 The Womersley solution

In [Womersley 1955], Womersley proposed an analytic harmonic solution of the linearized Navier-Stokes equations which is also a solution of the linearized RNSP equations (8.1). The Womersley solution is an important test case for numerical methods simulating blood flow in elastic arteries as it includes pulsatile effects, elastic deformation of the arterial wall and viscous dissipation. In [Lagrée 2000; Casulli et al. 2012; Dumbser et al. 2015], the authors

used the Womersley solution in a rigid axisymmetric tube to validate their numerical method. In this section, we compute the Womersley solution in an elastic artery as a first validation case of the multiring model (8.21). For a detailed description of the Womersley solution, see Subsection 2.4.2.

We consider a straight artery initially at rest:

$$\begin{cases} A(x, t = 0) = A_0 \\ Q_\alpha(x, t = 0) = 0 \quad \text{for } \alpha = 1, \dots, N_r. \end{cases} \quad (8.96)$$

We impose at the inlet a sinusoidal oscillation of the pressure:

$$p(x = 0, t) = \hat{p} \sin \left[2\pi \frac{t}{T_c} \right], \quad \hat{p} = \sqrt{\pi} K \hat{R}, \quad (8.97)$$

and at the outlet a zero reflection coefficient R_t to remove any backward traveling waves. The values of the geometrical and mechanical parameters describing the artery as well as those describing the inlet and outlet boundary conditions are presented in Table 8.1. The final time t_f is large enough to reach a periodic regime. The geometrical and mechanical parameters mimic physiological conditions and the value of \hat{R} is small enough such that the linear approximation required to obtain the Womersley solution is valid.

L	R_0	K	ρ	μ	\hat{R}	R_t	T_c	t_f	α
200	1	10^4	1	$2\pi \frac{\rho}{T_c} \frac{R_0^2}{\alpha^2}$	10^{-3}	0	0.5	$12T_c$	{5, 20}

Table 8.1 – Geometrical and mechanical parameters describing the artery and the inlet and outlet boundary conditions for the elastic Womersley example.

For the sake of illustration, we consider only two different Womersley numbers, $\alpha = 5$ and $\alpha = 20$, chosen to respectively represent flow conditions in small and large arteries. At small Womersley numbers ($\alpha = 5$), the viscous effect dominates, whereas at large Womersley numbers ($\alpha = 20$) the unsteady advection effect is dominant.

In Figure 8.2, we plot the velocity profiles obtained in $x = 25$ at $t \in \{0.2, 0.4, 0.5, 0.7\} T_c + 11T_c$ for $\alpha = 5$ (Figure 8.2 Left) and $\alpha = 20$ (Figure 8.2 Right). We use $N_x = 1600$ cells and $N_r = 128$ rings. We observe that in both cases ($\alpha = 5$ and $\alpha = 20$) the Womersley and the multiring solutions are in good accord for each recorded time. Small discrepancies between both solutions appear near the maximums of the velocity due to the numerical dissipation of the kinetic scheme and the nonlinearity of the numerical solutions.

In Figure 8.3, we represent the spatial evolution of the flow rate Q , the pressure p and the wall shear stress (WSS) τ_w obtained at time $t = 0.3T_c + 11T_c$ for $\alpha = 5$ (Figure 8.3 Left) and $\alpha = 20$ (Figure 8.3 Right). Once again, we use $N_x = 1600$ cells and $N_r = 128$ rings. For $\alpha = 20$, the Womersley and the multiring solutions overlap except at the local maximums and minimums of Q , p and τ_w , which are slightly dissipated by the numerical viscosity of the scheme. For $\alpha = 5$, both solutions match almost perfectly as the viscous dissipation is much larger than the numerical dissipation.

Next, we perform a convergence analysis in both the number of cells N_x and the number of rings N_r . In Figure 8.4, we plot the L_2 spatial error between the Womersley and the multiring solutions as a function of the dimensionless number of cells $\bar{N}_x = \lambda N_x / L$, where λ is the wavelength of the pressure pulse, and of the dimensionless number of rings $\bar{N}_r = N_r / \alpha$ for $\alpha = 5$ (Figure 8.4 Left) and $\alpha = 20$ (Figure 8.4 Right). We focus only on the flow rate Q and the WSS τ_w taken at time $t = 0.3T_c + 11T_c$. For both $\alpha = 5$ and $\alpha = 20$, we observe that increasing \bar{N}_x or \bar{N}_r is not equivalent. For low values of \bar{N}_x , increasing \bar{N}_r does not decrease the error significantly, whereas increasing \bar{N}_x does. On the contrary, for high values of \bar{N}_x , increasing \bar{N}_r significantly decreases the error, whereas increasing \bar{N}_x does not. This

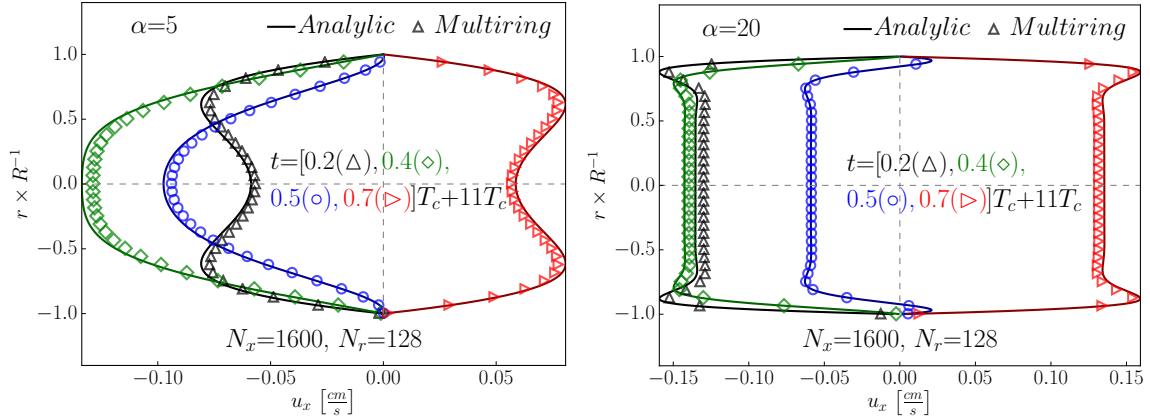


Figure 8.2 – Comparison between the velocity profiles obtained with the analytic Womersley solution (—) and with the multiring model using $N_x = 1600$ cells and $N_r = 128$ rings in $x = 25$ at times $t \in \{0.2(\Delta), 0.4(\diamond), 0.5(\circ), 0.7(\triangleright)\}T_c + 11T_c$.

Left: $\alpha = 5$.

Right: $\alpha = 20$.

We observe that the multiring solution agrees well with the analytic Womersley solution.

behavior is expected as wave propagation in the axial direction is the dominant physical mechanism of the Womersley solution and can only be captured if a sufficient number of cells \bar{N}_x is used. Only once a sufficient number of cells \bar{N}_x is used can we increase the number of rings \bar{N}_r to compute in detail the velocity profile. However, the behavior of the WSS τ_w for $\alpha = 20$ is different from the behavior of the other quantities. Indeed, the effect of increasing the number of rings \bar{N}_r for low values of \bar{N}_x is more significant than for the other quantities. This is due to the fact that for $\alpha = 20$, the boundary layer is thin, therefore increasing \bar{N}_r immediately allows to better capture the viscous behavior of the flow and therefore the WSS τ_w . As a rule of thumbs, we observe that $\bar{N}_x = 500$ and $\bar{N}_r = 2$ is the minimum mesh and ring refinements to obtain an accurate description of the Womersley solution.

To conclude this analysis, we study three additional flow configurations where we increase the nonlinearity of the elastic Womersley solution by changing the amplitude of the wall perturbation \hat{R} . We choose $\hat{R} \in \{10^{-3}, 10^{-2}, 10^{-1}, 3 \times 10^{-1}\}$. In Figure 8.5, we plot snapshots of the spatial evolution of the axial velocity profile u_x in the artery at time $t = 0.3T_c + 11T_c$ obtained for $\alpha = 20$ and using $N_x = 1600$ cells and $N_r = 128$ rings. The values of the other geometrical and mechanical parameters describing the artery are identical to those of Table 8.1. We observe that the multiring model (8.21) is able to compute with identical computational costs linear and nonlinear flow behaviors with small and large deformations of the arterial wall.

8.6.2 The steady linear elastic Poiseuille solution

In [Fung 2013], the author proposed a steady analytic solution of the linearized RNSP equations (8.1) in an elastic artery. As the Poiseuille solution, it describes the steady balance between the pressure gradient and the viscous radial dissipation term and is presented in Subsection 2.4.1. In [Casulli et al. 2012; Dumbser et al. 2015], the authors used this solution to validate their numerical code solving the axisymmetric RNSP equations (8.1). We reproduce here this solution using the multiring model (8.21).

We consider a straight artery initially at rest. We impose the pressure gradient by setting at the inlet and outlet constant pressures consistent with the analytic solution (2.46):

$$\begin{cases} p(x=0) = p_0 + \sqrt{\pi}KR_0\hat{R} \\ p(x=L) = p_0 - \sqrt{\pi}KR_0\hat{R}. \end{cases} \quad (8.98)$$

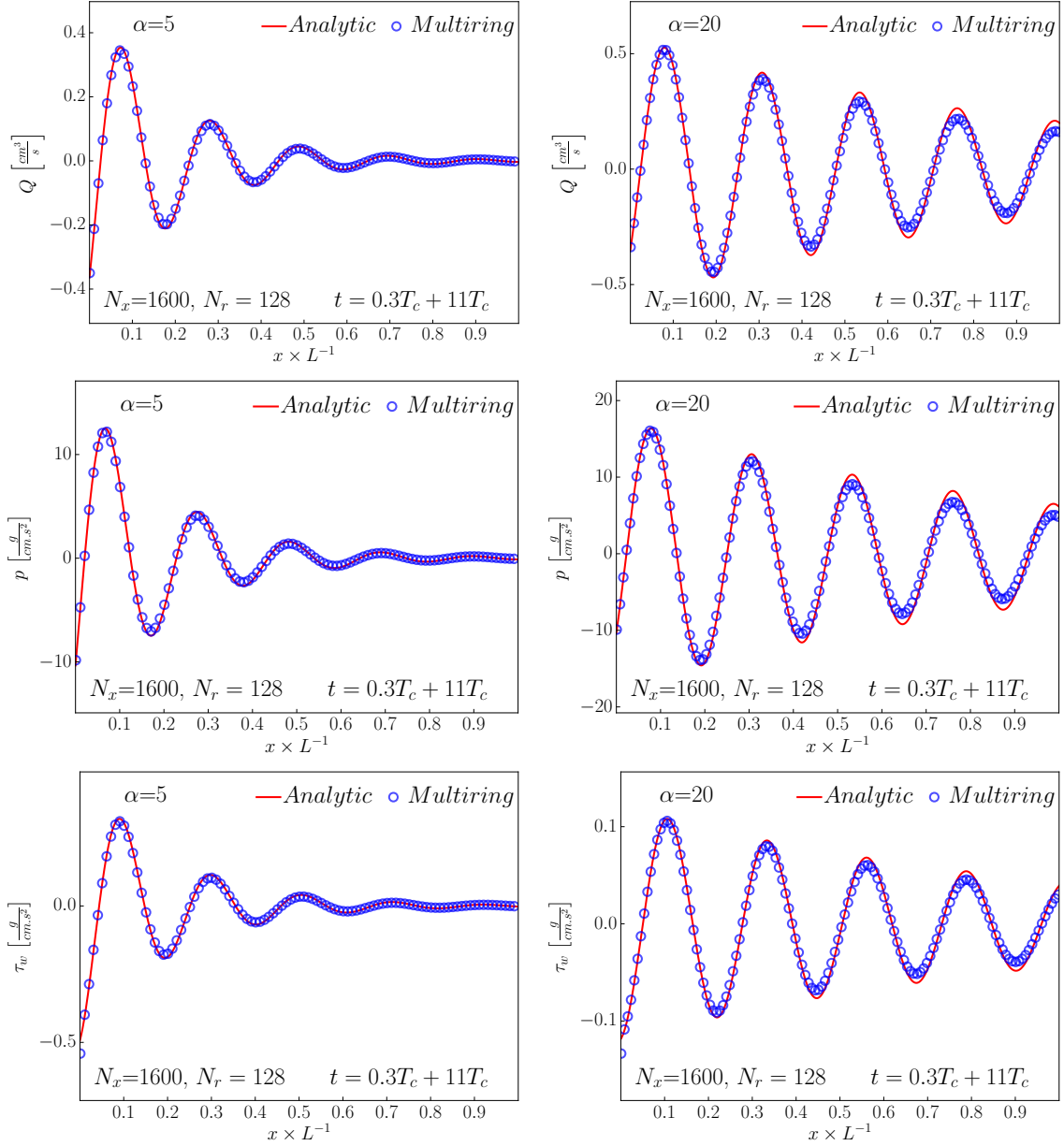


Figure 8.3 – Comparison between the flow rate Q , the pressure p and the WSS τ_w obtained with the analytic Womersley solution (—) and with the multiring model (○) using $N_x = 1600$ cells and $N_r = 128$ rings, at time $t = 0.3T_c + 11T_c$.

Left: $\alpha = 5$.

Right: $\alpha = 20$.

We observe that the multiring solutions agree well with the analytic solutions.

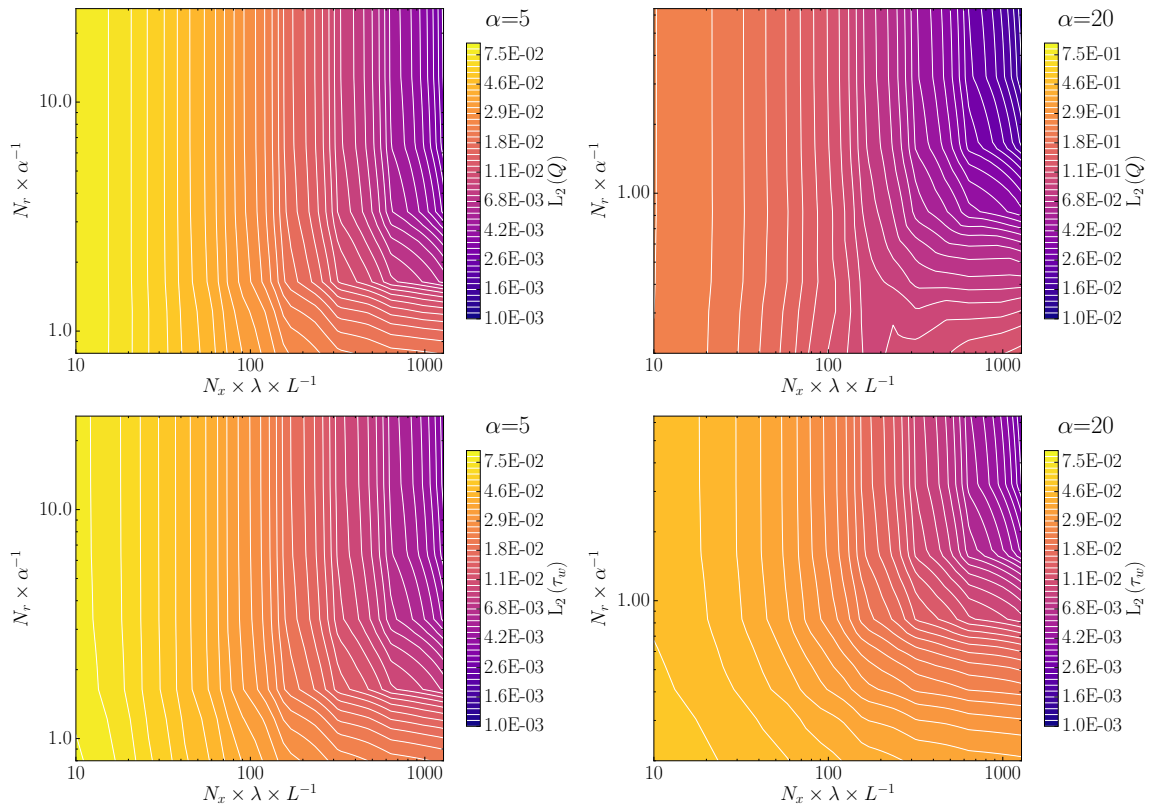


Figure 8.4 – Phase diagram of the L_2 spatial error between the Womersley and the multiring solutions as a function of $\lambda N_x/L$ and of N_r/α at time $t = 0.3T_c + 11T_c$.

Left: $\alpha = 5$.

Right: $\alpha = 20$.

Top: Flow rate Q .

Bottom: WSS τ_w .

For low values of $\lambda N_x/L$, increasing N_r/α does not decrease the error significantly, whereas increasing $\lambda N_x/L$ does. On the contrary, for high values of $\lambda N_x/L$, increasing N_r/α significantly decreases the error, whereas increasing $\lambda N_x/L$ does not.

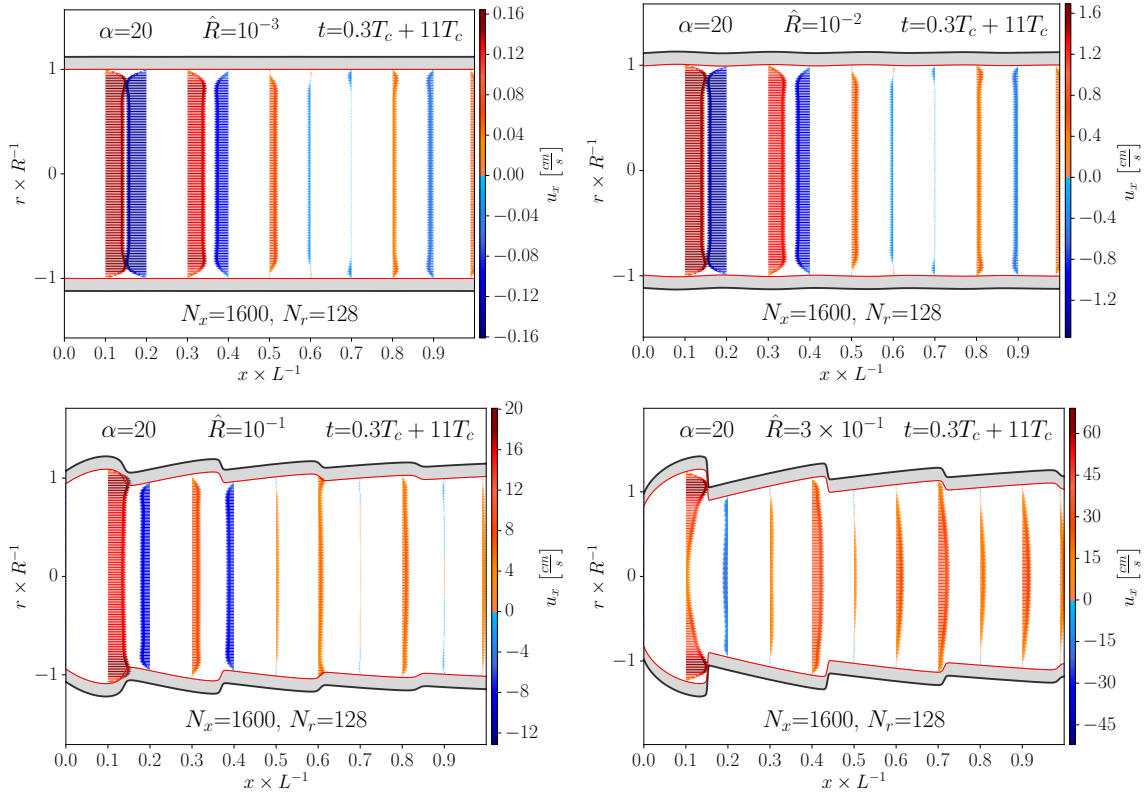


Figure 8.5 – Snapshots of the spatial evolution of the axial velocity u_x at $t = 0.3T_c + 11T_c$ obtained using $N_x = 1600$ cells and $N_r = 128$ rings for $\alpha = 20$.

Top: $\hat{R} \in \{10^{-3}, 10^{-2}\}$.

Bottom: $\hat{R} \in \{10^{-1}, 3 \times 10^{-1}\}$.

We observe that the multiring model is able to compute linear and nonlinear flow behaviors with small and large wall deformations.

For simplicity we set $p_0 = 0$. The values of the geometrical and mechanical parameters describing the artery as well as those describing the inlet and outlet boundary conditions are presented in Table 8.2. The final time t_f is large enough to reach a steady flow regime and the value of \hat{R} is small enough such that the linear approximation required to obtain the elastic Poiseuille solution is valid.

L	R_0	K	ρ	μ	\hat{R}	t_f
10	1	$\frac{10^2}{\sqrt{\pi}}$	1	1	10^{-1}	20

Table 8.2 – Geometrical and mechanical parameters describing the artery and the inlet and outlet boundary conditions for the steady linear elastic Poiseuille example.

In Figure 8.6, we plot the spatial evolution of the steady radius R (Figure 8.6 Left) and the steady axial velocity profiles taken in $x \in \{0, 0.2, 0.4, 0.6, 0.8, 0.99\}L$ (Figure 8.6 Right). We use $N_x = 800$ cells and $N_r = 64$ rings. We observe that for each recorded point the steady multiring numerical solution is in agreement with the steady analytic solution.

As this analytic solution is smooth enough, we perform a convergence analysis to determine the order of accuracy of the scheme. We consider the following mesh refinements $[N_x, N_r] \in \{[100, 8], [200, 16], [400, 32], [800, 64]\}$ and focus only on the radius R for simplicity. In Table 8.3, we compute the L_1 , L_2 and L_∞ spatial errors between the analytic solution (2.46) and the steady numerical solution for the radius R . We observe that the numerical solution converges at order 1, which is the expected order of convergence.

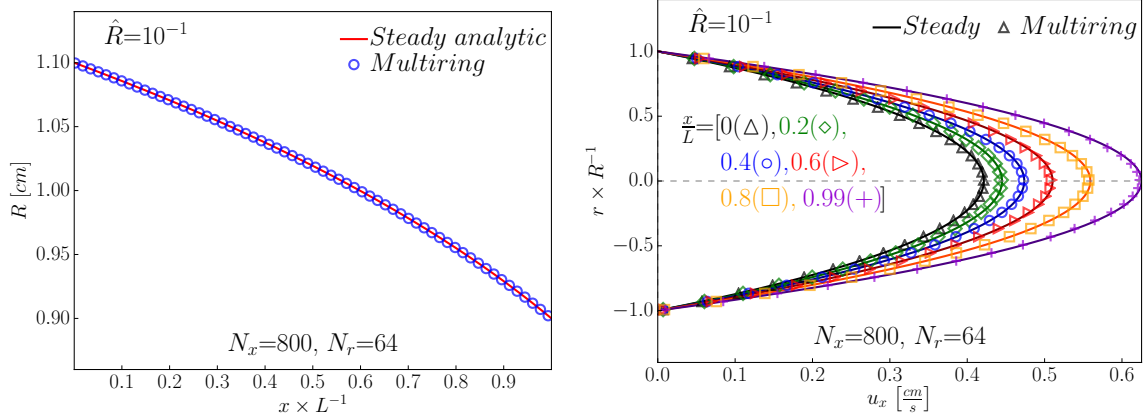


Figure 8.6 – Comparison between the steady analytic Poiseuille solution (—) and the multiring solution (marks) using $N_x = 800$ cells and $N_r = 64$ rings.

Left: Steady radius R .

Right: Steady axial velocity profiles u_x taken in $x \in \{0 (\Delta), 0.2 (\diamond), 0.4 (\circ), 0.6 (\triangleright), 0.8 (\square), 0.99 (+)\}L$.

We observe a good agreement between the analytic and the multiring numerical solutions.

N_x	N_r	$L_1(R)$	$O_{L_1(R)}$	$L_2(R)$	$O_{L_2(R)}$	$L_\infty(R)$	$O_{L_\infty(R)}$
100	8	1.29×10^{-3}	-	7.35×10^{-4}	-	5.36×10^{-4}	-
200	16	5.93×10^{-4}	-0.56	3.37×10^{-4}	-0.56	2.46×10^{-4}	-0.56
400	32	2.25×10^{-4}	-0.70	1.27×10^{-4}	-0.70	9.33×10^{-5}	-0.70
800	64	4.54×10^{-5}	-1.15	2.49×10^{-5}	-1.18	2.05×10^{-5}	-1.09

Table 8.3 – L_1 , L_2 and L_∞ spatial errors between the steady analytic solution (2.46) and the steady multiring numerical solution for the radius R obtain using $[N_x, N_r] \in \{[100, 8], [200, 16], [400, 32], [800, 64]\}$ cells and rings. We observe that the numerical solution converges at order 1, which is the expected order of convergence.

In the two previous examples, we have shown that the multiring model (8.21) is able to accurately capture steady and unsteady linear blood flow in a straight artery. We are therefore confident that the multiring model (8.21) can compute all relevant linear flow features encountered in large straight axisymmetric elastic arteries. However, the RNSP system of equations (8.1) is a rich dynamical system and is not limited to describing linear harmonic and steady solutions in elastic arteries. In the following sections, we will continue to validate the multiring model, the numerical scheme and the boundary conditions using nonlinear steady examples in rigid arteries with varying geometrical and mechanical properties.

8.7 Nonlinear examples in a rigid artery

8.7.1 Nonlinear transition from a flat to a Poiseuille velocity profile

In [Lagrée and Lorthois 2005], the authors studied the behavior of the RNSP system of equations (8.1) when computing steady flows in a rigid axisymmetric cylinder. They showed that it is able to describe the steady spatial transition from the Blasius [Schlichting 1968] to the Poiseuille flow regime, starting from a flat velocity profile at the inlet and evolving towards a fully developed Poiseuille velocity profile at the outlet. We reproduce here this phenomenon using the multiring model (8.21). The relevant dimensionless number in this

example is the Reynolds number $R_{e,R}$, defined as:

$$R_{e,R} = \frac{u_{x|x=0} R_{|x=0}}{\nu}, \quad (8.99)$$

and used to determine the relevant length and time scales in order to observe the steady spatial transition from the Blasius to the Poiseuille flow regime. Details on the determination of these scales can be found in [Lagrée and Lorthois 2005].

We consider a straight artery initially at rest. We impose at the inlet a steady velocity profile. We can not impose a flat velocity profile as it is not compatible with the no-slip boundary condition at the wall (8.19). Therefore we impose at the inlet a Von Kármán-Pohlhausen velocity profile [Pohlhausen 1921], describing a fourth-order approximation of the axial velocity profile in the viscous boundary layer:

$$u_x(x=0, r, t) = U_{in} \phi_{Pohlhausen}(r), \quad (8.100)$$

where:

$$\phi_{Pohlhausen}(r) = \begin{cases} \frac{1 - [1 - \eta]^3 [1 + [1 + \frac{\Delta}{6}] \eta]}{\frac{1}{30} [30 - 3 [6 + \frac{\Delta}{6}] \delta_{BL} + [4 + \frac{\Delta}{6}] \delta_{BL}^2]} & \text{if } \eta < 1 \\ \frac{1}{\frac{1}{30} [30 - 3 [6 + \frac{\Delta}{6}] \delta_{BL} + [4 + \frac{\Delta}{6}] \delta_{BL}^2]} & \text{if } \eta \geq 1, \end{cases} \quad (8.101)$$

with $\Delta = 12$ and $\eta = [1 - \frac{r}{R(x,t)}] / \delta_{BL}$. The parameter δ_{BL} is the estimated width of the boundary layer, that we choose here equal to $\delta_{BL} = l_{r,N_r} + l_{r,N_r-1}$. We impose at the outlet a zero reflection coefficient R_t to remove any backward traveling waves. The values of the geometrical and mechanical parameters describing the artery as well as those describing the inlet and outlet boundary conditions are presented in Table 8.4. The final time t_f is large enough to reach a steady flow regime. The geometrical and mechanical parameters mimic physiological conditions at the root of the aorta, where $R_{e,R} \approx 100$.

L	R_0	K	ρ	μ	U_{in}	R_t	t_f	$R_{e,R}$
$0.25 R_{e,R} R_{ x=0}$	1	10^7	1	$\rho \frac{U_{in} R_{ x=0}}{R_{e,R}}$	100	0	$0.5 \frac{R_{e,R} R_{ x=0}}{U_{in}}$	100

Table 8.4 – Geometrical and mechanical parameters describing the artery and the inlet and outlet boundary conditions for the steady rigid Poiseuille example.

As the multiring model (8.21) is intrinsically elastic, it is not possible to exactly simulate the flow of blood in a rigid cylinder. Nevertheless, by artificially increasing the arterial wall rigidity K (here $K = 10^7$), we penalize the wall's displacement and place ourselves in a quasi-rigid wall configuration.

To assess the quality of the multiring numerical results, we compare them to those of the steady numerical code presented in [Lagrée and Lorthois 2005]. This steady code was used to solve the steady RNSP system of equations (8.1) in a rigid tube and compared well with the results of an integral interactive boundary layer (IBL) code. In the following examples, all results of the steady code used as reference solutions are obtained using $N_x = 50000$ cells in the axial direction and $N_r = 1000$ cells in the radial direction, which is a very fine mesh.

In Figure 8.7, we plot the steady spatial evolution of the centerline velocity $u_{x|r=0}$ (Figure 8.7 Left) and of the pressure p (Figure 8.7 Right). We use $N_x \in \{800, 1600, 3200\}$ cells and $N_r = 32$ rings. We observe that as we increase the number of cells N_x , the steady multiring numerical solution converges towards the steady numerical solution and is able to describe the spatial transition from a flat velocity profile to a Poiseuille velocity profile. The number of cells N_x required to match the steady solution is relatively high due to the numerical dissipation of the kinetic scheme and since the transition from of flat to a Poiseuille velocity

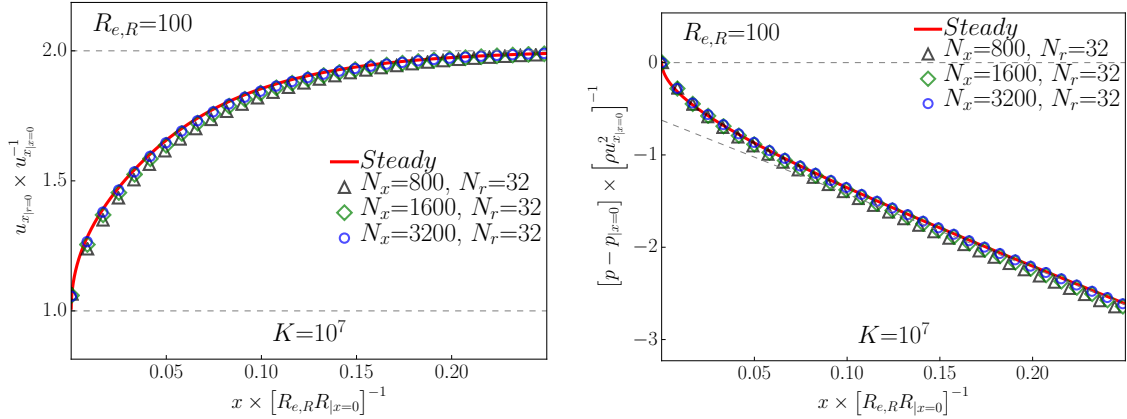


Figure 8.7 – Comparison between steady Poiseuille solutions obtained with the steady code [Lagrée and Lorthois 2005] (—) and with the multiring model using $N_x \in \{800 (\triangle), 1600 (\diamond), 3200 (\circ)\}$ cells and $N_r = 32$ rings.

Left: Steady centerline velocity $u_{x|r=0}$. The dashed lines represent the value of the flat centerline velocity ($u_{x|r=0} = u_{x|x=0}$) and the Poiseuille centerline velocity ($u_{x|r=0} = 2u_{x|x=0}$).

Right: Steady pressure p . The dashed line represents the pressure drop $-8x / (R_{e,R}R_{|x=0})$ of a Poiseuille flow.

For each quantity, the steady multiring numerical solution converges towards the steady numerical solution and we observe the transition from a flat to a Poiseuille velocity profile.

profile is a nonlinear phenomenon occurring on a short length scale (between $x = 0$ and $x = 0.15R_{e,R}R_{|x=0}$).

In Figure 8.8, we represent the steady velocity profiles taken in $x \in \{0.005, 0.01, 0.025, 0.05, 0.1, 0.2\}R_{e,R}R_{|x=0}$. We use $N_x \in \{800, 3200\}$ cells and $N_r = 32$ rings. For each recorded position, the steady multiring numerical velocity profiles converge towards the steady numerical velocity profiles as we increase the number of cells N_x . These results are coherent with the results presented in Figure 8.7.

8.7.2 Rigid wall stenosis and aneurysm

Stenoses and aneurysms are commonly encountered pathologies and correspond respectively to local constrictions and expansions of the neutral radius of the artery. The flow patterns in rigid stenoses and aneurysms have been studied by many authors [Wille 1981; Wille and Walløe 1981; Perktold 1987; Deplano and Siouffi 1999; Di Achille et al. 2014; Zaman et al. 2015; Wang et al. 2016a]. In [Lagrée and Lorthois 2005], the authors computed the numerical solution of the steady RNSP system of equations (8.1) in an axisymmetric rigid artery presenting a stenosis. They used the steady code presented in the previous section and were able to compute flow recirculations in case of severe stenoses. We use here the multiring model (8.21) to compute the steady flow in a rigid stenosis and in a rigid aneurysm. As in the previous section, the relevant dimensionless number is the Reynolds number $R_{e,R}$ (8.99).

We consider an artery initially at rest (eq. (8.96)). We impose at the inlet a steady Poiseuille velocity profile:

$$u_x(x=0, r, t) = 2U_{in} \left[1 - \frac{r^2}{R(x, t)^2} \right], \quad (8.102)$$

and at the outlet a zero reflection coefficient R_t to remove any backward traveling waves. The values of the geometrical and mechanical parameters describing the artery as well as those describing the inlet and outlet boundary conditions are presented in Table 8.5. The final time t_f is large enough to reach a steady flow regime. The geometrical and mechanical parameters mimic physiological conditions at the root of the aorta, where $R_{e,R} \approx 100$. The

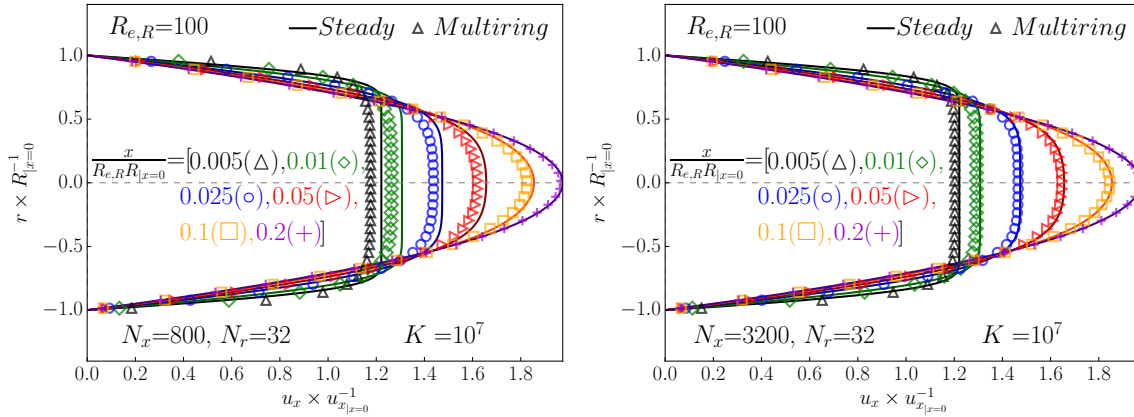


Figure 8.8 – Comparison between the steady velocity profiles obtained with the steady code [Lagrée and Lorthois 2005] (—) and with the multiring model for the steady rigid Poiseuille example taken in $x \in \{0.005 (\Delta), 0.01 (\diamond), 0.025 (\circ), 0.05 (\triangleright), 0.1 (\square), 0.2 (+)\}$ $R_{e,R}R_{|x=0}$. **Left:** $N_x = 800$ cells and $N_r = 32$ rings.

Right: $N_x = 3200$ cells and $N_r = 32$ rings.

We observe that the steady multiring velocity profiles converge towards the steady velocity profiles and accurately reproduce the transition from the Blasius to the Poiseuille flow regime.

stenosis and aneurysm considered here are described by the following variation of the neutral radius R_0 :

$$R_0 = \begin{cases} R_0 & \text{if } x < x_s \text{ or } x > x_f \\ R_0 \left(1 + \frac{\Delta R}{2} \left[1 + \cos \left(\pi + 2\pi \frac{x - x_s}{x_f - x_s} \right) \right] \right) & \text{if } x_s \leq x \leq x_f. \end{cases} \quad (8.103)$$

We choose $x_s = L/5$ and $x_f = 3L/5$ to satisfy the long-wave hypothesis. We set $\Delta R = -0.4$ to define the stenosis and $\Delta R = +0.4$ to define the aneurysm. We artificially increase the arterial wall rigidity K (here $K = 10^7$) to penalize the wall's displacement and place ourselves in a quasi-rigid wall configuration.

L	R_0	K	ρ	μ	U_{in}	R_t	t_f	$R_{e,R}$
0.25 $R_{e,R}R_{ x=0}$	1	10^7	1	$\rho \frac{U_{in}R_{ x=0}}{R_{e,R}}$	100	0	$0.5 \frac{R_{e,R}R_{ x=0}}{U_{in}}$	100

Table 8.5 – Geometrical and mechanical parameters describing the artery and the inlet and outlet boundary conditions for the steady rigid stenosis and aneurysm examples.

We compare the results of the multiring model (8.21) to those of the steady numerical code presented in [Lagrée and Lorthois 2005]. In [Chouly and Lagrée 2012], this steady code was used to solve the steady RNSP system of equations (8.1) in a rigid stenosis and compared well to the results of a finite element code for the incompressible Navier-Stokes equations. In the following examples, all results of the steady code used as reference solutions are obtained using $N_x = 50000$ cells in the axial direction and $N_r = 1000$ cells in the radial direction, which is a very fine mesh.

Flow in a stenosis

We first compute the steady flow in a rigid stenosis ($\Delta R = -0.4$). In Figure 8.9, we plot the steady spatial evolution of the centerline velocity $u_{x|r=0}$ (Figure 8.9 Left) and of the wall shear stress (WSS) τ_w (Figure 8.9 Right). We use $N_x \in \{800, 1600, 3200\}$ cells and $N_r = 32$ rings. We observe that as we increase the number of cells N_x , the steady multiring numerical solution for the centerline velocity $u_{x|r=0}$ converges towards the steady numerical solution. On the contrary, the steady multiring numerical solution for the WSS τ_w is already

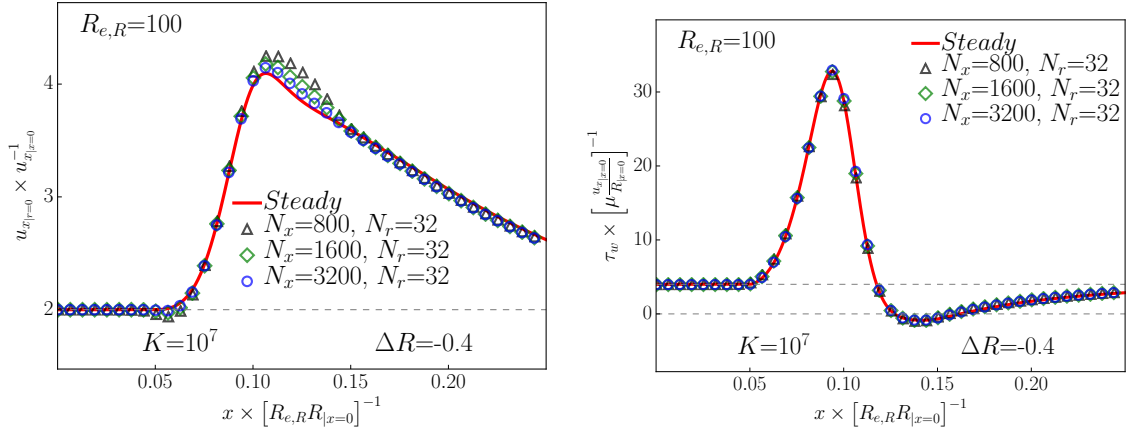


Figure 8.9 – Comparison between the solutions in the steady rigid stenosis obtained with the steady code [Lagrée and Lorthois 2005] (—) and with the multiring model using $N_x \in \{800 (\triangle), 1600 (\diamond), 3200 (\circ)\}$ cells and $N_r = 32$ rings.

Left: Steady centerline velocity $u_{x|r=0}$. The dashed line represents the value of the Poiseuille centerline velocity ($u_{x|r=0} = 2u_{x|x=0}$).

Right: Steady WSS τ_w . The dashed line represents the value of the Poiseuille WSS ($\tau_w = 4\mu u_{x|x=0}/R_{|x=0}$).

For each quantity, the steady multiring numerical solution converges towards the steady numerical solution.

converged for $N_x = 800$. Indeed, the number of rings N_r used is sufficient to obtain an accurate description of the shape of the velocity profile near the wall. We also note that the WSS τ_w becomes negative after the stenosis, indicating that the multiring model is able to capture flow recirculations. Finally, the steady WSS τ_w is similar to the one obtained in [Morgan and Young 1974; Smith 1976; Siegel et al. 1994].

In Figure 8.10, we represent the steady velocity profiles taken in $x \in \{0.05, 0.075, 0.1, 0.125, 0.15, 0.175\}R_{e,R}R_{|x=0}$. We use $N_x = 3200$ cells and $N_r = 32$ rings. For each recorded position, the steady multiring numerical velocity profiles agree well with the steady numerical velocity profiles. We observe that after the stenosis, a small jet-like region of high velocities forms in the center of the artery and a region of low and negative velocities is created near the wall. These results are coherent with the results presented in Figure 8.9 and with the velocities profiles obtained in [Morgan and Young 1974].

Flow in an aneurysm

We compute here the steady flow in a rigid aneurysm ($\Delta R = +0.4$). In Figure 8.11, we plot the steady spatial evolution of the centerline velocity $u_{x|r=0}$ (Figure 8.11 Left) and of the wall shear stress (WSS) τ_w (Figure 8.11 Right). We use $N_x \in \{800, 1600, 3200\}$ cells and $N_r = 32$ rings. For each quantity, the steady multiring numerical solution converges towards the steady numerical solution. We also note that even though the aneurysm is not large enough to create a flow recirculation, the WSS τ_w is almost negative in the center of the aneurysm. Finally, the steady WSS τ_w is similar to the one obtained in [Budwig et al. 1993; Finol and Amon 2002].

In Figure 8.12, we represent the steady velocity profiles taken in $x \in \{0.05, 0.075, 0.1, 0.125, 0.15, 0.175\}R_{e,R}R_{|x=0}$. We use $N_x = 3200$ cells and $N_r = 32$ rings. For each recorded position, the steady multiring numerical velocity profiles agree well with the steady numerical velocity profiles.

The results presented previously indicate that for a high arterial wall rigidity, the multiring

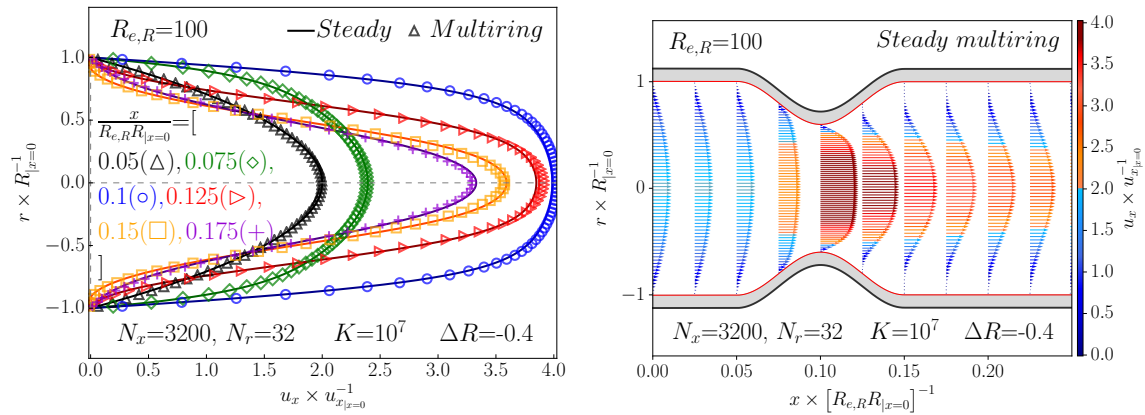


Figure 8.10 – Comparison between the steady velocity profiles obtained with the steady code [Lagrée and Lorthois 2005] (—) and with the multiring model for the steady rigid stenosis example using $N_x = 3200$ cells and $N_r = 32$ rings.

Left: Velocity profiles taken in $x \in \{0.05 (\Delta), 0.075 (\diamond), 0.1 (\circ), 0.125 (\triangleright), 0.15 (\square), 0.175 (+)\} R_{e,R}R_{|x=0}$.

Right: 2D visualization of the steady flow in the rigid stenosis.

We observe that the multiring velocity profiles are in good accord with the steady velocity profiles.

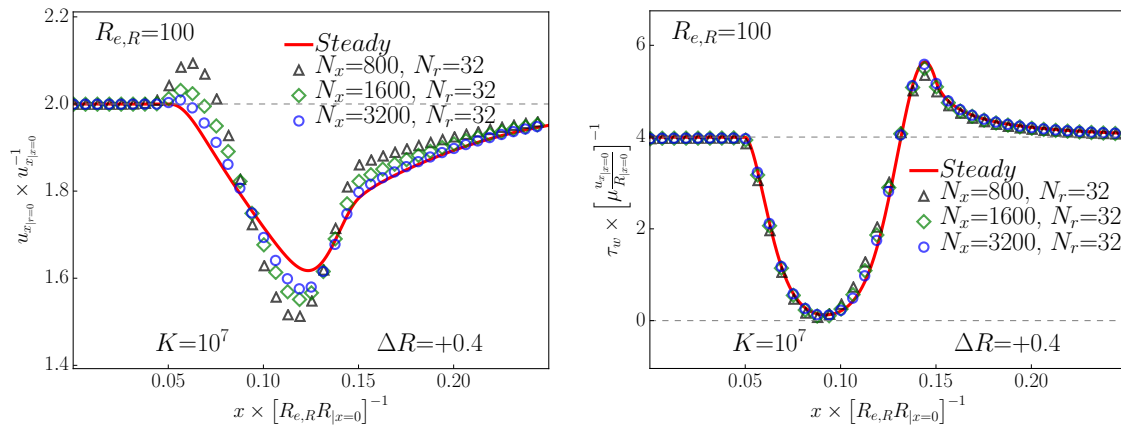


Figure 8.11 – Comparison between the solutions in the steady rigid aneurysm obtained with the steady code [Lagrée and Lorthois 2005] (—) and with the multiring model using $N_x \in \{800 (\Delta), 1600 (\diamond), 3200 (\circ)\}$ cells and $N_r = 32$ rings.

Left: Steady centerline velocity $u_{x|r=0}$. The dashed line represents the value of the Poiseuille centerline velocity ($u_{x|r=0} = 2u_{x|x=0}$).

Right: Steady WSS τ_w . The dashed line represents the value of the Poiseuille WSS ($\tau_w = 4\mu u_{x|x=0}/R_{|x=0}$).

For each quantity, the steady multiring numerical solution converges towards the steady numerical solution.

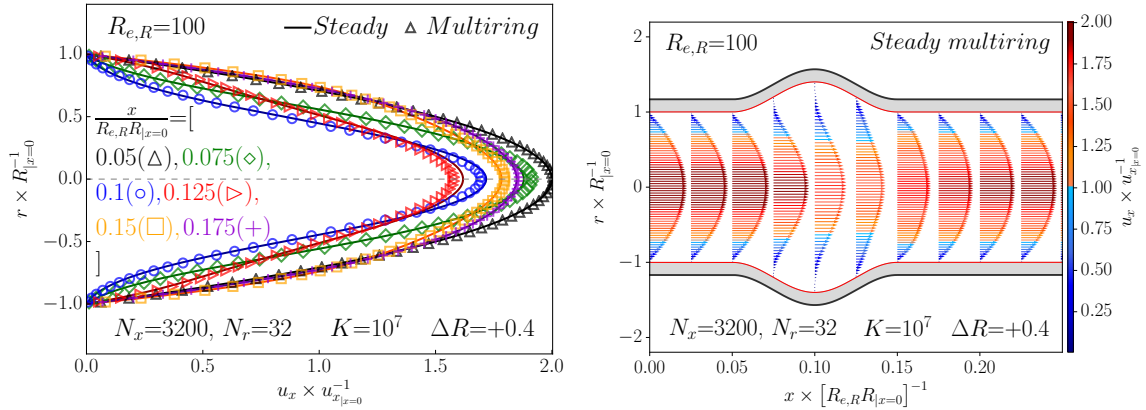


Figure 8.12 – Comparison between the steady velocity profiles obtained with the steady code [Lagrée and Lorthois 2005] (—) and with the multiring model for the steady rigid aneurysm example using $N_x = 3200$ cells and $N_r = 32$ rings.

Left: Velocity profiles taken in $x \in \{0.05 (\triangle), 0.075 (\diamond), 0.1 (\circ), 0.125 (\triangleright), 0.15 (\square), 0.175 (+)\} R_{e,R}R_{|x=0}$.

Right: 2D visualization of the steady flow in the rigid aneurysm.

We observe that the steady multiring velocity profiles are in good accord with the steady velocity profiles.

model (8.21) is able to compute the characteristic steady nonlinear flow features in a rigid artery. Indeed, we have shown that it can describe the nonlinear steady transition from a flat to a Poiseuille velocity profile, the acceleration of the flow in a stenosis, the deceleration of the flow in an aneurysm as well as small flow recirculations after the stenosis. It can also correctly compute the variation of the WSS and the pressure loss. We are therefore assured that the multiring model (8.21) correctly describes all relevant steady and unsteady, linear and nonlinear blood flow features in quasi-rigid and elastic straight, constricted (stenosis) and expanded (aneurysm) arteries.

Next, we use the multiring model to compute unsteady blood flow in an elastic stenosis.

8.8 Unsteady flow in an elastic stenosis

In physiological conditions, the arteries are elastic and the flow of blood is pulsatile in nature. Hence we compute here with the multiring model (8.21) a periodic flow in an elastic artery. The Womersley number α (2.41), the Reynolds number $R_{e,R}$ (8.99) and the Shapiro number S_h (8.36) are the relevant dimensionless numbers in this example. Here S_h is defined as:

$$S_h = \frac{U_{in}}{c} \quad \text{with} \quad c = \sqrt{\sqrt{\pi} \frac{K}{2\rho} R}. \quad (8.104)$$

We consider an artery initially at rest. We impose at the inlet a periodic Pohlhausen velocity profile (eq. (8.101)), mimicking the flow ejected by the heart in the aorta:

$$u_x(x=0, r, t) = U_{in} \phi_{Pohlhausen}(r) \max\left(0, \sin\left(2\pi \frac{t}{T_c}\right)\right), \quad (8.105)$$

where T_c is the period of the flow. At the outlet we impose a zero reflection coefficient R_t to remove any backward traveling waves. The values of the geometrical and mechanical parameters describing the artery as well as those describing the inlet and outlet boundary conditions are presented in Table 8.6 and are given in "cgs". The final time t_f is large enough to reach a periodic flow regime. The geometrical and mechanical parameters mimic physiological conditions at the root of the aorta, where $R_{e,R} \approx 100$, $\alpha \approx 15$ and $S_h \approx 10^{-2}$. As in the previous section, the stenosis is described by the neutral radius R_0 (8.103) with

$x_s = L/5$, $x_f = 3L/5$ and $\Delta R = -0.4$.

L	R_0	K	ρ	μ	U_{in}	R_t	T_c	t_f	$R_{e,R}$	α	S_h	
0.25	$R_{e,R}R_{ x=0}$	1	10^5	1	$\rho \frac{U_{in}R_{ x=0}}{R_{e,R}}$	$S_h c$	0	$\frac{2\pi}{\nu} \frac{R_0^2}{\alpha^2}$	$5T_c$	100	15	10^{-2}

Table 8.6 – Geometrical and mechanical parameters describing the artery and the inlet and outlet boundary conditions for the unsteady elastic stenosis example.

In Figure 8.13, we plot the temporal evolution of the pressure p (Figure 8.13 Top Left), of the pressure gradient $\partial_x p$ (Figure 8.13 Top Right), of the flow rate Q (Figure 8.13 Bottom Left) and of the WSS τ_w (Figure 8.13 Bottom Right) in $x \in \{0.025, 0.1, 0.175\} R_{e,R}R_{|x=0}$. We use $N_x = 3200$ cells and $N_r = 32$ rings. We observe that for each recorded positions, a periodic flow regime is reached after 4 periods. During systole ($nT_c < t < \frac{3}{2}nT_c$, $n \in \mathbb{N}$), the pulse wave propagates in the artery and the pressure p is higher upstream of the stenosis, in $x = 0.025R_{e,R}R_{|x=0}$. The pressure gradient $\partial_x p$ is therefore negative and the flow rate Q as well as the WSS τ_w are positive. On the contrary, during diastole ($\frac{3}{2}nT_c < t < 2nT_c$, $n \in \mathbb{N}$), the pulse wave exits the artery and the pressure p is higher downstream of the stenosis, in $x = 0.175R_{e,R}R_{|x=0}$. The pressure gradient $\partial_x p$ is then positive and the flow rate Q and the WSS τ_w are negative. Moreover, the presence of the stenosis creates a reflection of the incoming pulse wave, resulting in higher pressure values and a smaller flow rate Q upstream the stenosis, in $x = 0.025R_{e,R}R_{|x=0}$. Finally, the WSS is maximum in the stenosis, in $x = 0.1R_{e,R}R_{|x=0}$, as the flow is accelerated due to the constriction.

In Figure 8.14, we decompose the flow motion over one period (the fourth period) and focus on four different instants of the cycle: the end of diastole (or the beginning of systole) at $t = 4T_c$, the peak of systole at $t = 0.25T_c + 4T_c$, the end of systole (or the beginning of diastole) at $t = 0.5T_c + 4T_c$ and the middle of diastole at $t = 0.75T_c + 4T_c$. For each instant, we plot the velocity profiles in the artery (Figure 8.14 Left) and the spatial evolution of the pressure p (Figure 8.14 Center) and the WSS τ_w (Figure 8.14 Right). At times $t = 4T_c$, $t = 0.5T_c + 4T_c$ and $t = 0.75T_c + 4T_c$, we observe that the shapes of the pressure p waveforms are almost identical. The same can be said of the WSS τ_w . At these times, the pressure gradient $\partial_x p$ is positive, indicating that the pulse wave has left the artery. This positive pressure gradient reverses the flow, but only near the wall, as indicated by the negative WSS τ_w . Indeed, the inertia of the flow in the core of the artery is too strong to observe a complete flow reversal in one period. At $t = 0.25T_c + 4T_c$, the pressure p and WSS τ_w resemble the steady pressure and WSS observed in Figure 8.9. This indicates that a quasi-steady flow regime is reached at the peak of systole since the period T_c of the flow is larger than the characteristic time of propagation of the pulse wave.

The results presented in Figure 8.13 and Figure 8.14 are similar to those obtained in [Young et al. 1975]. They indicate that the multiring model (8.21) is capable of describing the unsteady flow in a elastic stenosis and that it computes the expected unsteady flow behaviors such as wave reflections and flow recirculations.

8.9 Conclusion

In Chapter 8, we have presented a two-dimensional (2D) nonlinear axisymmetric multiring model to compute blood flow in elastic arteries. This model results from the integration of the RNSP equations (8.1) over concentric rings of fluid in an elastic artery, providing a unified framework where both the motion of the fluid and the displacement of the arterial wall are dealt with simultaneously. Its mathematical structure as a system of balance laws allowed us to use a robust, conservative and positive *finite volume* numerical method to compute steady and unsteady linear and nonlinear flows in quasi-rigid and elastic arteries.

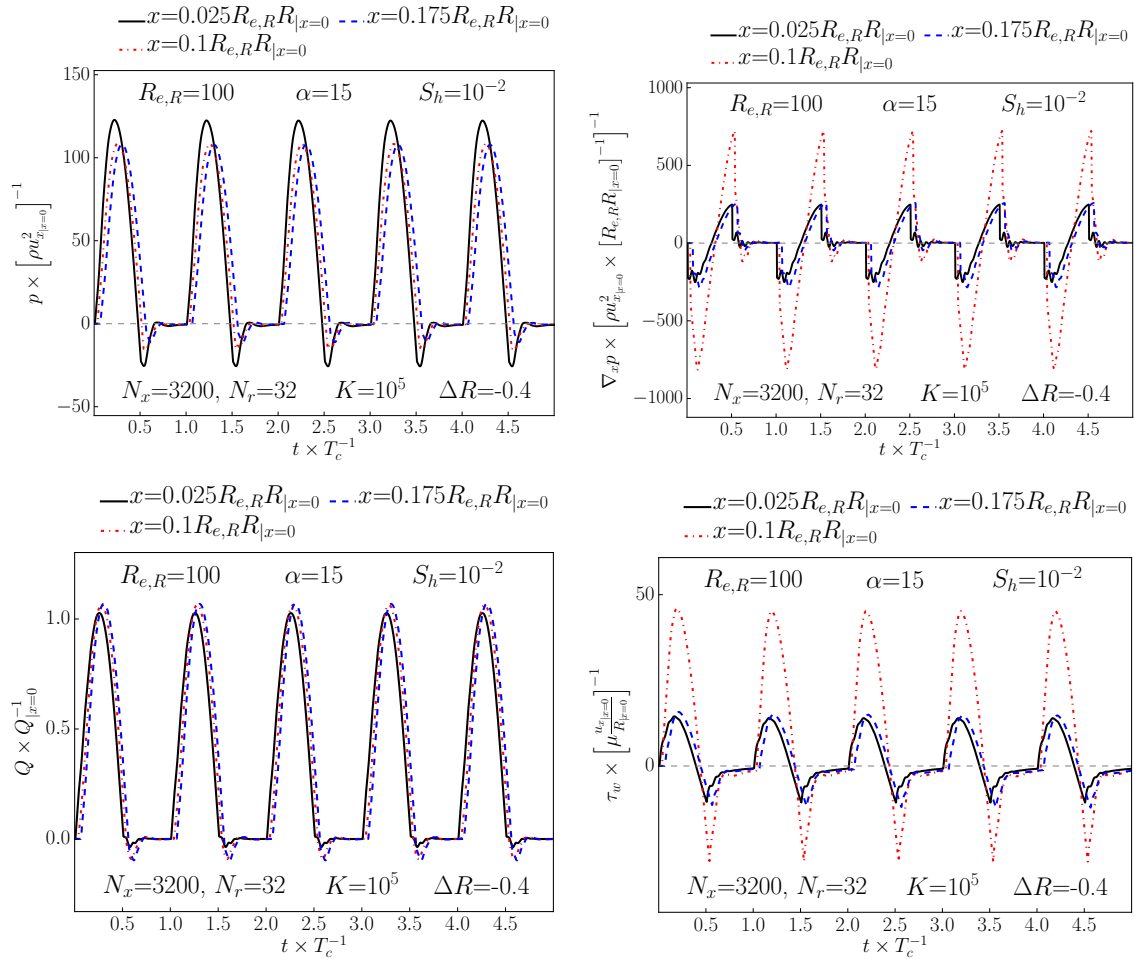


Figure 8.13 – Unsteady flow in the elastic stenosis computed in $x \in \{0.025 (—), 0.1 (---), 0.175 (-\cdot-)\} R_{e,R} R_{|x=0}$ obtained using $N_x = 3200$ cells and $N_r = 32$ rings.

Top Left: Pressure p .

Top Right: Pressure gradient $\partial_x p$.

Bottom Left: Flow rate Q .

Bottom Right: WSS τ_w .

We observe that after four cycles a periodic state is reached. We notice evidence of wave propagation and reflection as well as flow recirculation.

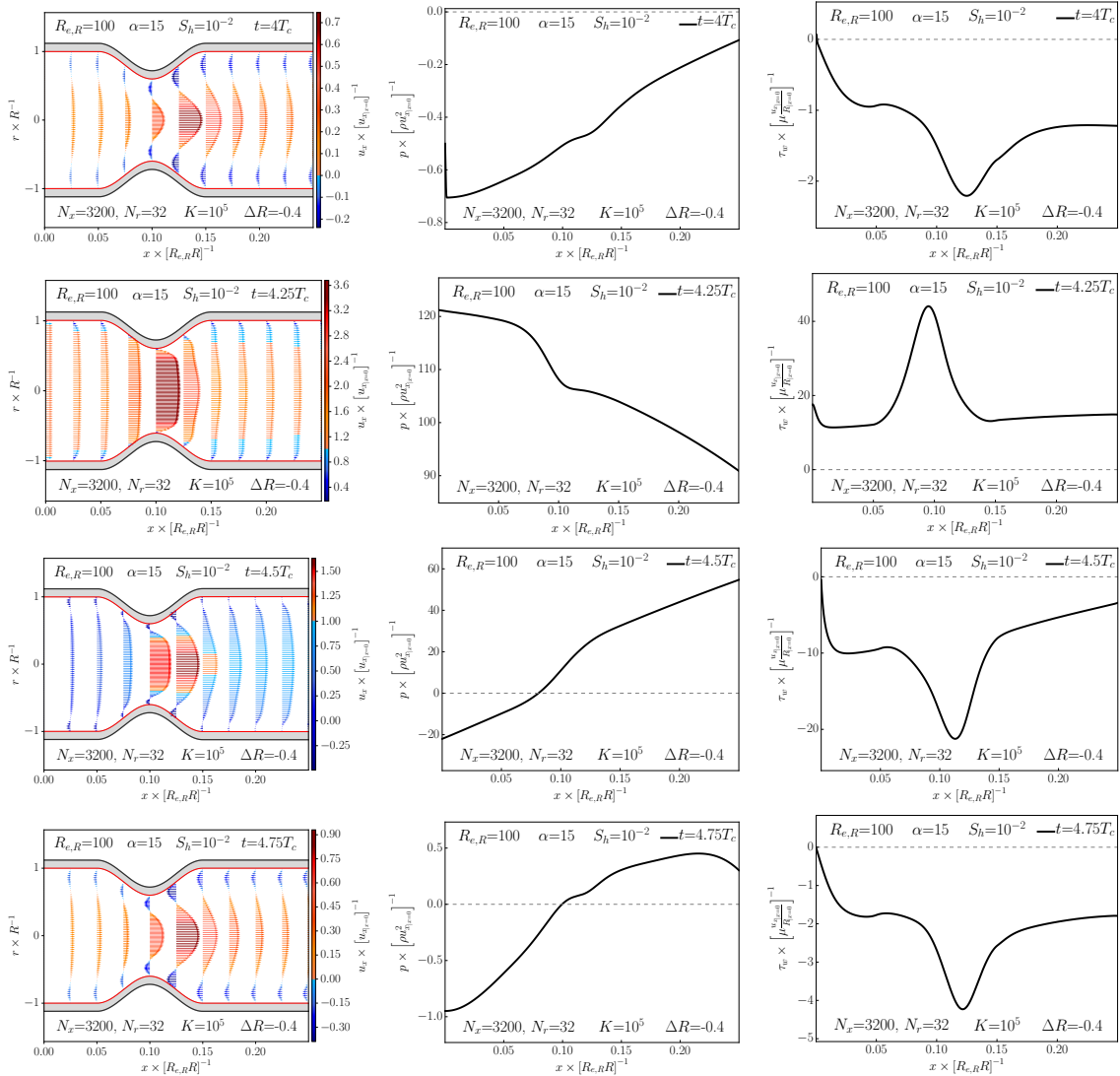


Figure 8.14 – Snapshots of the spatial evolution of the unsteady flow in the elastic stenosis taken at times $t \in \{0, 0.25, 0.5, 0.75\}T_c + 4T_c$ and obtained using $N_x = 3200$ cells and $N_r = 32$ rings.

Left: Axial velocity u_x .

Center: Pressure p .

Right: WSS τ_w .

We observe a backflow near the wall created by the positive pressure gradient at $t \in \{0, 0.5, 0.75\}T_c + 4T_c$. However, the inertia in the core of the artery is too strong to observe a complete flow reversal in one period. At the peak of systole $t = 0.25T_c + 4T_c$, the shapes of the pressure p and the WSS τ_w resemble those obtained in Figure 8.9, indicating that a quasi-steady flow regime is reached.

The multiring model and the numerical method were validated on multiple physiological blood flow examples. For each of the considered test cases, the multiring solution agreed very well with the reference solution for the velocity profiles, the wall shear stress (WSS) and other averaged quantities such as the flow rate or the pressure, even when large arterial wall deformations were considered. In the presence of pathologies such as stenoses or aneurysms, the multiring model captured the expected flow behaviors, and in particular flow recirculation, downstream of the stenosis and in the aneurysm. In comparison, classical one-dimensional (1D) models can only compute average quantities such as the flow rate or the pressure and can not describe flow recirculations. This study shows that the multiring model can serve as a superior alternative to 1D models to accurately compute blood flow in large elastic arteries at a reduced computational cost and could also prove to be a reliable substitute to three-dimensional (3D) models when simple arterial configurations are considered. This method can be extended to other pressure laws to describe the flow in veins and viscoelastic tubes or the propagation of a water hammer (Allevi's equation).

In future works, we plan to compare the 2D multiring model with a 1D model and to couple both models. Indeed, through our collaboration with Pr. Matsukawa from the *University of Doshisha* in Kyotanabe, Japan, we have access to a simple experimental setup described in Figure 8.15. This experiment allows us to measure at two different points the pressure and flow waveforms and therefore capture the propagation and reflection of pulses in straight and stenosed vessels (see Figure 8.16). This is the perfect framework to truly assess the differences between the 1D and 2D blood flow models.

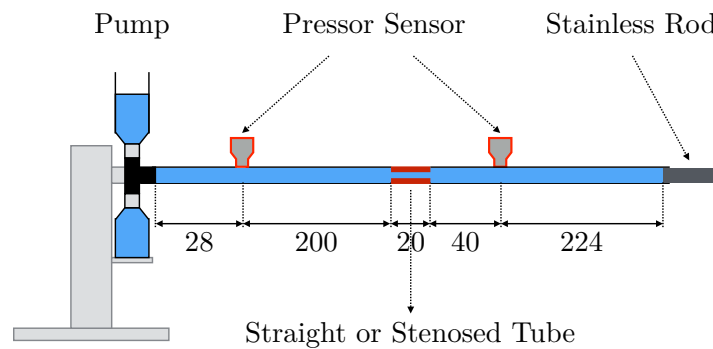


Figure 8.15 – *Experimental setup allowing us to measure the pressure and flow waveforms in straight or stenosed tubes closed at the outlet (stainless rod).*

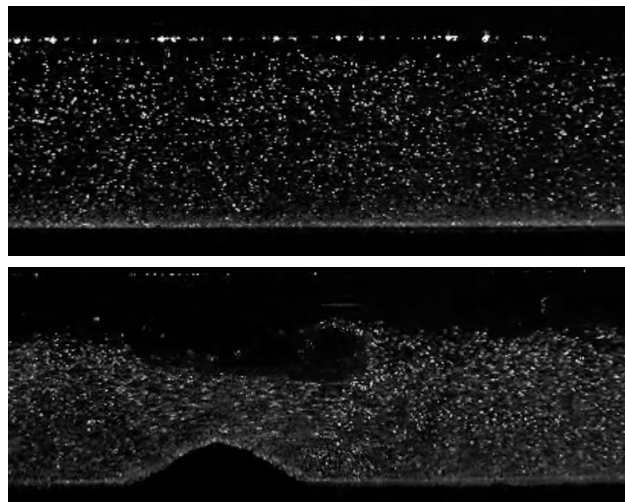


Figure 8.16 – *Flow visualizations in straight and stenosed tubes.*

One-dimensional non-Newtonian blood flow equations

We present here a non-Newtonian extension of the 1D blood flow equations. We take into account time-dependent non-Newtonian behaviors using a structure function that describes the state of aggregation of red blood cells. The text in this chapter deals with the derivation of the model and the numerical method used to solve it and is greatly inspired from the following article, currently *in revision* in the Journal of non-Newtonian Fluid Mechanics:

- A.R. Ghigo, P.-Y. Lagrée, and J.-M. Fullana. 1D generalized time dependent non-newtonian blood flow model. 2017d.

Contents

9.1	Introduction	201
9.2	1D time-dependent non-Newtonian blood flow model	202
9.2.1	The 1D blood flow model	202
9.2.2	Stress model: Newtonian	203
9.2.3	Stress model: non-Newtonian	204
9.2.4	Time-dependent 1D non-Newtonian blood flow model	205
9.2.5	Numerical scheme	205
9.3	Analysis of the non-Newtonian stress model	206
9.3.1	Steady flow: Analogy with the simplified Cross model	206
9.3.2	Constant shear rate	207
9.3.3	Zero shear rate	208
9.4	Comparison with experimental data	208
9.4.1	Single shear-step	209
9.4.2	Multiple shear-steps	210
9.4.3	Triangle shear solicitation	211
9.5	Elementary bifurcation	211
9.6	Idealized asymmetric network	213
9.6.1	Healthy network	214
9.6.2	Pathological network	215
9.7	Conclusion	215

9.1 Introduction

One-dimensional (1D) blood flow models, presented in Chapter 2, are used in medical applications to provide physiological insights on hemodynamics in large networks of the macro- and micro-circulations (see Chapter 7). They capture the pulse wave propagation dynamics in large networks and enable for example patient-specific surgical planning [Marchandise et al. 2009; Audebert et al. 2017b; Ghigo et al. 2017a]. The success of 1D modelling relies on the speed and accuracy at which 1D models compute blood pressure, flow rate and cross-sectional area in elastic arteries and arterioles. In comparison, three-dimensional approaches are much more costly and time-consuming, especially in deformable elastic vessels and are therefore restricted to small networks of only a few arteries [Blanco et al. 2009; Vignon-Clementel et al. 2010; Sankaran et al. 2012; Cuomo et al. 2017]. Reduced-order models such as 1D models are then used to provide physiological boundary conditions to these 3D approaches [Formaggia et al. 2001; Blanco et al. 2007, 2009; Formaggia et al. 2013].

In many regions of the systemic network, low shear regimes are reached (typically the shear rate $\dot{\gamma} \leq 1$) as a consequence of the pulsatility of blood flow, of recirculation areas created by stenoses, aneurysms and bifurcations and of the decrease in shear with vessel ramification. In such low shear regions, blood behaves as a non-Newtonian fluid and exhibits shear-thinning, viscoelastic and thixotropic behaviors. At low shear rates, molecular mechanisms trigger the aggregation of red blood cells (RBCs) into long column-like structures called "rouleaux", whereas at higher shear rates, these structures are deformed, disaggregated and the RBCs re-align in the direction of the flow. This reversible aggregation-disaggregation process is responsible for the shear-thinning behavior of blood. The different timescales of the aggregation and disaggregation processes are at the origin of the thixotropic response of blood. Finally, viscoelasticity stems from the elasticity of RBCs and the change of dissipation mechanisms at low and high shear rates [Cross 1965; Thurston 1972, 1975; Bureau et al. 1980; Quemada and Droz 1982].

There exists strong evidence that this non-Newtonian behavior of blood influences the progression of many cardiovascular pathologies, such as atherosclerosis, through local modifications of the hemodynamics [Verdier 2003]. Developing constitutive models of blood rheology is therefore of critical importance in cardiovascular simulations.

Existing non-Newtonian constitutive models can be roughly categorized as either time-independent or time-dependent models. Time-independent constitutive models describe only for the shear-thinning behavior of blood and are particularly relevant in shear-dominated steady flows [Cho and Kensey 1991; Yilmaz et al. 2008; Apostolidis and Beris 2014]. Due to their simplicity, they are the most commonly used non-Newtonian blood flow models in two-dimensional (2D) and three-dimensional (3D) numerical simulations. Time-independent models have been applied to study intracranial aneurysms [Bernsdorf and Wang 2009; Tian et al. 2013], stenoses [Nandakumar et al. 2015; Jahangiri et al. 2017], coronary arteries [Apostolidis et al. 2016], idealized arterial trees [Gijzen et al. 1999b,a; Weddell et al. 2015; Moreau and Mauroy 2015] and heart valves [De Vita et al. 2016]. In most of these works, non-Newtonian effects were observed proving the relevance of modeling the complex rheology of blood. Time-dependent constitutive models include viscoelastic and thixotropic effects as well as shear-thinning effects in the steady flow limit. They were developed based on an analogy between blood and a viscoelastic Maxwell material [Bird 1976]. In [Owens 2006; Moyers-Gonzalez et al. 2008a], a generalized Maxwell model was derived based on polymer network theory, and successive improvements enabled the description of the Fahreus and Fahreus-Lindquist effects. In [Yeleswarapu et al. 1998; Anand and Rajagopal 2004; Anand et al. 2013], a generalized Oldroyd-B model was proposed and improved based on a thermodynamics approach. Time-dependent models were successfully incorporated into

3D simulations [Fang and Owens 2006; Duarte et al. 2008; Moyers-Gonzalez et al. 2008b; Bodnár et al. 2011; Anand et al. 2013] and good agreement was found with experimental data in simple steady and pulsatile flows.

However, in almost every application previously mentioned, the mechanics and distensibility of the vessel wall were neglected. Moreover, non-Newtonian effects in large networks of arteries have seldom been studied. Even in 1D applications blood is almost always assumed Newtonian. Only in [Perdikaris et al. 2015; Sochi 2016] have the authors considered its non-Newtonian behavior, respectively using a model proposed in [Pries et al. 1992] and a power-law model. In [Apostolidis et al. 2015], the authors have proposed a reduced-order non-Newtonian model with a particular focus on the thixotropic behaviors of the yield stress. However, the authors obtained a semiquantitative agreement with experimental data from Bureau [Bureau et al. 1979, 1980] and Sousa [Sousa et al. 2013] and the model was not coupled to a blood flow numerical solver.

The goal of this work is to provide a simple and accurate 1D time-dependent non-Newtonian blood flow model and apply it to study large networks of elastic arteries. The rheological model we propose involves a simplified viscoelastic Maxwell model with shear and structure dependent coefficients and a kinetic equation describing the aggregation-disaggregation of RBCs which are considered as a homogeneous single phase.

In Section 9.2 we recall the 1D blood flow model (2.67) and present the non-Newtonian shear stress model and its integration in the 1D blood flow model (2.67). In Section 9.3, we describe analytic solutions of the rheological model in different flow conditions and exhibits its shear-thinning, thixotropic and viscoelastic behaviors. Then, in Section 9.4 we compare the results of the model to published experimental rheological data. Finally, in Section 9.5 and Section 9.6 we investigate the influence of the non-Newtonian model on blood flow in synthetic arterial networks with and without stenoses.

9.2 1D time-dependent non-Newtonian blood flow model

9.2.1 The 1D blood flow model

A thorough derivation of the 1D blood flow model starting from the Navier-Stokes equations is performed in Chapter 2. Two main hypotheses are involved in this derivation. First, the flow is assumed to be axisymmetric, implying that the geometry and both the inlet and outlet boundary are also axisymmetric. Second, the radius R of the artery is considered small with respect to the wavelength λ of the cardiac pulse wave, which is the characteristic axial lengthscale. In Chapter 2, we refer to this assumption as the long-wave hypothesis. Combining both hypotheses we obtain the reduced Navier-Stokes-Prandtl (RNSP) equations (2.43), that we then integrate over the cross-sectional area of an artery of length L (see Figure 9.1). Through this exact integration or averaging process, we obtain the 1D mass and momentum equations expressed at time t in the axial position x :

$$\begin{cases} \frac{\partial A}{\partial t} + \frac{\partial Q}{\partial x} = 0 \\ \frac{\partial Q}{\partial t} + \frac{\partial}{\partial x} \left[\psi \frac{Q^2}{A} \right] + \frac{A}{\rho} \frac{\partial p}{\partial x} = \frac{2\pi R}{\rho} \tau_{rx} |_{r=R}. \end{cases} \quad (9.1a)$$

$$\quad (9.1b)$$

The variables A and Q are respectively the cross-sectional area and the axial flow rate and are defined as:

$$A = 2\pi \int_{r=0}^R r dr \quad \text{and} \quad Q = 2\pi \int_{r=0}^R u_x r dr, \quad (9.2)$$

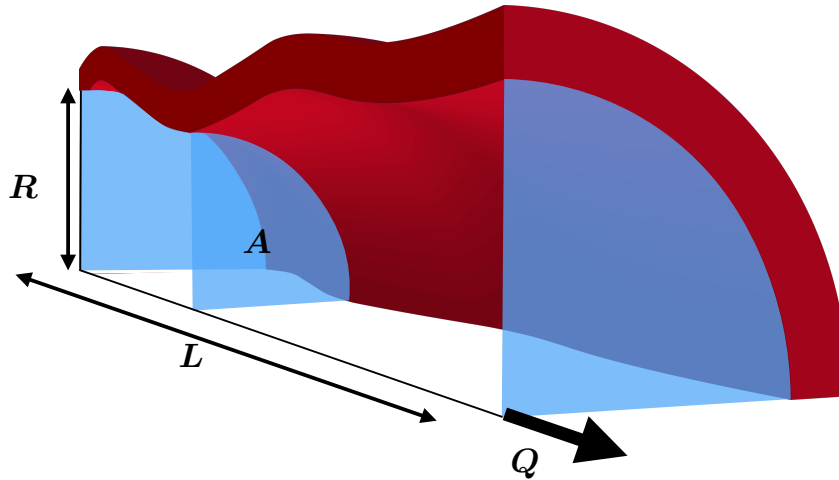


Figure 9.1 – One-dimensional representation of the fluid domain contained in an axisymmetric cylindrical artery. For clarity, only one-fourth of the artery of length L is represented. The variable Q is the flow rate and $A = \pi R^2$ is the cross-sectional area of the artery.

where R is the instantaneous radius of the artery. Finally, the coefficient ψ , defined as:

$$\psi = 2\pi \frac{A}{Q^2} \int_{r=0}^R r u_x^2 dr, \quad (9.3)$$

is the nonlinear shape factor. This coefficient depends on the axial velocity profile which is lost in the averaging process. We therefore assume an *a priori* shape of the velocity profile and set $\psi = 1$, which corresponds to a flat velocity profile assumption. See Subsection 2.5.2 for more details.

The closure relation connecting the cross-sectional area A and the pressure p is provided by viscoelastic thin-wall law (3.18), that we recall here:

$$p = p_{ext} + K \left[\sqrt{A} - \sqrt{A_0} \right] + K_\nu \frac{\partial A}{\partial t}, \quad (9.4)$$

where p_{ext} is the external pressure and A_0 is the neutral cross-sectional area. The coefficients K and K_ν are respectively the arterial rigidity and the viscoelastic coefficient. More details on the viscoelastic behavior of the arterial wall can be found in Chapter 3.

The last remaining unknown is the wall shear stress (WSS) $\tau_{rx}|_{r=R}$ and its definition is the subject of the following Subsection 9.2.2 and Subsection 9.2.3.

9.2.2 Stress model: Newtonian

We briefly recall here the definition of the WSS $\tau_{rx}|_{r=R}$ in the case of a Newtonian fluid in the 1D framework. Under Newtonian hypothesis, the shear stress τ_{rx} can be expressed as a function of a constant viscosity μ and the shear rate:

$$\tau_{rx} = \mu \left[\frac{\partial u_r}{\partial x} + \frac{\partial u_x}{\partial r} \right]. \quad (9.5)$$

The long-wave approximation allows us to simplify the expression for the shear rate at the wall $\dot{\gamma}|_{r=R}$:

$$\dot{\gamma}|_{r=R} \approx \frac{\partial u_x}{\partial r}|_{r=R}, \quad (9.6)$$

and we obtain the following Newtonian WSS model:

$$\tau_{rx}|_{r=R} = \mu \dot{\gamma}|_{r=R}. \quad (9.7)$$

Furthermore, 1D closure hypotheses suggest that we may rewrite the axial velocity u_x as:

$$u_x = \phi \left(\frac{r}{R(x,t)}, t \right) U(x,t), \quad (9.8)$$

where $U = Q/A$ is the averaged velocity and ϕ is the shape of the velocity profile. The expression for the wall shear rate then becomes:

$$\dot{\gamma}|_{r=R} = U \frac{\partial \phi}{\partial r} \Big|_{r=R}. \quad (9.9)$$

The average velocity U can be computed using the 1D model (9.1). However, as was mentioned in Subsection 9.2.1, the shape of the velocity profile ϕ is lost in the integration process and remains an unknown of the problem. We must therefore once again assume an *a priori* shape of the velocity profile. For example, for a Couette flow $\dot{\gamma} = -U/R$, for a Poiseuille flow $\dot{\gamma} = -4U/R$ and it is common in large arteries to use $\dot{\gamma} = -11U/R$ [Sherwin et al. 2003a; Wang et al. 2016b]. Without loss of generality, we assume in the following that $\dot{\gamma} = -U/R$.

Combining the previous equations, we finally obtain a closed-form expression for the Newtonian WSS:

$$\tau_{rx}|_{r=R} = -\mu \frac{U}{R}, \quad (9.10)$$

and we recover the classical viscous contribution $C_f U$ in the 1D momentum equation (2.67b), with $C_f = -2\pi\nu$. For clarity reasons, we drop the subscript $|_{r=R}$ in the following and write the WSS as τ_{rx} and the shear rate as $\dot{\gamma}$.

9.2.3 Stress model: non-Newtonian

Following the approach proposed in [Owens 2006], we build a transient reduced-order constitutive model for blood. We first split the WSS into a structural and a Newtonian component:

$$\tau_{rx} = \tau_{st} + \mu_\infty \dot{\gamma}, \quad (9.11)$$

where τ_{st} represents the structure dependent stress and μ_∞ the viscosity of blood in the high-shear asymptotic limit. Following [Owens 2006], we describe the time and space evolution of τ_{st} using the generalized Maxwell equations involving the Jaumann derivative of τ_{st} . Using the 1D long-wave and axisymmetric hypotheses, these equations simplify into a 1D viscoelastic Maxwell equation, representing the combined contributions of an elastic spring and a viscous dashpot:

$$\lambda_{st} \frac{\partial \tau_{st}}{\partial t} + \tau_{st} = \mu_{st} \dot{\gamma} \quad (9.12)$$

where λ_{st} is a characteristic elastic relaxation time and μ_{st} is the structural viscosity.

Next, we introduce a structure dependence in the Maxwell equation (9.12). We assume that the whole structure of blood, comprising of RBCs and rouleaux, can be described by a single parameter f varying between 0 for a completely disaggregated structure and 1 for a fully aggregated one. We then hypothesize that both λ_{st} and μ_{st} linearly depend on this structure parameter f :

$$\begin{cases} \lambda_{st} = \lambda_a f & (9.13a) \\ \mu_{st} = [\mu_0 - \mu_\infty] f. & (9.13b) \end{cases}$$

where λ_a is a characteristic aggregation time and μ_0 is the viscosity of blood in the low shear asymptotic limit. The equations (9.13a) and (9.13b) express the simplest possible dependence between the structure parameter f and the blood parameters.

Using an approach inspired from polymer theory [Cross 1965; Owens 2006], we describe the evolution of f using a kinetic equation representing the transport of f and the competition

between aggregation and disaggregation of blood structure:

$$\frac{\partial f}{\partial t} + U \frac{\partial f}{\partial x} = \frac{1-f}{\lambda_a} - \frac{f}{\lambda_d}, \quad (9.14)$$

where λ_d is a characteristic disaggregation time. As shear is the driving disaggregation mechanism, we define λ_d as the inverse of the shear rate $\dot{\gamma}$:

$$\lambda_d = \frac{1}{\delta|\dot{\gamma}|}, \quad (9.15)$$

where δ is a fitting coefficient. Compared to other existing simplified structural models, we incorporate advection in the kinetic equation as structure can be transported in the arteries.

Finally, yield stress can be taken into account through the change of variables $\tau'_{st} = \tau_{st} - \tau_y$, where τ_y is the yield stress. However, we assume that $\tau_y = 0$ in the following. We also neglect the effects of hematocrit variations and suppose a fixed hematocrit $H = 0.45$ (45% of blood volume occupied by RBCs). Nevertheless, these effects could be included in the model through a transport equation for H and hematocrit dependent coefficients (see [Pries et al. 1992] for details).

9.2.4 Time-dependent 1D non-Newtonian blood flow model

Replacing the pressure p by its expression (9.4), we obtain the closed-form 1D system of equations, describing the conservation of mass and the balance of momentum in a viscoelastic artery:

$$\left\{ \begin{array}{l} \frac{\partial A}{\partial t} + \frac{\partial Q}{\partial x} = 0 \end{array} \right. \quad (9.16a)$$

$$\left\{ \begin{array}{l} \frac{\partial Q}{\partial t} + \frac{\partial}{\partial x} \left[\frac{Q^2}{A} + \frac{K}{3\rho} A^{\frac{3}{2}} \right] = \frac{2\pi R}{\rho} \tau_{rx} + C_\nu \frac{\partial^2 Q}{\partial x^2}. \end{array} \right. \quad (9.16b)$$

with $C_\nu = AK_\nu/\rho$ and:

$$\left\{ \begin{array}{l} \dot{\gamma} = -\frac{U}{R} \end{array} \right. \quad (9.17a)$$

$$\tau_{rx} = \tau_{st} + \mu_\infty \dot{\gamma} \quad (9.17b)$$

$$\lambda_{st} \frac{\partial \tau_{st}}{\partial t} + \tau_{st} = \mu_{st} \dot{\gamma} \quad (9.17c)$$

$$\left\{ \begin{array}{l} \frac{\partial f}{\partial t} + U \frac{\partial f}{\partial x} = \frac{1-f}{\lambda_a} - \frac{f}{\lambda_d} \end{array} \right. \quad (9.17d)$$

$$\mu_{st} = [\mu_0 - \mu_\infty] f \quad (9.17e)$$

$$\lambda_{st} = \lambda_a f \quad (9.17f)$$

$$\left\{ \begin{array}{l} \lambda_d = \frac{1}{\delta|\dot{\gamma}|}, \end{array} \right. \quad (9.17g)$$

where μ_0 , μ_∞ , λ_a and δ are constants to be determined using available rheological data.

9.2.5 Numerical scheme

System (9.16) is dominantly hyperbolic. In physiological conditions, the flow speed is smaller than the wave speed, therefore the flow is always subcritical and shock-like phenomena do not occur. To capture the propagation of pulse waves, we solve System (9.16) using a second-order Adam-Bashforth time-integration scheme coupled to a *finite-volume* kinetic numerical scheme [Audebert et al. 2017b; Ghigo et al. 2017b] presented in Chapter 4. The rheological System (9.17) is explicitly updated using the same time integration scheme as

the hyperbolic System (9.16) and the transport equation is solved using an upwind scheme, where the velocity is given by the kinetic numerical flux [Bouchut 2004]. The treatment of inlet and outlet boundary conditions as well as bifurcations is classical and we refer the readers to Chapter 4, Chapter 6 and [Wang et al. 2015; Murillo and García-Navarro 2015; Ghigo et al. 2017b] for more details.

9.3 Analysis of the non-Newtonian stress model

We analyze the time-dependent behavior of the 1D non-Newtonian stress model (9.17) derived in the previous section. To simplify the analysis, we consider idealized flow conditions where we assume that all quantities are independent of the axial position x , and hence decouple the rheological model (9.17) from the 1D blood flow model (9.16).

9.3.1 Steady flow: Analogy with the simplified Cross model

We consider here a steady flow, for which the rheological model (9.17) simplifies to:

$$\begin{cases} f_s = \frac{1}{1 + \frac{\lambda_a}{\lambda_d}} & (9.18a) \\ \tau_s = \mu_{st}\dot{\gamma} = [\mu_0 - \mu_\infty] f_s \dot{\gamma} & (9.18b) \end{cases}$$

This steady state is the result of the balance between aggregation and disaggregation, and the equilibrium value of the structure function (9.18a) explicitly depends on the aggregation time scales λ_a and λ_d :

- If $\lambda_a \gg \lambda_d$, then $f \approx 0$ and structure disaggregation is dominant;
- If $\lambda_a \ll \lambda_d$, then $f \approx 1$ and structure aggregation is dominant.

In this steady case, we can explicitly define the apparent viscosity $\mu(\dot{\gamma}) = \frac{\tau_{rx}}{\dot{\gamma}}$ using equations (9.18a) and (9.18b):

$$\mu(\dot{\gamma}) = \mu_{st} + \mu_\infty = \mu_\infty + \frac{\mu_0 - \mu_\infty}{1 + \frac{\lambda_a}{\lambda_d}}, \quad (9.19)$$

which exhibits the expected shear-thinning behavior. Equation (9.19) is identical to the simplified Cross constitutive model [Steffan et al. 1990]:

$$\mu = \mu_\infty + \frac{\mu_0 - \mu_\infty}{1 + \lambda_c \dot{\gamma}}. \quad (9.20)$$

By analogy with (9.19) we have:

$$\lambda_c = \lambda_a \delta. \quad (9.21)$$

Table 9.1 summarizes the parameter values of the simplified Cross constitutive model taken from [Cho and Kensey 1991].

μ_∞	μ_0	λ_c
0.05	1.3	8

Table 9.1 – Parameter values of the simplified Cross constitutive model taken from [Cho and Kensey 1991]

In the following, we use the values of μ_0 and μ_∞ presented in Table 9.1. We determine the remaining unknown parameters λ_a and δ using the value of the constant λ_c and experimental data presented in [Quemada and Droz 1982]. The complete set of parameters of the rheological model (9.17) is presented in Table 9.2.

9.3.2 Constant shear rate

We study here the disaggregation under a constant shear rate $\dot{\gamma}_c$ of a fluid initially at rest. At $t = 0$, we assume that $f = 1$ and $\tau_{st} = 0$. The kinetic equation for the structure function writes:

$$\frac{df}{dt} = \frac{1-f}{\lambda_a} - \frac{f}{\lambda_d}. \quad (9.22)$$

The solution of the previous equation (9.22) is:

$$f = f_\infty + [1 - f_\infty] e^{-\frac{t}{\lambda_c}}, \quad (9.23)$$

where $f_\infty = \lambda_c/\lambda_a$ and $1/\lambda_c = 1/\lambda_a + 1/\lambda_d$. Injecting expression (9.23) in equation (9.12) we obtain the following expression for the structure stress τ_{st} :

$$\tau_{st} = [\mu_0 - \mu_\infty] \dot{\gamma}_c \frac{[1 - f_\infty] \frac{t}{\lambda_a} + [f_\infty]^2 \left[e^{\frac{t}{\lambda_c}} - 1 \right]}{1 + f_\infty \left[e^{\frac{t}{\lambda_c}} - 1 \right]}. \quad (9.24)$$

When $t \rightarrow \infty$, we find the following asymptotic values of f and τ_{st} :

$$\begin{cases} f_{t \rightarrow \infty} = f_\infty & (9.25a) \\ \tau_{st, t \rightarrow \infty} = [\mu_0 - \mu_\infty] \dot{\gamma}_c f_\infty. & (9.25b) \end{cases}$$

System (9.25) is identical to the steady system (9.18). The model therefore exhibits a characteristic viscoelastic property, that is the transitions from an initially aggregated state ($f = 1$, $\tau_{st} = 0$) towards a steady equilibrium state (9.25), where aggregation and disaggregation are perfectly balanced.

At intermediate times $0 < t < \infty$, the model exhibits a thixotropic behavior depending on the choice of the characteristic aggregation and disaggregation timescales λ_a and λ_d . Indeed, for given values of λ_a and λ_d , it is possible to find the analytic expression for the time $t_{\tau, max}$ at which the maximum value of τ_{st} is reached:

$$t_{\tau_{st}, max} = \lambda_c \left[1 + \frac{1}{1 - \frac{\lambda_c}{\lambda_a}} + W \left(\left[\frac{\lambda_a}{\lambda_c} - 1 \right] e^{-\left[1 + \frac{1}{1 - \frac{\lambda_c}{\lambda_a}} \right]} \right) \right], \quad (9.26)$$

with:

$$\tau_{st, max} = \tau_{st, t \rightarrow \infty} \left[1 + W \left(\left[\frac{\lambda_a}{\lambda_c} - 1 \right] e^{-\left[1 + \frac{1}{1 - \frac{\lambda_c}{\lambda_a}} \right]} \right) \right], \quad (9.27)$$

where W is the *Lambert-W* function, which is the inverse function of $f(w) = we^w$. From expressions (9.26) and (9.27), simple calculations allow us to show that $0 < t_{\tau_{st}, max} < \infty$ and $\tau_{st, max} \geq \tau_{st, t \rightarrow \infty}$. We can therefore conclude that in this case the model exhibits a characteristic thixotropic behavior at finite times, represented by an overshoot of the structure shear stress τ_{st} with respect to the asymptotic steady value $\tau_{st, t \rightarrow \infty}$. The magnitude of the overshoot depends on the value of the characteristic aggregation times λ_a and λ_d :

- if $\lambda_a \gg \lambda_d$ (equivalently $\dot{\gamma} \gg 1 \text{ s}^{-1}$), then $\lambda_c \approx \lambda_d$ and we have:

$$\tau_{st, max} \gg \tau_{st, t \rightarrow \infty}. \quad (9.28)$$

Disaggregation occurs at a much smaller timescale than aggregation due to the high shear rate value. This results in large variations of the structure of blood at small times ($t \leq t_d$) and therefore a large overshoot of the structure shear stress τ_{st} before the system relaxes towards the steady state.

- if $\lambda_a \ll \lambda_d$ (equivalently $\dot{\gamma} \ll 1 \text{ s}^{-1}$), then $\lambda_c \approx \lambda_a$ and we have:

$$\tau_{st, max} \approx \tau_{st, t \rightarrow \infty}. \quad (9.29)$$

Aggregation occurs at a much smaller timescale than disaggregation due to the low shear

rate value. This results in almost no variation of the structure of blood and therefore no overshoot of the structure shear stress τ_{st} .

9.3.3 Zero shear rate

We study here the reaggregation of a fluid at rest. At $t = 0$, we assume that $f = f_0$ and $\tau_{st} = \tau_{st,0}$. The kinetic equation for the structure function writes:

$$\frac{df}{dt} = -\frac{1+f}{\lambda_a}. \quad (9.30)$$

The solution of equation (9.30) writes:

$$f = 1 + [f_0 - 1] e^{-\frac{t}{\lambda_a}}. \quad (9.31)$$

Injecting expression (9.31) in equation (9.12) we obtain the following expression for the structure stress τ_{st} :

$$\tau_{st} = \tau_{st,0} \frac{f_0}{f_0 - 1 + e^{\frac{t}{\lambda_a}}}. \quad (9.32)$$

When $t \rightarrow \infty$, we find the asymptotic values of f and τ_{st} :

$$\begin{cases} f_{t \rightarrow \infty} = 1 & (9.33a) \\ \tau_{st,t \rightarrow \infty} = 0. & (9.33b) \end{cases}$$

The model exhibits here another characteristic viscoelastic property, that is the relaxation towards a fully aggregated state. The phenomenon is driven only by the characteristic aggregation timescale λ_a as in the absence of shear $\lambda_d \rightarrow \infty$.

The asymptotic analysis conducted in this section highlights the shear-thinning, viscoelastic and thixotropic behaviors of the rheological model (9.17) proposed in the previous section. In the following sections, we compare the numerical results, where spatial variations occur, to the analytic results previously obtained and to experimental results in order to assess if the model is able to quantitatively describe the flow behavior of blood.

9.4 Comparison with experimental data

We propose to compare the numerical results of the 1D non-Newtonian model (9.16)–(9.17) to experimental data available in the literature. We use the results of Bureau et al. [Bureau et al. 1980] and McMillan [McMillan et al. 1987], where the authors systematically studied using a coaxial cylinder microviscometer the response of blood to step and triangular shear solicitations.

In Subsection 9.4.1, Subsection 9.4.2 and Subsection 9.4.3, we consider a single artery in which we impose the flow rate at the inlet and a non-reflecting boundary condition at the outlet. The time-evolution of the inlet flow rate depends on the considered experimental test case. Its magnitude is given by the following expression, designed to impose a chosen shear rate $\dot{\gamma}_{in}$:

$$Q_{in}(\dot{\gamma}_{in}) = \frac{1}{\frac{\partial \phi}{\partial r}} A \dot{\gamma}_{in} \quad (9.34)$$

We recall that without loss of generality, we use $\frac{\partial \phi}{\partial r}|_{r=R} = -\frac{1}{R}$. We assume that blood enters the artery in a fully disaggregated state ($f = 0$). For each simulation, the initial conditions are the following, describing the asymptotic behavior of a fluid at rest:

$$\begin{cases} Q = 0 & \text{and} & A = A_0 & (9.35a) \\ f = 1 & \text{and} & \tau_{st} = 0. & (9.35b) \end{cases}$$

The parameters of the blood constitutive model (9.17) are summarized in Table 9.2.

ρ	μ_∞	μ_0	λ_a	δ
1	0.05	1.3	5	1.5

Table 9.2 – Parameters of the blood constitutive model (9.17), based on an analogy with the simplified Cross constitutive model [Steffan et al. 1990] and experimental data from [Quemada and Droz 1982].

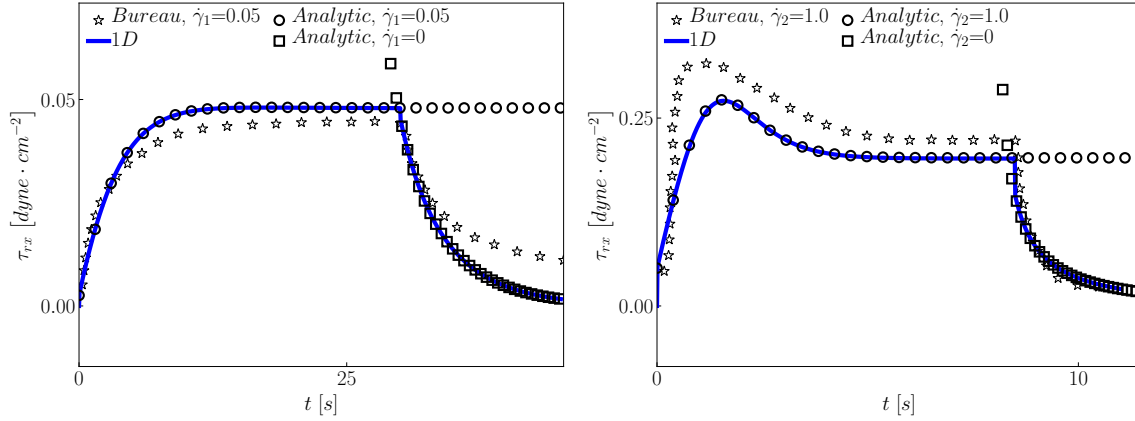


Figure 9.2 – Time evolution of the shear stress τ_{rx} with a step-change in shear rate: comparison between experimental data from Bureau [Bureau et al. 1979] (\star), results of the 1D blood flow model (9.16) (—) and analytic solutions (9.24) (\circ) and (9.32) (\square).

Left: Low shear viscoelastic regime with $\dot{\gamma}_1 = 0.05$ for $\Delta t_1 = 30$ and then $\dot{\gamma}_1 = 0$.

Right: High shear thixotropic regime (overshoot) with $\dot{\gamma}_2 = 1$ for $\Delta t_2 = 8.5$ and then $\dot{\gamma}_2 = 0$. There is a qualitative and quantitative match between experimental data and numerical results, and a perfect match between analytic and numerical results.

The geometrical and mechanical parameters describing the artery are given in Table 9.3.

L	A	K	C_v
10	1	10^4	0

Table 9.3 – Geometrical and mechanical parameters describing the artery.

Finally, the time- and space-discretization parameters are described in Table 9.4.

Δt	Δx	Order
10^{-4}	5×10^{-2}	2

Table 9.4 – Numerical parameters describing the time discretization and the mesh.

9.4.1 Single shear-step

In a series of experiments, Bureau et al. [Bureau et al. 1979] obtained experimental data on the behavior of a blood sample in controlled flow conditions. They subjected the sample to a step-change in shear rate:

$$\dot{\gamma}(t) = \begin{cases} \dot{\gamma}_{1,2} & \text{for } 0 \leq t < \Delta t_{1,2} \\ 0 & \text{for } \Delta t_{1,2} \leq t. \end{cases} \quad (9.36)$$

To highlight the viscoelastic and thixotropic behaviors of blood separately, they considered a low shear regime for which $\dot{\gamma}_1 = 0.05$ and $\Delta t_1 = 30$ and a high shear regime for which $\dot{\gamma}_2 = 1$ and $\Delta t_2 = 8.5$.

In Figure 9.2, we compare the measured experimental shear stress to the 1D numerical shear

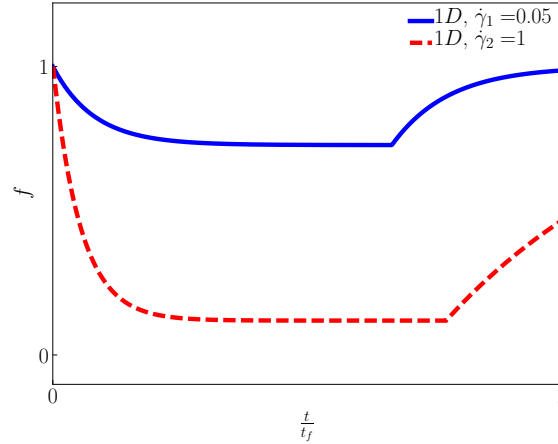


Figure 9.3 – Time evolution of the structure function f with a step-change in shear rate, computed using the 1D blood flow model (9.16).

— Low shear viscoelastic regime with $\dot{\gamma}_1 = 0.05$ for $\Delta t_1 = 30$ and then $\dot{\gamma}_1 = 0$.

-- High shear thixotropic regime with $\dot{\gamma}_2 = 1$ for $\Delta t_2 = 8.5$ and then $\dot{\gamma}_2 = 0$.

In the high shear regime, there is a large decrease of the structure function on a short timescale, leading to the thixotropic behavior observed in Figure 9.2 Right.

stress computed by mimicking the experimental flow conditions. As these flow conditions are similar to those studied analytically in Subsection 9.3.2 and Subsection 9.3.3, we also compare the experimental and numerical shear stresses to the analytic solutions (9.24) and (9.32). We observe that for both flow conditions $\dot{\gamma}_1$ and $\dot{\gamma}_2$, the experimental data from Bureau [Bureau et al. 1979] agree qualitatively and semiquantitatively with the 1D numerical results. Moreover, the analytic and 1D numerical results are perfectly matched. The data presented in Figure 9.2 Left are characteristic of a viscoelastic material: the shear stress rises continuously towards the equilibrium steady value, and then relaxes in the absence of shear towards a fully aggregated state. On the contrary, the data plotted in Figure 9.2 Right present the characteristic overshoot of a thixotropic material. These two behaviors of blood are analyzed in Subsection 9.3.2 and can be explained focusing on the evolution of the structure f , presented in Figure 9.3. At low shear values ($\dot{\gamma}_1$), the structure of blood is not significantly altered. At higher shear rates ($\dot{\gamma}_2$), large variations of the structure of blood occur on a short timescale, leading to memory effects and a thixotropic overshoot of the shear stress.

The comparison with analytic solutions validates the 1D numerical scheme and the agreement with experimental results indicates that systems (9.16)-(9.17) using the set of parameters presented in Table 9.2 provide a satisfactory description of the time-dependent behavior of blood.

9.4.2 Multiple shear-steps

Experimental data from McMillan *et al.* [McMillan et al. 1987] describe the time-dependent shear stress response of blood to two successive shear-steps of amplitude $\dot{\gamma} = 8$ and of length $\Delta t = 2.5$. The experiment was repeated three times, each time decreasing the time delay Δt_d between the consecutive shear-steps, during which no shear was applied.

In Figure 9.4 Left, we compare the time evolution of the experimental and 1D numerical shear stresses for different time delays $\Delta t_d \in \{1.5, 1, 0.5\}$. Both solutions are qualitatively and quantitatively comparable and we observe the expected viscoelastic relaxation and thixotropic transient overshoot. Results in Figure 9.4 Right correlate the increase of the overshoot amplitude with larger variations of the structure, as blood has more time to

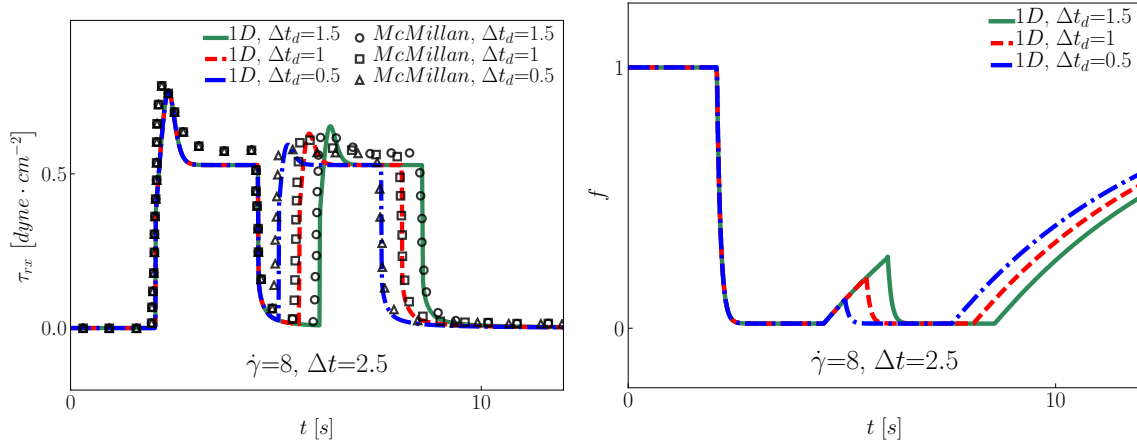


Figure 9.4 – Comparison between experimental data from McMillan [McMillan et al. 1987] and numerical results of the 1D blood flow model (9.16) describing two successive step-changes in shear rate of amplitude $\dot{\gamma} = 8$ and of length $\Delta t = 2.5$ for a time delay $\Delta t_d \in \{1.5$ (exp. \circ , 1D —), 1 (exp. \square , 1D -- --), 0.5 (exp. \triangle , 1D -- --).

Left: Shear stress τ_{rx} .

Right: Structure function f .

There is a qualitative and quantitative agreement between experimental and numerical data. The thixotropic overshoot increases with Δt_d as structure variations are more important.

reaggregate when Δt_d increases.

9.4.3 Triangle shear sollicitation

Bureau et al. [Bureau et al. 1980] also obtained experimental hysteresis curves for blood by imposing a triangular shear rate sollicitation to the sample:

$$\dot{\gamma}(t) = \begin{cases} \dot{\gamma}_{1,2} \frac{t}{t_{1,2}} & \text{for } 0 \leq t < t_{1,2} \\ \dot{\gamma}_{1,2} \left[2 - \frac{t}{t_{1,2}} \right] & \text{for } t_{1,2} \leq t \leq 2t_{1,2}. \end{cases} \quad (9.37)$$

To highlight the viscoelastic and thixotropic behaviors of blood separately, the authors considered a low shear regime ($\dot{\gamma}_1 = 0.12$ and $t_1 = 13$) and a high shear regime ($\dot{\gamma}_2 = 1.03$ and $t_2 = 47.6$).

In Figure 9.5, we plot the experimental and numerical variations of the shear stress τ_{rx} with respect to the shear rate $\dot{\gamma}$. In the low-shear regime $\dot{\gamma}_1$ plotted in Figure 9.5 Left, the viscoelastic behavior of blood is highlighted and the experimental and numerical results match very well. In the high-shear regime displayed on Figure 9.5 Right, thixotropic effects are dominant. For the increasing shear part of the curve, the experimental and numerical results are well matched. However, for the decreasing shear part, the experimental behavior is not reproduced, even though the shear stress amplitudes are similar.

The results presented in Subsection 9.4.1, Subsection 9.4.2 and Subsection 9.4.3 indicate that the 1D blood flow model (9.16) coupled to the rheological model (9.17) allows us to compute numerical results similar to well-known experimental data form [Bureau et al. 1979, 1980; McMillan et al. 1987]. We can now move towards more complex simulation in large networks of elastic arteries.

9.5 Elementary bifurcation

Bifurcations are elementary constituents of an arterial network and connect a parent artery p to two daughter arteries d_1 and d_2 . They are responsible for the reflection of the incoming

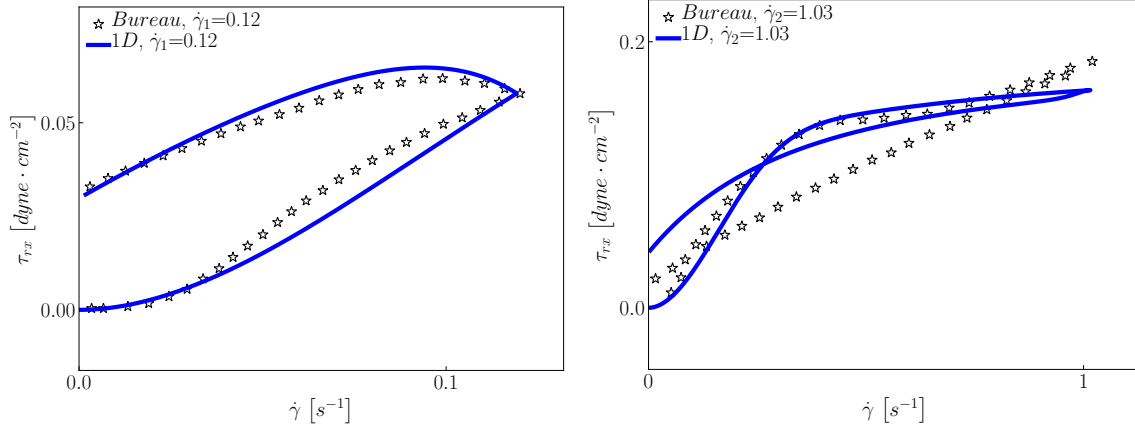


Figure 9.5 – Hysteresis curves of the evolution the shear stress τ_{rx} as a function of the shear rate $\dot{\gamma}$ under a triangular shear solicitation: comparison between experimental data from Bureau [Bureau et al. 1980] (\star) and 1D numerical results (—).

Left: Low shear viscoelastic regime with $\dot{\gamma}_1 = 0.12$ and $t_1 = 13$.

Right: High shear thixotropic regime with $\dot{\gamma}_2 = 1.03$ and $t_2 = 47.6$.

There is a qualitative and quantitative match between experimental data and numerical results.

pulse wave as they represent impedance discontinuities in the network. Due to the complex flow patterns they generate, the non-Newtonian behavior of blood can be particularly important in these configurations.

In a symmetric bifurcation, we compare here the 1D non-Newtonian blood flow model (9.16)–(9.17) with its Newtonian counterpart. The geometrical and mechanical properties of the bifurcation are presented in Table 9.5 and correspond to average properties of large arteries. At the inlet of the parent artery p , we impose the flow rate Q_{in} to mimic the behavior of the heart:

$$Q_{in}(t) = Q_h \max\left(0, \sin\left(2\pi \frac{t}{T_h}\right)\right), \quad 0 \leq t \leq 10T_h, \quad (9.38)$$

with $T_h = 1$. We choose the maximum flow rate $Q_h \in \{1, 10, 100\}$ to describe the flow in different regions of the systemic network. We also assume that blood enters the artery in a fully disaggregated state ($f = 0$). At the outlet of the daughter arteries d_1 and d_2 , we set a non-reflecting boundary condition as in Section 9.4. Finally, the initial conditions are (9.35) and the time- and space-discretization parameters of the network are described in Table 9.4. We present data obtained after 4 periods to ensure that the system has reached a periodic state.

L_{p,d_1,d_2}	R_{p,d_1,d_2}	K_{p,d_1,d_2}	C_v
10	1	10^4	0

Table 9.5 – Geometrical and mechanical parameters describing the properties of the parent artery p and the daughter arteries d_1 and d_2 .

In Figure 9.6, we compare the structure f (Left), shear stress τ_{rx} (Center) and pressure p (Right) waveforms computed with the Newtonian and non-Newtonian 1D blood flow models in the middle of the parent artery p and the daughter artery d_1 . We do not present results for the artery d_2 as they are identical to those of artery d_1 due to the symmetry of the bifurcation. As we decrease the flow rate ($Q = 100$ to $Q = 1$ from top to bottom in Figure 9.6), the shearing forces decrease allowing the RBCs to aggregate. As a consequence, in both arteries the structure function f and the shear stress $|\tau_{rx}|$ increase compared to the Newtonian case, with up to 100% differences for $Q_h = 1$. The pressure then rises to

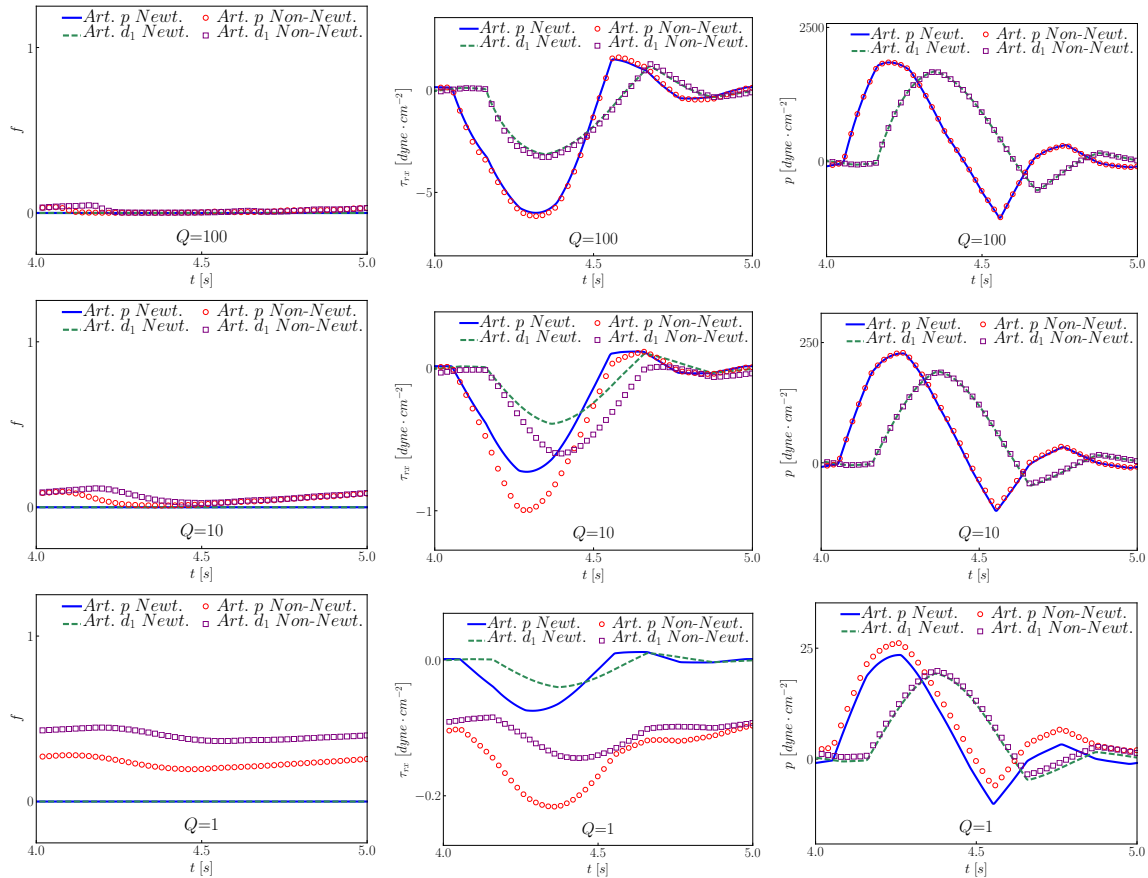


Figure 9.6 – Temporal evolution of the flow waveforms in an arterial bifurcation taken in the middle of parent artery p and the daughter artery d_1 : comparison between the Newtonian (artery p —, artery d_1 --) and the non-Newtonian (artery p \circ , artery d_1 \square) 1D blood flow models.

Left: Structure function f .

Center: Shear stress τ_{rx} .

Right: Pressure p .

Top: $Q = 100$.

Middle: $Q = 10$.

Bottom: $Q = 1$.

As the flow rate decreases, the aggregation increases, leading to a higher shear stress $|\tau_{rx}|$ and an increase of the pressure p .

compensate the increased viscous stresses and maintain a normal flow. Note that the value of f is higher and the value of $|\tau_{rx}|$ is lower in artery d_1 than in artery p as the flow coming from artery p splits in two to vascularize both daughter arteries.

These results indicate that non-Newtonian effects are important in certain bifurcations and can lead to modification of the WSS stress patterns and an increase of pressure. They are corroborated by similar data obtained in different 3D studies [Weddell et al. 2015; Apostolidis et al. 2016] of bifurcations. In the following, we build on this analysis and study non-Newtonian effects in large networks of arteries.

9.6 Idealized asymmetric network

Reduced-order 1D blood flow models have been designed to capture the wave propagation dynamics in large networks. In this framework, we analyze how non-Newtonian effects affect the network hemodynamics using the 1D time-dependent non-Newtonian model (9.16)–(9.17).

We consider an idealized asymmetric arterial tree made only of elementary bifurcations linked together to form a network. In each elementary bifurcation a parent artery p connects to two daughter arteries d_α and d_β . Given the mechanical and geometrical properties of the parent artery p , we construct the daughter arteries using the following relationships, presented in [Olufsen 1999; Olufsen et al. 2000] and used more recently in [Blanco et al. 2014; Perdikaris et al. 2015], which describe the physiological evolution the arteries' geometrical and mechanical properties along the network:

$$\begin{cases} R_\alpha = \alpha R_p & (9.39a) \end{cases}$$

$$\begin{cases} R_\beta = \beta R_p & (9.39b) \end{cases}$$

$$\begin{cases} L = 50R & (9.39c) \end{cases}$$

$$\begin{cases} K = \frac{4}{3} \frac{R}{\sqrt{\rho l}} [k_1 e^{k_2 R} + k_3] & (9.39d) \end{cases}$$

$$\begin{cases} \dot{\gamma} = -4 \frac{U}{R}, & (9.39e) \end{cases}$$

where $\alpha = 0.9$ and $\beta = 0.6$ are asymmetry coefficients and $k_1 = 2 \times 10^7$ dyne \cdot cm $^{-4}$, $k_2 = -22.53$ cm $^{-1}$ and $k_3 = 8.65 \times 10^5$ dyne \cdot cm $^{-4}$. The aim of this study is to understand how the size of the network, dependent on the level n_l of vessel ramifications, influences the aggregation process. For a given value of n_l , we construct the network by adding the corresponding number n_b of bifurcations and the number n_a of arteries. Table 9.6 presents the values of n_l , n_a and n_b used in the following.

n_l	n_b	n_a
2	3	7
4	15	31
6	63	127
n	$2^n - 1$	$2^{n+1} - 1$

Table 9.6 – Number n_l of level of vessel ramifications, number n_b of bifurcations and number n_a of arteries of an idealized asymmetric network

At the root of the network, the radius of the artery is $R_0 = 1$ cm and we impose the same pulsatile the flow rate (9.38) as in the previous Section 9.5, with $Q_h = 100$ and $T_h = 1$. We also assume that blood enters the artery in a fully disaggregated state ($f = 0$). At the leaves of the network (terminal segments), we set as in the previous Section 9.5 non-reflecting boundary conditions. We therefore detach ourselves from classical resistive boundary conditions and construct the network dynamics by adding successive levels of vessel ramifications. These boundary conditions are invariant with n_l and provide us with the adequate framework to study network-size effects.

Finally, the initial conditions are (9.35) and the time- and space-discretization parameters of the network are described in Table 9.7. We present data obtained after 9 periods to ensure that the system has reached a periodic state.

Δt	Δx	Order
10^{-5}	10^{-1}	2

Table 9.7 – Numerical parameters describing the time discretization and the mesh

9.6.1 Healthy network

We construct three healthy networks with $n_l \in \{2, 4, 6\}$. In Figure 9.7, we plot the distribution of the structure function f in the three networks at 4 characteristic times of the

last cardiac cycle: $t_1 = 9T_h$, $t_2 = 9.25T_h$, $t_3 = 9.5T_h$ and $t_4 = 9.75T_h$.

We observe clear effects of network size and asymmetry on the aggregation of RBCs. At $t = 9T_h$, the aggregation is stronger for $n_l = 2$, as the reflective behavior of the network is smaller due to the smaller number of bifurcations. At $t = 9.25T_h$, the inlet flow rate reaches its maximum value and blood is globally disaggregated for $n_l = \{2, 4, 6\}$. Nevertheless, for $n_l = 4$ and $n_l = 6$, aggregated regions remain in the left hand side (l.h.s.) large extremity arteries. These regions belong to high ramification levels and have not yet been reached by the incoming pulse wave. At $t = 9.5$, all RBCs have been disaggregated by the incoming pulse. Finally at $t = 9.75$, RBCs reaggregate in the l.h.s. large arteries since there is no flow coming from the heart and the reflected waves have been damped by viscous effects. Furthermore, the shear rate $\dot{\gamma}$ is lower in these larger arteries. Overall, aggregation dynamics depend on the size and asymmetry of the network and aggregation occurs principally in the large arteries of the l.h.s. and their immediate daughter arteries. In these arteries, the structure function reaches the critical value of $f \approx 0.1$, at which blood displays viscoelastic and thixotropic effects (see Subsection 9.4.2).

These results indicate that we must take into account non-Newtonian effects in networks presenting large arteries or a high level of vessel ramifications. Furthermore, these results highlight the importance of vessel topology as the asymmetry of the network influences the aggregation dynamics.

9.6.2 Pathological network

In the literature, non-Newtonian blood effects have been particularly studied in elementary pathological networks [Fan et al. 2009; Weddell et al. 2015; Apostolidis et al. 2016]. However, as observed before, the size and asymmetry of the network plays an important role in the aggregation dynamics. To characterize how pathologies can modify the flow and aggregation in a large network, we introduce two severe stenoses of 90% of obstruction each in the 3 networks presented above. One is located on the l.h.s., in the large radius branch of the network and the other is on the r.h.s., in the small radius branch. The exact position of both stenoses is represented in Figure 9.8 by a circle (\circ).

As previously, we plot in Figure 9.8 the distribution of the structure function f in the three networks ($n_l \in \{2, 4, 6\}$) at the same 4 characteristic times of the last cardiac cycle: $t_1 = 9T_h$, $t_2 = 9.25T_h$, $t_3 = 9.5T_h$ and $t_4 = 9.75T_h$. For $n_l \in \{4, 6\}$, the presence of the stenoses results in a higher aggregation in the arteries downstream of the stenoses compared to Figure 9.7. On the contrary for $n_l = 2$, the value of the structure f is lower than in Figure 9.7 as the stenoses create reflections that contribute to the disaggregation process. These results show that aggregation effects are amplified in pathological networks as the flow is reduced downstream of the stenoses. Upstream of the stenoses, aggregation is reduced due to additional reflected waves produced by the stenoses.

The numerical results presented in this section demonstrate that non-Newtonian behaviors can exist in healthy and pathological networks. Even if these non-Newtonian behaviors are small, they are non-negligible. They affect in particular the WSS distribution in the networks, which plays an important role in cardiovascular pathogenesis. The non-Newtonian aspect of blood must therefore be taken into account to accurately compute network hemodynamics, especially in pathological networks.

9.7 Conclusion

In Chapter 9, we have proposed 1D generalized non-Newtonian blood flow model, based on a classical 1D approach for the conservation mass and the balance of momentum, but

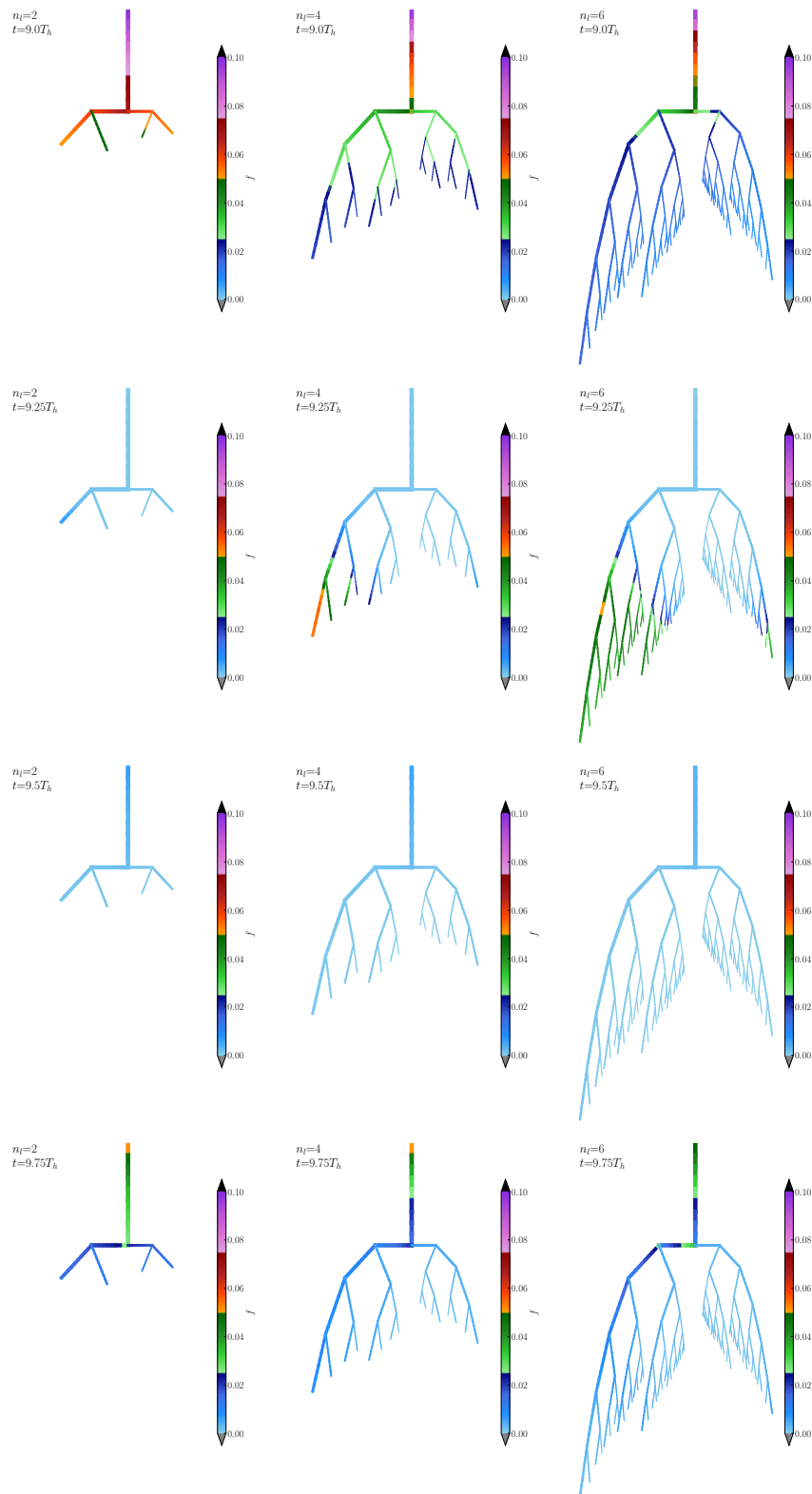


Figure 9.7 – Snapshots at $t_1 = 9T_h$, $t_2 = 9.25T_h$, $t_3 = 9.5T_h$ and $t_4 = 9.75T_h$ of the distribution of the structure function f in three healthy networks with increasing levels of ramification $n_l \in \{2$ (Left), 4 (Center), 6 (Right) $\}$. Aggregation occurs mainly in the large arteries on the l.h.s of the network and in their immediate daughter arteries. Aggregation depends on the pulsatility of the flow, the size and the asymmetry of the network.

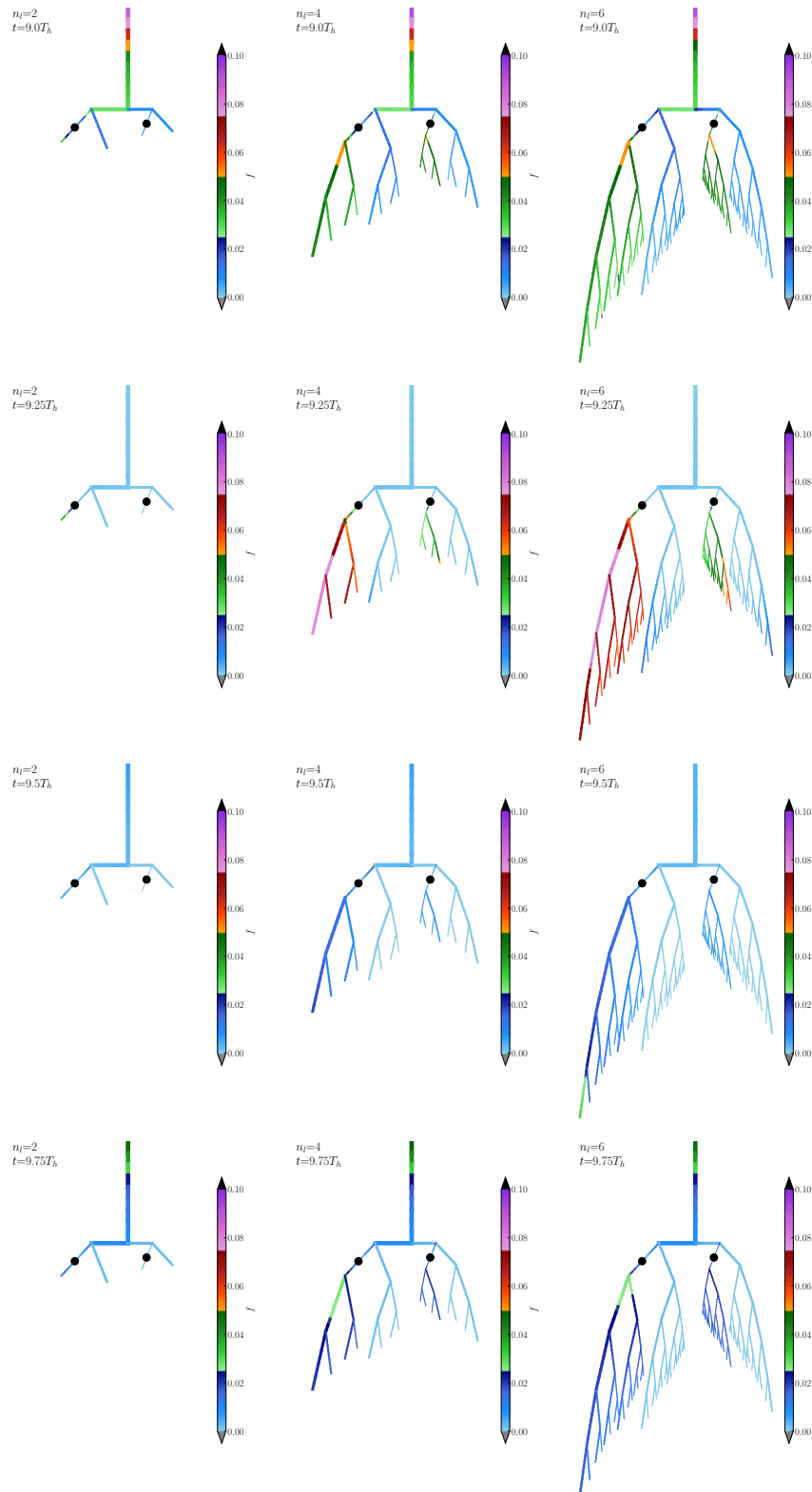


Figure 9.8 – Snapshots at $t_1 = 9T_h$, $t_2 = 9.25T_h$, $t_3 = 9.5T_h$ and $t_4 = 9.75T_h$ of the distribution of the structure function f in three pathological networks with increasing levels of ramification $n_l \in \{2$ (Left), 4 (Center), 6 (Right) $\}$, presenting two stenosis marked by the black circles (\circ). Aggregation now occurs in the large arteries on the l.h.s of the network and in their immediate daughter arteries but also on the r.h.s, downstream of the stenosis. In the arteries upstream of the stenoses, aggregation is reduced due to the additional reflections created by the stenoses.

including time- and structure-dependent viscous effects. The evolution of the shear stress is governed by a Maxwell equation with coefficients depending on the state of aggregation of RBCs. The balance between aggregation and shear-dependent disaggregation is described by a kinetic equation, which is a particular case of a structural model for viscoelastic fluids. We note that this approach is not restricted to blood rheology and could be applied to other structured fluids.

We have confronted the numerical predictions of our 1D blood flow model to experimental data available in the literature [Bureau et al. 1979, 1980; McMillan et al. 1987], and we have shown that the model reproduces qualitatively and quantitatively the rheology of blood. We have further investigated the non-Newtonian effects in arterial networks of increasing size and demonstrated how the pulsatility of the flow and the network topology contribute to the aggregation process, which occurs mainly in the large arteries and their immediate daughter arteries. The aggregation of RBCs is further increased downstream of pathologies such as stenoses.

In the entire study, we have assumed, in a 1D framework, that the wall shear rate $\dot{\gamma}|_{r=R}$ solely contributes to the disaggregation process as structure is represented by a single homogeneous phase. The shear rate $\dot{\gamma}|_{r=R}$ therefore governs the evolution of the blood structure near the wall and in the bulk of the flow. In reality, the axial velocity profile varies with time and space leading to variations of $\dot{\gamma}$ along the radius of the artery. In particular, for axisymmetric flow, $\dot{\gamma}|_{r=0} = 0$. By using the wall shear rate $\dot{\gamma}|_{r=R}$ to govern the disaggregation process in the entire artery we have overestimated the shearing effects and therefore underestimated the non-Newtonian effects. However, we have also assumed an *a priori* shape of the velocity profile, which is valid for experimental validation (see Section 9.4) but an approximation for network flows. In Section 9.5 and Section 9.6, we have assumed a Poiseuille flow everywhere in the network, as is classically done in 1D applications, and therefore underestimated the value of $\dot{\gamma}$. To overcome those limitations due to the loss of the velocity profile in the 1D averaging process, we plan in future works to use the 2D multiring framework developed in Chapter 8 to compute the axial velocity profile and introduce radial variations in the aggregation process.

Keeping in mind these limitations inherent to the 1D framework, the 1D generalized non-Newtonian blood flow model presented here will be useful in the future to help understanding the hemodynamics in healthy and pathological networks of the micro- and macro-circulation.

Chapter 10

Conclusion and perspectives

Contents

10.1 Conclusion	220
10.2 Perspectives	220
10.2.1 Short term perspectives	221
10.2.2 Long term perspectives	221

This thesis dealt with mathematical modeling and numerical simulations of blood flow in large arteries through the use of reduced-order blood flow models. These models capture at low computational and modeling costs the wave propagation dynamics in large networks of arteries which are essential to reproduce *in vivo* waveforms. However, their simplicity stems from modeling assumptions that partially hinder their ability to accurately reproduce the hemodynamics in specific pathological situations.

The overall goal of this thesis was therefore to revisit the main hypotheses used to derive the reduced-order models and to propose improvements through numerical methods and complementary models. Our focus was set on three particular issues:

- the viscoelasticity of the arterial wall (Chapter 3);
- the shape of the velocity profile, especially in pathological vessels (Chapter 8);
- the non-Newtonian behavior of blood (Chapter 9).

Additionally, through fruitful collaborations with the clinicians Dr. Salam Abou Taam (Hôpital Privé Claude Galien, Quincy-sous-Sénart, France), Dr. Julien Gaudric (Hôpital La Pitié Salpêtrière, Paris, France) and especially Dr. Teresa Politi (Faculdade de Medicina, Buenos Aires, Argentina), we also addressed more clinical issues concerning the origin of the dirotic notch, extracorporeal bypass surgeries and aortic and Iliac clamping (Chapter 7). These clinical issues led to a reflection on outflow boundary conditions (Chapter 6) and to the development of well-balanced numerical methods able to capture 1D hemodynamics in pathological vessels (Chapter 5). Concerning this last point, the method was introduced to us by Dr. Olivier Delestre (Université de Nice Sophia-Antipolis, Nice, France) with which we have collaborated since then. We were also greatly helped by Pr. Jacques Sainte-Marie (UPMC, Paris, France) and Dr. Emmanuel Audusse (Université Paris 13, Villetaneuse, France) on mathematical and numerical issues. Finally, a lasting collaboration with Pr. Mami Matsukawa and her students, Shimpei Ono and Shinya Shimada, has allowed us to collect experimental data on wave propagation in straight and stenosed tubes that we will use to validate our numerical methods.

As each part of this thesis was ended with a specific conclusion, we propose here a global conclusion and some perspectives.

10.1 Conclusion

Blood in the large and small elastic arteries is driven by the periodic contraction of the heart. This periodic inflow generates waves that elastically propagate in the arterial network and are subjected to reflection at arterial junctions and in the peripheral vascular sites (arterioles), to viscous dissipation and to viscoelastic diffusion (viscosity of the arterial wall). The speed at which these waves propagate is large, allowing us to simplify the governing equations for blood flow and derive a one-dimensional (1D) long wave blood flow model. This 1D model naturally accounts for wave propagation through its hyperbolic mathematical structure and has been extensively used in the literature. However, modeling assumptions are required to describe the viscous effect of blood, the viscoelastic effect of the arterial wall and the rheology of blood itself.

Indeed, 1D blood flow models are unable to describe the spatial and temporal evolution of the velocity profile in the artery, and therefore can not properly evaluate the wall shear stress (WSS), which is an important hemodynamical factor in the development of cardiovascular pathologies. To overcome this limitation, we have proposed a two-dimensional (2D) extension of the 1D model, able to dynamically compute the velocity profile and provide an accurate estimation of the WSS. We have shown that this 2D model can compute flow recirculation in stenoses (constrictions) and aneurysms (expansions), can account for large deformation of the arterial wall and does not require an adaptation of the radial mesh. Obviously, the computational costs of the 2D model is greater than those of the 1D model, yet its modeling cost are lower as there are no unknown parameters linked to the velocity profile. Moreover, the computational and modeling costs of the 2D blood flow model are still greatly inferior to those of three-dimensional (3D) fluid-structure interaction (FSI) models.

The viscosity of the arterial wall is also an important feature of arterial wall dynamics that is often discarded in 1D blood flow simulations. Indeed, it is difficult to measure the viscosity of the wall without direct access to arterial wall samples. Fortunately, using *ex vivo* measurements provided by our collaboration with Pr. Armentano (Favaloro University, Buenos Aires, Argentina), we were able to evaluate the viscoelastic behavior of the arterial wall of sheep, which allowed us to show that a nonlinear Kelvin-Voigt viscoelastic model is necessary to accurately capture the deformation of the arterial wall under pressure solicitations.

Finally, we have dealt with the issue of blood rheology by proposing a 1D non-Newtonian blood flow model as an alternative to the classical 1D Newtonian blood flow models. This model takes into account the time-dependent aggregation of red blood cells (RBCs) into long column-like structures called rouleaux and is therefore able to describe the viscoelastic, shear-thinning and thixotropic behaviors of blood. These non-Newtonian behaviors contribute to a better description of blood, particularly in low-shear flow regimes (diastole, severe stenoses, aneurysms, ...).

The combination of these three approaches provides valuable tools to improve the modeling of blood flow in large elastic arteries, leading to better hemodynamical predictions and improved clinical diagnosis.

10.2 Perspectives

There are multiple perspectives for the work presented in this thesis, and we have organized them into short and long term perspectives.

10.2.1 Short term perspectives

The work presented in this thesis has essentially dealt with blood flow in the large and small arteries. However, the cardiovascular system is a closed-loop circuit. Therefore, it is imperative to implement a heart model, organ models and models for the pulmonary and venous circulations in order to obtain a complete numerical model of the cardiovascular system. This model could then be applied to study medical issues such as arterio-venous fistula and compensation mechanisms of the heart during clamping, bypass surgeries and extracorporeal circulation procedures. A parameter estimation strategy should also be implemented in order to apply the model to patient-specific clinical issues. Finally, the code should be made open-source to create a community of users that would contribute to its improvement and increase the chances of producing a clinically relevant help-to-decision tool for clinicians.

On a more technical note, the 2D multiring model we have proposed should be efficiently coupled to the 1D model and their differences should be compared using analytic test cases such as the Womersley solution as well as experimental data. The work on control-volume junction modeling should also be continued and improved by considering for example that the 2D Shallow water equations are valid in junctions, thereby enabling the proper description of the flow rate.

Overall, interactions with clinicians should be increased to guide the research towards clinically relevant problematics.

10.2.2 Long term perspectives

Concerning the long term perspectives, we think that the future of cardiovascular modeling does not lie in full 3D simulations of blood flow in large networks. Indeed, even if the issues of 3D computational and modeling costs were resolved, clinicians are usually only interested in small portions of the arterial network and regions far from the points of interest do not require a 3D detailed treatment. We therefore think that a model adaptation strategy is more relevant, similar to mesh adaptation strategies commonly used in numerical simulations. Far from the region of interest, we would use reduced-order models to provide global information to more detailed models used only in the region of interest. Contrary to studies that have already used such an approach, the choice of model refinement would be dynamical and guided by modeling error estimators and the complete panel of blood flow models would be used (0D, 1D, 2D and 3D). This approach is particularly appropriate for cardiovascular modeling as blood flow is periodic and the arterial network is naturally segmented. This model adaptation strategy would drastically reduce the modeling costs as reduced-order models require much less parameters than full 3D FSI models and would provide an efficient and accurate blood flow modelization tool for clinicians that could be applied to strongly multiscale problems such as the study of lower-extremity arterial disease.

Growth and remodeling models should also be considered, especially of the microcirculation, as they play an important part in the development of cardiovascular diseases and peripheral circulation. The study of drug transport is also an interesting field of research, with the objective of determining the optimal injection point in order to reach a specific target. This could potentially reduce the doses at which antibiotics are administered and slow down the increasing resistance of bacteria.

At very long term, a full body model should be developed, including the cardiovascular system as well as bones, muscles, the digestive system, . . . However, this global human model raises many modeling and numerical issues, including estimating the colossal amount of parameters it implies, that must be resolved before ever hoping to reach such an objective.

Bibliography

- W.M. Abbott, A. Callow, W. Moore, R. Rutherford, F. Veith, and S. Weinberg. Evaluation and performance standards for arterial prostheses. *Journal of vascular surgery*, 17(4): 746–756, 1993. [144](#)
- J. Alastruey, K.H. Parker, J. Peiró, S.M. Byrd, and S.J. Sherwin. Modelling the circle of willis to assess the effects of anatomical variations and occlusions on cerebral flows. *Journal of biomechanics*, 40(8):1794–1805, 2007. [8](#)
- J. Alastruey, K.H. Parker, J. Peiró, and S.J. Sherwin. Lumped parameter outflow models for 1-d blood flow simulations: effect on pulse waves and parameter estimation. *Communications in Computational Physics*, 4(2):317–336, 2008. [7](#), [8](#), [48](#), [49](#), [98](#), [114](#), [121](#)
- J. Alastruey, K.H. Parker, J. Peiró, and S.J. Sherwin. Analysing the pattern of pulse waves in arterial networks: a time-domain study. *Journal of Engineering Mathematics*, 64(4): 331–351, 2009. [49](#), [68](#), [98](#), [99](#), [142](#), [143](#), [167](#)
- J. Alastruey, A.W. Khir, K.S. Matthys, P. Segers, S.J. Sherwin, P.R. Verdonck, K.H. Parker, and J. Peiró. Pulse wave propagation in a model human arterial network: assessment of 1-D visco-elastic simulations against in vitro measurements. *Journal of biomechanics*, 44(12):2250–2258, 2011. [6](#), [7](#), [9](#), [26](#), [32](#), [45](#), [98](#), [113](#), [114](#), [146](#)
- J. Alastruey, K.H. Parker, and S.J. Sherwin. Arterial pulse wave haemodynamics. In *11th International Conference on Pressure Surges*, pages 401–442. Virtual PiE Led t/a BHR Group: Lisbon, Portugal, 2012. [4](#), [28](#), [99](#), [110](#)
- L. Allievi. Teoria del colpo d’ariete, Atti Collegio Ing. Arch. English translation by Halmos E.E. 1929, The Theory of Waterhammer. *Trans. ASME*, 1913. [16](#)
- D. Ambrosi, A. Quarteroni, and G. Rozza. *Modeling of physiological flows*, volume 5. Springer Science & Business Media, 2012. [2](#)
- M. Anand and K.R. Rajagopal. A shear-thinning viscoelastic fluid model for describing the flow of blood. *Int. J. Cardiovasc. Med. Sci*, 4(2):59–68, 2004. [201](#)
- M. Anand, J. Kwack, and A. Masud. A new generalized oldroyd-b model for blood flow in complex geometries. *International Journal of Engineering Science*, 72:78–88, 2013. [201](#), [202](#)
- A.J. Apostolidis and A.N. Beris. Modeling of the blood rheology in steady-state shear flows. *Journal of Rheology*, 58(3):607–633, 2014. [201](#)

- A.J. Apostolidis, M.J. Armstrong, and A.N. Beris. Modeling of human blood rheology in transient shear flows. *Journal of Rheology*, 59(1):275–298, 2015. [202](#)
- A.J. Apostolidis, A.P. Moyer, and A.N. Beris. Non-Newtonian effects in simulations of coronary arterial blood flow. *Journal of Non-Newtonian Fluid Mechanics*, 233:155–165, 2016. [201](#), [213](#), [215](#)
- N.D. Appleton, D. Bosanquet, G. Morris-Stiff, H. Ahmed, P. Sanjay, and M.H. Lewis. Extra-anatomical bypass grafting – A single surgeon’s experience. *Annals of the Royal College of Surgeons of England*, 92(6):499, 2010. [144](#)
- R.L. Armentano, J.G. Barra, J. Levenson, A. Simon, and R.H. Pichel. Arterial wall mechanics in conscious dogs assessment of viscous, inertial, and elastic moduli to characterize aortic wall behavior. *Circulation Research*, 76(3):468–478, 1995. [32](#), [146](#)
- R.L. Armentano, J.G. Barra, F.M. Pessana, D.O. Craiem, S. Graf, D.B. Santana, and R.A. Sanchez. Smart smooth muscle spring-dampers. *IEEE Engineering in Medicine and Biology Magazine*, 1(26):62–70, 2007. [9](#), [32](#)
- R.L. Armentano, L.J. Cymberknop, W. Legnani, F.M. Pessana, D. Craiem, S. Graf, and J.G. Barra. Arterial pressure fractality is highly dependent on wave reflection. In *Engineering in Medicine and Biology Society (EMBC), 2013 35th Annual International Conference of the IEEE*, pages 1960–1963. IEEE, 2013. [156](#), [159](#), [162](#), [163](#), [164](#), [165](#)
- C.J. Arthurs, K.D. Lau, K.N. Asrress, S.R. Redwood, and C.A. Figueroa. A mathematical model of coronary blood flow control: simulation of patient-specific three-dimensional hemodynamics during exercise. *American Journal of Physiology-Heart and Circulatory Physiology*, 310(9):H1242–H1258, 2016. [167](#)
- C. Audebert, M. Bekheit, P. Bucur, E. Vibert, and I.E. Vignon-Clementel. Partial hepatectomy hemodynamics changes: Experimental data explained by closed-loop lumped modeling. *Journal of Biomechanics*, 50:202–208, 2017a. [7](#)
- C. Audebert, P. Bucur, M. Bekheit, E. Vibert, I.E. Vignon-Clementel, and J.-F. Gerbeau. Kinetic scheme for arterial and venous blood flow, and application to partial hepatectomy modeling. *Computer Methods in Applied Mechanics and Engineering*, 314:102–125, 2017b. [45](#), [46](#), [167](#), [177](#), [201](#), [205](#)
- E. Audusse and M.-O. Bristeau. A well-balanced positivity preserving second-order scheme for shallow water flows on unstructured meshes. *Journal of Computational Physics*, 206(1):311–333, 2005. [46](#), [179](#)
- E. Audusse, F. Bouchut, M.-O. Bristeau, R. Klein, and B. Perthame. A fast and stable well-balanced scheme with hydrostatic reconstruction for shallow water flows. *SIAM Journal on Scientific Computing*, 25(6):2050–2065, 2004. [65](#), [67](#)
- E. Audusse, M.-O. Bristeau, B. Perthame, and J. Sainte-Marie. A multilayer Saint-Venant system with mass exchanges for shallow water flows. Derivation and numerical validation. *ESAIM: Mathematical Modelling and Numerical Analysis*, 45(01):169–200, 2011. [169](#), [175](#), [176](#), [177](#), [179](#), [180](#)
- E. Audusse, F. Benkhaldoun, S. Sari, M. Seaid, and P. Tassi. A fast finite volume solver for multi-layered shallow water flows with mass exchange. *Journal of Computational Physics*, 272:23–45, 2014. [176](#), [177](#)

- E. Audusse, F. Bouchut, M.-O. Bristeau, and J. Sainte-Marie. Kinetic entropy inequality and hydrostatic reconstruction scheme for the Saint-Venant system. *Mathematics of Computation*, page 1, 2016. [67](#)
- A.P. Avolio. Multi-branched model of the human arterial system. *Medical and Biological Engineering and Computing*, 18(6):709–718, 1980. [116](#)
- G.R. Barrenechea and F. Chouly. A finite element method for the resolution of the Reduced Navier-Stokes/Prandtl equations. *ZAMM-Journal of Applied Mathematics and Mechanics/Zeitschrift für Angewandte Mathematik und Mechanik*, 89(1):54–68, 2009. [168](#)
- J.B. Bassingthwaighe. Fractal vascular growth patterns. *Acta stereologica*, 11(Suppl 1):305, 1992. [157](#)
- M. Beckmann, V. Jacomella, M. Kohler, M. Lachat, A. Salem, B. Amann-Vesti, and M. Husmann. Risk stratification of patients with peripheral arterial disease and abdominal aortic aneurysm using aortic augmentation index. *PloS one*, 10(10):e0139887, 2015. [156](#)
- A. Bermúdez and M.E. Vázquez. Upwind methods for hyperbolic conservation laws with source terms. *Computers & Fluids*, 23(8):1049–1071, 1994. [64](#), [179](#)
- J. Bernsdorf and D. Wang. Non-newtonian blood flow simulation in cerebral aneurysms. *Computers & Mathematics with Applications*, 58(5):1024–1029, 2009. [201](#)
- D. Bessems, M. Rutten, and F. van De Vosse. A wave propagation model of blood flow in large vessels using an approximate velocity profile function. *Journal of Fluid Mechanics*, 580:145–168, 2007. [168](#)
- R. B. Bird. Useful non-Newtonian models. *Annual Review of Fluid Mechanics*, 8(1):13–34, 1976. [201](#)
- R.B. Bird, R.C. Armstrong, O. Hassager, and C.F. Curtiss. *Dynamics of polymeric liquids*, volume 1. Wiley New York, 1977. [32](#)
- P.J. Blanco, R.A. Feijóo, and S.A. Urquiza. A unified variational approach for coupling 3D–1D models and its blood flow applications. *Computer Methods in Applied Mechanics and Engineering*, 196(41):4391–4410, 2007. [201](#)
- P.J. Blanco, M.R. Pivello, S.A. Urquiza, and R.A. Feijóo. On the potentialities of 3D–1D coupled models in hemodynamics simulations. *Journal of Biomechanics*, 42(7):919–930, 2009. [201](#)
- P.J. Blanco, S.M. Watanabe, E.A. Dari, M.A.R.F. Passos, and R.A. Feijóo. Blood flow distribution in an anatomically detailed arterial network model: criteria and algorithms. *Biomechanics and modeling in mechanobiology*, 13(6):1303–1330, 2014. [8](#), [107](#), [123](#), [124](#), [214](#)
- P.J. Blanco, S.M. Watanabe, M.A.R.F. Passos, P.A. Lemos, and R.A. Feijóo. An anatomically detailed arterial network model for one-dimensional computational hemodynamics. *IEEE Transactions on Biomedical Engineering*, 62(2):736–753, 2015. [8](#), [123](#), [124](#)
- T. Bodnár, A. Sequeira, and M. Prosi. On the shear-thinning and viscoelastic effects of blood flow under various flow rates. *Applied Mathematics and Computation*, 217(11):5055–5067, 2011. [202](#)

- E. Boileau, P. Nithiarasu, P.J. Blanco, L.O. Müller, F.E. Fossan, L.R. Hellevik, W.P. Donders, W. Huberts, M. Willemet, and J. Alastruey. A benchmark study of numerical schemes for one-dimensional arterial blood flow modelling. *International journal for numerical methods in biomedical engineering*, 31(10), 2015. [8](#), [45](#), [112](#), [113](#), [114](#), [123](#), [124](#), [125](#)
- P.-A. Bois. *Introduction à la mécanique théorique des fluides*. Ellipses, 2000. [88](#)
- A. Borlotti, Y. Li, K.H. Parker, and A.W. Khir. Experimental evaluation of local wave speed in the presence of reflected waves. *Journal of biomechanics*, 47(1):87–95, 2014. [142](#), [156](#)
- F. Bouchut. Construction of BGK models with a family of kinetic entropies for a given system of conservation laws. *Journal of Statistical Physics*, 95(1-2):113–170, 1999. [46](#), [177](#)
- F. Bouchut. *Nonlinear stability of finite Volume Methods for hyperbolic conservation laws and Well-Balanced schemes for sources*. Springer Science & Business Media, 2004. [45](#), [69](#), [86](#), [87](#), [206](#)
- F. Bouchut and T. Morales De Luna. A subsonic-well-balanced reconstruction scheme for shallow water flows. *SIAM Journal on Numerical Analysis*, 48(5):1733–1758, 2010. [65](#), [71](#), [72](#), [73](#), [96](#)
- E.L. Boulpaep, W.F. Boron, M.J. Caplan, L. Cantley, P. Igarashi, P.S. Aronson, and E.G. Moczydlowski. Medical Physiology a Cellular and Molecular Approach. *Signal Transduct*, 48:27, 2009. [128](#), [142](#)
- R.P. Brent. *Algorithms for minimization without derivatives*. Courier Corporation, 2013. [119](#)
- M.-O. Bristeau and B. Coussin. Boundary conditions for the shallow water equations solved by kinetic schemes. 2001. [48](#), [49](#), [182](#)
- R. Budwig, D. Elger, H. Hooper, and J. Slippery. Steady flow in abdominal aortic aneurysm models. *Journal of biomechanical engineering*, 115(4A):418–423, 1993. [193](#)
- M. Bureau, J.C. Healy, D. Bourgoïn, and M. Joly. Etude rhéologique en régime transitoire de quelques échantillons de sangs humains artificiellement modifiés. *Rheologica Acta*, 18(6):756–768, 1979. [202](#), [209](#), [210](#), [211](#), [218](#)
- M. Bureau, J.C. Healy, D. Bourgoïn, and M. Joly. Rheological hysteresis of blood at low shear rate. *Biorheology*, 17(1-2):191, 1980. [9](#), [201](#), [202](#), [208](#), [211](#), [212](#), [218](#)
- R.H. Byrd, P. Lu, J. Nocedal, and C. Zhu. A limited memory algorithm for bound constrained optimization. *SIAM Journal on Scientific Computing*, 16(5):1190–1208, 1995. [119](#)
- E.I. Cabrera Fischer, D. Bia, J.M. Camus, Y. Zócalo, E. De Forteza, and R.L. Armentano. Adventitia-dependent mechanical properties of brachiocephalic ovine arteries in in vivo and in vitro studies. *Acta Physiologica*, 188(2):103–111, 2006. [34](#)
- S. Čanić. Blood flow through compliant vessels after endovascular repair: wall deformations induced by the discontinuous wall properties. *Computing and visualization in science*, 4(3):147–155, 2002. [64](#)
- S. Čanić, D. Lamponi, A. Mikelić, and J. Tambača. Self-consistent effective equations modeling blood flow in medium-to-large compliant arteries. *Multiscale Modeling & Simulation*, 3(3):559–596, 2005. [168](#)
- Su. Čanić, C.J. Hartley, D. Rosenstrauch, J. Tambača, G. Guidoboni, and A. Mikelić. Blood flow in compliant arteries: an effective viscoelastic reduced model, numerics, and experimental validation. *Annals of Biomedical Engineering*, 34(4):575–592, 2006. [168](#)

- C.G. Caro, T.J. Pedley, and W.A. Seed. The Mechanics of the Circulation. *Cardiovascular physiology*. London: Medical and Technical Publishers, 1974. [2](#)
- M.J. Castro, A. Pardo Milanés, and C. Parés. Well-balanced numerical schemes based on a generalized hydrostatic reconstruction technique. *Mathematical Models and Methods in Applied Sciences*, 17(12):2055–2113, 2007. [76](#)
- M.J. Castro Díaz, J.A. López-García, and C. Parés. High order exactly well-balanced numerical methods for shallow water systems. *Journal of Computational Physics*, 246: 242–264, 2013. [76](#), [78](#)
- V. Casulli, M. Dumbser, and E.F. Toro. Semi-implicit numerical modeling of axially symmetric flows in compliant arterial systems. *International journal for numerical methods in biomedical engineering*, 28(2):257–272, 2012. [168](#), [183](#), [185](#)
- N. Cavallini and V. Coscia. One-dimensional modelling of venous pathologies: Finite volume and WENO schemes. In *Advances in Mathematical Fluid Mechanics*, pages 147–170. Springer, 2010. [45](#), [67](#)
- N. Cavallini, V. Caleffi, and V. Coscia. Finite volume and WENO scheme in one-dimensional vascular system modelling. *Computers & Mathematics with Applications*, 56(9):2382–2397, 2008. [45](#), [47](#)
- J.R. Cebral, M.A. Castro, S. Appanaboyina, C.M. Putman, D. Millan, and A.F. Frangi. Efficient pipeline for image-based patient-specific analysis of cerebral aneurysm hemodynamics: technique and sensitivity. *IEEE transactions on medical imaging*, 24(4):457–467, 2005. [6](#)
- A.-L. Charles, A.-S. Guilbert, J. Bouitbir, G.-D. Marco, I. Enache, J. Zoll, F. Piquard, B. Geny, et al. Effect of postconditioning on mitochondrial dysfunction in experimental aortic cross-clamping. *British Journal of Surgery*, 98(4):511–516, 2011. [156](#)
- D. Chemla, J.-L. Hebert, C. Coirault, S. Salmeron, K. Zamani, and Y. Lecarpentier. Matching dirotic notch and mean pulmonary artery pressures: implications for effective arterial elastance. *American Journal of Physiology-Heart and Circulatory Physiology*, 271(4): H1287–H1295, 1996. [128](#)
- K.M. Chinnaiyan, T. Akasaka, T. Amano, J.J. Bax, P. Blanke, B. De Bruyne, T. Kawasaki, J. Leipsic, H. Matsuo, Y. Morino, et al. Rationale, design and goals of the HeartFlow assessing diagnostic value of non-invasive FFR CT in Coronary Care (ADVANCE) registry. *Journal of cardiovascular computed tomography*, 11(1):62–67, 2017. [2](#)
- C. Chnafa, S. Mendez, and F. Nicoud. Image-based large-eddy simulation in a realistic left heart. *Computers & Fluids*, 94:173–187, 2014. [6](#)
- C. Chnafa, K. Valen-Sendstad, O. Brina, V.M. Pereira, and D.A. Steinman. Improved reduced-order modelling of cerebrovascular flow distribution by accounting for arterial bifurcation pressure drops. *Journal of biomechanics*, 51:83–88, 2017. [8](#)
- Y.I. Cho and K.R. Kensey. Effects of the non-Newtonian viscosity of blood on flows in a diseased arterial vessel. Part 1: Steady flows. *Biorheology*, 28(3-4):241–262, 1991. [201](#), [206](#)
- F. Chouly and P.-Y. Lagrée. Comparison of computations of asymptotic flow models in a constricted channel. *Applied Mathematical Modelling*, 36(12):6061–6071, 2012. [168](#), [192](#)

- C. Contarino, E.F. Toro, G.I. Montecinos, R. Borsche, and J. Kall. Junction-Generalized Riemann Problem for stiff hyperbolic balance laws in networks: An implicit solver and ADER schemes. *Journal of Computational Physics*, 315:409–433, 2016. [8](#), [99](#)
- R. Courant, K. Friedrichs, and H. Lewy. On the partial difference equations of mathematical physics. *IBM journal*, 11(2):215–234, 1967. [47](#), [180](#)
- W. Cousins and P.-A. Gremaud. Boundary conditions for hemodynamics: The structured tree revisited. *Journal of Computational Physics*, 231(18):6086–6096, 2012. [7](#), [8](#), [98](#), [114](#), [116](#), [117](#), [118](#), [119](#), [120](#)
- D. Craiem and R.L. Armentano. A fractional derivative model to describe arterial viscoelasticity. *Biorheology*, 44(4):251–263, 2007. [32](#)
- D. Craiem, F.J. Rojo, J.M. Atienza, R.L. Armentano, and G.V. Guinea. Fractional-order viscoelasticity applied to describe uniaxial stress relaxation of human arteries. *Physics in medicine and biology*, 53(17):4543, 2008. [32](#)
- M.M. Cross. Rheology of non-Newtonian fluids: a new flow equation for pseudoplastic systems. *Journal of colloid science*, 20(5):417–437, 1965. [9](#), [201](#), [204](#)
- H. Crystal, S. Holman, Y.W. Lui, A. Baird, H. Yu, R. Klein, D. Rojas-Soto, R. Leung, D. Gustafson, and G. Stebbins. Association of the fractal dimension of retinal arteries and veins with quantitative brain MRI measures in HIV-infected and uninfected women (P4. 067). *Neurology*, 86(16 Supplement):P4–067, 2016. [165](#)
- F. Cuomo, S. Roccabianca, D. Dillon-Murphy, N. Xiao, J.D. Humphrey, and C.A. Figueroa. Effects of age-associated regional changes in aortic stiffness on human hemodynamics revealed by computational modeling. *PloS one*, 12(3):e0173177, 2017. [201](#)
- L.J. Cymberknop, W. Legnani, F.M. Pessana, D. Bia, Y. Zócalo, and R.L. Armentano. Stiffness indices and fractal dimension relationship in arterial pressure and diameter time series in-vitro. In *Journal of Physics: Conference Series*, volume 332, page 012024. IOP Publishing, 2011. [157](#), [163](#)
- L.J. Cymberknop, W. Legnani, F.M. Pessana, A. Crottogini, and R.L. Armentano. Coronary arterial stiffness is related with a loss of fractal complexity in the aortic pressure. In *Engineering in Medicine and Biology Society (EMBC), 2012 Annual International Conference of the IEEE*, pages 4200–4203. IEEE, 2012. [157](#), [158](#), [163](#)
- L.J. Cymberknop, R.L. Armentano, F.M. Pessana, M.R. Alfonso, and W. Legnani. Mapping the fractal dimension of arterial pressure. In *IUPESM 2015. World Congress on Medical Physics & Biomedical Engineering*, pages 7–12, 2015. [157](#), [164](#)
- G. Dahlgren, F. Veintemilla, G. Settergren, and J. Liska. Left ventricular end-systolic pressure estimated from measurements in a peripheral artery. *Journal of cardiothoracic and vascular anesthesia*, 5(6):551–553, 1991. [128](#)
- R. Dalman. *Operative techniques in vascular surgery*. Lippincott Williams & Wilkins, 2015. [156](#)
- W.R. Davidson and E.C. Fee. Influence of aging on pulmonary hemodynamics in a population free of coronary artery disease. *The American journal of cardiology*, 65(22):1454–1458, 1990. [2](#)

- F. De Vita, M.D. de Tullio, and R. Verzicco. Numerical simulation of the non-newtonian blood flow through a mechanical aortic valve. *Theoretical and Computational Fluid Dynamics*, 30(1-2):129–138, 2016. [201](#)
- O. Delestre and P.-Y. Lagrée. A "well-balanced" finite volume scheme for blood flow simulation. *International Journal for Numerical Methods in Fluids*, 72(2):177–205, 2013. [8](#), [45](#), [46](#), [52](#), [64](#), [65](#), [67](#), [79](#), [81](#), [179](#)
- O. Delestre, C. Lucas, P.-A. Ksinant, F. Darboux, C. Laguerre, T.-N. Vo, F. James, S. Cordier, et al. SWASHES: a compilation of shallow water analytic solutions for hydraulic and environmental studies. *International Journal for Numerical Methods in Fluids*, 72(3):269–300, 2013. [76](#)
- O. Delestre, A.R. Ghigo, J.-M. Fullana, and P.-Y. Lagrée. A shallow water with variable pressure model for blood flow simulation. *Networks and Heterogeneous Media*, 11(1):69–87, 2016. [52](#), [65](#), [67](#), [68](#), [69](#), [79](#), [81](#), [179](#)
- V. Deplano and M. Siouffi. Experimental and numerical study of pulsatile flows through stenosis: Wall shear stress analysis. *Journal of Biomechanics*, 32(10):1081–1090, 1999. [191](#)
- P Di Achille, G Tellides, CA Figueroa, and JD Humphrey. A haemodynamic predictor of intraluminal thrombus formation in abdominal aortic aneurysms. In *Proc. R. Soc. A*, volume 470, page 20140163. The Royal Society, 2014. [191](#)
- D. Drzisga, T. Köppl, U. Pohl, R. Helmig, and B. Wohlmuth. Numerical modeling of compensation mechanisms for peripheral arterial stenoses. *Computers in biology and medicine*, 70:190–201, 2016. [8](#)
- A.S.R. Duarte, A.I.P. Miranda, and P.J. Oliveira. Numerical and analytical modeling of unsteady viscoelastic flows: The start-up and pulsating test case problems. *Journal of Non-Newtonian Fluid Mechanics*, 154(2):153–169, 2008. [202](#)
- M. Dumbser, U. Iben, and M. Ioriatti. An efficient semi-implicit finite volume method for axially symmetric compressible flows in compliant tubes. *Applied Numerical Mathematics*, 89:24–44, 2015. [183](#), [185](#)
- W. Eckhaus. *Asymptotic analysis of singular perturbations*, volume 9. Elsevier, 2011. [18](#)
- H.A. Erbay, S. Erbay, and S. Dost. Wave propagation in fluid filled nonlinear viscoelastic tubes. *Acta mechanica*, 95(1):87–102, 1992. [32](#)
- B. Erkut and O.A. Onk. Effect of N-acetylcysteine and allopurinol combination to protect spinal cord ischemia/reperfusion injury induced by aortic cross-clamping in rat model. *Journal of cardiothoracic surgery*, 10(1):95, 2015. [156](#)
- L. Euler. Principia pro motu sanguinis per arterias determinando. *Opera posthuma mathematica et physica anno*, pages 814–823, 1844. [8](#), [168](#)
- H.L. Falsetti, R.E. Mates, R.J. Carroll, R.L. Gupta, and A.C. Bell. Analysis and correction of pressure wave distortion in fluid-filled catheter systems. *Circulation*, 49(1):165–172, 1974. [129](#)
- Y. Fan, W. Jiang, Y. Zou, J. Li, J. Chen, and X. Deng. Numerical simulation of pulsatile non-Newtonian flow in the carotid artery bifurcation. *Acta Mechanica Sinica*, 25(2):249–255, 2009. [215](#)

- J. Fang and R.G. Owens. Numerical simulations of pulsatile blood flow using a new constitutive model. *Biorheology*, 43(5):637–660, 2006. [202](#)
- F. Fantin, A. Mattocks, C.J. Bulpitt, W. Banya, and C. Rajkumar. Is augmentation index a good measure of vascular stiffness in the elderly? *Age and ageing*, 36(1):43–48, 2007. [156](#)
- C. Farhat, P. Geuzaine, and C. Grandmont. The discrete geometric conservation law and the nonlinear stability of ALE schemes for the solution of flow problems on moving grids. *Journal of Computational Physics*, 174(2):669–694, 2001. [6](#), [167](#)
- E.D. Fernández-Nieto, E.H. Koné, T.M. De Luna, and R. Bürger. A multilayer shallow water system for polydisperse sedimentation. *Journal of Computational Physics*, 238:281–314, 2013. [177](#)
- C.A. Figueroa, I.E. Vignon-Clementel, K.E. Jansen, T.J.R. Hughes, and C.A. Taylor. A coupled momentum method for modeling blood flow in three-dimensional deformable arteries. *Computer methods in applied mechanics and engineering*, 195(41):5685–5706, 2006. [6](#), [167](#)
- E.A. Finol and C.H. Amon. Flow-induced wall shear stress in abdominal aortic aneurysms: Part I – Steady flow hemodynamics. *Computer Methods in Biomechanics & Biomedical Engineering*, 5(4):309–318, 2002. [193](#)
- P. Flaud, P. Guesdon, and J.-M. Fullana. Experiments of draining and filling processes in a collapsible tube at high external pressure. *The European Physical Journal Applied Physics*, 57(3):31101, 2012. [58](#)
- J. Flores, J. Alastruey, and E.C. Poiré. A Novel Analytical Approach to Pulsatile Blood Flow in the Arterial Network. *Annals of biomedical engineering*, pages 1–22, 2016. [168](#)
- L. Formaggia, J.-F. Gerbeau, F. Nobile, and A. Quarteroni. On the coupling of 3D and 1D Navier–Stokes equations for flow problems in compliant vessels. *Computer Methods in Applied Mechanics and Engineering*, 191(6):561–582, 2001. [201](#)
- L. Formaggia, D. Lamponi, and A. Quarteroni. One-dimensional models for blood flow in arteries. *Journal of engineering mathematics*, 47(3-4):251–276, 2003. [8](#), [24](#), [28](#), [99](#), [168](#), [174](#)
- L. Formaggia, D. Lamponi, M. Tuveri, and A. Veneziani. Numerical modeling of 1D arterial networks coupled with a lumped parameters description of the heart. *Computer methods in biomechanics and biomedical engineering*, 9(5):273–288, 2006. [45](#)
- L. Formaggia, A. Quarteroni, and A. Veneziani. *Cardiovascular Mathematics: Modeling and simulation of the circulatory system*, volume 1. Springer Science & Business Media, 2010. [2](#)
- L. Formaggia, A. Quarteroni, and C. Vergara. On the physical consistency between three-dimensional and one-dimensional models in haemodynamics. *Journal of Computational Physics*, 244:97–112, 2013. [201](#)
- O. Frank. Die grundform des arteriellen pulses. *Zischr F Biol*, 37:483–526, 1899. [6](#)
- J.-M. Fullana and S. Zaleski. A branched one-dimensional model of vessel networks. *Journal of Fluid Mechanics*, 621:183–204, 2009. [8](#), [45](#), [99](#)
- J.-M. Fullana, F. Cros, P. Flaud, and S. Zaleski. Filling a collapsible tube. *Journal of Fluid Mechanics*, 494:285–296, 2003. [58](#)

- Y. Fung. *Biomechanics: Mechanical Properties of Living Tissues*. 1993. [32](#)
- Y.-C. Fung. *Biomechanics: Circulation*. Springer Science & Business Media, 2013. [11](#), [19](#), [185](#)
- D. Gallagher, A. Adji, and M.F. O'Rourke. Validation of the transfer function technique for generating central from peripheral upper limb pressure waveform. *American journal of hypertension*, 17(11):1059–1067, 2004. [159](#)
- S. Gelman. The pathophysiology of aortic cross-clamping and unclamping. *The Journal of the American Society of Anesthesiologists*, 82(4):1026–1057, 1995. [156](#)
- M.S. Ghidaoui, M. Zhao, D.A. McInnis, and D.H. Axworthy. A review of water hammer theory and practice. *Applied Mechanics Reviews*, 58(1/6):49, 2005. [16](#)
- A.R. Ghigo, S. Abou Taam, X. Wang, P.-Y. Lagrée, and J.-M. Fullana. A one-dimensional arterial network model for bypass graft assessment. *Medical Engineering & Physics*, 2017a. [8](#), [9](#), [26](#), [32](#), [99](#), [145](#), [146](#), [147](#), [201](#)
- A.R. Ghigo, O. Delestre, J.-M. Fullana, and P.-Y. Lagrée. Low-Shapiro hydrostatic reconstruction technique for blood flow simulation in large arteries with varying geometrical and mechanical properties. *Journal of Computational Physics*, 331:108–136, 2017b. [8](#), [46](#), [174](#), [177](#), [205](#), [206](#)
- A.R. Ghigo, J.-M. Fullana, and P.-Y. Lagrée. A 2D nonlinear multiring model for blood flow in large elastic arteries. *Journal of Computational Physics*, 350:136–165, 2017c.
- A.R. Ghigo, P.-Y. Lagrée, and J.-M. Fullana. 1D generalized time dependent non-newtonian blood flow model. 2017d.
- A.R. Ghigo, X.-F. Wang, R. Armentano, J.-M. Fullana, and P.-Y. Lagrée. Linear and non-linear viscoelastic arterial wall models: application on animals. *Journal of Biomechanical Engineering*, 139(1):011003, 2017e.
- F.J.H. Gijssen, E. Allanic, F.N. van De Vosse, and J.D. Janssen. The influence of the non-Newtonian properties of blood on the flow in large arteries: unsteady flow in a 90 curved tube. *Journal of biomechanics*, 32(7):705–713, 1999a. [201](#)
- F.J.H. Gijssen, F.N. van De Vosse, and J.D. Janssen. The influence of the non-Newtonian properties of blood on the flow in large arteries: steady flow in a carotid bifurcation model. *Journal of biomechanics*, 32(6):601–608, 1999b. [201](#)
- L. Gosse. *Computing qualitatively correct approximations of balance laws*, volume 2. Springer, 2013. [30](#), [67](#)
- L. Gosse and A.-Y. LeRoux. Un schéma-équilibre adapté aux lois de conservation scalaires non-homogènes. *CR Acad. Sci. Paris Sér. I Math*, 323(5):543–546, 1996. [64](#), [179](#)
- S. Gottlieb. On high order strong stability preserving Runge–Kutta and multi step time discretizations. *Journal of Scientific Computing*, 25(1):105–128, 2005. [48](#)
- J.M. Greenberg and A.-Y. LeRoux. A well-balanced scheme for the numerical processing of source terms in hyperbolic equations. *SIAM Journal on Numerical Analysis*, 33(1):1–16, 1996. [64](#), [179](#)
- S.E. Greenwald and C.L. Berry. Improving vascular grafts: the importance of mechanical and haemodynamic properties. *The Journal of pathology*, 190(3):292–299, 2000. [144](#), [145](#)

- B. Gryglewska, M. Necki, M. Żelawski, M. Cwynar, T. Baron, M. Mrozek, and T. Grodzicki. Fractal dimensions of skin microcirculation flow in subjects with familial predisposition or newly diagnosed hypertension. *Cardiol J*, 18(1):26–32, 2011. [165](#)
- D. Guan, F. Liang, and P.-A. Gremaud. Comparison of the Windkessel model and structured-tree model applied to prescribe outflow boundary conditions for a one-dimensional arterial tree model. *Journal of biomechanics*, 49(9):1583–1592, 2016. [7](#), [8](#), [114](#), [118](#), [119](#), [120](#)
- M. Guillot, A.-L. Charles, T.N. Chamaroux-Tran, J. Bouitbir, A. Meyer, J. Zoll, F. Schneider, and B. Geny. Oxidative stress precedes skeletal muscle mitochondrial dysfunction during experimental aortic cross-clamping but is not associated with early lung, heart, brain, liver, or kidney mitochondrial impairment. *Journal of vascular surgery*, 60(4):1043–1051, 2014. [156](#)
- A. Guyton and J. Hall. Textbook of medical physiology 11th edition Elsevier Inc. *Philadelphia PA*, 2006. [128](#), [142](#)
- E.E. Han, M. Hantke, and G. Warnecke. Exact Riemann solutions to compressible Euler equations in ducts with discontinuous cross-section. *Journal of Hyperbolic Differential Equations*, 9(03):403–449, 2012. [29](#)
- W. Harvey. Exercitatio anatomica de motu cordis et Sanguinis in animalibus. movement of the heart and blood in animals; translated by k.j. franklin, 1957. [1](#)
- J.-L. Hébert, Y. Lecarpentier, K. Zamani, C. Coirault, G. Daccache, D. Chemla, N. Wuilliez, and L. Larsonneur. Relation between aortic dirotic notch pressure and mean aortic pressure in adults. *The American journal of cardiology*, 76(4):301–306, 1995. [128](#)
- E. Hermeling, K.D. Reesink, L.M. Kornmann, R.S. Reneman, and A.P.G. Hoeks. The dirotic notch as alternative time–reference point to measure local pulse wave velocity in the carotid artery by means of ultrasonography. *Journal of hypertension*, 27(10):2028–2035, 2009. [142](#)
- E. Hermeling, A.P.G. Hoeks, M.H.M. Winkens, J.L. Waltenberger, R.S. Reneman, A.A. Kroon, and K.D. Reesink. Noninvasive assessment of arterial stiffness should discriminate between systolic and diastolic pressure ranges. *Hypertension*, 55(1):124–130, 2010. [142](#)
- M. Higashidate, K. Tamiya, T. Beppu, and Y. Imai. Regulation of the aortic valve opening: in vivo dynamic measurement of aortic valve orifice area. *The Journal of Thoracic and Cardiovascular Surgery*, 110(2):496–503, 1995. [128](#)
- T. Higuchi. Approach to an irregular time series on the basis of the fractal theory. *Physica D: Nonlinear Phenomena*, 31(2):277–283, 1988. [159](#)
- S. Hirschfeld, J. Liebman, G. Borkat, and C. Bormuth. Intracardiac pressure-sound correlates of echographic aortic valve closure. *Circulation*, 55(4):602–604, 1977. [128](#)
- R. Holenstein, P. Niederer, and M. Anliker. A viscoelastic model for use in predicting arterial pulse waves. *J Biomech Eng*, 102(4):318–325, 1980. [32](#)
- G.A. Holzapfel and R.W. Ogden. Constitutive modelling of arteries. In *Proceedings of the Royal Society of London A: Mathematical, Physical and Engineering Sciences*, volume 466, pages 1551–1597. The Royal Society, 2010. [6](#)
- G.A. Holzapfel, T.C. Gasser, and R.W. Ogden. A new constitutive framework for arterial wall mechanics and a comparative study of material models. *Journal of elasticity and the physical science of solids*, 61(1-3):1–48, 2000. [6](#), [167](#)

- T.J.R. Hughes and J. Lubliner. On the one-dimensional theory of blood flow in the larger vessels. *Mathematical Biosciences*, 18(1):161–170, 1973. [24](#), [25](#)
- T.J.R. Hughes, W.K. Liu, and T.K. Zimmermann. Lagrangian-Eulerian finite element formulation for incompressible viscous flows. *Computer methods in applied mechanics and engineering*, 29(3):329–349, 1981. [6](#), [167](#)
- Y. Ikenaga, S. Nishi, Y. Komagata, M. Saito, P.-Y. Lagree, T. Asada, and M. Matsukawa. Experimental study on the pressure and pulse wave propagation in viscoelastic vessel tubes – Effects of liquid viscosity and tube stiffness. *IEEE transactions on ultrasonics, ferroelectrics, and frequency control*, 60(11):2381–2388, 2013. [9](#), [24](#)
- E. Isaacson and B. Temple. Nonlinear resonance in systems of conservation laws. *SIAM Journal on Applied Mathematics*, 52(5):1260–1278, 1992. [29](#)
- G.N. Jager. *Electrical model of the human systemic arterial tree*. PhD thesis, University of Utrecht, 1965. [12](#)
- M. Jahangiri, M. Saghafian, and M.R. Sadeghi. Numerical simulation of non-Newtonian models effect on hemodynamic factors of pulsatile blood flow in elastic stenosed artery. *Journal of Mechanical Science and Technology*, 31(2):1003–1013, 2017. [201](#)
- J. Kalder, P. Keschenau, S.J. Hanssen, A. Greiner, I.C.V. Windsant, L.N. Kennes, R. Tolba, F.W. Prinzen, W.A. Buurman, M.J. Jacobs, et al. The impact of selective visceral perfusion on intestinal macrohemodynamics and microhemodynamics in a porcine model of thoracic aortic cross-clamping. *Journal of vascular surgery*, 56(1):149–158, 2012. [156](#)
- R.D. Kamm and A.H. Shapiro. Unsteady flow in a collapsible tube subjected to external pressure or body forces. *Journal of Fluid Mechanics*, 95(01):1–78, 1979. [58](#)
- K. Katseni, A. Chalkias, T. Kotsis, N. Dafnios, V. Arapoglou, G. Kaparos, E. Logothetis, N. Iacovidou, E. Karvouni, and K. Katsenis. The effect of perioperative ischemia and reperfusion on multiorgan dysfunction following abdominal aortic aneurysm repair. *BioMed research international*, 2015, 2015. [156](#)
- A.W. Khir and K.H. Parker. Measurements of wave speed and reflected waves in elastic tubes and bifurcations. *Journal of biomechanics*, 35(6):775–783, 2002. [142](#), [156](#)
- H.J. Kim, I.E. Vignon-Clementel, J.S. Coogan, C.A. Figueroa, K.E. Jansen, and C.A. Taylor. Patient-specific modeling of blood flow and pressure in human coronary arteries. *Annals of biomedical engineering*, 38(10):3195–3209, 2010. [167](#)
- D.J. Korteweg. Über die Fortpflanzungsgeschwindigkeit des Schalles in elastischen Röhren. *Annalen der Physik*, 241(12):525–542, 1878. [16](#), [17](#), [26](#), [175](#)
- Y. Kotake, T. Yamada, H. Nagata, J. Takeda, and H. Shimizu. Descending aortic blood flow during aortic cross-clamp indicates postoperative splanchnic perfusion and gastrointestinal function in patients undergoing aortic reconstruction. *British journal of anaesthesia*, page aes095, 2012. [156](#)
- P.-Y. Lagrée. An inverse technique to deduce the elasticity of a large artery. *The European Physical Journal Applied Physics*, 9(02):153–163, 2000. [9](#), [26](#), [168](#), [183](#)
- P.-Y. Lagrée and S. Lorthois. The RNS/Prandtl equations and their link with other asymptotic descriptions: application to the wall shear stress scaling in a constricted pipe. *International Journal of Engineering Science*, 43(3):352–378, 2005. [9](#), [19](#), [168](#), [189](#), [190](#), [191](#), [192](#), [193](#), [194](#), [195](#)

- R. Lal, B. Mohammadi, and F. Nicoud. Data assimilation for identification of cardiovascular network characteristics. *International Journal for Numerical Methods in Biomedical Engineering*, 2016. 114
- J.W. Lambert. On the nonlinearities of fluid flow in nonrigid tubes. *Journal of the Franklin Institute*, 266(2):83–102, 1958. 168
- G. Lanzino, A.A. Rabinstein, and R.D. Brown. Treatment of carotid artery stenosis: medical therapy, surgery, or stenting? In *Mayo Clinic Proceedings*, volume 84, pages 362–368. Elsevier, 2009. 147
- R.D. Latham, N. Westerhof, P. Sipkema, B.J. Rubal, P. Reuderink, and J.P. Murgo. Regional wave travel and reflections along the human aorta: a study with six simultaneous micromanometric pressures. *Circulation*, 72(6):1257–1269, 1985. 128, 164
- S. Laurent, J. Cockcroft, L. van Bortel, P. Boutouyrie, C. Giannattasio, D. Hayoz, B. Pannier, C. Vlachopoulos, I. Wilkinson, and H. Struijker-Boudier. Expert consensus document on arterial stiffness: methodological issues and clinical applications. *European heart journal*, 27(21):2588–2605, 2006. 162
- R.J. LeVeque. *Numerical methods for conservation laws*. Springer Science & Business Media, 1992. 52
- R.J. LeVeque. *Finite volume methods for hyperbolic problems*, volume 31. Cambridge university press, 2002. 29, 45
- M.N. Levy, B.M. Koeppen, and B.A. Stanton. *Berne & Levy principles of physiology*. Elsevier Health Sciences, 2005. 128
- F. Liang, S. Takagi, R. Himeno, and H. Liu. Multi-scale modeling of the human cardiovascular system with applications to aortic valvular and arterial stenoses. *Medical & biological engineering & computing*, 47(7):743–755, 2009. 7, 99
- F. Liang, K. Fukasaku, H. Liu, and S. Takagi. A computational model study of the influence of the anatomy of the circle of Willis on cerebral hyperperfusion following carotid artery surgery. *Biomedical engineering online*, 10(1):84, 2011. 8
- J. Liao and J. Farmer. Arterial stiffness as a risk factor for coronary artery disease. *Current atherosclerosis reports*, 16(2):387, 2014. 156
- J. Lighthill. *Waves in fluids*. Cambridge Univ. Press, 1978. 52
- S. Lim, P.M. Halandras, N.U. Saqib, Y.A. Ching, E. Vilella, T. Park, H. Son, and J.S. Cho. Comparison of suprarenal aortic cross-clamping with supraceliac aortic cross-clamping for aortic reconstruction. *Journal of vascular surgery*, 64(4):941–947, 2016. 156
- S.C. Ling and H.B. Atabek. A nonlinear analysis of pulsatile flow in arteries. *Journal of Fluid Mechanics*, 55(03):493–511, 1972. 168
- C. Liu, D. Zheng, A. Murray, and C. Liu. Modeling carotid and radial artery pulse pressure waveforms by curve fitting with gaussian functions. *Biomedical Signal Processing and Control*, 8(5):449–454, 2013. 159
- C. Liu, L. Zhao, and C. Liu. Effects of blood pressure and sex on the change of wave reflection: evidence from gaussian fitting method for radial artery pressure waveform. *PloS one*, 9(11):e112895, 2014. 159

- T.-P. Liu. Nonlinear resonance for quasilinear hyperbolic equation. *Journal of mathematical physics*, 28(11):2593–2602, 1987. [29](#)
- B.B. Mandelbrot. *Fractals: Form, Chance, and Dimension*. WH Freeman and Company, 1977. [157](#)
- D.L. Mann, D.P. Zipes, P. Libby, and R.O. Bonow. *Braunwald’s heart disease: a textbook of cardiovascular medicine*. Elsevier Health Sciences, 2014. [128](#), [142](#)
- L. Mannoni and E.-J. Marey. La mémoire de l’oeil. *Milan/Paris, Mazzotta/La Cinémathèque française*, 1999. [5](#)
- E. Marchandise, M. Willemet, and V. Lacroix. A numerical hemodynamic tool for predictive vascular surgery. *Medical engineering & physics*, 31(1):131–144, 2009. [144](#), [201](#)
- E.J. Marey. *Physiologie médicale de la circulation du sang basée sur l’étude graphique des mouvements du coeur et du pouls artériel avec applications aux maladies de l’appareil circulatoire*. A. Delahaye, 1863. [5](#)
- P.L. Marino. *Marino’s the ICU Book*. Lippincott Williams & Wilkins, 2013. [128](#)
- V. Martin, F. Clément, A. Decoene, and J.-F. Gerbeau. Parameter identification for a one-dimensional blood flow model. In *ESAIM: Proceedings*, volume 14, pages 174–200. EDP Sciences, 2005. [45](#)
- K.S. Matthys, J. Alastruey, J. Peiró, A.W. Khir, P. Segers, P.R. Verdonck, K.H. Parker, and S.J. Sherwin. Pulse wave propagation in a model human arterial network: assessment of 1-d numerical simulations against in vitro measurements. *Journal of biomechanics*, 40(15): 3476–3486, 2007. [6](#), [8](#), [99](#), [113](#), [114](#), [142](#)
- M. Mayr, T. Klöppel, W.A. Wall, and M.W. Gee. A temporal consistent monolithic approach to fluid-structure interaction enabling single field predictors. *SIAM Journal on Scientific Computing*, 37(1):B30–B59, 2015. [6](#), [167](#)
- D.E. McMillan, J. Strigberger, and N.G. Utterback. Rapidly recovered transient flow resistance: a newly discovered property of blood. *American Journal of Physiology-Heart and Circulatory Physiology*, 253(4):H919–H926, 1987. [208](#), [210](#), [211](#), [218](#)
- V. Melicher and V. Gajdošík. A numerical solution of a one-dimensional blood flow model–moving grid approach. *Journal of Computational and Applied Mathematics*, 215(2):512–520, 2008. [45](#)
- C.J. Mills, I.T. Gabe, J.H. Gault, D.T. Mason, J. Ross, E. Braunwald, and J.P. Shillingford. Pressure-flow relationships and vascular impedance in man. *Cardiovascular Research*, 4(4):405–405, 1970. [164](#)
- W.R. Milnor. Hemodynamics (2nd edn). *Williams and Wilkins: Baltimore*, 1989. [6](#)
- A.I. Moens. *Die pulskurve*. EJ Brill, 1878. [17](#), [26](#), [175](#)
- G.I. Montecinos, L.O. Müller, and E.F. Toro. Hyperbolic reformulation of a 1D viscoelastic blood flow model and ADER finite volume schemes. *Journal of Computational Physics*, 266:101–123, 2014. [9](#), [26](#), [32](#), [41](#), [45](#)
- B. Moreau and B. Mauroy. Murray’s law revisited: Quémada’s fluid model and fractal trees. *Journal of rheology*, 59(6):1419–1430, 2015. [201](#)

- B.E. Morgan and D.F. Young. An integral method for the analysis of flow in arterial stenoses. *Bulletin of Mathematical Biology*, 36:39–53, 1974. [193](#)
- M. Moyers-Gonzalez, R.G. Owens, and J. Fang. A non-homogeneous constitutive model for human blood. Part 1. model derivation and steady flow. *Journal of Fluid Mechanics*, 617:327–354, 2008a. [201](#)
- M.A. Moyers-Gonzalez, R.G. Owens, and J. Fang. A non-homogeneous constitutive model for human blood. part III. Oscillatory flow. *Journal of Non-Newtonian Fluid Mechanics*, 155(3):161–173, 2008b. [202](#)
- L.O. Müller and P.J. Blanco. A high order approximation of hyperbolic conservation laws in networks: application to one-dimensional blood flow. *Journal of Computational Physics*, 300:423–437, 2015. [8](#), [47](#), [99](#)
- L.O. Müller and E.F. Toro. A global multiscale mathematical model for the human circulation with emphasis on the venous system. *International journal for numerical methods in biomedical engineering*, 30(7):681–725, 2014. [7](#), [8](#), [45](#), [67](#), [99](#), [167](#)
- L.O. Müller, C. Parés, and E.F. Toro. Well-balanced high-order numerical schemes for one-dimensional blood flow in vessels with varying mechanical properties. *Journal of Computational Physics*, 242:53–85, 2013. [8](#), [28](#), [46](#), [64](#), [76](#), [168](#)
- L.O. Müller, P.J. Blanco, S.M. Watanabe, and R.A. Feijóo. A high-order local time stepping finite volume solver for one-dimensional blood flow simulations: application to the ADAN model. *International journal for numerical methods in biomedical engineering*, 2016a. [8](#), [46](#), [47](#)
- L.O. Müller, G. Leugering, and P.J. Blanco. Consistent treatment of viscoelastic effects at junctions in one-dimensional blood flow models. *Journal of Computational Physics*, 314:167–193, 2016b. [8](#), [9](#), [32](#), [50](#)
- J.P. Murgo, S.A. Altobelli, J.F. Dorethy, J.R. Logsdon, and G.M. McGranahan. Normal ventricular ejection dynamics in man during rest and exercise. *Am Heart Assoc Monogr*, 46:92–101, 1975. [157](#)
- J.P. Murgo, N. Westerhof, J.P. Giolma, and S.A. Altobelli. Aortic input impedance in normal man: relationship to pressure wave forms. *Circulation*, 62(1):105–116, 1980. [142](#), [157](#), [159](#), [164](#), [165](#)
- J. Murillo and P. García-Navarro. A Roe type energy balanced solver for 1D arterial blood flow and transport. *Computers & Fluids*, 117:149–167, 2015. [8](#), [45](#), [46](#), [49](#), [64](#), [76](#), [206](#)
- S.E. Musicant, Ma.E. Giswold, C.J. Olson, G.J. Landry, R.A. Taylor, L.M. and Yeager, J.M. Edwards, and G.L. Moneta. Postoperative duplex scan surveillance of axillofemoral bypass grafts. *Journal of vascular surgery*, 37(1):54–61, 2003. [144](#)
- J.P. Mynard and P. Nithiarasu. A 1D arterial blood flow model incorporating ventricular pressure, aortic valve and regional coronary flow using the locally conservative Galerkin (LCG) method. *Communications in Numerical Methods in Engineering*, 24(5):367–417, 2008. [8](#), [45](#), [143](#)
- J.P. Mynard and K. Valen-Sendstad. A unified method for estimating pressure losses at vascular junctions. *International journal for numerical methods in biomedical engineering*, 31(7), 2015. [8](#), [98](#), [99](#)

- N. Nandakumar, K.C. Sahu, and M. Anand. Pulsatile flow of a shear-thinning model for blood through a two-dimensional stenosed channel. *European Journal of Mechanics-B/Fluids*, 49:29–35, 2015. [201](#)
- R.M. Nerem, W.A. Seed, and N.B. Wood. An experimental study of the velocity distribution and transition to turbulence in the aorta. *Journal of Fluid Mechanics*, 52(01):137–160, 1972. [6](#)
- W. Nichols, M. O’Rourke, and C. Vlachopoulos. *McDonald’s blood flow in arteries: theoretical, experimental and clinical principles*. CRC press, 2011. [2](#)
- W.W. Nichols and D.G. Edwards. Arterial elastance and wave reflection augmentation of systolic blood pressure: deleterious effects and implications for therapy. *Journal of cardiovascular pharmacology and therapeutics*, 6(1):5–21, 2001. [164](#)
- S. Noelle, Y. Xing, and C.-W. Shu. High-order well-balanced finite volume WENO schemes for shallow water equation with moving water. *Journal of Computational Physics*, 226(1): 29–58, 2007. [76](#)
- A. Noordergraaf, P.D. Verdouw, and H.B.K. Boom. The use of an analog computer in a circulation model. *Progress in Cardiovascular Diseases*, 5(5):419–439, 1963. [7](#)
- L. Norgren, W.R. Hiatt, J.A. Dormandy, M.R. Nehler, K.A. Harris, F.G..R Fowkes, TASC II Working Group, et al. Inter-society consensus for the management of peripheral arterial disease (TASC II). *European Journal of Vascular and Endovascular Surgery*, 33(1):S1–S75, 2007. [144](#)
- M.S. Olufsen. Structured tree outflow condition for blood flow in larger systemic arteries. *American journal of physiology-Heart and circulatory physiology*, 276(1):H257–H268, 1999. [98](#), [114](#), [214](#)
- M.S. Olufsen, C.S. Peskin, W.Y. Kim, E.M. Pedersen, A. Nadim, and J. Larsen. Numerical simulation and experimental validation of blood flow in arteries with structured-tree outflow conditions. *Annals of biomedical engineering*, 28(11):1281–1299, 2000. [8](#), [98](#), [114](#), [117](#), [214](#)
- M.S. Olufsen, N.A. Hill, G.D.A. Vaughan, C. Sainsbury, and M. Johnson. Rarefaction and blood pressure in systemic and pulmonary arteries. *Journal of fluid mechanics*, 705: 280–305, 2012. [114](#)
- M.F. O’Rourke and A.P. Avolio. Pulsatile flow and pressure in human systemic arteries. *Circulation Research*, 46(3):363–372, 1980. [128](#)
- R.G. Owens. A new microstructure-based constitutive model for human blood. *Journal of Non-Newtonian Fluid Mechanics*, 140(1):57–70, 2006. [201](#), [204](#)
- M.F. O’Rourke, J.A. Staessen, C. Vlachopoulos, D. Duprez, et al. Clinical applications of arterial stiffness; definitions and reference values. *American journal of hypertension*, 15(5): 426–444, 2002. [128](#), [156](#)
- S. Pant, B. Fabrèges, J.-F. Gerbeau, and I.E. Vignon-Clementel. A methodological paradigm for patient-specific multi-scale CFD simulations: from clinical measurements to parameter estimates for individual analysis. *International journal for numerical methods in biomedical engineering*, 30(12):1614–1648, 2014. [114](#)
- C. Parés. Numerical methods for nonconservative hyperbolic systems: a theoretical framework. *SIAM Journal on Numerical Analysis*, 44(1):300–321, 2006. [64](#)

- K.H. Parker. A brief history of arterial wave mechanics. *Medical & biological engineering & computing*, 47(2):111–118, 2009. [4](#)
- K.H. Parker. The reservoir-wave model. *Artery Research*, 2017. [7](#)
- T.J. Pedley, B.S. Brook, and R.S. Seymour. Blood pressure and flow rate in the giraffe jugular vein. *Philosophical Transactions of the Royal Society of London B: Biological Sciences*, 351(1342):855–866, 1996. [67](#)
- P. Perdikaris and G.E. Karniadakis. Fractional-order viscoelasticity in one-dimensional blood flow models. *Annals of biomedical engineering*, 42(5):1012–1023, 2014. [7](#), [9](#), [32](#), [98](#)
- P. Perdikaris, L. Grinberg, and G.E. Karniadakis. An effective fractal-tree closure model for simulating blood flow in large arterial networks. *Annals of biomedical engineering*, 43(6):1432–1442, 2015. [8](#), [107](#), [114](#), [116](#), [117](#), [120](#), [202](#), [214](#)
- K. Perktold. On the paths of fluid particles in an axisymmetrical aneurysm. *Journal of biomechanics*, 20(3):311–317, 1987. [191](#)
- B. Perthame and C. Simeoni. A kinetic scheme for the Saint-Venant system with a source term. *Calcolo*, 38(4):201–231, 2001. [46](#)
- M.R. Pinsky, L. Brochard, J. Mancebo, and M.R. Pinsky. *Applied physiology in intensive care medicine*. Springer, 2006. [128](#), [142](#)
- K. Pohlhausen. Zur näherungsweise integration der differentialgleichung der laminaren grenzschicht. *ZAMM-Journal of Applied Mathematics and Mechanics/Zeitschrift für Angewandte Mathematik und Mechanik*, 1(4):252–290, 1921. [190](#)
- M.T. Politi, A.R. Ghigo, J.M. Fernández, I. Khelifa, J. Gaudric, J.-M. Fullana, and P.-Y. Lagrée. The dicrotic notch analyzed by a numerical model. *Computers in Biology and Medicine*, 72:54–64, 2016a. [98](#), [156](#), [167](#)
- M.T. Politi, S.A. Wray, J.M. Fernández, J. Gaudric, A.R. Ghigo, P.-Y. Lagrée, C. Capurro, J.-M. Fullana, and R. Armentano. Impact of arterial cross-clamping during vascular surgery on arterial stiffness measured by the augmentation index and fractal dimension of arterial pressure. *Health and Technology*, 6(3):229–237, 2016b.
- J. Pottecher, M. Guillot, E. Belaidi, A.-L. Charles, A. Lejay, A. Gharib, P. Diemunsch, and B. Geny. Cyclosporine A normalizes mitochondrial coupling, reactive oxygen species production, and inflammation and partially restores skeletal muscle maximal oxidative capacity in experimental aortic cross-clamping. *Journal of vascular surgery*, 57(4):1100–1108, 2013. [156](#)
- L. Prandtl. Motion of fluids with very little viscosity. *N.A.C.A. Technical Memorandum*, (452), 1928. [16](#), [19](#)
- A.R. Pries, D. Neuhaus, and P. Gaehtgens. Blood viscosity in tube flow: dependence on diameter and hematocrit. *American Journal of Physiology-Heart and Circulatory Physiology*, 263(6):H1770–H1778, 1992. [126](#), [202](#), [205](#)
- C. Puelz, S. Čanić, B. Rivière, and C.G. Rusin. Comparison of reduced models for blood flow using Runge–Kutta discontinuous Galerkin methods. *Applied Numerical Mathematics*, 2017. [8](#), [9](#), [24](#), [45](#)

- A. Quarteroni, A. Veneziani, and C. Vergara. Geometric multiscale modeling of the cardiovascular system, between theory and practice. *Computer Methods in Applied Mechanics and Engineering*, 302:193–252, 2016. [99](#), [167](#)
- D. Quemada and R. Droz. Blood viscoelasticity and thixotropy from stress formation and relaxation measurements: a unified model. *Biorheology*, 20(5):635–651, 1982. [9](#), [201](#), [206](#), [209](#)
- M.U. Qureshi, G.D.A. Vaughan, C. Sainsbury, M. Johnson, C.S. Peskin, M.S. Olufsen, and N.A. Hill. Numerical simulation of blood flow and pressure drop in the pulmonary arterial and venous circulation. *Biomechanics and modeling in mechanobiology*, 13(5):1137–1154, 2014. [114](#)
- R. Raghu, I.E. Vignon-Clementel, C.A. Figueroa, and C.A. Taylor. Comparative study of viscoelastic arterial wall models in nonlinear one-dimensional finite element simulations of blood flow. *Journal of biomechanical engineering*, 133(8):081003, 2011. [9](#), [32](#)
- J.K. Raines, M.Y. Jaffrin, and A.H. Shapiro. A computer simulation of arterial dynamics in the human leg. *Journal of biomechanics*, 7(1):77–91, 1974. [81](#)
- A.B. Ramachandra, A.M. Kahn, and A.L. Marsden. Patient-Specific Simulations Reveal Significant Differences in Mechanical Stimuli in Venous and Arterial Coronary Grafts. *Journal of Cardiovascular Translational Research*, 9(4):279–290, 2016. [167](#)
- P. Reymond, F. Merenda, F. Perren, D. Rüfenacht, and N. Stergiopoulos. Validation of a one-dimensional model of the systemic arterial tree. *American Journal of Physiology-Heart and Circulatory Physiology*, 297(1):H208–H222, 2009. [8](#), [9](#), [26](#), [32](#)
- P. Reymond, Y. Bohraus, F. Perren, F. Lazeyras, and N. Stergiopoulos. Validation of a patient-specific one-dimensional model of the systemic arterial tree. *American Journal of Physiology-Heart and Circulatory Physiology*, 301(3):H1173–H1182, 2011. [8](#), [9](#), [32](#)
- P.L. Roe. Upwind differencing schemes for hyperbolic conservation laws with source terms. In *Nonlinear hyperbolic problems*, pages 41–51. Springer, 1987. [64](#), [179](#)
- N. Rognant, O. Rouvière, M. Janier, Q.H. Lê, P. Barthez, M. Laville, and L. Juillard. Hemodynamic responses to acute and gradual renal artery stenosis in pigs. *American journal of hypertension*, 23(11):1216–1219, 2010. [148](#)
- V.V. Rusanov. Calculation of Intersection of Non-Steady Shock Waves with Obstacles. *J Comput Math Phys USSR*, 1:267–279, 1961. [47](#)
- M. Saito, Y. Ikenaga, M. Matsukawa, Y. Watanabe, T. Asada, and P.-Y. Lagrée. One-dimensional model for propagation of a pressure wave in a model of the human arterial network: comparison of theoretical and experimental results. *Journal of Biomechanical Engineering*, 133(12):121005, 2011. [5](#), [27](#), [45](#), [174](#)
- J. Sampson, A. Easton, and M. Singh. Moving boundary shallow water flow above parabolic bottom topography. *Anziam Journal*, 47:373–387, 2006. [91](#)
- S. Sankaran, Ma.E. Moghadam, A.M. Kahn, E.E. Tseng, J.M. Guccione, and A.L. Marsden. Patient-specific multiscale modeling of blood flow for coronary artery bypass graft surgery. *Annals of biomedical engineering*, 40(10):2228–2242, 2012. [6](#), [7](#), [167](#), [201](#)
- S. Sarkar, H.J. Salacinski, G. Hamilton, and A.M. Seifalian. The mechanical properties of infrainguinal vascular bypass grafts: their role in influencing patency. *European journal of vascular and endovascular surgery*, 31(6):627–636, 2006. [149](#)

- I. Sazonov, A.W. Khir, W.S. Hacham, E. Boileau, J.M. Carson, R. van Loon, C. Ferguson, and P. Nithiarasu. A novel method for non-invasively detecting the severity and location of aortic aneurysms. *Biomechanics and Modeling in Mechanobiology*, pages 1–18, 2017. [8](#)
- H. Schlichting. *Boundary-layer theory*. McGraw-Hill, 1968. [189](#)
- P. Segers, N. Stergiopulos, P. Verdonck, and R. Verhoeven. Assessment of distributed arterial network models. *Medical and Biological Engineering and Computing*, 35(6):729–736, 1997. [34](#), [36](#), [99](#), [142](#)
- P. Segers, F. Dubois, D. de Wachter, and P. Verdonck. Role and relevancy of a cardiovascular simulator. *Cardiovascular Engineering*, 3:48–56, 1998. [5](#)
- A.H. Shapiro. Steady flow in collapsible tubes. *Journal of Biomechanical Engineering*, 99(3):126–147, 1977. [29](#), [175](#)
- V. Sharma. Deterministic chaos and fractal complexity in the dynamics of cardiovascular behavior: perspectives on a new frontier. *Open Cardiovasc Med J*, 3:110–123, 2009. [157](#), [158](#)
- S.J. Sherwin, L. Formaggia, J. Peiro, and V. Franke. Computational modelling of 1D blood flow with variable mechanical properties and its application to the simulation of wave propagation in the human arterial system. *International Journal for Numerical Methods in Fluids*, 43(6-7):673–700, 2003a. [8](#), [28](#), [45](#), [64](#), [99](#), [146](#), [204](#)
- S.J. Sherwin, V. Franke, J. Peiró, and K. Parker. One-dimensional modelling of a vascular network in space-time variables. *Journal of Engineering Mathematics*, 47(3-4):217–250, 2003b. [8](#)
- T. Shinozaki, R.S. Deane, and J.E. Mazuzan. The dynamic responses of liquid-filled catheter systems for direct measurements of blood pressure. *Anesthesiology*, 53(6):498–504, 1980. [129](#)
- J.M. Siegel, C.P. Markou, D.N. Ku, and S.R. Hanson. A scaling law for wall shear rate through an arterial stenosis. *Journal of biomechanical engineering*, 116(4):446–451, 1994. [193](#)
- A. Siviglia and M. Toffolon. Steady analysis of transcritical flows in collapsible tubes with discontinuous mechanical properties: implications for arteries and veins. *Journal of Fluid Mechanics*, 736:195–215, 2013. [175](#)
- F.T. Smith. Flow through constricted or dilated pipes and channels: Part 2. *The Quarterly Journal of Mechanics and Applied Mathematics*, 29(3):365–376, 1976. [19](#), [168](#), [193](#)
- N.P. Smith, A.J. Pullan, and P.J. Hunter. An anatomically based model of transient coronary blood flow in the heart. *SIAM Journal on Applied mathematics*, 62(3):990–1018, 2002. [25](#), [26](#)
- T. Sochi. The flow of power law fluids in elastic networks and porous media. *Computer methods in biomechanics and biomedical engineering*, 19(3):324–329, 2016. [202](#)
- P.C. Sousa, J. Carneiro, R. Vaz, A. Cerejo, F.T. Pinho, M.A. Alves, and M.S.N. Oliveira. Shear viscosity and nonlinear behavior of whole blood under large amplitude oscillatory shear. *Biorheology*, 50(5-6):269–282, 2013. [202](#)

- R.L. Spilker, J.A. Feinstein, D.W. Parker, V.M. Reddy, and C.A. Taylor. Morphometry-based impedance boundary conditions for patient-specific modeling of blood flow in pulmonary arteries. *Annals of biomedical engineering*, 35(4):546–559, 2007. [120](#)
- H. Steffan, W. Brandstätter, G. Bachler, and R. Pucher. Comparison of newtonian and non-newtonian blood flow in stenotic vessels using numerical simulation. In *Biofluid Mechanics*, pages 479–485. Springer, 1990. [206](#), [209](#)
- D.A. Steinman, J.B. Thomas, H.M. Ladak, J.S. Milner, B.K. Rutt, and J.D. Spence. Reconstruction of carotid bifurcation hemodynamics and wall thickness using computational fluid dynamics and MRI. *Magnetic Resonance in Medicine*, 47(1):149–159, 2002. [6](#)
- M. Strocchi, C. Contarino, Q. Zhang, R. Bonmassari, and E.F. Toro. A global mathematical model for the simulation of stenoses and bypass placement in the human arterial system. *Applied Mathematics and Computation*, 300:21–39, 2017. [8](#)
- Z. Sun, S. Inaba, and F. Xiao. Boundary Variation Diminishing (BVD) reconstruction: A new approach to improve Godunov schemes. *Journal of Computational Physics*, 322:309–325, 2016. [62](#)
- S.P. Suter and R. Skalak. The history of Poiseuille’s law. *Annual Review of Fluid Mechanics*, 25(1):1–20, 1993. [19](#)
- L.G. Svensson, E.S. Crawford, K.R. Hess, J.S. Coselli, and H.J. Safi. Experience with 1509 patients undergoing thoracoabdominal aortic operations. *Journal of Vascular Surgery*, 17(2):357–370, 1993. [156](#)
- A. Swillens and P. Segers. Assessment of arterial pressure wave reflection: methodological considerations. *Artery Research*, 2(4):122–131, 2008. [156](#)
- T.L. Szabo. *Diagnostic ultrasound imaging: inside out*. Academic Press, 2004. [16](#)
- T. Takahashi. *Microcirculation in fractal branching networks*. Springer, 2014. [165](#)
- K. Takazawa, N. Tanaka, K. Takeda, F. Kurosu, and C. Ibukiyama. Underestimation of vasodilator effects of nitroglycerin by upper limb blood pressure. *Hypertension*, 26(3):520–523, 1995. [159](#)
- C.A. Taylor, T.J.R. Hughes, and C.K. Zarins. Finite element modeling of blood flow in arteries. *Computer methods in applied mechanics and engineering*, 158(1):155–196, 1998. [6](#), [167](#)
- M.G. Taylor. An experimental determination of the propagation of fluid oscillations in a tube with a visco-elastic wall; together with an analysis of the characteristics required in an electrical analogue. *Physics in medicine and biology*, 4(1):63, 1959. [9](#), [31](#)
- T.E. Tezduyar. Computation of moving boundaries and interfaces and stabilization parameters. *International Journal for Numerical Methods in Fluids*, 43(5):555–575, 2003. [6](#), [167](#)
- T.E. Tezduyar, S. Sathe, T. Cragin, B. Nanna, B.S. Conklin, J. Pausewang, and M. Schwaab. Modelling of fluid–structure interactions with the space–time finite elements: Arterial fluid mechanics. *International Journal for Numerical Methods in Fluids*, 54(6-8):901–922, 2007. [6](#), [167](#)
- W.C. Thacker. Some exact solutions to the nonlinear shallow-water wave equations. *Journal of Fluid Mechanics*, 107:499–508, 1981. [91](#)

- M. Thiriet. *Biology and mechanics of blood flows. Part II: Mechanics and medical aspects*. Springer Science & Business Media, 2007. [2](#)
- L.H. Thomas. Elliptic problems in linear difference equations over a network. *Watson Sci. Comput. Lab. Rept., Columbia University, New York*, 1, 1949. [50](#), [182](#)
- G.B. Thurston. Viscoelasticity of human blood. *Biophysical journal*, 12(9):1205–1217, 1972. [9](#), [201](#)
- G.B. Thurston. Elastic effects in pulsatile blood flow. *Microvascular research*, 9(2):145–157, 1975. [9](#), [201](#)
- F.-B. Tian, L. Zhu, P.-W. Fok, and X.-Y. Lu. Simulation of a pulsatile non-newtonian flow past a stenosed 2D artery with atherosclerosis. *Computers in biology and medicine*, 43(9):1098–1113, 2013. [201](#)
- E.F. Toro. *Shock-capturing methods for free-surface shallow flows*. Wiley, 2001. [64](#)
- E.F. Toro and A. Siviglia. Flow in collapsible tubes with discontinuous mechanical properties: mathematical model and exact solutions. *Communications in Computational Physics*, 13(02):361–385, 2013. [64](#)
- J.V. Tyberg, J.E. Davies, Z. Wang, W.A. Whitelaw, J.A. Flewitt, N.G. Shrive, D.P. Francis, A.D. Hughes, K.H. Parker, and J.-J. Wang. Wave intensity analysis and the development of the reservoir–wave approach. *Medical & biological engineering & computing*, 47(2):221–232, 2009. [7](#)
- D. Valdez-Jasso, M.A. Haider, H.T. Banks, D.B. Santana, Y.Z. Germán, R.L. Armentano, and M.S. Olufsen. Analysis of viscoelastic wall properties in ovine arteries. *IEEE transactions on biomedical engineering*, 56(2):210–219, 2009. [9](#), [31](#), [32](#), [33](#), [36](#), [38](#)
- D. Valdez-Jasso, D. Bia, Y. Zócalo, R.L. Armentano, M.A. Haider, and M.S. Olufsen. Linear and nonlinear viscoelastic modeling of aorta and carotid pressure–area dynamics under in vivo and ex vivo conditions. *Annals of biomedical engineering*, 39(5):1438–1456, 2011. [38](#)
- F.N. van de Vosse and M.E.H. van Dongen. *Cardiovascular Fluid Mechanics — Lecture notes . Faculty of Applied Physics, Faculty of Mechanical Engineering, Eindhoven University of Technology, Eindhoven, Netherlands*, 1998. [11](#)
- G.C. Van den Bos, N. Westerhof, and O.S. Randall. Pulse wave reflection: can it explain the differences between systemic and pulmonary pressure and flow waves? A study in dogs. *Circulation Research*, 51(4):479–485, 1982. [128](#)
- M. Van Dyke. *Perturbation methods in Fluid Mechanics*. *Applied mathematics and mechanics* (, 8, 1964. [18](#)
- C. Verdier. Review Article: Rheological Properties of Living Materials. From Cells to Tissues. *Journal of Theoretical Medicine*, 5(2):67–91, 2003. [9](#), [201](#)
- I.E. Vignon and C.A. Taylor. Outflow boundary conditions for one-dimensional finite element modeling of blood flow and pressure waves in arteries. *Wave Motion*, 39(4):361–374, 2004. [7](#), [110](#), [114](#)
- I.E. Vignon-Clementel, C.A. Figueroa, K.E. Jansen, and C.A. Taylor. Outflow boundary conditions for three-dimensional finite element modeling of blood flow and pressure in arteries. *Computer methods in applied mechanics and engineering*, 195(29):3776–3796, 2006. [7](#)

- I.E. Vignon-Clementel, A.L. Marsden, and J.A. Feinstein. A primer on computational simulation in congenital heart disease for the clinician. *Progress in Pediatric Cardiology*, 30(1):3–13, 2010. [6](#), [167](#), [201](#)
- L. Wang, B. Shi, and Z. Chai. A lattice boltzmann study of the asymmetry effect on the hemodynamics in stented fusiform aneurysms. *Computers & Mathematics with Applications*, 71(1):328–348, 2016a. [191](#)
- X.-F. Wang, J.-M. Fullana, and P.-Y. Lagrée. Verification and comparison of four numerical schemes for a 1D viscoelastic blood flow model. *Computer methods in biomechanics and biomedical engineering*, 18(15):1704–1725, 2015. [8](#), [23](#), [44](#), [45](#), [46](#), [47](#), [49](#), [50](#), [56](#), [68](#), [81](#), [99](#), [130](#), [168](#), [174](#), [206](#)
- X.-F. Wang, S. Nishi, M. Matsukawa, A.R. Ghigo, P.-Y. Lagrée, and J.-M. Fullana. Fluid friction and wall viscosity of the 1D blood flow model. *Journal of biomechanics*, 49(4):565–571, 2016b. [9](#), [24](#), [146](#), [204](#)
- Z. Wang, G. Li, and O. Delestre. Well-balanced finite difference weighted essentially non-oscillatory schemes for the blood flow model. *International Journal for Numerical Methods in Fluids*, 2016c. [26](#), [47](#), [79](#)
- S.M. Wartman, K. Woo, A. Yaeger, M. Sigman, S.G. Huang, S.W. Ham, V. Rowe, and F.A. Weaver. Outcomes after abdominal aortic aneurysm repair requiring a suprarenal cross-clamp. *Journal of vascular surgery*, 60(4):893–899, 2014. [156](#)
- S.M. Watanabe, P.J. Blanco, and R.A. Feijóo. Mathematical model of blood flow in an anatomically detailed arterial network of the arm. *ESAIM: Mathematical Modelling and Numerical Analysis*, 47(4):961–985, 2013. [8](#), [107](#)
- J.C. Weddell, J. Kwack, P.I. Imoukhuede, and A. Masud. Hemodynamic analysis in an idealized artery tree: differences in wall shear stress between Newtonian and non-Newtonian blood models. *PloS one*, 10(4):e0124575, 2015. [201](#), [213](#), [215](#)
- B.E. Westerhof, I. Guelen, N. Westerhof, J.M. Karemaker, and A. Avolio. Quantification of wave reflection in the human aorta from pressure alone: proof of principle. *Hypertension*, 48(4):595–601, 2006. [128](#), [156](#)
- N. Westerhof. *Analog Studies of Human Systemic Arterial Hemodynamics (PhD dissertation)*. PhD thesis, Philadelphia, PA: University of Pennsylvania, 1968. [12](#)
- N. Westerhof and A. Noordergraaf. Arterial viscoelasticity: a generalized model. Effect on input impedance and wave travel in the systematic tree. *Journal of Biomechanics*, 3(3):357–379, 1970. [9](#), [31](#)
- N. Westerhof and B.E. Westerhof. Waves and Windkessels reviewed. *Artery Research*, 2017. [7](#)
- N. Westerhof, F. Bosman, C.J. De Vries, and A. Noordergraaf. Analog studies of the human systemic arterial tree. *Journal of Biomechanics*, 2(2):121–43, 1969. [7](#)
- N. Westerhof, P.K. Sipkema, G.C. van Den Bos, and G. Elzinga. Forward and backward waves in the arterial system. *Cardiovascular research*, 6(6):648–656, 1972. [7](#), [97](#), [128](#), [156](#)
- S.Ø. Wille. Pulsatile pressure and flow in an arterial aneurysm simulated in a mathematical model. *Journal of biomedical engineering*, 3(2):153–158, 1981. [191](#)

- S.Ø. Wille and L. Walløe. Pulsatile pressure and flow in arterial stenoses simulated in a mathematical model. *Journal of biomedical engineering*, 3(1):17–24, 1981. [191](#)
- M. Willemet, V. Lacroix, and E. Marchandise. Inlet boundary conditions for blood flow simulations in truncated arterial networks. *Journal of biomechanics*, 44(5):897–903, 2011. [45](#)
- M. Willemet, V. Lacroix, and E. Marchandise. Validation of a 1D patient-specific model of the arterial hemodynamics in bypassed lower-limbs: simulations against in vivo measurements. *Medical engineering & physics*, 35(11):1573–1583, 2013. [8](#), [144](#)
- J.R. Womersley. XXIV. Oscillatory motion of a viscous liquid in a thin-walled elastic tube. I: The linear approximation for long waves. *The London, Edinburgh, and Dublin Philosophical Magazine and Journal of Science*, 46(373):199–221, 1955. [19](#), [168](#), [183](#)
- M.M. Wynn, C. Acher, E. Marks, T. Engelbert, and C.W. Acher. Postoperative renal failure in thoracoabdominal aortic aneurysm repair with simple cross-clamp technique and 4 C renal perfusion. *Journal of vascular surgery*, 61(3):611–622, 2015. [156](#)
- N. Xiao, J.D. Humphrey, and C.A. Figueroa. Multi-scale computational model of three-dimensional hemodynamics within a deformable full-body arterial network. *Journal of computational physics*, 244:22–40, 2013. [6](#), [7](#), [167](#)
- D. Xiu and S.J. Sherwin. Parametric uncertainty analysis of pulse wave propagation in a model of a human arterial network. *Journal of Computational Physics*, 226(2):1385–1407, 2007. [45](#)
- K.K. Yeleswarapu, M.V. Kameneva, K.R. Rajagopal, and J.F. Antaki. The flow of blood in tubes: theory and experiment. *Mechanics Research Communications*, 25(3):257–262, 1998. [201](#)
- F. Yilmaz, M.Y. Gundogdu, et al. A critical review on blood flow in large arteries; relevance to blood rheology, viscosity models, and physiologic conditions. *Korea-Australia Rheology Journal*, 20(4):197–211, 2008. [201](#)
- D.F. Young, N.R. Cholvin, and A.C. Roth. Pressure drop across artificially induced stenoses in the femoral arteries of dogs. *Circulation research*, 36(6):735–743, 1975. [196](#)
- M. Zagzoule and J.-P. Marc-Vergnes. A global mathematical model of the cerebral circulation in man. *Journal of biomechanics*, 19(12):1015–1022, 1986. [8](#)
- A. Zaman, N. Ali, and O.A. Bég. Numerical simulation of unsteady micropolar hemodynamics in a tapered catheterized artery with a combination of stenosis and aneurysm. *Medical & biological engineering & computing*, pages 1–14, 2015. [191](#)
- M. Zamir. On fractal properties of arterial trees. *Journal of theoretical biology*, 197(4):517–526, 1999. [116](#)
- M. Zamir. Arterial branching within the confines of fractal L-system formalism. *The Journal of general physiology*, 118(3):267–276, 2001. [157](#)
- M.T. Zundel, M. Pattyn, T.C. Chelimsky, and M.L. Riess. Arterial flow waveforms, vascular tone, and chronic fatigue: a case report. *Autonomic Neuroscience*, 190:58–60, 2015. [128](#), [142](#)